NUREG/CR-6389
BMI-2187

IPIRG-2 Task 1 – Pipe System Experiments with Circumferential Cracks in Straight-Pipe Locations

Final Report
September 1991 – November 1995

Manuscript Completed: June 1996
Date Published: February 1997

Prepared by
P. Scott, R. Olson, C. Marschall, D. Rudland,
R. Francini, R. Wolterman, A. Hopper, G. Wilkowski

Battelle
505 King Avenue
Columbus, OH 43201

M. Mayfield, NRC Project Manager

Prepared for
Division of Engineering Technology
Office of Nuclear Regulatory Research
U.S. Nuclear Regulatory Commission
Washington, DC 20555-0001
NRC Job Code D2060

ABSTRACT

This report presents the results from Task 1 of the Second International Piping Integrity Research Group (IPIRG-2) program. The rationale for and objective of Task 1 was to build on the results of the First IPIRG program by evaluating: (1) the fracture behavior of circumferentially cracked pipe subjected to more complex load histories, such as simulated seismic load histories, (2) cracks at geometric discontinuities, such as elbow girth welds, (3) smaller circumferential surface cracks, more typical of those considered in in-service flaw evaluations, subjected to dynamic, cyclic load histories, and (4) circumferential through-wall-cracked pipe subjected to dynamic, cyclic load histories. As a result of these Task 1 efforts, it was shown that: (1) the load-carrying capacity of a cracked pipe subjected to a simulated seismic load history is no worse than that of a cracked pipe subjected to the single-frequency excitation evaluated in IPIRG-1, (2) cracks at elbow girth welds can be adequately analyzed using methods previously developed for cracks in straight pipe, and (3) analysis methods previously developed and verified for large circumferential surface cracks and circumferential through-wall cracks work equally well for smaller cracks, even when subjected to more complex load histories.

DISCLAIMER

CONTENTS

CONTENTS

CONTENTS

CONTENTS

CONTENTS

Page

LIST OF FIGURES

CONTENTS

CONTENTS

CONTENTS

CONTENTS

CONTENTS

CONTENTS

CONTENTS

Page

CONTENTS

CONTENTS

CONTENTS

Page

CONTENTS

CONTENTS

CONTENTS

CONTENTS

Page

LIST OF TABLES

CONTENTS

CONTENTS

CONTENTS

CONTENTS

EXECUTIVE SUMMARY

This report presents the results from Task 1 of the Second International Piping Integrity Research Group (IPIRG-2) program. The IPIRG-2 program was an international group program managed by the U.S. Nuclear Regulatory Commission (U.S. NRC) and funded by a consortium of organizations from fifteen nations. The objective of the IPIRG-2 program was to extend the state-of-the-art in pipe fracture technology for assessing the integrity of flawed nuclear power plant piping. This was done by building on the results of the first IPIRG program (IPIRG-1) and other related programs.

During the past ten years, a number of pipe fracture programs have been conducted worldwide. Two of the more recent pipe fracture programs were the IPIRG-1 and Short Cracks in Piping and Piping Welds programs, both of which were conducted at Battelle-Columbus. The primary focus of the IPIRG-1 program was the investigation of the behavior of circumferentially flawed piping and piping systems subjected to high-rate, cyclic loadings typical of a seismic event. Whereas the focus of the IPIRG-1 program was on the load history, the focus of the Short Cracks in Piping and Piping Welds program was the evaluation of the behavior of shorter crack lengths, typical of the circumferential crack lengths considered in Leak-Before-Break (LBB) and in-service flaw evaluations.

Even though both the IPIRG-1 and Short Cracks programs extended the pipe fracture experimental database considerably, there were still a number of gaps in the database at the completion of these programs. The rationale for and specific objectives of the IPIRG-2 program were to fill some of these gaps. The identified gaps which were addressed as part of Task 1 of the IPIRG-2 program included:

- An evaluation of the fracture behavior of cracked piping subjected to a simulated seismic load history,
- An assessment of the American Society of Mechanical Engineers (ASME), R6, and other flaw evaluation criteria for the case where the piping system is subjected to different stress components, i.e., primary membrane (P_m), primary bending (P_b), thermal expansion (P_e), and seismic anchor motion (SAM) stresses,
- An evaluation of the case where the crack is close to a fitting, such as an elbow, instead of in straight pipe,
- An evaluation of smaller surface cracks, more typical of those considered in an in-service flaw evaluation, when subjected to a combination of inertial and displacement-controlled stresses, and
- An evaluation of the stability and fracture behavior of through-wall-cracked pipe subjected to combined inertial and displacement-controlled stresses.

In order to address these gaps in the experimental database, nine pipe fracture experiments were conducted as part of Task 1: two simulated seismic pipe system experiments, two elbow girth weld experiments, two short surface-cracked pipe experiments, and three short through-wall-cracked pipe experiments. Data from eight companion experiments from previous programs were available for comparison with the results from the Task 1 experiments. These companion experiments were similar to the nine Task 1 experiments,

except they involved either simpler load histories (quasi-static or single-frequency versus simulated seismic), simpler crack location geometries (straight pipe versus elbow girth weld cracks), or larger crack sizes.

In addition to the pipe experiments, there were a number of related activities which had to be undertaken before the questions (i.e., the gaps in the technology) identified above, which formed the basis for the formation of Task 1, could be addressed.

Before the first pipe-system experiment could be conducted, the IPIRG pipe loop facility had to be rebuilt because the pipe loop facility was damaged during the last IPIRG-1 pipe-system experiment. In addition, a new restraint system capable of holding the two halves of the pipe loop together in the event of a double-ended-guillotine-break (DEGB) had to be designed and constructed in order to reduce the possibility of damaging the facility again. Finally, the hydraulic system used to apply loads to the pipe had to be modified to permit longer duration simulated seismic experiments. Once the pipe loop facility was rebuilt, an uncracked pipe-system experiment was conducted in order to assess the response of the rebuilt pipe loop. As part of this uncracked pipe system experiment, the damping characteristics and first few natural frequencies of the rebuilt pipe loop were measured. It was found that the piping system response for the new pipe loop was consistent with that previously measured in IPIRG-1.

One of the major activities associated with the conduct of the simulated-seismic, pipe-system experiments was the design of a representative simulated-seismic load history to be applied to the pipe loop. The resultant load history was designed to be compatible with the U.S. NRC Standard Review Plan (SRP) 3.7.1 (Seismic Design Parameters), U.S. NRC Regulatory Guide 1.60 (Design Response Spectra for Seismic Design of Nuclear Power Plants), U.S. NRC Regulatory Guide 1.61 (Damping Values for Seismic Design of Nuclear Power Plants), and ASME Boiler and Pressure Vessel Code, Appendix N. The load history was derived from an analysis of a pressurized water reactor (PWR) nuclear plant on a soil foundation with many simplifying assumptions. The frequency content, spectral amplitudes, and resultant stresses were reasonably consistent with actual plant design.

Task 1 also involved a series of material characterization tests. For each Task 1 test specimen material, quasi-static and dynamic, tensile and fracture toughness tests were conducted as part of this effort, or as part of one of the previous pipe fracture programs conducted at Battelle. In addition, for a few selected materials, quasi-static and dynamic, cyclic, fracture toughness tests were conducted. The material properties generated as part of this and the other related programs were used in the subsequent analyses of the pipe experiments.

The analyses of these experiments (both Task 1 and companion experiments) was to have included an evaluation of maximum moment predictions as well as an assessment of the margins in a piping design as a consequence of using an elastic finite element analysis to predict cracked pipe applied stresses. A problem was encountered with the elastic finite element analyses of the pipe system experiments. Based on careful review of the experimental data, the primary restraint system incorporated into the test specimen for the pipe-system experiments influenced the behavior of the cracked test specimen. For the same experimental applied displacements (i.e., the same single-frequency excitation), the resultant experimental displacements and moments at the cracked test specimen were much higher for the case when the restraint system was in place when compared with the case when the restraint system was not in place. Finite element analyses, however, generally showed no such difference. Regardless of how the restraint system was modeled, the influence of the restraint system on the finite element analyses results was minimal. Only by reducing

Young's modulus by 12 percent for the entire pipe loop could the presence of the restraint system substantially alter the system response. The experimental data were carefully checked and found to be valid. Because the experimental material property data do not support a low elastic modulus, there were questions about the validity of the elastic stress analyses results for this single-frequency excitation experiment. By implication, there were questions about the validity of the elastic stress analyses for the other experiments which used the restraint device, i.e., the simulated-seismic, pipe-system experiments. As a result, such elastic stress calculations were deemed of questionable value, and as such were not performed. Consequently, it was not possible to address the issue of how the ASME Code, R6, and other flaw evaluation criteria handle the different stress components, i.e., primary membrane, primary bending, thermal expansion, or seismic anchor motion stresses when using uncracked pipe elastic stress analysis values.

The fracture prediction analyses involved comparing the experimental stresses with predictions based on existing fracture analysis methods for straight pipe. In this way, differences in pipe/crack dimensions and material property data between the Task 1 and companion experiments could be properly considered.

The results for all these efforts, i.e., pipe experiments, material characterization efforts, and analyses of experiments, are described in detail in the report that follows.

As a result of the Task 1 efforts, several important conclusions were made. The first four conclusions are related to the identified gaps in the technology discussed above which provided the rationale for the conduct of Task 1. The remaining conclusions were other major findings which naturally came about as a result of the efforts associated with Task 1.

- The load-carrying capacity of a circumferentially cracked pipe subjected to a simulated-seismic load history is no worse than the load-carrying capacity of a cracked pipe subjected to a single-frequency, cyclic load history. This conclusion should be qualified by saying that it may be an artifact of the specific simulated-seismic forcing function applied to the Task 1 experiments. Because the cycles prior to maximum load were primarily elastic for the particular simulated seismic history that was used, these experiments can probably be analyzed as if they were dynamic monotonic experiments. If some other simulated-seismic history were used, with a more gradual buildup of the large amplitude cycles, then the extent of cyclic degradation that occurs may be greater. Note, as part of one of the IPIRG-2 round-robin problems, four different but "equal" displacement time histories were created from the same peak-broadened acceleration response spectrum. The maximum moments induced in a linear finite element model of the IPIRG pipe system were similar (to within 20 percent) but the time, number, and buildup of the moment peaks were substantially different.

- The load-carrying capacity of circumferential cracks at geometric discontinuities, such as at the junction of an elbow to a straight pipe section, can be analyzed using methods previously developed for cracks in straight pipe sections.

- The analysis methods previously developed and verified for large surface cracks for which the plasticity is confined to the cracked section are appropriate for the analysis of smaller crack sizes for which plasticity may not be confined to the crack section. This conclusion is consistent with the findings of the Short Cracks in Piping Welds program. However, the results

from this program extended the findings from the Short Cracks program by generalizing this finding to the case of dynamic loadings.

- The previously developed circumferential through-wall-cracked pipe analyses, which have only been verified using quasi-static, monotonic pipe fracture data, work equally well for the case of a through-wall-cracked dynamic, cyclic pipe system experiment.

- The use of an idealized constant depth crack shape geometry assumed by such analysis methodologies as ASME Section XI, can result in a significant underprediction of the failure stresses for a situation where the crack is in a weld or the crack is irregular in shape. If real cracks are found in service, then additional inspection efforts may be warranted to further define the crack shape in order to avoid excess conservatism.

- For flaw evaluation purposes, the weld crown should not be included with the pipe wall thickness when making moment predictions to insure a conservative underprediction. (In reality, it is unlikely if it will be known if the flaw is centered in the weld or near the toe of the weld, where the weld crown height is less.) Furthermore, if the weld crown is ground off, then the results from Task 1 suggest that the analyses of the stainless steel weld experiments are still sufficiently conservative, but this may not be true for the carbon steel weld experiments. In hindsight, it might have been better to conduct the IPIRG experiments with the weld crown removed, since typically, for UT flaw sizing, the weld crown is ground off in service.

- The use of quasi-static stress-strain data and quasi-static toughness data results in the best predictions of the quasi-static experiments. The use of quasi-static stress-strain data and dynamic toughness data gives the best predictions for the dynamic experiments. Consequently, the development of dynamic stress-strain data is probably not necessary. (However, if the uncracked pipe is experiencing plastic strains, then the dynamic stress-strain curve may be needed.) It is of further note that for the ASME Code Case N-494-3 and R6 approaches, the differences in the predictions for the dynamic pipe-system experiments when using quasi-static and dynamic J-R curve data were relatively insignificant. Consequently, for these code approaches, one should be able to use quasi-static stress-strain and quasi-static J-R curve data.

- There appears to be a threshold for the effective stress ratio ($R_{effective}$) above which the effect of cyclic loading can be ignored. This threshold value of $R_{effective}$ may be material dependent, which is consistent with the laboratory specimen test results from Task 3 of this program. The material dependence of the threshold value of $R_{effective}$ has been attributed to the relative toughness of the material. The higher toughness materials require greater compressive loads (more negative stress ratios) to resharpen the crack tip and voids ahead of the crack after a tensile loading.

- For the ferritic materials evaluated in this program, a flow stress based on actual material property data (i.e., the average of yield and ultimate) agreed well with the ASME Code definition of flow stress of $2.4S_m$, where S_m is based on actual material data adhering to the spirit of the criteria specified in Article 2110 of Appendix III of the Section III Division 1 appendices of the 1989 Edition of the ASME Code, i.e., S_m(Actual). On the other hand, the flow stresses based on actual material data for the ferritic materials were up to 40 percent higher than the $2.4S_m$(Code) values. For the austenitic materials evaluated, a flow stress based on

actual material data is significantly less than the flow stress based on a $3S_m$(Actual) definition while the average of the yield and ultimate strength definition of flow stress was approximately 10 percent less than the $3S_m$(Code) definition. The S_m(Actual) term was introduced as a means for evaluating the technical basis of the ASME Code procedures by analyzing the pipe experiments as if the pipes used had the minimum properties defined in Section II of the ASME Code.

- For 16-inch nominal diameter pipe, and accounting for differences between the actual strength of the material and the Code specified strength parameter (i.e., S_m), the ASME Section XI Z-factors for austenitic weld and ferritic base metal and weld cracks each have an inherent degree of inaccuracy (i.e., conservatism) of approximately 1.4 to 1.5 when compared with the Dimensionless-Plastic-Zone-Parameter (DPZP) "best fit" Z-factors. This finding is contrary to what has been reported in the past where it was indicated that the degree of inaccuracy, or conservatism, associated with the ferritic criteria was much greater than that for the austenitic criteria. The differences in fracture ratios between the two criteria are more the result of differences in the relative strength factors between actual and Code tensile strength properties than they are the result of differences in the basic criteria of Z-factor formulations. The inherent degree of inaccuracy between the current Section XI Z-factors and the DPZP "best-fit" Z-factors increases with pipe diameter. The ASME Section XI Z-factors agree fairly closely with the DPZP Z-factors based on the 95-percent confidence level fits of the experimental data.

- The degree of inaccuracy, or conservatism, associated with the R6 Revision 3 Option 1 method is comparable with that for the ASME criteria, i.e., Appendix C for austenitic pipes, Appendix H for ferritic pipes, and Code Case N-494-3 for austenitic and ferritic pipes. Like the R6 approach, ASME Code Case N-494-3 is a FAD-based approach that allows for the use of actual yield and ultimate strength data instead of Code-specified strength parameters, i.e., S_m values. The analyses conducted in this effort for the R6 and Code Case N-494-3 methods used actual strength data and the procedures in the Windows version of the NRCPIPES computer code (Version 3.0).

ACKNOWLEDGMENTS

The IPIRG Program was an international group program coordinated by the U.S. Nuclear Regulatory Commission's Electrical, Materials, and Mechanical Engineering Branch of the Office of Nuclear Regulatory Research under Contract No. NRC-04-91-063 to Battelle. Mr. Michael Mayfield was the U.S. NRC program manager. Dr. Allen Hopper was the Battelle program manager.

The members of the IPIRG-2 Program and their representatives to the IPIRG Technical Advisory Group (TAG) were:

Bulgaria	
- CUAEPP	Mr. Y. Yanev
Canada	
- AECB(*)	Dr. B. Jarman(**), Mr. J. K. Pereira
- Ontario Hydro	Mr. M. Kozluk
Czech Republic	
- NRI	Dr. J. Zdárek, Dr. M. Brumovsky, Dr. P. Kadečka, Mr. J. Palyza
France	
- EDF(*)	Mr. C. Faidy(**), Mr. P. Le Delliou
- CEA	Ms. F. Gantenbein, Mr. E. Debec-Mathet
- Framatome	Dr. Ph. Gilles
Hungary	
- HAEC	Mr. A. Fehérvári
Italy	
- ANPA-DISP(*)	Dr. C. Maricchiolo(**)
Japan	
- CRIEPI(*)	Dr. K. Kashima(**), Mr. N. Miura
Lithuania	
- VATESI	Mr. P. Vaisnys
Republic of China	
- INER/AEC(*)	Dr. Li-Fu Lin(**)

(*) Contractual organization

(**) TAG representative

Republic of Korea	
- KINS(*)	Dr. J. B. Lee(**), Dr. Y. H. Choi
- SKKU	Dr. Y. J. Kim
Slovak Republic	
- VUJE	Dr. L. Kupca
- NRA	Dr. J. Misak
Sweden	
- SKI(*)	Dr. G. Hedner(**)
- SAQ	Dr. B. Brickstad
Switzerland	
- KKL(*)	Mr. R. Wanner(**)
- HSK	Dr. D. H. Njo
United Kingdom	
- Nuclear Electric(*)	Dr. T. C. Chivers(**), Dr. J. Darlastan
United States	
- U.S. NRC-RES(*)	Mr. M. Mayfield(**)
- U.S. NRC-NRR(*)	Mr. K. Wichman(**)
- EPRI(*)	Mr. S. Gosselin(**), Dr. Y. K. Tang

We would like to express our appreciation for the support and interest of the IPIRG members in this program.

We would also like to thank Ms. Nadine Blay and Ms. Francois Gantenbein of CEA for their suggestions and input into the linear-elastic stress analyses of the IPIRG pipe-system experiments. We would like to thank Mr. Jesus Hidalgo, a visiting scientist at Battelle from the Materials Engineering Branch of the Nuclear Safety and Safeguards National Commission in Mexico, who conducted a number of the fracture analyses discussed in this report. We would like to thank others at Battelle who have helped in these efforts. Technicians who have contributed include: Mr. J. Anthony, Mr. E. Blakesley, Mr. R. Gertler, Mr. P. Held, Mr. P. Mincer, Mr. M. Oliver, Mr. D. Rider, Mr. D. Shoemaker, and Mr. G. Wall. We also would like to recognize Mrs. V. Kreachbaum, Ms. Brenda Fuller, and Ms. Judy Ward for their assistance in preparing this report.

(*) Contractual organization

(**) TAG representative

NOMENCLATURE

1. SYMBOLS

a	Crack depth
a_{cl}	Crack depth at the crack centerline
a_{max}	Crack depth at the deepest location along the crack front
a_o	Original crack length
a_1	Crack depth referenced to the inside pipe surface for weld crack experiments
a_2	Crack depth referenced to the inside surface of the counterbore for weld crack experiments
â	Reduced thickness length in LBB.ENG analyses
b	Uncracked ligament length (w-a)
C	Circumferential
C_1	Statistically-based parameter from plastic-zone-size screening criteria
C_2	Coefficient in power-law J-R curve equation
c	Distance from neutral bending axis
D	Pipe diameter
D_i	Inside pipe diameter
D_m	Mean pipe diameter
D_o	Outside pipe diameter
d_{CB}	Depth of the counterbore
E	Elastic modulus
E′	$E/(1-\nu^2)$
E_N	Normalized electric potential used in through-wall crack expression
E_0	Baseline reference d-c EP reading for uncracked pipe adjusted to represent a reading taken with a probe spacing equal to the crack centerline d-c EP probe spacing

EP_c	Crack centerline electric potential accounting for any zero offsets
EP_N	Normalized electric potential used in surface-crack expression
$E_{0.25}$	Electric potential reading for a crack 25 percent of the pipe circumference in length
$E_{0.5}$	Electric potential reading for a/t equal to 0.5
f_1	Function from GE/EPRI J-estimation scheme for calculating elastic component of J
F_1	Elastic f-function in GE/EPRI method
G	Modulus of rigidity
H(a/t)	Function from SC.ENG1 and SC.ENG2 J-estimation schemes
H_B	Function from LBB.ENG2 J-estimation scheme
h_{wc}	Height of the weld crown
h_1, h_2, h_4	Functions in EPRI/GE J-estimation scheme
I	Area moment of inertia
I_B	Function from LBB.ENG2 J-estimation scheme
J	J-integral fracture parameter
J_{cyc}	J due to cyclic loading
J_e	Elastic component of J
J_i	J at crack initiation
J_M	Modified form of J
J_{mono}	J due to monotonic loading
J_p	Plastic component of J
J_R	Crack growth resistance
J_{2mm}	J at 2 mm of crack extension
k	Stiffness
K	LEFM stress intensity factor fracture parameter

K_I	Applied linear elastic stress intensity factor
K_{Ib}	Stress intensity fracture due to bending stresses
K_{Ic}	Material toughness expressed in terms of K
K_{Im}	Stress intensity factor due to membrane stresses
K_r	Ratio of K_I to $K_r(a)$ from R6 analysis
l	Total crack length of a surface planar flaw oriented in the plane normal to the pressure retaining surface for an ASME Section XI analysis
L	Length parameter in SC.TNP analyses
L_B	Function from LBB.ENG2 J-estimation scheme
L_r	Load ratio in R6 analysis
L_w	Length of weld in LBB.ENG analyses
M	Moment
m	Mass
m_1	Exponent in power law extrapolated J-R curve equation
M_L^c	Net-Section-Collapse moment for a circumferentially surface-cracked pipe used in SC.ENG1 and SC.ENG2 analyses
M_L^d	Net-Section-Collapse moment for an uncracked pipe with a reduced thickness, t_e, used in SC.ENG1 and SC.ENG2 analyses
M_{max}	Maximum moment
M_o	Limit moment for a cracked pipe under pure bending
n	Strain-hardening exponent in Ramberg-Osgood equation
P	Total failure stress
p	Pressure
P_b	Bending stress
P_e	Thermal expansion stress

Nomenclature

P_m	Membrane stress
P_{NSC}	Net-Section-Collapse predicted failure stress
R	Stress or load ratio, i.e., minimum stress (load)/maximum stress (load)
$R_{effective}$	Effective stress ratio for a pipe experiment accounting for the stress contribution due to internal pipe pressure
R_m	Mean pipe radius
S_m	ASME code design stress intensity
S_m(Actual)	S_m based on measured tensile properties
S_m(Code)	S_m based on ASME Section II Code properties
S_u	ASME Section II Part D ultimate strength
S_y	ASME Section II Part D yield strength
t	Time, or pipe thickness
t_1	Wall thickness of the pipe referenced to the inside pipe surface and excluding the weld crown height
t_2	Wall thickness of the pipe referenced to the inside surface of the counterbore and excluding the weld crown height
t_3	Wall thickness of the pipe referenced to the inside pipe surface and including the weld crown height
t_4	Wall thickness of the pipe referenced to the inside surface of the counterbore and including the weld crown height
t_e	Reduced wall thickness representation of cracked section in LBB.ENG2 method
V	Compliance function from GE/EPRI J-estimation scheme method
X	Dynamic response parameter
X_o	Static response parameter
W	Width of compact specimen
Z	Stress multipliers in Section XI to account for low toughness

α	Ramberg-Osgood parameter
β	Angle from bottom of pipe to neutral bending axis
δ	Displacement
δ_{cyc}	Incremental cyclic plastic displacement from a cyclic test
δ_i	Displacement at crack initiation from a monotonic test
Δa	Change in crack length or depth, i.e., crack growth
ϵ	Strain
ϵ_o	Ramberg-Osgood reference strain
ψ	Angle between the crack centerline and the location where the crack is deepest
ζ	Damping ratio (fraction of critical damping)
ν	Poisson's ratio
η	Geometric constant used in general analytical procedure where the plastic component of J is calculated using experimental load, displacement, and crack growth data
ϕ	Pipe rotation
σ	Stress
σ_b	Bending stress
$\sigma_{b_{analysis}}$	Predicted bending stress from the analysis
$\sigma_{B_{max}}$	Maximum bending stress
$\sigma_{B_{min}}$	Minimum bending stress
$\sigma_{B_{expt}}$	Experimental bending stress at maximum moment
σ_f	Flow stress
σ_m	Membrane stress due to internal pipe pressure
σ_o	Ramberg-Osgood reference stress
σ_u	Ultimate strength

σ_y	Yield strength
θ	Half crack angle
ω	Excitation frequency
ω_o	First natural frequency

2. ACRONYMS AND INITIALISMS

ACS	Aged cast stainless
A/D	Analog-to-Digital
AECB	Atomic Energy Control Board (Canada)
AISI	American Iron and Steel Institute
AIT	American Institute of Taiwan
ANPA-DISP	Agenzia Najionale per la Protezion dell'Ambiarte (Italy)
ASME	American Society of Mechanical Engineers
ASTM	American Society for Testing and Materials
BCD	Battelle-Columbus Division (U.S.A.)
BMI	Battelle Memorial Institute (U.S.A.)
BWR	Boiling Water Reactor
B&W	Babcock and Wilcox (U.S.A.)
CEA	Commissariat A L'Energie Atomique (France)
CEGB	Central Electric Generating Board, United Kingdom (now Nuclear Electric)
CMO	Crack-mouth opening
CMOD	Crack-mouth-opening displacement
COD	Crack-opening displacement
CRIEPI	Central Research Institute of Electric Power Industry (Japan)

CS	Carbon steel
CSBM	Carbon steel base metal
CSW	Carbon steel weld
C(T)	Compact (Tension)
CUAEPP	Commercial Use of Atomic Energy for Peaceful Purposes Agency (Bulgaria)
d-c	Direct current
d-c EP	Direct-current electric potential
DEGB	Double-ended guillotine break
DPZP	Dimensionless plastic-zone parameter
DP3II	Degraded Piping Program - Phase II
DSA	Dynamic strain aging
DW	Dead weight
Dyn	Dynamic
EDF	Electricité de France
EDM	Electric-discharge machine
EP	Normalized electric potential
EPFM	Elastic-plastic fracture mechanics
EPRI	Electric Power Research Institute (U.S.A.)
FAC	Failure assessment curve
FAD	Failure assessment diagram
FEA	Finite element analysis
FEM	Finite element method
FC	Fatigue crack
GE	General Electric (U.S.A.)

HAEC	Hungarian Atomic Energy Commission
HSK	Hauptabteilung für die Sicherheit der Kernanlagen (Swtizerland)
IHI	Ishikawajima-Harima Heavy Industries (Japan)
INER/AEC	Institute of Nuclear Energy Research/Atomic Energy Commission (Republic of China)
Int.	Intermediate (strain rate)
IPIRG	International Piping Integrity Research Group
IPIRG-1	First International Piping Integrity Research Group
IPIRG-2	Second International Piping Integrity Research Group
JAERI	Japanese Atomic Energy Research Institute
J-R	J-resistance (curve)
KfK	Kernfortschangszantran Karlsruhe (Germany)
KINS	Korea Institute of Nuclear Safety
KKL	Kernkraftwerk Leibstadt AG (Switzerland)
LBB	Leak-Before-Break
L-C	Orientation that indicates crack plane is normal to longitudinal axis (L) and crack growth direction is circumferential (C)
LVDT	Linear variable differential transformer
LWR	Light water reactor
MPA	Materialprüfungsanstalt (Germany)
MSS	Manufacturers' Standardization Society of the Valve and Fittings Industry
NDE	Nondestructive evaluation
NRA	Nuclear Regulatory Authority (Slovak Republic)
NRC	Nuclear Regulatory Commission (U.S.A.)
NRC-NRR	Nuclear Regulatory Commission - Office of Nuclear Reactor Regulation (U.S.A.)

NRC-RES	Nuclear Regulatory Commission - Office of Nuclear Reactor Research (U.S.A.)
NRI	Nuclear Research Institute (Czech Republic)
NSC	Net-Section-Collapse
NUPEC	Nuclear Power Engineering Test Center (Japan)
OBE	Operational Basis Earthquake
PIFRAC	PIping FRACture mechanics material property database
PSD	Power spectral density
PVP	Pressure Vessel and Piping
PWR	Pressurized Water Reactor
QS	Quasi-static
ROC-AEC	Republic of China - Atomic Energy Commission
RPV	Reactor Pressure Vessel
RT	Room temperature
SAM	Seismic anchor motion
SAW	Submerged-arc weld
SC	Surface crack
SEM	Scanning electron microscope
SEN(T)	Side Edge Notch (Tension)
SKI	Statens Kärnkraftinspektion (Swedish Nuclear Power Inspectorate)
SKKU	Sung Kyun Kwan University (Korea)
SMAW	Shielded-metal-arc weld
SMiRT	Structural Mechanics in Reactor Technology
SMN	Sharp machine notch
SMTS	Specified minimum tensile strength

SMYS	Specified minimum yield strength
SRP	Standard Review Plan
SS	Stainless steel
SSBM	Stainless steel base metal
SSE	Safe shutdown earthquake
SSW	Stainless steel weld
TAG	Technical Advisory Group
TIG	Tungsten-inert-gas weld
TWC	Through-wall crack
U.S.	United States
U.S. NRC	United States Nuclear Regulatory Commission
VATESI	State Nuclear Energy Safety Inspection of the Republic of Lithuania
VUJE	Vyskumny Ustav Jadravyeh Elektrarni (Nuclear Power Plant Research Institute of Slovakia)

PREVIOUS REPORTS IN SERIES

Reports from this Program

"Summary of Results from the IPIRG-2 Round-Robin Analyses," NUREG/CR-6337, BMI-2186, January 1996.

"The Effect of Cyclic and Dynamic Loads on Carbon Steel Pipe," NUREG/CR-6438, BMI-2188, February 1996.

"Design of the IPIRG-2 Simulated Seismic Forcing Function," NUREG/CR-6439, BMI-2189, February 1996.

"Deterministic and Probabilistic Evaluations for Uncertainty in Pipe Fracture Parameters in Leak-Before-Break and In-Service Flaw Evaluations," NUREG/CR-6443, BMI-2191, June 1996.

"Fracture Behavior of Circumferentially Surface-Cracked Elbows," NUREG/CR-6444, BMI-2192, December 1996.

"Development of a J-Estimation Scheme for Internal Circumferential and Axial Surface Cracks in Elbows," NUREG/CR-6445, BMI-2193, June 1996.

"The Effect of Cyclic and Dynamic Loading on the Fracture Resistance of Nuclear Piping Steels," NUREG/CR-6440, BMI-2190, December 1996.

Reports from the IPIRG-1 Program

"Evaluation and Refinement of Leak-Rate Estimation Models," NUREG/CR-5128, BMI-2164, Revision 1, June 1994.

"Loading Rate Effects on Strength and Fracture Toughness of Pipe Steels Used in Task 1 of the IPIRG Program," Topical Report, NUREG/CR-6098, BMI-2175, October 1993.

"Stability of Cracked Pipe Under Inertial Stresses," NUREG/CR-6233, BMI-2177, Volume 1, August 1994.

Previous Related Documents from NRC's Short Cracks in Piping and Piping Welds Program

"Short Cracks in Piping and Piping Welds," First Semiannual Report, NUREG/CR-4599, BMI-2173, Vol. 1, No. 1, March 1991.

"Short Cracks in Piping and Piping Welds," Second Semiannual Report, NUREG/CR-4599, BMI-2173, Vol. 1, No. 2, April 1992.

"Short Cracks in Piping and Piping Welds," Third Semiannual Report, NUREG/CR-4599, BMI-2173, Vol. 2, No. 1, September 1992.

"Short Cracks in Piping and Piping Welds," Fourth Semiannual Report, NUREG/CR-4599, BMI-2173, Vol. 2, No. 2, February 1993.

"Short Cracks in Piping and Piping Welds," Fifth Semiannual Report, NUREG/CR-4599, BMI-2173, Vol. 3, No. 1, October 1993.

"Short Cracks in Piping and Piping Welds," Sixth Semiannual Report, NUREG/CR-4599, BMI-2173, Vol. 3, No. 2, March 1994.

"Short Cracks in Piping and Piping Welds," Progress Report, NUREG/CR-4599, BMI-2173, Vol. 4, No. 1, April 1995.

"Assessment of Short Through-Wall Circumferential Cracks in Pipes," NUREG/CR-6235, BMI-2178, April 1995.

"Fracture Behavior of Short Circumferential Short-Surface-Cracked Pipe," NUREG/CR-6298, BMI-2183, November 1995.

"Fracture Evaluations of Fusion Line Cracks in Nuclear Pipe Bimetallic Welds," NUREG/CR-6297, BMI-2182, April 1995.

"Effect of Dynamic Strain Aging on the Strength and Toughness of Nuclear Ferritic Piping at LWR Temperatures," NUREG/CR-6226, BMI-2176, October 1994.

"Effects of Toughness Anisotropy and Combined Loading on Fracture Behavior of Ferritic Nuclear Pipe," NUREG/CR-6299, BMI-2184, April 1995.

"Refinement and Evaluation of Crack-Opening Analyses for Circumferential Through-Wall Cracks in Pipes," NUREG/CR-6300, April 1995.

"Probabilistic Pipe Fracture Evaluations for Leak-Rate Detection Applications," NUREG/CR-6004, BMI-2174, April 1995.

"Stainless Steel Submerged Arc Weld Fusion Line Toughness," NUREG/CR-6251, BMI-2180, April 1995.

"Validity Limits in J-Resistance Curve Determination: Volume 1: An Assessment of the J_M Parameter," NUREG/CR-6264, BMI-2181, Vol. 1, February 1995.

"Validity Limits in J-Resistance Curve Determinations: Volume 2: A Computational Approach to Ductile Crack Growth Under Large-Scale Yielding Condition," NUREG/CR-6264, BMI-2181, Vol. 2, February 1995.

Previous Related Documents from NRC's Degraded Piping Program - Phase I Reports

"The Development of a Plan for the Assessment of Degraded Nuclear Piping by Experimentation and Tearing Instability Fracture Mechanics Analysis," NUREG/CR-3142, Vols. 1 and 2, June 1983.

Previous Related Documents from NRC's Degraded Piping Program - Phase II Reports

"Degraded Piping Program - Phase II," Semiannual Report, NUREG/CR-4082, BMI-2120, Vol. 1, Oct. 1984.

"Degraded Piping Program - Phase II," Semiannual Report, NUREG/CR-4082, BMI-2120, Vol. 2, June 1985.

"Degraded Piping Program - Phase II," Semiannual Report, NUREG/CR-4082, BMI-2120, Vol. 3, March 1986.

"Degraded Piping Program - Phase II," Semiannual Report, NUREG/CR-4082, BMI-2120, Vol. 4, July 1986.

"Degraded Piping Program - Phase II," Semiannual Report, NUREG/CR-4082, BMI-2120, Vol. 5, Dec. 1986.

"Degraded Piping Program - Phase II," Semiannual Report, NUREG/CR-4082, BMI-2120, Vol. 6, April 1988.

"Degraded Piping Program - Phase II," Semiannual Report, NUREG/CR-4082, BMI-2120, Vol. 7, March 1989.

"Degraded Piping Program - Phase II," Semiannual Report, NUREG/CR-4082, BMI-2120, Vol. 8, March 1989.

"NRC Leak-Before-Break (LBB.NRC) Analysis Method for Circumferentially Through-Wall Cracked Pipes Under Axial Plus Bending Loads," Topical Report, NUREG/CR-4572, BMI-2134, March 1986.

"Elastic-Plastic Finite Element Analysis of Crack Growth in Large Compact Tension and Circumferentially Through-Wall-Cracked Pipe Specimen--Results of the First Battelle/NRC Analysis Round Robin," Topical Report, NUREG/CR-4573, BMI-2135, September 1986.

"An Experimental and Analytical Assessment of Circumferential Through-Wall Cracked Pipes Under Pure Bending," Topical Report, NUREG/CR-4574, BMI-2136, June 1986.

"Predictions of J-R Curves With Large Crack Growth From Small Specimen Data," Topical Report, NUREG/CR-4575, BMI-2137, September 1986.

"An Assessment of Circumferentially Complex-Cracked Pipe Subjected to Bending," Topical Report, NUREG/CR-4687, BMI-2142, September 1986.

"Analysis of Cracks in Stainless Steel TIG Welds," Topical Report, NUREG/CR-4806, BMI-2144, November 1986.

"Approximate Methods for Fracture Analyses of Through-Wall Cracked Pipes," Topical Report, NUREG/CR-4853, BMI-2145, January 1987.

"Assessment of Design Basis for Load-Carrying Capacity of Weld-Overlay Repair," Topical Report, NUREG/CR-4877, BMI-2150, February 1987.

"Analysis of Experiments on Stainless Steel Flux Welds," Topical Report, NUREG/CR-4878, BMI-2151, February 1987.

"Experimental and Analytical Assessment of Circumferentially Surface-Cracked Pipes Under Bending," Topical Report, NUREG/CR-4872, BMI-2149, April 1987.

Other Related Program Reports

"Validation of Analysis Methods for Assessing Flawed Piping Subjected to Dynamic Loading," NUREG/CR-6234, ANL-94/22, BMI-2178, August 1994.

1.0 INTRODUCTION

This report presents the results from Task 1 of the Second International Piping Integrity Research Group (IPIRG-2) program. The IPIRG-2 program is an international group program managed by the U.S. Nuclear Regulatory Commission (U.S. NRC) and funded by a consortium of organizations from 15 nations including: Bulgaria, Canada, Czech Republic, France, Hungary, Italy, Japan, Republic of Korea, Lithuania, Republic of China, Slovak Republic, Sweden, Switzerland, the United Kingdom, and the United States.

The objective of the program was to build on the results of the IPIRG-1 and other related programs by extending the state-of-the-art in pipe fracture technology through the development of data needed to verify engineering methods for assessing the integrity of nuclear power plant piping systems that contain defects. The IPIRG-2 program included five main tasks:

Task 1 - Pipe System Experiments with Flaws in Straight Pipe and Welds

Task 2 - Fracture of Flawed Fittings

Task 3 - Cyclic and Dynamic Load Effects on Fracture Toughness

Task 4 - Resolution of Issues From IPIRG-1 and Related Programs

Task 5 - Information Exchange Seminars and Workshops, and Program Management.

The scope of this report is to present the results from the experiments and analyses associated with Task 1 (Pipe System Experiments with Flaws in Straight Pipe and Welds). The rationale and objectives of this task are discussed after a brief review of experimental data which existed after the IPIRG-1 program.

1.1 Status of Experimental Database After IPIRG-1

During the past ten years, a number of pipe fracture experimental programs have been conducted worldwide. Some of the key programs include those conducted in Japan (Refs. 1.1 through 1.4), Germany (Refs. 1.5 through 1.12), Italy (Ref. 1.13), France (Refs. 1.14 and 1.15), and the United States (Refs. 1.16 through 1.25). In the United States, the key experimental piping programs have been the Piping Reliability Program (Refs. 1.16 and 1.17) jointly sponsored by the U.S. NRC and the Electric Power Research Institute (EPRI), the U.S. NRC sponsored Degraded Piping Program (Ref. 1.18), the U.S. NRC sponsored Short Cracks in Piping and Piping Welds Program (Refs. 1.19 through 1.21), and the First International Piping Integrity Research Group (IPIRG-1) Program (Refs. 1.22 through 1.24). As part of the Short Cracks Program, a database of pipe fracture experiments conducted worldwide was developed. This database, CIRCUMCK.WK1, includes the test conditions, test results, and material property data for over 700 circumferentially-cracked pipe fracture experiments. (Note, a companion axially-cracked pipe fracture database (AXIALCK.WK1) was also developed as part of the Short Cracks

program (Ref. 1.25) and a database of cracked elbow and tee experiments (ELBOWCK.WK1 and TEECK.WK1) were developed as part of Task 2 of the IPIRG-2 program.

At the beginning of the IPIRG-1 and Short Cracks programs, there were a number of pipe fracture technology issues which needed to be addressed. The primary focus of the IPIRG-1 program was an experimental task that investigated the behavior of circumferentially-cracked piping and piping systems subjected to high-rate, cyclic loadings typical of a seismic event. As part of the IPIRG-1 program, both separate effects straight pipe experiments (i.e., pure inertial and pure displacement-controlled loading experiments), and combined inertial and displacement-controlled loading pipe system experiments were conducted. The combined loading pipe system experiments were conducted in a pipe loop experimental facility specially designed and built for the IPIRG-1 program. The pipe system was an expansion loop with over 30 m (100 feet) of 16-inch nominal diameter pipe and five long radius elbows. The five cracked pipe system experiments conducted as part of the IPIRG-1 program evaluated five different materials using nominally the same loading history, i.e., an increasing amplitude sinusoidal waveform superimposed on a linear ramp. The excitation frequency for these pipe system experiments was approximately 85 to 90 percent of the first natural frequency of the piping system.

Whereas the primary focus on the IPIRG-1 program was on the loading history, the primary focus of Short Cracks in Piping and Piping Welds Program was to evaluate the fracture behavior of shorter crack lengths, more typical of the crack lengths considered in Leak-Before-Break (LBB) and in-service flaw evaluations. The nominal through-wall-crack length evaluated in the Degraded Piping and IPIRG-1 programs was 37-percent of the pipe circumference and the nominal surface-crack size evaluated in these programs was 50-percent of the pipe circumference in length and 66-percent of the pipe wall thickness in depth. For these crack sizes, most of the plasticity associated with the experiment was confined to the crack plane. The nominal through-wall-crack length for the Short Cracks program was in the range of 6- to 8-percent of the pipe circumference, typical of the crack lengths considered in LBB analyses for large diameter pipes, and the nominal surface crack size was 25-percent of the pipe circumference in length and 50-percent of the pipe wall thickness in depth, more typical of the crack sizes considered for in-service flaw evaluations. For these smaller crack sizes, significant plasticity occurs in the pipe remote from the crack, which must be accounted for in the analyses.

1.2 Rationale and Objective for Task 1

Even though both the IPIRG-1 and Short Cracks programs had extended the pipe fracture experimental database, there were still a number of gaps in the database at the completion of these programs. The rationale for and objective of the IPIRG-2 program was to fill some of these gaps. The identified gaps in the database which were addressed as part of Task 1 of the IPIRG-2 program included:

The fracture behavior of piping under simulated seismic loading conditions was evaluated. As alluded to earlier, the cracked-pipe-system experiments conducted previously as part of the IPIRG-1 program all involved a single-frequency excitation. In the IPIRG-2 program, experiments were conducted with a time simulated-seismic excitation.

The role of different stress components, i.e., primary membrane (P_m), primary bending (P_b), thermal expansion (P_e), inertial, and seismic anchor motion (SAM), was assessed for the American Society of Mechanical Engineers (ASME), R6, and other flaw evaluation criteria.

The case where a crack is close to a fitting, such as an elbow, instead of in straight pipe was also evaluated. In the programs previously discussed, the crack had always been located in a section of straight pipe or in a weld joining two sections of straight pipe. Locating the cracks in straight pipe facilitated the analyses. However, in actual plant situations, cracks often occur at the junction of a straight pipe section and a fitting due to the natural stress riser that exists at this type of geometric discontinuity.

The fracture behavior of shorter crack sizes was considered. The crack sizes in the pipe system experiments conducted during IPIRG-1 were large enough that the plasticity was confined to the crack section. Shorter crack lengths were considered as part of the Short Cracks program, but the loading condition for those experiments was quasi-static four-point bending or combined pressure and quasi-static four-point bending. In addition, as part of the IPIRG-1 program, it was found that the elastic stress margin, which is the ratio of the elastically calculated stress from an elastic finite element analysis to the experimental stress, was close to 1.0. This value was significantly less than the value observed from the uncracked pipe experiments conducted as part of the joint EPRI/NRC Piping Reliability Program (Refs. 1.16 and 1.17). It was thought at the time of the completion of the IPIRG-1 program that if shorter crack sizes were evaluated in the IPIRG-2 program, then the elastic stress margins would increase due to the additional plasticity which would occur remote from the crack section for the shorter crack experiments.

The stability and fracture behavior of through-wall-cracked pipe subjected to combined inertial and displacement-controlled stresses such as exist in a pipe system was evaluated. Each of the cracked pipe-system experiments conducted during IPIRG-1 evaluated surface-cracked pipe specimens. No through-wall-cracked pipe system data existed. Since the United States LBB criteria embodied in Standard Review Plan (SRP) 3.6.3 is based on a circumferential through-wall crack analysis, it was decided to conduct a circumferential through-wall-cracked pipe-system experiment to help further validate those criteria.

1.3 Scope and Structure of Task 1

In order to address the gaps in the experimental database described above, the experimental test matrix shown in Table 1.1 for Task 1 of the IPIRG-2 program was developed. The Task 1 test matrix included nine experiments consisting of five pipe system experiments, three companion quasi-static bending experiments, and one dynamic four-point bend experiment on a smaller diameter pipe specimen. The first two experiments listed in Table 1.1 (Experiments 1-1 and 1-2) were simulated seismic pipe system experiments for which companion single-frequency pipe system and companion quasi-static four-point bending experiments using the same test materials and flaw geometries had already been conducted. By comparing the results from the two simulated-seismic experiments with the results from the companion single-frequency and quasi-static four-point bending experiments, one can determine what effect a more complex load history with multiple-frequency content has on the fracture behavior of these materials.

Table 1.1 Test matrix for IPIRG-2 Task 1 experiments

Experiment No.	Crack Geometry[1]	Material[2]	Crack Location	Loading History
1-1	SC	SSBM	Straight Pipe Base Metal	Simulated Seismic
1-2	SC	CSBM	Straight Pipe Base Metal	Simulated Seismic
1-3	SC	CSW	Elbow-to-Pipe Girth Weld	Single Frequency
1-4	SC	CSW	Elbow-to-Pipe Girth Weld	Quasi-Static Monotonic Bend
1-5	SC	SSW	Pipe-to-Pipe Girth Weld	Single Frequency
1-6	SC	SSW	Pipe-to-Pipe Girth Weld	Quasi-Static Monotonic Bend
1-7	TWC	CSBM	Straight Pipe Base Metal	Simulated Seismic
1-8	TWC	CSBM	Straight Pipe Base Metal	Quasi-Static Monotonic Bend
1-9[3]	TWC	CSBM	Straight Pipe Base Metal	Dynamic Monotonic Bend

(1) SC = Surface crack; TWC = through-wall crack.
(2) SSBM = Stainless steel base metal; CSBM = carbon steel base metal; CSW = carbon steel weld; SSW = stainless steel weld.
(3) 6-inch nominal diameter pipe test; all other tests were on 16-inch nominal diameter pipe.

The two materials evaluated in these experiments were a stainless steel base metal (Experiment 1-1) and a carbon steel base metal (Experiment 1-2).

The second set of experiments listed in Table 1.1 (Experiments 1-3 and 1-4) were experiments for which the crack was located in a girth weld at the junction of a straight pipe section and a long radius elbow. The bulk of the existing data in the circumferentially cracked-pipe fracture database, CIRCUMCK.WK1, were developed for the case of cracks in straight pipe sections or for the case of cracks in welds joining two sections of straight pipe. Relative to cracks in straight pipe, little has been done to study the problem of cracks in elbows or other fittings. This represents a significant gap in the experimental database because field experience suggests that cracks in and adjacent to fittings are a potential concern. In Task 2 of this program, the issue of cracks in elbows were examined. The two Task 1 elbow-to-pipe girth weld experiments (Experiments 1-3 and 1-4) examined the effect of cracks in the weld joining an elbow to a straight pipe. The weld procedure used for these welds was the same Babcock and Wilcox (B&W) carbon steel submerged-arc weld (SAW) procedure used in the straight pipe, pipe system experiment in IPIRG-1 (Experiment 1.3-4) and in a straight pipe quasi-static four-point bend experiment conducted as part of the Degraded Piping Program (Experiment 4141-8). Experiment 1-3 was a single-frequency pipe-system experiment. The forcing function used in this experiment was similar to the one used to excite the pipe system during the three stainless steel pipe system experiments conducted as part of IPIRG-1. Experiment 1-4 was a quasi-static bend experiment. The load frame used to apply the quasi-static bending loads for this experiment was the same load frame used in the quasi-static elbow experiments conducted as part of Task 2 of the IPIRG-2 program.

The third set of experiments listed in Table 1.1 (Experiments 1-5 and 1-6) were short surface crack experiments in which the crack was located in the center of a stainless steel submerged-arc weld (SAW). The weld procedure used to fabricate these welds was the same weld procedure used in the Degraded

Piping and IPIRG-1 programs. The crack size evaluated in these experiments was 25-percent of the pipe circumference in length and 50-percent of the pipe wall thickness in depth. This was the same nominal surface-crack geometry used in the quasi-static, surface-cracked pipe experiments conducted during the Short Cracks in Piping and Piping Welds program. This crack size is more representative of the crack size considered in an in-service flaw evaluation than the larger crack sizes used in the Degraded Piping and IPIRG-1 programs.

The final set of experiments listed in Table 1.1 (Experiments 1-7, 1-8, and 1-9) were short circumferential through-wall-cracked pipe experiments. Each of the prior pipe system experiments conducted as part of the IPIRG-1 and IPIRG-2 programs evaluated the case of an internal circumferential surface crack. Such experiments were pertinent for assessing the in-service flaw evaluation criteria and some non-U.S. LBB criteria. However, since the United States LBB criteria, as spelled out in the U.S. NRC Draft Standard Review Plan (SRP) 3.6.3, is based on a circumferential through-wall crack, it was deemed necessary to conduct a set of experiments with a circumferential through-wall crack. Furthermore, since the Draft SRP 3.6.3 considers a relatively short through-wall crack, the crack size chosen for these experiments was the shortest crack size that could be tested in the IPIRG pipe loop experimental facility without introducing significant plasticity remote from the test section.

Prior to the conduct of the nine pipe experiments listed in Table 1.1, the pipe system experimental facility had to be refurbished. During the last pipe system experiment conducted as part of the IPIRG-1 program (Experiment 1.3-7), a failure of the restraint system occurred after the pipe test specimen severed into two pieces. Significant damage was done to the experimental facility as a result of this failure. Prior to the conduct of the first IPIRG-2 experiment, the damaged experimental facility had to be reconstructed, a new restraint system capable of holding the two halves of the pipe loop together in the event of a double-ended-guillotine-break (DEGB) had to be designed and constructed, and additional accumulator capacity had to be incorporated into the hydraulic system to accommodate the longer duration simulated seismic pipe system experiments. Details of each of these support activities will be discussed during the course of this report, in addition to the discussion of the experiments.

1.4 References

1.1 "Technical Report on the Piping Reliability Proving Tests at the Japan Atomic Energy Research Institute," Report JAERI-M-93-076, March 1993.

1.2 Shibata, K., and others, "Ductile Fracture Behavior of Circumferentially Cracked Type 304 Stainless Steel Piping Under Bending Loads," *Nuclear Engineering and Design*, Vol. 94, pp 221-231, 1986.

1.3 "Proving Test on the Integrity of Carbon Steel Piping in LWRs," Summary NUPEC Report, 1986.

1.4 Yagawa, G., and others, "Research Activities on Fracture Mechanics for Nuclear Piping in Japan," *Nuclear Engineering and Design*, Vol. 98, pp 231-241, 1987.

1.5 Stoppler, W., and others, "Crack Behavior of Piping Under Internal Pressure and Simultaneous External Bending Moment," *Nuclear Engineering and Design*, Vol. 112, pp 173-182, 1989.

1.6 Kussmoud, K., and others, "Research Project 1500 - 279 Phenomenological Pipe and Vessel Burst Tests," MPA Final Report, Contract No. 8180 00 000, Nov. 1989.

1.7 Sturm, D., and others, "The Behavior of Dynamically Loaded Pipes with Circumferential Flaws Under Internal Pressure and External Bending Loads," *Nuclear Engineering and Design*, Vol. 96, pp 99-113, 1986.

1.8 Grüter, L., and others, "Crack Resistance Properties of Through-Cracks in Austenitic Straight Pipes (DN700) Under Bending," *Nuclear Engineering and Design*, Vol. 108, pp 447-456, 1988.

1.9 Azodi, D., and others, "Fracture Mechanics Evaluations of Precracked Cylinderical Vessels Subjected to Limit Load Conditions," SMiRT-12, Paper G04/2, August 1993.

1.10 Julisch, P., and others, "Exclusion of Rupture for Welded Piping Systems of Power Stations by Component Tests and Failure Approaches," SMiRT-12, Paper GF09/2, August 1993.

1.11 Stoppler, W., and others, "Crack Growth and Fracture Behavior of Pipes with Circumferential Defects Under Internal Pressure and Superimposed Alternating Bending Moment Load," 18th MPA Seminar, Vol. 1, Paper No. 13, Oct. 1992.

1.12 Schulze, H., and others, "Fracture Mechanics Analysis of the Initiation and Propagation of Circumferential and Longitudinal Cracks in Straight Pipes and Pipe Bends," *Nuclear Engineering and Design*, Vol. 58, pp 19-31, 1980.

1.13 Milella, P., "Outline of Nuclear Piping Research Conducted in Italy," *Nuclear Engineering and Design*, Vol. 98, pp 210-229, 1987.

1.14 Moulin, D., and others, "Crack Initiation and Experimental Determination of J in Bending for Elbows and Pipes of Austenitic Steel," PVP Vol. 165, pp 89-94, July 1989.

1.15 Garcia, J., and others, "Evaluation of Critical Sizes of Part-Through Cracks on 3-Inch Austenitic Stainless Steel Piping," SMiRT-8, Vol. G, pp 201-208, 1985.

1.16 Tang, H., and others, "Experimental Investigation of High Energy Pipe Leak and Rupture Phenomena," ASME Special Publication PVP Vol. 98-8, *Fracture, Fatigue, and Advanced Mechanics*, 1985.

1.17 "Piping and Fitting Dynamic Reliability Program - Project Summary, Vol. 1," EPRI TR-102792, Vols. 1-5, 1995.

1.18 Wilkowski, G., and others, "Degraded Piping Program - Phase II: Summary of Technical Results and Their Significance to Leak-Before-Break and In-Service Flaw Acceptance Criteria - March 1984 - January 1989," NUREG/CR-4082 Vol. 8, March 1989.

1.19 Brust, F., and others, "Assessment of Short Through-Wall Circumferential Cracks in Pipes," NUREG/CR-6235, April 1995.

1.20 Krishnaswamy, P., and others, "Fracture Behavior of Short Circumferentially Surface-Cracked Pipe," NUREG/CR-6298, November 1995.

1.21 Scott, P., and others, "Fracture Evaluations of Fusion Line Cracks in Nuclear Pipe Bimetallic Welds," NUREG/CR-6297, April 1995.

1.22 Scott, P., and others, "Stability of Cracked Pipe Under Inertial Stresses," NUREG/CR-6233, Vol. 1, August 1994.

1.23 Scott, P., and others, "The Effect of Dynamic and Cyclic Loading During Ductile Tearing on Circumferentially Cracked Pipe: Experimental Results," PVP Vol. 280, pp 207-220, June 1994.

1.24 Scott, P., and others, "The IPIRG-1 Pipe System Fracture Tests: Experimental Results," PVP Vol. 280, pp 135-151, June 1994.

1.25 Wilkowski, G. M., and others, "Short Cracks in Piping and Piping Welds," Seventh program Report: March 1993 - December 1994, NUREG/CR-4899, Vol. 4, No. 1, January 1995.

2.0 MATERIAL CHARACTERIZATION

In this section, the results of the material characterization efforts for the Task 1 materials are discussed. The discussion begins with a description of the materials selected for use as test specimens and materials used in the construction of the pipe loop. Next, the results of the tensile (both quasi-static and dynamic), fracture toughness (both quasi-static and dynamic), and dynamic modulus tests are presented. The section concludes with a discussion of the results. Further details of these material characterization efforts are presented in Reference 2.1.

2.1 Material Selection

First, the materials selected for test specimens and for the fabrication of the piping loop are described.

2.1.1 Test Specimen Materials

Seven different materials were evaluated for the five pipe-system experiments and the four 4-point bend experiments conducted as part of Task 1 (see Table 2.1). (The material used for constructing the pipe loop was ASTM A710, Grade A, Class 3 steel. Information regarding this material is provided in the next section, Piping Loop Materials.) The seven materials chosen for the cracked-pipe experiments included three A106 Grade B carbon steel pipes, two heats of an SA-358 Type 304 stainless steel pipe, and submerged-arc welds in both the A106B and Type 304 materials. These materials were chosen to provide a range of fracture toughness values typical of nuclear power plant piping. In addition, test specimens were prepared from 25.4-mm (1-inch) thick plate materials containing a submerged-arc, single-Vee butt weld prepared using procedures similar to those used in the submerged-arc welding of the pipes. As is shown in Table 2.1, these plate welds included one for carbon steel and two for Type 304 stainless steels.

The stainless steel and carbon steel base metals were nuclear grade materials obtained from canceled nuclear plants. The welding employed submerged-arc welding (SAW) procedures obtained from nuclear plant vendors in the United States. Each of these materials (base metals and welds) had been characterized at quasi-static loading rates as part of the Degraded Piping program (Ref. 2.2), and at dynamic loading rates as part of the IPIRG-1 program (Ref. 2.1). An additional carbon-steel weld (DP2-F55W) in 25.4-mm (1-inch) thick plate material was characterized in this program. The stainless steels have a very high toughness and were expected to reach limit load conditions during the pipe fracture experiments. The carbon steel materials have toughness values near the lower bound from the ASME Code, and their failure was expected to fall in the elastic-plastic fracture mechanics (EPFM) regime.

The two carbon steel welds discussed in this report also had unusually low fracture toughness values. In fact, the J-resistance (J-R) curve for one of these welds, namely, Pipe Weld DP2-F29W, formed the basis for the lower bound J-R curve incorporated into Section XI IWB-3650 of the ASME Code. The stainless steel pipe weld discussed in this report, namely, DP2-A8W, had a toughness value close to the lower bound toughness value used in Section XI IWB-3640 for submerged-arc welds. The two stainless steel plate welds discussed herein were slightly tougher than the pipe weld discussed in this report, namely, DP2-A8W, which had a toughness value close to the lower bound toughness value used in Section XI

Table 2.1 Materials used in IPIRG-2 Task 1 pipe experiments and companion experiments conducted during the Degraded Piping (Ref. 2.2), IPIRG-1 (Ref. 2.3), or a Battelle/EPRI (Ref. 2.4) program

Experiment No.	Material	Identification No.	Pipe Dimensions	
			Schedule	Nominal Diameter, inch
1.3-1	ASTM A710 Grade A, Class 3, low-carbon precipitation hardening steel pipe	IP-F3	100	16
-	ASTM A710 Grade A, Class 3, low-carbon precipitation hardening steel pipe	IP-F5	100	16
4112-8, 1.3-2, 1-2	ASTM A106 Grade B carbon steel pipe	DP2-F29	100	16
1-7, 1-8	ASTM A106 Grade B carbon steel pipe	DP2-F23	140	16
1-9	ASTM A106 Grade B carbon steel pipe	DP2-F22	80	6
EPRI 13S	ASTM A358 Type 304 stainless steel pipe	DP2-A8	100	16
1-1	ASTM A358 Type 304 stainless steel pipe	DP2-A8I	100	16
1.3-3	ASTM A358 Type 304 stainless steel pipe	DP2-A8II	100	16
4141-8, 1.3-4, 1-3, 1-4	Submerged-arc weld in ASTM A106 Grade B carbon steel pipe	DP2-F29W	100	16
N.A.[a]	Submerged-arc weld in carbon steel plate	DP2-F55W	25.4-mm (1 inch) plate material	
N.A.[a]	Submerged-arc weld in carbon steel plate	DP2-F40W	25.4-mm (1-inch) plate material	
4141-4, 1.3-5, 1-5, 1-6	Submerged-arc weld in ASTM A358 Type 304 stainless steel pipe	DP2-A8W	100	16
N.A.	Submerged-arc weld in Type 304 stainless steel plate	DP2-A45W1	25.4-mm (1-inch) plate material	
N.A.	Submerged-arc weld in Type 304 stainless steel plate	DP2-A45W2	25.4-mm (1-inch) plate material	

(a) Not applicable.

IWB-3640 for submerged-arc welds. The two stainless steel plate welds discussed herein were slightly tougher than the pipe weld.

Each of these materials was selected, in part, because a companion quasi-static pipe fracture experiment had been conducted previously as part of the Degraded Piping Program (Ref. 2.2) or a previous EPRI program conducted at Battelle (Ref. 2.4).

2.1.2 Piping Loop Materials

Two different materials were used in the fabrication of the pipe loop, one for the straight sections and another for the elbows. Both materials were used in 16-inch diameter Schedule 100 (26.2 mm [1.03 inch] thick) and Schedule 160 (40.4 mm [1.59 inch] thick) nominal sizes. The straight pipe sections, manufactured by Cameron Iron Works of Houston, Texas, are seamless extrusions of ASTM A710, Grade A, Class 3, low-carbon, precipitation-hardening alloy steel. This steel is required to have a yield strength of at least 515 MPa (75 ksi) and a tensile strength of at least 585 MPa (85 ksi) at ambient temperature. The elbows, which were fabricated by Flo-Bend Incorporated of Tulsa, Oklahoma, have a material designation WPHY-65, which is a designation of the Manufacturers Standardization Society of the Valve and Fitting Industry, Inc., in specification MSS SP-75. These carbon steel elbows were heat treated by quenching and tempering and are required to have a yield strength of at least 448 MPa (65 ksi) and a tensile strength of at least 531 MPa (77 ksi) at ambient temperature.

Both materials were chosen for their strength and weldability. To use the pipe loop for multiple experiments, materials were needed with sufficiently high yield strengths to preclude yielding remote from the cracked section. If yielding did occur remote from the crack, energy supplied by the hydraulic actuator used to shake the pipe would have been absorbed at those locations so that there would be less energy available to drive the crack. If this energy absorption should occur, larger (i.e., more costly) servo-hydraulic equipment would have been required to conduct these experiments.

It should be noted that the pipe loop was partially reconstructed between the IPIRG-1 and IPIRG-2 programs. Specifically, three of the five elbows and some of the Schedule 100 straight-pipe sections were replaced. This report contains material characterization data for the straight pipes and elbows used in both the original loop and the partially rebuilt loop. The original pipe loop is identified as Loop No. 1 in this report and the partially reconstructed pipe loop as Loop No. 2.

2.2 Tensile Test Results

Summary graphs and tables of tensile test results are presented in this section. Table 5.7 in Section 5.0 provides the Ramberg-Osgood coefficients derived from the graphs of engineering stress versus engineering strain that are included in this section. The Ramberg-Osgood equation is commonly written as:

$$\epsilon/\epsilon_o = \sigma/\sigma_o + \alpha(\sigma/\sigma_o)^n \qquad (2\text{-}1)$$

where σ is stress, σ_o is a reference stress (sometimes yield stress or sometimes flow stress is used), ϵ is strain, and ϵ_o is a reference strain equal to σ_o/E, where E is Young's modulus. This expression will produce a straight line having a slope of n and an intercept of log α if log $(\epsilon/\epsilon_o - \sigma/\sigma_o)$ is plotted against log (σ/σ_o). The Ramberg-Osgood equation is used by many fracture analysts to fit a mathematical expression to the stress-strain data.

The procedures used in collecting the necessary stress-strain data at dynamic rates of loading for these tensile tests are provided in detail in Reference 2.1.

2.2.1 A106 Grade B Carbon Steel

2.2.1.1 Pipe DP2-F29

Tensile specimens were machined from a section of the ASTM A106 Grade B carbon steel pipe material (DP2-F29) and subjected to quasi-static-loading rate tests at room temperature, 149 C (300 F), and 288 C (550 F), and to dynamic-loading rate tests at 288 C (550 F). All specimens were machined such that the tensile axis was parallel with the pipe axis. The results of those tests are summarized in Table 2.2 and Figure 2.1. Notice in Figure 2.1 that the actual quasi-static yield strength at room temperature was approximately 114 percent of the ASME Section II Part D specified minimum yield strength (SMYS), and the actual quasi-static tensile strength was approximately 125 percent of the ASME Section II Part D specified minimum tensile strength (SMTS). The elevation of the tensile strength at the higher temperatures in the quasi-static tests and the lowering of the strength at 288 C (550 F) with increasing strain rate are indications of dynamic strain aging (DSA) sensitivity (Refs. 2.5 to 2.7). Figure 2.2 shows engineering stress-strain curves from tensile tests for this carbon steel at 288 C (550 F) for three different strain rates. This steel exhibited pronounced serrations on the stress-strain curves at the intermediate rate which is another indication of DSA.

Figure 2.3 shows the variation of strength and ductility with strain rate for this carbon steel tested at 288 C (550 F). As was noted earlier, the ultimate strength dropped significantly with increasing strain rate. However, the yield strength and ductility were relatively unaffected by increased strain rate.

Table 2.2 Tensile properties of ASTM A106 Grade B carbon steel pipe (DP2-F29)

Spec. Ident. No.	Temperature, C	Temperature, F	Strain Rate, s^{-1}	0.2-Percent Offset Yield Strength, MPa	0.2-Percent Offset Yield Strength, ksi	Ultimate Tensile Strength, MPa	Ultimate Tensile Strength, ksi	Elongation, Percent in 25.4 mm (1.0 inch)
F29-1[a]	22	72	$2x10^{-4}$	277	40.2	524	76.0	29.6
F29-2[a]	22	72	$2x10^{-4}$	276	40.0	513	74.4	29.6
F29-3[a]	149	300	$2x10^{-4}$	252	36.6	610	88.5	18.1
F29-4[a]	149	300	$2x10^{-4}$	251	36.4	596	86.4	19.1
F29-5[a]	288	550	$2x10^{-4}$	241	34.9	618	89.7	24.0
F29-6[a]	288	550	$2x10^{-4}$	234	33.9	601	87.2	24.0
F-29-1	288	550	$2.6x10^{-2}$	240	34.8	546	79.2	--
F-29-2	288	550	$2.6x10^{-2}$	236	34.2	554	80.4	--
F29-101	288	550	1	235[b]	34.1	503	72.9	19.6
F29-103	288	550	1	230[b]	33.3	511	74.1	23.0
F-29-102	288	550	10	234[b]	34.0	443	64.2	24.1
F-29-104	288	550	10	228[b]	33.0	435	63.1	19.6
SA-106 Gr. B	22	72	QS[c]	241[d]	35.0[d]	414[e]	60.0[e]	--
SA-106 Gr. B	288	550	QS[c]	187[f]	27.1[f]	414[g]	60.0[g]	--

(a) Round-bar, threaded-end specimens; all others were flat pin-loaded specimens.
(b) Approximate value only, due to uncertainties in stress-strain curves at small strains.
(c) Quasi-static.
(d) S_y at 22 C (72 F) from ASME Section II Part D.
(e) S_u at 22 C (72 F) from ASME Section II Part D.
(f) S_y at 288 C (550 F) from ASME Section II Part D.
(g) S_u at 288 C (550 F) from ASME Section II Part D.

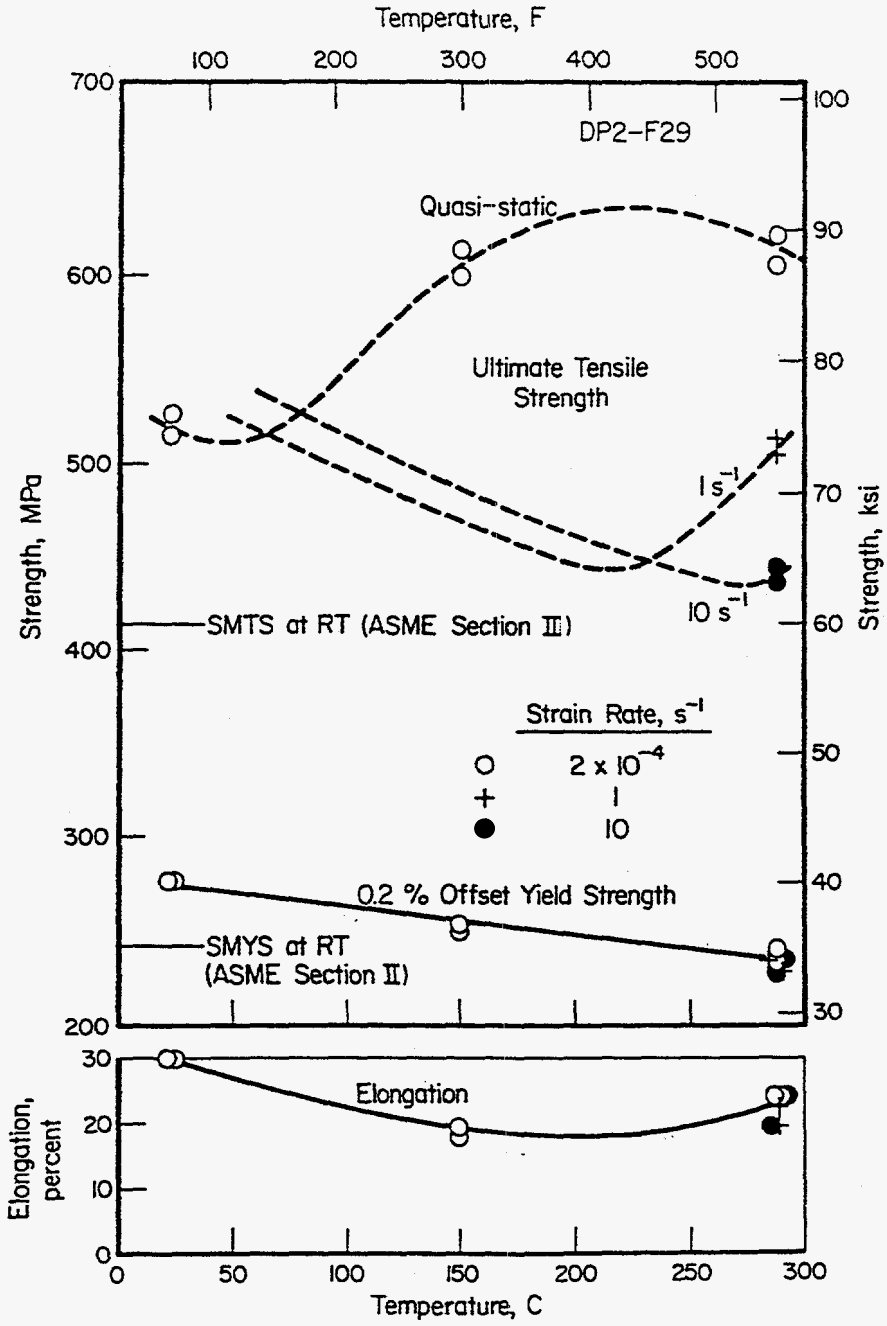

Figure 2.1 Tensile properties versus temperature for A106 Grade B carbon steel pipe (DP2-F29)

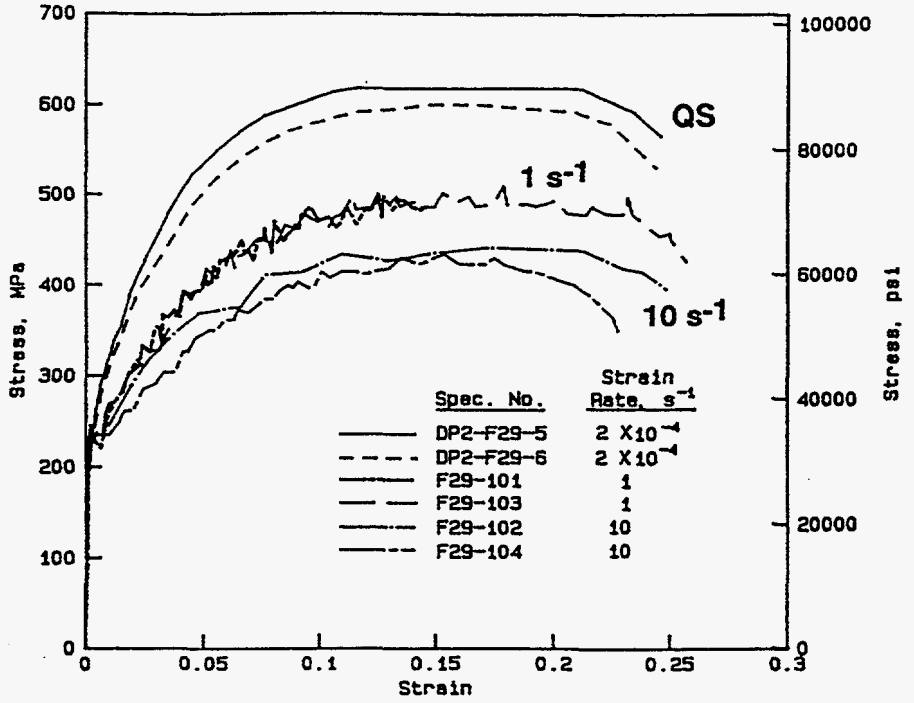

Figure 2.2 Engineering stress-strain curves at 288 C (550 F) for A106 Grade B carbon steel pipe (DP2-F29) tested at several different strain rates

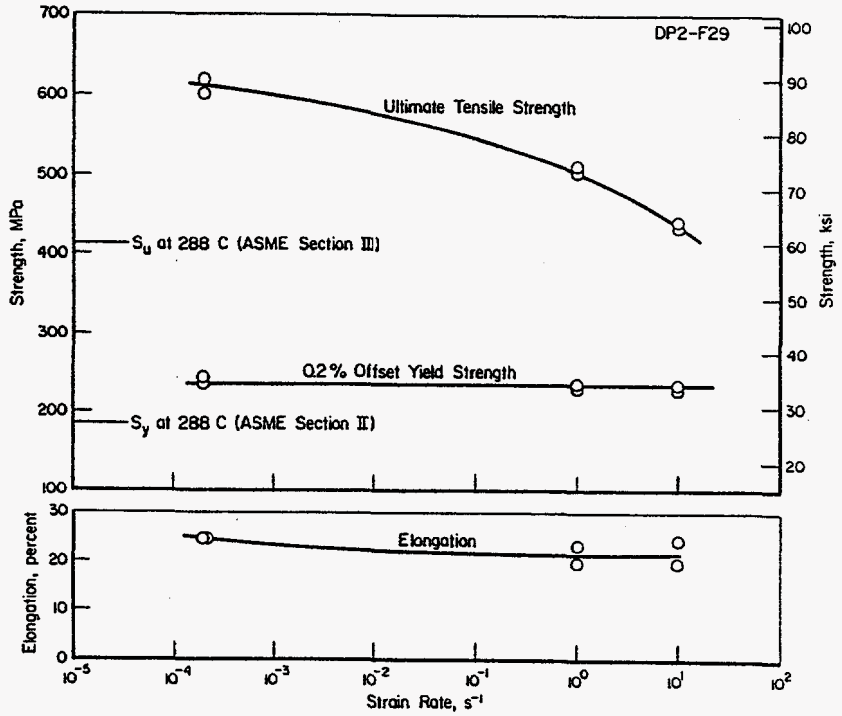

Figure 2.3 Tensile properties at 288 C (550 F) versus strain rate for A106 Grade B carbon steel pipe (DP2-F29)

The ASME Section II Part D yield strength (S_y) and ultimate strength (S_u) values at 288 C (550 F) are also indicated in Figure 2.3. The actual yield strength at both quasi-static and dynamic-loading rates was approximately 125 percent of the ASME code value for this pipe at 288 C (550 F). The ultimate strength at quasi-static test rates was approximately 145 percent of the ASME code value at 288 C (550 F), but decreased to approximately 105 percent of the ASME code value at a strain rate of 10/second.

2.2.1.2 Pipe DP2-F23

Tensile specimens were machined from a section of Pipe DP2-F23; some were subjected to quasi-static-loading-rate tests and some to dynamic-loading-rate tests at 288 C (550 F). All specimens were machined such that the tensile axis was parallel with the pipe axis. The results of those tests are summarized in Table 2.3. Included also in Table 2.3 are the ASME Section II Part D specified minimum yield strength and minimum tensile strength values. Notice in Table 2.3 that the actual yield strength in quasi-static tests at 288 C (550 F) was approximately 116 percent of the ASME Section II Part D specified minimum yield strength, and the actual tensile strength was approximately 122 percent of the ASME Section II Part D specified minimum tensile strength. However, at the higher strain rate, the actual tensile strength was only about 109 percent of the ASME Section II Part D specified minimum tensile strength.

Figure 2.4 shows engineering stress-strain curves from quasi-static-loading-rate tensile tests at 288 C (550 F). Corresponding curves for the higher strain-rate tests are not shown because reliable strain data were not obtained from the optical strain recording device employed in those tests. For those tests, yield strength values were estimated from graphs of stress versus stroke.

Figure 2.5 shows the variation of strength and ductility with strain rate for Pipe DP2-F23 at 288 C (550 F). The significant lowering of the ultimate tensile strength at 288 C (550 F) with increasing strain rate is indicative of the susceptibility of this steel to dynamic strain aging (Refs. 2.5 to 2.7). Notice also in Figure 2.5 that the ductility decreased and the yield strength increased with increasing strain rate.

Table 2.3 Tensile properties of ASTM A106 Grade B carbon steel pipe (DP2-F23) at 288 C (550 F)

Specimen Identification Number	Strain Rate, s^{-1}	0.2-Percent Offset Yield Strength, MPa	0.2-Percent Offset Yield Strength, ksi	Ultimate Tensile Strength, MPa	Ultimate Tensile Strength, ksi	Elongation, Percent in 25.4 mm (1 inch)
DP2-F23-3t[a]	$2x10^{-4}$	223	32.2	514	74.6	33.0
DP2-F23-4t[a]	$2x10^{-4}$	210	30.5	499	72.3	32.7
DP2-F23A	1	273[b]	39.7[b]	442	64.1	29.9
DP2-F23B	1	234[b]	33.9[b]	451	65.4	30.2
DP2-F23C	1	269[b]	39.0[b]	461	66.8	28.9
SA-106-Gr.B	QS[c]	187[d]	27.1[d]	414[e]	60[e]	-

(a) Round-bar, threaded-end specimens; all others were flat, pin-loaded specimens.
(b) Approximate value due to uncertainties in stress-strain curve at small strains.
(c) Quasi-static.
(d) S_y at 288 C (550 F) from ASME Section II Part D.
(e) S_u at 288 C (550 F) from ASME Section II Part D.

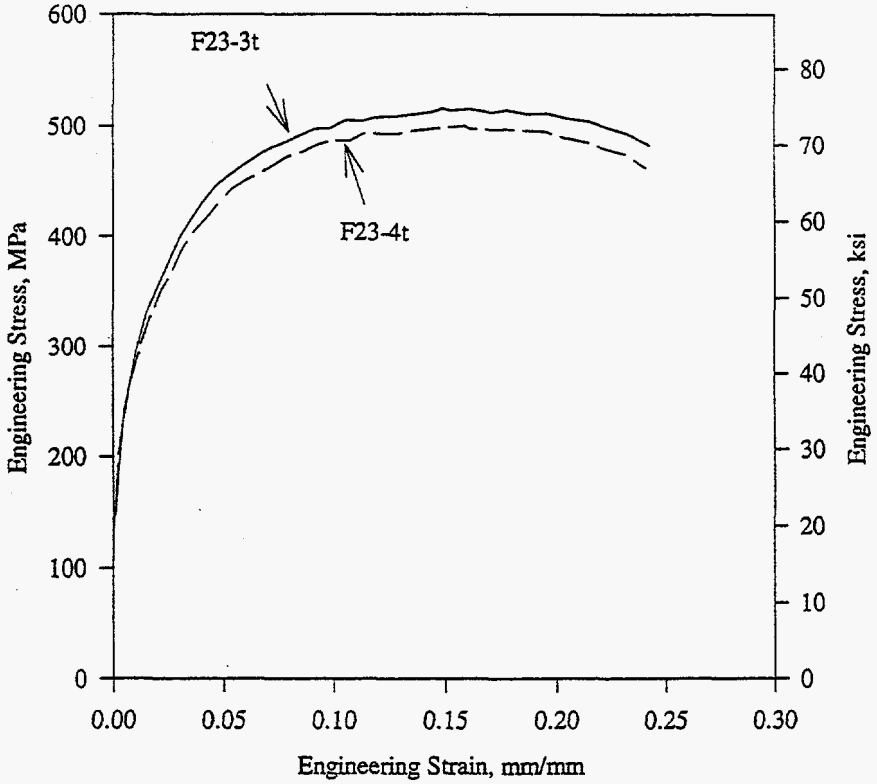

Figure 2.4 Engineering stress-strain curves at 288 C (550 F) for specimens from A106 Grade B carbon steel pipe (DP2-F23) tested at quasi-static loading rates

2.2.1.3 Pipe DP2-F22

Tensile specimens were machined from Pipe DP2-F22; some were subjected to quasi-static-loading-rate tests and some to dynamic-loading-rate tests at 288 C (550 F). All specimens were machined such that the tensile axis was parallel with the pipe axis. The results of the tests are summarized in Table 2.4, which includes also ASME Section II Part D minimum yield and tensile strength values. Notice in Table 2.4 that the actual yield strength in quasi-static tests at 288 C (550 F) was approximately 137 percent of the ASME Section II Part D specified minimum yield strength, and the actual tensile strength was approximately 142 percent of the ASME Section II Part D specified minimum tensile strength. However, at the higher strain rate, the actual tensile strength was only 127 percent of the ASME Section II Part D specified minimum tensile strength.

Figure 2.6 shows engineering stress-strain curves from the quasi-static tests conducted at 288 C (550 F). Corresponding curves for the specimen tested at a greater strain rate are not shown because reliable data were not obtained from the optical extensometer used to measure strain in that test. A value for yield strength was obtained from a graph of stress versus stroke.

Figure 2.7 shows the variation of strength and ductility with strain rate for Pipe DP2-F22 at 288 C (550 F). The significant lowering of the ultimate tensile strength that accompanied the increase in strain rate indicates that the steel is susceptible to dynamic strain aging (Refs. 2.5 to 2.7). As was the case for Pipe DP2-F23 (see Figure 2.5), the percentage elongation of Pipe DP2-F22 was decreased and the yield strength was increased by increasing the strain rate.

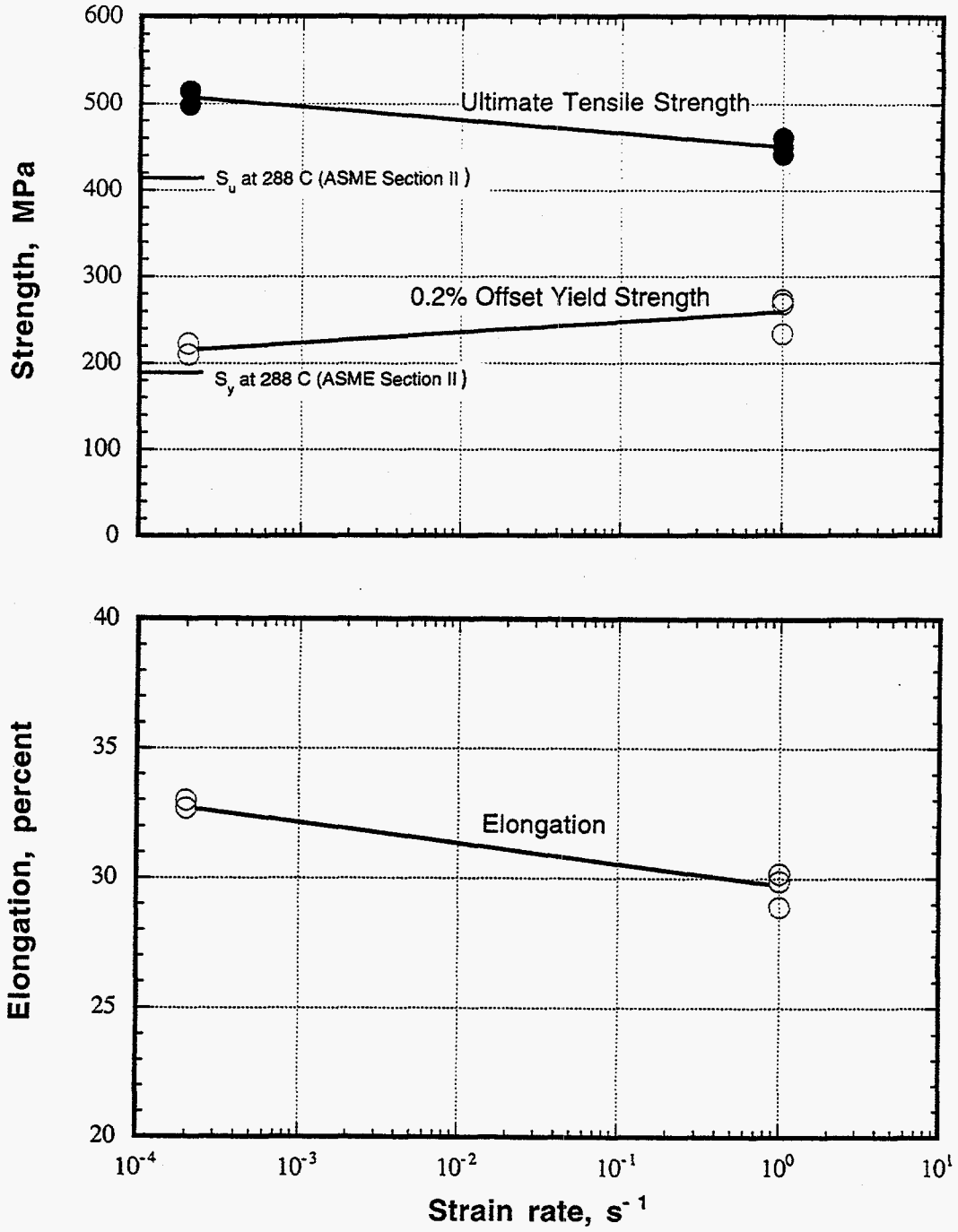

Figure 2.5 Tensile properties at 288 C (550 F) versus strain rate for specimens from ASTM A106 Grade B carbon steel pipe (DP2-F23)

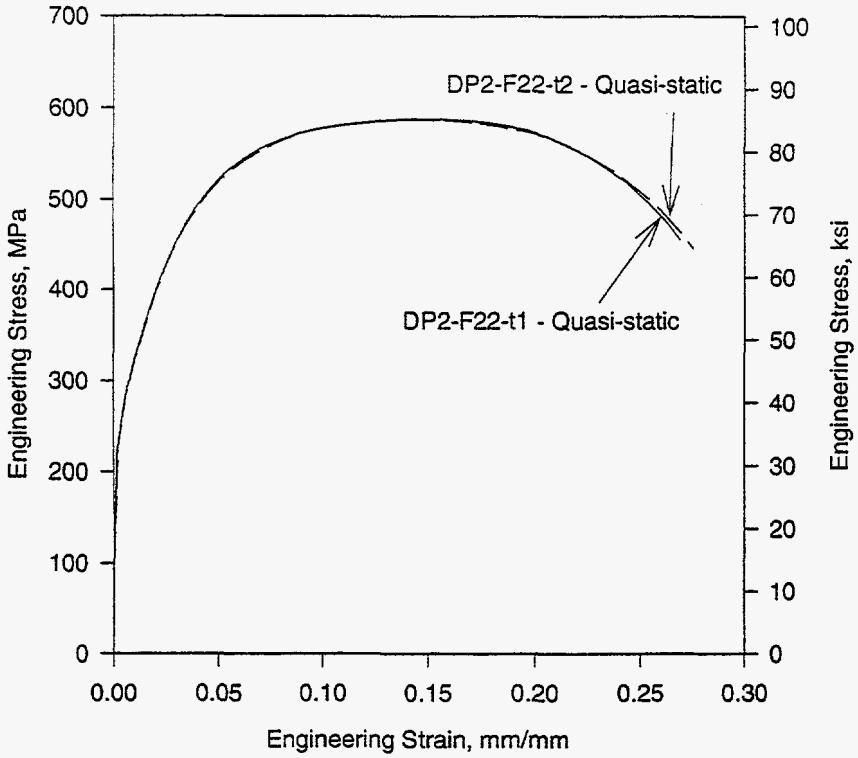

Figure 2.6 Engineering stress-strain curves at 288 C (550 F) for ASTM A106 Grade B carbon steel pipe (DP2-F22) tested at quasi-static loading rates

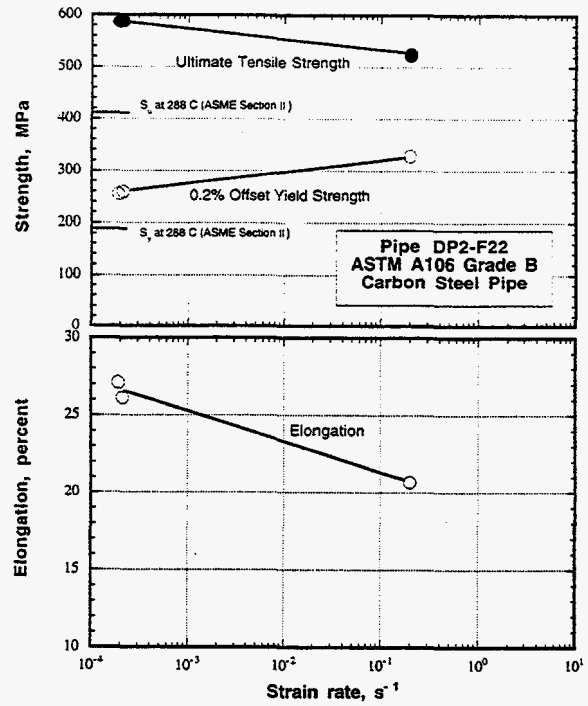

Figure 2.7 Tensile properties at 288 C (550 F) versus strain rate for A106 Grade B carbon steel pipe (DP2-F22)

Table 2.4 Tensile properties of ASTM A106 Grade B carbon steel pipe (DP2-F22) at 288 C (550 F)

Specimen Identification Number	Strain Rate, s^{-1}	0.2-Percent Offset Yield Strength, MPa	ksi	Ultimate Tensile Strength, MPa	ksi	Elongation, Percent in 25.4 mm (1 inch)
DP2-F22-t1[a]	$2x10^{-4}$	259	37.5	588	85.3	26.1
DP2-F22-t2[a]	$2x10^{-4}$	255	37.0	587	85.2	27.1
DP2-F22B	0.2	328[b]	47.5[b]	526	76.5	20.7
SA-106 Gr.B	QS[c]	187[d]	27.1[d]	414[e]	60[e]	--

(a) Round-bar, threaded-end specimens; the other was a flat, pin-loaded specimen.
(b) Approximate value due to uncertainties in stress-strain curve at small strains.
(c) Quasi-static.
(d) S_y at 288 C (550 F) from ASME Section II Part D.
(e) S_u at 288 C (550 F) from ASME Section II Part D.

2.2.2 Type 304 Stainless Steel

Tensile properties are summarized in Table 2.5 for all tensile tests, both at quasi-static and dynamic loading rates, conducted on the ASTM A358 Type 304 stainless steel pipe material (DP2-A8).* (Note, during the course of the IPIRG-2 program, it was discovered that the stainless steel pipe material which had always been referred to as DP2-A8 was actually from two different heats of stainless steel pipe. The tensile properties for both of these heats (now referred to as DP2-A8I and DP2-A8II) are included in Table 2.5.) All specimens were machined such that the tensile axis was parallel with the pipe axis. Figure 2.8 shows the effect of test temperature on tensile properties. Note that the tensile strength, yield strength, and fracture elongation were decreased by increasing the test temperature. (Note, the tensile properties of DP2-A8I and DP2-A8II were virtually the same. Consequently, the discussion which follows is a generic discussion applicable to either material. In addition, for the analyses presented in Section 5 these generic DP2-A8 tensile data are used throughout.) As was noted earlier, strength decreases are the expected result of increasing the test temperature; however, the reason for the decrease in fracture elongation as temperature was raised is not known. The reduction in fracture elongation is too great to be attributed to experimental scatter.

Notice in Figure 2.8 that the actual quasi-static yield strength of this material at room temperature was approximately 140 percent of the ASME Section II Part D specified minimum yield strength (SMYS). The actual quasi-static tensile strength at room temperature for this material was also approximately 140 percent of the ASME Section II Part D specified minimum tensile strength (SMTS).

Figure 2.9 shows engineering stress-strain curves for tensile specimens of this stainless steel material tested at 288 C (550 F) at several different strain rates. As can be seen in Figure 2.9 and Table 2.5, the differences in tensile properties for the two heats of stainless steel are minimal. Table 2.5 and Figure 2.10

*Some of the quasi-static tensile test results were available from the Degraded Piping Program (Ref. 2.2).

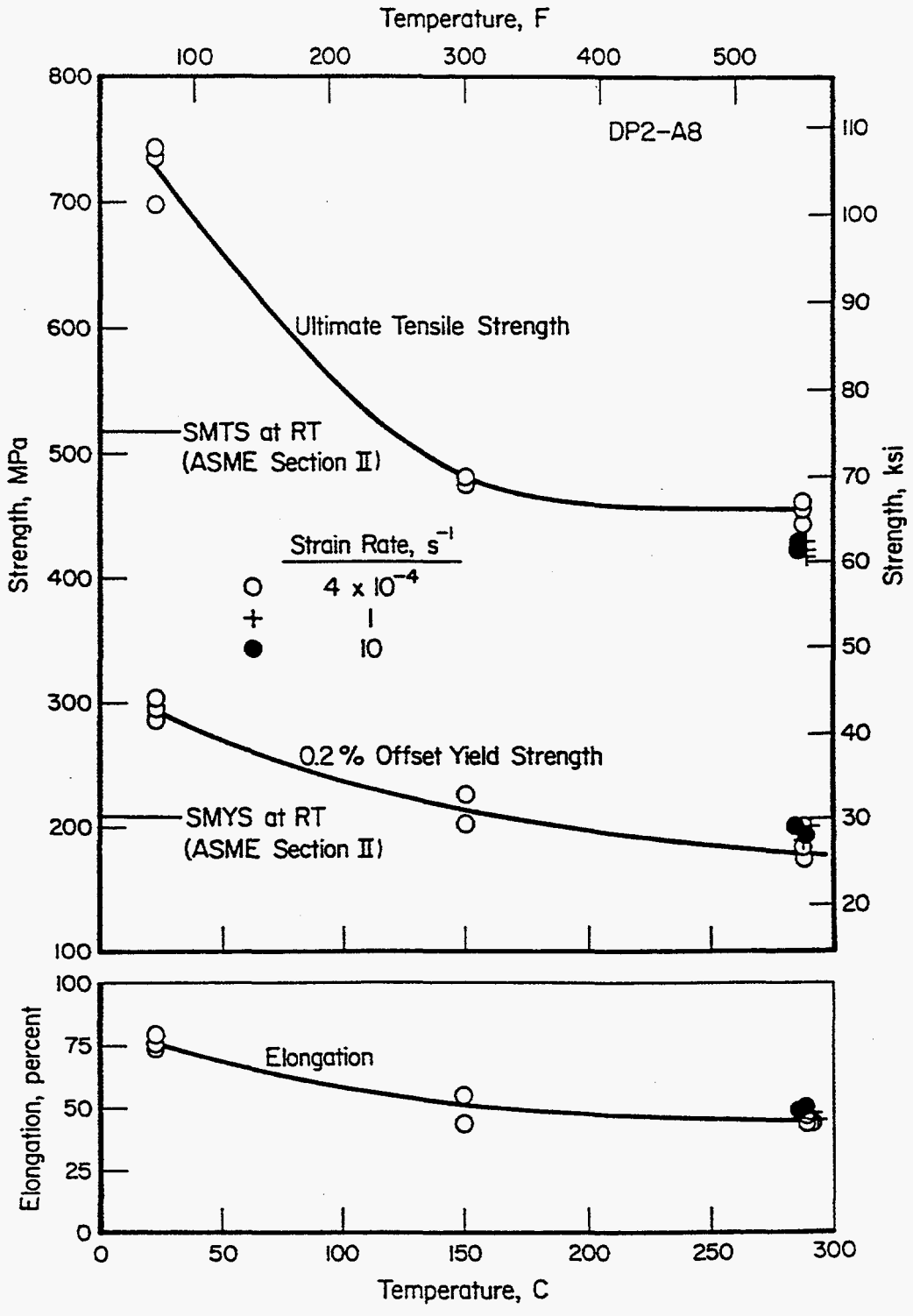

Figure 2.8 Tensile properties versus test temperature for A358 Type 304 stainless steel pipes (DP2-A8I and DP2-A8II)

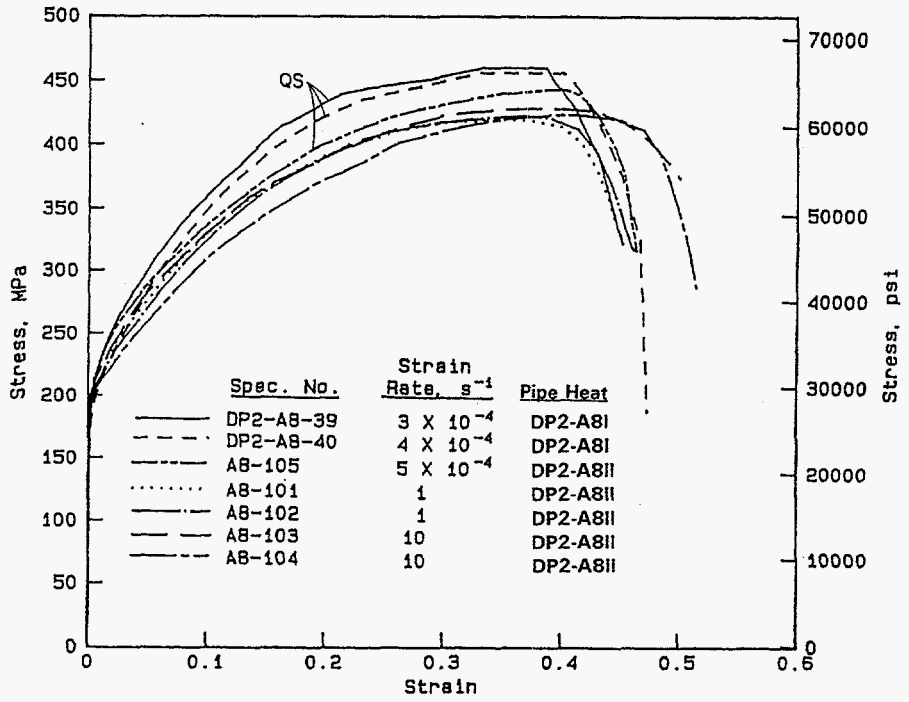

Figure 2.9 Engineering stress-strain curves at 288 C (550 F) for A358 Type 304 stainless steel pipes (DP2-A8I and DP2-A8II) tested at several different strain rates

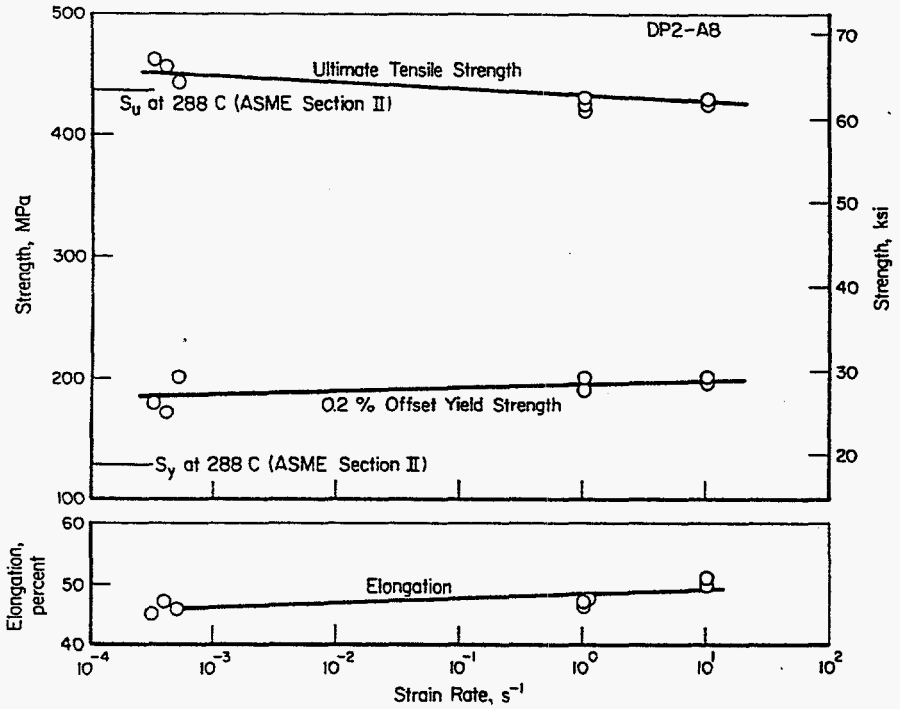

Figure 2.10 Tensile properties at 288 C (550 F) versus strain rate for A358 Type 304 stainless steel pipes (DP2-A8I and DP2-A8II)

Table 2.5 Tensile properties of ASTM A358 Type 304 stainless steel pipes (DP2-A8I and DP2-A8II)

Specimen Ident. Number	Pipe/Heat Ident. Number	Temperature, C	Temperature, F	Strain Rate, s^{-1}	0.2-Percent Offset Yield Strength, MPa	0.2-Percent Offset Yield Strength, ksi	Ultimate Tensile Strength, MPa	Ultimate Tensile Strength, ksi	Elongation, Percent in 25.4 mm (1.0 inch)
A8-48[a]	DP2-A8I	22	72	$4x10^{-4}$	287	41.6	698	101.2	79.4
A8-35[a]	DP2-A8I	22	72	$4x10^{-4}$	295	42.8	743	107.8	75.9
A8-36[a]	DP2-A8I	22	72	$4x10^{-4}$	303	43.9	736	106.7	74.3
A8-37[a]	DP2-A8I	149	300	$4x10^{-4}$	225	32.6	481	69.8	43.5
A8-38[a]	DP2-A8I	149	300	$3x10^{-4}$	202	29.3	476	69.1	54.8
A8-105	DP2-A8II	288	550	$5x10^{-4}$	200[b]	29.0	443	64.3	45.7
A8-39[a]	DP2-A8I	288	550	$3x10^{-4}$	180	26.1	461	66.8	45.0
A8-40[a]	DP2-A8I	288	550	$4x10^{-4}$	171	24.8	456	66.2	47.0
A8-100	DP2-A8II	288	550	1	N.D.	N.D.	430	62.4	47.0
A8-101	DP2-A8II	288	550	1	200[b]	29.0	420	60.9	47.1
A8-102	DP2-A8II	300	572	1	190[b]	27.5	423	61.3	46.5
A8-103	DP2-A8II	288	550	10	200[b]	29.0	429	62.2	49.8
A8-104	DP2-A8II	288	550	10	194[b]	28.1	423	61.4	50.8
SA-358 TP304		22	72	QS[c]	207[d]	30.0[d]	517[e]	75.0[e]	--
SA-358 TP304		288	550	QS[c]	130[f]	18.8[f]	438[g]	63.5[g]	--

(a) Round-bar, threaded-end specimen; all others were flat, pin-loaded specimens.
(b) Approximate value only, due to uncertainties in stress-strain curves at small strains.
(c) Quasi-static.
(d) S_y at 22 C (72 F) from ASME Section II Part D.
(e) S_u at 22 C (72 F) from ASME Section II Part D.
(f) S_y at 288 C (550 F) from ASME Section II Part D.
(g) S_u at 288 C (550 F) from ASME Section II Part D.

summarize the effect of strain rate on tensile properties. Ultimate tensile strength values showed a slight decrease, while yield strength and fracture elongation values showed a slight increase with increasing strain rate.

The ASME Section II Part D yield strength (S_y) and ultimate strength (S_u) values at 288 C (550 F) are also indicated in Figure 2.10. The actual yield strength value was above the ASME S_y value for all strain rates investigated. The actual ultimate strength values were above the ASME S_u value at low strain rates and, at the higher strain rates, the actual ultimate strength values were very close to the ASME S_u value.

2.2.3 Carbon Steel Submerged-Arc Welds

Data for two different carbon steel submerged-arc welds are included in this report. One of the welds, identified as DP2-F29W, was a circumferential weld in an A106 Grade B carbon steel pipe that was characterized in the Degraded Piping program and the IPIRG-1 program. The second weld, identified as DP2-F55W, was a butt welded carbon steel plate of 25.4 mm (1 inch) thickness, characterized in the IPIRG-2 program. Both welds were prepared by United McGill Corporation using procedures recommended by Babcock and Wilcox. The chemical compositions for the two welds were in close agreement. Table 2.6 provides a comparison of the material property data (tensile and fracture toughness) obtained for the two welds; additional information about the mechanical properties of the two welds follows.

Table 2.6 Comparison of IPIRG-1 DP2-F29W and IPIRG-2 DP2-F55W material properties at 288 C (550 F)

Material Property	DP2-F29W	DP2-F55W
Quasi-static Yield Strength, MPa	356	359
Quasi-static Ultimate Strength, MPa	556	612
QS J at Crack Initiation, kJ/m^2	82.3	65.4
QS dJ/da, MJ/m^3	68.0	46.3
Dynamic J at Crack Initiation, kJ/m^2	125.3	98.7
Dynamic dJ/da, MJ/m^3	101.7	92.9

2.2.3.1 Pipe Weld DP2-F29W

A submerged-arc girth weld (DP2-F29W) in the ASTM A106 Grade B carbon steel material was subjected to tensile tests only at 288 C (550 F) at three different strain rates. No tensile test results are available at other temperatures for this material. All specimens were machined longitudinal to the pipe axis and the test weld was centered in the gage length of the specimen. Tensile properties are summarized in Table 2.7 and engineering stress-strain curves are presented in Figure 2.11. As was the case for the carbon steel base metal, this material exhibited very pronounced serrations at the intermediate strain rate, indicative of DSA.

Table 2.7 Tensile properties of submerged-arc weld (DP2-F29W) in ASTM A106 Grade B carbon steel pipe at 288 C (550 F)

Specimen Identification Number	Strain Rate, s^{-1}	0.2-Percent Offset Yield Strength, [a] MPa	ksi	Ultimate Tensile Strength, MPa	ksi	Elongation, Percent in 25.4 mm (1.0 inch)
F29W-107	$2x10^{-4}$	356	51.7	556	80.7	20.4
F29W-101	1	368	53.4	487	70.6	14.8
F29W-104	1	396	57.4	495	71.8	14.5
F29W-103	10	347	50.3	446	64.7	21.8
F29W-106	10	345	50.0	454	65.8	21.9

(a) Approximate values only, due to uncertainties in stress-strain curves at small strains.

Figure 2.12 shows the tensile properties of this submerged-arc weld as a function of strain rate in tests conducted at 288 C (550 F). Notice the similarity of the behavior exhibited by the carbon steel weld metal to that exhibited by the carbon steel base metal in Figure 2.3. In particular, the decreasing tensile strength with increasing strain rate is obvious. Thus, even though tensile tests on the pipe weld metal were conducted only at 288 C (550 F), it appears that the carbon steel weld metal was displaying susceptibility to DSA in a manner very similar to that for the carbon steel base metal.

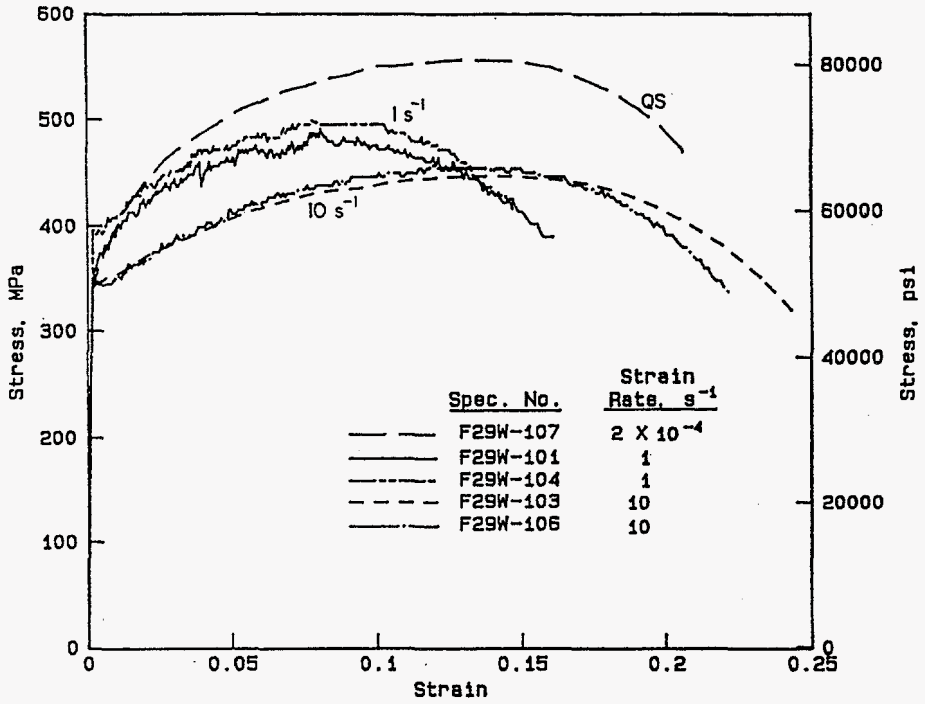

Figure 2.11 Engineering stress-strain curves at 288 C (550 F) for a submerged-arc weld (DP2-F29W) in an A106 Grade B carbon steel pipe, tested at several different strain rates

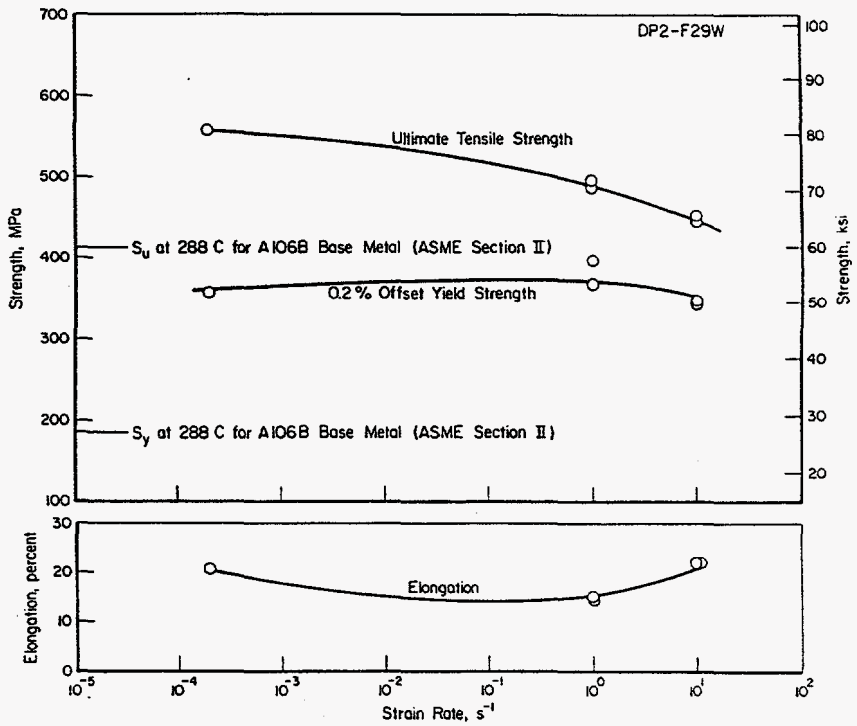

Figure 2.12 Tensile properties at 288 C (550 F) versus strain rate for a submerged-arc weld (DP2-F29W) in an A106 Grade B carbon steel pipe

In comparing the carbon steel base metal tensile test results to the carbon steel weld metal results, it was found that the weld metal ultimate strength at 288 C (550 F) was below that of the base metal at quasi-static rates and approached the base metal ultimate strength at a strain rate of 10/second. The weld metal yield strength was well above the base metal yield strength at all strain rates investigated.

2.2.3.2 Plate Weld DP2-F55W

Sub-size round-bar tensile specimens having a 6.35 mm (0.25 inch) diameter gage section were tested to determine the quasi-static-loading-rate tensile properties of this weld metal at 288 C (550 F). The specimens were oriented such that the tensile axis was perpendicular to the weld centerline. An extensometer of 12.7 mm (0.5 inch) gage length was used to measure axial strain. The nominal strain rate was 2×10^{-4} s^{-1}. No dynamic-loading-rate tensile tests were performed.

Quasi-static tensile properties at 288 C (550 F) are summarized in Table 2.8 and engineering stress-strain curves are shown in Figure 2.13. As was shown previously in Table 2.6, Plate Weld DP2-F55W had a yield strength comparable to that of Pipe Weld DP2-F29W and an ultimate tensile strength that exceeded that of Pipe Weld DP2-F29W by approximately 10 percent.

Table 2.8 Tensile properties at 288 C (550 F) of a submerged-arc weld (DP2-F55W) in a carbon steel plate

Specimen Identification Number	0.2-Percent Offset Yield Strength, MPa	ksi	Ultimate Tensile Strength, MPa	ksi	Elongation, percent in 12.7 mm (0.5 inch)
DP2-F55W-T1	328	47.6	608	88.2	30.1
DP2-F55W-T2	390	56.5	615	89.2	30.6

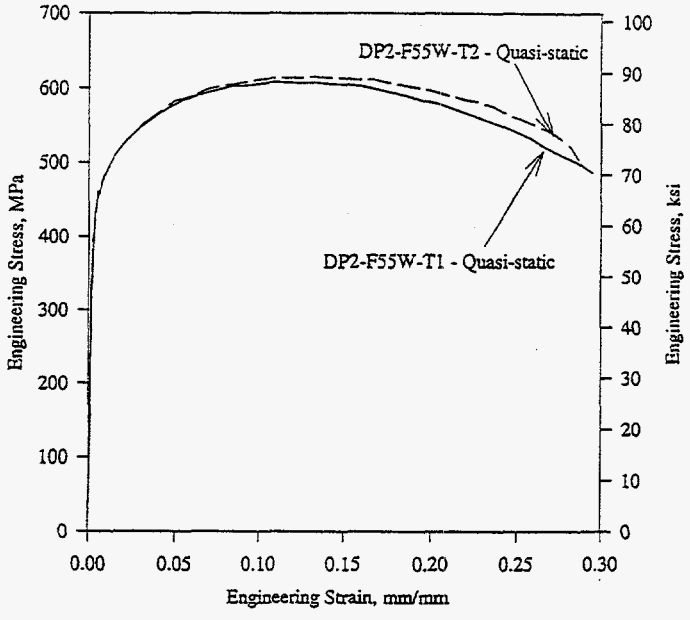

Figure 2.13 Engineering stress-strain curves at 288 C (550 F) for a submerged-arc weld (DP2-F55W) in a carbon steel pipe, tested at quasi-static loading rates

2.2.4 Stainless Steel Submerged-Arc Welds

Data for three different submerged-arc welds are included in this report. One of the welds, identified as DP2-A8W, was a circumferential weld in an ASTM A358 Type 304 stainless steel pipe that was characterized in the Degraded Piping program and the IPIRG-1 program. A second weld, identified as DP2-A45W1, was a butt-welded Type 304 stainless steel plate of 25.4 mm (1 inch) thickness, characterized in the Degraded Piping program. The third weld, identified as DP2-A45W2, was similar to and was made from the same plate material as DP2-A45W1, but was characterized in the Short Cracks in Piping and Piping Welds program.

Each of the three welds was prepared by United McGill Corporation using procedures recommended by the General Electric Company. The chemical compositions of the three welds are compared in Table 2.9 and, for the most part, are in reasonable agreement. Table 2.10 provides a comparison of the material property data (both tensile and fracture toughness) obtained for the three welds from quasi-static tests at 288 C (550 F). Additional information about the mechanical properties of the three welds follows.

2.2.4.1 Pipe Weld DP2-A8W

Figure 2.14 shows engineering stress-strain curves for the submerged-arc weld (SAW) metal (DP2-A8W) in ASTM A358 Type 304 stainless steel pipe tested at 288 C (550 F) at several different strain rates. No tensile test results are available at other temperatures for this material. All specimens were machined such

Table 2.9 Chemical composition of three stainless steel submerged-arc weld metals in percent by weight

	DP2-A8W	DP2-A45W1	DP2-A45W2
C	0.06	0.07	0.03
Mn	2.1	1.87	2.26
P	0.024	0.029	0.032
S	0.005	0.010	0.010
Si	0.79	0.62	0.89
Cu	0.04	0.25	0.26
Sn	0.006	(a)	0.010
Ni	8.9	8.70	9.6
Cr	20.8	19.83	19.7
Mo	0.046	0.19	0.10
Al	0.016	(a)	0.015
V	0.046	0.05	0.070
Nb	0.007	(a)	0.012
Zr	0.008	(a)	0.015
Ti	0.006	(a)	0.006
B	0.0010	(a)	0.0008
Ca	(a)	(a)	0.0008
Co	0.069	0.11	0.13
W	0.00	(a)	0.0
Se	(a)	(a)	0.00

(a) Not determined.

Table 2.10 Summary table showing the average yield and ultimate strength, J_i, and dJ/da values for quasi-static testing rates at 288 C (550 F) for Welds DP2-A45W1, DP2-A45W2, and DP2-A8W

Weld Identification Number	Plate or Pipe Weld	Program Which Developed Data	0.2-Percent Offset Yield Strength, MPa	0.2-Percent Offset Yield Strength, ksi	Ultimate Tensile Strength, MPa	Ultimate Tensile Strength, ksi	J_i, kJ/m^2	J_i, in-lb/in^2	dJ/da[a], MJ/m^3	dJ/da[a], in-lb/in^3
DP2-A45W1	Plate	Degraded Piping	325	47.1[b]	466	67.6[b]	108[c]	616[c]	109	15,800
DP2-A45W2	Plate	Short Cracks	366	53.1[b]	503	72.9[b]	59.7[d]	341[d]	160	23,250
							47.3[e]	270[e]	147	21,350
DP2-A8W	Pipe	IPIRG-1	258	37.4[f]	469	68.0[f]	55.2[d]	315[d]	135	19,550
		Average	316	45.9	479	69.5	67.4	385	138	19,990

(a) Using data from initial portion of J-R curve from 0.15 mm (0.006 inch) < Δa < 1.5 mm (0.060 inch).
(b) Round-bar tensile specimen with 19 mm (0.75 inch) gage section which was made up entirely of weld metal.
(c) Data from fatigue precracked nonside-grooved 1T C(T) specimens. (Note that this value is an average of two tests. There were also 3T and 9.5T specimens tested with the same thickness. See NUREG/CR-4575, Table 3.1.)
(d) Data from fatigue precracked 20-percent side-grooved specimens.
(e) Data from fatigue precracked nonside-grooved specimens.
(f) Flat, pin-loaded tensile specimens with a 20.3 mm (0.8 inch) gage section which was made up entirely of weld metal.

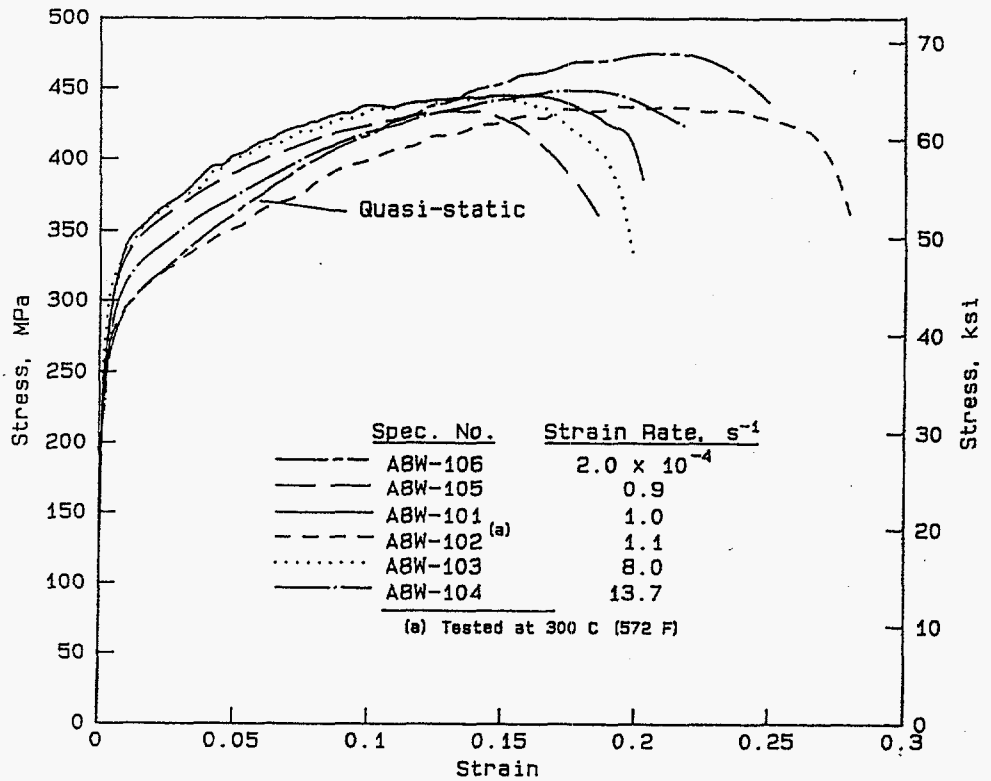

Figure 2.14 Engineering stress-strain curves at 288 C (550 F) for a submerged-arc weld (DP2-A8W) in A358 Type 304 stainless steel pipe, tested at several different strain rates

that the tensile axis was parallel with the pipe axis and had the test weld centered in the gage length of the specimen. Table 2.11 and Figure 2.15 summarize the effect of strain rate on the tensile properties at 288 C (550 F).

Table 2.11 Tensile properties of submerged-arc weld (DP2-A8W) in ASTM A358 Type 304 stainless steel pipe at 288 C (550 F)

Specimen Identification Number	Strain Rate, s^{-1}	0.2-Percent Offset Yield Strength, MPa	ksi	Ultimate Tensile Strength, MPa	ksi	Elongation, Percent in 20.3 mm (0.8 inch)
A8W-106	$2.0x10^{-4}$	258	37.4	469	68.0	26.4
A8W-105	0.9	283	41.0	430	62.4	19.4
A8W-101	1.0	288	41.8	443	64.2	23.3
A8W-102[a]	1.1	270	39.1	436	63.2	30.1
A8W-103	8.0	308	44.6	442	64.1	22.8
A8W-104	13.7	266	38.6	444	64.4	24.5

(a) Tested at 300 C (572 F).

The strength results for the SAW are similar to those for the base metal in this pipe (see Figure 2.10). Both materials showed slightly lower ultimate tensile strength and slightly higher yield strength values with increasing strain rate. Fracture elongation values, on the other hand, were increased slightly by strain rate for the base metal and decreased slightly for the weld metal.

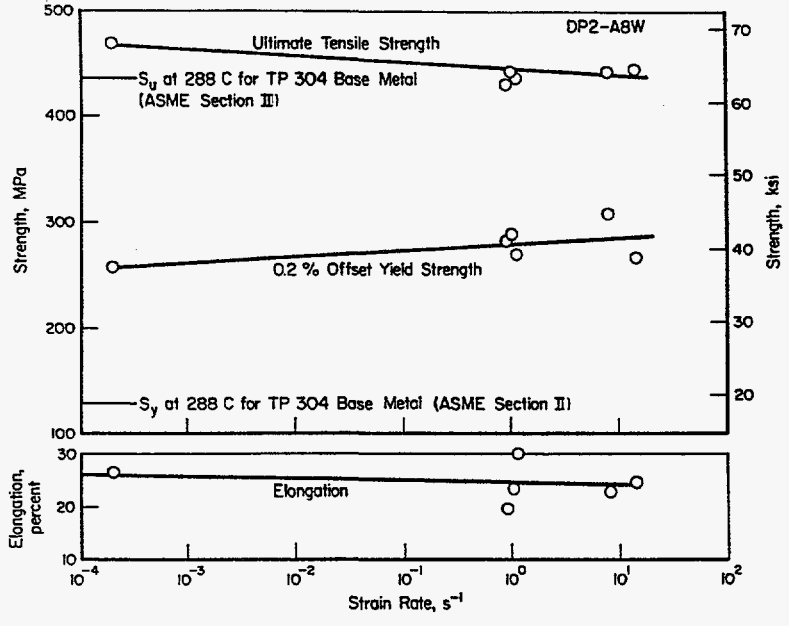

Figure 2.15 Tensile properties at 288 C (550 F) versus strain rate for submerged-arc weld (DP2-A8W) in A358 Type 304 stainless steel pipe

In comparing the stainless steel base metal tensile test results to the stainless steel SAW results, it was found that the SAW yield strength values and ultimate strength values at 288 C (550 F) exceeded those of the base metal at all strain rates investigated.

2.2.4.2 Plate Weld DP2-A45W1

Round-bar tensile specimens having threaded ends were machined such that the tensile axis was normal to the welding direction and parallel with the plate rolling direction. The reduced-section of each specimen was made up entirely of weld metal from near the weld crown where the deposition process was completely submerged arc. The results of tensile tests conducted at quasi-static loading rates at 288 C (550 F) are shown in Table 2.12 and engineering stress-strain curves are shown in Figure 2.16. No dynamic-loading-rate tensile tests were conducted on this weld metal.

Table 2.12 Tensile properties at 288 C (550 F) of a submerged-arc weld (DP2-A45W1) in a Type 304 stainless steel plate

Specimen Identification Number	0.2-Percent Offset Yield Strength, MPa	ksi	Ultimate Tensile Strength, MPa	ksi	Elongation, Percent in 12.7 mm (0.5 inch)	Reduction of Area, Percent
A45SW-1	339	49.1	470	68.1	30.0	46.0
A45SW-2	310	45.0	463	67.1	33.0	42.4
Average	325	47.1	466	67.6	31.5	44.2

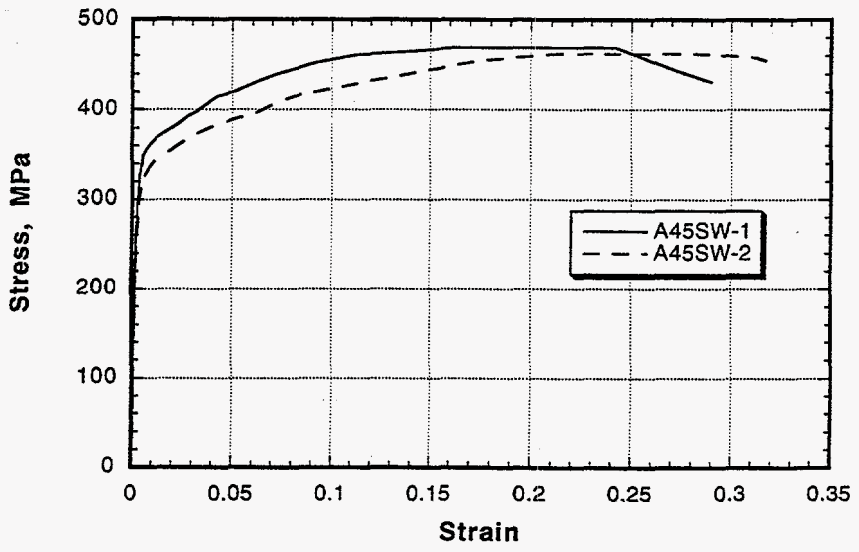

Figure 2.16 Engineering stress-strain curves at 288 C (550 F) for a submerged-arc weld (DP2-A45W1) in a Type 304 stainless steel plate tested at quasi-static loading rates

2.2.4.3 Plate Weld DP2-A45W2

Round-bar tensile specimens having threaded ends were machined such that the tensile axis was normal to the weld centerline. The reduced section of each specimen was made up entirely of weld metal from near the crown of the weld where the metal deposition process was completely submerged arc. Table 2.13 and Figure 2.17 summarize the quasi-static-loading-rate tensile properties at room temperature and 288 C (550 F). As is commonly observed in austenitic stainless steels, both strength and ductility values were lower at 288 C (550 F) than at room temperature.

Table 2.13 Tensile properties of a submerged-arc weld (DP2-A45W2) in a Type 304 stainless steel plate

Specimen Number	Test Temperature, C	Test Temperature, F	0.2-Percent Offset Yield Strength, MPa	0.2-Percent Offset Yield Strength, ksi	Ultimate Tensile Strength, MPa	Ultimate Tensile Strength, ksi	Elongation, Percent in 12.7 mm (0.5 inch)	Reduction of Area, Percent
A45W2-1	22	72	405	58.7	610	88.5	24.4	64.0
A45W2-2	22	72	375	54.4	581	84.3	24.6	55.0
A45W2-3	288	550	374	54.3	510	74.0	15.5	63.0
A45W2-4	288	550	357	51.8	495	71.8	13.7	54.0

Figure 2.18 shows engineering stress-strain curves for this plate weld material at the two temperatures investigated. No dynamic-loading-rate tensile tests were conducted on this weld.

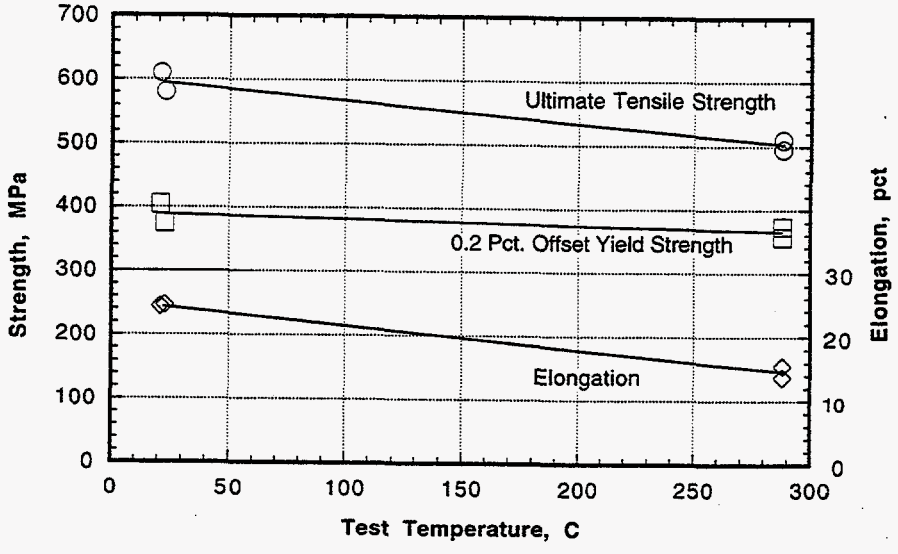

Figure 2.17 Tensile properties versus test temperature for a submerged-arc weld (DP2-A45W2) in a Type 304 stainless steel plate

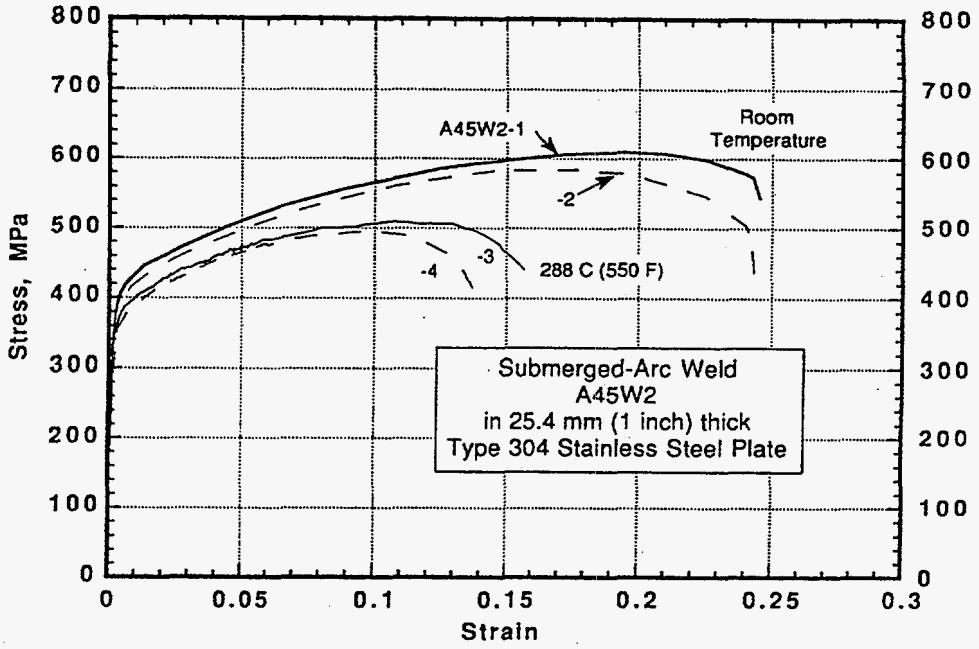

Figure 2.18 Engineering stress-strain curves for a submerged-arc weld (DP2-A45W2) in a Type 304 stainless steel plate

2.2.5 A106 Grade B 90-Degree Long Radius Elbow

Tensile specimens were machined from the elbow's extrados. The elbow identification number from which these specimens were machined was IP2-FE17. Four tensile specimens were machined from the elbow's centerline and four tensile specimens were machined from one of the ends of the elbow (End B). Round-bar tensile specimens with a 6.35-mm (0.25-inch) diameter gage section, that were oriented such that the tensile axis was parallel to the elbow axis, were used to characterize the tensile properties of this material at quasi-static loading rates. An extensometer of 12.7 mm (0.5 inch) gage length was used to measure axial strain in these quasi-static tests. Flat, pin-loaded tensile specimens with integral flags were used for the dynamic-loading-rate tensile tests. The gage section for these dynamic tensile tests had a width of 6.35 mm (0.25 inch), a thickness of 3.18 mm (0.125 inch), and a gage length of 25.4 mm (1.0 inch). Strain in the gage section of these dynamic tests was to be monitored using a nonconducting optical strain-measuring device. However, during the course of these high-strain-rate tests, it was noticed that the strain-measuring device was not producing reasonable strain readings. Therefore, some of the strain data are not reported here. For the strain data that are reported, a high- temperature clip-gage extensometer was used to measure the dynamic strains in lieu of the optical device.

Table 2.14 is a summary table of the tensile properties for these tests. Engineering stress-strain curves for the tensile tests are presented in Figure 2.19. As can be seen in Table 2.14 and Figure 2.19, there was a reduction of approximately 10 percent in the ultimate tensile strength of this material with increasing strain rate.

Table 2.14 Elbow IP2-FE17 tensile property summary

Specimen Identification Number	Specimen Location in Elbow's Extrados	Strain Rate, s^{-1}	0.2-Percent Offset Yield Strength, MPa	0.2-Percent Offset Yield Strength, ksi	Ultimate Tensile Strength, MPa	Ultimate Tensile Strength, ksi	Elongation, Percent in 25.4 mm (1 inch)
IP2-FE17T1	Centerline	2×10^{-4}	208.3	30.21	449.5	65.19	28.3
IP2-FE17T2	Centerline	2×10^{-4}	215.0	31.18	446.4	64.75	29.1
IP2-FE17T3	End B	2×10^{-4}	210.4	30.51	452.2	65.58	28.2
IP2-FE17T4	End B	2×10^{-4}	203.3	29.49	443.9	64.38	29.5
IP2-FE17-HT1	Centerline	1.0	265.5[a]	38.50	404.0	58.55	30.4
IP2-FE17-HT2	Centerline	1.0	273.7[a]	39.70	412.7	59.86	30.4
IP2-FE17-HT3	End B	1.0	248.9	36.10	386.7	56.09	21.9
IP2-FE17-HT4	End B	1.0	192.4	27.90	404.0	58.59	25.2

(a) Optical strain-measuring device used. Yield strengths were calculated using stroke instead of strain.

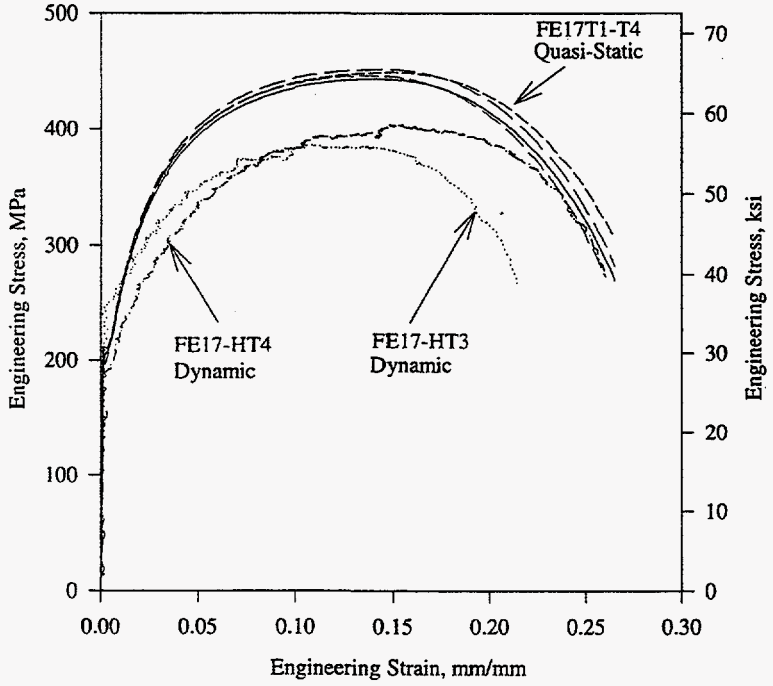

Figure 2.19 Engineering stress-strain curves at 288 C (550 F) for an A106 Grade B elbow (IP2-FE17)

2.2.6 ASTM A710 Carbon Steel Straight-Pipe Loop Material

As was noted in Section 2.1.2, the pipe loop was partially rebuilt between the IPIRG-1 and IPIRG-2 programs. Both the original loop (Loop No. 1) and the partially reconstructed loop (Loop No. 2) were fabricated from ASTM A710, Grade A, Class 3, low-carbon, precipitation-hardening alloy steel in both Schedule 100 and 160 thicknesses. The straight pipes used in Loop No. 1 were Pipes IP-F3 and IP-F4 (Schedule 100 and 160, respectively); in Loop No. 2, Pipe IP-F5 (Schedule 100) was used to replace the damaged sections of Pipe IP-F3. Longitudinal tensile tests were conducted at quasi-static loading rates by both the manufacturer of the pipes and Battelle. Table 2.15 summarizes the results of those tests. Figure 2.20 shows the Battelle stress-strain curves at room temperature and 288 C (550 F) for Pipe IP-F3 (Schedule 100) and Figure 2.21 shows stress-strain curves for Pipe IP-F5 (Schedule 100) at 288 C (550 F). No data were developed at Battelle for the Schedule 160 pipe.

Table 2.15 Quasi-static tensile property data for ASTM A710, Grade A, Class 3, low-carbon precipitation-hardening alloy steel pipe used in Loop No. 1 (IP-F3 and IP-F4) and Loop No. 2 (IP-F5)

Pipe Identification	Schedule	Heat	Temperature, C	Temperature, F	0.2-Percent Offset Yield Strength, MPa	0.2-Percent Offset Yield Strength, ksi	Ultimate Tensile Strength, MPa	Ultimate Tensile Strength, ksi	Elongation, Percent	Reduction of Area, Percent
IP-F3[a]	100	47453	20	68	555	80.5	678	98.3	27.1	78.0
IP-F3[b]	100	47453	22	72	530	76.9	753	94.7	27.5	76.6
IP-F3[b]	100	47454	22	72	560	81.2	665	96.4	27.3	76.7
IP-F3[a]	100	47453	288	550	463	67.1	621	90.1	21.8	72.9
IP-F4[b]	160	47549	22	72	538	78.0	656	95.1	27.3	75.9
IP-F5[a]	100	54473	288	550	537	77.9	658	95.4	21.3	(c)
IP-F5[a]	100	54473	288	550	543	78.7	658	95.4	22.0	(c)

(a) Battelle data.
(b) Manufacturer's data.
(c) Not determined.

2.2.7 WPHY-65 Carbon Steel Elbow Material

Pipe loop elbows were manufactured from WPHY-65 carbon steel in both Schedule 100 and 160 thicknesses. Longitudinal tensile tests were conducted at room temperature by the manufacturer. Tables 2.16 and 2.17 show the results for Loop No. 1 elbows and Loop No. 2 elbows, respectively. Also shown in Tables 2.16 and 2.17 are 0.2 percent offset yield strength values obtained in two different types of tests conducted at Battelle--monotonic and cyclic loading. The cyclic tests were conducted to assess the susceptibility of this material to cyclic strain softening, as described in the next paragraph. The monotonic tests were conducted to provide baseline data and, except for Specimens H-3 and B-3 in Table 2.17, were discontinued at 1 percent strain, just as were the cyclic tests.

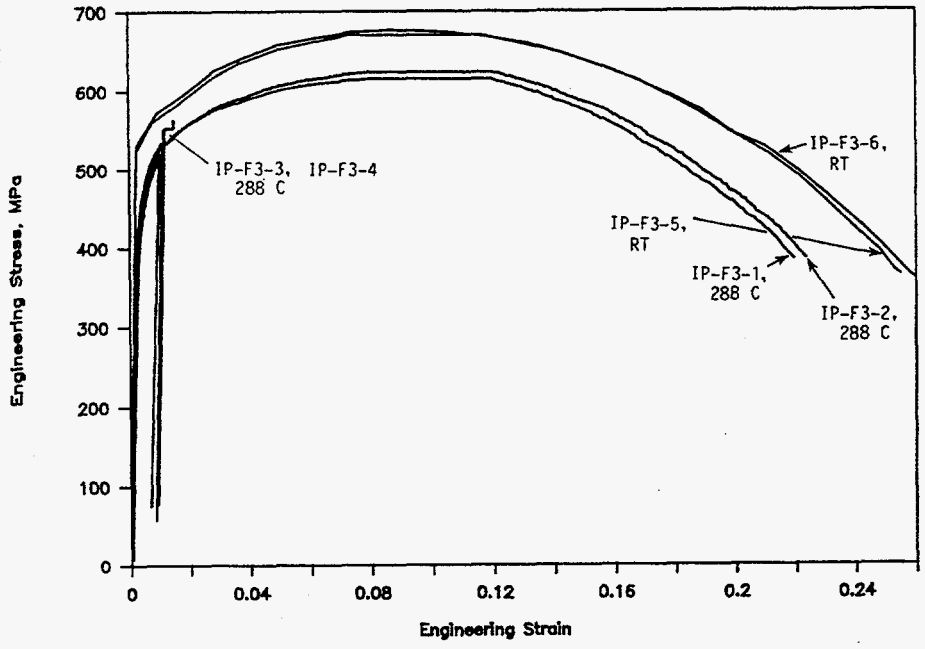

Figure 2.20 Engineering stress-strain curves for ASTM A710, Grade A, Class 3, Schedule 100 straight pipe (IP-F3) used in Loops No. 1 and No. 2

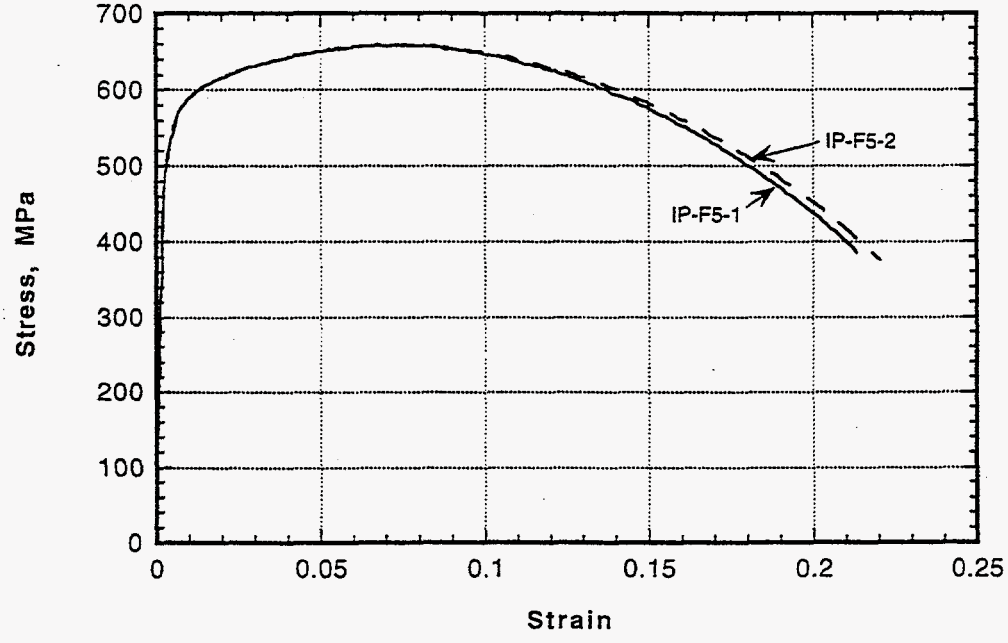

Figure 2.21 Engineering stress-strain curves at 288 C (550 F) for ASTM A710, Grade A, Class 3 Schedule 100 straight pipe (IP-F5) used in Loop No. 2

Consequently, the Battelle tests provided no ultimate strength values for the Loop No. 1 elbow materials. The room temperature yield strength values, determined from Battelle's monotonic-loading tests (see Tables 2.16 and 2.17), are in close agreement with the manufacturer's results for Elbows IP-FE7, IP-FE11 and IP-FE12. However, for Elbow IP-FE6, the manufacturer's yield strength value is approximately 25 percent greater than the value determined at Battelle.

Incremental step shake-down tests were conducted at Battelle on the pipe loop elbow materials to assess the susceptibility of the elbows to cyclic strain softening. In this test, a tensile specimen is load cycled in the following manner: (a) load cycles are fully reversed, (b) starting at zero, the amplitude of each successive cycle is increased in a step-wise fashion to a maximum of 1.0 percent strain, and (c) at the maximum strain, the amplitude of each successive cycle is reduced back to zero strain. The cyclic loading history is repeated until the resulting stress-strain curve shows no further changes with cycling. Figures 2.22 and 2.23 show envelope data for the incremental step tests on the elbow materials and Tables 2.16 and 2.17 give values of the 0.2 percent offset yield strength determined from the curves. From the figures and the tables, it is apparent that the elbow material cyclically softens at room temperature and cyclically hardens at elevated temperature.

Table 2.16 Tensile properties for WPHY-65 carbon steel elbows used in Loop No. 1

Spec. Ident. Number	Test Temperature, C	Test Temperature, F	Test Type	0.2-Percent Offset Yield Strength, MPa	0.2-Percent Offset Yield Strength, ksi	Ultimate Tensile Strength, MPa	Ultimate Tensile Strength, ksi	Elongation, Percent	Reduction of Area, Percent
			Elbow IP-FE6, Schedule 100, Heat No. Y025 FN						
N.A.[a]	RT	RT	Monotonic	545	79.0	662	96.0	32	75
IP-FE6-3	21	70	Monotonic	431	62.5	(b)	(b)	(b)	(b)
IP-FE6-4	21	70	Cyclic[c]	408	59.2	(b)	(b)	(b)	(b)
IP-FE6-1	288	550	Monotonic	346	50.2	(b)	(b)	(b)	(b)
IP-FE6-2	288	550	Cyclic[c]	556	80.7	(b)	(b)	(b)	(b)
			Elbow IP-FE7, Schedule 160, Heat No. 780419						
N.A.[a]	RT	RT	Monotonic	448	65.0	593	86.0	36	66
IP-FE7-3	21	70	Monotonic	450	65.2	(b)	(b)	(b)	(b)
IP-FE7-4	21	70	Cyclic[c]	390	56.6	(b)	(b)	(b)	(b)
IP-FE7-1	288	550	Monotonic	418	60.6	(b)	(b)	(b)	(b)
IP-FE7-2	288	550	Cyclic[c]	574	83.2	(b)	(b)	(b)	(b)

(a) Not applicable; tensile properties shown are from manufacturer's mill certifications.
(b) Ultimate strength, elongation, and reduction of area were not determined because test was discontinued after 1 percent strain.
(c) Incremental step shake-down tests were conducted to assess susceptibility to cyclic strain softening.

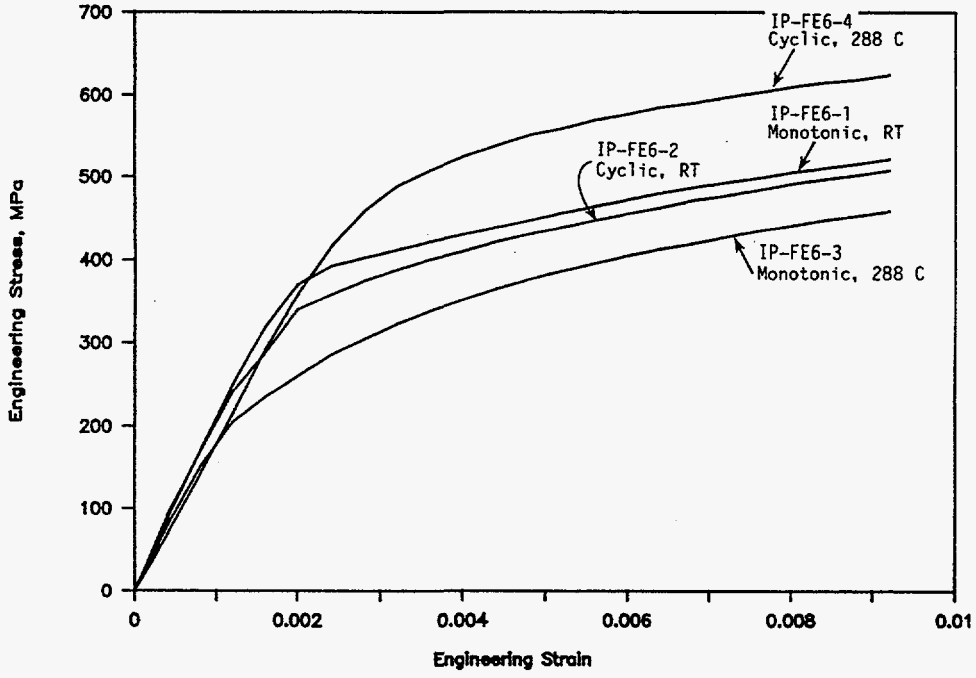

(a) IP-FE6 (Schedule 100)

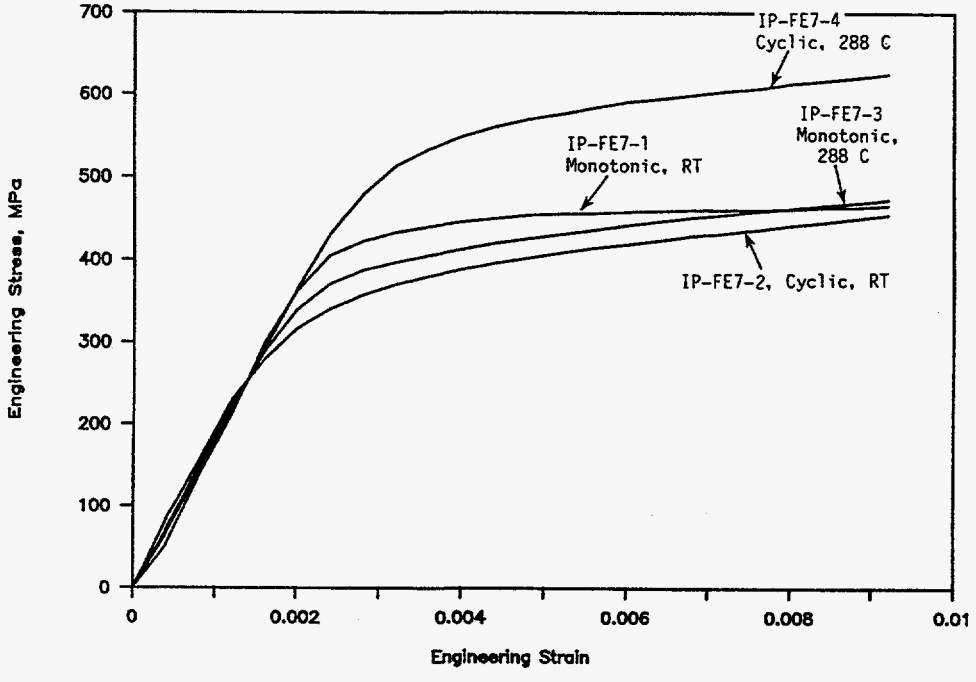

(b) IP-FE7 (Schedule 160)

Figure 2.22 Envelopes of engineering stress-strain curves at 288 C (550 F) from incremental step tests for WPHY-65, Schedule 100 and 160 elbows from Loop No. 1 (IP-FE6 and IP-FE7, respectively)

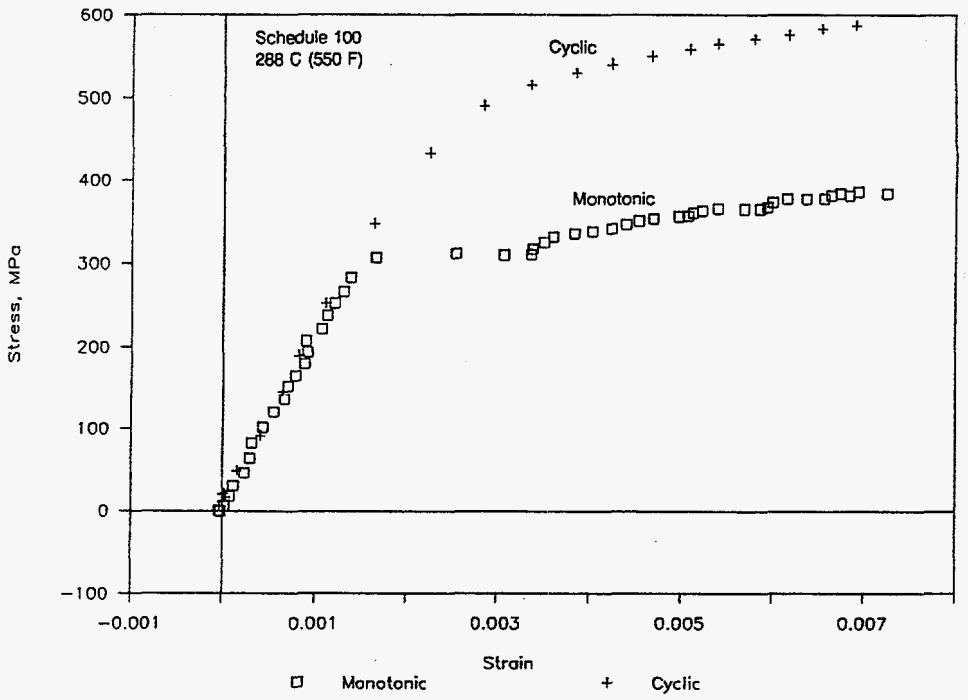

(a) IP-FE11 (Schedule 100)

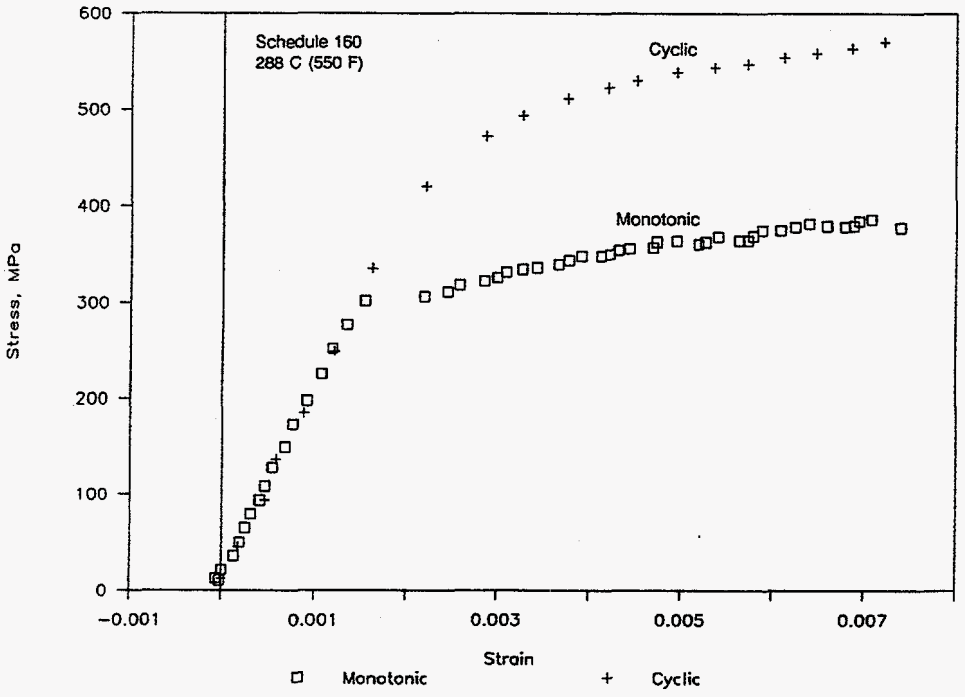

(b) IP-FE12 (Schedule 160)

Figure 2.23 Envelopes of engineering stress-strain curves at 288 C (550 F) from incremental step tests for WPHY-65, Schedule 100 and 160 elbows from Loop No. 2 (IP-FE11 and IP-FE12, respectively)

Table 2.17 Results of monotonic loading and cyclic loading tensile tests for WPHY-65 Schedule 100 and 160 elbows used in Loop No. 2

Specimen Identification Number	Test Temperature, C	F	Monotonic Yield Strength, MPa	ksi	Cyclic Yield Strength, MPa	ksi	Ultimate Tensile Strength, MPa	ksi
Elbow IP-FE11, Schedule 100, Heat H10536								
H-1	288	550	326	47.3	548	79.5	--	--
H-2	288	550	367	53.2	549	79.6	--	--
H-3	288	550	370	53.7	--	--	693	100.5
		Average	354	51.4	548	79.5	693	100.5
H-4	22	72	458	66.4[a]	374	54.2	--	--
H-5	22	72	457	66.3[a]	378	54.8	--	--
		Average	457	66.3[a]	376	54.5		
N.A.[b]	RT	RT	449	65.1	--	--	657	95.3
Elbow IP-FE12, Schedule 160, Heat BO757								
B-1	288	550	344	49.9	537	77.9	--	--
B-2	288	550	339	49.2	534	77.4	--	--
B-3	288	550	361	52.4	--	--	668	96.9
		Average	348	50.5	535	77.7	668	96.9
B-4	22	72	439	63.7[a]	364	52.8	--	--
B-5	22	72	456	66.1[a]	367	53.2	--	--
		Average	447	64.9[a]	365	53.0		
N.A.[b]	RT	RT	448	65.0	--	--	641	93.0

(a) Lower yield point values. These materials exhibited a distinct upper and lower yield point at room temperature.
(b) Tensile properties shown are from manufacturer's mill certifications.

2.3 Monotonic-Loading J-R Curve Test Results

Summary graphs and tables of both quasi-static and dynamic, monotonic-loading J-R curve tests are presented in this section. (The results of a series of quasi-static and dynamic, cyclic-loading C(T) specimen tests for selected Task 1 materials are presented in Section 2.4.) Side-grooved compact tension [C(T)] specimens were machined from the pipes in the L-C orientation which simulates growth of a circumferential through-wall crack. The procedures used to convert the load, load-line displacement, and electric potential data into the J-resistance curves (J versus Δa) presented herein are provided in detail in Reference 2.1.

Actual rates of loading in the C(T) tests, expressed as dJ/dt up to the point of crack initiation, are summarized in Table 2.18. The loading rates in the rapid-loading tests were about 2,500 to 4,500 times faster and averaged approximately 3,700 times faster than those in quasi-static-loading tests.

2.3.1 A106 Grade B Carbon Steel

2.3.1.1 Pipe DP2-F29

Load-displacement curves for C(T) specimens machined from the ASTM A106 Grade B carbon steel pipe material (DP2-F29) and tested at 288 C (550 F) are shown in Figure 2.24. They reveal large effects

Table 2.18 Actual loading rates for tests of C(T) specimens

Pipe Identification Number	Material Type	Approximate dJ/dt, kJ/m²/s (in-lb/in²/s)			$dJ/dt_{RL}/dJ/dt_{QS}$
		Quasi-static	Rapid Loading		
DP2-F29	ASTM A106, Grade B carbon-steel pipe	0.17 (0.97)	420	(2,400)	2,470
DP2-F23	ASTM A106 Grade B carbon-steel pipe	0.14 (0.80)	526	(3,000)	3,680
DP2-F22	ASTM A106 Grade B carbon-steel pipe	0.12 (0.68	362	(2,065)	3,040
DP2-F29W	Submerged-arc girth weld in ASTM A106 Grade B pipe	0.13 (0.74)	520	(2,970)	4,000
DP2-F55W	Submerged-arc weld in carbon-steel plate	0.11 (0.62)	495	(2,820)	4,490
DP2-A8	ASTM A358, Type 304 stainless-steel pipe	1.8 (10.3)	7,250	(41,400)	4,025
DP2-A8W	Submerged-arc girth weld in ASTM A358, Type 304 pipe	0.13 (0.74)	570	(3,250)	4,385
DP2-A45W1	Submerged-arc weld in Type 304 stainless steel plate	0.18 (1.03)	(a)		(a)
DP2-A45W2	Submerged-arc weld in Type 304 stainless steel plate	0.10 (0.57)	(a)		(a)

(a) No dynamic C(T) tests were conducted.

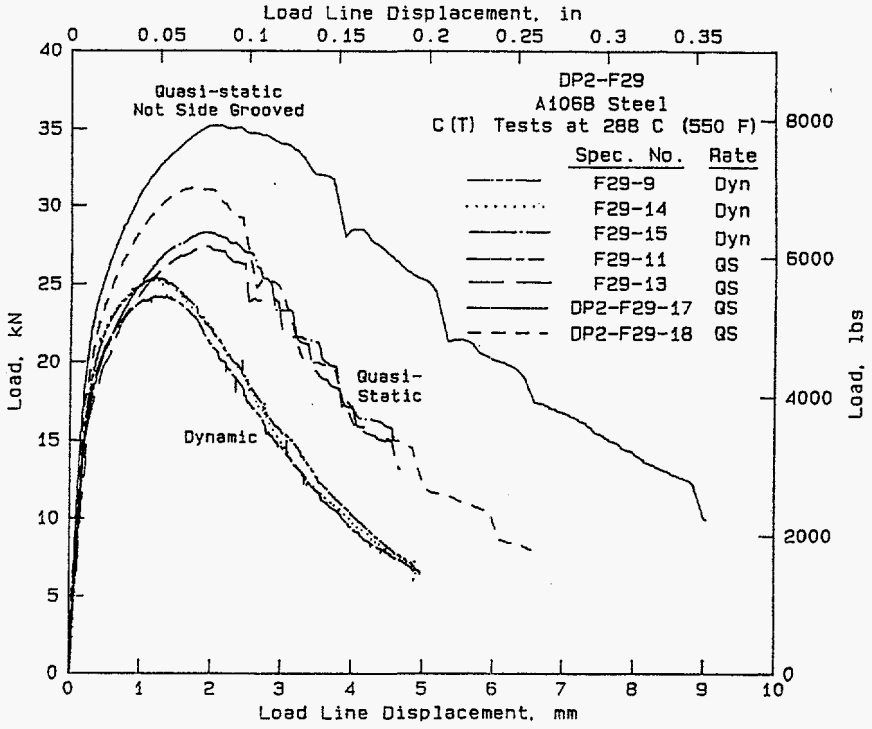

Figure 2.24 Load-displacement curves at 288 C (550 F) for C(T) specimens from A106 Grade B carbon steel pipe (DP2-F29)

of dynamic loading for this pipe, namely, substantial lowering of the load-displacement curve and virtual elimination of significant crack jumps that were observed in the quasi-static tests. The curve that lies above all the others in Figure 2.24 was for a specimen that was not side-grooved (Spec. No. F29-17).

J-resistance curves for this A106B steel are shown in Figure 2.25 and values of J_i and dJ/da are summarized in Table 2.19. For the quasi-static tests, the J-R curves were terminated at the point of the first significant crack jump because there is no agreed-upon method for calculating J during and after a crack instability. It is evident from the results in Figure 2.25 and Table 2.19 that both J_i and dJ/da were lowered as a result of increasing the displacement rate by a factor of approximately 2,500; J_i values decreased by approximately 35 percent and dJ/da values decreased by approximately 45 percent as the displacement rate was increased.

Included for comparison in Figure 2.25 are the ASME Section XI IWB-3650 reference J-R curves for A106 Grade B and A516 Grade 70 carbon steel. Notice that the quasi-static test results for the carbon steel specimens lie slightly below the ASME J-R curve for A106 Grade B steel, and the dynamic test results lie significantly below the J-R curve for A106 Grade B carbon steel and approximately on the ASME curve for A516 Grade 70 carbon steel.

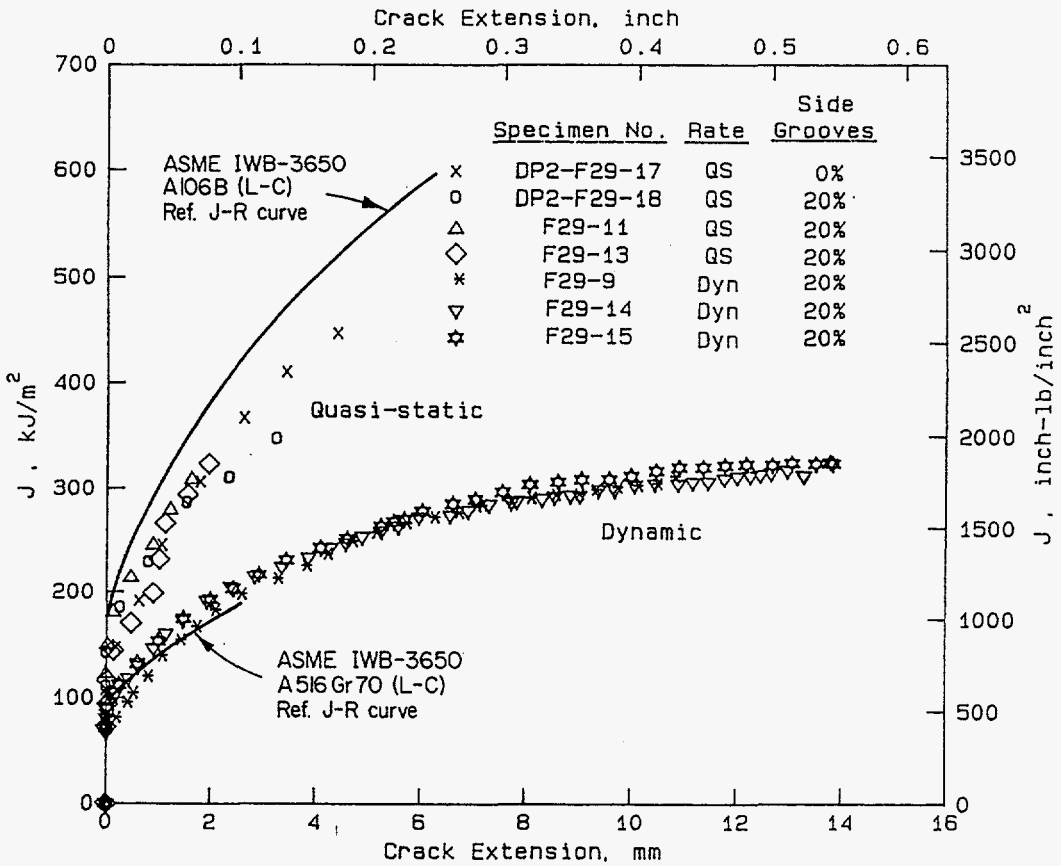

Figure 2.25 J-resistance curves at 288 C (550 F) for compact specimens from A106 Grade B carbon steel pipe (DP2-F29)

Table 2.19 J_i and dJ/da values at 288 C (550 F) for C(T) specimens from A106 Grade B carbon steel pipe (DP2-F29)

Specimen Identification Number	Percent Side-Grooves	Rate[a]	J at Initiation, kJ/m^2	J at Initiation, $in\text{-}lb/in^2$	dJ/da, MJ/m^3	dJ/da, $in\text{-}lb/in^3$
F29-17	0	QS	111	635	113	16,410
F29-18	20	QS	149	850	89	12,910
F29-11	20	QS	147	840	100	14,550
F29-13	20	QS	92	525	125	18,200
F29-9	20	Dyn	68	390	62	8,930
F29-14	20	Dyn	88	505	55	8,020
F29-15	20	Dyn	89	510	56	8,140

(a) QS = quasi-static; Dyn = dynamic.

2.3.1.2 Pipe DP2-F23

Load-displacement curves for 1T C(T) specimens machined from Pipe DP2-F23 and tested at 288 C (550 F) are shown in Figure 2.26. Notice that neither of the loading rates resulted in crack jumps, such as were evident in specimens machined from Pipe DP2-F29. However, the specimens subjected to dynamic loading exhibited load-displacement curves that were slightly below those for specimens subjected to quasi-static loading.

J-resistance curves are shown in Figure 2.27 and values of J_i and dJ/da are summarized in Table 2.20. Increasing the displacement rate appears to cause a modest increase in the J_i values and a modest decrease in the dJ/da values for this A106 Grade B pipe material.

2.3.1.3 Pipe DP2-F22

Load-displacement curves for 0.5T planform C(T) specimens, 9.1 mm (0.36 inch) thick, machined from Pipe DP2-F22 and tested at 288 C (550 F) are shown in Figure 2.28 and J-R curves are shown in Figure 2.29. Values of J_i and dJ/da are summarized in Table 2.21. For this A106 Grade B pipe, increasing the displacement rate had a marked effect on the shape of the load-displacement curve and lowered both the value of J at crack initiation and the value of dJ/da. Also, as shown by the load drops in Figure 2.28, dynamic loading produced several crack jumps that were not evident at quasi-static loading rates.

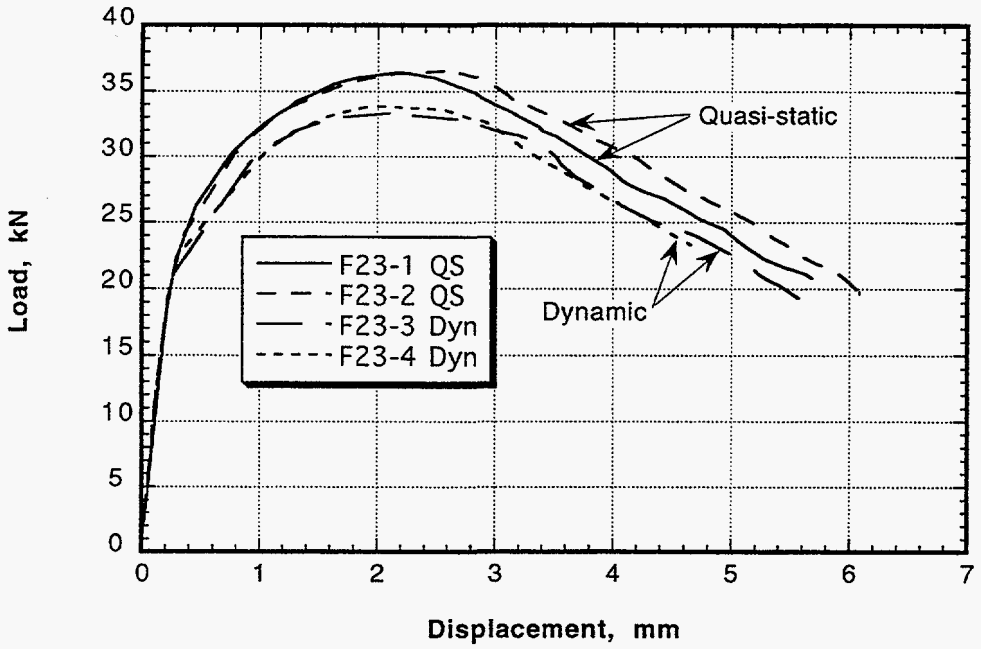

Figure 2.26 Load-displacement curves at 288 C (550 F) for C(T) specimens from A106 Grade B carbon steel pipe (DP2-F23)

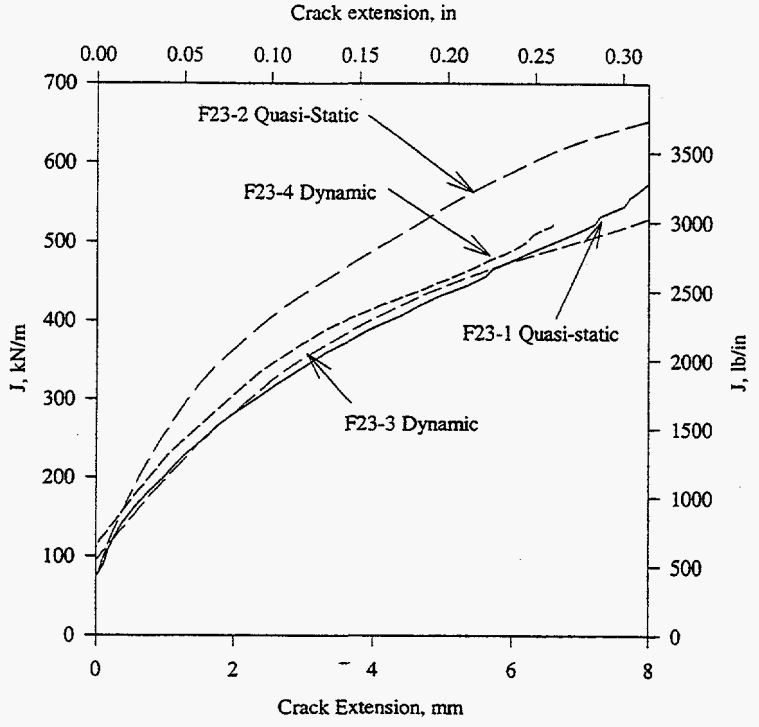

Figure 2.27 J-resistance curves at 288 C (550 F) for C(T) specimens from A106 Grade B carbon steel pipe (DP2-F23)

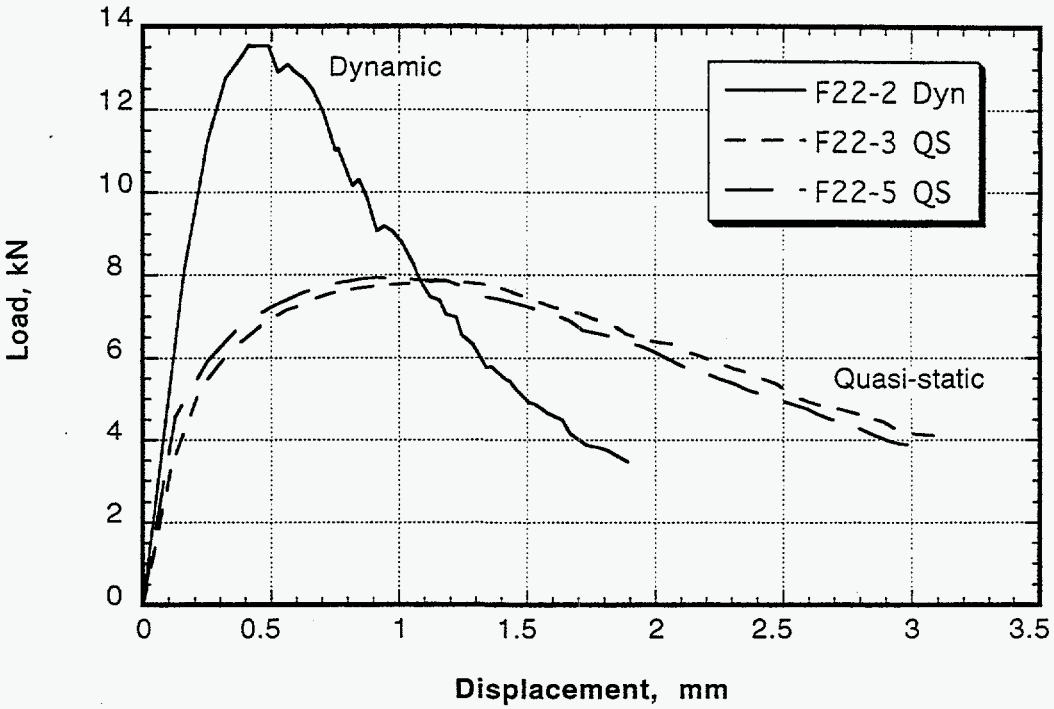

Figure 2.28 Load-displacement curves at 288 C (550 F) for C(T) specimens from A106 Grade B carbon steel pipe (DP2-F22)

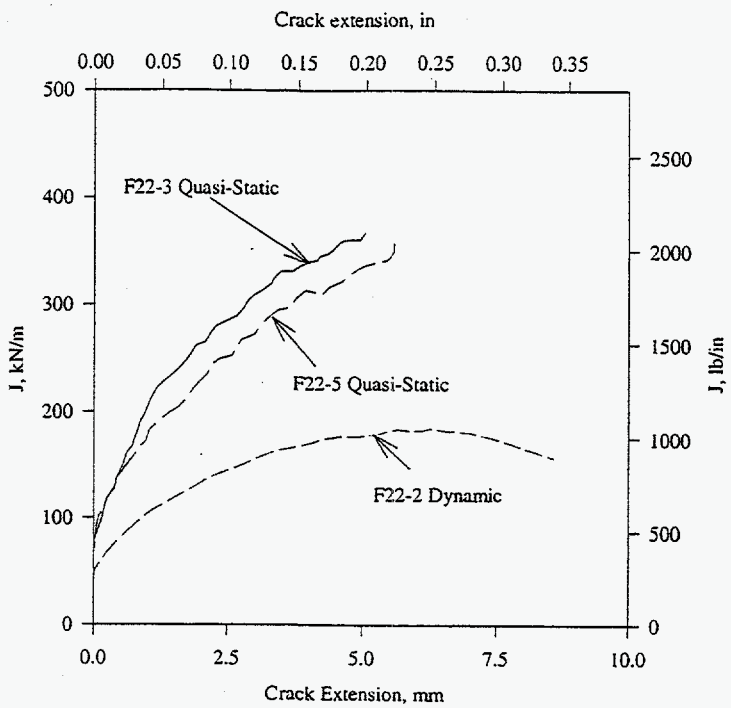

Figure 2.29 J-resistance curves at 288 C (550 F) for C(T) specimens from A106 Grade B carbon steel pipe (DP2-F22)

Table 2.20 J_i and dJ/da values at 288 C (550 F) for ASTM A106 Grade B carbon steel pipe (DP2-F23)

Specimen Identification Number	Rate	J at Initiation, kJ/m^2	J at Initiation, in-lb/in^2	dJ/da[a], MJ/m^2	dJ/da[a], in-lb/in^3
DP2-F23-1	Quasi-static	74.3	424	104.6	15,170
DP2-F23-2	Quasi-static	69.3	396	159.5	23,130
DP2-F23-3	Dynamic	94.9	542	98.5	14,290
DP2-F23-4	Dynamic	115.4	659	99.5	14,440

(a) Determined for crack extension between 0.15 and 1.5 mm (0.006 and 0.06 inch).

Table 2.21 J_i and dJ/da values at 288 C (550 F) for ASTM A106 Grade B carbon steel pipe (DP2-F22)

Specimen Identification Number	Rate	J at Initiation, kJ/m^2	J at Initiation, in-lb/in^2	dJ/da[a], MJ/m^3	dJ/da[a], in-lb/in^3
DP2-F22-3	Quasi-static	77.1	440	108.3	15,710
DP2-F22-5	Quasi-static	65.3	373	94.2	13,660
DP2-F22-2	Dynamic	43.6	249	42.7	6,190

(a) Determined for crack extension between 0.15 and 1.5 mm (0.006 and 0.06 inch).

2.3.2 Type 304 Stainless Steel

J-resistance curves for L-C orientation C(T) specimens machined from the ASTM A358, Type 304 stainless pipe materials (DP2-A8I and DP2-A8II) are presented in Figure 2.30 and values of J_i and dJ/da are summarized in Table 2.22. Note, unlike the tensile test results, the J-R curves for the two heats of DP2-A8, i.e., DP2-A8I and DP2-A8II, were substantially different. The value of J at crack initiation (J_i) for DP2-A8I was approximately 60 percent higher than the J_i value for DP2-A8II at both quasi-static and dynamic loading rates. The results for both heat of materials show that increasing the displacement rate by a factor of approximately 4000 raised J_i significantly but had little effect on dJ/da.

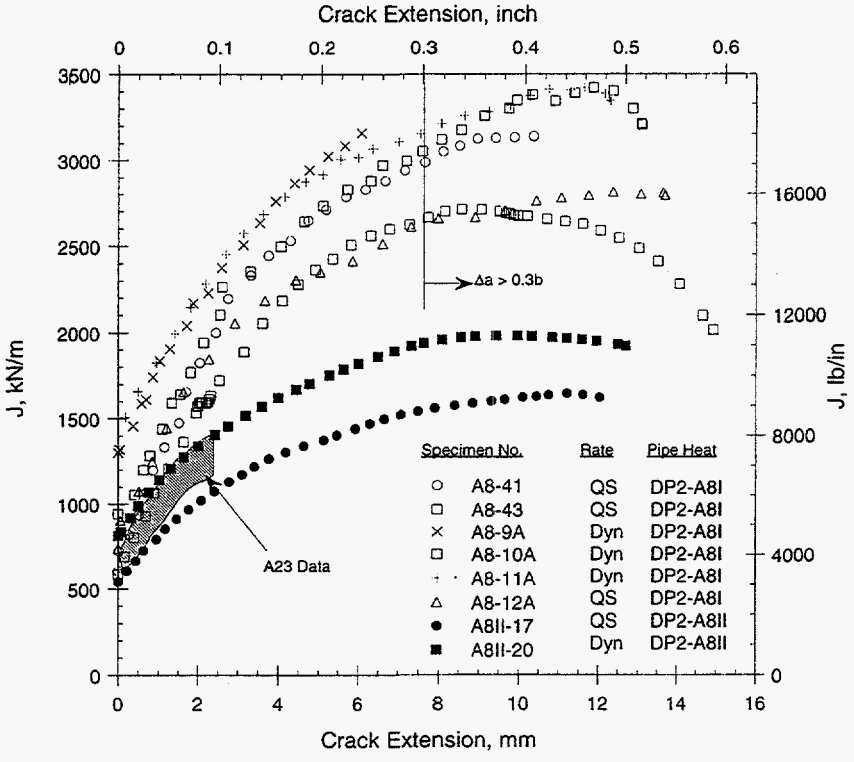

Figure 2.30 J-resistance curves at 288 C (550 F) for C(T) specimens from A358 Type 304 stainless steel pipes (DP2-A8I and DP2-A8II)

Table 2.22 J_i and dJ/da values at 288 C (550 F) for ASTM A358, Type 304 stainless steel pipes (DP2-A8I and DP2-A8II)

Specimen Ident. Number	Pipe/Heat Ident. Number	Percent Side-Grooves	Rate[a]	J at Initiation, kJ/m²	J at Initiation, in-lb/in²	dJ/da, MJ/m³	dJ/da, in-lb/in³
A8-41	A8I	0	QS	710	4,050	610	88,500
A8-43	A8I	20	QS	623	3,555	524	76,000
A8-12a	A8I	20	QS	854	4,875	481	69,720
A8II-17	A8II	20	QS	546	3,120	264	38,300
A8-9a	A8I	20	Dyn	1,302	7,430	500	72,470
A8-10a	A8I	20	Dyn	943	5,385	566	82,060
A8-11a	A8I	20	Dyn	1,399	7,985	388	56,320
A8II-20	A8II	20	Dyn	815	4,655	326	47,300

(a) QS = quasi-static, Dyn = dynamic.

Also shown for comparison in Figure 2.30 are results for a smaller-diameter 6-inch Type 304 stainless steel pipe (DP2-A23) tested in IPIRG-1 Subtasks 1.1 and 1.2. Notice that for most specimens, the larger pipe (DP2-A8) exhibited somewhat greater toughness than did the smaller pipe (DP2-A23).

2.3.3 Carbon Steel Submerged-Arc Welds

2.3.3.1 Pipe Weld DP2-F29W

Load-displacement curves are shown in Figure 2.31 for C(T) specimens machined from submerged-arc weld material (DP2-F29W) in ASTM A106 Grade B carbon steel pipe. The curves are seen to be similar up to maximum load but thereafter the curves for dynamic-loading-rate tests are substantially above the curve for the single quasi-static-loading-rate test.

J-resistance curves are shown in Figure 2.32 and values of J_i and dJ/da are summarized in Table 2.23, which show that both J_i and dJ/da were increased approximately 50 percent as a result of increasing dJ/dt by a factor of approximately 4,000. These results for weld metal are in marked contrast to those for carbon steel base metals (DP2-F29, -F23, and F-22; see Tables 2.19, 2.20, and 2.21) where dynamic loading tended to decrease dJ/da in each of the three carbon steels and to decrease J_i in two of the three (DP2-F29 and -F22).

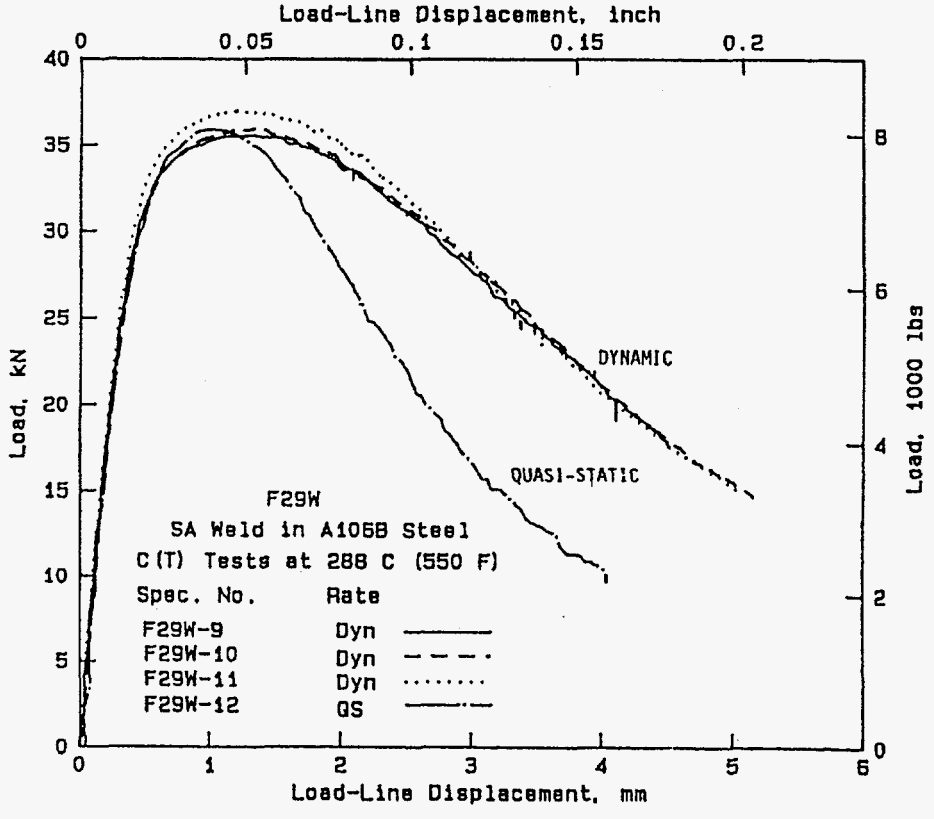

Figure 2.31 Load-displacement curves at 288 C (550 F) for C(T) specimens from a submerged-arc weld (DP2-F29W) in an A106 Grade B carbon steel pipe

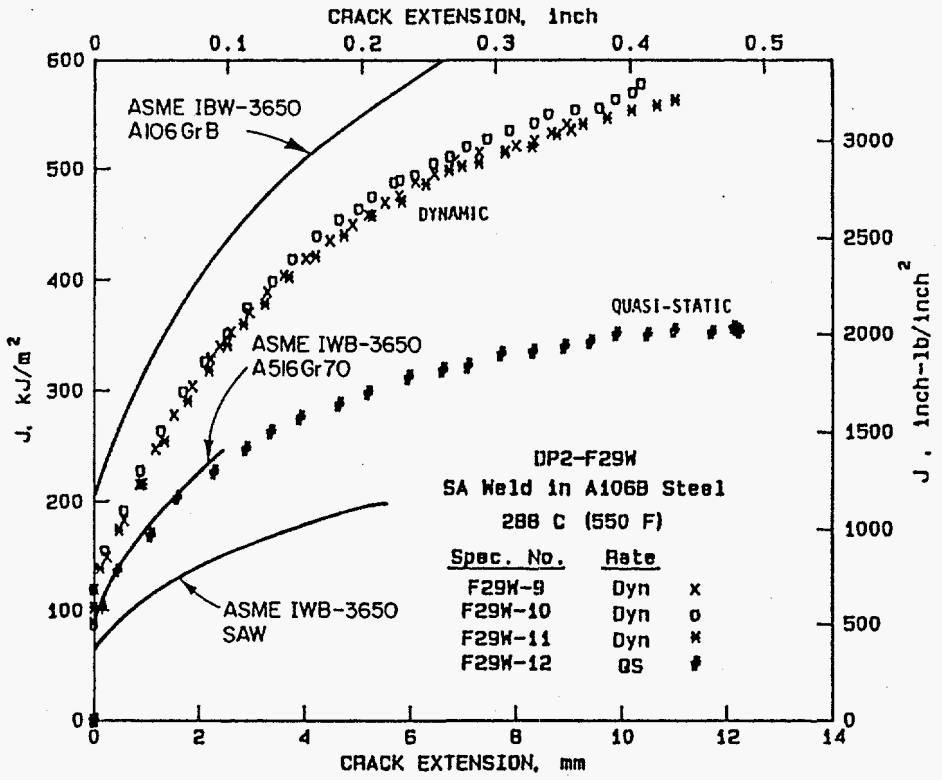

Figure 2.32 J-resistance curves at 288 C (550 F) for C(T) specimens from a submerged-arc weld (DP2-F29W) in an A106 Grade B carbon steel pipe

Table 2.23 J_i and dJ/da values at 288 C (550 F) for submerged-arc weld (DP2-F29W) in ASTM A106 Grade B carbon steel pipe

Specimen Identification Number	Percent Side-Grooves	Rate[a]	J at Initiation, kJ/m²	J at Initiation, in-lb/in²	dJ/da, MJ/m³	dJ/da, in-lb/in³
F29W-12	20	QS	82.3	470	68.0	9,860
F29W-9	20	Dyn	118	675	109	15,760
F29W-10	20	Dyn	131	745	102	14,820
F29W-11	20	Dyn	127	725	93.9	13,620

(a) QS = quasi-static, Dyn = dynamic.

Also shown in Figure 2.32 are the ASME IWB-3650 J-R curves for two ferritic steel base metals and a ferritic steel submerged-arc weld. The ASME curve for the submerged-arc weld in Figure 2.32 is based on results obtained in the Degraded Piping Program in which a weld was prepared in a 25.4 mm (1 inch) plate of A516 Grade 70 steel, using the same procedures as for the weld studied here. J-R curves for 1T C(T) specimens machined from that earlier weld can be found in Figures 3.3.17 and 3.3.18 of Reference 2.8. Note in Figure 2.32 that the data from both quasi-static and dynamic tests on specimens machined from Pipe Weld DP2-F29W lie above the ASME curve for a submerged-arc weld and, even in the worst case (quasi-static tests), are approximately equal to the ASME curve for A516 Grade 70 base metal.

2.3.3.2 Plate Weld DP2-F55W

Three 0.5T side-grooved C(T) specimens were tested at 288 C (550 F); one of the tests was conducted at a quasi-static-loading rate and the other two were conducted at dynamic loading rates. Each specimen was machined from the plate weld such that the crack growth direction was along the centerline of the weld. Load-displacement curves for the three tests are shown in Figure 2.33. As was the case for the pipe weld, DP2-F29W, dynamic testing of the plate weld metal raised the load-displacement curve significantly.

J-resistance curves are shown in Figure 2.34 and values of J_i and dJ/da are summarized in Table 2.24. These results indicate that J_i was increased approximately 50 percent and dJ/da was increased approximately 100 percent as a result of increasing the displacement rate by a factor of approximately 4,500.

2.3.4 Stainless Steel Submerged-Arc Welds

2.3.4.1 Pipe Weld DP2-A8W

J-resistance curves for L-C oriented C(T) specimens machined from submerged-arc weld metal (DP2-A8W) in ASTM A358 Type 304 stainless steel pipe are presented in Figure 2.35, and values of J_i and dJ/da are summarized in Table 2.25. The results indicate that the submerged-arc weld was affected

Table 2.24 J_i and dJ/da values at 288 C (550 F) for a submerged-arc weld (DP2-F55W) in a carbon steel plate

Specimen Identification Number	Rate[a]	J at Initiation, kJ/m²	J at Initiation, in-lb/in²	dJ/da[b], MJ/m²	dJ/da[b], in-lb/in³
DP2-F55W-2	QS	65.4	373	46.3	6,720
DP2-F55W-3	Dyn	91.3	521	86.2	12,500
DP2-F55W-4	Dyn	106.0	605	99.3	14,400

(a) QS = Quasi-static; Dyn = Dynamic.
(b) Determined for crack growth of 0.15 mm to 1.5 mm (0.006 inches to 0.060 inch).

Table 2.25 J_i and dJ/da values at 288 C (550 F) for a submerged-arc weld (DP2-A8W) in an ASTM A358, Type 304 stainless steel pipe

Specimen Identification Number	Percent Side-Grooves	Rate[a]	J at Initiation, kJ/m²	J at Initiation, in-lb/in²	dJ/da, MJ/m³	dJ/da, in-lb/in³
A8W-110	20	QS	55	315	135	19,550
A8W-107	20	Dyn	140	800	180	26,140
A8W-108	20	Dyn	116	660	205	29,700
A8W-111	20	Dyn	(b)	(b)	(b)	(b)

(a) QS = quasi-static, Dyn = dynamic.
(b) No electric potential data were obtained for Specimen No. A8W-111; hence, the J-R curve could not be calculated.

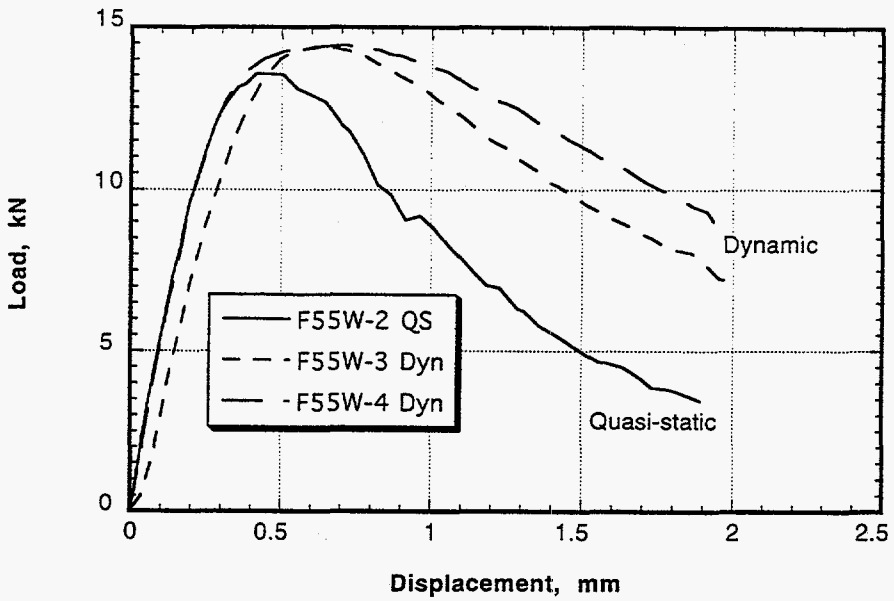

Figure 2.33 Load-displacement curves at 288 C (550 F) for C(T) specimens from a submerged-arc weld (DP2-F55W) in a carbon steel plate

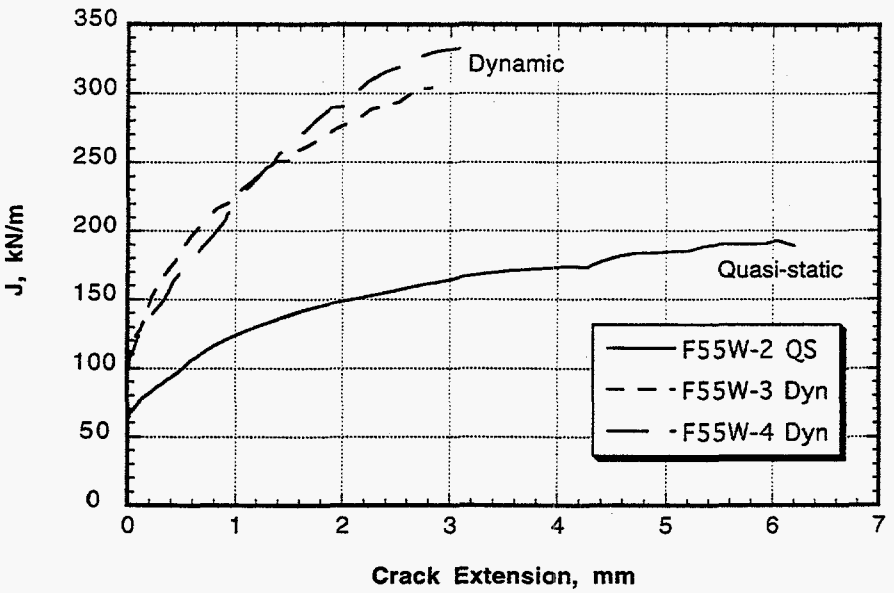

Figure 2.34 J-resistance curves at 288 C (550 F) for C(T) specimens from a submerged-arc weld (DP2-F55W) in a carbon steel plate

somewhat more than was the base metal when the displacement rate was increased by a factor of approximately 4,400. J_i was more than doubled and dJ/da was increased by about 40 percent as a result of dynamic loading. Notice also in Figure 2.35 that the toughness of this submerged-arc weld metal was much lower than that of the base metal. That finding is in agreement with results obtained for Type 304 plate material, both base metal and submerged-arc weld metal, in the Degraded Piping Program (Ref. 2.8). The submerged-arc weld in Reference 2.8 was made by the same procedures as were used in this program and exhibited quasi-static J-R curves in 1T C(T) specimens that were very similar to that for the stainless steel weld studied here, whose quasi-static J-R curve is shown in Figure 2.35 (see Figures 3.3.14 and 3.3.15 in Reference 2.8).

2.3.4.2 Plate Weld DP2-A45W1

1T C(T) specimens were machined from Plate Weld DP2-A45W1 such that the crack growth direction was along the weld centerline. Unlike the C(T) specimens machined from Pipe Weld DP2-A8W, the specimens from plate weld DP2-A45W1 contained no side grooves. Two specimens were tested using quasi-static loading at 288 C (550 F). No dynamic-loading rate tests were conducted on this weld.

J-resistance curves for the nonside-grooved specimens tested quasi-statically at 288 C (550 F) are shown in Figure 2.36. These curves are seen to lie above those in Figure 2.35 for Pipe Weld DP2-A8W, but that

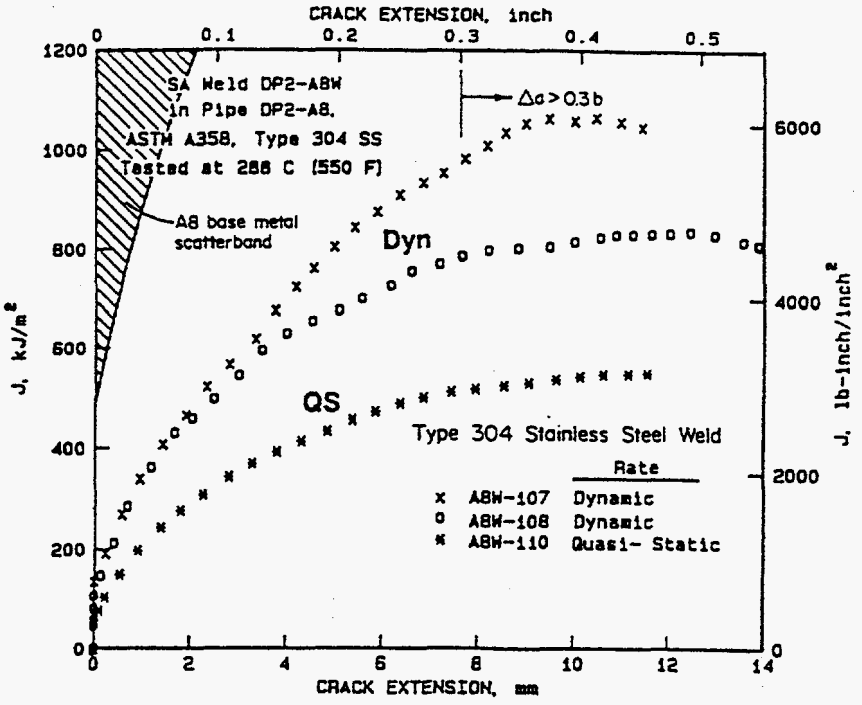

Figure 2.35 J-resistance curves at 288 C (550 F) for compact specimens from a submerged-arc weld (DP2-A8W) in a A358 Type 304 stainless steel pipe

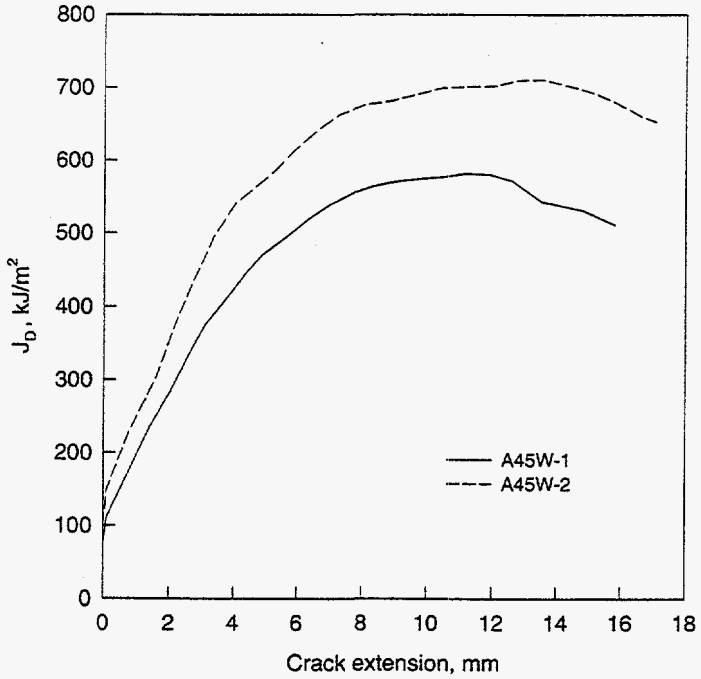

Figure 2.36 J-resistance curves at 288 C (550 F) for nonside-grooved 1T C(T) specimens from a submerged-arc weld (DP2-A45W1) in a Type 304 stainless steel plate

result would be expected because the specimens for the plate weld were not side grooved. Values of J_i and dJ/da are summarized in Table 2.26.

Table 2.26 J_i and dJ/da values at 288 C (550 F) for nonside-grooved 1T C(T) specimens from a submerged-arc weld (DP2-A45W1) in a Type 304 stainless steel plate

Specimen Identification Number	Percent Side-Grooves	J at Initiation, kJ/m^2	J at Initiation, in-lb/in^2	dJ/da,[a] MJ/m^3	dJ/da,[a] in-lb/in^3
A45W-1	0	96.0	548	103.6	15,030
A45W-2	0	120.0	684	114.3	16,570

(a) Calculated for crack extension between 0.15 and 1.5 mm (0.006 and 0.060 inch).

2.3.4.3 Plate Weld DP2-A45W2

1T C(T) specimens were machined from Plate Weld DP2-A45W2 such that the crack growth direction was along the centerline of the weld. Three specimens were side grooved 20 percent and three were not side grooved. One specimen from each group was tested at a quasi-static-loading rate at room temperature and two were tested quasi-statically at 288 (550 F). No dynamic-loading-rate tests were conducted on this weld.

J-resistance curves are shown in Figure 2.37 for the nonside-grooved specimens and in Figure 2.38 for the side-grooved specimens. J_i and dJ/da values are summarized in Table 2.27. Notice that the J-R curves in both figures were lowered significantly by increasing the test temperature from room temperature to 288 C (550 F). Notice also that the J-R curves at 288 C (550 F) for the side-grooved specimens in Figure 2.38 lie above that for Pipe Weld DP2-A8W in Figure 2.35.

Table 2.27 J_i and dJ/da values at 288 C (550 F) for C(T) specimens from a submerged-arc weld (DP2-A45W2) in a Type 304 stainless steel plate

Specimen Identification Number	Test Temperature, C	F	Percent Side-Grooves	J at Initiation, kJ/m²	in-lb/in²	dJ/da, MJ/m³	in-lb/in³
A45W2-1	20	68	20	114	649	334	48,400
A45W2-2	288	550	20	58	332	169	24,500
A45W2-3	288	550	20	61	350	152	22,000
A45W2-4	20	68	0	106	605	289	41,900
A45W2-5	288	550	0	38	215	111	16,100
A45W2-6	288	550	0	57	326	183	26,600

2.4 Cyclic-Load J-R Curve Test Results

Summary graphs and tables for both quasi-static and dynamic, cyclic-load J-R curve tests conducted at 288 C (550 F) for selected Task 1 materials are presented in this section. The materials for which cyclic-load J-R curve tests were conducted were the stainless steel base metals (DP2-A8I and DP2-A8II), the stainless steel SAW (DP2-A8W), and the carbon steel SAW (DP2-F40W).

2.4.1 Stainless Steel Base Metals (DP2-A8I and DP2-A8II)

Six cyclically-loaded and eight monotonically-loaded C(T) specimen tests were conducted at 288 C (550 F) on these stainless steel materials. For four of the cyclically-loaded specimens, the stress ratio (R) was -0.3 and for the other two it was -1. Each specimen was tested with a fixed cyclic-displacement increment (δ_{cyc}/δ_i) equal to 0.1. Stable crack growth occurred throughout each test.

Figure 2.39 shows the quasi-static, monotonic-loading and quasi-static, cyclic-loading J-R curves for these materials. Table 2.28 shows fracture toughness values (i.e., J_i and dJ/da values) taken from the J-R curves. The bar graphs in Figure 2.40 summarize the effect of cyclic loading on fracture toughness. Note that they contain a third toughness parameter (J at 2 mm of crack extension) in addition to J_i and dJ/da. From Figures 2.39 and 2.40 and Table 2.28, it is clear that the material DP2-A8II was more strongly affected by cyclic loading than was material DP2-A8I. The effect was especially pronounced at dynamic rates (comparing the change in J_i values from the dynamic, monotonic test (A8II-20) to the dynamic cyclic, R = -0.3 test (A8II-15) with the change in J_i values from the quasi-static, monotonic test (A8II-17) to the quasi-static, cyclic, R = -0.3 test (A8II-21). The effect of cyclic loading was also much more pronounced at the R = -1 condition than it was at the R = -0.3 condition for both materials.

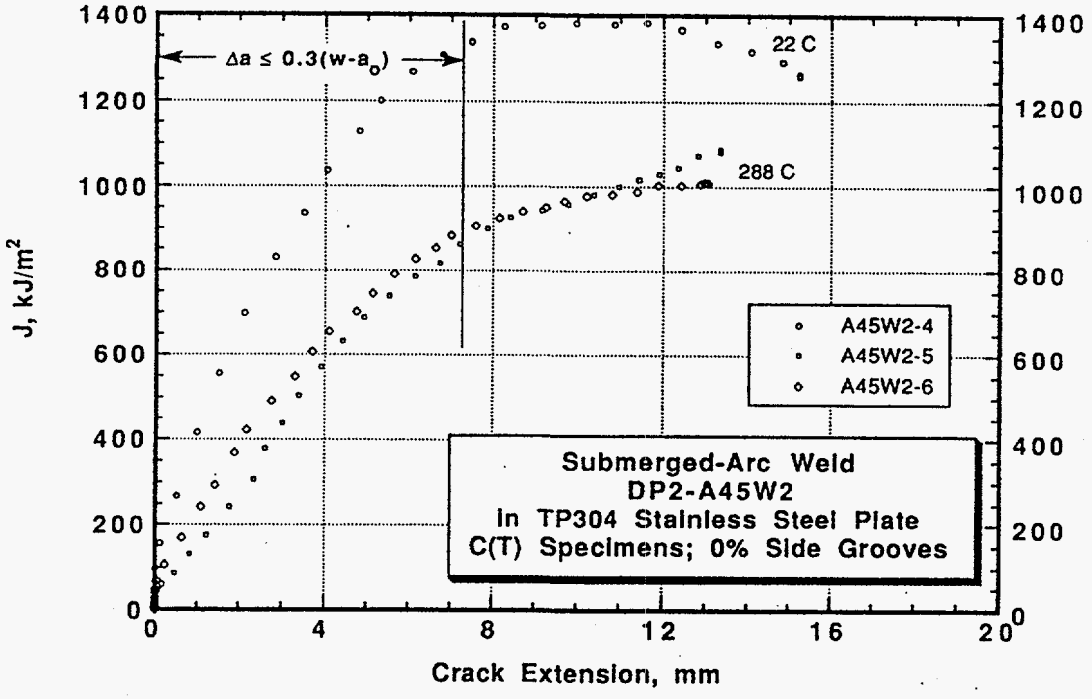

Figure 2.37 J-resistance curves at 288 C (550 F) for nonside-grooved C(T) specimens from a submerged-arc weld (DP2-A45W2) in a Type 304 stainless steel plate

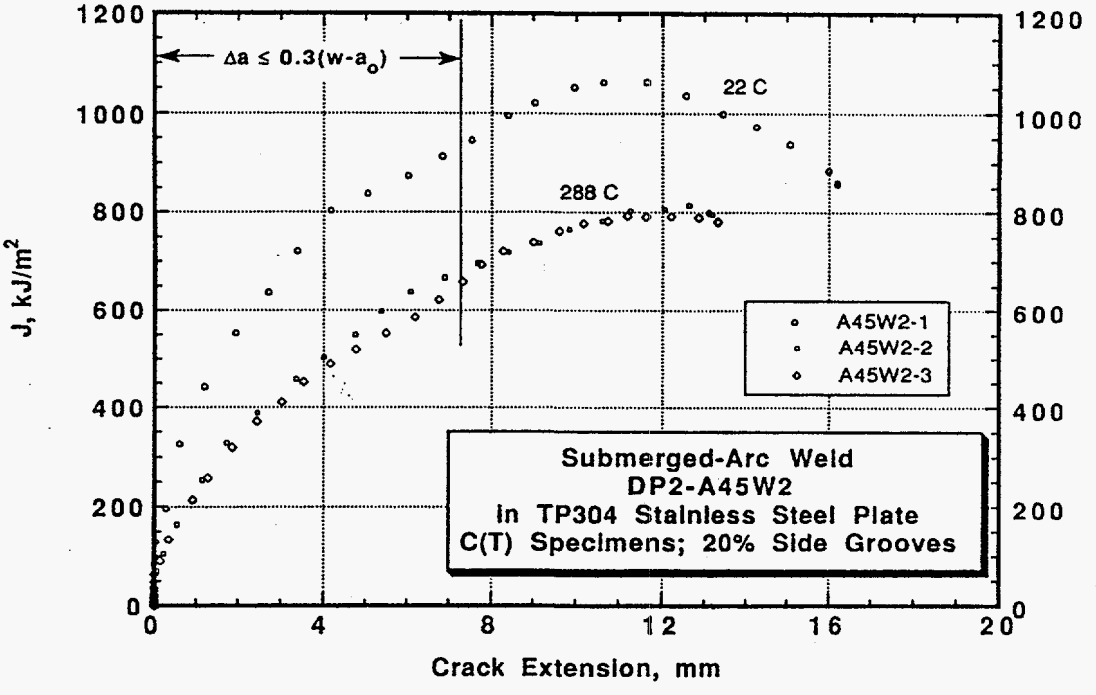

Figure 2.38 J-resistance curves at 288 C (550 F) for side-grooved C(T) specimens from a submerged-arc weld (DP2-A45W2) in a Type 304 stainless steel plate

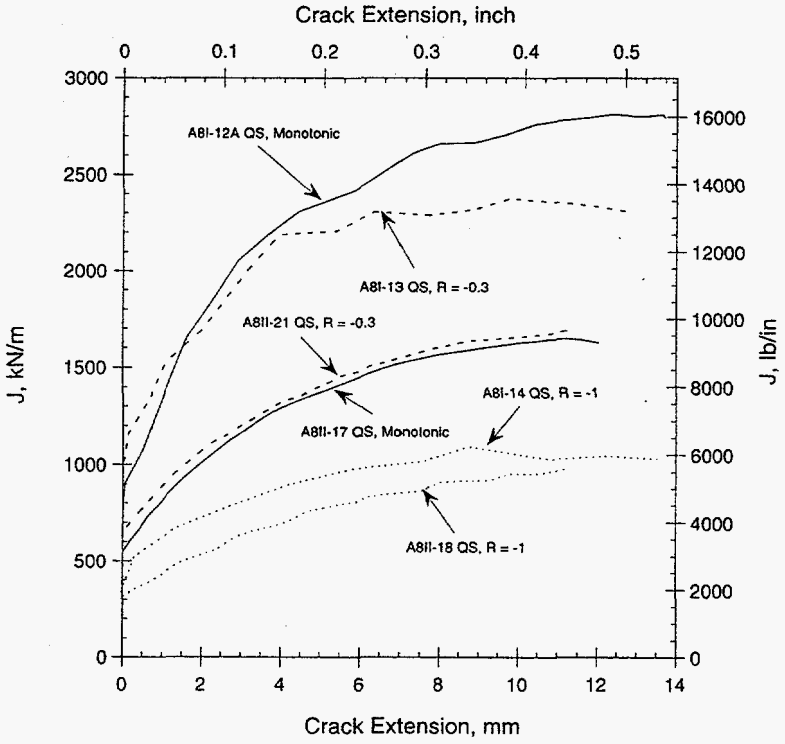

Figure 2.39 Quasi-static, monotonic and quasi-static, cyclic loading J-R curves at 288 C (550 F) for the two A358 Type 304 stainless steel pipes (DP2-A8I and DP2-A8II)

Table 2.28 C(T) specimen fracture toughness summary for ASTM A358, Type 304 stainless steel pipes (DP2-A8I and DP2-A8II) tested quasi-statically at 288 C (550 F)

Specimen Ident. Number	Pipe/Heat Ident. Number	Cyclic History	J at Initiation		dJ/da	
			kJ/m^2	in-lb/in^2	MJ/m^3	in-lb/in^3
A8-41[a]	A8I	QS R = 1	710	4,050	610	88,500
A8-43	A8I	QS R = 1	623	3,555	524	76,000
A8-12a	A8I	QS R = 1	854	4,875	481	69,270
A8II-17	A8II	QS R = 1	546	3,120	264	38,300
A8-13	A8I	QS R = -0.3	952	5,435	287	41,600
A8-14	A8I	QS R = -1	356	2,032	214	31,000
A8II-21	A8II	QS R = -0.3	652	3,723	240	34,800
A8II-18	A8II	QS R = -1	313	1,787	114	16,500
A8-9a	A8I	Dyn R = 1	1,302	7,430	500	72,470
A8-10a	A8I	Dyn R = 1	943	5,385	566	82,060
A8-11a	A8I	Dyn R = 1	1,399	7,985	388	56,320
A8II-20	A8II	Dyn R = 1	815	4,655	326	47,300
A8I-22	A8I	Dyn R = -0.3	1,297	7,405	334	48,440
A8II-15	A8II	Dyn R = -0.3	395	2,255	123	17,840

(a) Not side grooved.

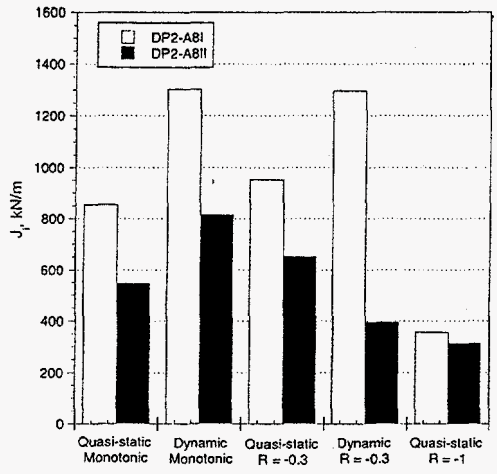

(a) J_i

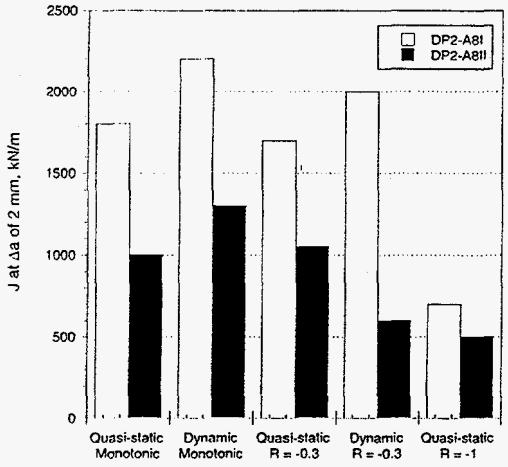

(b) J at 2 mm of crack extension

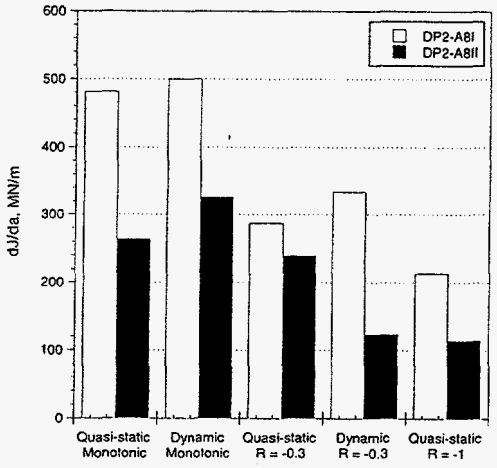

(c) dJ/da

Figure 2.40 Fracture resistance parameters at 288 C (550 F) for the ASTM A358, Type 304 stainless steel pipes (DP2-A8I and DP2-A8II)

2.4.2 Stainless Steel SAW (DP2-A8W)

A total of seven cyclic-load C(T) specimen tests were conducted at 288 C (550 F) on this stainless steel weld material, four at quasi-static-loading rates and three at dynamic-loading rates. Each specimen was sidegrooved 10 percent per side to insure that the crack remained in the original crack plane. The stress ratios for these tests were -0.6 and -1.0. Duplicate tests were conducted for all combinations of loading rate and stress ratio, except for the dynamic, R = -0.6 condition, where only one specimen was tested. All specimens were tested with a fixed cyclic displacement increment (δ_{cyc}/δ_i) equal to 0.1. Stable crack growth occurred throughout each test.

Figures 2.41 and 2.42 show the quasi-static- and dynamic-loading-rate J-R curves, respectively, for this stainless steel SAW (DP2-A8W). Table 2.29 shows fracture toughness values (i.e., J_i and dJ/da values) from the graphs. The figures and table include the results from both monotonic and cyclic tests, for comparison purposes. As can be seen, there is a noticeable variability in toughness between certain specimens tested under nominally identical conditions. The differences in results between the two dynamic, monotonic-load tests and between the two quasi-static-load, R = -1 tests are especially large. These differences may be due to inhomogeneities in the weld metal.

Table 2.29 Fracture toughness summary for submerged-arc weld (DP2-A8W) in ASTM A358, Type 304 stainless steel pipe tested at 288 C (550 F)

Specimen Identification Number	Loading Rate	Stress Ratio, R	δ_{cyc}/δ_i	J at Initiation, kJ/m²	J at Initiation, in-lb/in²	dJ/da, MJ/m³	dJ/da, in-lb/in³
A8W-110	QS	1	N/A	55	315	135	19,550
A8W-107	Dyn	1	N/A	140	800	180	26,140
A8W-108	Dyn	1	N/A	116	660	205	29,700
A8W-101c	QS	-1	0.1	39	225	30.2	4,380
A8W-102c	QS	-1	0.1	57	328	38.3	5,560
A8W-103c	QS	-0.6	0.1	46	265	72.9	10,570
A8W-104c	QS	-0.6	0.1	59	336	62.6	9,080
A8W-106c	Dyn (4Hz)	-1	0.1	47	254	55.0	7,980
A8W-107c	Dyn (4Hz)	-1	0.1	34	192	46.8	6,790
A8W-108c	Dyn (4Hz)	-0.6	0.1	61	343	72.6	10,529

Figure 2.43 summarizes the effects of cyclic and dynamic loading on three different fracture toughness parameters. In this figure, the values from the duplicate specimens have been averaged. Looking first at the effects of cyclic loading at a quasi-static rate, J_i was lowered only slightly at R = -0.6 and R = -1. However, both J at 2 mm of crack extension and dJ/da were lowered significantly by cyclic loading, with

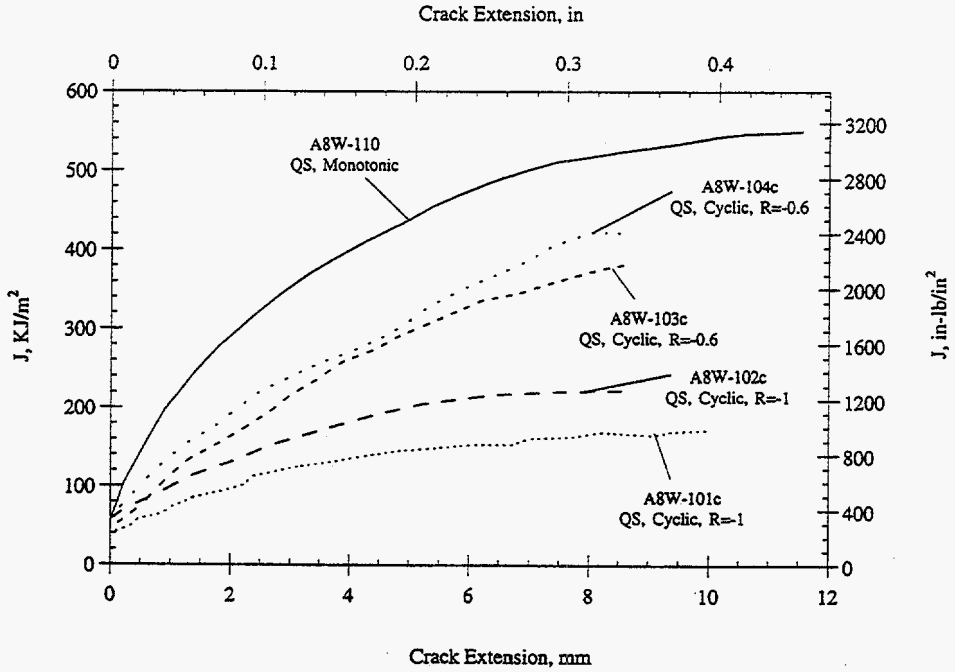

Figure 2.41 Quasi-static, monotonic loading and quasi-static, cyclic loading J-R curves at 288 C (550 F) for a submerged-arc weld (DP2-A8W) in an ASTM A358, Type 304 stainless steel pipe

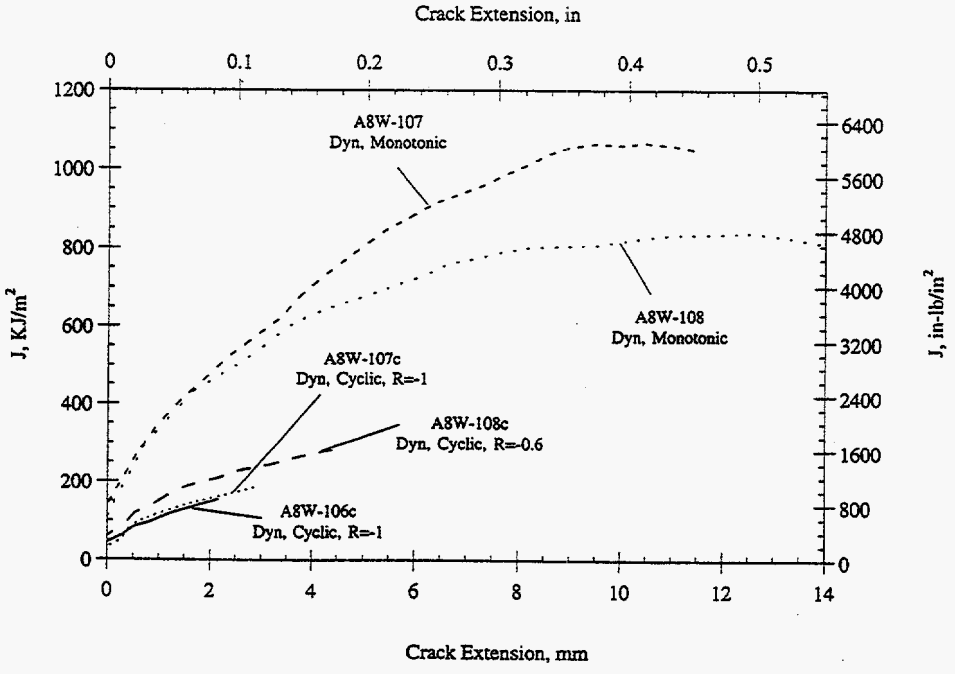

Figure 2.42 Dynamic, monotonic loading and dynamic, cyclic loading J-R curves at 288 C (550 F) for a submerged-arc weld (DP2-A8W) in an ASTM A358, Type 304 stainless steel pipe

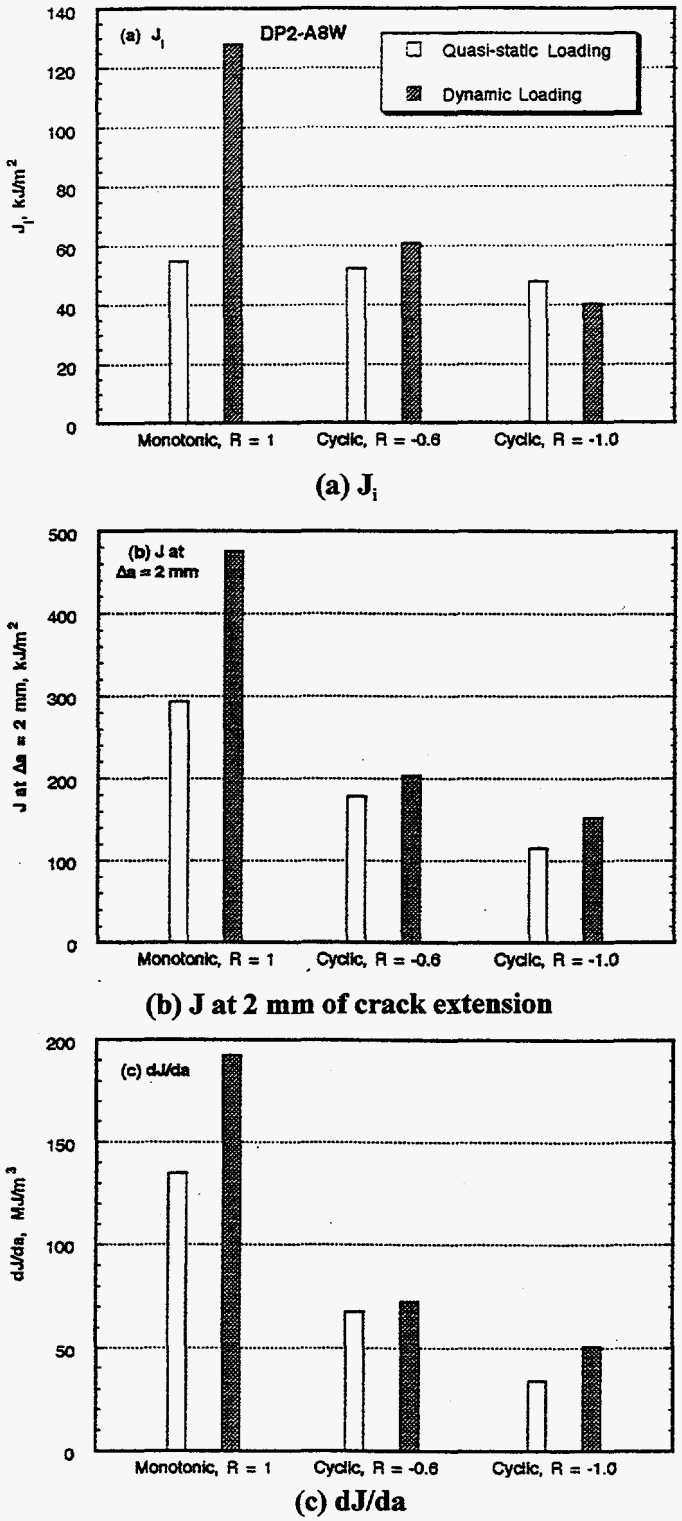

Figure 2.43 Fracture resistance parameters at 288 C (550 F) for a submerged-arc weld (DP2-A8W) in an ASTM A358, Type 304 stainless steel pipe

the effect becoming more severe as R became more negative. With respect to dynamic-loading effects, large increases in each toughness parameter were observed in the monotonic loading tests. In the cyclic tests, dynamic loading produced small beneficial effects on toughness relative to quasi-static loading, except for J_i at R = -1, where a small detrimental effect was observed.

The results from these cyclic-load tests indicate that the damage done by the cyclic loading outweighs the beneficial effects of dynamic loading for this material.

2.4.3 Carbon Steel SAW (DP2-F40W)

A total of seven cyclic-load C(T) specimens tests were conducted on this carbon steel weld material at 288 C (550 F), three at quasi-static-loading rates and four at dynamic-loading rates. Each test specimen was sidegrooved 10 percent per side to ensure that the crack remained in the original plane of the crack. The stress ratios for these tests were -0.6 and -1.0. Duplicate tests were conducted for all combinations of loading rate and stress ratio, except for the quasi-static, R = -0.6 condition, where only one specimen was tested. All specimens were tested with a fixed cyclic displacement increment (δ_{cyc}/δ_i) equal to 0.1. Stable crack growth occurred throughout each test. For comparison, two monotonic-load tests were conducted, one at a quasi-static rate and one at a dynamic rate.

Figures 2.44 and 2.45 show the quasi-static- and dynamic-loading rate J-R curves, respectively, for the carbon steel SAW (DP2-F40W). Table 2.30 shows fracture toughness values (i.e., J_i and dJ/da values) from the graphs.

Table 2.30 Fracture toughness summary for a submerged-arc weld (DP2-F40W) in a carbon steel plate tested at 288 C (550 F)

Specimen Identification Number	Loading Rate	Stress Ratio, R	δ_{cyc}/δ_i	J at Initiation, kJ/m²	J at Initiation, in-lb/in²	dJ/da, MJ/m³	dJ/da, in-lb/in³
F40W-1c	QS	1	N/A	65.5	374	29.3	4,250
F40W-4c	Dyn	1	N/A	56.4	322	113.2	16,420
F40W-5c	QS	-1	0.1	30.1	172	26.2	3,800
F40W-7c	QS	-0.6	0.1	47.3	270	29.3	4,250
F40W-8c	QS	-1	0.1	30.3	173	33.6	4,870
F40W-10c	Dyn (4 Hz)	-1	0.1	38.6	220	43.3	6,280
F40W-11c	Dyn (4Hz)	-1	0.1	33.7	192	37.2	5,390
F40W-12c	Dyn (4Hz)	-0.6	0.1	48.5	277	56.5	8,190
F40W-13c	Dyn (4Hz)	-0.6	0.1	33.4	191	58.8	8,530

As was the case for the stainless steel weld tests, there was some variability between specimen results, probably due to inhomogeneities in the weld metal.

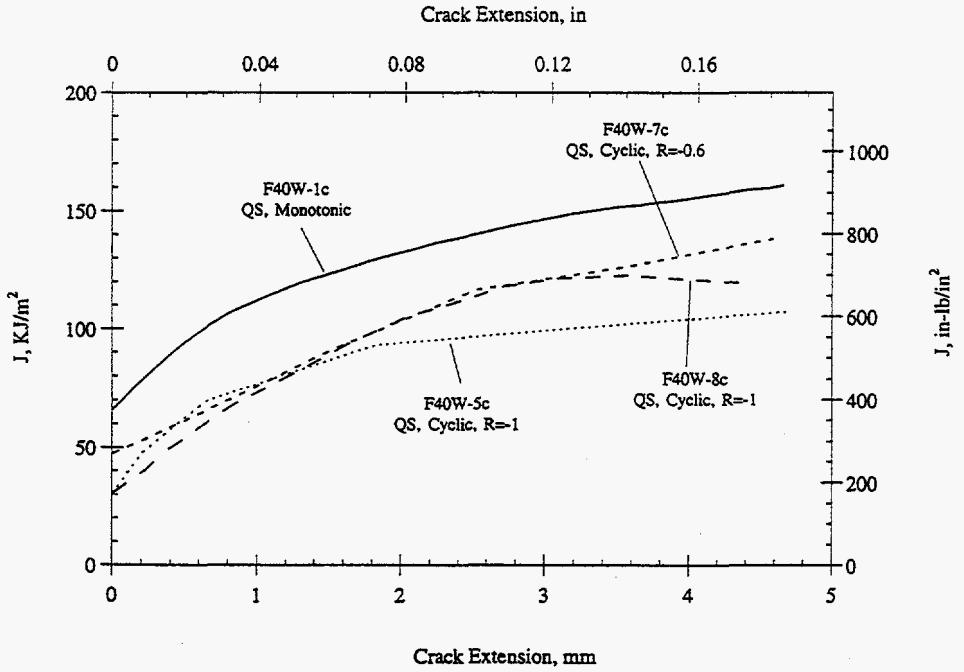

Figure 2.44 Quasi-static, monotonic loading and quasi-static, cyclic loading J-R curves at 288 C (550 F) for a submerged-arc weld (DP2-F40W) in a carbon-steel plate

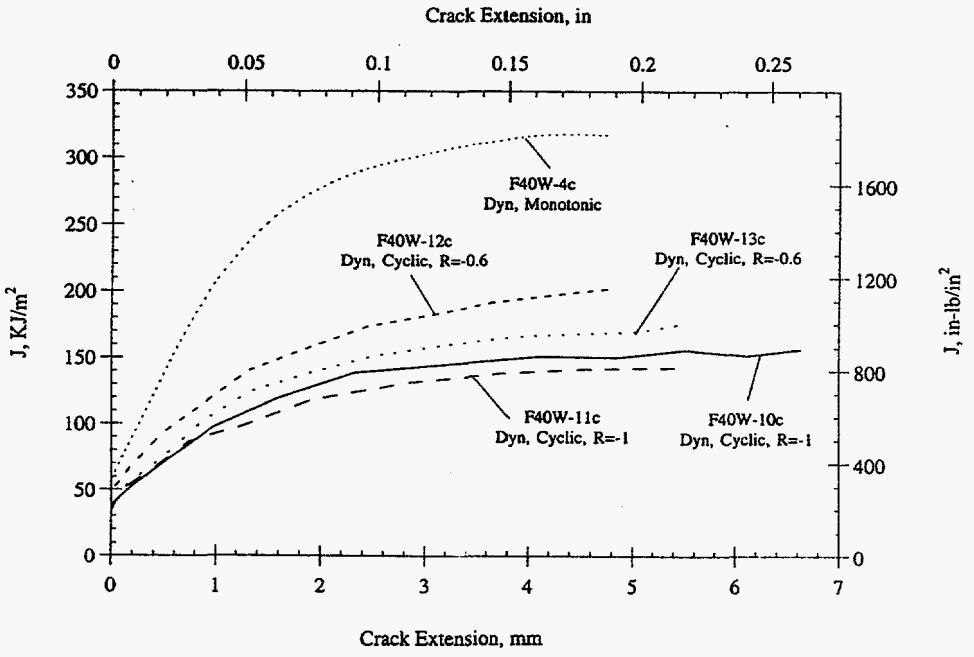

Figure 2.45 Dynamic, monotonic loading and dynamic, cyclic loading J-R curves at 288 C (550 F) for a submerged-arc weld (DP2-F40W) in a carbon steel plate

Figure 2.46 summarizes the effects of cyclic and dynamic loading on three different fracture toughness parameters; values from the duplicate specimens have been averaged. It is seen that cyclic loading at a quasi-static rate caused a marked reduction in J_i and a modest reduction in J at 2 mm of crack extension relative to quasi-static monotonic loading, with the effects on each of those properties becoming more damaging as R became more negative. Little effect of quasi-static cyclic loading was observed for dJ/da. Dynamic loading produced mostly beneficial results relative to quasi-static loading for this carbon steel weld, as was the case also for the stainless steel weld (see Figure 2.43). The only exceptions were for the J_i parameter for both monotonic loading and R = -0.6 cyclic loading, where the dynamic-loading-rate values were slightly less than those for the quasi-static loading rate.

2.5 Dynamic Modulus Tests

2.5.1 A710 Steel Straight-Pipe Loop Material and WPHY-65 Steel Elbow Material

Because modulus is such an important factor in predicting the behavior of the pipe and in converting measured strains to bending moments, a direct determination of modulus as a function of temperature was made using a dynamic modulus device. In a dynamic modulus measurement, the resonant frequency of a vibrating specimen is measured. Knowing the mass of the specimen and its geometry, and making corrections for thermal expansion, the modulus of the specimen can be inferred from the frequency equation for the specimen. By inducing different vibrational modes, it is possible to determine both Young's modulus (E) and the torsion modulus (G) from the same test specimen. Poisson's ratio (ν) can then be calculated from the relation

$$\nu = (E/2G) - 1 \qquad (2\text{-}2)$$

In the IPIRG-1 program, E was determined by Battelle as a function of temperature for Pipe IP-F3, the Loop No. 1 A710, low-carbon, precipitation-hardening, Schedule 100 straight-pipe steel. The results are shown in Figure 2.47. The values of E at room temperature and at 288 C (550 F) were found to be 212.9 GPa (30,900 ksi) and 197.9 GPa (28,700 ksi), respectively.

In the IPIRG-2 program, dynamic modulus tests were conducted at selected temperatures at CNS Company, Incorporated, in Fullerton, California, on the A710 straight pipe loop material (IP-F5) used in the partial reconstruction of the pipe loop, and on the WPHY-65 elbow materials from both the original loop (Loop No. 1) and the reconstructed loop (Loop No. 2). The results of the tests conducted at CNS are presented in Figure 2.48 through 2.50, which show Young's modulus, torsion modulus, and Poisson's ratio, respectively, as functions of temperature. The "old" and "new" designations in the legends for Figures 2.48 through 2.50 refer to the materials used in the construction of Loop No. 1 and Loop No. 2, respectively.

As can be seen in Figure 2.48, the Young's modulus of the Loop No. 2 straight pipe (IP-F5) at 288 C (550 F) was 194.0 GPa (28,100 ksi), which is approximately 2 percent less than that for the Loop No. 1 straight pipe material (IP-F3, see Figure 2.47). At room temperature, the Young's modulus values of the two straight pipe materials agreed within approximately 0.5 percent. All five of the materials subjected to

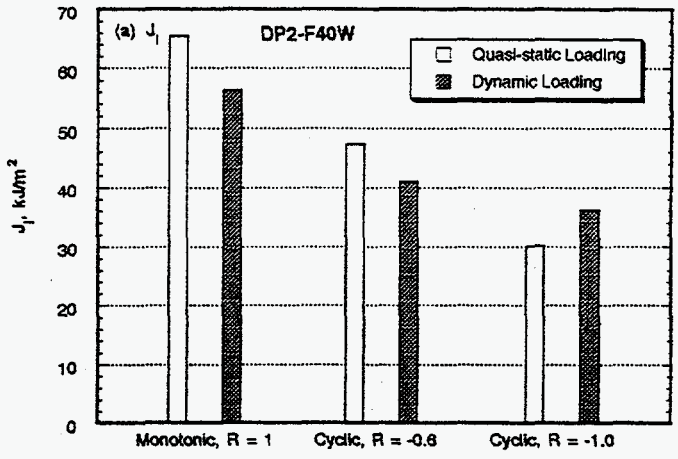

(a) J_i

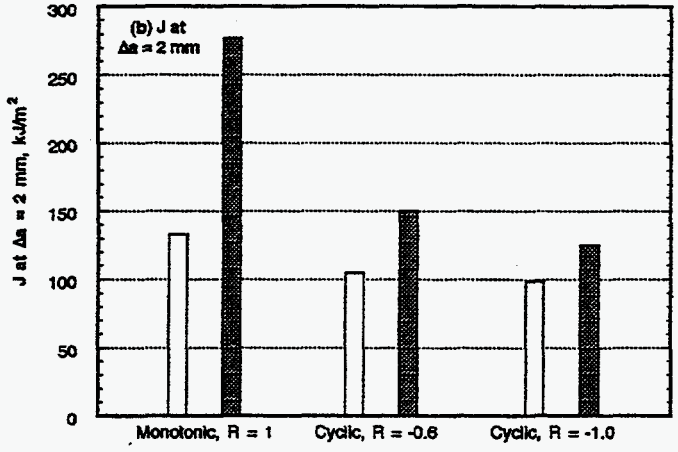

(b) J at 2 mm of crack extension

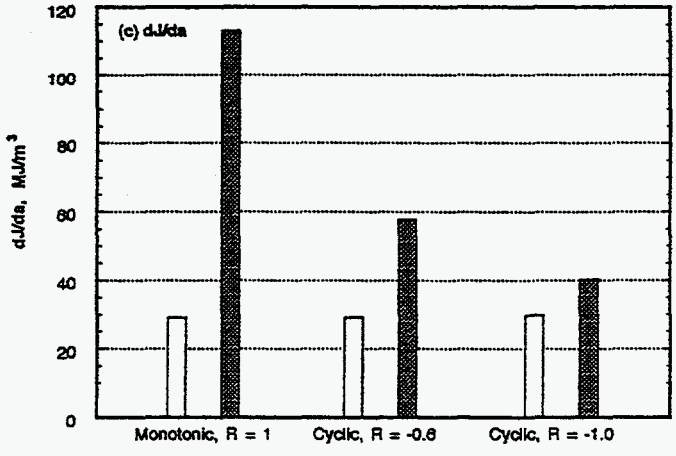

(c) dJ/da

Figure 2.46 Fracture resistance parameters at 288 C (550 F) for a submerged-arc weld (DP2-F40W) in a carbon steel plate

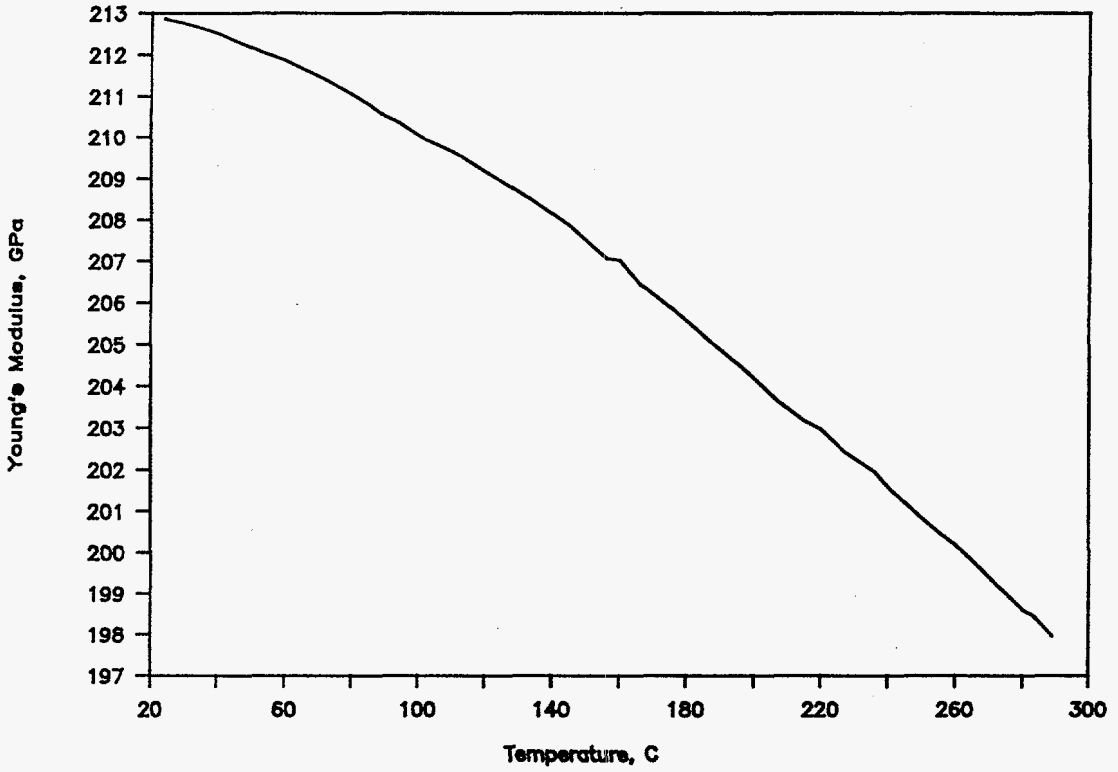

Figure 2.47 Young's modulus versus temperature for the ASTM A710, Grade A, Class 3 Schedule 100 straight-pipe (Pipe IP-F3) from Loop No. 1

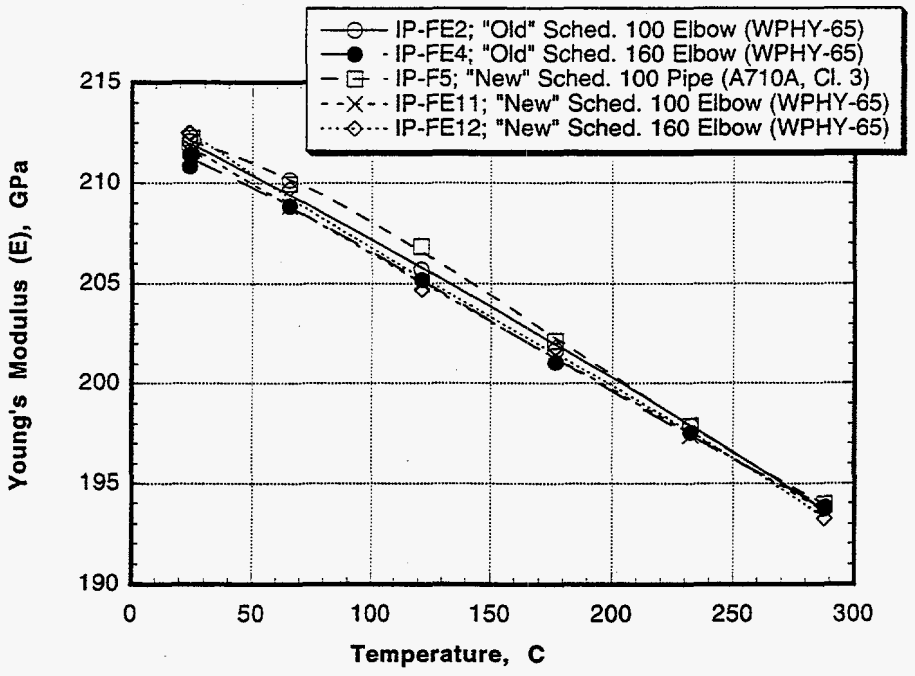

Figure 2.48 Young's modulus versus temperature for Loop No. 1 ("old") and Loop No. 2 ("new") ASTM A710, Grade A, Class 3 straight pipe and WPHY-65 elbow materials

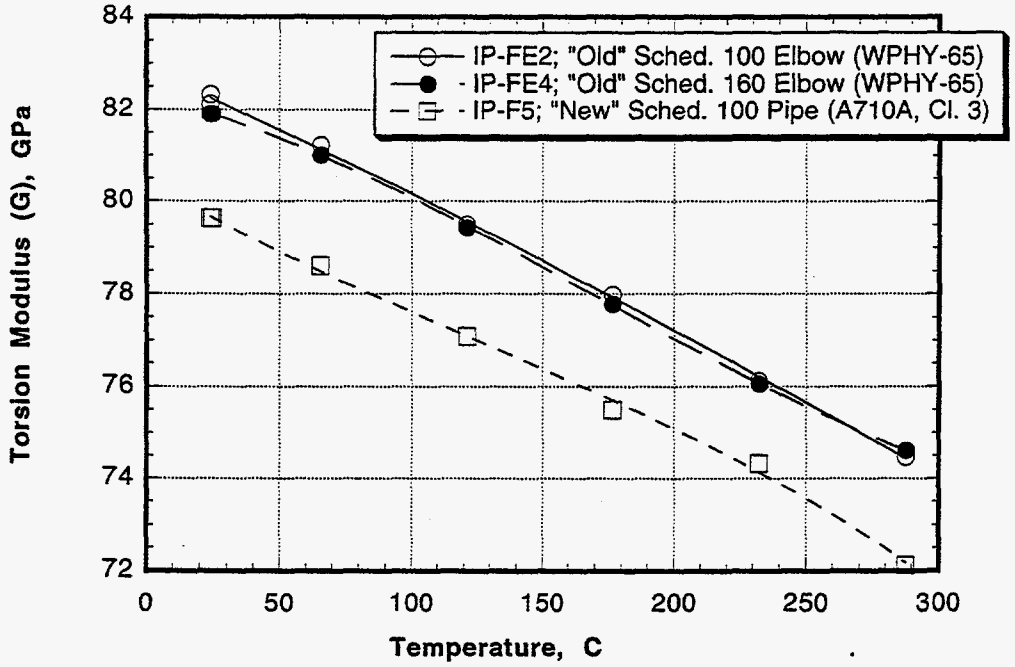

Figure 2.49 Torsion modulus versus temperature for Loop No. 1 ("old") and Loop No. 2 ("new") ASTM A710, Grade A, Class 3 straight pipe and WPHY-65 elbow materials

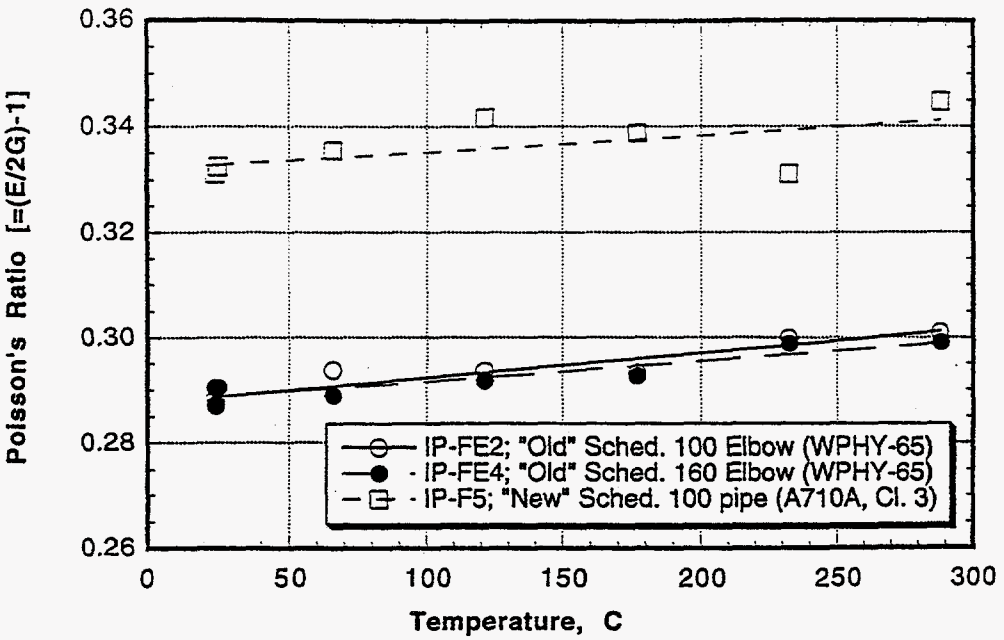

Figure 2.50 Poisson's ratio versus temperature for Loop No. 1 ("old") and Loop No. 2 ("new") ASTM A710, Grade A, Class 3 straight pipe and WPHY-65 elbow materials

dynamic modulus tests at CNS showed reasonably close agreement in Young's modulus values from room temperature to 288 C (550 F).

As is shown in Figure 2.49, only three of the materials (one straight pipe and two elbows) were tested to determine torsion modulus values. The other two elbows were not tested in torsion because the specimen size and shape for those materials, which differed from those of the other three materials, were not suitable for reliable determination of torsion modulus values. Notice in Figure 2.49 that the two elbow materials tested showed good agreement in torsion modulus values from room temperature to 288 C (550 F); the straight pipe material, on the other hand, displayed torsion values that are approximately 2.5 percent below those of the elbows. The reasons for the difference in torsion modulus between the straight pipe and the elbows are uncertain. The effect of the difference in torsion modulus values between the straight pipe and the elbows on Poison's ration is seen in Figure 2.50, where the Poison's ratio values (equal to [E/2G]-1) for the straight pipe are seen to be approximately 14 percent greater than those for the elbows.

Details of which materials were used in the different locations in the refurbishing of the pipe loop are provided in Appendix A, Figure A.1. As can be seen in that figures, Leg 2 was fabricated from the "old" IPIRG-1 straight pipe material (IP-F3), and Legs 1, 3, and 4 were fabricated from the "new" IPIRG-2 straight pipe material (IP-F5). Elbows 1 and 5 were "old" elbows and Elbows 2, 3, and 4 were "new" elbows.

2.6 Discussion of Results

2.6.1 Dynamic-Loading-Rate Effects on Properties

The effect of increasing the rate of displacement in tensile and C(T) tests conducted at 288 C (550 F) for materials used in Task 1 is summarized in Table 2.31. Also included in Table 2.31 are results from two 152-mm (6-inch) diameter pipes investigated in the IPIRG-1 program, A106B carbon steel (DP2-F30) and A376 Type 304 stainless steel (DP2-A23). Table 2.31 shows the approximate percentage change in tensile properties as the strain rate was increased by a factor of approximately 10^4 to 10^5, and the approximate percentage change in several toughness parameters (J_i, J at 2 mm of crack extension, and dJ/da) as the value of dJ/dt was increased by a factor of 2,500 to 4,500 times that in the quasi-static-loading-rate tests.

The results shown in Table 2.31 reveal that the carbon steel materials responded to increasing strain rate at 288 C (550 F) in a significantly different manner than did the stainless steel materials. The carbon steels, because of the fact that each was susceptible to dynamic strain aging, showed marked effects of strain rate on tensile strength. Of special importance to nuclear piping applications, the tensile strength at 288 C (550 F) of all four carbon steel base metals and of the single SAW investigated were lowered substantially by the increased strain rate, as was the fracture elongation of the base metals. The stainless steels, on the other hand, showed little change in either strength or elongation. Each of the stainless steels did exhibit a higher yield strength with increasing strain rate, whereas the yield strength of two of the carbon steel base metals and of the single SAW investigated was virtually unchanged; the indicated increase in yield strength with increasing strain rate for the other two carbon steel base metals (DP2-F23 and -F22) was based on estimated yield strength values in the dynamic tests.

The observed differences between the two types of materials in tensile tests were carried over into the J-R curve tests as well. Each of the stainless steel base metals and the single SAW investigated increased in toughness as dJ/dt was increased, as evidenced by J_i values, J values after 2 mm of crack extension, and by dJ/da values.[a] In some cases, the gain was modest and in other cases the gain was substantial. The carbon steels, on the other hand, exhibited marked differences between base metal and weld metal in their response to increasing dJ/dt in C(T) tests at 288 C (550 F). All four of the carbon steel base metals showed a decrease in dJ/da as dJ/dt was increased while three of the four showed a decrease in J_i and J at 2 mm of crack extension as dJ/dt was increased. The three SAW's, however, were affected beneficially by increasing dJ/dt, namely, both J at 2 mm of crack extension and dJ/da were increased substantially.

Table 2.31 Summary of dynamic-loading-rate effects on tensile properties and fracture resistance properties at 288 C (550 F)

		Approximate Percentage Change in Indicated Property as Strain Rate was Increased[(a)]					
Ident. Number	Type of Steel	Yield Strength	Ultimate Tensile Strength	Elongation	J_i	J at $\Delta a = 2$mm	dJ/da[(b)]
DP2-F30	A106B carbon steel pipe	0	-20	-35	-15	-20[(c)]	-15
DP2-F29	A106B carbon steel pipe	0	-30	-15	-35	-40	-45
DP2-F23	A106B carbon steel pipe	+19[(d)]	-11	-10	+46	+5	-25
DP2-F22	A106B carbon steel pipe	+28[(d)]	-10	-22	-39	-49	-58
DP2-F29W	Submerged-arc weld in A106B carbon steel pipe	0	-20	+5	+55	+70	+50
DP2-F40W	Submerged-arc weld in carbon steel pipe	(e)	(e)	(e)	-15	(e)	+285
DP2-F55W	Submerged-arc weld in carbon steel plate	(e)	(e)	(e)	+51	+93	+100
DP2-A23	A376 Type 304 stainless steel pipe	+35	+5	+5	+5	+15	+20
DP2-A8I	A358 Type 304 stainless steel pipe	+10[(f)]	-5[(f)]	+10[(f)]	+52	+20	-5
DP2-A8II	A358 Type 304 stainless steel pipe	+10[(f)]	-5[(f)]	+10[(f)]	+49	+30	+20
DP2-A8W	Submerged-arc weld in A358 Type 304 stainless steel pipe	+10	-5	-10	+135	+60	+45
DP2-A45W1	Submerged-arc weld in stainless steel plate	(e)	(e)	(e)	(e)	(e)	(e)
DP2-A45W2	Submerged-arc weld in stainless steel plate	(e)	(e)	(e)	(e)	(e)	(e)

(a) For tensile tests, strain rate was increased from approximately 10^{-4} s^{-1} to 10 s^{-1}; for C(T) tests, dJ/dt in dynamic tests was 2,500 to 4,500 times that in quasi-static tests.
(b) dJ/da was determined over the crack-extension range from 0.15 to 1.5 mm (0.006 to 0.060 in.).
(c) The change in J was determined at $\Delta a = 0.5$ mm (0.02 inch) because of limited stable crack growth in this material.
(d) Based on estimated yield strengths in dynamic tests.
(e) Not determined.
(f) The tensile properties of the stainless steel pipes (DP2-A8I and DP2-A8II) are essentially the same.

The findings regarding the occurrence of crack jumps in the carbon-steel materials are summarized in Table 2.32. The only consistent trend observed was that carbon steel welds appear to be less likely to

(a) One exception was the DP2-A8I which showed a slight decrease in dJ/da.

The findings regarding the occurrence of crack jumps in the carbon-steel materials are summarized in Table 2.32. The only consistent trend observed was that carbon steel welds appear to be less likely to exhibit crack jumps in C(T) tests at 288 C (550 F) than are carbon steel base metals. Among the four base metals in Table 2.32, two exhibited crack jumps in quasi-static tests at 288 C (550 F) and two did not. The response to increased displacement rate was different for each of the four.

Table 2.32 Summary of observations regarding the occurrence of crack jumps in C(T) tests of carbon steels at 288 C (550 F)

	Were Crack Jumps Observed?	
Material	**Quasi-static Tests**	**Dynamic Tests**
DP2-F30 base metal	Yes	Yes
DP2-F29 base metal	Yes	No
DP2-F23 base metal	No	No
DP2-F22 base metal	No	No
DP2-F29W weld metal	Slight	No
DP2-F55W weld metal	Slight	No

The reasons for the different strain rate response of the six carbon steel materials are not known with certainty. It can be hypothesized that the differences in response are the result of differences in the way in which interstitial atoms (nitrogen and carbon) interact with dislocations at 288 C (550 F) to produce the many unusual effects associated with dynamic strain aging. These differences could give rise to different temperature- and strain-rate dependence of dynamic strain aging among the six steels. Thus, their strength-versus-temperature curves might show peak strengths occurring at different temperatures, or they might display serrations on the stress-strain curve over different temperature ranges, and so on.

Even though the causes of the different behaviors among the six carbon steels cannot be adequately explained at this time, it is important to note that the results were clear in one regard; each of the carbon steel base metals and the single SAW investigated showed a lowering of tensile strength at 288 C (550 F) with increasing strain rate, and each of the four base metals showed a reduction in J at 2 mm of crack extension as dJ/dt was increased. Furthermore, each of the four base metals exhibited a drop in dJ/da as dJ/dt was raised. That result means that a similar response must be assumed in any other carbon steel pipe unless contrary evidence is available.

In addition to measuring displacement-rate effects, this investigation confirmed a result obtained in the Degraded Piping Program and the IPIRG-1 program, namely, the fracture resistance of submerged-arc welds in stainless steels is much poorer than that of base metal. The stainless steel SAW's studied in these programs displayed a J_i value that was only about 10 to 20 percent of the value for its base metal counterpart, and of about the same magnitude as that for the carbon steel SAW.

2.6.2 Effects of Cyclic Loading and Dynamic Cyclic Loading on Fracture Resistance

The effects of cyclic loading and dynamic cyclic loading on fracture resistance at 288 C (550 F) are summarized in Figures 2.51, 2.52, and 2.53 for DP2-A8I and DP2-A8II (stainless steel base metal), DP2-A8W (stainless steel SAW), and DP2-F40W (carbon steel SAW), respectively. The figures include three different fracture-resistance parameters—J at crack initiation (J_i), J at 2 mm of crack extension ($J_{2\,mm}$), and the slope of the J-Δa curve (dJ/da) for Δa values between 0.15 and 1.5 mm (0.006 and 0.060 inch). The value of each parameter has been normalized against the value of that parameter determined in a monotonic, quasi-static loading test. Values less than 1.0 for the normalized parameters indicate a loss of toughness from cyclic or dynamic cyclic loading.

For the stainless steel base metals (DP2-A8I and DP2-A8II) in Figure 2.51, cyclic loading at R = -1 had a strong adverse effect on each fracture resistance parameter, whereas at R = -0.3, the effects of cyclic loading were modest.

For the stainless steel SAW (DP2-A8W) in Figure 2.52, the effects of cyclic loading, both quasi-static and dynamic, were less adverse on J_i than on $J_{2\,mm}$ and dJ/da. For each of the three parameters, cyclic loading at R = -1 was more damaging than at R = -0.6. Except for J_i values at R = -1, dynamic cyclic loading had a smaller adverse effect on toughness than did quasi-static cyclic loading.

The results for the carbon steel SAW (DP2-F40W), shown in Figure 2.53, differed from those for the stainless steel SAW (see Figure 2.52) in that the J_i parameter for the carbon steel SAW was more adversely affected by cyclic loading than were $J_{2\,mm}$ and dJ/da. Also, the damaging effect of going from R = - 0.6 to R = -1.0 in the carbon steel SAW was less apparent than in the stainless steel SAW. The two welds were similar, however, in their reaction to dynamic cyclic loading; except for J_i varies at R = -0.6, dynamic cyclic loading of the carbon steel weld produced greater toughness values than did quasi-static cyclic loading.

The findings summarized in Figures 2.51 through 2.53 are too limited to permit firm conclusions to be drawn concerning the effects of cyclic and dynamic cyclic loading on fracture resistance of piping and piping welds. However, it appears that cyclic loading, especially at R = -1, is significantly damaging to one or more of the fracture resistance parameters (J_i, $J_{2\,mm}$, and dJ/da) described here. For the two welds in which dynamic cyclic loading was investigated, it appears that dynamic cyclic loading was no more detrimental to toughness than was quasi-static cyclic loading and, in some cases, was less damaging or even beneficial relative to quasi-static monotonic loading.

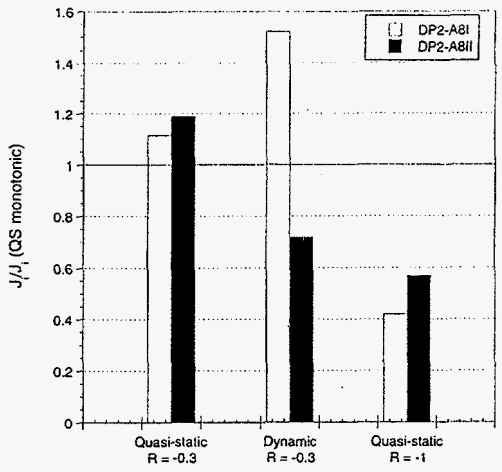

(a) J_i

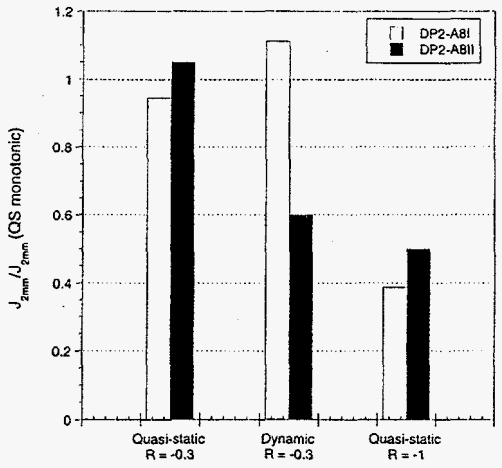

(b) J at 2 mm of crack extension

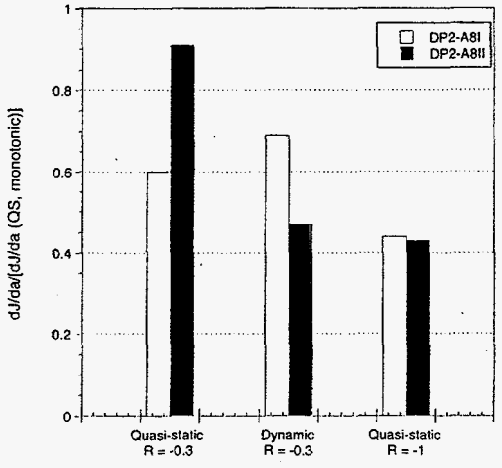

(c) dJ/da

Figure 2.51 Normalized fracture resistance parameters at 288 C (550 F) for the A358 Type 304 stainless steel pipes (DP2-A8I and DP2-A8II)

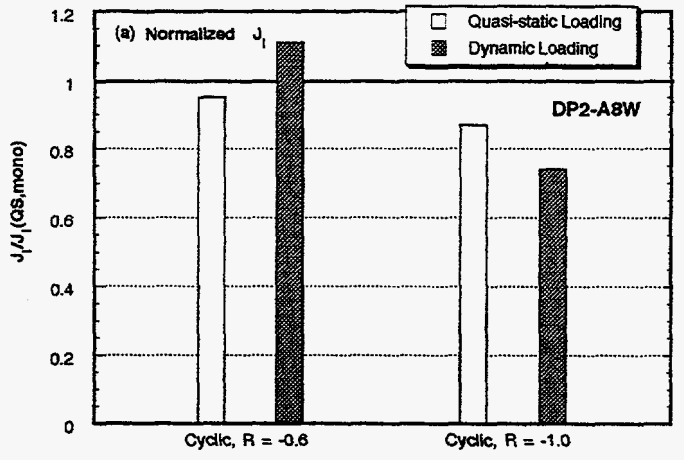

(a) J_i

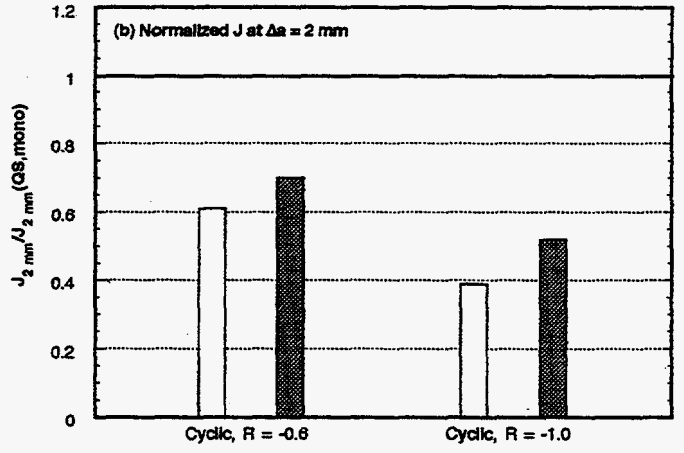

(b) J at 2 mm of crack extension

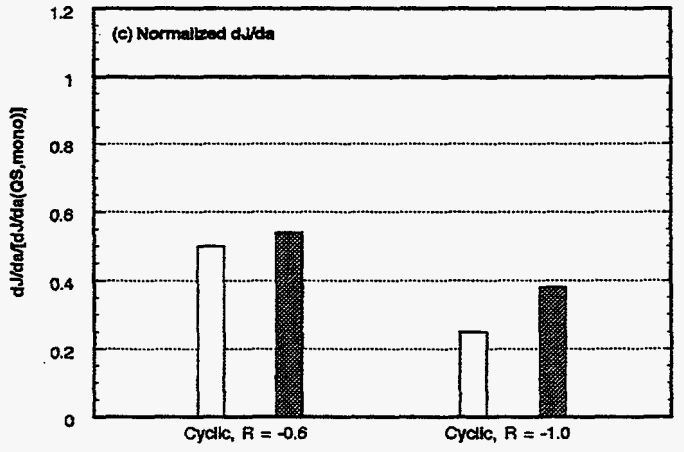

(c) dJ/da

Figure 2.52 Normalized fracture resistance parameters at 288 C (550 F) for a submerged-arc weld (DP2-A8W) in an A358 Type 304 stainless steel pipe

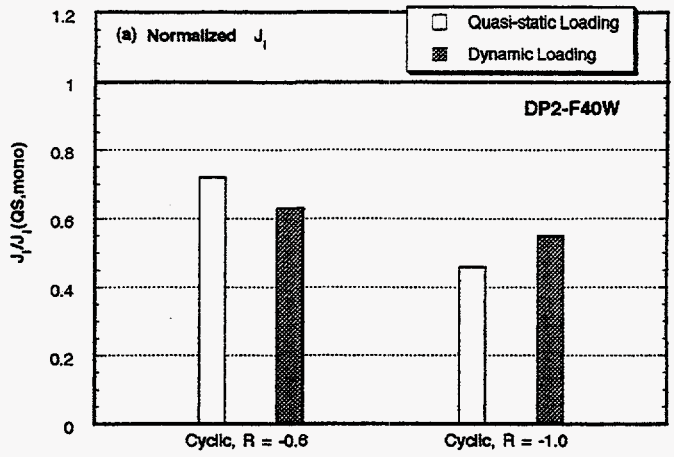

(a) J_i

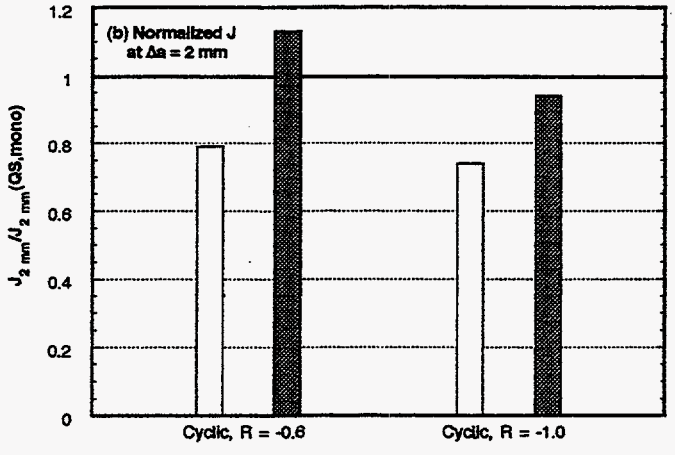

(b) J at 2 mm of crack extension

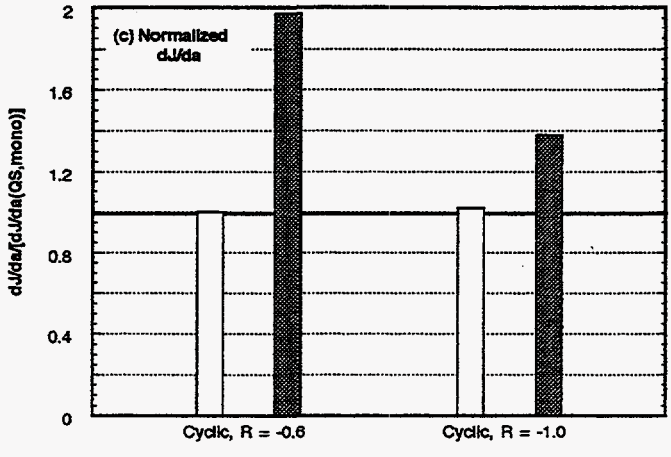

(c) dJ/da

Figure 2.53 Normalized fracture resistance parameters at 288 C (550 F) for a submerged-arc weld (DP2-F40W) in a carbon steel plate

2.7 References

2.1 Marschall, C. W., Landow, M. P., and Wilkowski, G. M., "Loading Rate Effects on Strength and Fracture Toughness of Pipe Steels Used in Task 1 of the IPIRG Program," NUREG/CR-6098, October 1993.

2.2 Wilkowski, G. M. and others, "Degraded Piping Program - Phase II, Summary of Technical Results and Their Significance to Leak-Before-Break and In-Service Flaw Acceptance Criteria," March 1984 - January 1989, NUREG/CR-4082, Vol. 8, March 1989.

2.3 Scott, P. and others, "The IPIRG-1 Pipe System Fracture Tests: Experimental Results," PVP Vol. 280, pp 135-151, June 1994.

2.4 Kanninen, M. F. and others, "Instability Predictions for Circumferentially Cracked Type 304 Stainless Steel Pipes Under Dynamic Loadings," Final Report on EPRI Project T118-2, by Battelle Columbus Laboratories, EPRI Report Number NP-2347, April 1982.

2.5 Baird, J. D., "Strain Aging of Steel -- A Critical Review," *Iron and Steel*, pp 450-457, September 1963.

2.6 Keh, A. S., Nakada, Y., and Leslie, W. C., "Dynamic Strain Aging in Iron and Steel," in *Dislocation Dynamics*, A. R. Rosenfield et al., Eds., McGraw-Hill, New York, pp 381-408, 1968.

2.7 Manjoine, M. J., "Influence of Rate of Strain and Temperature on Yield Stresses of Mild Steel," *J. of Applied Mechanics*, pp A211-A218, December 1944.

2.8 Wilkowski, G. M. and others, "Degraded Piping Program--Phase II," Sixth Program Report, October 1986 - September 1987, by Battelle Columbus Laboratories, NUREG/CR-4082, Vol. 6, April 1988.

3.0 EXPERIMENTAL SETUP AND TEST PROCEDURES

This section of the report describes the procedures for setting up and conducting the IPIRG-2 pipe experiments. First, the IPIRG-2 pipe system experimental facility is described. As part of this discussion, the special hardware used to realize the boundary conditions for the pipe loop is described. Next, the primary and secondary restraint systems, included in the facility design to guard against the pipe whip associated with a double-ended pipe break will be discussed. After this discussion, the results of the uncracked shakedown experiment for the recommissioned pipe loop will be discussed, i.e., the results of the natural frequency and damping characteristic evaluations will be presented. After discussing the IPIRG-2 pipe system facility, the test facilities used in the quasi-static straight pipe and quasi-static elbow girth weld bend experiments will be discussed. This section of the report concludes with a discussion of the general test procedures used during the conduct of these experiments.

3.1 The IPIRG-2 Pipe System Experimental Facility

The experimental pipe loop facility used in IPIRG-2 was rebuilt at the beginning of the IPIRG-2 program to repair damage done during the last IPIRG-1 pipe system experiment, i.e., Experiment 1.3-7. Figure 3.1 is an artist's conception of the IPIRG-2 experimental facility. The IPIRG-2 facility was unchanged from the IPIRG-1 facility except that two additional 190 liter (50 gallon) piston-type hydraulic accumulators were added to the servo-hydraulic system to accommodate longer duration simulated seismic pipe system experiments. The pipe loop was fabricated from predominantly 16-inch diameter Schedule 100 pipe. The same straight pipe (ASTM 710 Grade A Class 3) and elbow (WPHY65) materials were used in the construction of the IPIRG-2 facility as were used in the construction of the IPIRG-1 facility. Elbows 1, 2, 3, and 5 were Schedule 100 elbows while Elbow 4 was a Schedule 160 elbow. Elbows 2, 3, and 4 were new elbows procured as part of IPIRG-2 for the refurbishing project, while Elbows 1 and 5 were the same elbows as used in IPIRG-1. Figure 3.2 shows the physical dimensions of the pipe loop. For the straight pipe system experiments (i.e., Experiments 1-1, 1-2, 1-5, and 1-7) the wall thicknesses of the various sections of the loop were essentially unchanged from the pipe loop used in IPIRG-1. For the one elbow girth weld experiment (i.e., Experiment 1-3), the pipe sections around Elbow 4 were changed to allow for an additional moment cell just east of Elbow 4 and for the fact that the test elbow used in these experiments was a Schedule 100 elbow and not the Schedule 160 elbow used for the straight pipe experiments. Appendix A provides the detailed pipe loop dimensions, including wall thickness measurements, for the straight pipe system experiments and the elbow girth weld pipe system experiment.

The boundary conditions for the piping loop were realized by using various specialized pieces of hardware. At the two fixed ends, the pipe loop is welded to a 1500 pound class weld neck flange, which is bolted to a large steel frame that is buried in a large, heavily reinforced concrete mass. At the actuator location, the pipe, which is being forced in the east-west direction (see Figure 3.1), is restrained in the vertical direction and is free to rotate and translate in the other four degrees of freedom. At the two hanger locations, the pipe is restrained in both the vertical direction and the horizontal direction perpendicular to the pipe axis, but is free to translate and rotate in the other four degrees of freedom. At each of these three locations, large spherical bearings allow the pipe to rotate about all three axes and translate in the direction of the

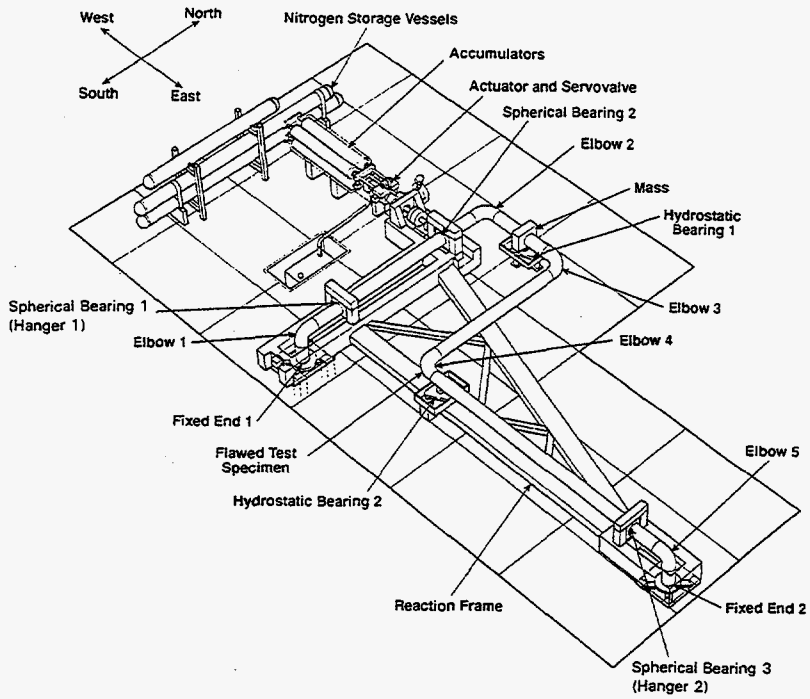

Figure 3.1 Artist's conception of the IPIRG-2 pipe system facility

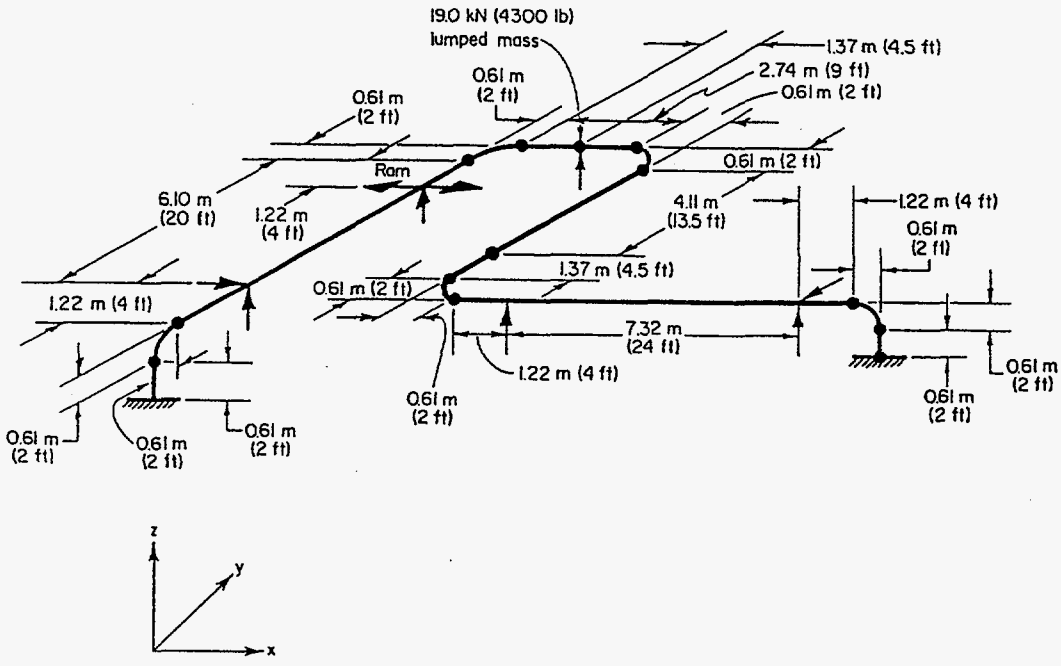

Figure 3.2 Physical dimensions of the pipe loop for straight pipe experiments conducted as part of Task 1

pipe axis. At the two vertical supports (hydrostatic bearings 1 and 2), the pipe is supported only in the vertical direction. In order to minimize any frictional forces in the horizontal plane at these two locations, the pipe is supported by hydrostatic bearings. Spherical bearings were used in conjunction with the hydrostatic bearings at these two locations to allow the pipe to rotate about each of the three axes.

System loads are applied by a 1,560 kN (350,000 pound) Moog Model 85-454 double-ended piston actuator (equal piston areas for both push and pull) with a 457 mm (18.0 inch) stroke capacity. The actuator is driven by a 7,600 liter per minute (2,000 gpm) Moog Model 79-507 three-stage servo-valve which is supplied with oil at 21 MPa (3,000 psi) by piston-type hydraulic accumulators with an oil capacity of 760 liters (200 gallons). Nitrogen gas to drive the accumulators is stored in separate pressure vessels.

The pipe loop is connected to an auxiliary expansion tank of 760 liters (200 gallons) capacity which is filled with air prior to the heat-up. This tank accommodates the expansion of the water as it is heated from ambient temperature to 288 C (550 F). It also provides an accumulator effect for maintaining the pressure at the test conditions. Heat for bringing the pipe loop to test temperature is supplied by heater tapes wrapped continuously around the exterior of the pipe. Water in the pipe loop is circulated by a pump connected to the two fixed ends to provide an even temperature distribution. The pipe loop is completely covered with fiberglass insulation.

3.2 DEGB Restraint Systems

The philosophy of the IPIRG-2 simulated seismic pipe system experiments was to load the test specimens with the complete loading history, even if the surface crack penetrated the pipe wall. Because this made the possibility for a double-ended-guillotine-break (DEGB) quite high, a means to control the motion of the two halves of the pipe loop in the event of a DEGB was incorporated into the test specimen. Figure 3.3 shows a schematic of the primary restraint system used for the straight pipe system experiments. The essential elements of the DEGB primary restraint system are: (1) a central rod to keep the two ends of the severed pipe together, (2) baffle plates to restrain the central rod and to limit the thrust force after the DEGB, and (3) a series of Belleville washers to cushion the impact loads on the rod. Analytical evaluations have shown that the presence of the restraint system does not have any significant influence on the rotation of the cracked section, fluid pressure on the crack faces, or the propensity towards a DEGB.

For the elbow girth weld pipe system experiment (i.e., Experiment 1-3), it was not possible to incorporate the central-rod primary restraint system into the test specimen due to the curvature of the test specimen. As a result, it was decided to restrain the two halves of the pipe loop in the event of a DEGB by simply minimizing the amount of subcooled water in the test specimen. This was accomplished by welding end caps into the pipe loop, 1.83 m (72 inches) on either side of Elbow 4, see Figure 3.4. (Each end cap had a 19 mm (0.75 inch) diameter hole in it to allow water circulation.) Restraint for Experiment 1-3 was also realized by the fact that since the forcing function for this experiment was a single frequency excitation, it was possible to shutdown the applied forcing function as soon as the crack in the test specimen penetrated the pipe wall. Consequently, based on experience from IPIRG-1, it was felt that the pipe system could be brought to rest before the resultant through-wall crack could grow completely around the pipe circumference.

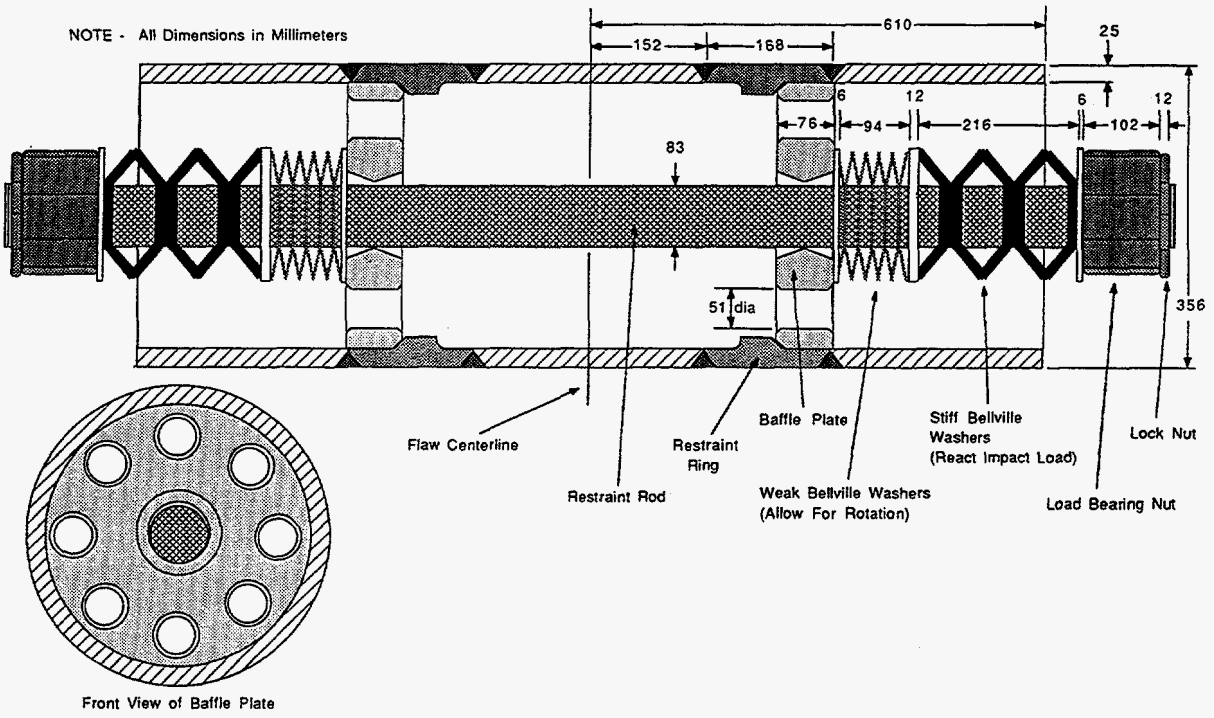

Figure 3.3 Primary restraint design used for straight pipe experiments conducted as part of Task 1

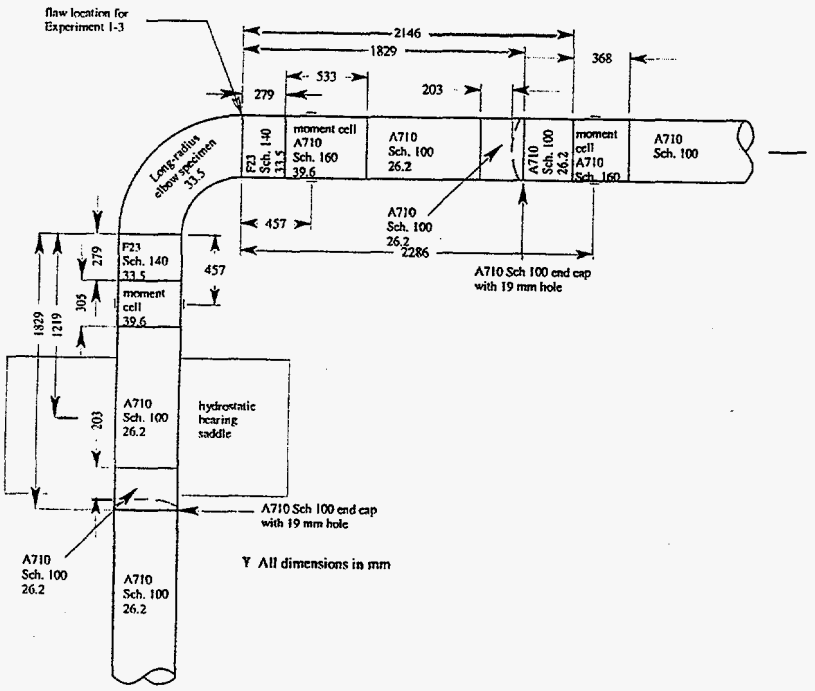

Figure 3.4 Schematic of pipe loop in vicinity of Elbow 4 for elbow girth weld pipe system experiment (Experiment 1-3) showing the end caps used to minimize the energy in the test specimen in the case of a DEGB

As a backup, in the event either primary restraint system (i.e., the central rod system for the straight pipe experiments or the end caps for the elbow girth weld pipe system experiment) failed to restrain the two halves of the pipe loop in the event of a DEGB, a secondary restraint system was incorporated into the overall system design. This secondary restraint system was a series of 8,800 kg (4,000 pound) bags of sand placed strategetically around the pipe loop, see Figure 3.5. The sand bags were stacked in layers of two and placed behind large oak timber frames. The thought behind this secondary restraint system was that if the primary restraint system failed, the whipping pipe would expend its energy moving the sand rather than causing other damage.

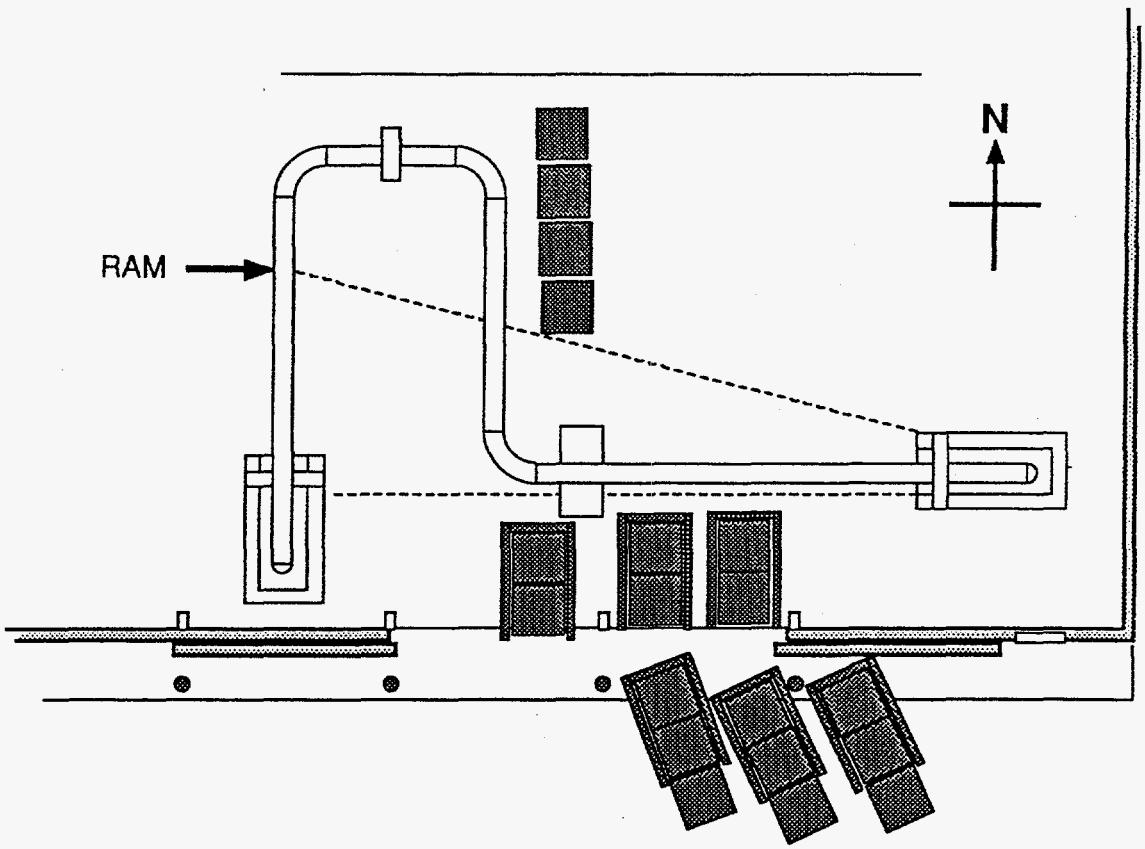

Figure 3.5 Typical layout of sand bags used as secondary restraint system

3.3 Uncracked Shakedown Experiment

Prior to the conduct of the first IPIRG-2 cracked pipe system experiment, an uncracked shakedown experiment was conducted. The purpose of this experiment was to ensure that the refurbished pipe loop facility was the same as the facility used in IPIRG-1. As part of this uncracked shakedown experiment, the damping and the first few natural frequencies of the refurbished facility were measured. The damping characteristics of the refurbished facility were assessed with the pipe loop at PWR conditions, i.e., 288 C (550 F) and 15.5 MPa (2,250 psi) internal pipe pressure. The procedures for quantifying the damping in the pipe system were the same as used in IPIRG-1. The pipe loop was excited with a small amplitude sinusoidal displacement at the actuator (approximately $\pm$1.5 mm [$\pm$0.06 inch]) at a frequency below the first natural frequency of the pipe loop. The frequency of the excitation was then increased until the resonant frequency of the pipe loop was found, as evident by large motions of the pipe loop and large actuator loads. After a few seconds of excitation at the resonant frequency, the input excitation was stopped, the actuator held fixed, and the pipe loop allowed to come to rest as indicated by the load falling to a static value. Actuator load was recorded continuously during this process. Figure 3.6 is a plot of the actuator load versus time record for the "ring down" portion of the damping test. The damping ratio, i.e., the fraction of critical damping for the piping system, can then be calculated from the experimental record of the damped free vibration of the piping system, Figure 3.6, using the log-decrement method. Following the procedures outlined above, the damping ratio for the recommissioned pipe system was determined to be approximately 0.45 percent. This agrees very well with the damping ratio previously determined for the IPIRG-1 facility of 0.5 percent.

The natural frequencies of the recommissioned facility were also determined at PWR conditions. The basic procedures were the same as used to determine the elevated temperature natural frequencies of the pipe loop during IPIRG-1. The procedure consisted of applying a bandwidth-limited random noise displacement signal, so called pink noise (broad-band random noise with equal energy in each octave frequency band, see Figure 3.7) to the actuator and measuring the acceleration of the pipe in response to the pink noise. A spectrum analyzer collected the acceleration response data for 30 seconds, averaged the data, and produced the acceleration response spectra. Two accelerometers were located on the pipe as shown in Figure 3.8, one on the extrados of Elbow 3 (Location 7 in Figure 3.8), and one on the top of the pipe at the junction of Elbow 3 and the straight pipe containing the test section (Location 8 in Figure 3.8). The Elbow 3 extrados location was chosen because it would likely experience significant motion for any in-plane modes while the other location was expected to respond to any out-of-plane modes.

The acceleration response spectra under PWR conditions for the in-plane modes for the refurbished IPIRG-2 facility and the IPIRG-1 facility are shown in Figures 3.9 and 3.10, respectively. The acceleration response spectra under PWR conditions for the out-of-plane modes are shown in Figures 3.11 and 3.12 for the IPIRG-2 and IPIRG-1 facilities, respectively. In all cases, there was a 31.1 kN (7,000 lbs.) preload on the actuator. Comparing Figure 3.9 with Figure 3.10 and Figure 3.11 with Figure 3.12, it can be seen that the response spectra for the recommissioned facility are very similar to those for the IPIRG-1 facility.

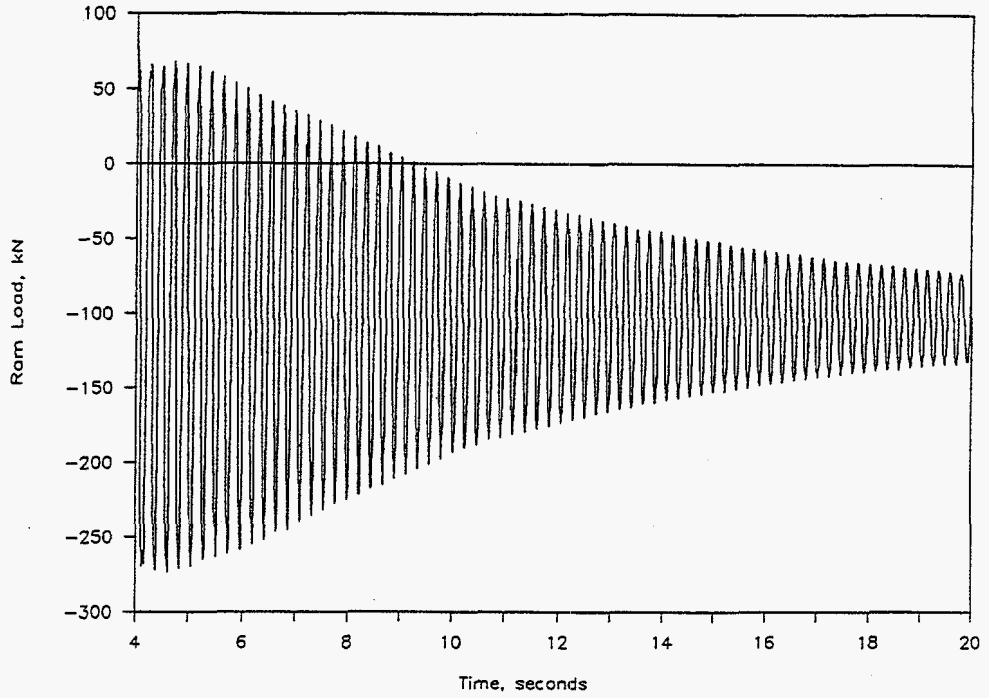

Figure 3.6 Plot of actuator load versus time for the "ring-down" portion of the damping test

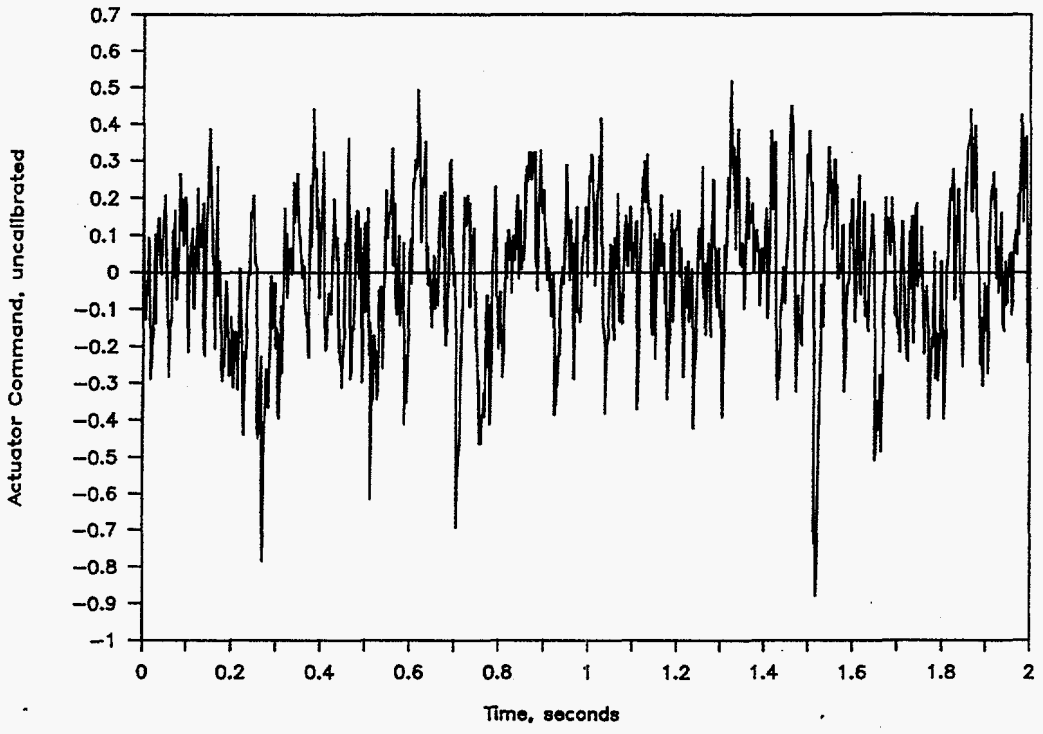

Figure 3.7 Typical pink noise actuator displacement input command signal

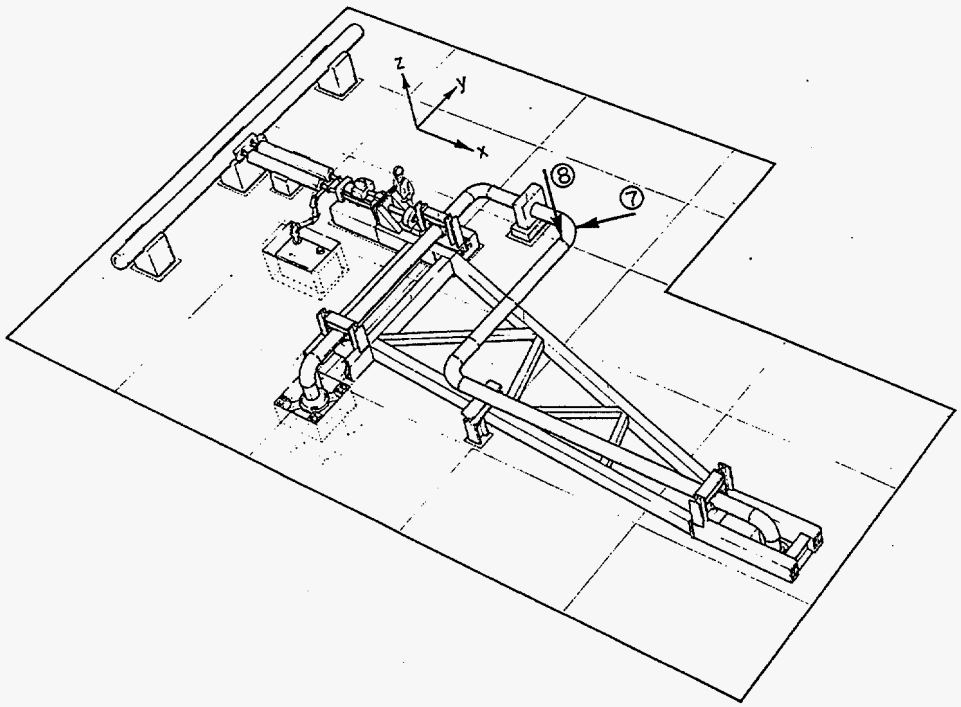

Figure 3.8 Accelerometer locations for actuator-driven excitation dynamic response measurements

The damping values and natural frequencies associated with the refurbished IPIRG-2 facility are compared with the damping values and natural frequencies for the IPIRG-1 facility in Table 3.1. (Note, the primary restraint system was not in place when the natural frequency and damping values were measured during the IPIRG-2 uncracked shakedown experiment. The mass of the restraint system was approximately 320 kg (700 lbs). ANSYS finite element calculations indicated that a lumped mass of this magnitude at the crack location would lower the first natural frequency of the piping system approximately 3 percent.) As can be seen in Table 3.1, the first natural frequency of the refurbished pipe loop adjusted for the reduction in natural frequency due to the presence of the restraint device was approximately 4.35 Hz. As can be seen in Table 3.1 and Figures 3.8 through 3.11, the differences in natural frequencies and damping values between the IPIRG-1 and IPIRG-2 facilities are minor. This seems to indicate that the objective of refurbishing the facility to the same specifications as used for IPIRG-1 was satisfied.

3.4 Experimental Facilities Used in IPIRG-2 Quasi-Static Companion Pipe Bend Experiments

The IPIRG-2 Task 1 test matrix included a total of eight pipe experiments, five dynamic pipe system and three quasi-static pipe bend experiments. The purpose of these companion quasi-static experiments was to provide experimental data to which the experimental results from the dynamic pipe system experiments could be compared for the cases where such data did not already exist. Two of the companion experiments were quasi-static four-point bend experiments where the crack was in a section of straight pipe and the third was a quasi-static bend experiment where the crack was in an elbow girth weld.

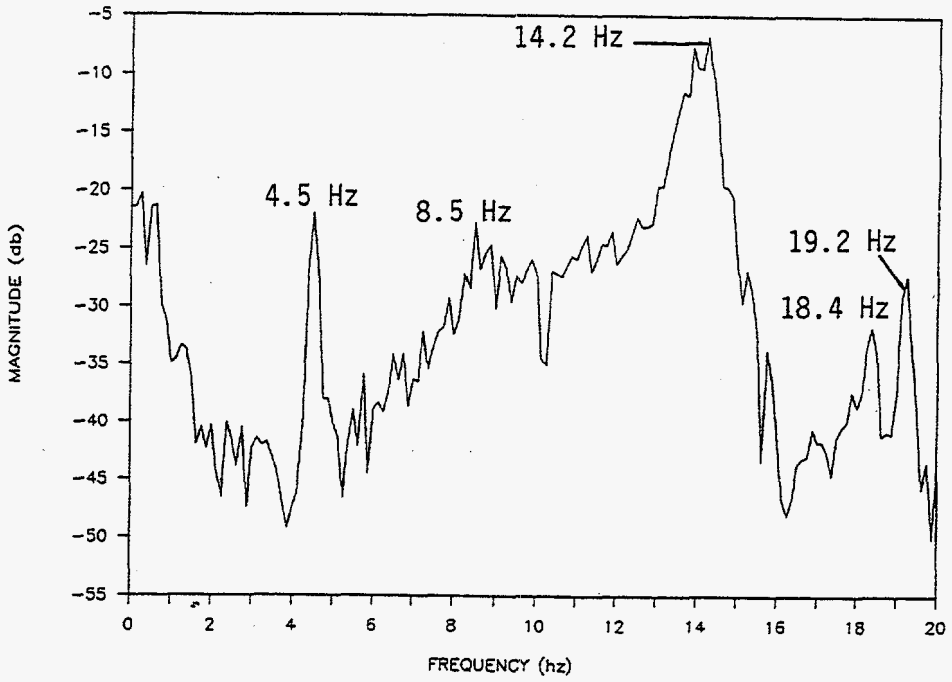

Figure 3.9 Acceleration response spectrum under PWR conditions for the in-plane modes for the IPIRG-2 facility

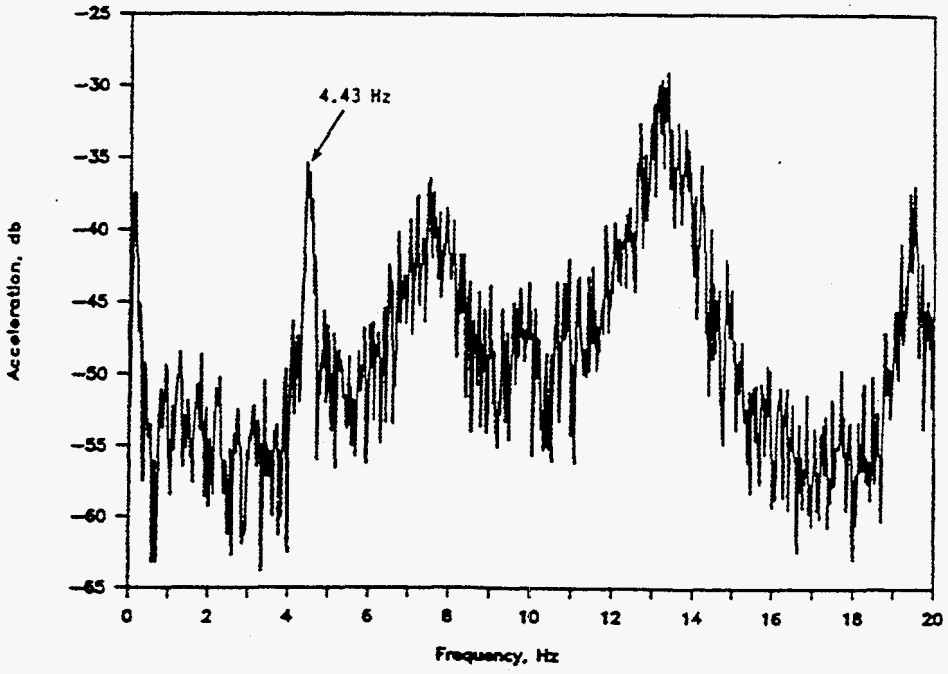

Figure 3.10 Acceleration response spectrum under PWR conditions for the in-plane modes for the IPIRG-1 facility

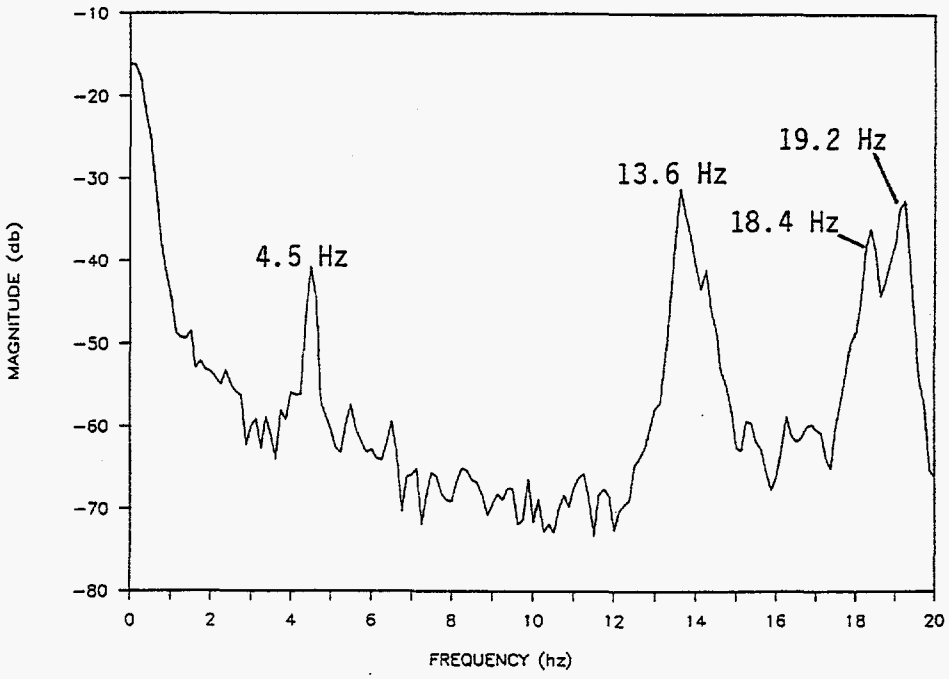

Figure 3.11 Acceleration response spectrum under PWR conditions for the out-of-plane modes for the IPIRG-2 facility

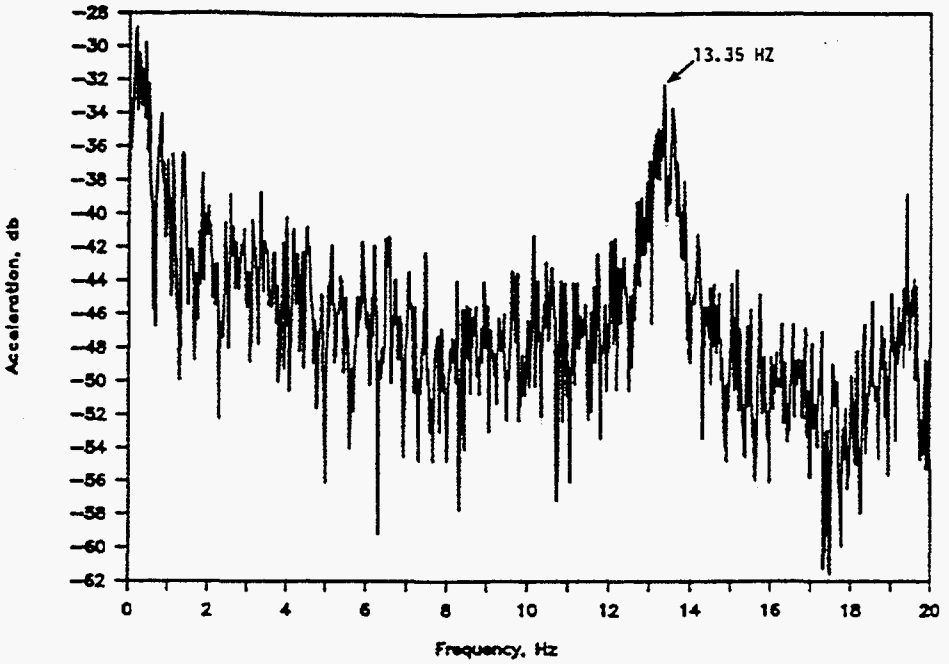

Figure 3.12 Acceleration response spectrum under PWR conditions for the out-of-plane modes for the IPIRG-1 facility

Table 3.1 Experimentally measured damping values and natural frequencies associated with the IPIRG-1 and IPIRG-2 pipe loop facilities at 288 C (550 F) and 15.5 MPa (2,250 psi) internal pipe pressure

		Natural Frequencies, Hz[2]			
	Damping[1], Percent Critical Damping	First	Second	Third	Fourth
IPIRG-1 Facility	0.5	4.43	7.7	13.35	19.5
IPIRG-2 Facility	0.45	4.5[3]	8.5[3]	14.2[3]	18.4[3]

(1) Measured through a system "ring-down" test and analyzed using the log-decrement analysis.
(2) Measured frequency response for an actuator-controlled input displacement using a bandwidth-limited random noise excitation signal with an actuator preload of 31.1 kN (7,000 lbs).
(3) Measurements made without the central rod primary restraint system in place.

The two straight pipe experiments were conducted in Battelle's large pipe bend facility located at Battelle's West Jefferson, Ohio test site. Figure 3.13 is a post-test photograph of the quasi-static four-point bend through-wall-cracked pipe specimen setup in this facility. The two hydraulic actuators associated with this facility, located at the vertical columns, are each capable of applying 2,000 kN (450 kips) of force to the test pipes. For the quasi-static companion experiments conducted as part of Task 1, the applied loads were measured with load cells in the load train. The applied forces from these actuators are reacted by a series of wire ropes at each end of the test pipes.

For the quasi-static bend elbow girth weld experiment, the large pipe bend facility was modified to accommodate the curved test specimen. Figure 3.14 is a pre-test photograph of the quasi-static bend elbow girth weld experiment set up in this facility. For this facility, a specially fabricated strongback was constructed on top of the existing large pipe bend facility. A 1500 pound class weld neck flange, with a section of high strength A710 Grade A Class 3 pipe welded to it, was bolted to this strongback. The elbow girth weld test specimen was welded to this straight pipe section. The elbow girth weld test specimen included both the test elbow and a section of A106 Grade B test pipe. In Figure 3.14 the crack was in the elbow girth weld joining the elbow girth weld test specimen to the vertical leg. The crack in the test weld was at the extrados of the elbow. Attached to the other end of elbow was a section of moment arm pipe. For this facility only one of the two hydraulic actuators associated with the large pipe bend facility was used. The east hydraulic actuator pulled down on the horizontal moment arm pipe, thus putting the extrados crack in the test elbow girth weld in tension.

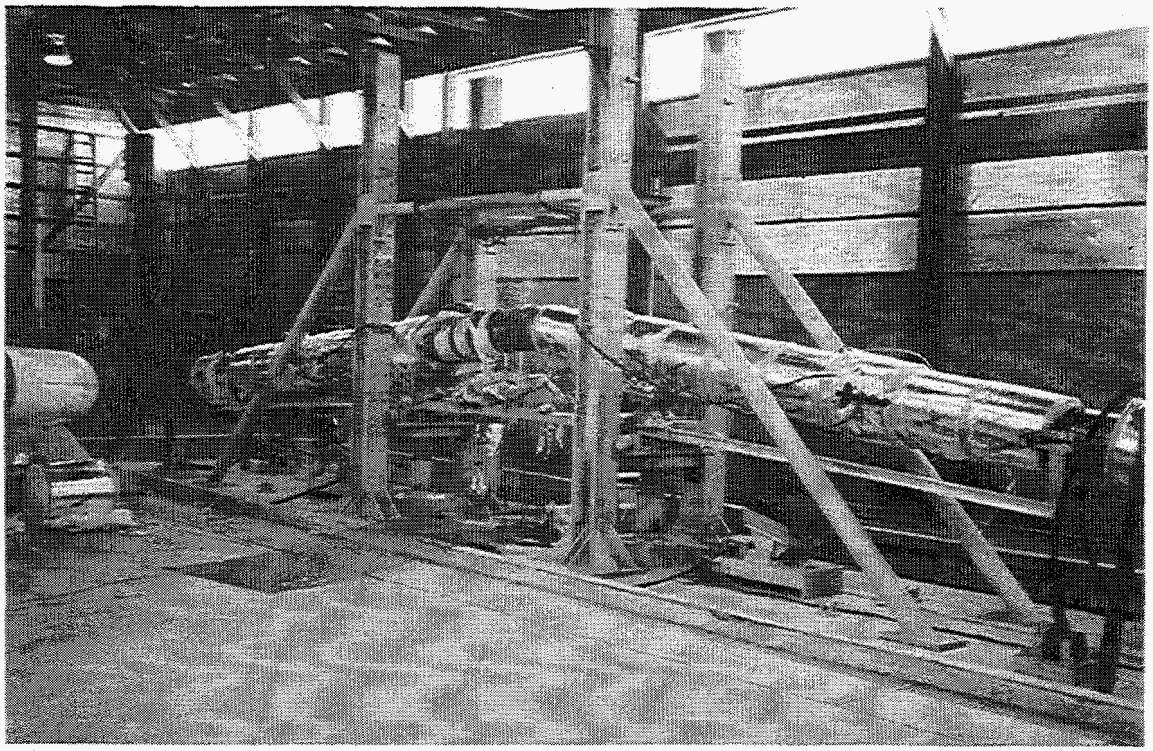

Figure 3.13 Post-test photograph of the quasi-static four-point-bend through-wall-cracked-pipe specimen set up in Battelle's large pipe bend facility

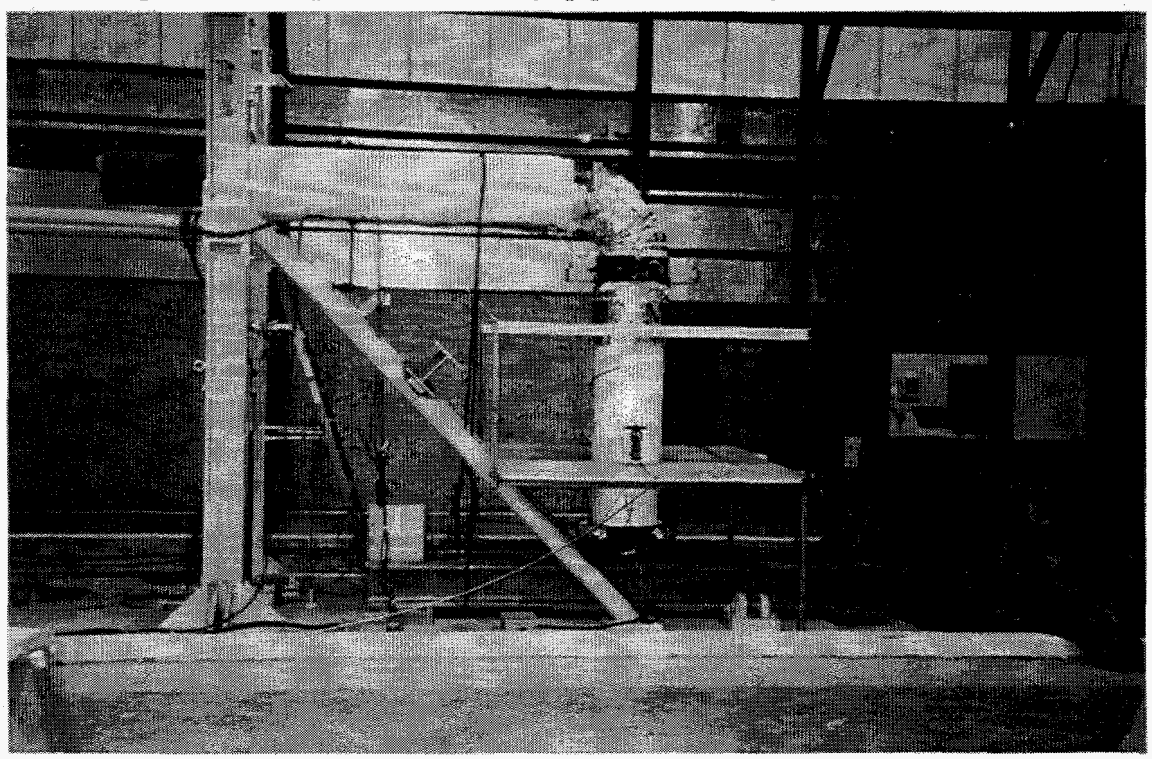

Figure 3.14 Pre-test photograph of the quasi-static bend elbow girth weld experiment setup in the quasi-static bend elbow facility

3.5 General Test Procedures

The IPIRG-2 Task 1 experiments were conducted following the procedures set forth in the Quality Assurance Document IPI2-PP-1, Revision 1, "Procedure for Performing Pipe Fracture Experiments Under Combined Inertial and Seismic/Dynamic Displacement Controlled Stresses". This document specified detailed checklist-type procedures for preparing the test specimens (Section 5.0), for setting up the dynamic pipe system experiments (Section 6.0), for conducting the pipe system experiments (Section 7.0), for conducting the companion quasi-static bend experiments (Section 8.0), and for documenting the results of the experiments (Section 9.0).

3.5.1 Test Specimen Preparation

The first step in preparing a test specimen for one of the IPIRG-2 Task 1 pipe experiments was to fabricate the test weld, if the experiment involved a crack in a weld. Four of the eight Task 1 experiments were weld crack experiments and four were base metal crack experiments. Of the four weld experiments, two involved stainless steel welds and two involved carbon steel welds. All of the welds were lower toughness flux welds, i.e., submerged-arc welds (SAW). The stainless steel weld procedure was obtained from the General Electric (GE) Corporation as part of the Degraded Piping Program (Ref. 3.1). The weld procedure is a typical pipe weld used in U.S. boiling water reactor (BWR) plants. The first two layers of Type 308 stainless steel weld metal are deposited by the gas-tungsten-arc process (sometimes called TIG welding). These TIG weld passes are followed by two layers of shielded-metal-arc weld (SMAW), with the balance of the weld being made by the submerged-arc weld (SAW) process. Of note is the fact that the initial TIG layers are much higher in toughness than the succeeding SMAW and SAW layers. However, since the surface cracks evaluated in this program and related programs were typically 50 to 66 percent of the pipe wall thickness in depth, the crack tip ended up in the lower toughness flux weld metal. It is also of note that fracture toughness data developed as part of the Degraded Piping Program for this weld procedure were used in the development of the technical basis for the stainless steel flux weld criteria embodied in Article IWB-3640 of Section XI of the ASME Code (Ref. 3.2).

The carbon steel weld procedure was obtained from Babcock and Wilcox (B&W). This was a C-Mn-Mo-Ni weld procedure first evaluated in a pipe fracture experiment during the Degraded Piping program, i.e., Experiment 4141-8. This same weld procedure was also used in an IPIRG-1 pipe system experiment, i.e., Experiment 1.3-4. The weld specification specified a single-Vee weld having a 6.4 mm (0.25 inch) gap. A 9.5 mm (0.38 inch) thick steel backing ring was used for the root pass. The filler metal met Specification SFA-5.23, Class EF2 (Linde 44) and the flux was Linde 80. The weld was stress relieved at 605 C (1125 F) for 1 hour. This weld procedure was used for about 10 percent of the pipe welds in B&W plants. The majority of the remaining B&W carbon steel pipe welds were fabricated using a procedure evaluated during the Short Cracks in Piping and Piping Welds Program (Ref. 3.3). The Short Cracks weld procedure was a lower toughness [J_i = 56 kJ/m^2 (320 in-lb/in^2 versus 82 kJ/m^2 (470 in-lb/in^2)] and lower nickel content [0.013 percent versus 0.60 weight percent] weld procedure than that used in the fabrication of the Degraded Piping and IPIRG welds. The filler metal for this Short Cracks weld met Specification SFA 5.23, Class EA3. The flux was Linde 80 as was the case for the welds evaluated as part of this program. All of the welds were fabricated by the United McGill Corporation of Columbus, Ohio.

After fabricating the test welds, the next step in the specimen preparation procedures was the introduction of a machined flaw. For the two simulated seismic pipe system experiments, Experiments 1-1 and

1-2, the machined surface flaws were introduced using a horizontal milling machine. For the two elbow girth weld experiments, Experiments 1-3 and 1-4, and the two short surface crack experiments, Experiments 1-5 and 1-6, the machined surface flaws were introduced using electric-discharge-machining (EDM) techniques. For the two 16-inch diameter short through-wall-cracked experiments, Experiments 1-7 and 1-8, the machined through-wall flaws were also introduced using EDM techniques. For the 6-inch nominal diameter bellows verification through-wall-cracked pipe experiment, Experiment 1-9, the machined flaw was introduced using a saw cut and sharpened with a jeweler's saw. For all of the experiments with the exception of the stainless steel base metal simulated seismic experiment and the 6-inch nominal diameter bellows verification experiment, Experiments 1-1 and 1-9, the machined flaws were sharpened and extended through fatigue loading.

Once the flaws were introduced into the test specimens, the flaws were instrumented with electric potential probes and crack-opening displacement devices, typically LVDTs. The instrumented test specimens were then welded to moment arm pipes (for the companion quasi-static experiments) or into the pipe system (for the dynamic pipe system experiments). The remainder of the instrumentation was then incorporated into the overall test specimen. Figure 3.15 shows a schematic of the instrumentation plan typically used for the IPIRG-2 Task 1 pipe system experiments. Table 3.2 is a summary table showing what instrumentation was used on the different Task 1 experiments.

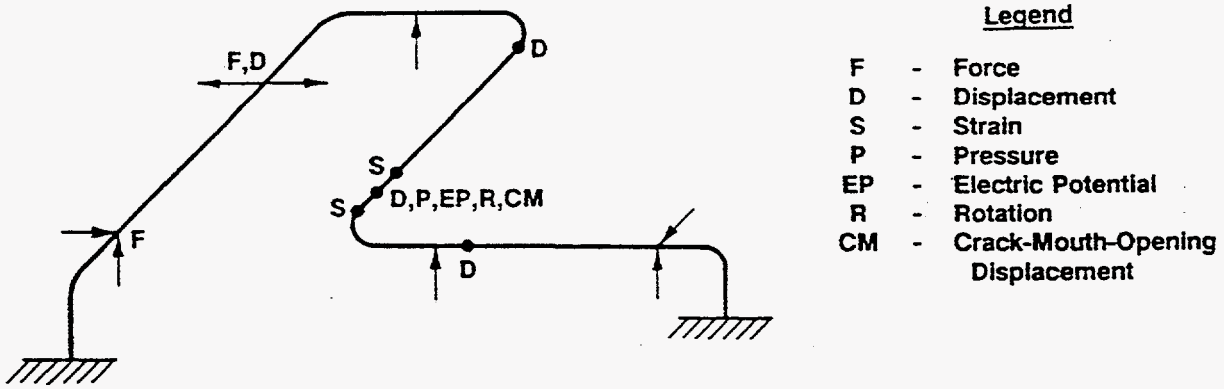

Figure 3.15 Schematic of the instrumentation plan typically used for the Task 1 pipe system experiments

In addition to the instrumentation listed in Table 3.2, there was often additional instrumentation incorporated into the overall instrumentation plan for the pipe system experiments to facilitate the shutdown of the experiment. For the single frequency pipe system experiments, a Battelle-built programmable attenuator was incorporated into the control logic to shut down the forcing function once

Table 3.2 Instrumentation used in IPIRG-2 Task 1 experiments

	Experiment No.								
	1-1	1-2	1-3	1-4	1-5	1-6	1-7	1-8	1-9
Applied Load or Moment	X	X	X	X	X	X	X	X	X
Applied Displacements	X	X	X	X	X	X	X	X	X
Pipe Displacements	X	X	X	X	X	X	X	X	
Rotation	X	X	X	X	X	X	X	X	
CMOD	X	X	X	X	X	X	X	X	
d-c EP	X	X	X	X	X	X	X	X	X
Pipe Pressure	X	X	X	X	X	X	X	X	X
Ovalization				X		X			
Reaction Force	X	X	X		X		X		
Strains			X	X					

the pressure inside the test specimen dropped below a preset value. Once the attenuator sensed a drop in internal pressure, the command signal controlling the motion of the hydraulic actuator exciting the pipe system was linearly attenuated over a 3 to 4 second time interval. For the simulated seismic pipe system experiments, the programmable attenuator was set up so that it needed to sense not only the drop in internal pressure, but also the occurrence of a pipe break, i.e., a double-ended-guillotine-break (DEGB). The instrumentation device used to sense the occurrence of the DEGB was a trip wire on the original compressive side of the test specimen, 180 degrees from the centerline of the surface crack.

3.5.2 Test Conditions

The test conditions for each of the pipe experiments conducted as part of Task 1 were representative of pressurized water reactor (PWR) conditions, 288 C (550 F) and 15.5 MPa (2,250 psi).

3.6 References

3.1 Wilkowski, G. M., and others, "Degraded Piping Program - Phase II: Summary of Technical Results and Their Significance to Leak-Before-Break and In-Service Flaw Acceptance Criteria - March 1984 - January 1989," NUREG/CR-4082, Vol. 8, March 1989.

3.2 American Society of Mechanical Engineering Boiler and Pressure Vessel Code, Section XI Article IWB-3640, July 1995.

3.3 Brust, F. W., and others, "Assessment of Short Through-Wall Circumferential Cracks in Pipes," NUREG/CR-6235, April 1995.

4.0 RESULTS OF IPIRG-2 TASK 1 PIPE FRACTURE EXPERIMENTS

In this section, the results of the IPIRG-2 Task 1 pipe fracture experiments will be presented. Table 4.1 shows the test matrix for the Task 1 experiments. Included in Table 4.1 are nine IPIRG-2 Task 1 experiments. Eight of these experiments were on 16-inch nominal diameter pipes. This is the same pipe size evaluated in the IPIRG-1 pipe system experiments. The ninth experiment listed in Table 4.1 is a 6-inch nominal diameter through-wall-cracked pipe experiment. This experiment was not in the original Task 1 test matrix. The original intent for this experiment was to evaluate the effectiveness of a bellows inside the pipe at providing a pressure seal for a circumferential through-wall crack. The intent for this experiment was not to collect pipe fracture data. However, some pipe fracture data were collected and due to limited data for experiments on pipes with a through-wall crack subjected to combined pressure and dynamic four-point bending, it was decided to analyze these data in more detail. Also included in Table 4.1 are eight companion experiments conducted as part of the Degraded Piping (Ref. 4.1), IPIRG-1 (Ref. 4.2), or a Battelle/EPRI (Ref. 4.3) program.

Table 4.1 Test matrix for IPIRG-2 Task 1 experiments and companion experiments from References 4.1, 4.2, and 4.3

Experiment No.	Program[1]	Crack Geometry[2]	Material[3]	Crack Location	Loading History
1-1	IPIRG-2	SC	SSBM	Straight Pipe Base Metal	Simulated Seismic
EPRI13S[4]	BCD/EPRI	SC	SSBM	Straight Pipe Base Metal	Quasi-Static Monotonic Bend
1.3-3	IPIRG-1	SC	SSBM	Straight Pipe Base Metal	Single Frequency
1-2	IPIRG-2	SC	CSBM	Straight Pipe Base Metal	Simulated Seismic
4112-8	DP3II	SC	CSBM	Straight Pipe Base Metal	Quasi-Static Monotonic Bend
1.3-2	IPIRG-1	SC	CSBM	Straight Pipe Base Metal	Single Frequency
1-3	IPIRG-2	SC	CSW	Elbow-to-Pipe Girth Weld	Single Frequency
1-4	IPIRG-2	SC	CSW	Elbow-to-Pipe Girth Weld	Quasi-Static Monotonic Bend
4141-8	DP3II	SC	CSW	Pipe-to-Pipe Girth Weld	Quasi-Static Monotonic Bend
1.3-4	IPIRG-1	SC	CSW	Pipe-to-Pipe Girth Weld	Single Frequency
1-5	IPIRG-2	SC	SSW	Pipe-to-Pipe Girth Weld	Single Frequency
1-6	IPIRG-2	SC	SSW	Pipe-to-Pipe Girth Weld	Quasi-Static Monotonic Bend
4141-4	DP3II	SC	SSW	Pipe-to-Pipe Girth Weld	Single Frequency
1.3-5	IPIRG-1	SC	SSW	Pipe-to-Pipe Girth Weld	Quasi-Static Monotonic Bend
1-7	IPIRG-2	TWC	CSBM	Straight Pipe Base Metal	Simulated Seismic
1-8	IPIRG-2	TWC	CSBM	Straight Pipe Base Metal	Quasi-Static Monotonic Bend
1-9[5]	IPIRG-2	TWC	CSBM	Straight Pipe Base Metal	Dynamic Monotonic Bend

(1) BCD/EPRI (Ref. 4.3); IPIRG-1 (Ref. 4.2); DP3II (Ref. 4.1).
(2) SC = Surface crack; TWC = through-wall crack.
(3) SSBM = Stainless steel base metal; CSBM = carbon steel base metal; CSW = carbon steel weld; SSW = stainless steel weld.
(4) Ambient temperature test; all other tests conducted at 288 C (550 F).
(5) 6-inch nominal diameter test; all other tests 16-inch nominal diameter.

These experiments are analyzed along with the IPIRG-2 data in Section 5.0. Comparing the results from these IPIRG-2 Task 1 experiments with those from the previously conducted companion experiments will help answer some of the fundamental questions which led to the IPIRG-2 program.

In the section that follows, the results from the two internal surface-cracked simulated seismic pipe system experiments will be presented first. This will be followed by a presentation of the results from the two elbow girth weld experiments. This discussion is followed by a presentation of the results from the three short surface-cracked pipe experiments. The section concludes with a discussion of the results from the three short through-wall-cracked pipe experiments.

4.1 Simulated Seismic Pipe System Experiments

Two surface-cracked pipe simulated seismic pipe system experiments, Experiments 1-1 and 1-2, were conducted as part of Task 1 of the IPIRG-2 program. A third simulated seismic through-wall cracked pipe experiment was also conducted. (This experiment will be discussed later in Section 4.4.) The objective of these two surface-cracked simulated seismic experiments was to gather experimental data for assessing the fracture behavior and stability of a circumferential internal surface crack in a representative piping configuration subjected to a simulated seismic load history. The cracked test specimens for these two experiments were sections of Type 304 stainless steel (Experiment 1-1) and A106 Grade B carbon steel (Experiment 1-2). Companion quasi-static monotonic four-point bend surface-cracked pipe experiments were conducted previously. One as part of a prior EPRI program conducted at Battelle (Ref. 4.3), Experiment EPRI 13S in Table 4.1, and one in the Degraded Piping Program (Ref. 4.1), Experiment 4112-8 in Table 4.1. For both of these companion four-point bend experiments, the test specimen was unpressurized. The stainless steel EPRI experiment (EPRI 13S) was conducted at ambient temperature, i.e., 22 C (68 F), and the carbon steel Degraded Piping Program experiment (4112-8) was conducted at 288 C (550 F). In addition to the quasi-static four-point bending experiments, companion single frequency pipe system experiments were also conducted as part of the IPIRG-1 program (Ref. 4.2) using these same two pipe materials. For these single frequency pipe system experiments, the test conditions were representative of pressurized water reactor (PWR) conditions; 288 C (550 F) temperature and 15.5 MPa (2,250 psi) internal pipe pressure. The test temperature and pressure for the simulated seismic pipe system experiments conducted as part of IPIRG-2 were the same. For each of these experiments, the nominal crack size was approximately 50 percent of the pipe circumference in length and 66 percent of the pipe wall thickness in depth. By comparing the results for the different load histories it is possible to see if there is a difference in the response of the cracked test section between the seismic load history, with its multiple frequency content, and that due to the single frequency and quasi-static monotonic load histories. Note, however, that due to differences in test specimen sizes and crack sizes, the reader is cautioned against making direct comparisons of results between experiments until the results have been normalized by the fracture prediction analyses in Section 5.0.

4.1.1 Design of the Simulated Seismic Forcing Function

The global objective of the simulated seismic experiments was to determine what effect, if any, variable amplitude, multi-frequency loading has on cracked pipe in a pipe system. The principal parameters of interest were maximum moment and propensity for a double-ended guillotine break (DEGB) after maximum moment was achieved.

The ideas governing the design of the seismic forcing function were embodied in three premises:

1. The objective of the design process was only to define an actuator displacement time-history, and not to necessarily explore the full probabilistic nature of true seismic events.

2. Accepted seismic design procedures were to be used.

3. The criteria for selecting a particular forcing function were principally based on the engineering requirements for the test system, i.e., servo-hydraulic constraints.

This design approach provided a framework for selecting possible technical approaches, limiting the scope of the design effort, and a rationale for assessing the merits of competing design alternatives.

The specific steps taken to implement the design approach were as follows:

1. The U.S. NRC Regulatory Guide 1.60 ground acceleration response spectrum provided the basic description of the seismic input.

2. An artificial time-history of ground acceleration was generated that is spectrum-consistent with Step 1 using the SIMQKE computer program. The artificial time-history was forced to be consistent with U.S. NRC Standard Review Plan 3.7.1 prescriptions for duration, frequency spacing, power spectral density (PSD), and spectra enveloping.

3. A simple, 9 degree-of-freedom model of a pressurized water reactor (PWR) plant was used as a transfer function between the time-history ground acceleration and an assumed location for the pipe system.

4. The relative motion between two "floors" in the PWR model represented the displacements to be applied to the pipe system.

5. The time-history of actuator motion for the IPIRG pipe loop was selected by finding a single-point excitation displacement time history that would give the same moment-time response at the crack location as the multi-point excitation defined in Step 4.

6. Scaling of the input ground acceleration was fixed by a desire to have the surface crack penetration be due to ductile tearing and not fatigue, and a need to maintain an adequate margin on servo-hydraulic capacities.

7. A finite element model of the pipe system, including a nonlinear representation of the cracks, was used to predict the response of the pipe system to the simulated seismic loading. The predicted response was the basis for Step 6.

Following these basic steps, a reasonably realistic seismic forcing function was developed. The forcing function included all of the essential elements of a true seismic event at a plant in a relatively simple fashion, without unnecessary complications. Additional details related to the design of the IPIRG-2 simulated seismic forcing function can be found in NUREG/CR-6439 (Ref. 4.4).

The basic seismic forcing function was developed on the basis of a 1.0 g earthquake. To satisfy the requirements for the IPIRG-2 simulated seismic experiments, the basic 1.0 g earthquake needed to be scaled. The test philosophy used for the IPIRG-2 simulated seismic experiments was to apply three increasing levels of loading:

1. "SSE" level - an excitation that would be considered representative of a safe shut-down earthquake (SSE) to demonstrate that the design basis for current plants is adequate. Significant crack propagation was not expected to occur under this loading.

2. "Test" level - best estimate of scaled basic forcing function that would result in surface crack penetration some time during the time history.

3. "Decision Tree" - a loading to be applied if the "Test" loading did not result in surface crack penetration or if the resultant crack opening due to the "Test" loading was small. Application of this load was contingent upon critical instrumentation being functional after the "Test" loading and the ability to be able to visually inspect the system by remote video (i.e., steam does not obscure the test section).

To define the various load levels, nonlinear spring, cracked-pipe finite element analyses were used. In these analyses, the cracked section was modeled as a nonlinear moment-rotation spring. Analyses were performed in the time domain and considered growth of surface or through-wall cracks, the occurrence of surface crack penetration, and transition of a surface crack to a through-wall crack.

Based on nonlinear cracked pipe analyses, the "Test" level excitation required to achieve surface crack penetration for the carbon steel and stainless steel base metal experiments was 1.25 g. Based on a nuclear plant stress survey, a 0.2 g excitation was selected for the "SSE" level loading. A 1.38 g level was chosen for the "Decision Tree" loading. In all cases, the forcing functions were just scaled from the basic 1.0 g level.

Figures 4.1 and 4.2 show the actuator displacement-time history for the "SSE" and "Test" level excitations, respectively. The seismic functions last 20 seconds: 5 seconds of build up, 10 seconds of stationary signal, and 5 seconds of decay. Compared to the IPIRG-1 forcing functions, the seismic functions are rich in frequency content and they show significant negative displacement excursions.

Figure 4.3 shows the response spectra for the simulated seismic load history. The damping values shown in this figure are representative of values for floor response spectra for nuclear power plants and are not equivalent to the damping associated with the IPIRG pipe loop. From Figure 4.3, it can be seen that the simulated seismic load history contains frequencies up to 40 Hz, with most of the large amplitude motions occurring in the 1 to 10 Hz range.

Although the seismic forcing function and the design of the pipe loop are rooted in plant practice, it is reasonable to question how representative the resulting stresses actually are. In order to make that assessment, Battelle obtained elastically-calculated stress data from actual plant piping system stress analyses and compared those data with the elastically-calculated crack section stresses for the IPIRG-2 pipe system. For this comparison, the actuator displacement-time history from the stainless steel base metal simulated seismic pipe system experiment was used as input. Battelle obtained the actual plant piping system stress data from two sources. One source of data was a presentation made by Mr. Nate Cofie of

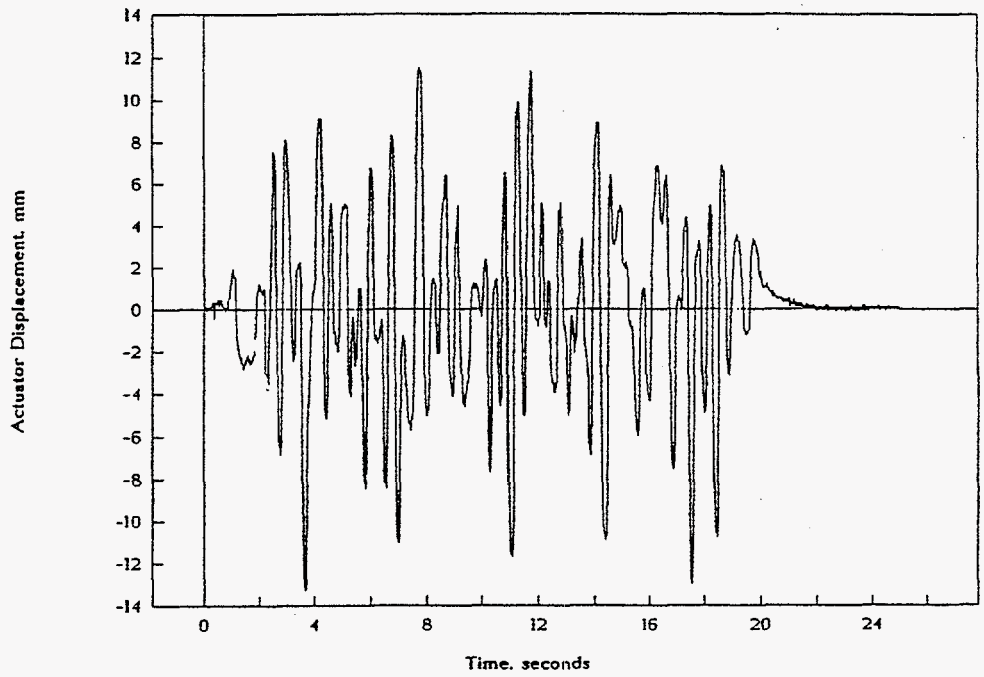

Figure 4.1 Actuator displacement versus time history for the "SSE" forcing function

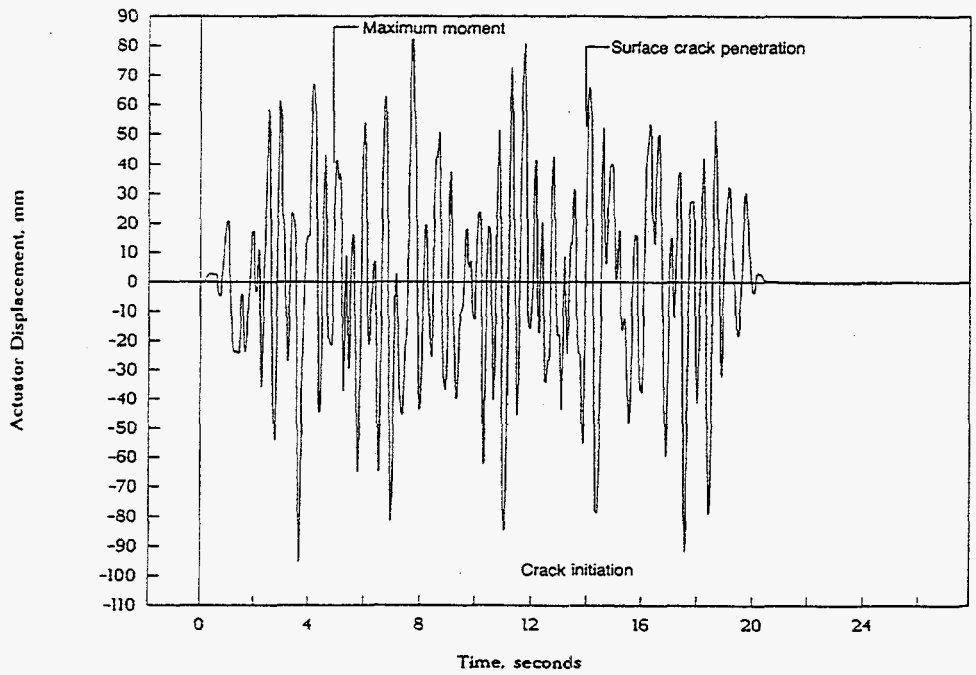

Figure 4.2 Actuator displacement versus time history for the "Test" forcing function

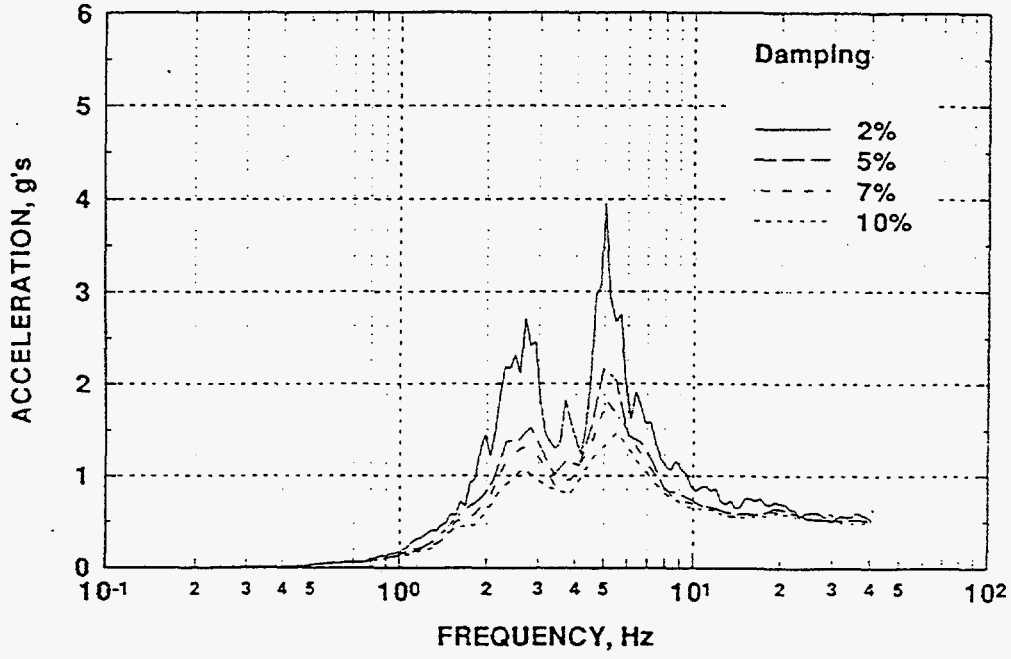

Figure 4.3 Response spectra of actuator motion for simulated seismic load history

Structural Integrity Associates, Inc. to the ASME Section XI Working Group on Pipe Flaw Evaluation in January 1994. As part of that presentation, elastically-calculated stresses for a number of welds in a number of piping systems were presented for four different plants. The welds chosen for comparison were from 12-inch nominal diameter pipe, because the pipe diameter was close to the 16-inch nominal diameter pipe in the IPIRG loop. The piping system stresses were broken down into four basic stress components: pressure, deadweight, thermal, and seismic due to the operational basis earthquake (OBE). In discussions between Battelle and Mr. Cofie, it was determined that he assumed that the stresses due to a safe shutdown earthquake (SSE) would be twice those due to an operational basis earthquake. As a result, the seismic stresses he presented were adjusted accordingly in order to allow for an equal comparison between his stresses and those calculated for the IPIRG pipe system subjected to a simulated SSE load history. Additional stress data were obtained from Mr. Steve Gosselin, the IPIRG TAG representative from EPRI. Mr. Gosselin presented some data he had obtained from Mr. Seth Swamy and Mr. Dulal Bhowmick of Westinghouse. Westinghouse presented elastically calculated normal operating (deadweight, thermal expansion, and pressure induced stresses) plus the safe shutdown earthquake (SSE) stresses for the weld connecting the hot leg to the nozzle on the reactor pressure vessel (see Figure 4.4) for two different plants.

Figure 4.5 shows a comparison of elastically-calculated stresses for actual plant piping systems and elastically-calculated stresses for the IPIRG pipe system using the actuator displacement-time history from the stainless steel base metal simulated seismic experiment as input. The IPIRG pipe system stresses are presented for both the "SSE" and "Test" forcing functions. As can be seen in Figure 4.5, the stresses due to the "SSE" excitation agree very well with the calculated stresses from the actual plant piping systems. As should be expected, the calculated stresses due to the "Test" forcing function are quite a bit higher than the calculated stresses from actual plant piping systems.

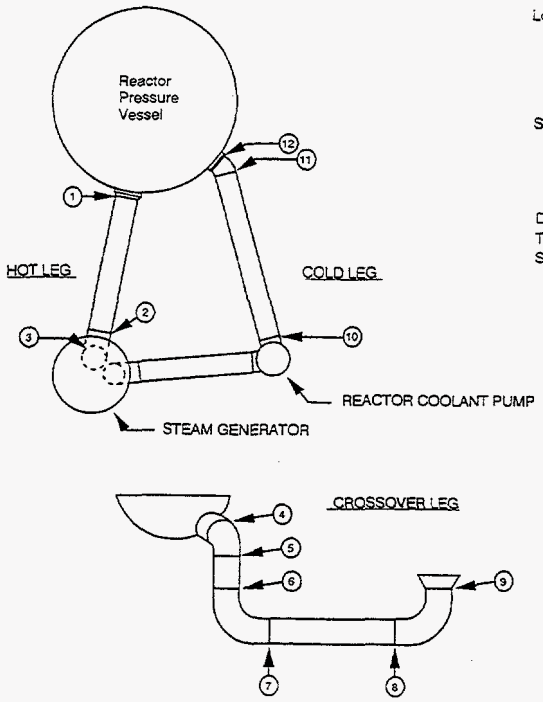

Location #1 is the Highest Stressed (typically)	Plant A	Plant B
Nominal Outer Diameter (in) =	34.0	34.0
Thickness (in) =	2.50	2.50
Pressure(psia) =	2250	2250
Temperature(°F) =	620	620
Stress Component (psi)		
Normal Stress (DW + Th + Press)	21660	19840
Faulted Stress (Normal + SSE)	23780	35130

DW = Deadweight
Th = Thermal Expansion
SSE = Seismic including Seismic Anchor Motion

Prepared By: Dulal Bhowmick
Verified By: Daniel E. Prager

Figure 4.4 Schematic of a Westinghouse loop piping system showing the location of the hot leg to reactor pressure vessel (RPV) weld for which Westinghouse provided elastically-calculated plant stresses for comparison with the IPIRG pipe loop stresses

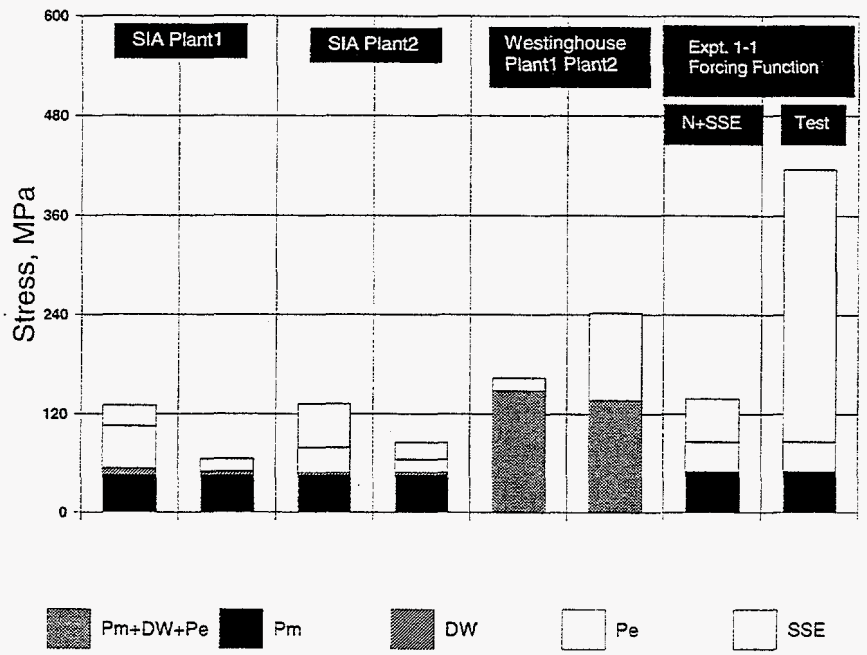

Figure 4.5 Comparison of elastically-calculated stresses for actual plant piping systems to elastically calculated stresses for the IPIRG pipe system

4.1.2 Experimental Results

The key results from the two surface-cracked simulated seismic experiments are shown in Table 4.2. Also included in Table 4.2 are the results for the companion quasi-static monotonic four-point bend and the companion single frequency pipe system experiments. Shown in Table 4.2 are the test conditions (pipe diameters, wall thicknesses, crack depths, crack lengths, test pressures, and test temperatures), material property data (yield and ultimate strengths and J values at crack initiation [J_i] from C(T) specimen tests), and moments at crack initiation and maximum moments for each of the six pertinent experiments. Table 4.2 and the subsequent figures typically show only the "Test" forcing function results. Unless showing the "SSE" data serves a specific purpose, the data from the "SSE" phase of the experiment are not included because the crack did not extend in either experiment as a result of this loading. This was as expected.

4.1.2.1 Experiment 1-1 Results

Figure 4.6 is a plot of the internal pipe pressure as a function of time for Experiment 1-1. The drop in pressure in this figure indicates the time when the surface crack penetrated the pipe wall. For Experiment 1-1 the time at surface crack penetration was 14.035 seconds into the "Test" forcing function.

Table 4.2 Key results from two simulated seismic pipe system experiments (1-1 and 1-2) plus two companion quasi-static monotonic experiments (EPRI 13S and 4112-8) and two companion single-frequency pipe system experiments (1.3-3 and 1.3-2)

Expt. No.	Outside Pipe Diameter, mm	Wall Thickness, mm	a/t[1]	2c/πD[2]	Test Pressure, MPa	Test Temperature, C	Yield[3] Strength, MPa	Ultimate[3] Strength MPa	J at[3] Crack Initiation C(T) Specimen, kJ/m²	Moment at Crack Initiation, kN-m	Maximum Moment, kN-m
1-1	417.1	25.53	0.628	0.527	15.5	288	171	456	854	594	598
EPRI 13S	413.5	28.32	0.66	0.58	0	18	295	743	2,277	970	1260
1.3-3	415.8	26.19	0.66	0.552	15.5	288	171	456	546	415	426
1-2	405.1	24.82	0.719	0.525	15.5	288	241	618	149	ND[4]	476
4112-8	402.6	26.42	0.662	0.532	0	288	241	618	149	689	748
1.3-2	403.9	25.70	0.727	0.525	15.5	288	241	618	149	ND[4]	341

(1) At the location where the crack was deepest.
(2) Total crack length on inside pipe surface divided by inside pipe circumference.
(3) Quasi-static material data.
(4) ND = Not determined.

Figure 4.7 is a plot of the crack section moment as a function of time for Experiment 1-1. The crack section moment data were taken as the average of the moments on either side of the crack. The assumption of a linear distribution of moment between moments on either side of the crack was confirmed with an ANSYS finite element analysis, see Figure 4.8, and was also found to hold true experimentally during the uncracked shakedown experiment conducted as part of the IPIRG-1 program (Experiment 1.3-1). The moments inferred from the measured strain gage data are for the dynamic component of moment only. The statically indicated component of the strain has been subtracted from the experimental data because it was not possible to separate the effects of pressure and thermal expansion from electrical drift in the strain gage circuits which occurred during the 48 hours of heatup. To be able to report total moment values (static plus dynamic), the static (time=0) values of moment due to pressure and thermal expansion stresses were determined from an ANSYS finite element analysis and then added to the dynamic moment values inferred from the measured strains. The ANSYS-calculated static value of moment for the crack location was 103.1 kN-m (913 in-kips). From Figure 4.7, it can be seen that the maximum total moment (static plus dynamic) at the crack section for Experiment 1-1 was 598 kN-m (5,290 in-kips) and occurred 5.03 seconds into the "Test" forcing function.

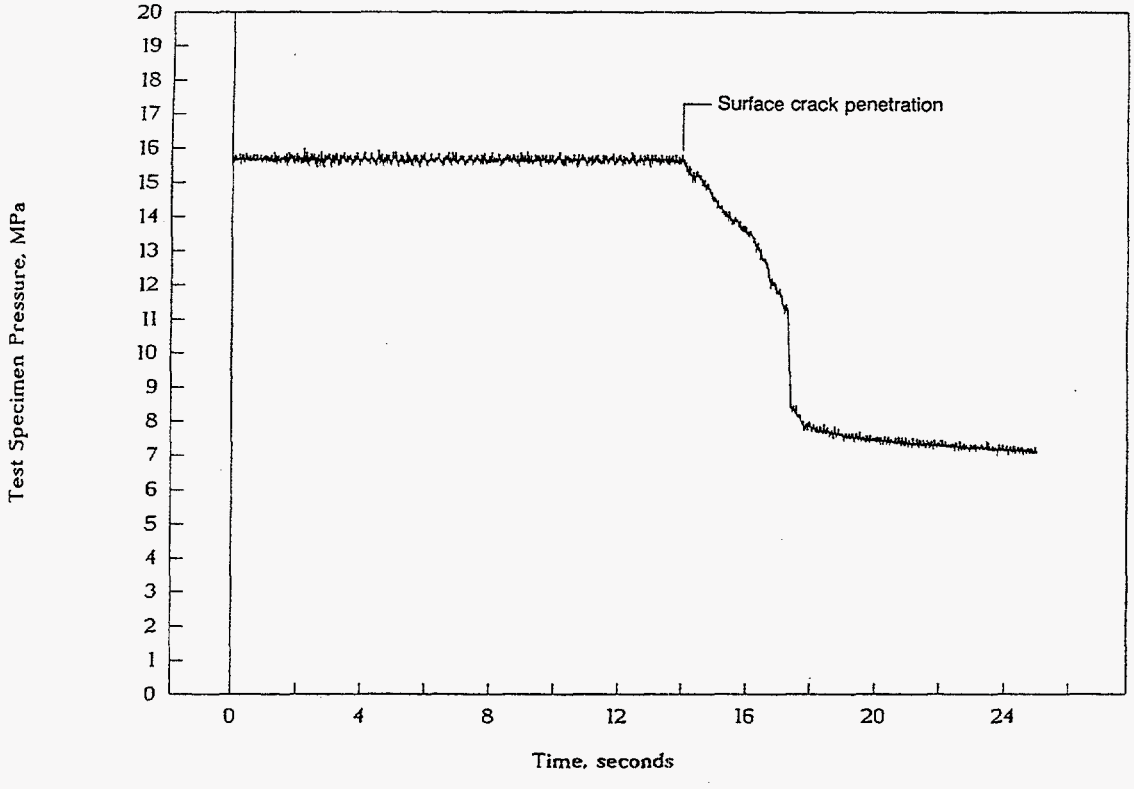

Figure 4.6 Experiment 1-1 test specimen pressure versus time history for the "Test" forcing function

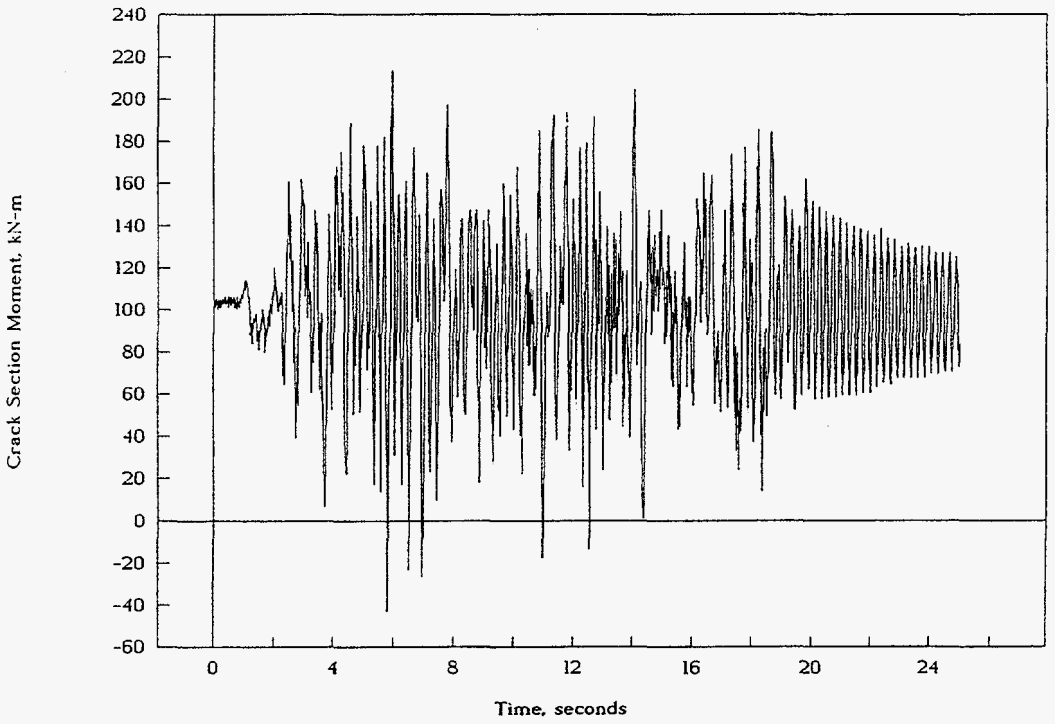

(a) "SSE" forcing function

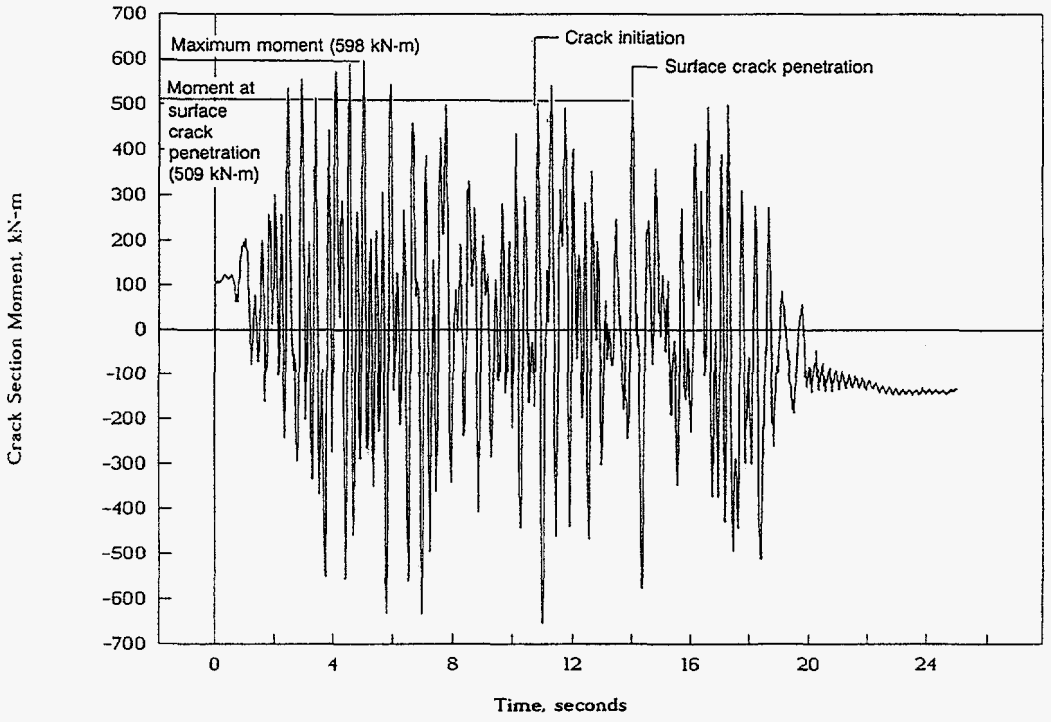

(b) "Test" forcing function

Figure 4.7 Experiment 1-1 crack section moment versus time history

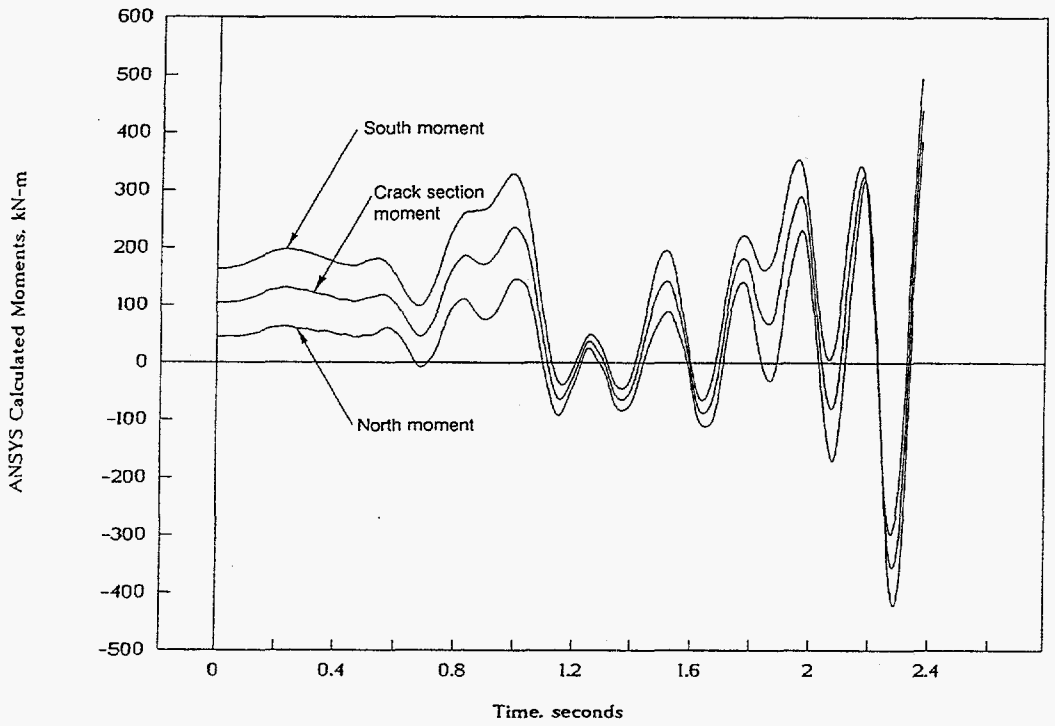

Figure 4.8 ANSYS calculated moments for Experiment 1-1 for the South moment cell, North moment cell, and crack location (Note, the moment at the crack location is the average of the moments at the North and South moment cells for the entire plot)

Figures 4.9 and 4.10 are bar charts showing histograms (number of occurrences) of experimental stresses (membrane plus bending) for the "SSE" and "Test" forcing functions, respectively, for the stainless steel base metal simulated seismic pipe system experiment (i.e., Experiment 1-1). For reference, the ASME Code yield strength value (S_y) for TP304 stainless steel at 288 C (550 F) is shown in the histogram for the "SSE" excitation, see Figure 4.9. For the "Test" forcing function histogram (Figure 4.10), the ASME Code yield strength (S_y) plus the Service Level B, C, and D limits are shown for reference. As can be seen in Figure 4.9, the maximum experimental stress was less than the ASME Code yield strength value (S_y) for 93 of the 98 cycles associated with the 20 second long "SSE" excitation. Furthermore, all 98 cycles resulted in maximum stresses less than the Service Level B limit of 194 MPa (28.2 ksi). Conversely, for the "Test" forcing function, only 13 of the 54 cycles associated with this excitation resulted in a maximum stress less than the ASME Code yield strength value of 130 MPa (18.8 ksi). In addition, the maximum experimental stress exceeded the Service Level C limit 11 times and the Service Level D limit three times. Figures 4.9 and 4.10 demonstrate the relative severity of the "Test" forcing function where compared with that of the "Normal plus SSE" excitation.

Figures 4.11 and 4.12 are plots of the crack section moment data from Experiment 1-1 as a function of the crack-mouth-opening-displacement (CMOD) and crack section rotation data, respectively. The overall characteristics of both figures are very similar. Both figures show an initial region where the response is cyclic, but linear in nature. After this initial linear-elastic cyclic response, a single, large-amplitude cycle occurs during which there is significant plasticity at the crack section. As can be seen from the CMOD-time and rotation-time response plots for this experiment, see Figures 4.13 and 4.14, this initial large

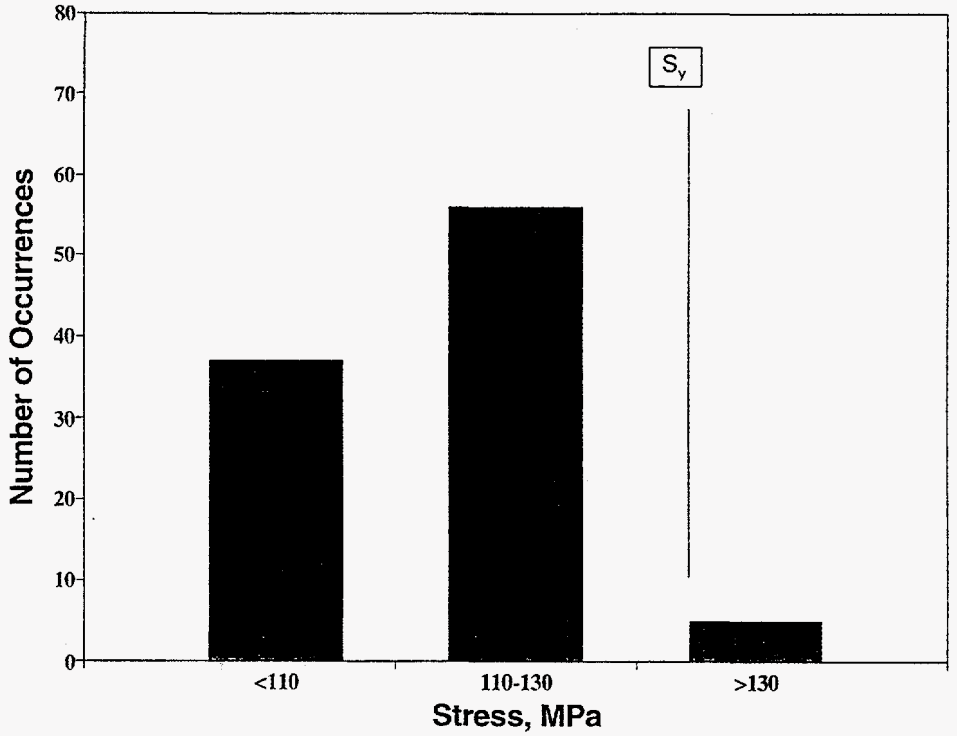

Figure 4.9 Histogram of experimental stress amplitudes (membrane plus bending) for the "SSE" excitation for Experiment 1-1

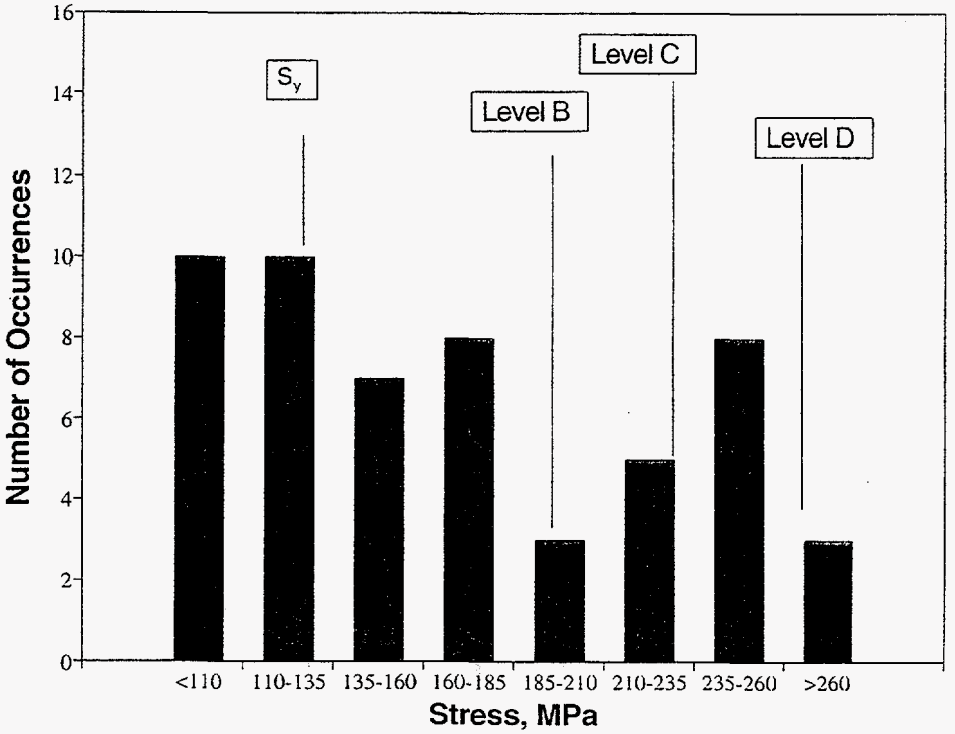

Figure 4.10 Histogram of experimental stress amplitudes (membrane plus bending) for the "Test" forcing function for Experiment 1-1

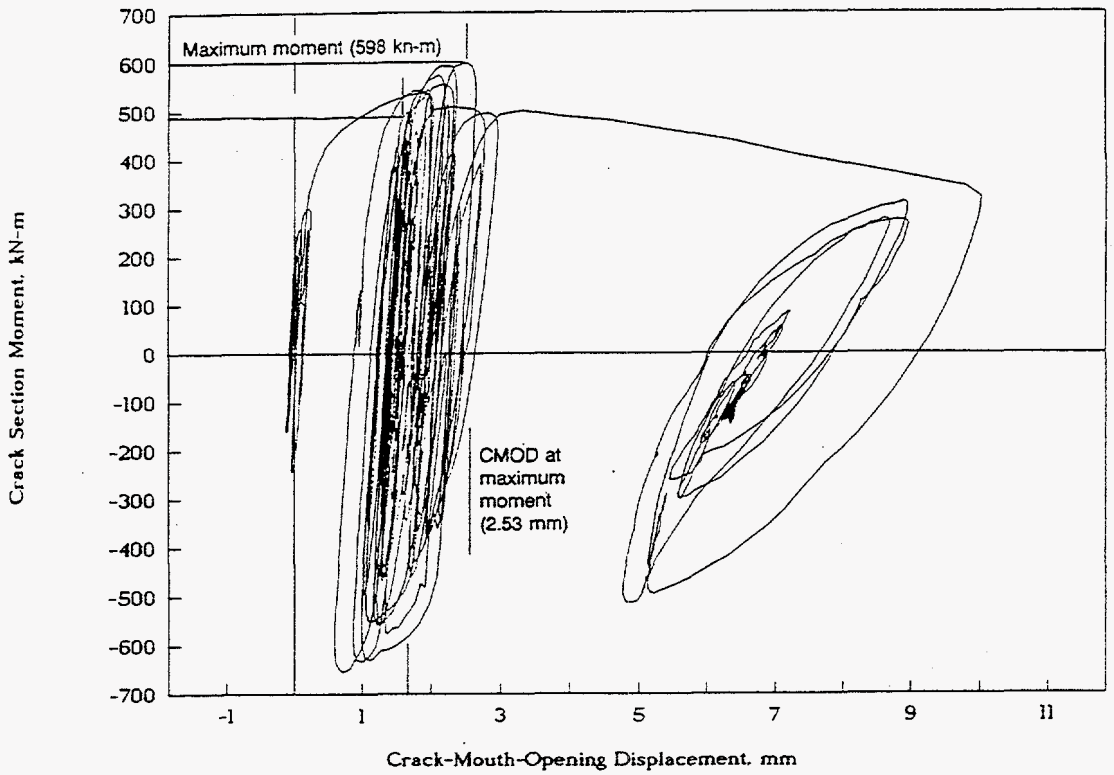

Figure 4.11 Crack section moment versus crack-mouth-opening displacement (CMOD) history for Experiment 1-1

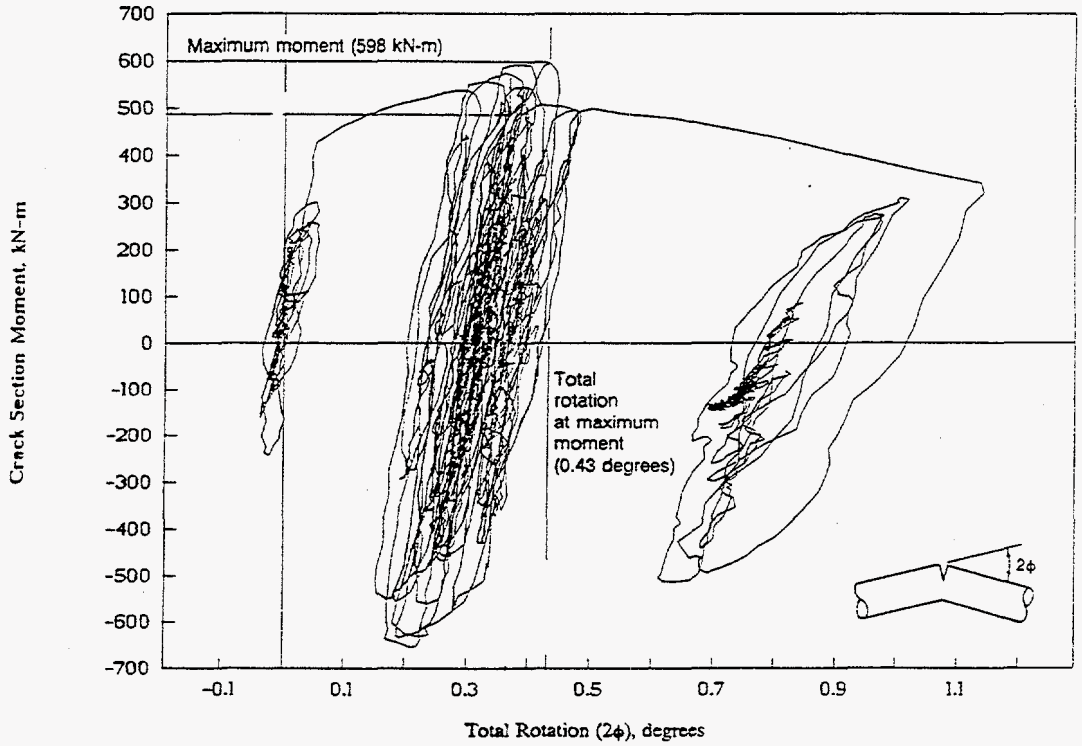

Figure 4.12 Crack section moment versus total rotation history for Experiment 1-1

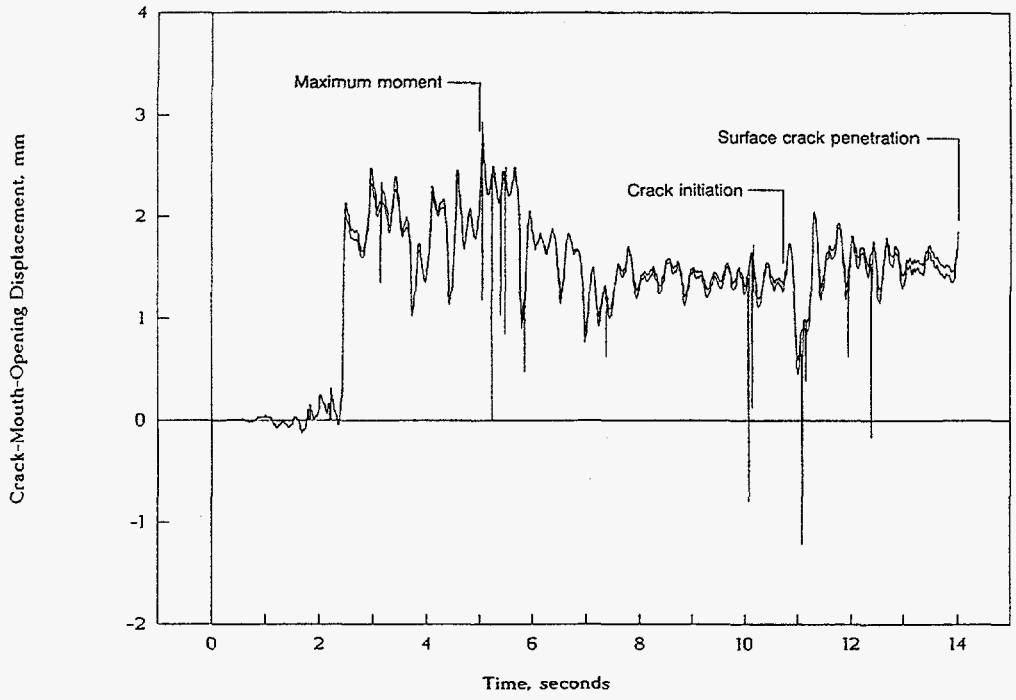

Figure 4.13 Crack-mouth-opening displacement (CMOD) versus time history for Experiment 1-1 (CMOD data are shown up to the instant of surface-crack penetration for both the crack centerline location and the location 51 mm (2 inches) from the crack centerline)

amplitude cycle occurs approximately 2.5 seconds after the start of the "Test" forcing function. After this one large amplitude cycle, both the moment-CMOD and moment-rotation responses again begin to cycle in a linear manner. The linear behavior continues until approximately 3.3 seconds after the surface crack penetrated the pipe wall. At that time, approximately 17.3 seconds into the "Test" forcing function, both the moment-CMOD and moment-rotation responses exhibit another large, plastic cycle. After this cycle, the stiffness of both the moment-CMOD and moment-rotation responses decrease dramatically.

It was not possible to clearly identify the time of crack initiation for Experiment 1-1. From a plot of the direct-current electric potential (d-c EP) versus the CMOD data for the increasing moment portion of a number of the large amplitude cycles, it was concluded that the crack probably initiated some time during the maximum moment cycle for the experiment, i.e., between 5.005 and 5.025 seconds into the forcing function. The applied crack section moments at 5.005 and 5.025 seconds into the "Test" forcing function were 506 kN-m (4,479 in-kips) and 594 kN-m (5,260 in-kips), respectively. Thus, the moment at crack initiation is probably between these two values.

The observed behavior of the d-c EP, CMOD, and moment data are consistent with the features observed on the fracture surface for this experiment. Figure 4.15 is a 6X magnification of the fracture surface at the center of the crack. The beachmarks clearly identify the growth of the crack as it was cycled. Figure 4.16 is a sketch of these beachmarks in the center region of the crack, with measurements of the crack extension for the major cycles. The first cycle of crack growth, Cycle G in Figure 4.17, caused approximately 0.125 mm (0.005 inches) of crack growth. The second cycle of crack growth, Cycle N in Figure 4.17, which

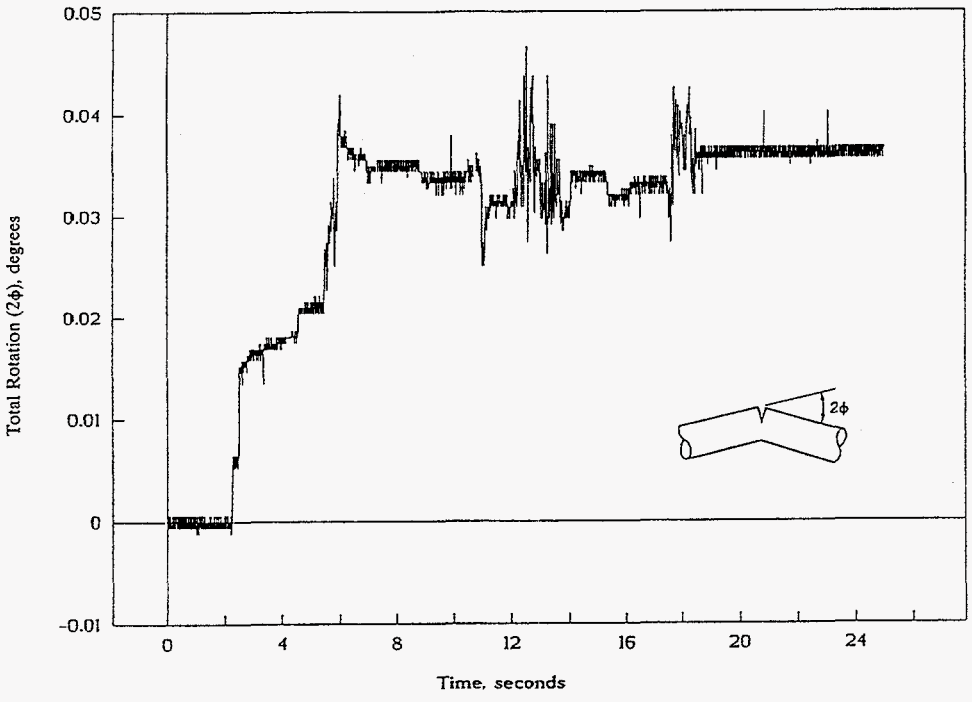

(a) During the "SSE" forcing function

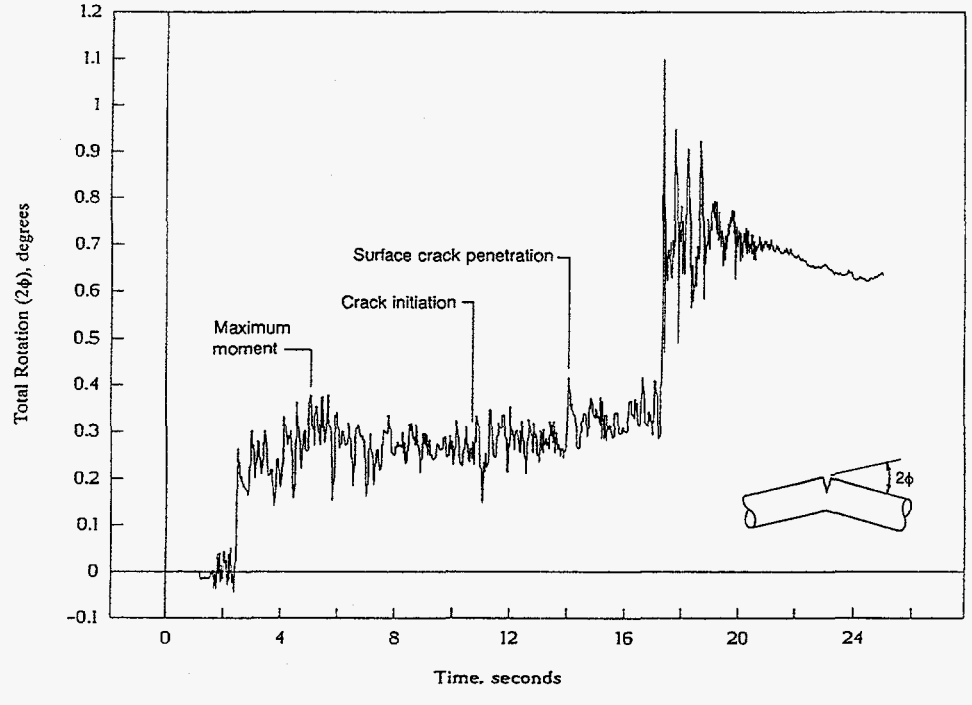

(b) During the "Test" forcing function

Figure 4.14 Experiment 1-1 total crack rotation versus time history (Data in this figure are from the fine rotation device)

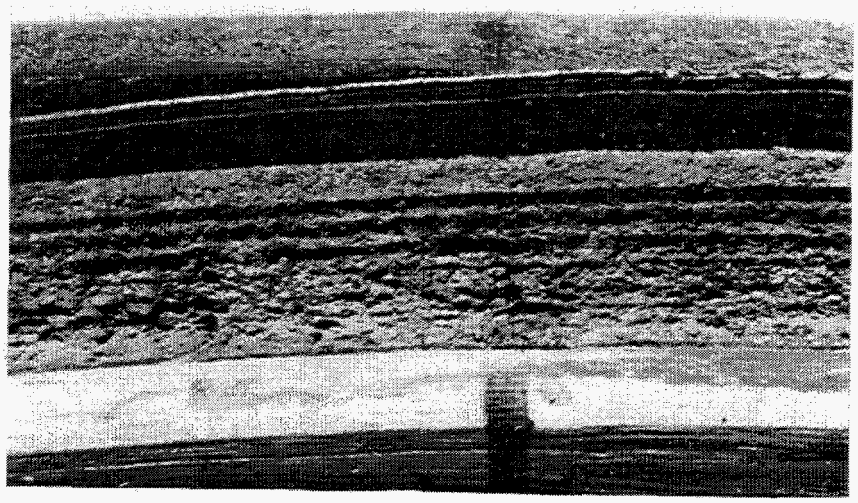

Figure 4.15 6X magnification of the fracture surface at the crack centerline for Experiment 1-1

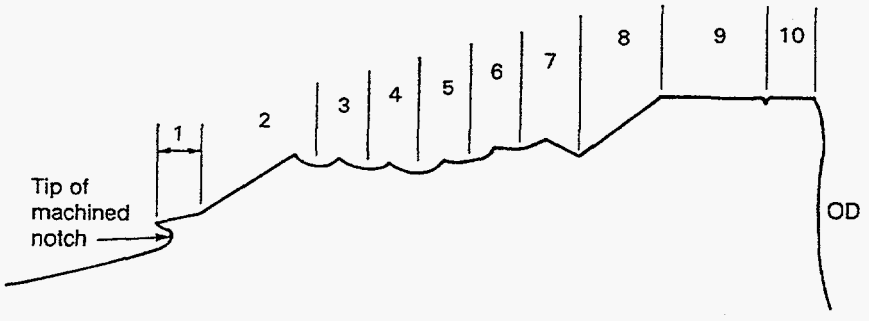

Location	Crack Growth, mm (inch)
1	0.127 (0.005)
2	1.219 (0.048)
3	0.406 (0.016)
4	0.508 (0.020)
5	0.610 (0.024)
6	0.559 (0.022)
7	0.533 (0.021)
8	0.813 (0.032)
9	1.245 (0.049)
10	0.406 (0.016)

Figure 4.16 Sketch of the beachmarks on the fracture surface in the center region of the crack showing the progression of the surface crack due to cyclic loading

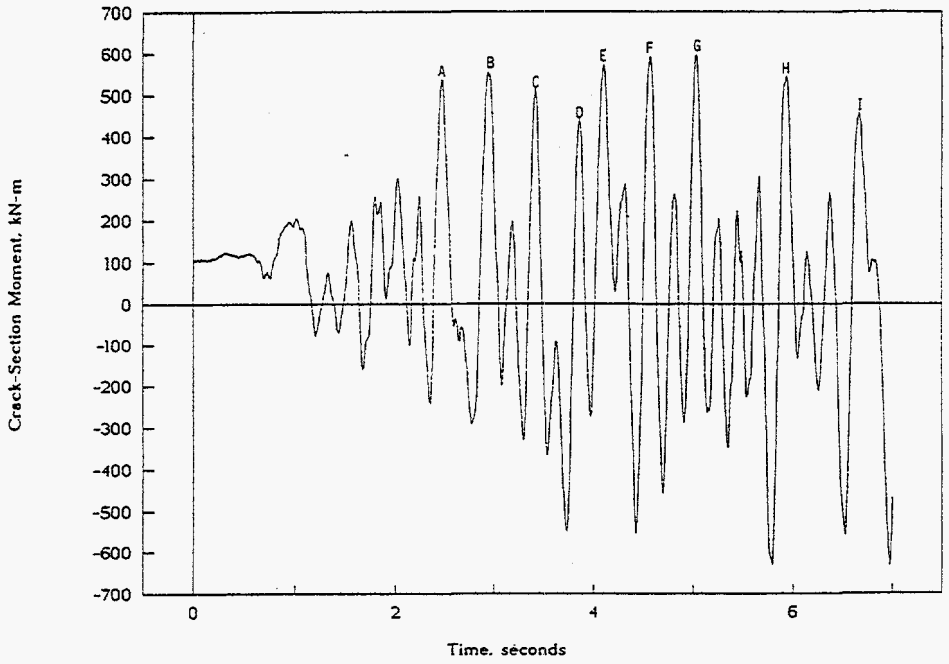

(a) 0-7 seconds

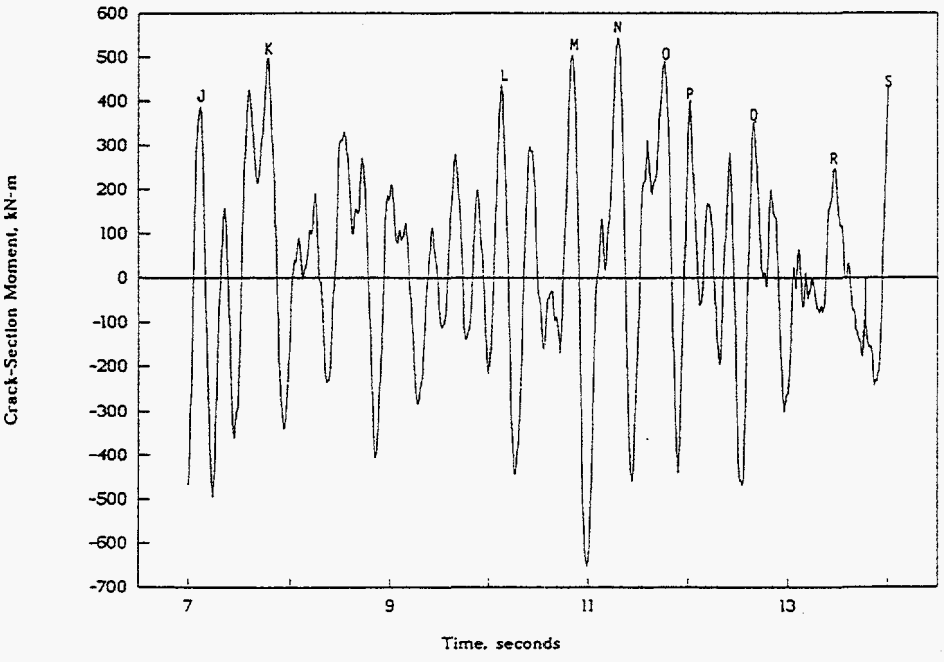

(b) 7-14 seconds

Figure 4.17 Moment-time plot for the "Test" forcing function for Experiment 1-1

occurred approximately 6 seconds after the first cycle of crack growth, caused approximately 1.22 mm (0.048 inches) of crack growth. Note, in between the crack initiation cycle (Cycle G) at 5 seconds into the forcing function and the second cycle of crack growth (Cycle N) approximately 11 seconds into the forcing function, the applied crack section moment value never got back to the same level as was reached at 5 seconds into the forcing function. Consequently, it is unlikely that any crack growth occurred during these lower amplitude cycles. It is also of note that the d-c EP data for the cycles for which crack growth was assumed to have occurred agreed very well with the measured crack growth from the fracture surface measurements in Figure 4.16.

Figure 4.18 shows the post-test measurements of the surface crack for Experiment 1-1. From Figure 4.18, it can be seen that the deepest point of the surface crack was close to the crack centerline location, i.e., within 25 mm (1-inch). The deepest point of the surface along the crack front was 62.8 percent of the pipe wall thickness in depth. The crack at the crack centerline location was 62.5 percent of the pipe wall thickness in depth.

4.1.2.2 Experiment 1-2 Results

Figure 4.19 is a plot of the internal pipe pressure as a function of time for Experiments 1-2. The drop in pressure in this figure indicates the time when the surface crack penetrated the pipe wall. For Experiment 1-2 the time at surface crack penetration was 2.46 seconds into the "Test" forcing function. Surface-crack penetration at 2.46 seconds into the forcing function is also evident in a plot of the crack-mouth-opening displacement versus time, see Figure 4.20.

Figure 4.21 is a plot of the crack section moment data as a function of time for Experiment 1-2. The same procedures were used to estimate the moment data for Experiment 1-2 as were used for Experiment 1-1. From Figure 4.21, it can be seen that the maximum total moment (static plus dynamic) at the crack section for Experiment 1-2 was 476 kN-m (4,210 in-kips) and occurred 2.46 seconds into the "Test" forcing function, i.e., surface crack penetration occurred at the time of maximum moment for the experiment.

Figure 4.22 is a plot of the crack section moment data as a function of the crack-mouth-opening-displacement (CMOD) for Experiment 1-2. The overall characteristics of this figure are similar to the initial portion of the moment-CMOD plot for Experiment 1-1. Figure 4.22 shows an initial region where the response is cyclic, but linear in nature. After this initial linear-elastic cyclic response, a single large amplitude cycle with significant plasticity at the crack section occurs. At the end of this single large amplitude cycle, surface crack penetration occurs. As was the case for Experiment 1-1, this initial large amplitude cycle occurs approximately 2.5 seconds after the start of the "Test" forcing function. For Experiment 1-2, the applied cyclic loadings continued until the test specimen severed, i.e., a double-ended-guillotine-break (DEGB) occurred (approximately 11 seconds into the "Test" forcing function). It is noteworthy that the time of the DEGB for Experiment 1-2, i.e., approximately 11 seconds, is the time when the first large amplitude cycle after the maximum moment cycle occurred during Experiment 1-1.

As was the case for Experiment 1-1, it was not possible to determine the instant of crack initiation for Experiment 1-2. However, an attempt to bound the crack initiation moment value was made by assuming that the crack initiated during the large amplitude cycle just prior to maximum moment, somewhere between the moment value when the CMOD data becomes nonlinear (approximately 345 kN-m [3,050 in-kips]), see Figure 4.22, and the maximum moment value (476 kN-m [4,210 in-kips]). It is also interesting to note that the carbon steel fracture surface did not exhibit the same "beachmark" appearance that the

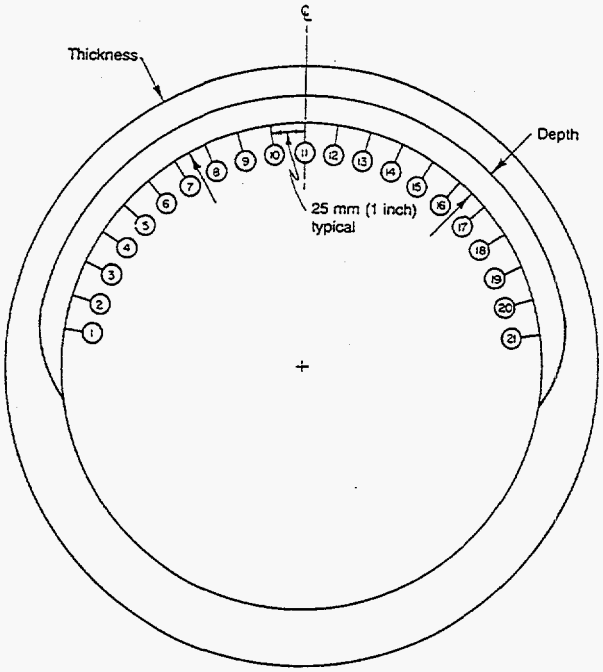

Location	Flaw Depth, mm	Wall Thickness, mm	a/t
1	11.49	25.55	0.450
2	11.67	25.48	0.458
3	12.04	25.55	0.471
4	12.24	25.35	0.483
5	12.73	25.60	0.497
6	13.07	25.37	0.515
7	13.12	25.55	0.513
8	13.02	25.15	0.518
9	13.84	25.65	0.540
10	14.82	25.70	0.577
11	16.04	25.68	0.625
12	16.21	25.81	0.628
13	15.34	25.73	0.596
14	13.97	25.55	0.547
15	13.02	25.63	0.508
16	12.09	25.58	0.473
17	11.19	25.68	0.436
18	11.18	25.63	0.436
19	11.30	25.60	0.441
20	10.80	25.40	0.425
21	11.35	25.65	0.443

Figure 4.18 Flaw geometry for Experiment 1-1

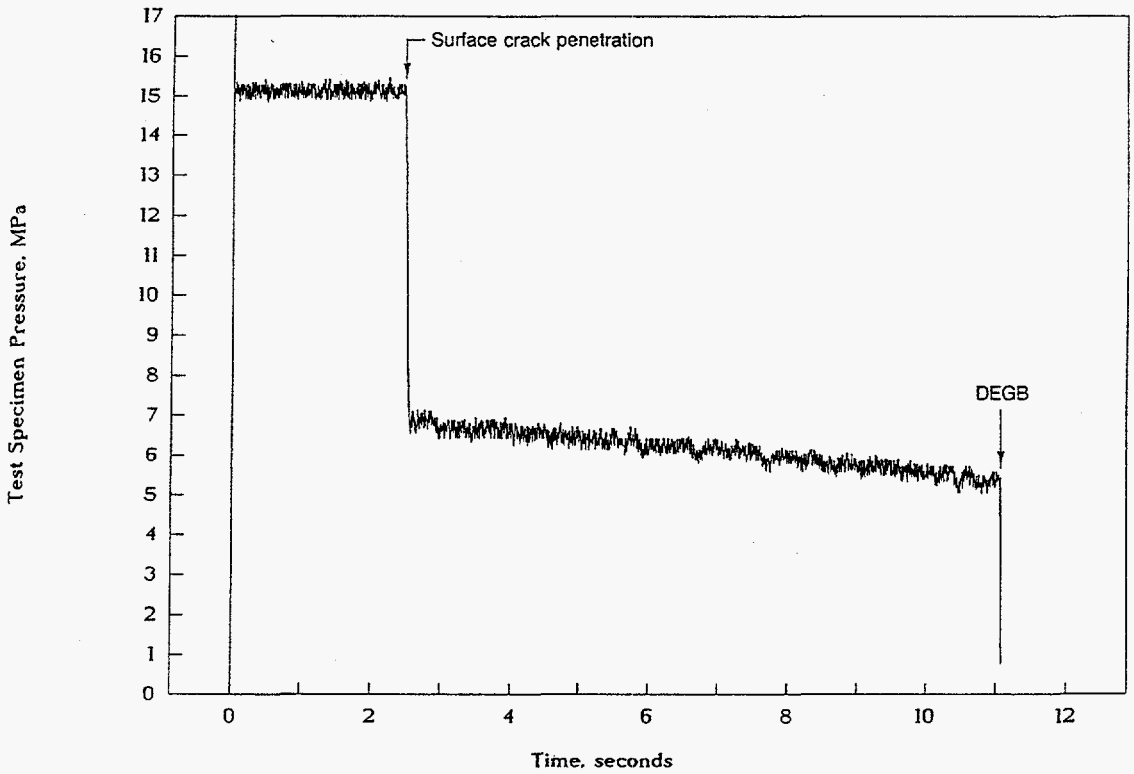

Figure 4.19 Experiment 1-2 crack location internal pressure history

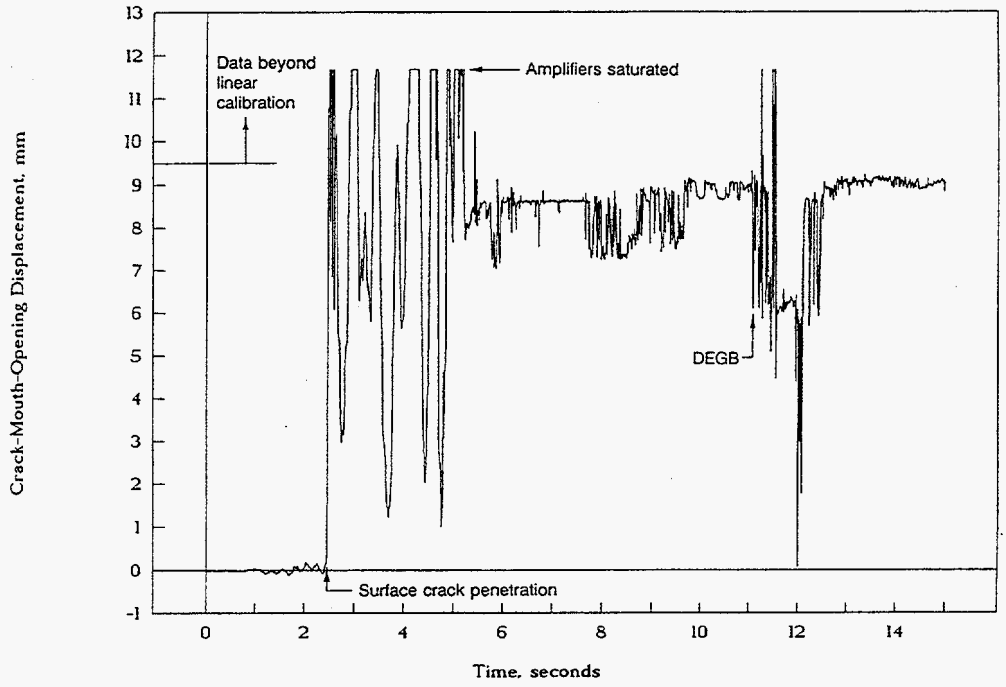

(a) For entire "Test" forcing function

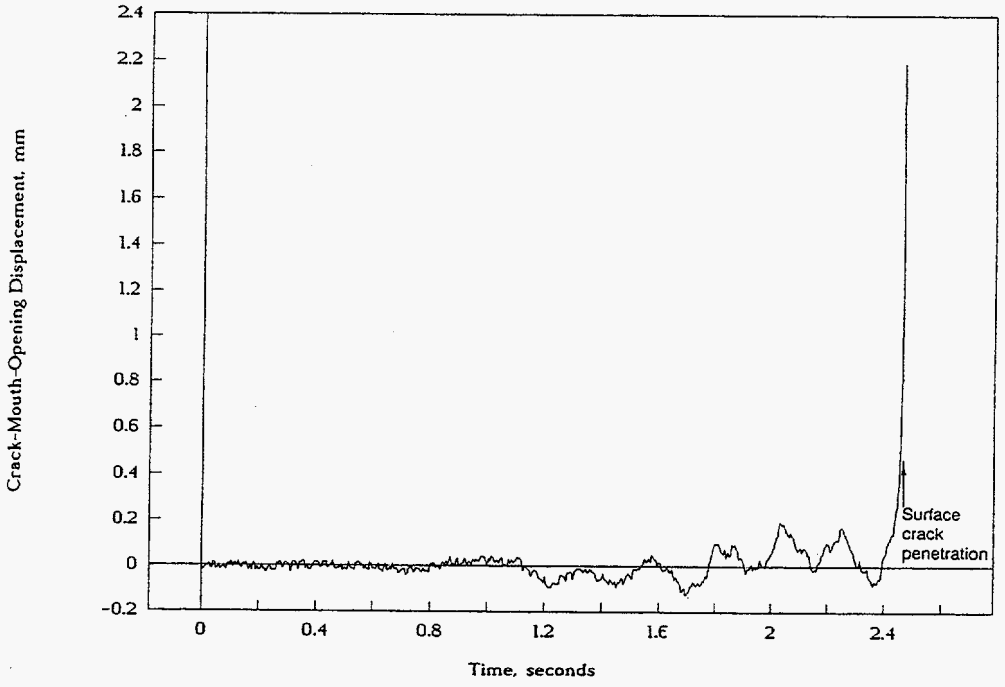

(b) Up to surface-crack penetration

Figure 4.20 Crack-mouth-opening displacement versus time history for Experiment 1-2

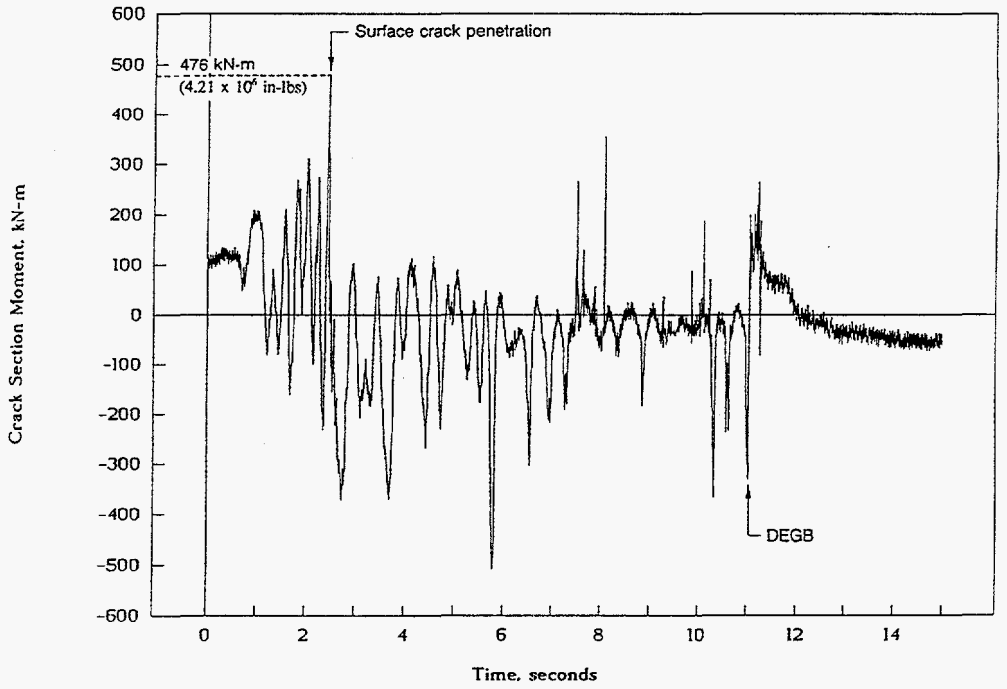

Figure 4.21 Moment-time history at the crack plane for Experiment 1-2

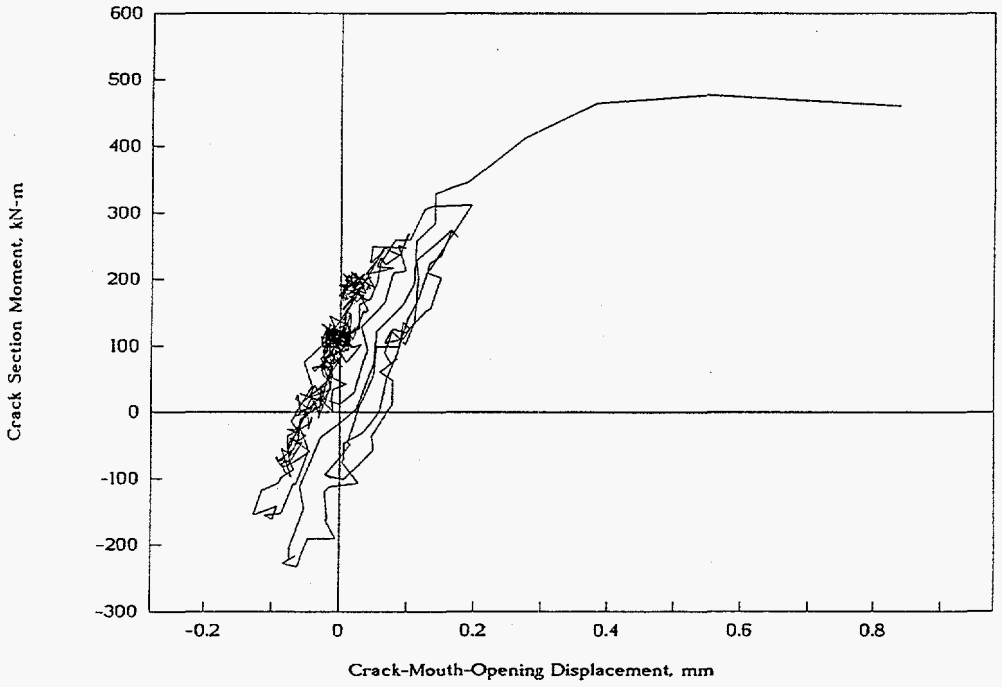

Figure 4.22 Experiment 1-2 plot of total crack section moment as a function of crack-mouth-opening displacement up to the instant of surface crack penetration

stainless steel specimen for Experiment 1-1 did. Consequently, it was not possible to estimate the cyclic surface crack growth.

Figure 4.23 is a photograph of the fracture for Experiment 1-2. After the surface crack penetrated the pipe wall, the through-wall crack continued to tear in a stable cyclic manner around the pipe circumference until the remaining ligament was only 6 percent of the pipe circumference. The remaining through-wall crack ligament at the start of the instability leading to the DEGB was only 76 mm (3 inches). This was the same remaining ligament which existed at the start of the instability for the aged cast stainless steel experiment (Experiment 1.3-7) from the IPIRG-1 program (Ref. 4.2). To a first approximation, the failure is a flow stress tensile failure due to the pressure forces.

Figure 4.24 shows the post-test measurements of the machined notch and the fatigue precrack for Experiment 1-2. From Figure 4.24, it can be seen that the deepest part of the crack was 100 mm (4-inches) around the inside pipe circumference from the crack centerline. The crack depth at this location was 71.9 percent of the pipe wall thickness. The crack depth at the crack centerline location was 59.2 percent of the pipe wall thickness. Various methods of handling such off-center cracks for fracture prediction analyses are discussed in Section 5.0.

4.2 Elbow-Girth Weld Experiments

Two elbow-girth weld pipe experiments, Experiments 1-3 and 1-4, were conducted as part of Task 1 of the IPIRG-2 program. Experiment 1-3 was a single frequency pipe system experiment using the same basic forcing function as used in previous IPIRG-1 experiments. Experiment 1-4 was a companion quasi-static monotonic bend experiment. The objective of these experiments was to gather experimental data for assessing the fracture behavior and stability of a circumferential internal surface crack located in a girth weld joining a straight pipe section and an elbow. The rationale for these experiments was to see if proximity to an elbow alters the fracture behavior when compared with straight pipe. To make this determination, the results from these two elbow girth weld experiments were compared with the results from two carbon steel weld straight pipe experiments conducted previously, a quasi-static monotonic four-point bend experiment from the Degraded Piping (Ref. 4.1) program (Experiment 4141-8) and a single frequency pipe system experiment from the IPIRG-1 (Ref. 4.2) program (Experiment 1.3-4). Note, due to differences in the test specimens and crack sizes, the reader is again cautioned against making direct comparisons of results between experiments until the results have been normalized by the fracture prediction analyses in Section 5.0.

The cracks for the two elbow-girth weld experiments were located in shop-fabricated submerged-arc welds (SAW) between sections of 16-inch nominal diameter, Schedule 140 carbon steel pipe and 16-inch nominal diameter, Schedule 100 carbon steel elbows. The inside diameter of the Schedule 140 pipe was machined prior to welding so that the wall thickness of the pipe matched the elbow. The weld procedure was a Babcock and Wilcox (B&W) carbon steel weld procedure that was used in straight pipe experiments in the Degraded Piping (Experiment 4141-8) and the IPIRG-1 (Experiment 1.3-4) programs.

The nominal internal surface flaw dimensions for these experiments were planned to be the same as those used in the previous Degraded Piping and IPIRG-1 program experiments; 50 percent of the pipe circumference in length and 66 percent of the pipe wall thickness in depth. The test temperature and

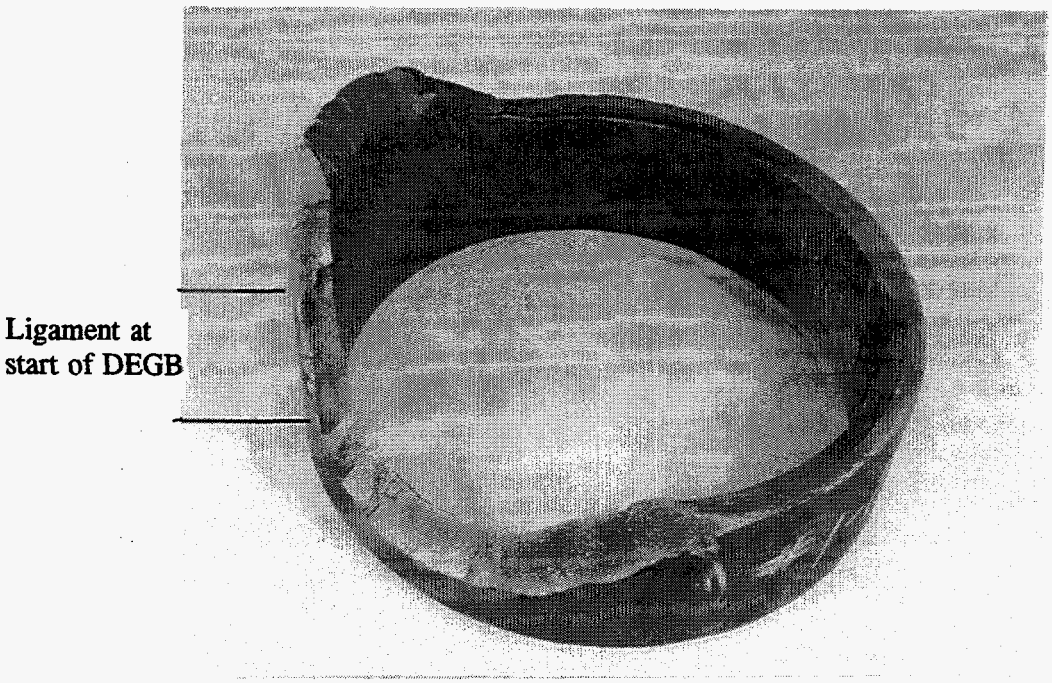

Figure 4.23 Photograph of fracture for Experiment 1-2

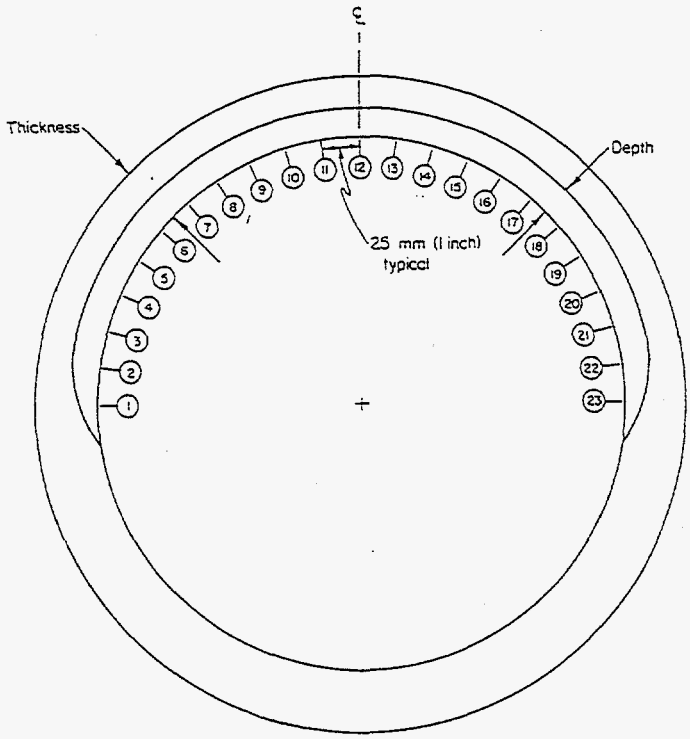

Crack length on inside pipe surface = 587 mm (23.1 inch)

Location	Crack-Depth(a), mm	Wall Thickness(t), mm	a/t
1	7.16	25.3	0.283
2	12.1	25.6	0.471
3	11.8	25.4	0.464
4	15.3	25.5	0.601
5	16.8	25.4	0.659
6	16.9	25.6	0.658
7	17.5	25.6	0.685
8	18.3	25.4	0.719
9	17.9	25.6	0.698
10	16.4	25.8	0.636
11	16.0	25.5	0.627
12	14.9	25.2	0.592
13	14.2	25.2	0.564
14	14.8	25.2	0.588
15	15.6	25.3	0.615
16	16.0	25.3	0.632
17	15.4	25.5	0.603
18	15.5	25.2	0.616
19	17.4	25.6	0.576
20	14.5	25.7	0.564
21	14.0	25.7	0.545
22	12.4	25.7	0.483
23	6.62	25.3	0.262

Figure 4.24 Flaw geometry for Experiment 1-2

pressure for all of the experiments (Degraded Piping, IPIRG-1, and IPIRG-2) were representative of PWR conditions; 288 C (550 F) and 15.5 MPa (2,250 psi).

4.2.1 Modifications to the Pipe Loop

In order to conduct the elbow-girth weld pipe system experiment (Experiment 1-3), the IPIRG pipe loop experimental facility had to be modified in the vicinity of Elbow 4. The modifications included: (1) replacing the original Schedule 160 Elbow 4 with a Schedule 100, A106 Grade B carbon steel elbow, (2) adding a new moment cell near the hydrostatic bearing just to the east of Elbow 4, and (3) welding end caps into the loop 1.83 m (72 inches) either side of Elbow 4, see Figure 3.4.

The new Schedule 100 elbow with a short length of pipe attached formed the test specimen for Experiment 1-3. The crack was located in the shop fabricated, submerged-arc weld (SAW) which joined the elbow to the short piece of straight pipe. The A106 Grade B carbon steel elbow was fabricated from the same heat of steel used in the carbon steel elbow experiments conducted as part of Task 2 of the IPIRG-2 program. The short piece of straight pipe was fabricated from a section of 16-inch nominal diameter, Schedule 140 carbon steel pipe which was obtained during the Degraded Piping Program from a canceled nuclear power plant. The wall thickness of the Schedule 140 pipe was machined prior to welding so that its wall thickness matched that of the test elbow. The new moment cell was incorporated into the overall facility so that the moment at the test section could be determined. From a free body analysis of the pipe loop, the moment at the elbow girth weld test section can be expressed as a function of the moment at the new moment cell and one of the existing moment cells. The end caps were incorporated into the modified facility to limit the volume of subcooled water in the actual test specimen in the event a DEGB occurred. This was done because it was not possible to incorporate the central rod primary restraint system into the test specimen design for curved test specimens.

4.2.2 Experimental Results

The key results from the two elbow-girth weld pipe experiments are shown in Table 4.3. Also included in Table 4.3 are the results for the two companion straight pipe experiments. Shown in Table 4.3 are the test conditions (i.e., pipe diameters, wall thicknesses, crack depths, crack lengths, test pressures, and test temperatures), material property data (yield and ultimate strengths and J values at crack initiation [J_i] from C(T) specimen tests), and moments at crack initiation and maximum moments for each of the four pertinent experiments.

4.2.2.1 Experiment 1-3 Results

Experiment 1-3 was a single frequency pipe system experiment with an internal circumferential surface crack in the center of a shop-fabricated elbow-girth weld. The single frequency excitation applied to the pipe loop was nominally the same single frequency excitation applied to the three stainless steel pipe system experiments conducted during IPIRG-1 (Experiments 1.3-3, 1.3-5, and 1.3-7) and Experiment 1-5 from this program. Figure 4.26 is a plot of the actuator displacement-time history for this experiment. Two loadings were applied because the crack just barely penetrated the pipe wall during the first loading. The experiment met the specified criteria in the test procedure for application of another loading: video not obscured, instrumentation functional, pressure maintained at nearly the original test pressure. The second forcing function was nominally identical to the first.

Table 4.3 Key results from two elbow-girth weld experiments (1-3 and 1-4) plus two companion pipe-to-pipe weld experiments (4141-8 and 1.3-5)

Experiment No.	Outside Pipe Diameter, mm	Wall Thickness, mm	a/t[1]	2c/πD[2]	Test Pressure, MPa	Yield[3] Strength, MPa	Ultimate[3] Strength, MPa	J at Crack Initiation C(T) Specimen[4], kJ/m²	Moment at Crack Initiation, kN-m	Maximum Moment, kN-m
1-3	406.7[5]	33.5[5]	0.815	0.50	15.5	223	514	82	668	815
1-4	406.9[5]	33.5[5]	0.748	0.50	15.5	223	514	82	713	798
4141-8	403.2	25.37	0.67	0.50	15.5	241	618	82	423	594
1.3-4	402.6	25.48	0.692	0.535	15.5	241	618	82	ND[6]	618

(1) At the location where the crack was the deepest; wall thickness does not include weld crown height.
(2) Total crack length on the inside pipe surface divided by the inside pipe circumference.
(3) Quasi-static data for the pipe base metal material.
(4) Quasi-static data for the weld metal.
(5) Pipe dimensions; not elbow dimensions.
(6) ND = Not determined.

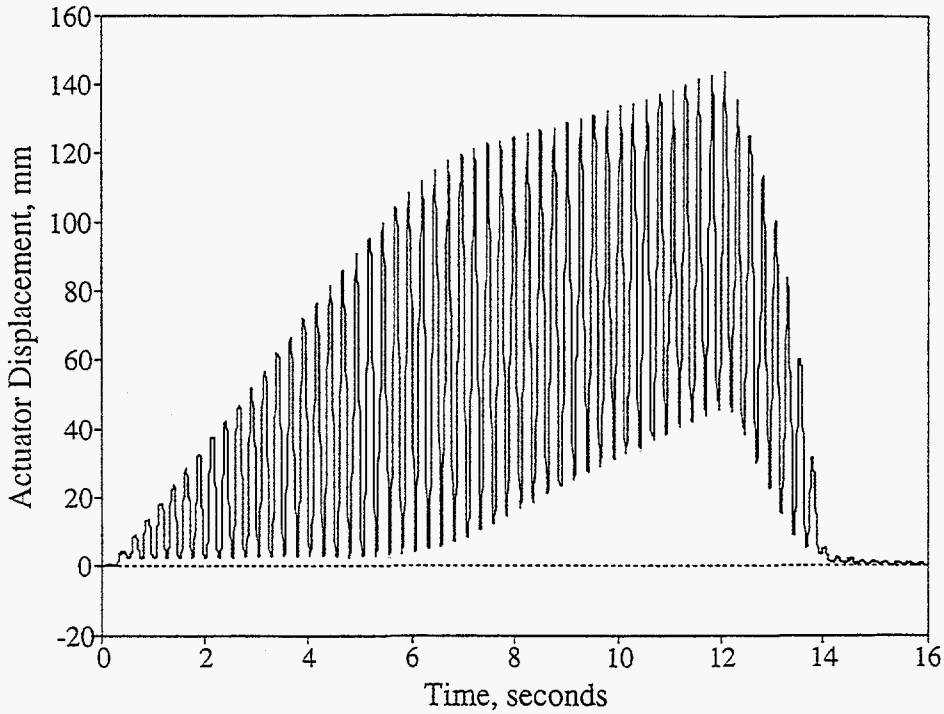

Figure 4.25 Experiment 1-3 actuator displacement versus time history for the first application of the forcing function

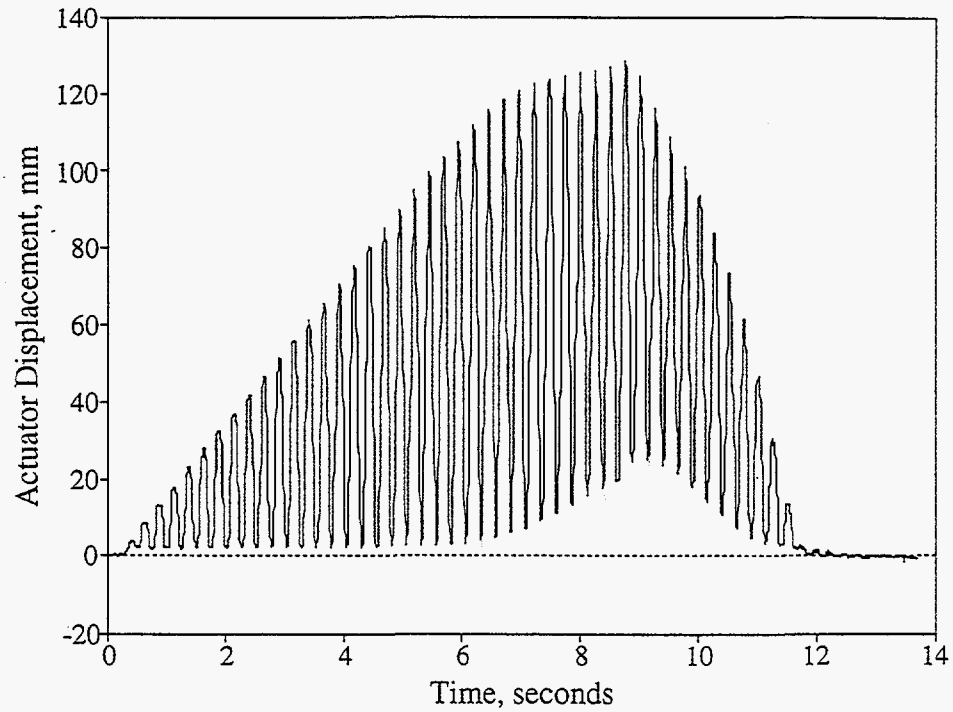

Figure 4.26 Experiment 1-3 actuator displacement versus time history for the second application of the forcing function

Figure 4.27 is a plot of the internal pipe pressure as a function of time for both applications of the forcing function for this experiment. Even though the surface crack penetrated the pipe wall during the first application of the forcing function, as evident by steam emanating from the crack section on the video, the internal test specimen pressure did not drop significantly. After the first application of the forcing function, and prior to the second application of the forcing function, the internal pipe pressure dropped slowly while preparations were made to apply the forcing function a second time. It took approximately 30 minutes to prepare the hydraulic system and data acquisition systems for the second application of the forcing function. During this 30 minute delay, the internal pipe pressure dropped from 15.5 MPa (2,250 psi) to approximately 12.4 MPa (1,800 psi). The sudden loss in pressure evident during the second loading in Figure 4.27, 8.7 seconds into the second application of the forcing function, corresponds to the time when the internal surface crack penetrated the pipe wall for the entire length of the surface crack.

Figure 4.28 is a plot of the crack section moment as a function of time for both applications of the forcing function for Experiment 1-3. The moment data in Figure 4.28 include both the dynamic moment values inferred from the strain gage data and the time = 0, static value of 160.1 kN-n (1,417 in-kips) inferred from the ANSYS finite element analysis. The maximum moment for this experiment was 814.9 kN-m (7,213 in-kips) and occurred approximately 7 seconds into the second application of the forcing function. Figures 4.29 and 4.30 are plots of the crack section moment as a function of the crack-mouth-opening displacement (CMOD) and crack-section rotation data, respectively, for both the first and second applications of the forcing function. The CMOD data were obtained from a high temperature/high pressure LVDT mounted across the crack on the inside pipe surface. The rotation data were obtained from a series of LVDTs mounted across the crack plane on the outside of the pipe. The overall characteristics of both figures are very similar, showing an increase in cyclic response as the forcing function increases.

In an attempt to ascertain when the surface crack initiated and began to grow during the first and second applications of the forcing function, an assessment of the unloading and loading compliance data was made for Experiment 1-3. Unloading compliance measurements are frequently used in laboratory specimens [e.g., C(T) specimens] to determine crack growth. In typical laboratory specimen tests, unloadings are done intentionally. In the IPIRG pipe system experiments, the unloadings occur naturally from the single frequency loading function. Figure 4.31 is a plot of the unloading and loading compliances (i.e., the slope of the CMOD-moment response for the elastic regions of the unloading and loading portions of the CMOD-moment curve) as a function of cycle number. It appears from Figure 4.31 that the unloading and loading compliance data begin to show an increase, which is indicative of crack growth, at approximately the 19th cycle of the first application of the forcing function. It was in this region that a detailed study of the d-c electric potential data was focused to determine the instant of crack initiation.

Figure 4.32 shows the d-c EP data for the first application of the forcing function for a set of d-c EP probes across the crack centerline. Upon investigating the crack centerline d-c EP data, it was noticed that after about 6 seconds into the first application of the forcing function (corresponding to the 25th cycle) the d-c EP began to act strangely. Instead of a constantly increasing peak electric potential value, random peak d-c EP values were observed. As the crack is growing during an increasing amplitude history, the d-c EP is expected to increase each cycle. However, this is not what is observed in this data. Since a portion of the surface crack penetrated the wall thickness early in the application of the first forcing function, it was

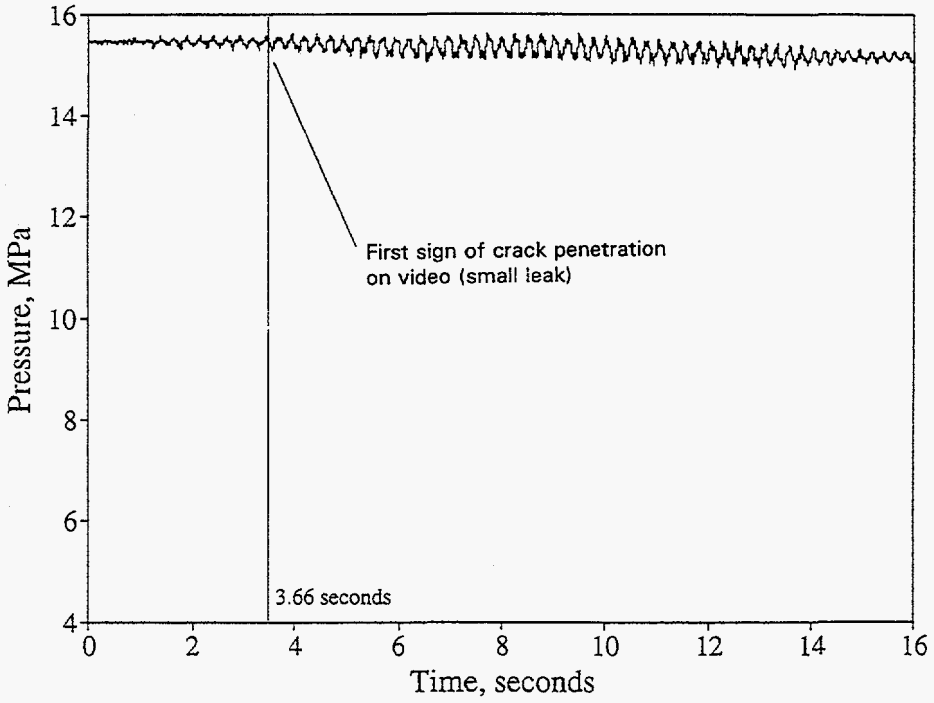

(a) First application of the forcing function

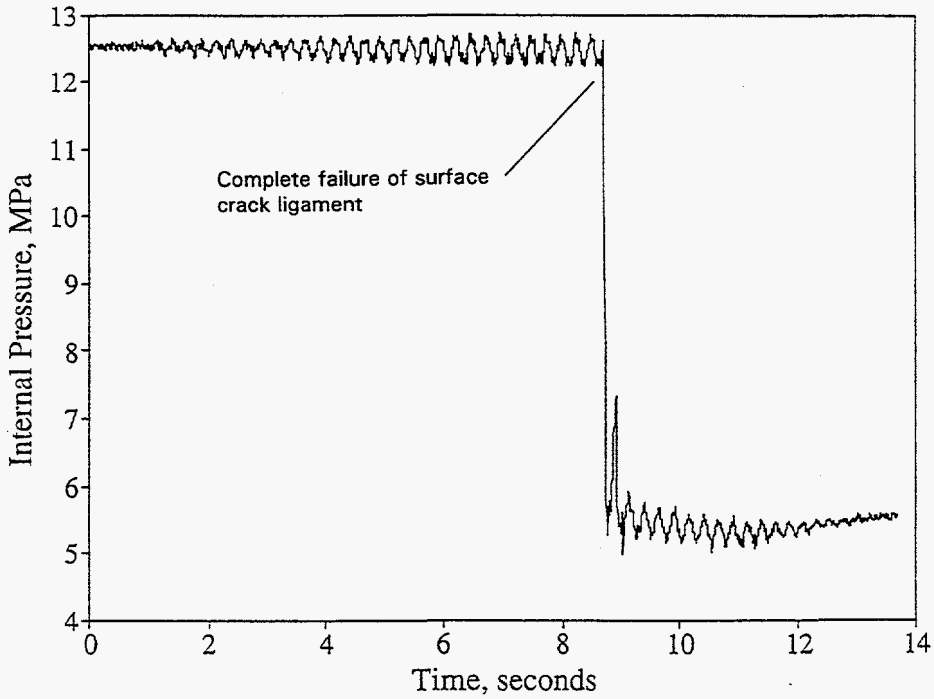

(b) Second application of the forcing function

Figure 4.27 Experiment 1-3 test specimen pressure versus time history

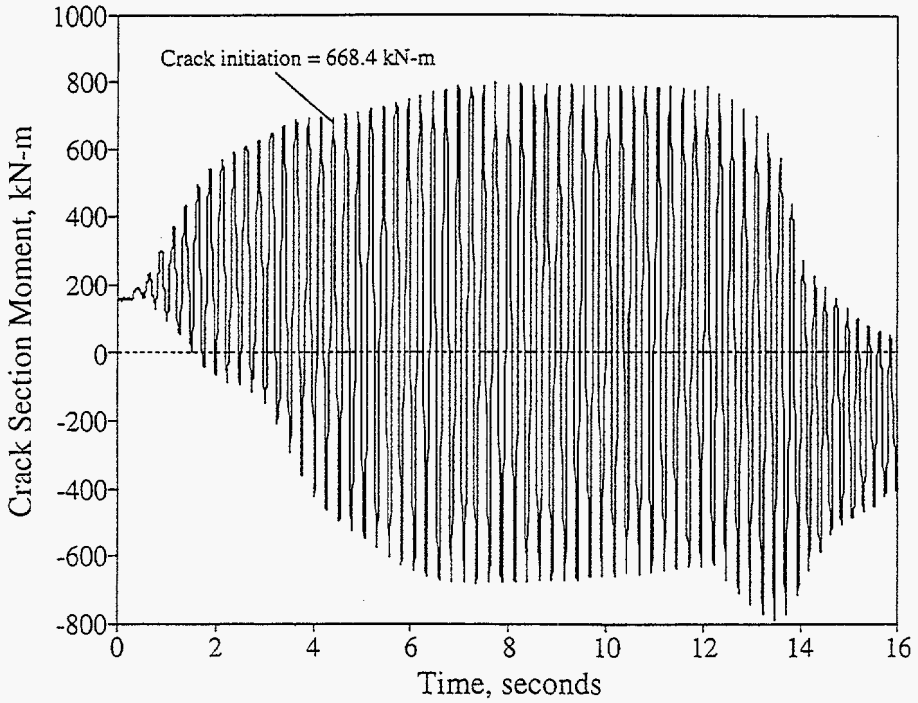

(a) First application of the forcing function

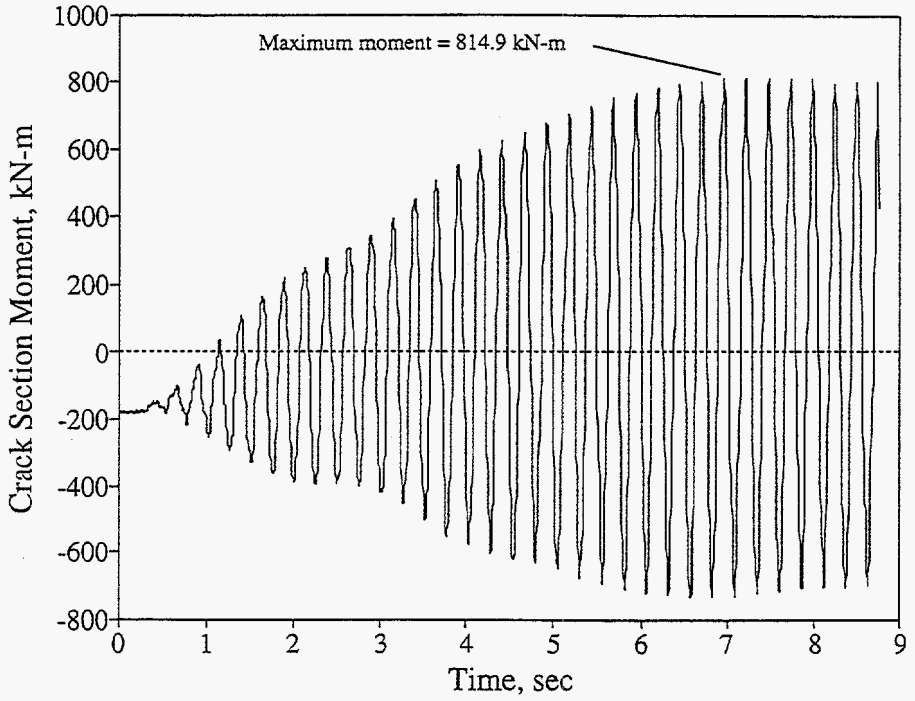

(b) Second application of the forcing function

Figure 4.28 Experiment 1-3 crack section moment versus time history

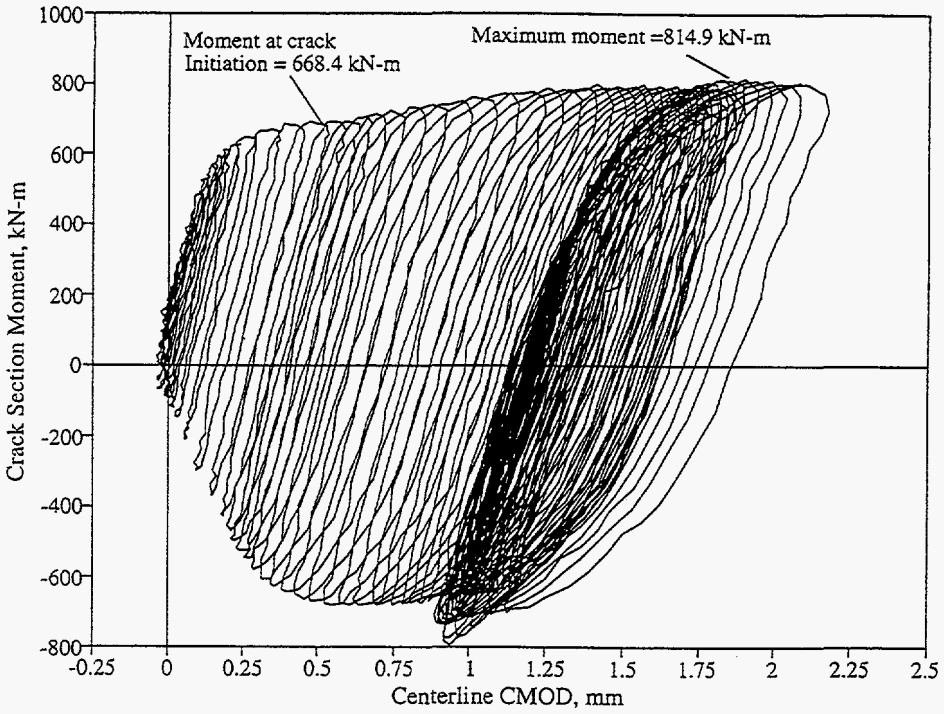

Figure 4.29 Crack section moment versus centerline CMOD for the entire loading history for Experiment 1-3

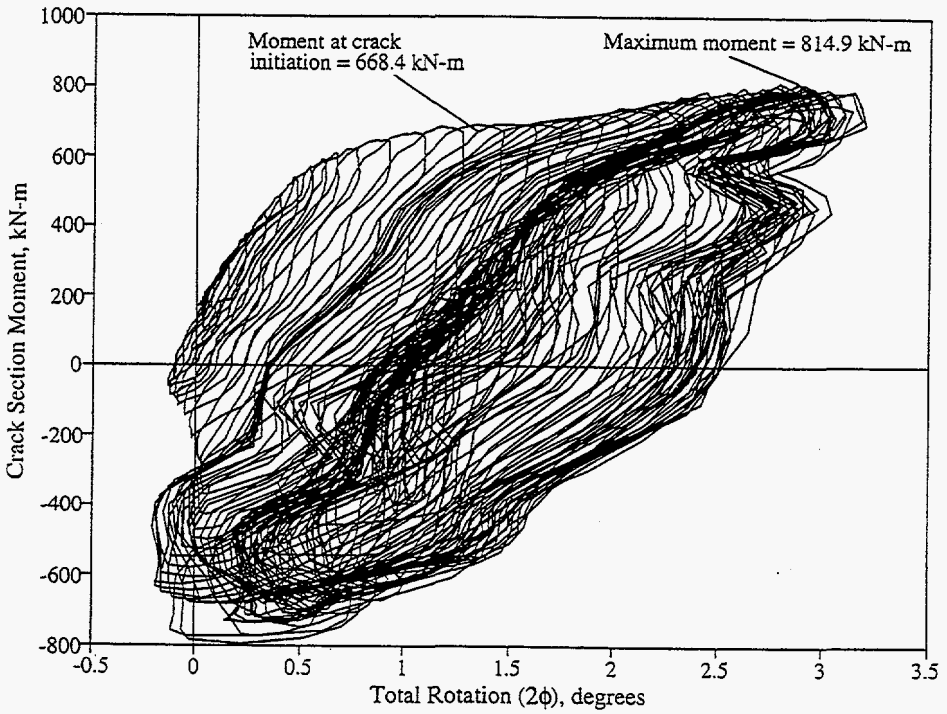

Figure 4.30 Crack section moment versus rotation (2ϕ) for the entire time history of Experiment 1-3

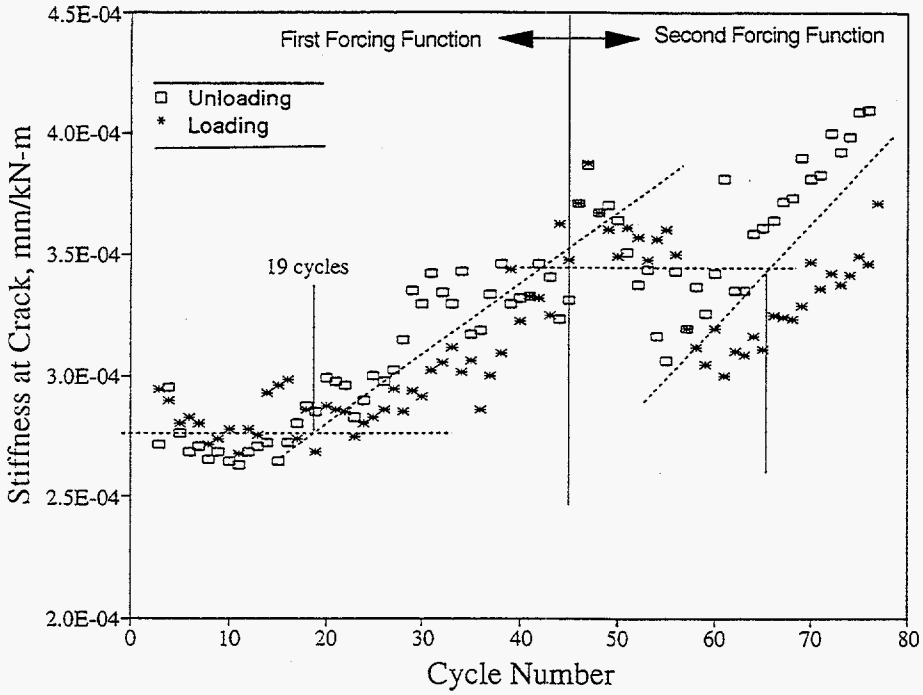

Figure 4.31 Unloading and loading compliance data for the entire loading history of Experiment 1-3

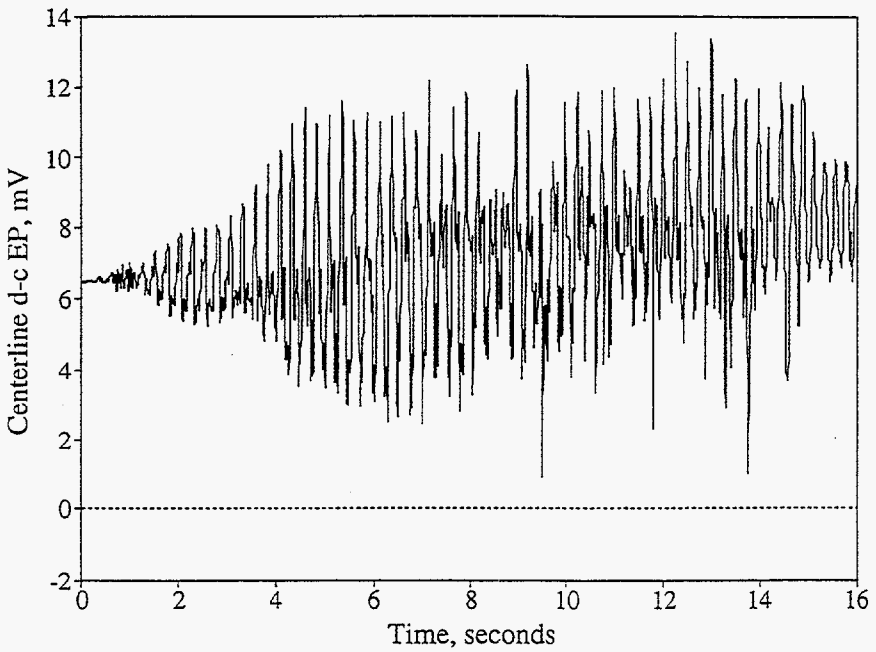

Figure 4.32 Experiment 1-3 centerline d-c EP versus time history for the first application of the forcing function

thought that the presence of a local through-wall crack may have affected the electric potential field at the crack centerline by altering the current density at that location. This inconsistency in the d-c EP data makes crack growth determination difficult. However, the data before the 25th cycle was used to determine the surface crack initiation point at the crack centerline. Figure 4.33 shows the centerline d-c EP data versus the centerline CMOD data for the 10th through 18th cycles of the first application of the forcing function. These data correspond to the positive increasing crack section moment data for each cycle. From this figure, it was estimated that the centerline of the crack initiated during the 16th cycle. This corresponds to a crack section moment of 668.4 kN-m (5,916 in-kips) and occurred 4.14 seconds after the start of the first application of the forcing function.

Figure 4.34 is a photograph of the fracture surface for Experiment 1-3. Post-test measurements from this fracture surface can be found in Figure 4.35. The crack grew through the thickness in the circumferential plane for about 50 percent of the initial remaining ligament and then grew as a slant fracture at a 45-degree angle. From this figure, it is also evident why the crack initially penetrated the wall well away from the centerline. The two outer, non-scalloped, electric-discharged machined (EDM) regions of the crack front were machined too deep producing a variable depth crack front. Figure 4.36a shows a magnified view of one of these locations, while Figure 4.36b shows a magnified view of the fracture surface at the crack centerline. Inspection of the fracture surface indicates that there were two crack initiation locations. The surface crack initially penetrated the wall at the location shown in Figure 4.36a; however, the crack-driving force was low enough that this through-wall crack did not influence the surface-crack growth until the slant fracture occurred. If the through-wall crack was growing, the fracture surface would show marks of circumferential growth; however, only radial crack growth is apparent on this fracture surface, see Figure 4.36b.

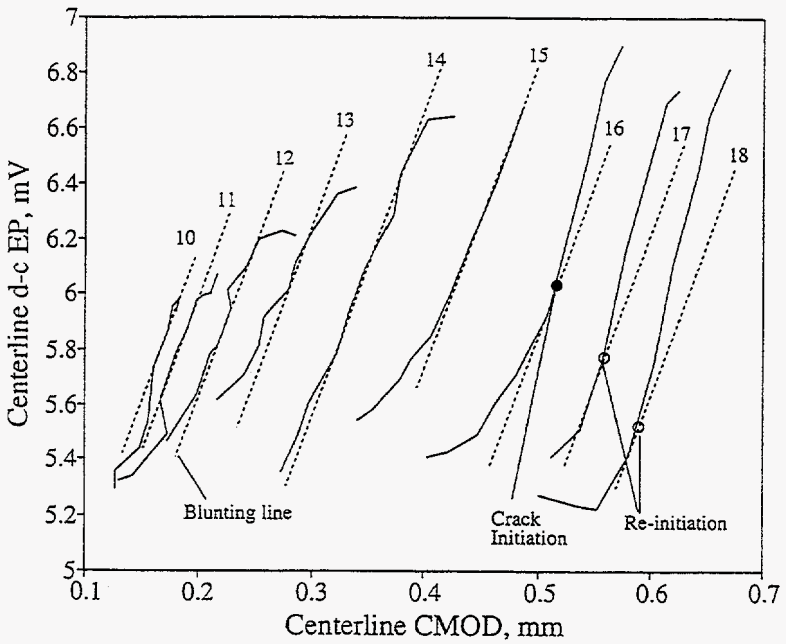

Figure 4.33 Experiment 1-3 centerline d-c EP versus centerline CMOD for Cycles 10 through 18 of the first application of the forcing function showing crack initiation and reinitiation (data shown correspond to positive, increasing crack section moment values)

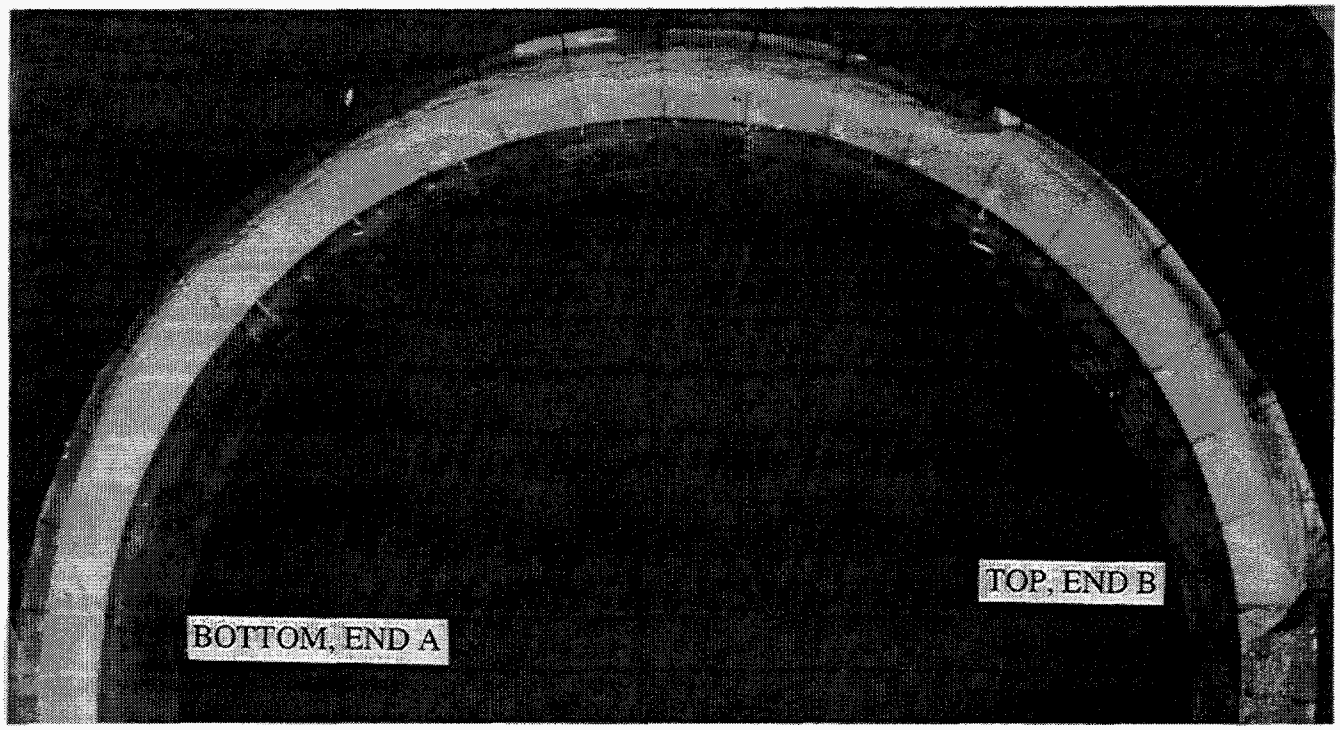

Figure 4.34 Photograph of the fracture surface for Experiment 1-3

4.2.2.2 Experiment 1-4 Results

Experiment 1-4 was a combined pressure and quasi-static monotonic bend experiment. The IPIRG elbow bend test facility constructed for the IPIRG-2 Task 2 elbow experiments was used for this experiment, see Figure 4.37. Figure 4.38 shows the applied load, including the dead weight load due to the weight of the pipe, water, and wire rope restraint system, as a function of the pipe displacement at the load point. The pipe displacement at the load point is the displacement due solely to the crack and the pipe, with the displacements due to the test machine compliance being accounted for. The maximum load for this experiment was 249.2 kN (56,020 lbs).

Figure 4.39 is a plot of the internal pipe pressure as a function of time for this experiment. Shortly after the start of the loading, an instrumentation fitting began to leak. While this fitting was leaking, the internal test specimen pressure was manually maintained at 15.5 MPa (2,250 psi). The sudden loss in pressure evident in Figure 4.39 corresponds to the internal surface crack penetrating the pipe wall.

Figure 4.40 is a plot of the crack section moment as a function the pipe displacement at the load point. The moment values were calculated from the total applied load data and the fixed moment arm length. The maximum moment for this experiment was 797.5 kN-m (7,059 in-kips). Figures 4.41 and 4.42 are plots of the crack section moment as a function of the crack centerline crack-mouth-opening displacement (CMOD) and total crack section rotation data, respectively, for Experiment 1-4. The CMOD data were obtained from a high temperature/high pressure LVDT mounted across the crack on the inside pipe surface. The rotation data were obtained from a series of LVDTs mounted across the crack plane on the outside of the pipe.

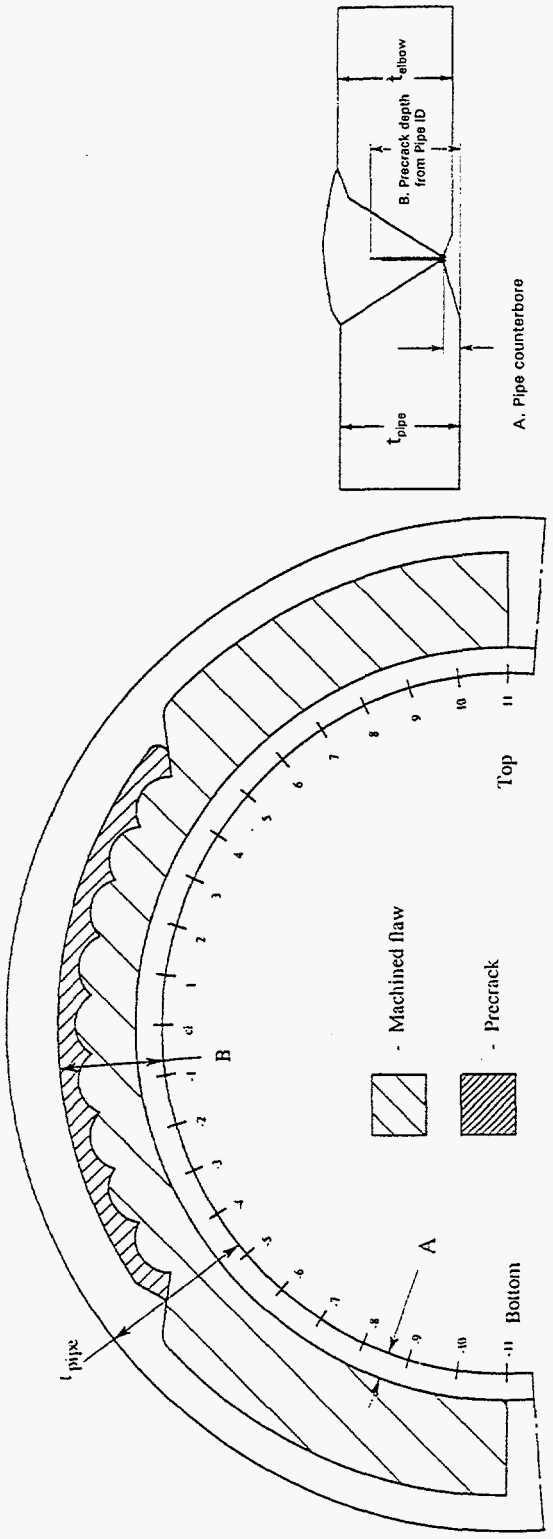

Location	Pipe Wall thickness, t mm	Height of weld crown, mm	Pipe Counterbore, A mm	Counter bore to precrack, mm	Crack depth from pipe ID, B mm	Initial a/t, B/t	Pipe Wall thickness, t inch	Height of weld crown, inch	Pipe Counterbore, A inch	Counter bore to precrack, inch	Crack depth from pipe ID, B inch
-11	32.7	4.5	6.7		23.0	0.705	1.286	0.178	0.264		0.907
-10	32.9	4.6	7.1		23.9	0.726	1.294	0.183	0.279		0.940
-9	33.2	3.9	6.1		23.5	0.708	1.308	0.152	0.240		0.926
-8	33.4	4.6	6.6		24.6	0.738	1.313	0.181	0.260		0.969
-7	33.5	4.0	6.2		24.9	0.742	1.319	0.159	0.245		0.979
-6	33.6	4.7	7.1	19.7	26.8	0.799	1.322	0.186	0.279	0.778	1.056
-5	33.6	4.8	6.5	20.7	27.2	0.810	1.323	0.188	0.256	0.817	1.072
-4	33.6	4.2	7.0	15.9	22.9	0.681	1.324	0.165	0.275	0.627	0.902
-3	33.8	3.7	6.9	15.2	22.1	0.652	1.332	0.146	0.270	0.599	0.869
-2	34.0	3.4	6.6	16.0	22.6	0.665	1.338	0.134	0.261	0.629	0.890
-1	34.1	4.6	7.0	16.2	23.3	0.683	1.342	0.179	0.278	0.639	0.916
0	34.0	4.6	7.2	16.1	23.2	0.684	1.337	0.183	0.282	0.632	0.914
1	34.0	4.0	7.0	16.0	23.1	0.679	1.337	0.159	0.277	0.631	0.908
2	33.9	4.2	6.5	16.1	22.5	0.665	1.334	0.164	0.255	0.632	0.887
3	34.0	4.5	7.6	15.0	22.6	0.666	1.337	0.177	0.301	0.590	0.890
4	34.0	3.8	7.4	15.2	22.6	0.665	1.338	0.148	0.292	0.599	0.890
5	33.9	4.9	7.6		27.6	0.815	1.335	0.193	0.300		1.088
6	33.6	5.2	7.6		27.0	0.802	1.324	0.203	0.299		1.062
7	33.6	5.3	7.4		26.7	0.793	1.324	0.207	0.293		1.050
8	33.8	3.8	7.3		25.8	0.764	1.330	0.151	0.289		1.016
9	33.7	5.2	7.6		25.6	0.759	1.327	0.206	0.301		1.007
10	33.3	5.8	7.8		25.3	0.759	1.310	0.230	0.308		0.995
11	32.9	4.1	7.7		24.2	0.734	1.296	0.160	0.304		0.951
Average	33.6	4.5	7.1	16.6	24.4	0.726	1.323	0.175	0.278	0.652	0.960

Figure 4.35 Post-test fracture surface measurements for Experiment 1-3

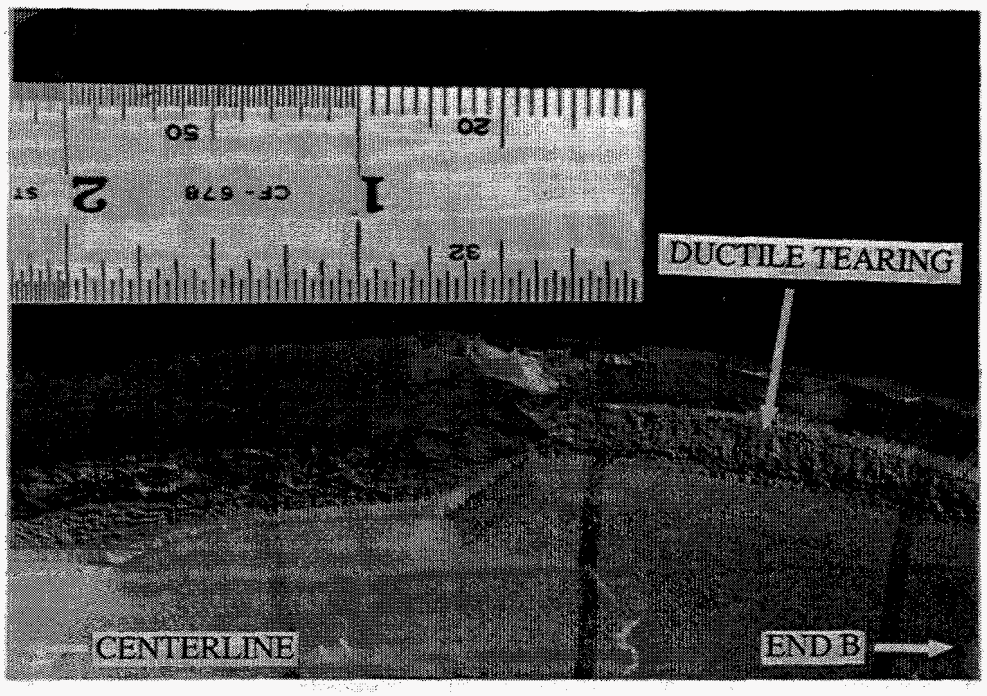

(a) At one of the crack front discontinuities

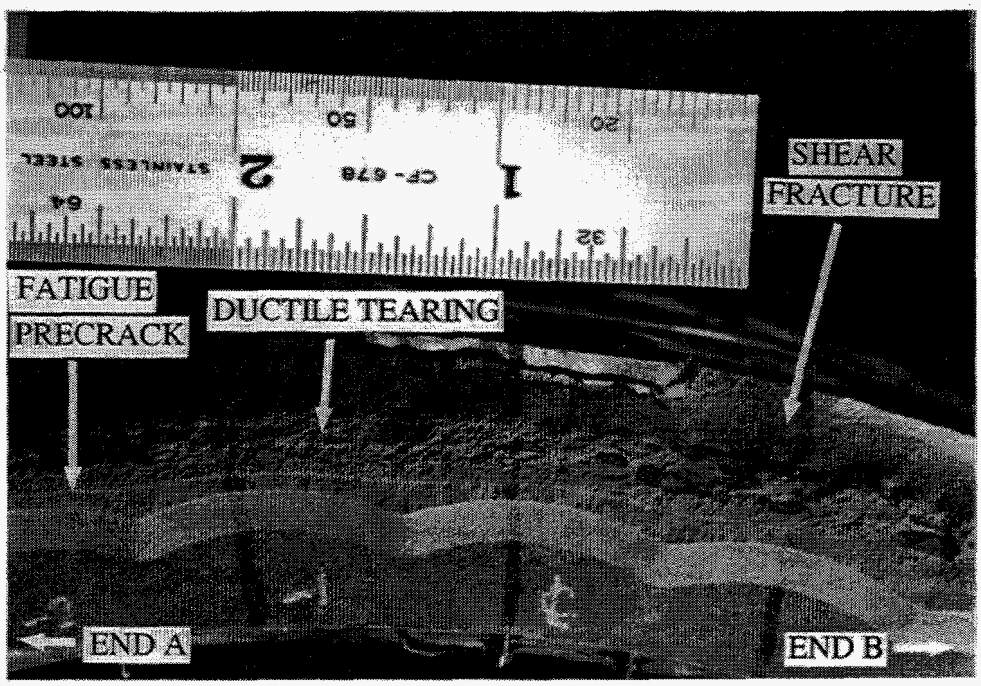

(b) At the crack centerline

Figure 4.36 Magnified view of the fracture surface for Experiment 1-3 (scale in inches)

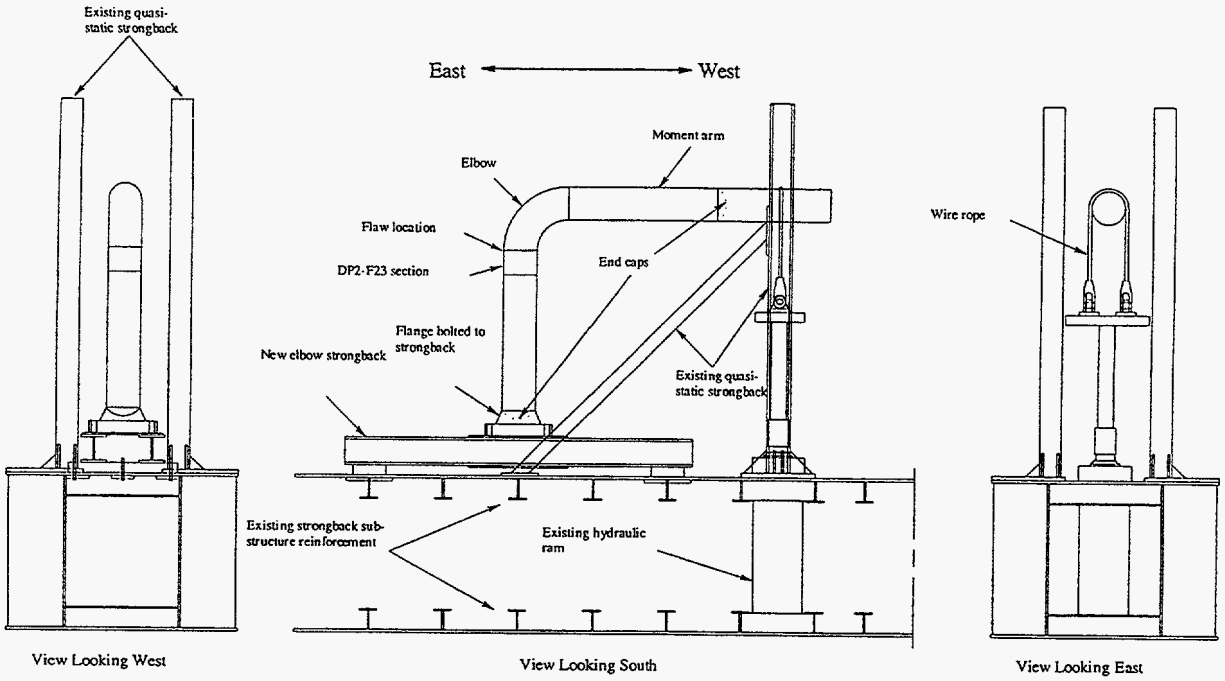

Figure 4.37 Elbow test facility

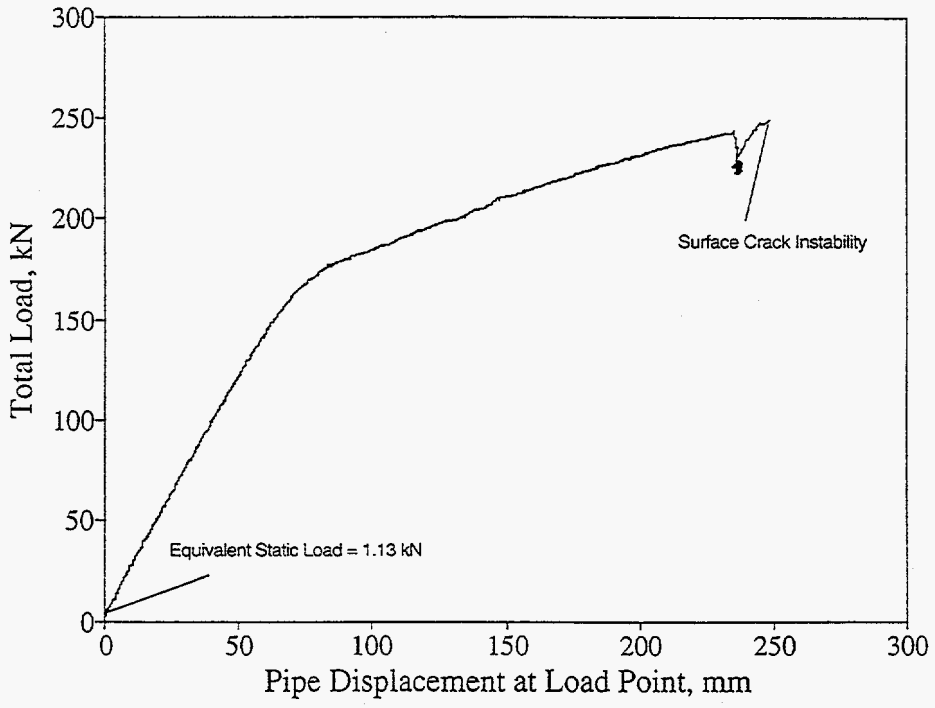

Figure 4.38 Applied load versus pipe displacement at the load point for Experiment 1-4 (Equivalent static load includes dead-weight and pressure effects)

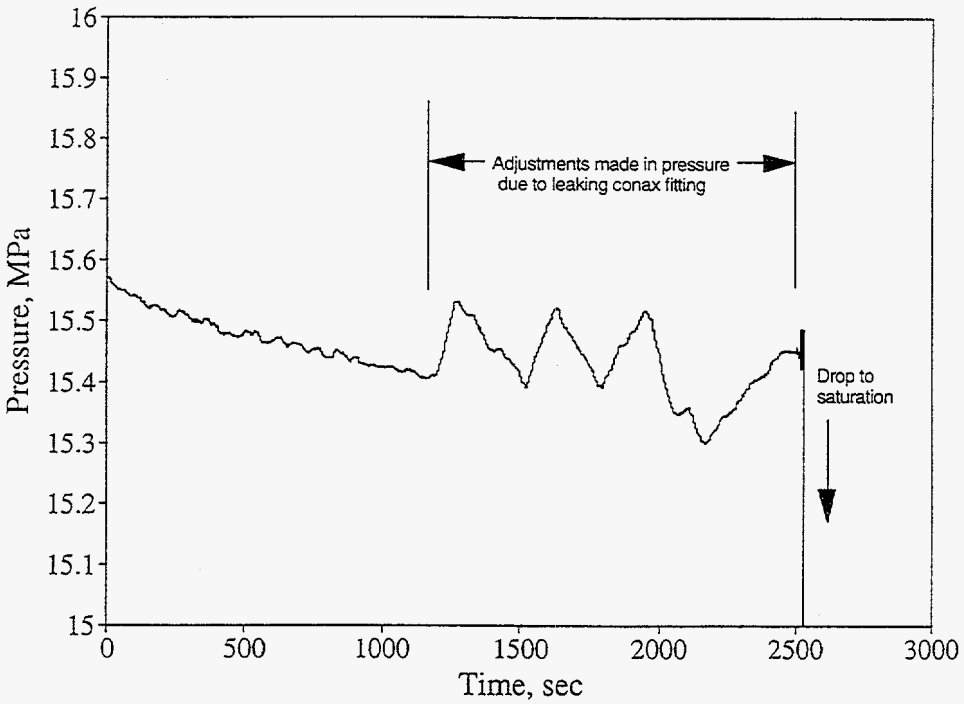

Figure 4.39 Internal pressure versus time for Experiment 1-4

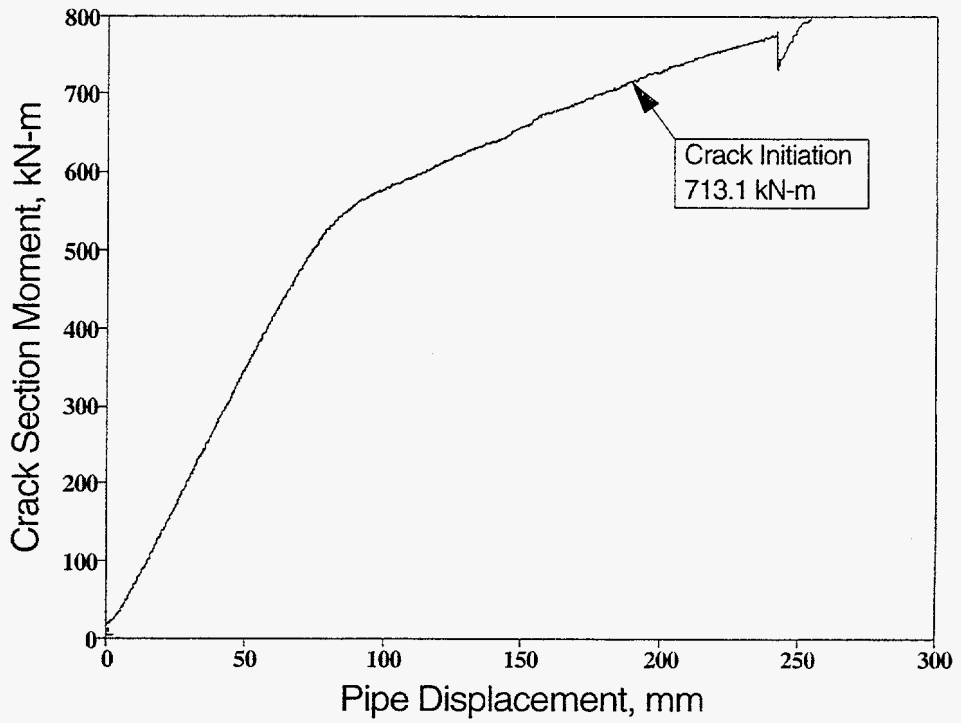

Figure 4.40 Crack-section moment as a function of pipe displacement at the load point for Experiment 1-4

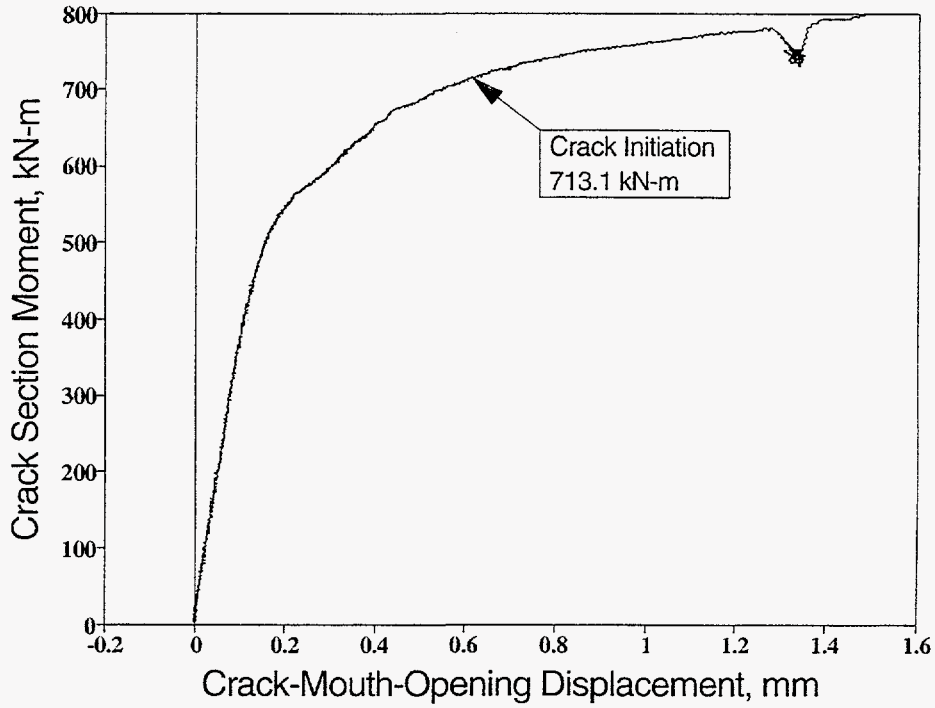

Figure 4.41 Crack-section moment as a function of crack centerline CMOD data for Experiment 1-4

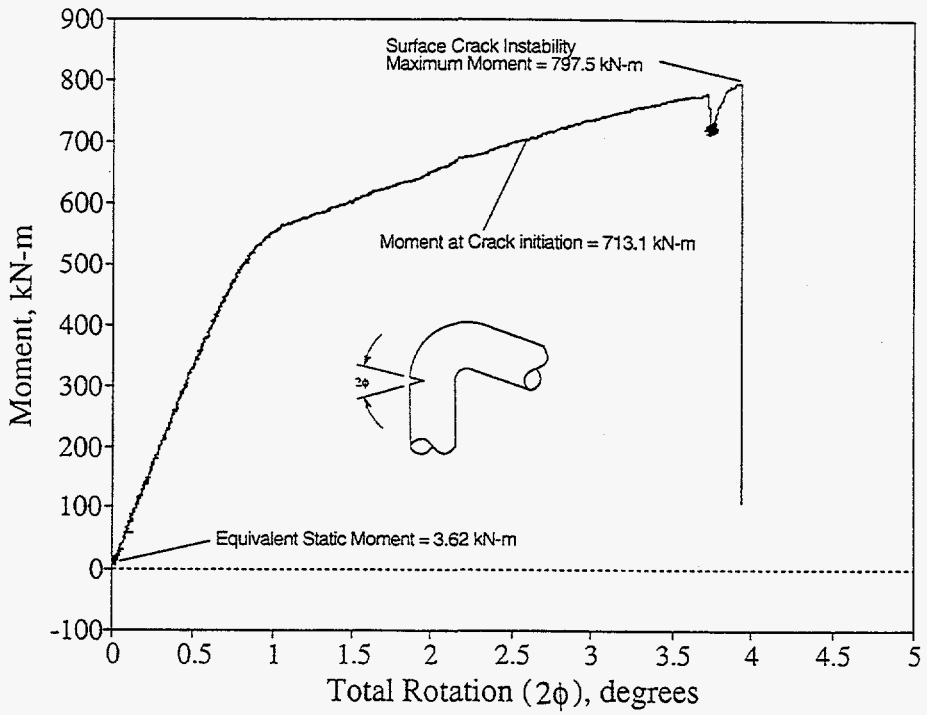

Figure 4.42 Crack-section moment versus total rotation data for Experiment 1-4

Figure 4.43 is a plot of the normalized crack centerline d-c EP (normalized by the base metal reference d-c EP data) as a function of the crack centerline CMOD data. The change in slope of the d-c EP versus CMOD data is indicative of crack initiation. From this figure, it appears that the surface crack initiated at a centerline CMOD value of approximately 0.61 mm (0.024 inch). From Figure 4.41, it can be seen that the applied moment at this value of CMOD is 713.1 kN-m (6,312 in-kips). Thus, the moment at crack initiation is approximately 89 percent of the maximum moment for the experiment.

To determine the surface crack growth from the d-c EP data, a polynomial fit was made to the d-c EP calibration data developed by Wilkowski (Ref. 4.5). A polynomial fit was developed to relate the normalized surface crack depth (a/t) in terms of the normalized electric potential data (EP_N):

$$a/t = 0.669(EP_N) - 0.193(EP_N)^2 + 0.02 + 0.024(EP_N)^3 \quad (4\text{-}1)$$

where

$$EP_N = (EP_c - E_o)/(E_{0.5} - E_o) \quad (4\text{-}2)$$

and

- t = wall thickness
- a = surface crack depth
- EP_c = the crack centerline d-c EP reading accounting for any zero offsets
- $E_{0.5}$ = the electric potential reading for a/t = 0.5 in the same pipe
- E_o = the baseline reference d-c EP reading for uncracked pipe adjusted to represent a reading taken with a probe spacing equal to the crack centerline d-c EP probe spacing

By knowing the normalized surface crack depth at the start of the experiment from post-test measurements of the fracture surface, one can solve for the normalized electric potential (EP) for that crack depth using Equation 4-1. Then substituting into Equation 4-2, the value for $E_{0.5}$ can be calculated using the value of E and E_o at crack initiation as measured in the experiment. Surface crack growth through the wall thickness can then be determined by inputting the normalized value of d-c EP from Equation 4-2 into Equation 4-1 for the experimental d-c EP data after crack initiation. Figure 4.44 presents the surface crack growth as a function of the pipe displacement at the load point for Experiment 1-4.

Figure 4.45 shows an overall photograph of the fracture surface for Experiment 1-4. Figure 4.46 shows a magnified view of the fracture surface at the crack centerline. From this figure, the initial scalloped EDM flaw and the fatigue precrack are clearly identifiable. Figure 4.47 shows the post-test measurements of the machined notch and the fatigue precrack for Experiment 1-4. From Figure 4.47, it can be seen that at the crack centerline, the normalized initial surface crack depth (a/t) was 67.7 percent of the pipe wall thickness. The average normalized initial surface crack depth was 67.5 percent of the pipe wall thickness. The deepest section of the crack (74.8 percent of the pipe wall thickness in depth) was approximately 125 mm (5 inches) from the crack centerline towards End A of the surface crack.

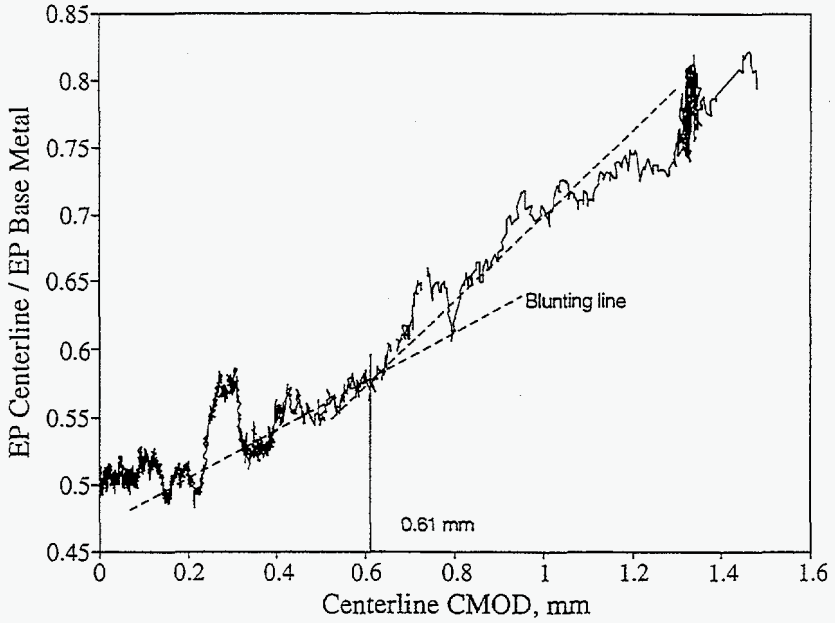

Figure 4.43 Normalized centerline d-c EP versus centerline crack-mouth-opening displacement for Experiment 1-4

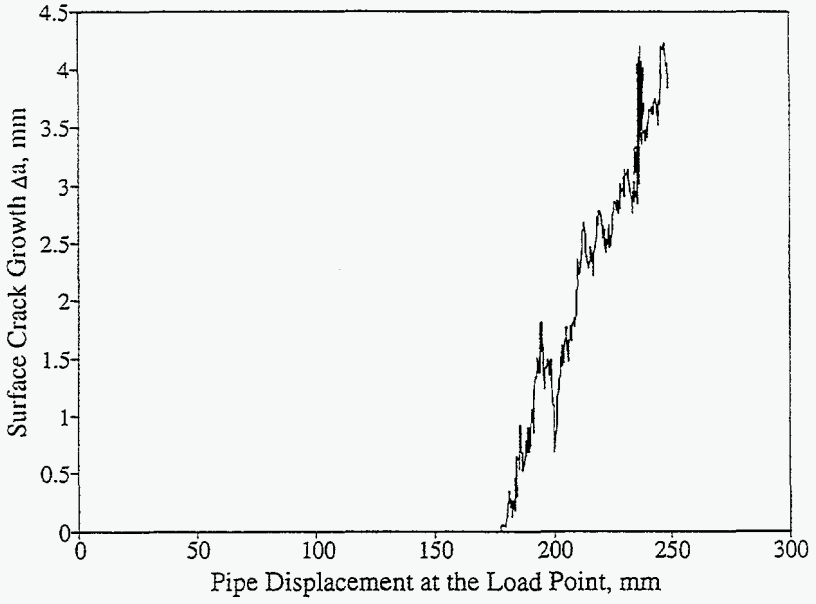

Figure 4.44 Surface crack growth versus pipe displacement at the load point for Experiment 1-4

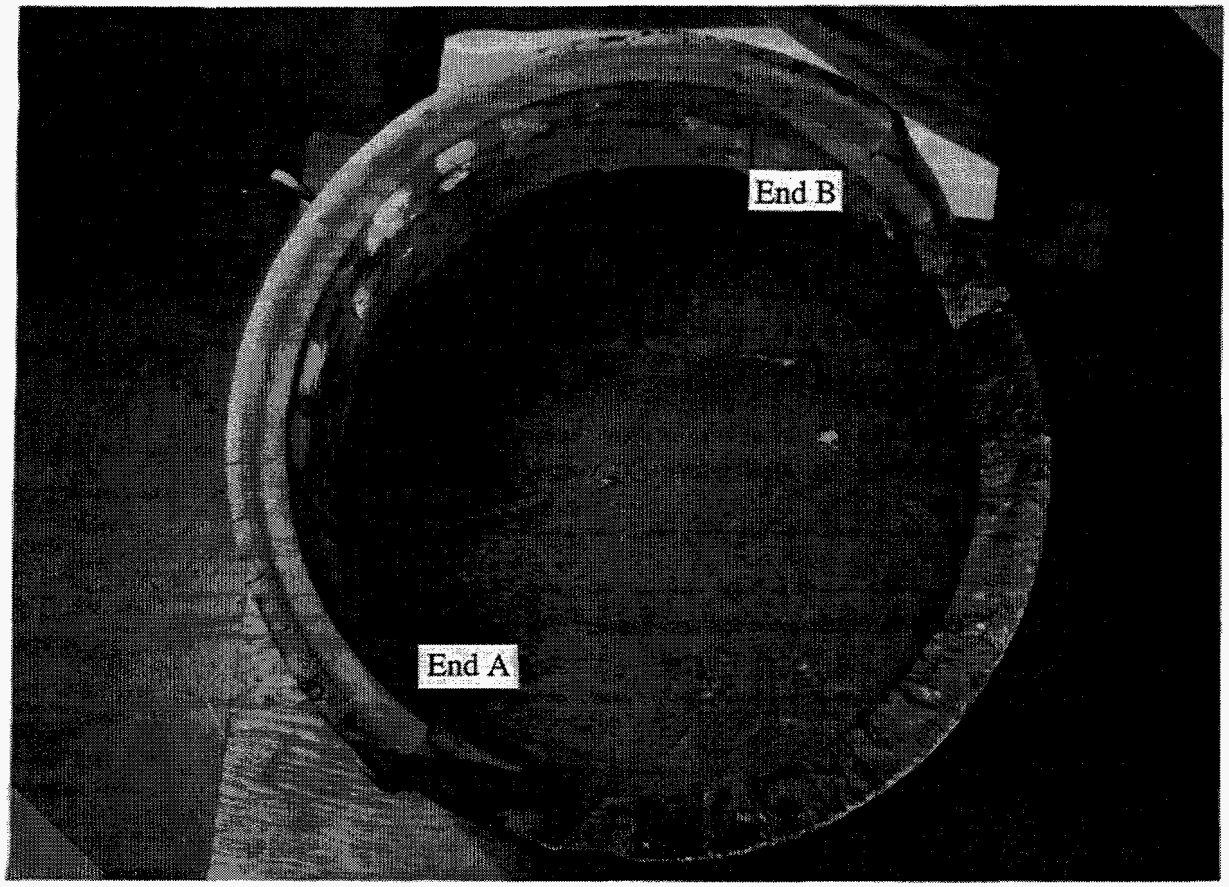

Figure 4.45 Photograph of fracture surface of Experiment 1-4

4.3 Short Surface Crack Experiments

Two short surface crack pipe experiments, Experiments 1-5 and 1-6, were conducted as part of Task 1 of the IPIRG-2 program. Experiment 1-5 was a single frequency pipe system experiment using the same basic forcing function as used in previous IPIRG single frequency pipe system experiments. Experiment 1-6 was a companion quasi-static four-point bend experiment. The objective of these experiments was to gather experimental data for assessing the fracture behavior of relatively short internal circumferential surface cracks. The rationale for conducting these experiments was to determine if the fracture prediction analysis methods previously developed and verified for the case of relatively large surface cracks are applicable to crack sizes more typical of the crack sizes used in in-service flaw evaluations. As part of the Short Cracks in Piping and Piping Welds Program (Ref. 4.6), it was shown that the previously developed analysis methods work for the shorter crack sizes considered as part of this effort for the case of quasi-static loading. However, no such data existed for the case of dynamic, cyclic loading. Experiments 1-5 and 1-6 were included in the IPIRG-2 test matrix to help fill this void in the database. To satisfy the objective of this effort, the results from these two short surface crack experiments are compared with the results from companion long surface cracked pipe experiments conducted previously as part of the Degraded Piping (Experiment 4141-4) and IPIRG-1 (Experiment 1.3-5) programs. Note, due to slight differences in test conditions and test specimen sizes, the reader is cautioned against making direct comparisons of results between experiments until the results have been normalized by the fracture prediction analyses in Section 5.0.

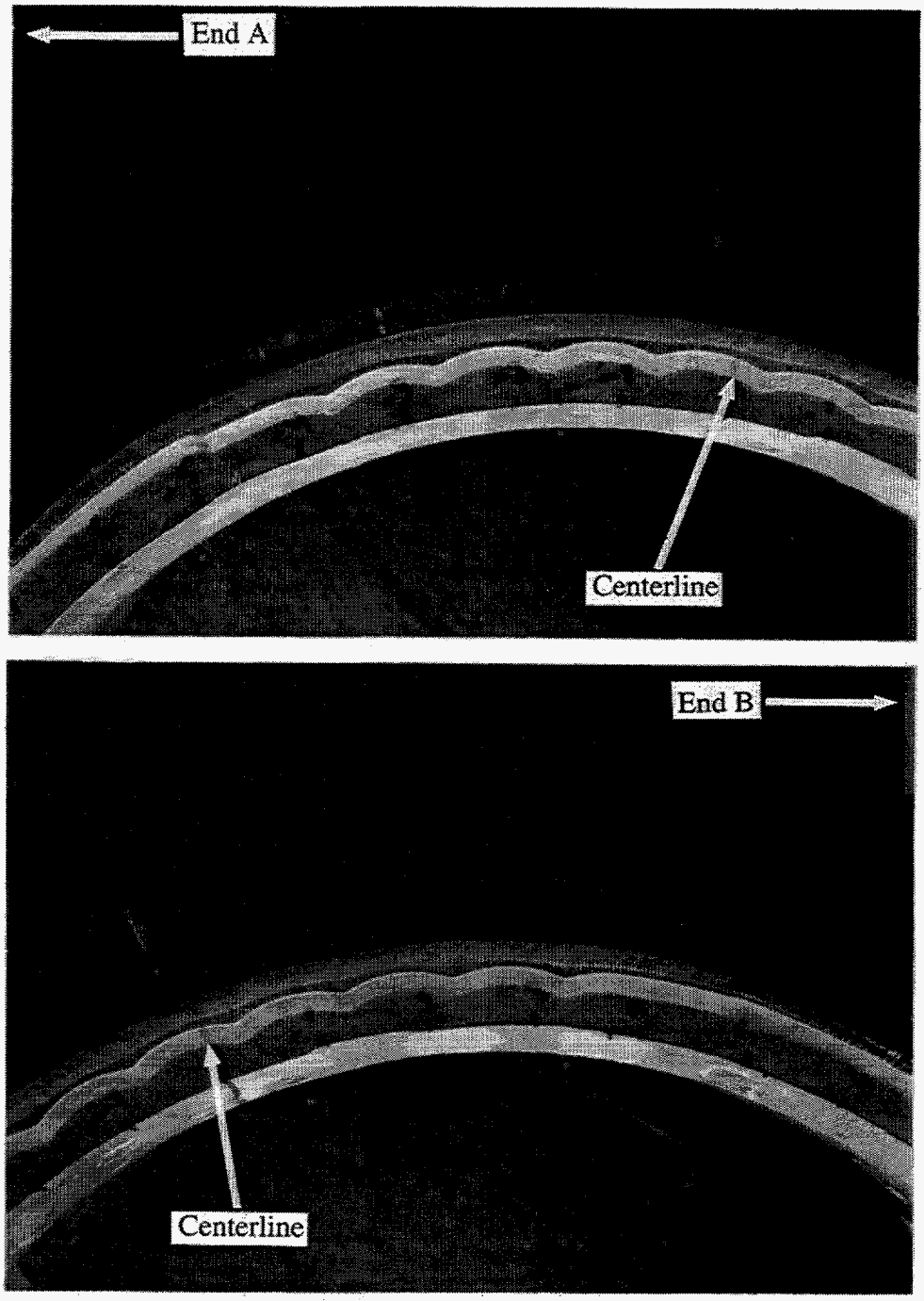

Figure 4.46 Views of the fracture surface at the flaw centerline for Experiment 1-4

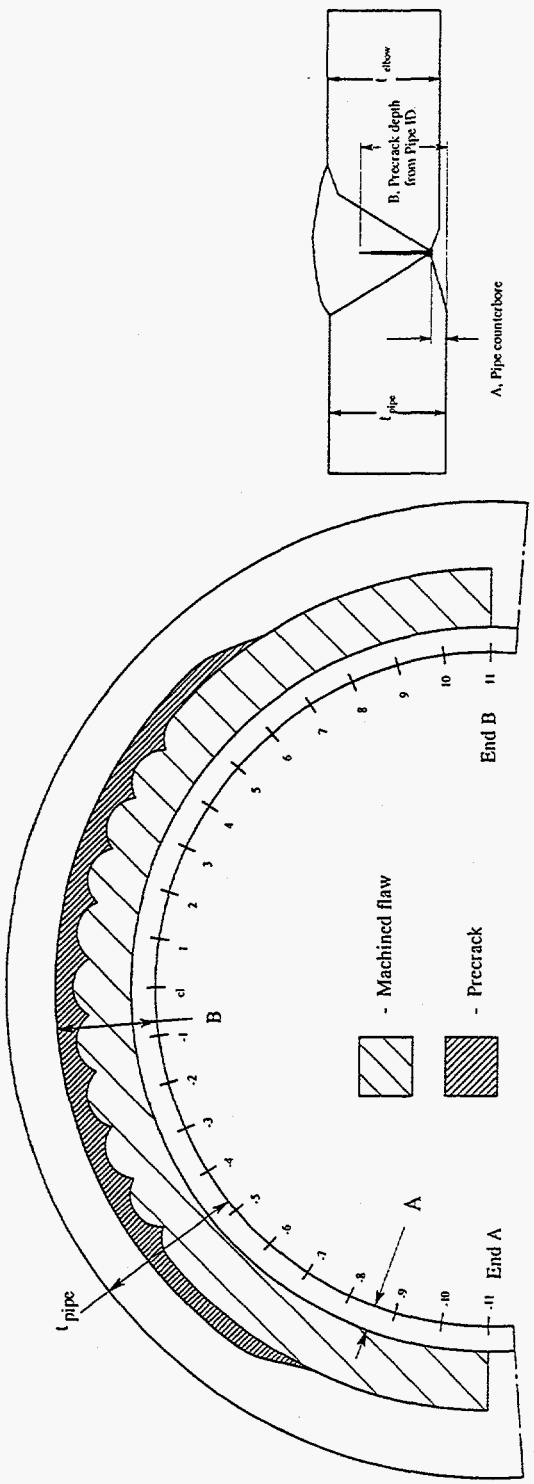

Location	Pipe Wall thickness, t mm	Height of weld crown, mm	Pipe Counterbore, A mm	Counter bore to precrack, mm	Crack depth from pipe ID, B mm	Initial a/t, B/t	Pipe Wall thickness, t inch	Height of weld crown, inch	Pipe Counterbore, A inch	Counter bore to precrack, inch	Crack depth from pipe ID, B inch
-11	33.5	4.5	6.0		23.6	0.706	1.318	0.177	0.235		0.930
-10	33.9	4.5	6.4		22.9	0.674	1.336	0.179	0.250		0.901
-9	33.7	4.9	7.0		22.9	0.679	1.326	0.193	0.274		0.901
-8	33.4	4.8	7.2		22.7	0.679	1.315	0.187	0.282		0.893
-7	33.3	5.6	7.6	16.1	23.7	0.711	1.311	0.220	0.299	0.634	0.933
-6	33.6	5.4	7.3	16.6	24.0	0.714	1.321	0.213	0.289	0.655	0.944
-5	33.5	5.7	7.5	17.6	25.0	0.748	1.318	0.225	0.294	0.693	0.986
-4	33.3	5.3	6.9	16.0	22.9	0.689	1.310	0.209	0.273	0.630	0.903
-3	33.3	5.2	6.9	15.9	22.8	0.685	1.310	0.205	0.271	0.627	0.898
-2	33.1	5.0	6.8	15.9	22.7	0.685	1.304	0.197	0.267	0.626	0.893
-1	33.1	4.7	6.6	15.8	22.4	0.678	1.303	0.185	0.262	0.622	0.883
0	33.4	4.0	6.6	16.0	22.6	0.677	1.314	0.158	0.261	0.629	0.890
1	33.6	4.2	7.3	15.3	22.6	0.671	1.324	0.165	0.288	0.601	0.888
2	33.7	3.8	6.4	15.5	21.9	0.652	1.325	0.148	0.253	0.611	0.864
3	33.6	4.3	7.0	15.0	22.1	0.656	1.324	0.171	0.277	0.592	0.869
4	33.6	3.9	6.5	15.8	22.4	0.666	1.322	0.155	0.257	0.624	0.881
5	33.9	2.9	6.5	15.5	21.9	0.648	1.334	0.116	0.255	0.610	0.864
6	33.9	3.8	6.3	14.7	21.0	0.619	1.333	0.149	0.248	0.578	0.826
7	33.8	3.7	6.5		21.2	0.627	1.332	0.145	0.255		0.835
8	33.9	2.8	6.3		21.5	0.634	1.336	0.111	0.248		0.848
9	34.1	2.6	6.3		22.4	0.657	1.341	0.100	0.249		0.882
10	34.1	3.1	6.3		23.0	0.673	1.344	0.120	0.247		0.905
11	34.0	3.7	6.8		24.0	0.705	1.340	0.145	0.266		0.945
Average	33.6	4.3	6.7	15.8	22.7	0.675	1.324	0.169	0.265	0.623	0.894

Figure 4.47 Post-test fracture surface measurements for Experiment 1-4

The nominal crack size used for these experiments was 25 percent of the pipe circumference in length and 50 percent of the pipe wall thickness in depth. This is the same nominal surface crack size used in the U.S. NRC Short Cracks in Piping and Piping Welds program (Ref. 4.6). The nominal surface crack size used in the Degraded Piping and IPIRG-1 programs was 50 percent of the pipe circumference in length and 66 percent of the pipe wall thickness in depth.

The internal surface cracks for both of these experiments were located in the center of a relatively low toughness shop-fabricated stainless steel submerged-arc weld. The weld procedure was a General Electric (GE) stainless steel weld procedure used previously in the quasi-static monotonic Degraded Piping Program experiment (Experiment 4141-4) and the single frequency pipe system IPIRG-1 experiment (Experiment 1.3-5). The test temperature and pressure for the two IPIRG-2 experiments and the IPIRG-1 experiment were representative of PWR conditions, i.e., 288 C (550 F) and 15.5 MPa (2,250 psi). The test specimen pressure for the quasi-static monotonic Degraded Piping Program experiment (4141-4) was 11.0 MPa (1,600 psi). The test temperature for this experiment was 288 C (550 F).

4.3.1 Experimental Results

The key results from the two Task 1 short surface-cracked pipe experiments are shown in Table 4.4. Also included in Table 4.4 are the results for the two companion, relatively large, surface-cracked pipe experiments conducted previously in the Degraded Piping and IPIRG-1 programs. The summary in Table 4.4 contains the test conditions (pipe diameters, wall thicknesses, crack depths, crack lengths, test pressures, and test temperatures), material property data (yield and ultimate strengths for the stainless steel base metal and J values at crack initiation [J_i] from C(T) specimen tests for the stainless steel weld), and moments at crack initiation and maximum moments for each of the four pertinent experiments.

4.3.1.1 Experiment 1-5 Results

Experiment 1-5 was a single frequency pipe system experiment. Figure 4.48 shows the displacement-time history forcing function for this experiment. The maximum applied displacement for this experiment was 71.9 mm (2.83 inches) and occurred 3.9 seconds after the initiation of the forcing function, after which attenuation of the forcing function occurred. Control logic for the forcing function was set up so that when the test specimen pressure dropped below 12.4 MPa (1,800 psi), the command signal was linearly attenuated over a 3 second interval. This shutdown sequence provided a gradual return of the actuator to its original starting position without inducing large forces, which could damage the test system. The maximum moment for the experiment and surface crack penetration occurred prior to the attenuation of the forcing function. The actuator displacement at the time of the maximum moment was 68.8 mm (2.71 inches).

Figure 4.49 is a plot of the test specimen internal pressure as a function of time. The initial test pressure was 15.5 MPa (2,250 psi). From Figure 4.49, it appears that the surface crack penetrated the pipe wall approximately 3.77 seconds after the initiation of the forcing function. However, closer examination of the crack-mouth-opening displacement (Figure 4.50), crack centerline electric potential (Figure 4.51), and crack section moment (Figure 4.52) versus time data indicate that the crack most likely penetrated the pipe wall 3.67 seconds after the start of the forcing function.

Table 4.4 Key results from two short surface-crack stainless steel weld pipe experiments (1-5 and 1-6) and two companion long surface-crack stainless steel weld pipe experiments (4141-4 and 1.3-5)

Experiment No.	Outside Pipe Diameter, mm	Wall[1] Thickness, mm	a/t[2]	2c/πD[3]	Test Pressure, MPa	Test Temperature, C	Yield[4] Strength, MPa	Ultimate[4] Strength, MPa	J at Crack Initiation C(T) Specimen[5], kJ/m²	Moment at Crack Initiation, kN-m	Maximum Moment, kN-m
1-5	415.3	22.15	0.427	0.267	15.5	288	171	456	55	ND[6]	776
1-6	412.7	22.86	0.649	0.27	15.5	288	171	456	55	614	697
4141-4	413.5	23.65	0.633	0.50	11.0	288	171	456	55	498	501
1.3-5	416.1	22.56	0.574	0.532	15.5	288	171	456	55	460	493

(1) Excluding counterbore and weld crown.
(2) At the location where the crack was the deepest; wall thickness does not include counterbore or weld crown.
(3) Total crack length on the inside pipe surface divided by the inside pipe circumference.
(4) Quasi-static data for the pipe base metal material.
(5) Quasi-static data for the weld metal.
(6) ND = Not determined.

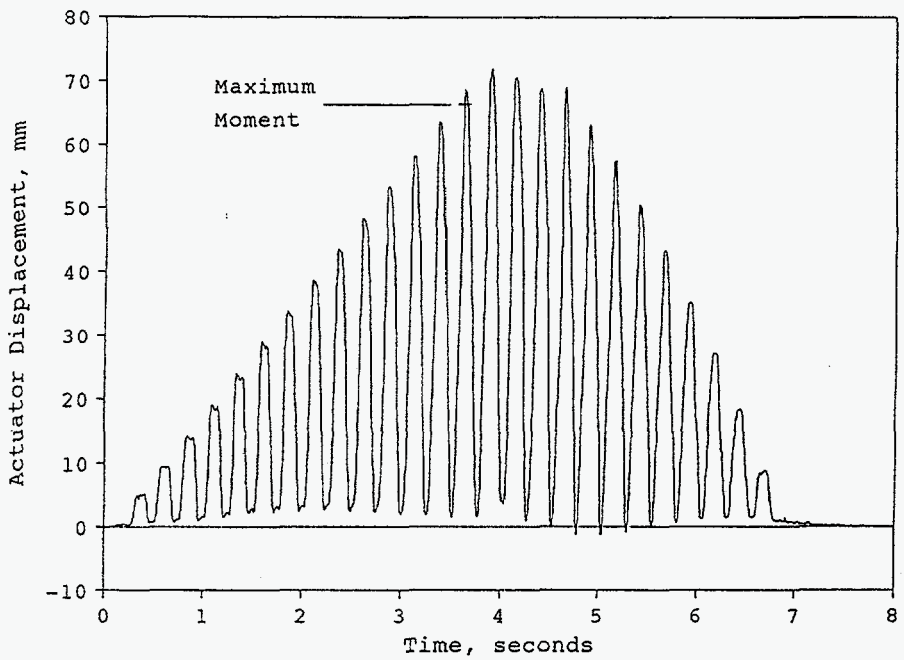

Figure 4.48 Experiment 1-5 actuator displacement versus time history

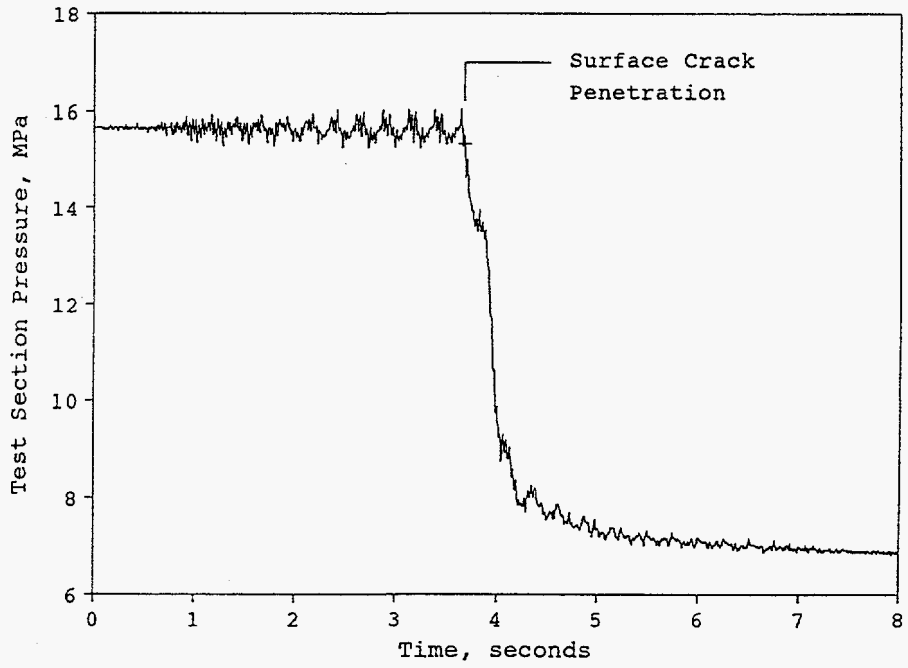

Figure 4.49 Experiment 1-5 test specimen pressure versus time history

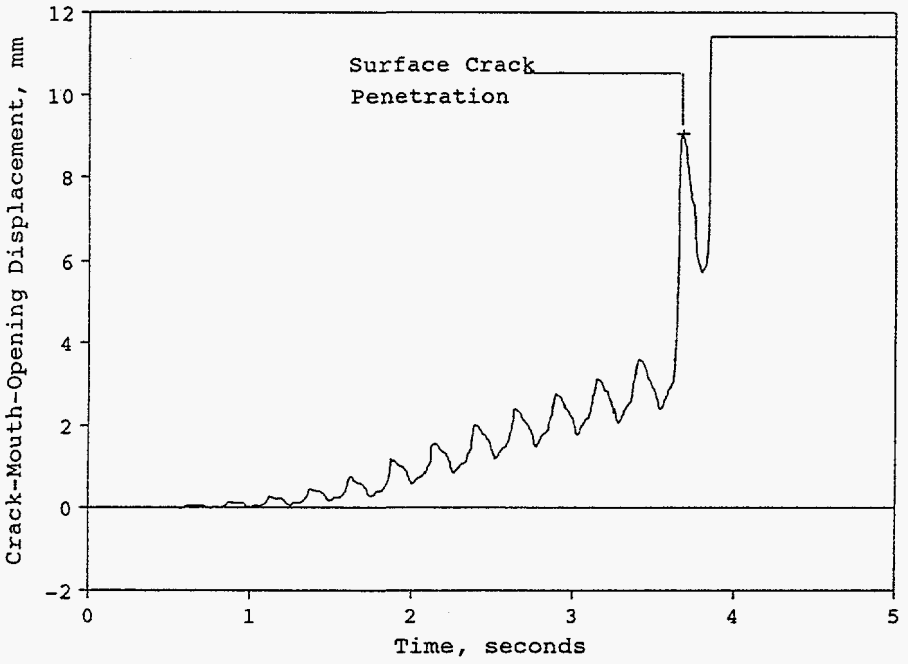

Figure 4.50 Experiment 1-5 crack centerline crack-mouth-opening displacement (CMOD) versus time history

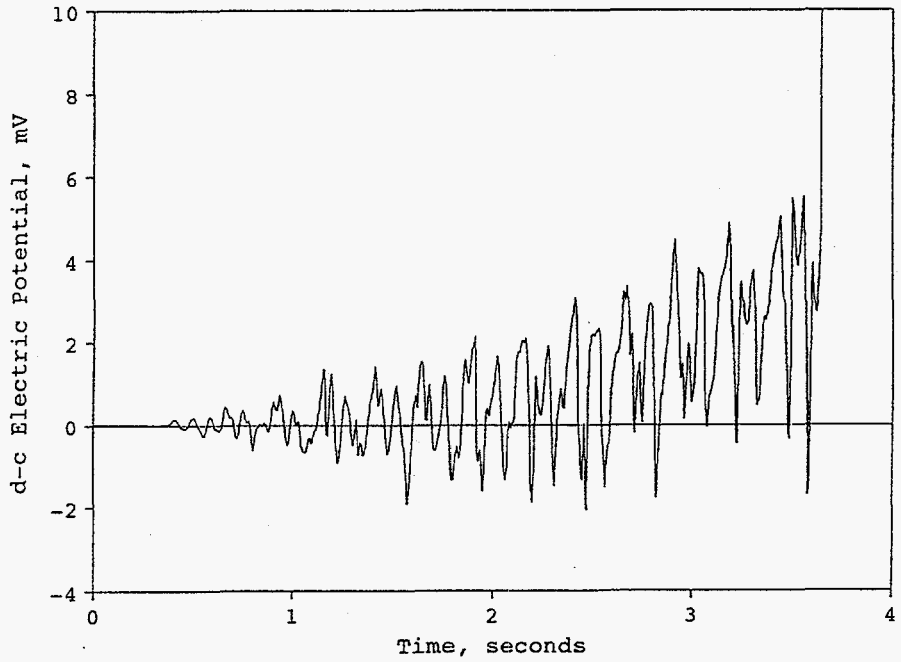

Figure 4.51 Experiment 1-5 crack centerline d-c electric potential versus time history

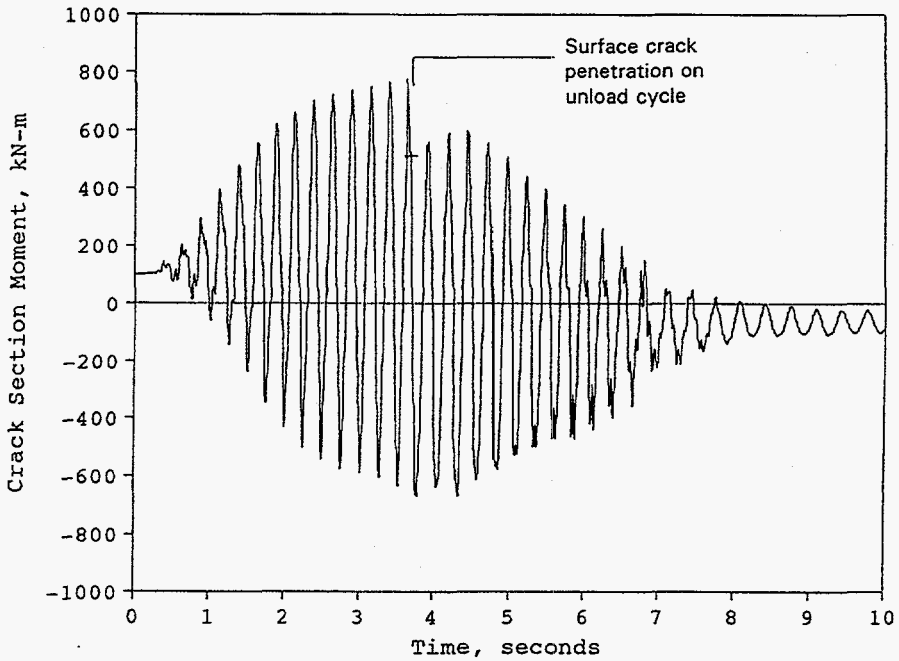

Figure 4.52 Experiment 1-5 crack-section moment versus time history

Figure 4.50 shows the crack centerline crack-mouth-opening displacement (CMOD) versus time data for Experiment 1-5. Worth noting from Figure 4.50 is the fact that the signal from the centerline LVDT is relatively clean for the entire load history, even after the surface crack penetrated the pipe wall and fluid was escaping through the crack opening. The LVDT was set up so that its initial position was intentionly offset 3.2 mm (0.125 inch) to the closing CMOD side. Consequently, the calibrated opening range of the LVDT was 9.5 mm (0.375 inch). Beyond that range, the output of the device becomes nonlinear. The fact that the signal saturates at approximately 11.5 mm (0.45 inch) of CMOD is a result of the voltage input to the Analog-to-Digital (A/D) converter saturating at 10 volts.

The total (dynamic plus static) moment at the crack section as a function of time is shown in Figure 4.52. From this figure it can be seen that the maximum crack section moment during this experiment was 776.2 kN-m (6,870 in-kips). The crack section moment at the time of surface crack penetration was 514.1 kN-m (4,550 in-kips), which is only 66.2 percent of the maximum moment for the experiment. It appears that the surface crack penetrated the pipe wall on the first unloading cycle after the maximum moment cycle, 0.035 seconds after the maximum moment for the experiment was achieved.

Figures 4.53 and 4.54 are plots of the total crack section moment as a function of the crack-mouth-opening displacement (CMOD) and crack-section rotation data, respectively, for Experiment 1.5. The overall characteristics of both figures are similar, showing an increasing cyclic response consistent with the forcing function.

It was not possible to detect the instant of crack initiation from the d-c EP versus CMOD data. The cyclic loadings and unloadings caused compressive plasticity at the crack which affected the material's electrical resistivity. This severely complicated the interpretation of the data, see Figure 4.55. As a result, the cycle during which the crack initiated had to be estimated based on post-test examination of the fracture surface. Figure 4.56 is an overall view of the fracture surface for this experiment. Figure 4.57 is a 5X magnification of the fracture at the center of the crack. This section of the fracture surface was examined using a scanning electron microscope (SEM) to document and measure the progress of the surface crack due to the cyclic loadings. The beachmarks on the fracture surface clearly identify the progress of the surface crack as it grew due to cyclic loading. Figure 4.58 shows a sketch of these beachmarks in the center region of the crack, with measurements of the extension of the crack front for each of the load cycles between crack initiation and surface-crack penetration. This figure shows eight distinct regions of crack growth and crack arrest. Previous test data showed that the surface crack penetrated the pipe wall during the 14th loading cycle; therefore, the surface crack was estimated to have initiated during the sixth loading cycle. The exact load (or moment) at crack initiation could not be determined for this experiment. However, based on the moment time data in Figure 4.52, it was estimated that the crack initiated between 481 kN-m (4,260 in-kips) and 557 kN-m (4,930 in-kips).

The depth of the initial machined notch plus the fatigue precrack and the pipe wall thickness were measured post-test at 13 locations along the length of the surface crack, see Figure 4.59. The crack depth measurements reported in Figure 4.59 include the depth of the weld counterbore. The crack depth to wall thickness ratio (a/t) at the crack centerline was 0.495. This was the location where the crack was deepest.

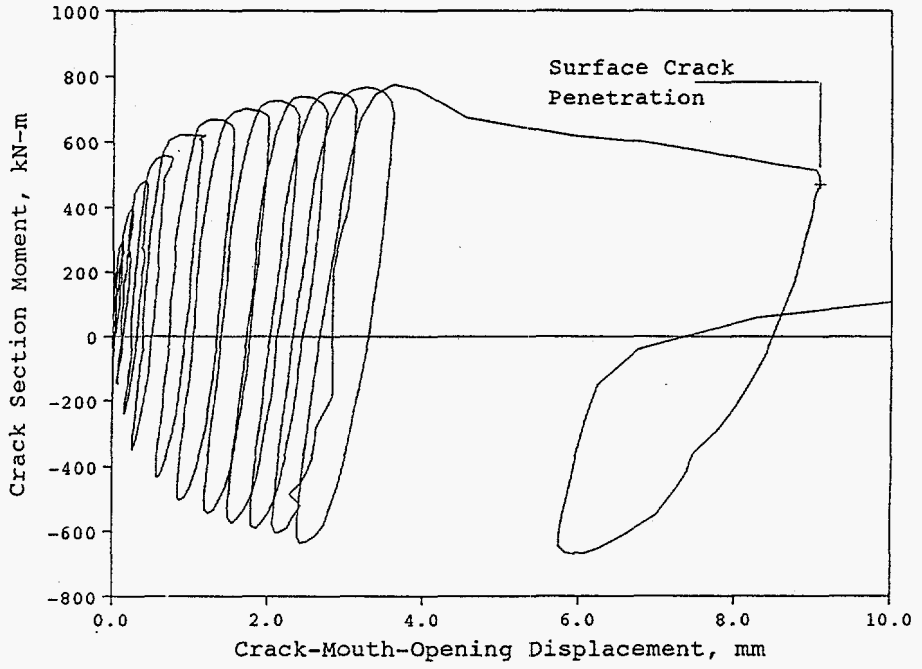

Figure 4.53 Crack-section moment versus crack-mouth-opening displacement (CMOD) history for Experiment 1-5 (CMOD data are from the centerline LVDT)

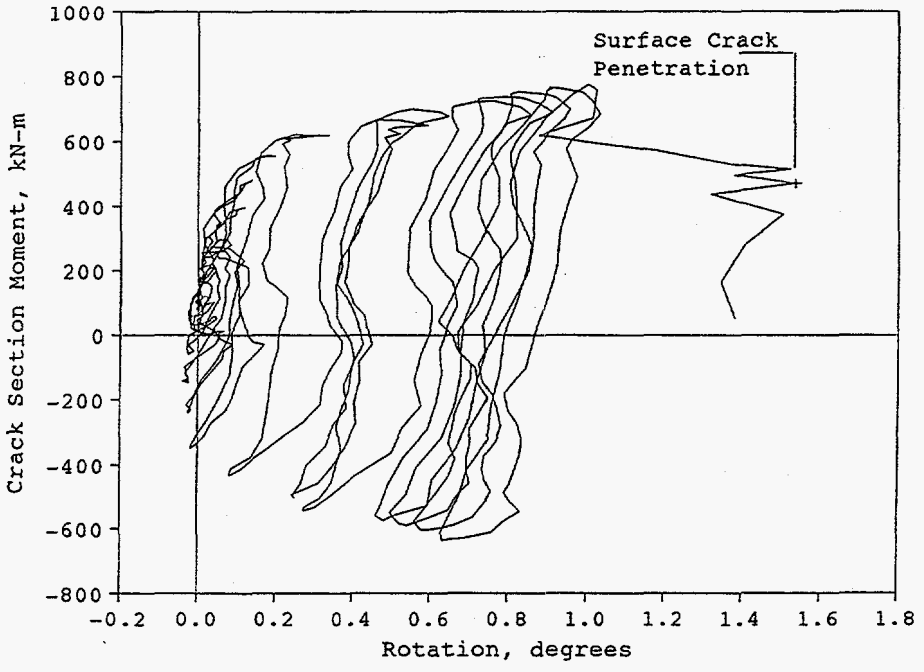

Figure 4.54 Crack-section moment versus total rotation history for Experiment 1-5 (Rotation data are from the coarse rotation device)

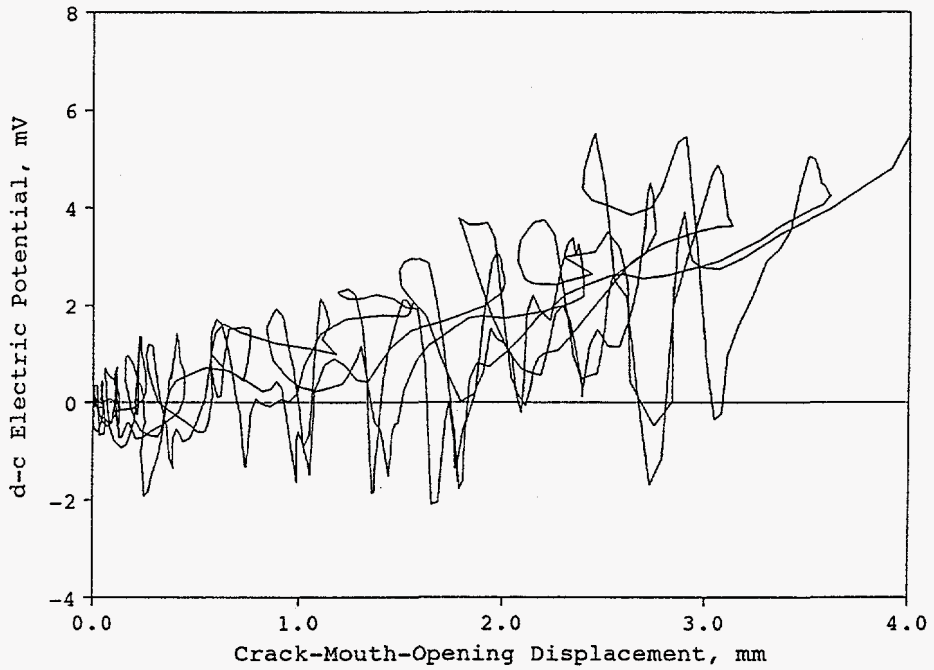

Figure 4.55 Crack centerline d-c electric potential versus crack-mouth-opening displacement (CMOD) history for Experiment 1-5 (CMOD data are based on the centerline LVDT)

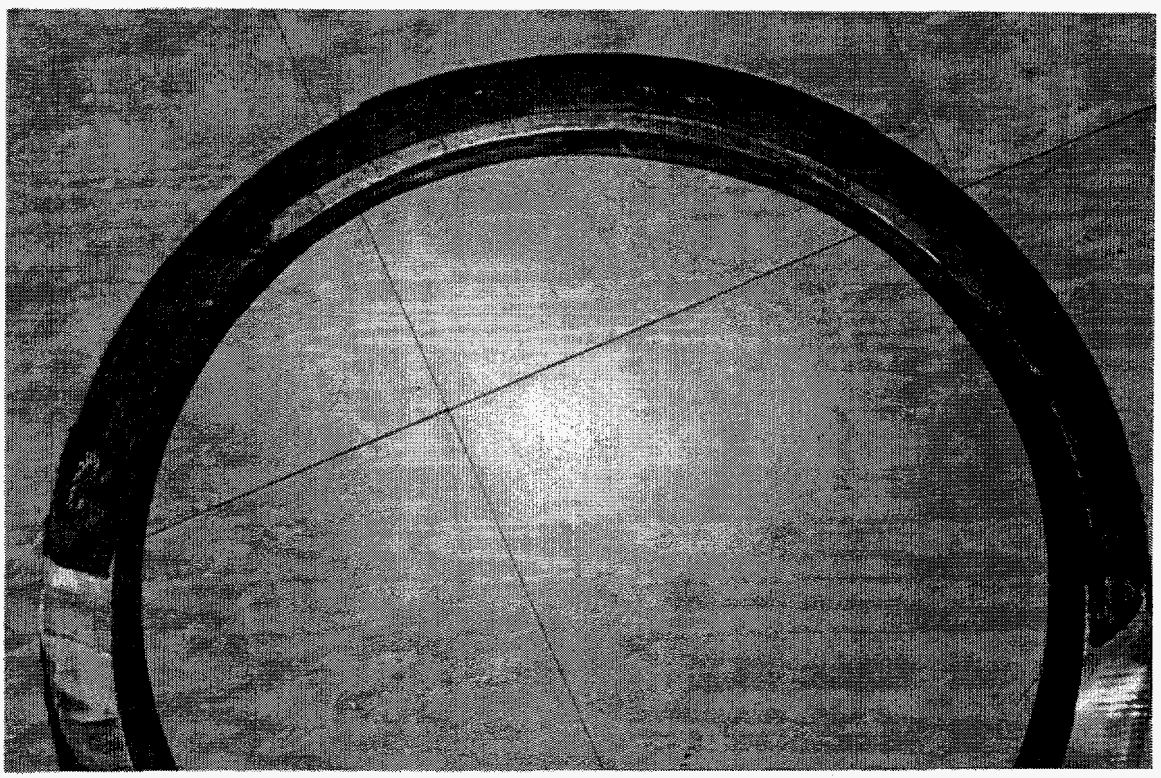

Figure 4.56 Overall view of the fracture surface from Experiment 1-5

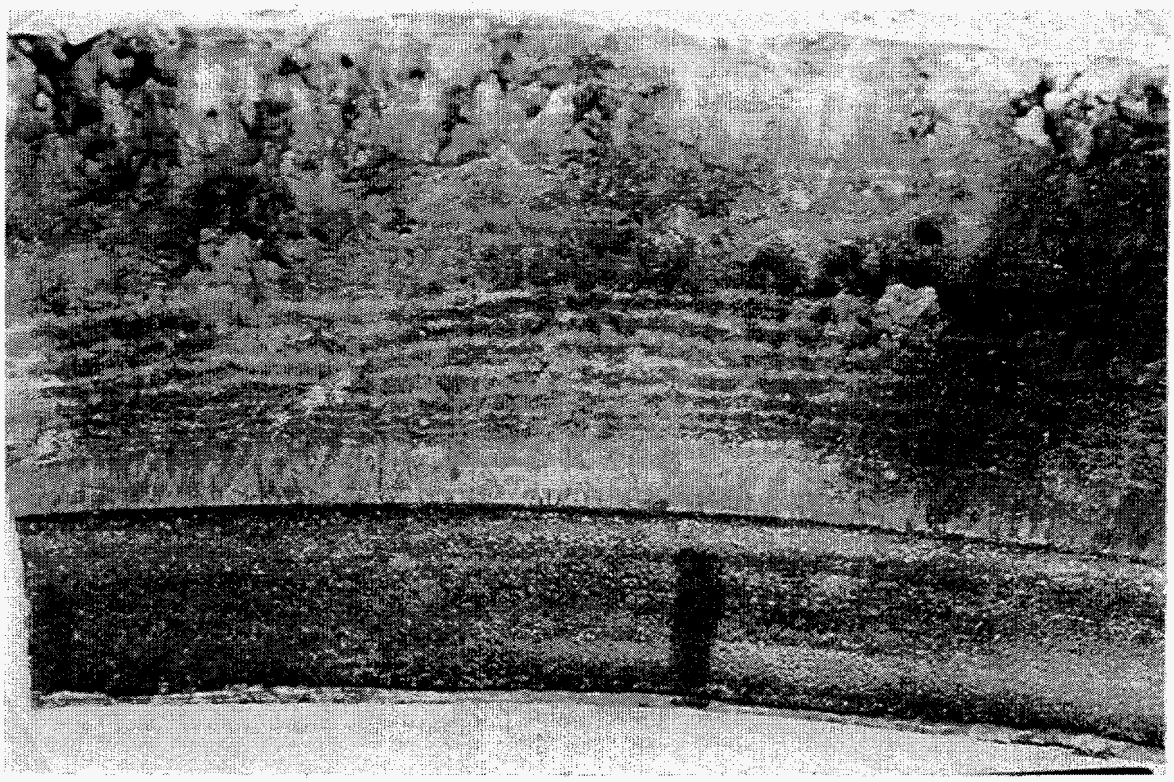

Figure 4.57 5X magnification of the fracture surface for Experiment 1-5 at the crack centerline

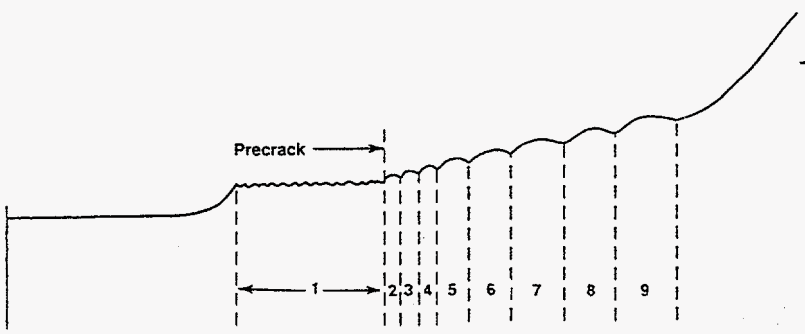

Segment	Crack Growth, mm (inch)
1	2.4130 (0.095)
2	0.3302 (0.013)
3	0.3556 (0.014)
4	0.3556 (0.014)
5	0.5842 (0.023)
6	0.7620 (0.030)
7	0.8636 (0.034)
8	0.8890 (0.035)
9	1.0160 (0.040)

Figure 4.58 Sketch of the fracture surface for Experiment 1-5 in the center region of the crack showing the progression of the surface crack due to cyclic loading

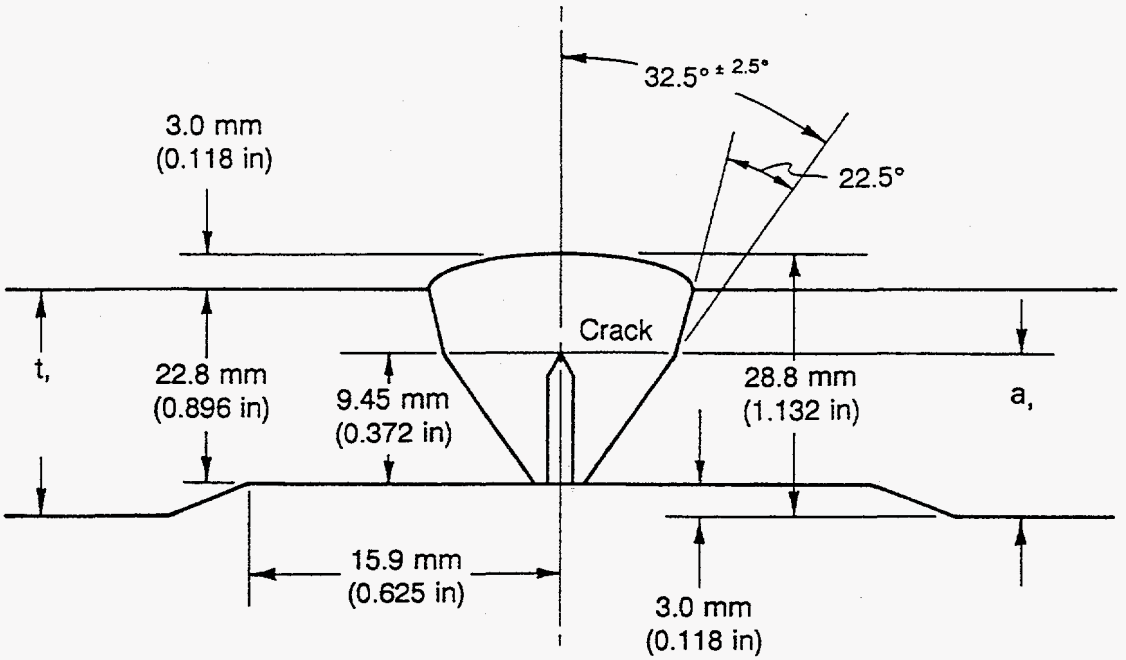

(a) Crack and weld section dimensions

Location	a Crack Depth Including Counterbore, mm	t Base Metal Wall Thickness, mm	a/t
1	3.00	25.1	0.120
2	11.4	25.2	0.453
3	11.0	25.0	0.439
4	11.4	25.3	0.452
5	11.6	25.1	0.461
6	11.5	25.3	0.453
7	12.5	25.1	0.495
8	12.1	25.3	0.479
9	11.3	25.2	0.449
10	11.1	24.9	0.444
11	10.3	25.1	0.410
12	10.3	25.1	0.412
13	3.00	25.1	0.120

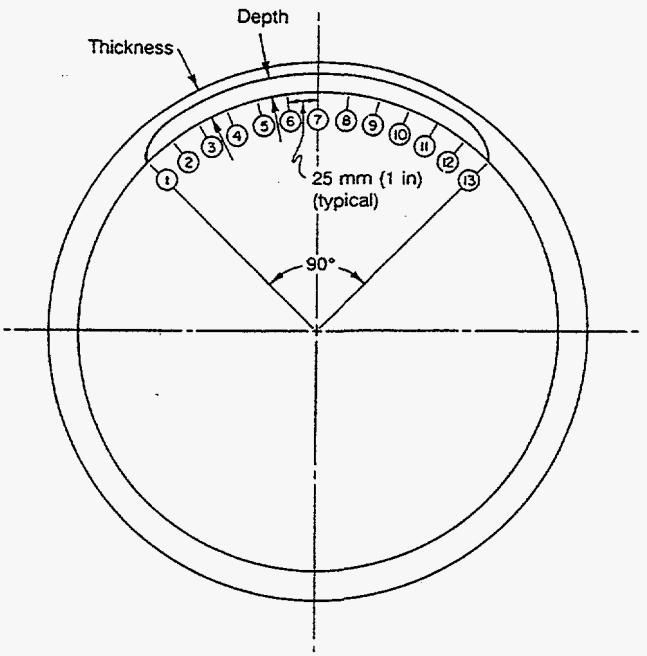

(b) Crack depth locations and measurements

Figure 4.59 Flaw geometry for Experiment 1-5

4.3.1.2 Experiment 1-6 Results

Experiment 1-6 was the quasi-static monotonic companion experiment to Experiment 1-5. Figure 4.60 is a plot of the total applied load as a function of the pipe displacement at the load point for this experiment. The total applied load is the total load measured from the load cells at the two actuators plus the "dead-weight" load due to the weight of the pipe, the water inside the pipe, and the restraint cables. The pipe displacement at the load point is the displacement due solely to the pipe and crack. The pipe displacement at the load point does not include the added displacement due to the compliance of the test frame. The load-displacement curve shown in Figure 4.60 shows a relatively smooth loading behavior up to the point when the surface crack penetrates the pipe wall. At that point, there was an abrupt drop in load as the surface crack grew unstable through the pipe wall thickness. The point where the crack became unstable occurred near the maximum load for the experiment. The maximum load for this experiment was 339 kN (76,200 lbs).

Figures 4.61 and 4.62 show the crack section moment as a function of the crack-mouth-opening displacement (CMOD) and crack section rotation data, respectively, for Experiment 1-6. The maximum moment for the experiment was 697 kN-m (6,169 in-kips).

Figure 4.63 shows the change in the crack centerline d-c EP signal ("current on" minus "current off") as a function of the crack centerline CMOD data for Experiment 1-6. A change in slope of the d-c EP versus CMOD data indicates crack initiation. To aid in the determination of the instant of crack initiation, linear regression lines have been included on Figure 4.63 for the data when the CMOD was less than 1.0 mm (0.04 inch) (i.e., in the region where the crack definitely had not initiated) and for the data when the

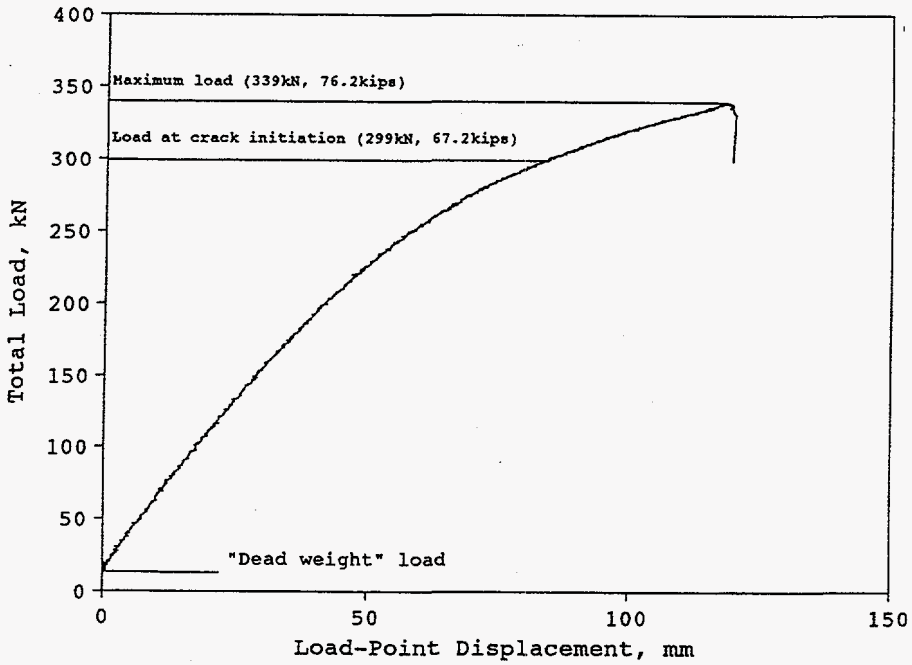

Figure 4.60 Total load versus pipe displacement at the load-point for Experiment 1-6

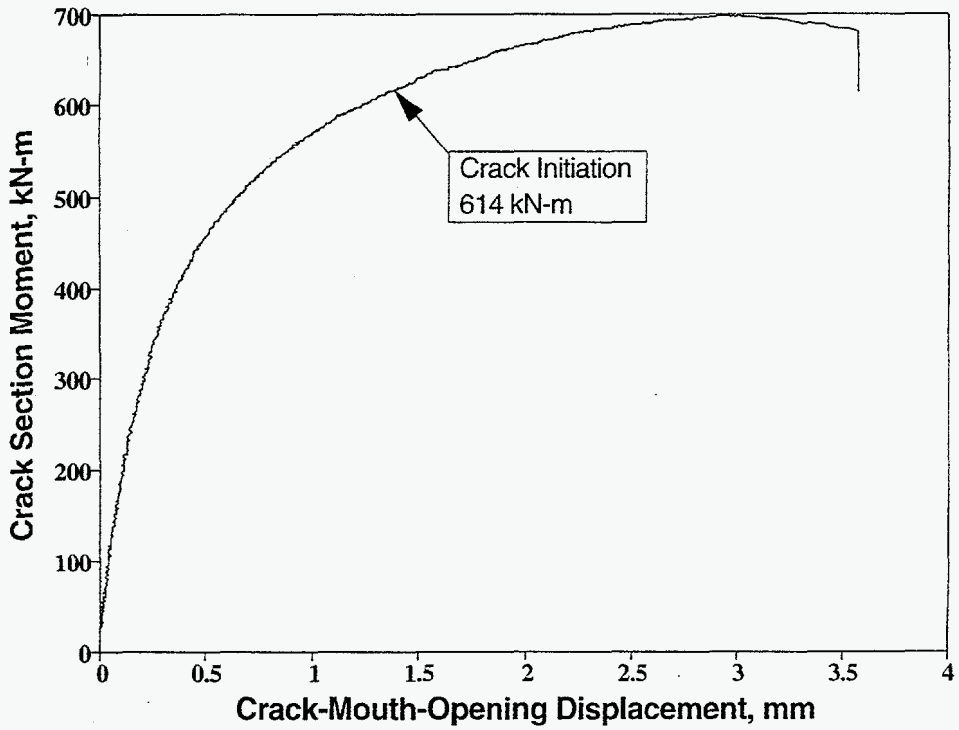

Figure 4.61 Crack-section moment versus CMOD for Experiment 1-6

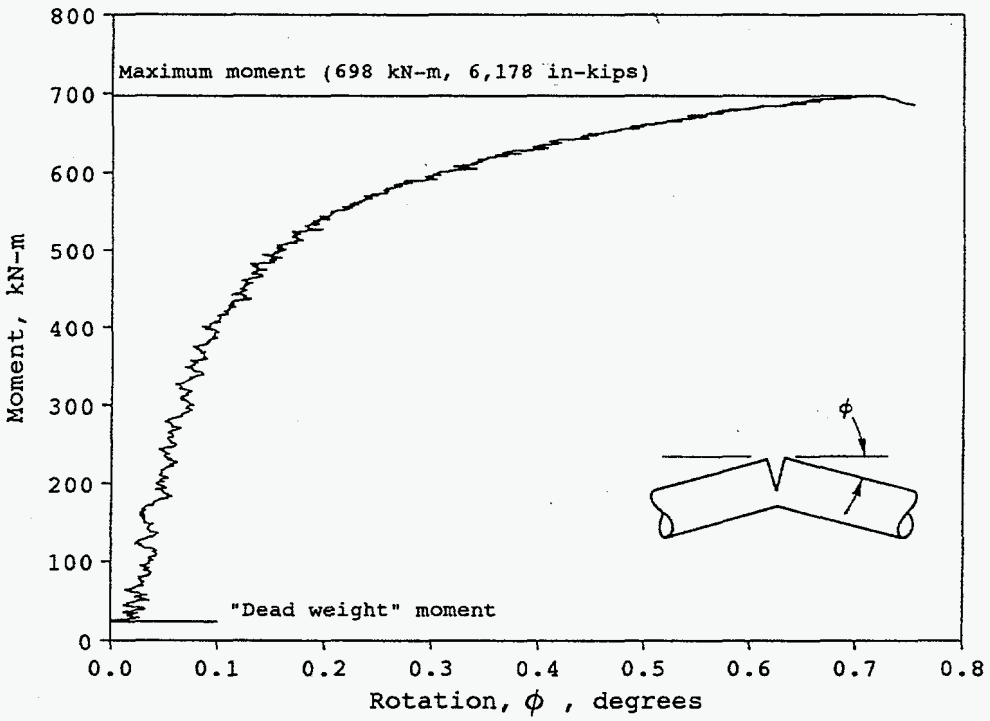

Figure 4.62 Pipe moment versus half rotation for Experiment 1-6

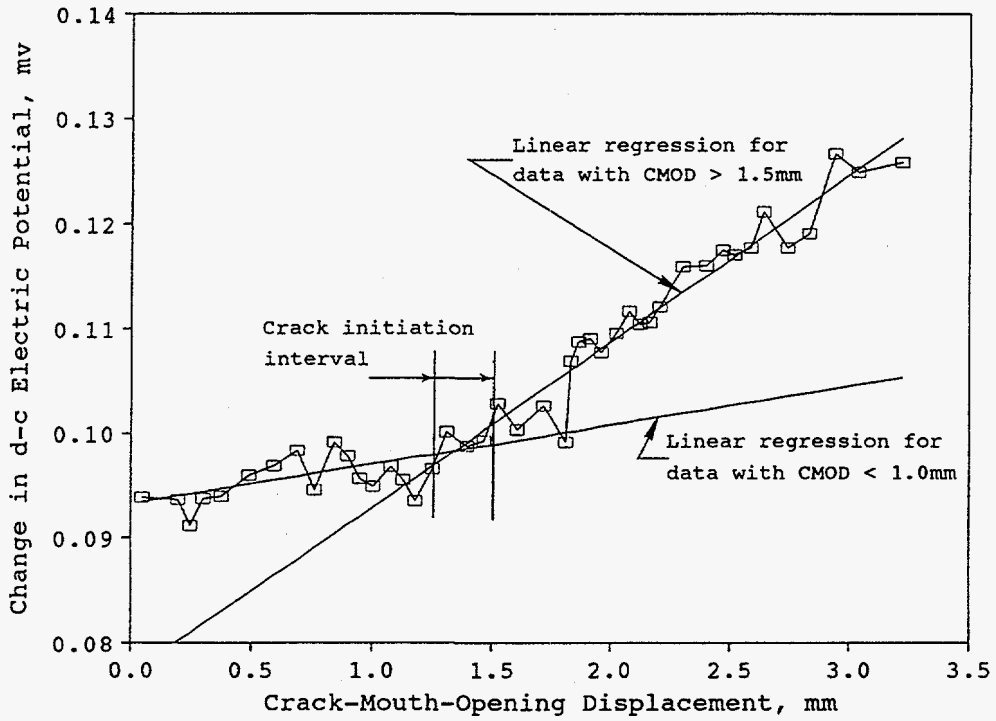

Figure 4.63 Change in d-c electric potential ("current on" minus "current off") as a function of crack-mouth-opening displacement for Experiment 1-6

CMOD was greater than 1.5 mm (0.06 inch) (i.e., in the region where the crack had definitely initiated). From Figure 4.63, it appears that the surface crack initiated and began to grow through the pipe wall thickness at a CMOD value of approximately 1.35 mm (0.053 inch). From Figure 4.61, the crack section moment at this CMOD value is 614 kN-m (5,435 in-kips), approximately 88 percent of the maximum moment for the experiment. Surface crack growth was determined from the d-c EP data using the same procedures previously discussed for Experiment 1-4. Figure 4.64 shows the surface crack growth as a function of the pipe displacement at the load point for Experiment 1-6.

The depth of the initial machined notch plus the fatigue precrack and the pipe wall thickness were measured post-test for Experiment 1-6, see Figure 4.65. The crack depth measurements include the depth of the weld counterbore. The wall thickness is the thickness of the pipe wall, excluding the weld crown height. The crack depth to wall thickness ratio (a/t) at the crack centerline was 0.687.

4.4 Short Through-Wall Cracked Pipe Experiments

Three short through-wall cracked pipe experiments were conducted as part of Task 1 of the IPIRG-2 program. They were Experiments 1-7, 1-8, and 1-9, see Table 4.1. The objective of these experiments was to gather experimental data for assessing the fracture behavior and stability of a short circumferential

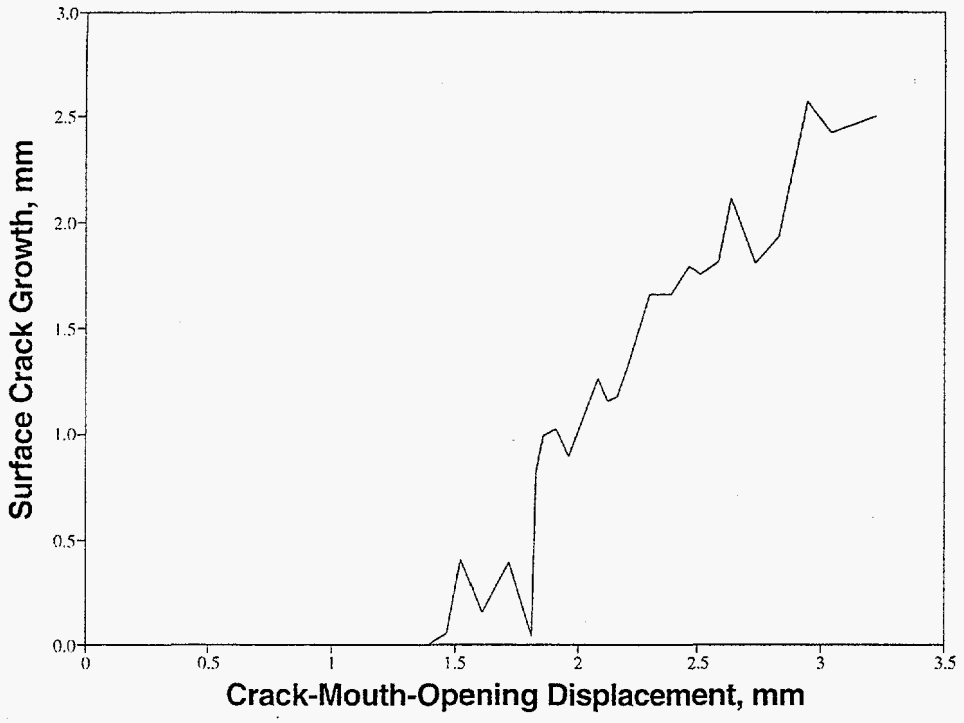

Figure 4.64 Surface crack growth as a function of crack-mouth-opening displacement for Experiment 1-6

through-wall crack. Through-wall-cracks are of interest because the U.S. NRC's Leak-Before-Break (LBB) criteria are based on a through-wall crack analysis; a detectable leaking through-wall crack must be shown to remain stable during an upset condition such as a seismic event.

The cracked test specimens for the first two through-wall-cracked pipe experiments listed in Table 4.1 (Experiments 1-7 and 1-8) were sections of a 16-inch nominal diameter, Schedule 140, A106 Grade B carbon steel pipe which had been machined so that the wall thickness matched that of Schedule 100 pipe, i.e., 26.2 mm (1.03 inches). The circumferential through-wall crack length for these experiments was approximately 152 mm (6 inches), 12 percent of the outside pipe circumference. The test specimen for the third through-wall cracked pipe experiment listed in Table 4.1 (Experiment 1-9) was a section of 6-inch nominal diameter, Schedule 80, A106 Grade B carbon steel pipe. The circumferential through-wall crack length for this experiment was approximately 132 mm (5.2 inches), approximately 25 percent of the pipe circumference.

The forcing function for Experiment 1-7 was a simulated seismic load history. The simulated seismic forcing function applied during this experiment was similar to that used for the two simulated seismic experiments discussed previously, i.e., Experiments 1-1 and 1-2. The same "SSE" excitation forcing function was applied to the piping system as had been done in the past experiments. This "SSE" excitation was followed shortly thereafter by the application of an increased amplitude version of the "SSE" excitation. The amplitude of this "Test" forcing function was approximately 20 percent higher than the amplitude of the "Test" forcing functions used in the two other simulated seismic experiments. Then, since the through-wall crack did not extend to the ends of the external patch after the application of the

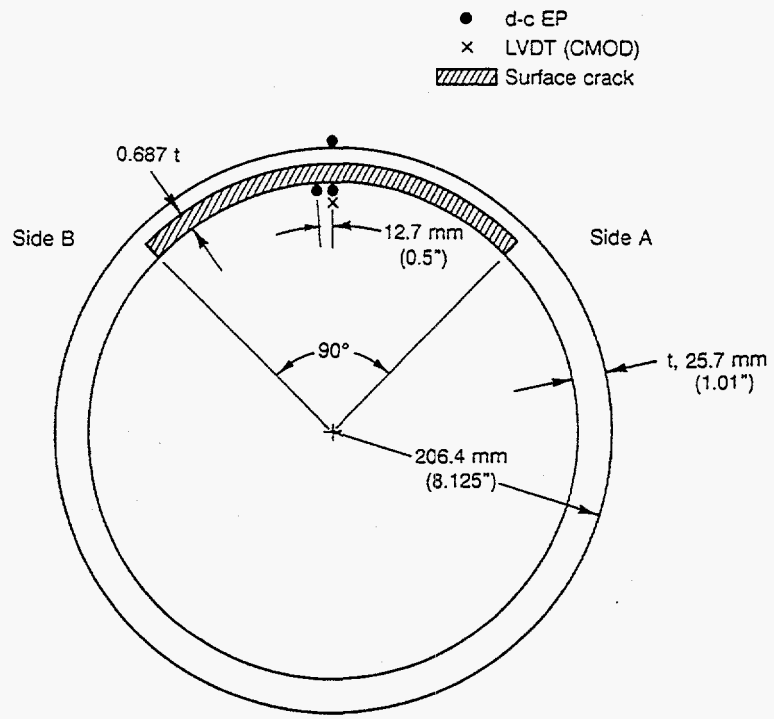

(a) Cross section of pipe at the crack plane

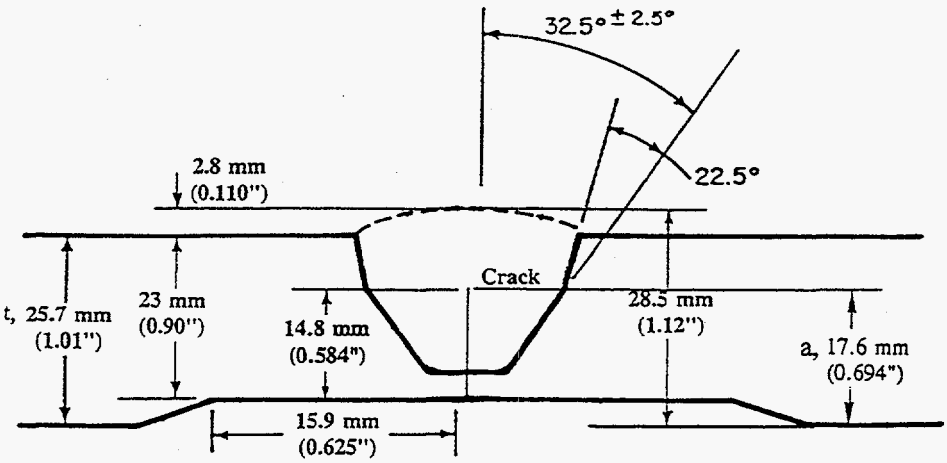

(b) Cross section of weld

Figure 4.65 Flaw geometry for Experiment 1-6

"Test" forcing function, a third "Decision Tree" forcing function was applied to the pipe system. This third level of excitation was exactly the same as the second loading, i.e., the "Test" forcing function. Figures 4.66 through 4.68 show the actuator displacement-time histories for the "SSE", "Test", and "Decision Tree" forcing functions applied during this experiment.

The load history applied during Experiment 1-8 was quasi-static monotonic four-point bending. The loading rate for this experiment was approximately 0.025 mm/second (0.001 inches/second) for most of the experiment and 1.14 mm/second (0.045 inches/second) for the final stages of the experiment. For Experiment 1-9 the load history was dynamic four-point bending. The original intent of Experiment 1-9 was to evaluate a through-wall crack sealing method which was to be used for Experiments 1-7 and 1-8. The loading rate for this experiment was approximately 108 mm/second (4.24 inches/second).

The test temperature and pressure for the short through-wall-cracked pipe experiments were representative of PWR conditions; 288 C (550 F) and 15.5 MPa (2,250 psi), respectively.

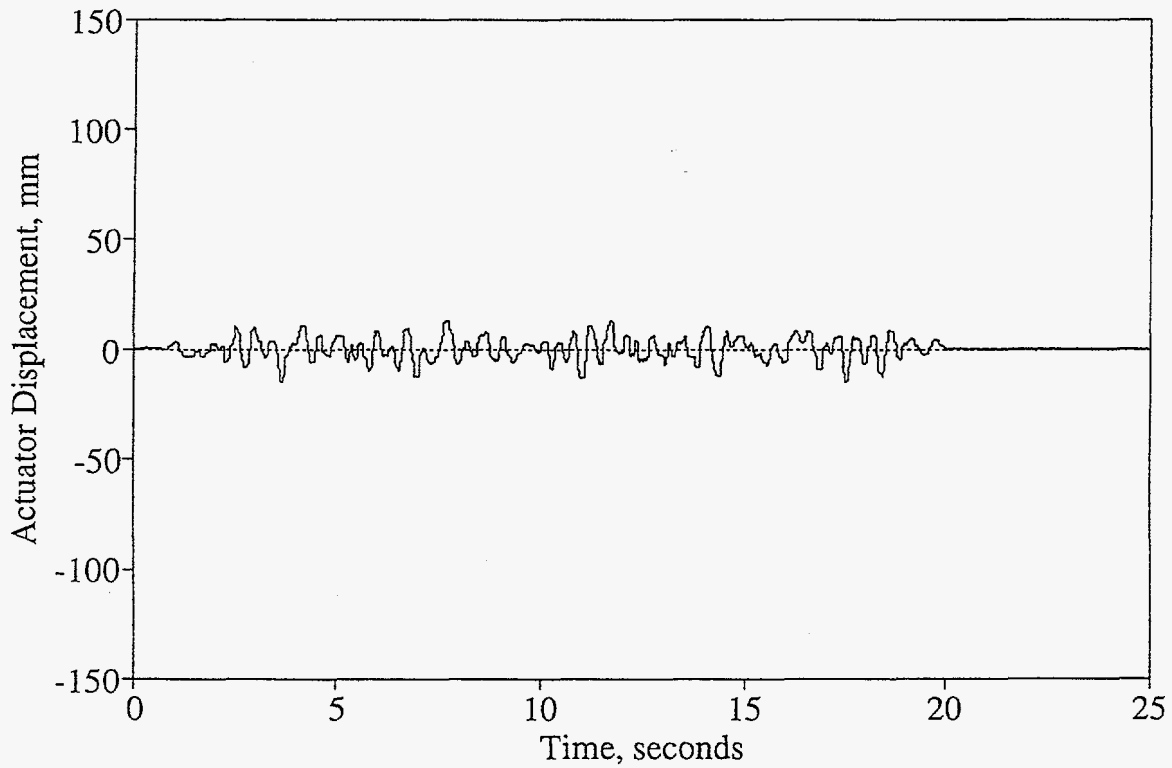

Figure 4.66 Experiment 1-7 "SSE" actuator displacement versus time history

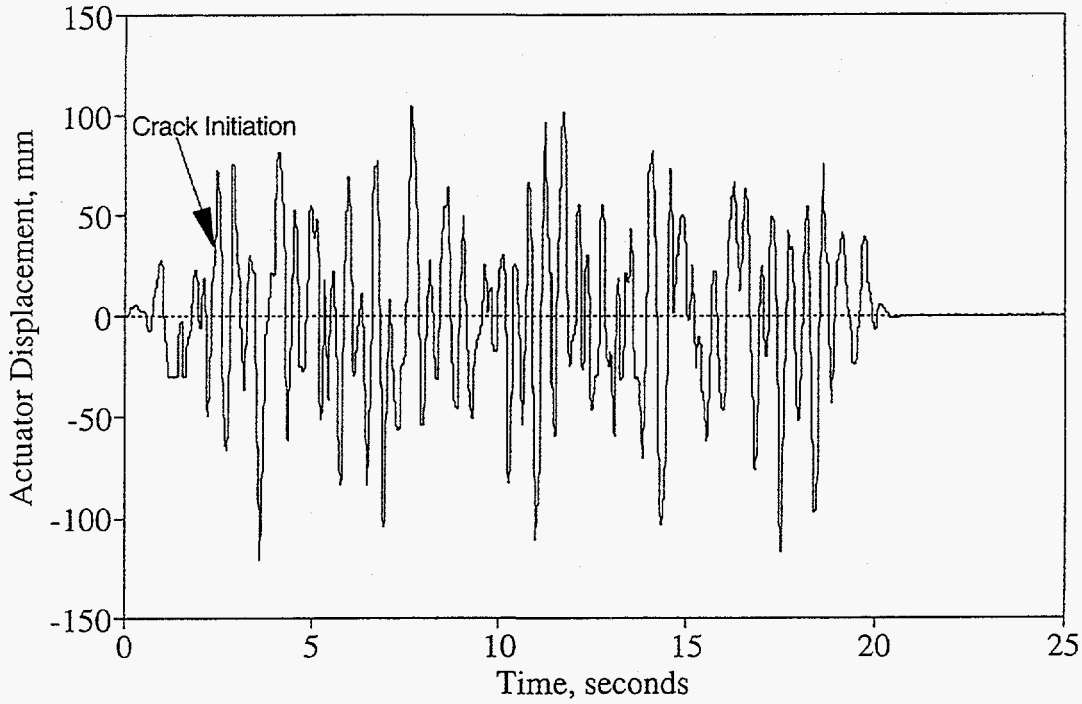

Figure 4.67 Experiment 1-7 "Test" actuator displacement versus time history

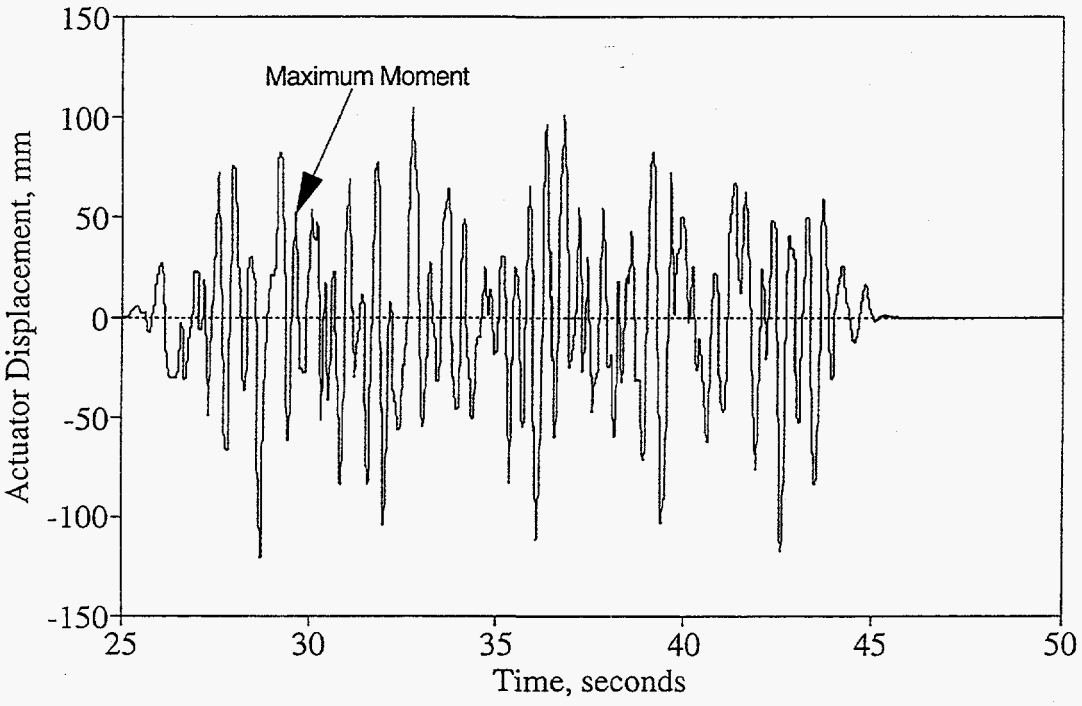

Figure 4.68 Experiment 1-7 "Decision Tree" actuator displacement versus time history

4.4.1 Development of Through-Wall Crack Pressure Sealing Method

One of the challenges in conducting elevated temperature, pressurized, through-wall-cracked pipe experiments is sealing the through-wall crack. In the past, thin metal patches have been successfully used to seal the pressure inside axial through-wall-cracked pipe specimens at room temperature. However, during the Degraded Piping Program (Ref. 4.1) the adhesives used to bond the patches to the inside pipe surface were found to be ineffective at the test temperatures of interest. Thus, alternative means of sealing the through-wall cracks were tried during the Degraded Piping Program. The through-wall crack sealing method used during the Degraded Piping Program was a bladder made of Viton rubber. This sealing method worked reasonably well for some of the smaller diameter pipe experiments, i.e., 6-inch nominal diameter. However, for the larger, 16-inch nominal diameter pipe experiments, the failure rate of this method was found to be unacceptable. This sealing method was also used during the IPIRG-1 program for some of the 6-inch nominal diameter inertially-loaded pipe experiments (Ref. 4.7). The success rate of the bladders for these short duration dynamically-loaded pipe experiments was better than previously experienced for the quasi-statically loaded pipe experiments from the Degraded Piping Program. However, as a result of the marginal performance of these internal bladders, especially for the larger 16-inch nominal diameter experiments of interest for this effort, it was decided to pursue an alternative method of sealing the through-wall crack.

4.4.1.1 Full 360-Degree Welded Bellows

The first method considered for sealing the pressurized through-wall-cracked test specimens was a full 360-degree thin metal bellows welded to the inside of the test specimen. A 149.4-mm (5.88-inch) outside diameter by 0.81 mm (0.032 inch) thick bellows fabricated from Inconel sheet was welded to the inside surface of a 6-inch nominal diameter carbon steel through-wall-cracked test specimen which had its inside surface machined to match the outside diameter of the stainless steel bellows. This sealed test specimen was then welded to a series of moment arm pipes and subjected to a combined pressure plus bending load history. This internal full-bellows design worked very well at sealing the pressurized through-wall crack. In fact, the data from this "proof-of-concept" test were of such quality and value that it was decided to document the results from this test in the same manner as the primary pipe experiments conducted as part of Task 1. This "proof-of-concept" test was given the number Experiment 1-9. The results of Experiment 1-9 are discussed in detail later in this section of this report.

The internal full-bellows method worked too well. The full bellows maintained the internal pipe pressure until the through-wall crack in the test specimen had grown to such an extent that it reached a critical through-wall-crack size. As a result, the test specimen experienced a near instantaneous double-ended-guillotine-break (DEGB) with a resultant large release of energy. A similar near instantaneous DEGB in the 16-inch diameter pipe would be unacceptable, so an alternative sealing method design for Experiments 1-7 and 1-8 was needed.

4.4.1.2 Patch Design

Four alternative designs for sealing the pressurized through-wall-cracked test specimens for Experiments 1-7 and 1-8 were considered. These involved (1) a full bellows with a mechanical puncture device, (2) a curved plate, (3) a partial welded bellows, and (4) a partial formed bellows.

Design Criteria

The primary design criteria for the sealing method is that it must be able to seal the through-wall-cracked pipe so that it does not leak until the maximum load has been reached in the experiment. The experiments are conducted at a pressure of 15.5 MPa (2,250 psi) and a test temperature of 288 C (550 F). The LBB.ENG2 method was used to estimate the COD versus moment relationship for Experiments 1-7 and 1-8. Figure 4.69 shows the results of these calculations for two quasi-static material J-R curves. A COD of 8.0 mm (0.31 inch) was chosen for the design. This value is well beyond the maximum load and allows for some uncertainty in the actual experimental COD.

The second design criteria was that the moment across the crack due to the seal should be less than 2 percent of the bending moment on the pipe at any instant. The third design criteria is that the sealing device must permit the controlled release of pressure sometime after maximum moment is obtained. Finally, the plastic strain in the seal should be less than half of the failure strain of the material.

Each of the designs considered allowed for the controlled release of the pressure by limiting the circumferential length of the patch, i.e., before the through-wall crack could go unstable, it would grow beyond the patch and relieve pressure.

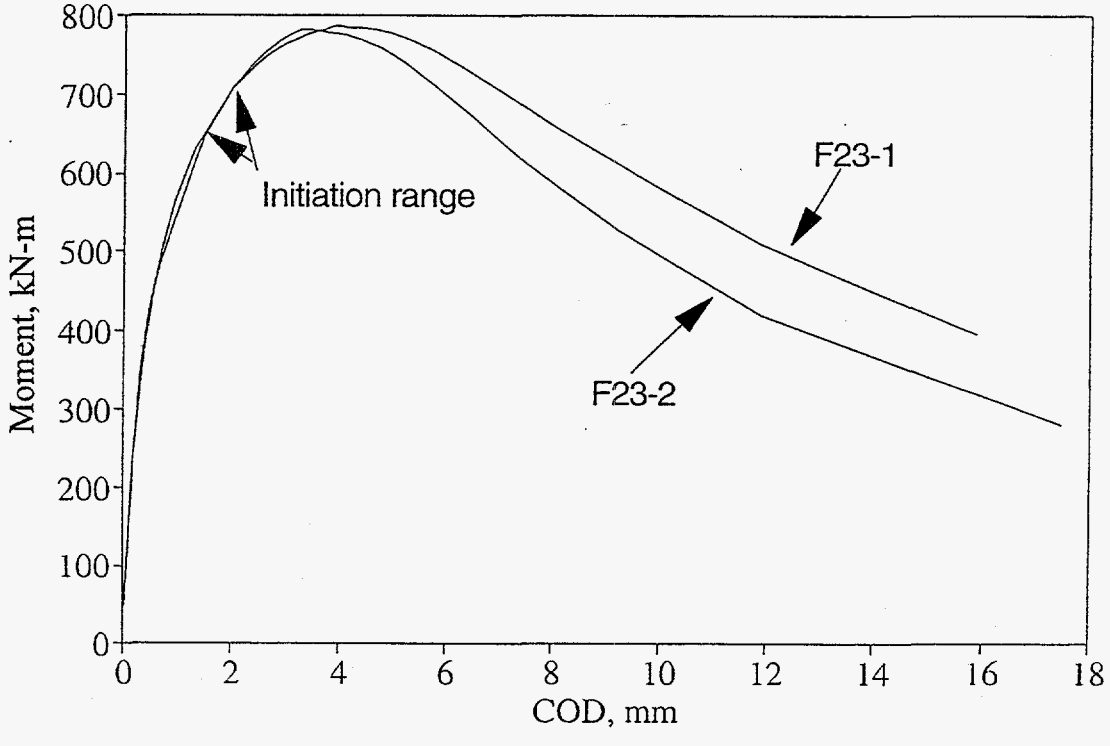

Figure 4.69 LBB.ENG2 moment-COD calculations for Experiments 1-7 and 1-8

Full Bellows With a Mechanical Puncture Device

Experiment 1-9 showed that a thin internal bellows could retain pressure very effectively. If a mechanical puncture device could be added to the system that would rupture the bellows prior to the through-wall crack reaching a critical size, then the internal bellows could be made to work. Spring-load penetrators, pyrotechnic devices, and stationary sharp points that would contact the bellows when the CMOD got large enough were considered, but were considered too unpredictable or unreliable. Hence, the full bellows with puncture device idea was abandoned.

Curved Plate Analysis Results

The curved plate design consisted of a 4.75 mm (0.187 inch) thick plate over the crack attached to a 0.89 mm (0.035 inch) sheet. Figure 4.70 shows a model of this design. The model was analyzed under plane strain conditions. The 4.75 mm (0.187 inch) plate is thick enough that it does not extrude through the crack as it opens. The 0.89 mm (0.035 inch) sheet is used as an elastic-plastic element to accommodate the crack opening displacements by stretching. Both the plate and sheet were assumed to be made from annealed Type 304 stainless steel with a yield strength of 137.9 MPa (20.0 ksi). The coefficient of friction between the pipe wall and the stainless steel was assumed to be 0.15.

The results of the curved plate analysis are shown in Figure 4.71. This figure shows the equivalent plastic strains at a COD of 7.72 mm (0.304 inch). At the maximum COD, the maximum principle strain is 0.169 mm/mm. An estimate of the moment across the crack due to the seal is shown in Figure 4.72.

The moments in the curved plate develop very rapidly and then level off. They are the result of the tensile loading on the sheet. This means that in the early stages of the experiments the moments across the crack will be a high percentage of the total moment (approximately 5 percent at a COD of 0.5 mm [0.02 inch]).

Figure 4.70 Model of curved plate design

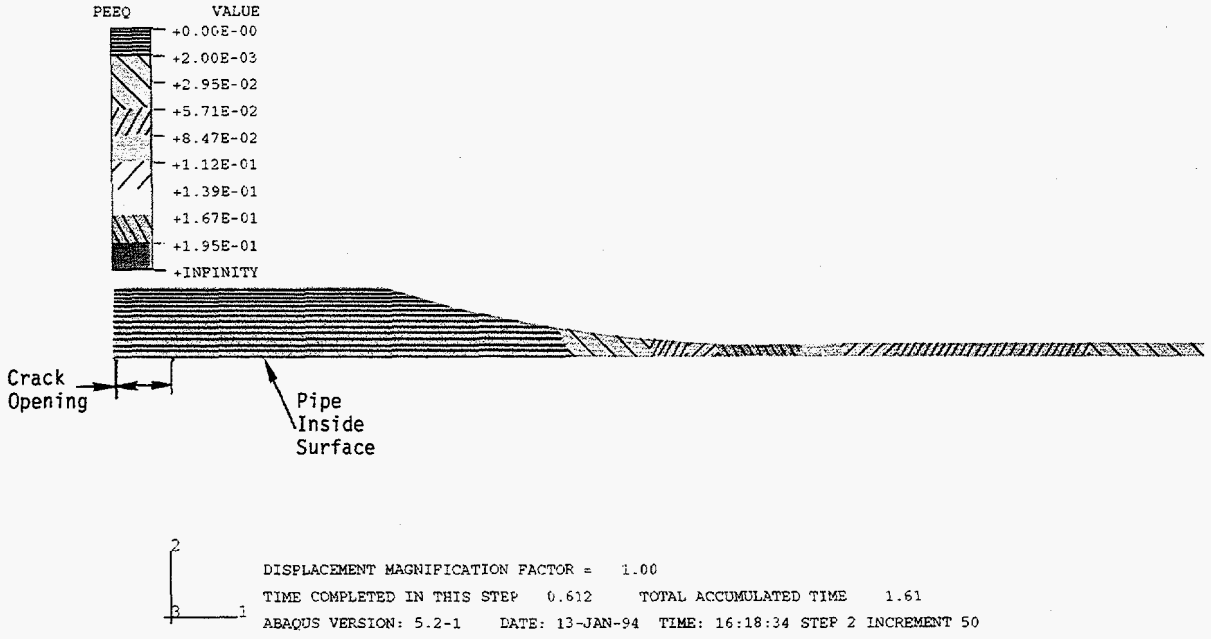

Figure 4.71 Results of curved plate analysis

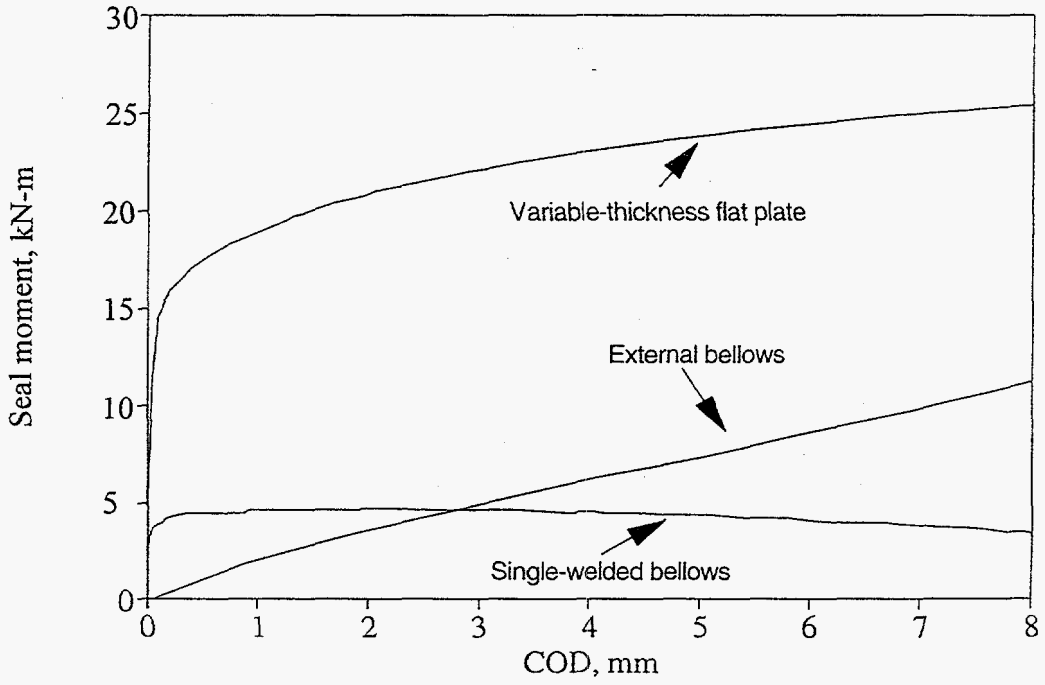

Figure 4.72 Calculated moment across the crack due to the presence of the curved plate seal

Any attempt to reduce these moments by making the sheet thinner results in higher strains in the sheet. The strains in the sheet are not just a function of thickness, but also a function of the frictional forces between the plate and the pipe. This means that the length of the plate that can strain to accommodate the COD is limited by the frictional shear forces. The simplest way to explain these results is to imagine that there were no frictional forces on the plate. In this case the sheet would strain uniformly when the COD was applied to it and any thickness sheet could be used as long as it could take the strain. When friction is present the shear forces build up along the length of the sheet until the sheet begins to yield. This buildup of frictional shear forces reduces the length of the sheet that can strain as a result of the applied displacement due to the COD. The result is that any attempt to reduce the thickness of the sheet to bring the moment across the crack to design levels results in the strains in the sheet being higher than design levels.

Partial Welded Bellows Analysis Results

The partial welded bellows consisted of a 0.89 mm (0.035 inch) thick sheet of annealed Type 304 stainless steel that is formed into a single flat convolution. Figure 4.73 shows a half model of the convolution. The model was analyzed under plane strain conditions. The material properties were assumed to be the same as those used for the flat plate model.

The results of this analysis are shown in Figure 4.74. This figure shows the equivalent plastic strains at a COD of 7.92 mm (0.312 inch). At maximum COD, the maximum principle strain is 0.29 mm/mm. The moment across the crack due to the COD is shown in Figure 4.72.

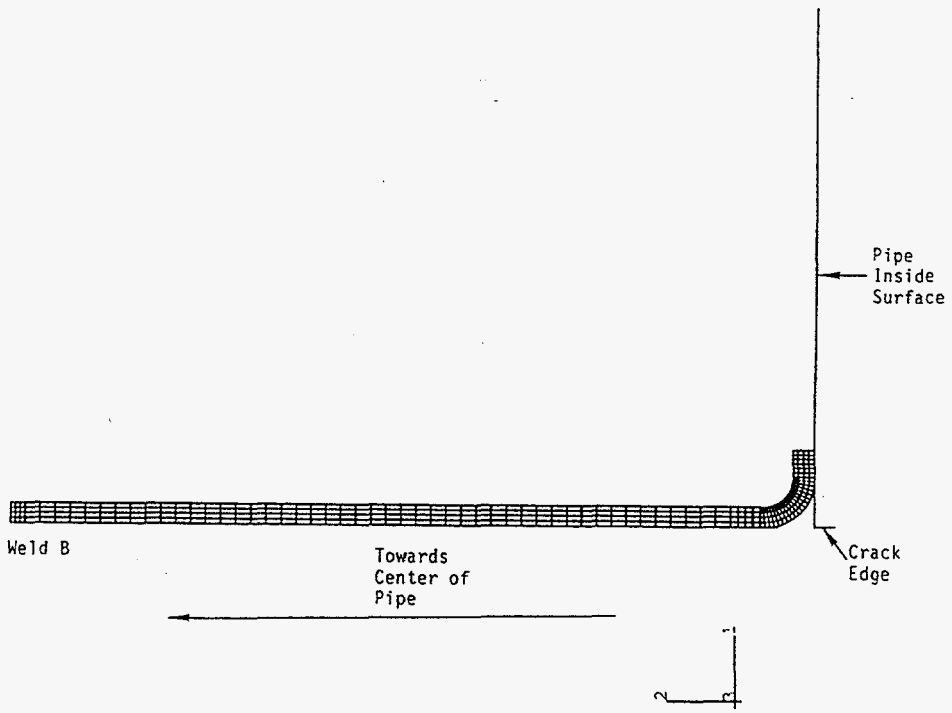

Figure 4.73 Half model of a partial welded bellows convolution

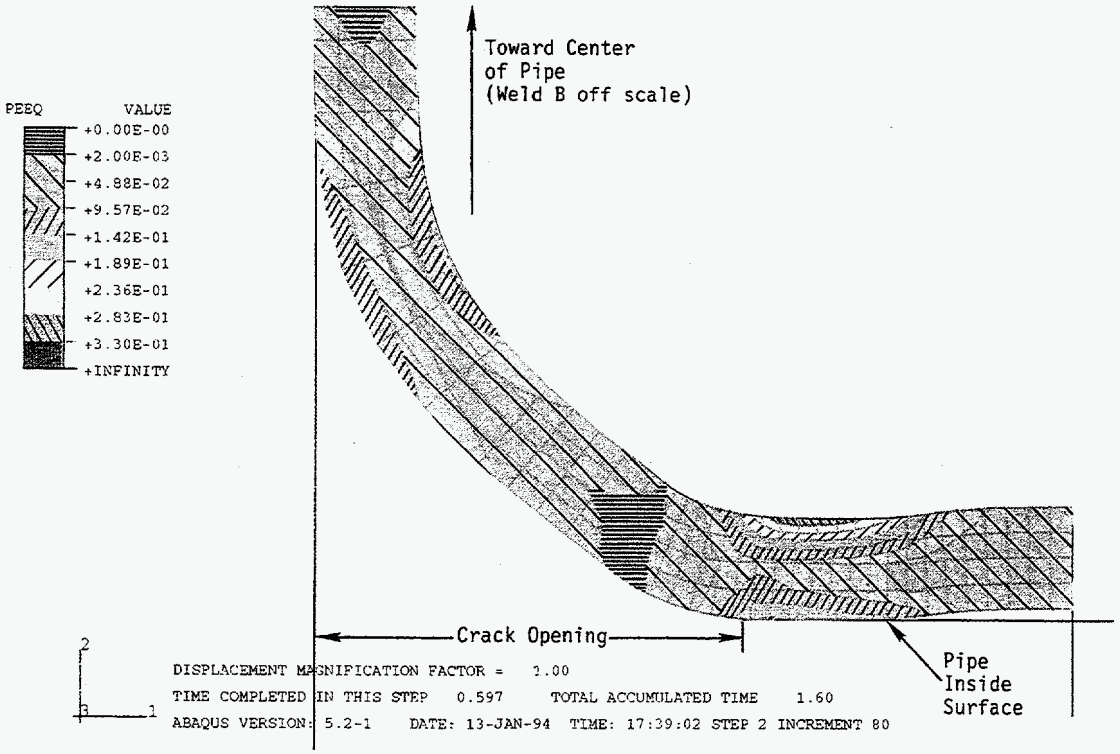

Figure 4.74 Results of partial welded bellows design analysis

The moments rise quickly, as they did in the curved plate design, however, they are much lower than in the curved plate. These moments decrease slightly with increasing COD. In this case the strains are extremely high. This seal accommodates the COD by bending. Hinges are formed where the plate meets the pipe wall and where the two plates come together. The length over which this bending can take place is limited by the pressure which is holding the bellows closed and the bending stiffness of the sheet.

Because the displacements are due to bending, the strains can be reduced by making the sheet thinner, but this increases the risk of extruding the bellows through the crack. The effects of increasing the thickness and/or yield strength of the bellows was not thoroughly investigated because of the advantages of the final external bellows design. One aspect of this analysis that should be noted is that the high strains in the bellows (0.29 mm/mm maximum) make both the model and the actual bellows extremely sensitive to the stress-strain characteristics of the bellows material. Small deviations in material properties at these large strains could result in a failure of the bellows.

External Bellows Analysis Results

The external bellows consisted of a single 50.8 mm (2 inch) radius semi-circular cross-section convolution placed on the outside of the pipe. The ends of this convolution were sealed with a spherical head. Figure 4.75 shows a sketch of the bellows while Figure 4.76 shows the model that was analyzed. The material used for the external bellows was 3.18 mm (0.125 inch) thick Inconel 625. Inconel 625 was chosen because it has a higher yield strength than Type 304 stainless steel and, at the same time, a high ductility. The yield strength for the Inconel was assumed to be 276 MPa (40 ksi). The high yield is required to keep the wall reasonably thin and still withstand the pressure inside the pipe. The high elongation is required so that the design can readily incorporate some material plasticity. In addition, the

coefficient of thermal expansion of the Inconel closely matches that of the carbon steel pipe that the bellows will be welded onto. This eliminates residual stresses and cracking in the weld.

The analysis of the external bellows design assumed plane strain conditions. The results of this analysis are shown in Figure 4.77. This figure shows the equivalent plastic strains at a COD of 7.62 mm (0.30 inch). At the maximum COD, the maximum principle strain is 0.076 mm/mm. Figure 4.72 shows the moment across the crack for this design.

This design meets all of the criteria. The strains in the bellows were the lowest for any of the designs. In addition, the moments across the crack were essentially linear. At a COD of 8.0 mm (0.31 inch) the moment is 2 percent of the bending load on the pipe. Besides meeting the design criteria, there was another factor that made the external welded bellows design desirable. This is the fact that if the bellows began to leak during the quasi-static test, the test could have been stopped to repair or replace the bellows. In the case of the dynamic test, if a leak developed, nothing could have been done to repair the leak once the test had begun. However, the dynamic test was such a short duration test, that the pressure in the test specimen would not have had a chance to decrease much. Furthermore, if a leak was detected before the initiation of the experiment, i.e., a leak caused during fatigue precracking, the option of repairing or replacing the bellows would have been available. None of the other sealing methods could have been repaired without cutting the test specimen.

The external bellows was fabricated by spin forming. The semi-circular cross-section was formed in a full circle and cut into three 120 degree segments. The spherical heads were formed separately. The heads were cut to the contour of the pipe and welded onto the semi-circular portion of the bellows. This weld was a tig weld and used Inconel 625 filler rod.

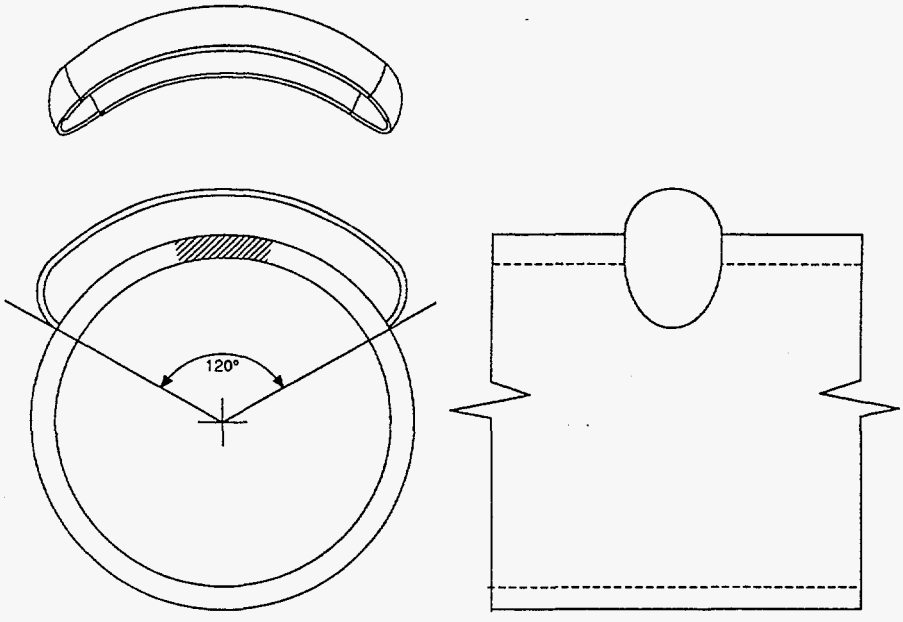

Figure 4.75 Sketch of external bellows concept to be used to seal through-wall-cracked test specimens

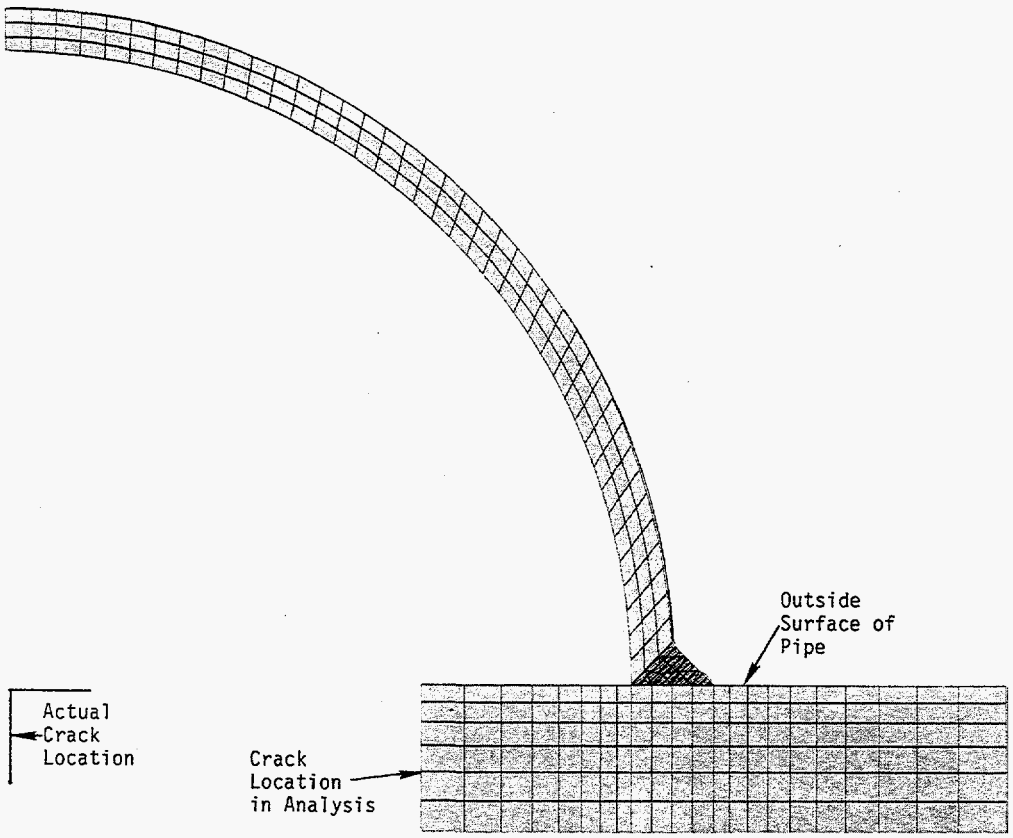

Figure 4.76 Model of external bellows design

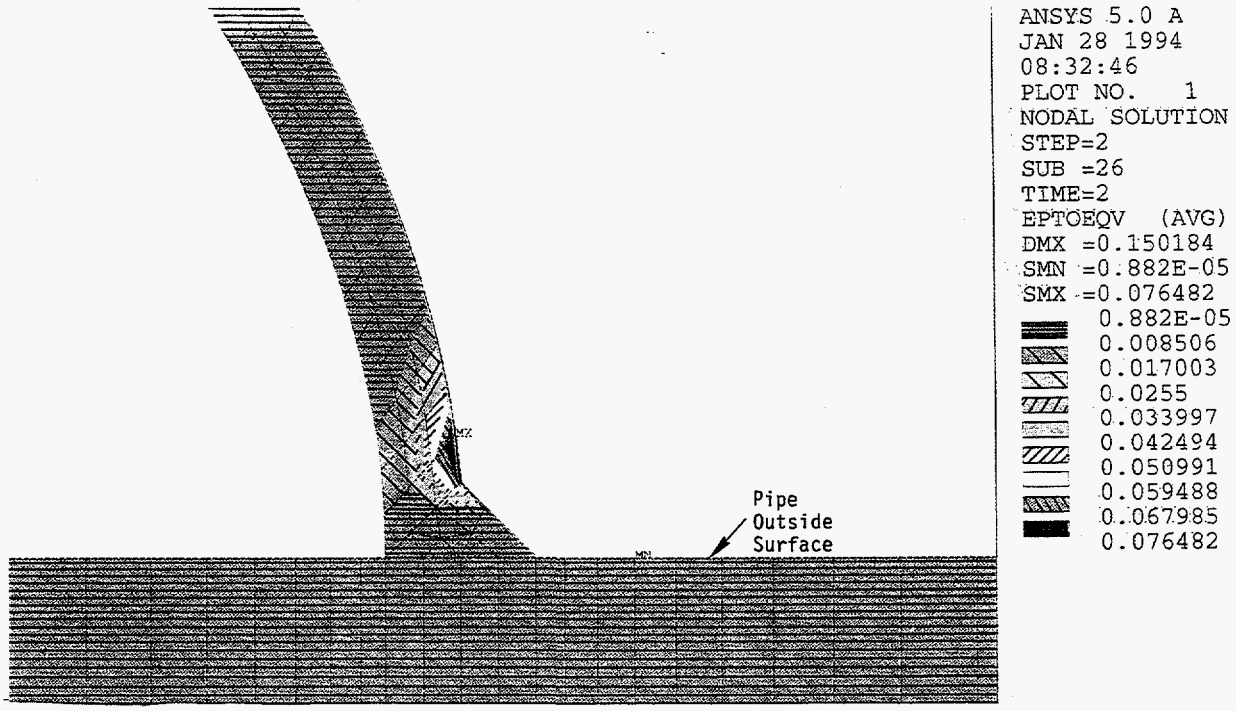

Figure 4.77 Results of plane strain analysis of external bellows design

The most critical aspect of the design was the weld between the bellows and the pipe. With the proper weld procedure and filler selection, the strength of the weld was similar to that of the Inconel 625. The finite element model of the external bellows included weld properties obtained from the supplier of the weld metal. The weld was made with Inconel 82 filler rod. This filler rod was recommended for Inconel 625 to carbon steel welds. The weld followed a procedure that had been developed for long continuous welds that minimizes the possibility of cracking by using a series of joined-up discontinuous welds.

4.4.2 Experimental Results

The key results from the three short through-wall cracked pipe experiments are summarized in Table 4.5. Included in Table 4.5 are the test conditions (pipe diameters, wall thicknesses, crack lengths, test pressures, and test temperatures), material property data (yield and ultimate strengths and J values at crack initiation [J_i] from C(T) specimen tests), and moments at crack initiation and maximum moments for each of these experiments.

4.4.2.1 Experiment 1-7 Results

The experimental results from the simulated seismic through-wall-cracked pipe system experiment will be presented first. The experiment was conducted in three loading phases. For the first phase, the piping system was excited with a forcing function which resulted in stresses representative of the stresses a piping system may experience as a result of normal operating conditions plus a Safe Shutdown Earthquake (SSE).

Table 4.5 Key results from the three short through-wall-cracked pipe experiments conducted as part of Task 1 of the IPIRG-2 program

Experiment No.	Outside Pipe Diameter, mm	Wall Thickness, mm	$2c/\pi D$	Test Pressure, MPa	Test Temperature, C	Yield(1) Strength, MPa	Ultimate(1) Strength, MPa	J at Crack Initiation C(T) Specimen(1), kJ/m^2	Moment at Crack Initiation, kN-m	Maximum Moment, kN-m
1-7	399.8	26.39	0.12	15.5	288	223	514	74.3	611	852
1-8	399.3	26.16	0.12	15.5	288	223	514	74.3	621	1.038
1-9	168.9	11.18	0.249	15.5	288	259	588	77.1	47.5	54.3

(1) Quasi-static data.

It was expected that the "SSE" excitation would not cause the through-wall crack to extend in length. Consequently, a second, and a possible third, excitation were planned. The second excitation was referred to as the "Test" forcing function. The actuator displacement amplitudes associated with the "Test" forcing function for Experiment 1-7 were approximately 20 percent higher than the actuator displacement amplitudes associated with the "Test" forcing functions for Experiments 1-1 and 1-2 because of the larger moment carrying capacity of the smaller flaw. Since the "Test" forcing function failed to cause the through-wall crack to extend during Experiment 1-7, a third loading was applied. This third level of excitation was referred to as the "Decision Tree" excitation.

The "SSE" loading was completely benign, as expected. The crack did not extend and so the "SSE" data are unremarkable. The "Test" and "Decision Tree" loadings did cause crack growth and are discussed in the following.

Figures 4.78a and 4.78b are plots of the test specimen internal pipe pressure as a function of time for Experiment 1-7. The initial test pressure was 15.5 MPa (2,250 psi). It appears that the through-wall crack penetrated the patch approximately 17.4 seconds after the start of the "Decision Tree" forcing function, i.e., 42.4 seconds after the start of the "Test" forcing function. As will be shown later, the d-c EP data showed that the crack initiated 2.435 seconds after the start of the "Test" forcing function.

The moments for this experiment were determined using the methods outlined previously for Experiments 1-1 and 1-2. The total (dynamic plus static) moments at the crack plane as a function of time for the duration of the "Test" and "Decision Tree" forcing functions are shown in Figures 4.79a and 4.79b. The maximum moment for the experiment occurred 4.65 seconds into the "Decision Tree" excitation, i.e., 29.65 seconds after the start of the "Test" forcing function. The maximum moment for the experiment was 852 kN-m (7,540 in-kips). Figures 4.80 and 4.81 are plots of the total crack section moment as a function of the crack-mouth-opening displacement (CMOD) and crack-section rotation data, respectively, for both the "Test" and "Decision Tree" forcing functions. The overall characteristics of both figures are very similar. Both figures show an initial region where the response is cyclic, but linear in nature. After this initial linear-elastic cyclic response, a single large amplitude cycle occurs during which the crack initiates. This initial large amplitude cycle occurs approximately 2.43 seconds into the "Test" forcing function. After this large cycle, both the moment-CMOD and moment-rotation response again begin to cycle in a linear manner. Both continue to do so until approximately 17.25 seconds after the start of the "Test" forcing function. At that time, both the moment-CMOD and moment-rotation response exhibit another cycle during which significant plasticity occurs. (Note, similar behavior was also observed for the other two simulated seismic experiments, Experiments 1-1 and 1-2.). Finally at 17.35 seconds after the start of the "Decision Tree" excitation, a very large jump occurs in both the CMOD and rotation data. These jumps are associated with a large decrease in moment-carrying capacity and stiffness at the crack section.

In an attempt to determine when the through-wall crack initiated and began to grow during the course of the "Test" forcing function, an assessment of the unloading compliance data was made for Experiment 1-7. Figure 4.82 is a plot of the unloading compliance (i.e., the slope of the CMOD-moment response for the unloading portion of the moment-CMOD curve) as a function of time. It appears from Figure 4.82 that the unloading compliance data began to show a decrease, which is indicative of crack growth, sometime between 2 and 3 seconds into the forcing function. Consequently, this was the region where attention was focussed when examining the d-c EP versus CMOD data to establish crack initiation. Figure 4.83 is a plot of the crack centerline d-c EP data as a function of crack centerline CMOD data for the loading portion of

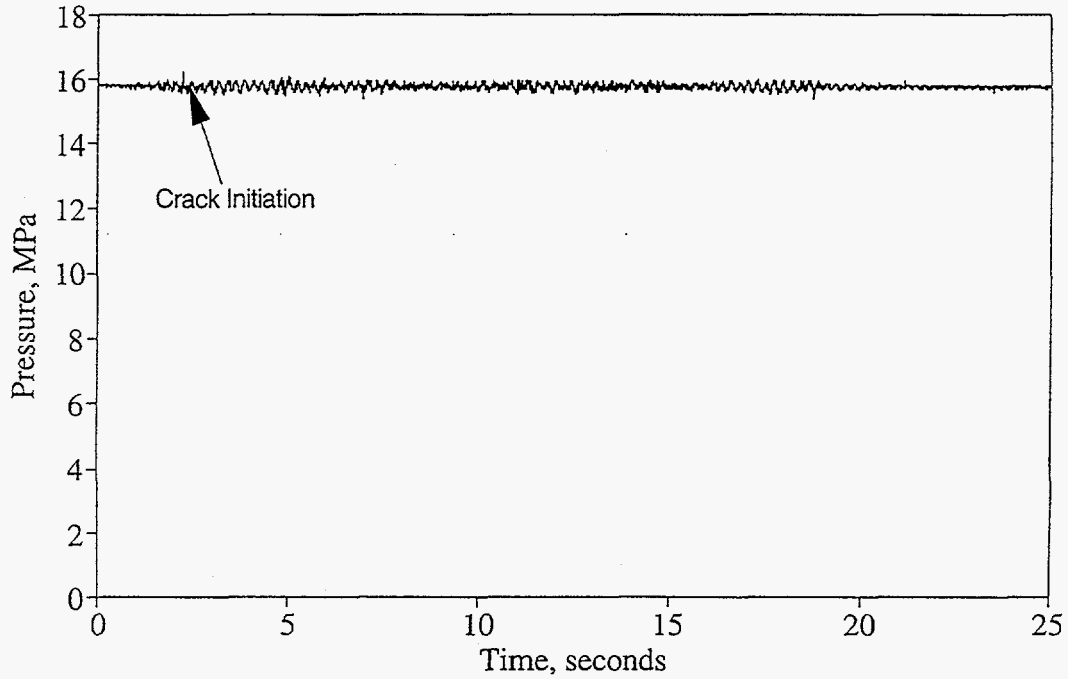

(a) "Test" forcing function

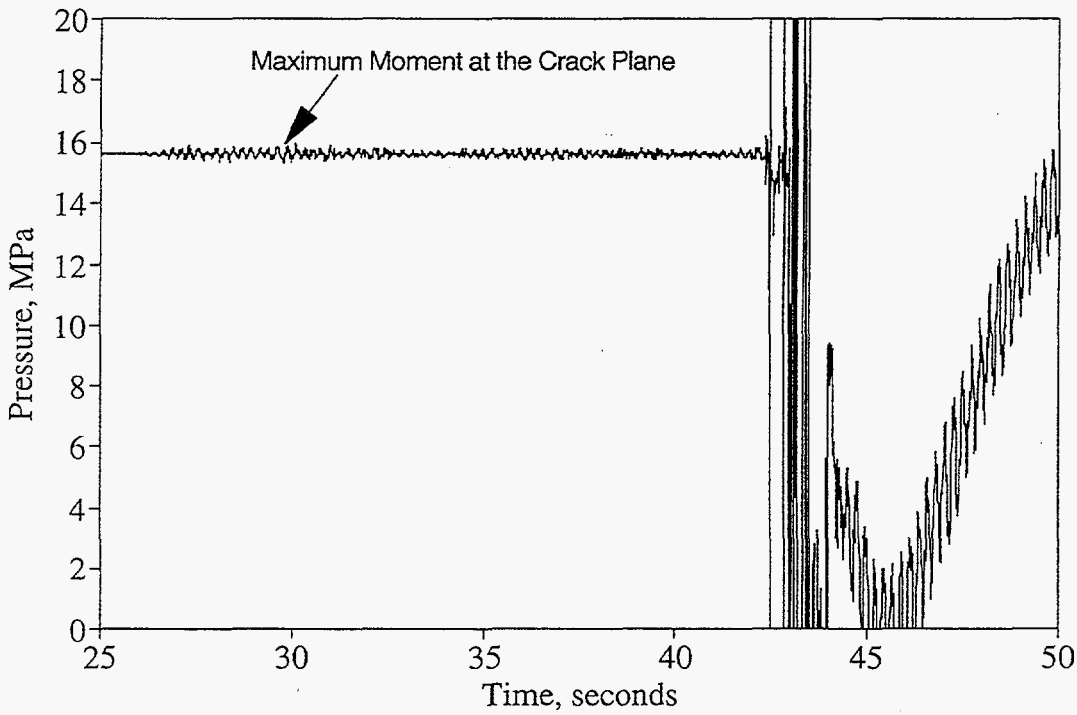

(b) "Decision Tree" forcing function

Figure 4.78 Experiment 1-7 test specimen pressure versus time history

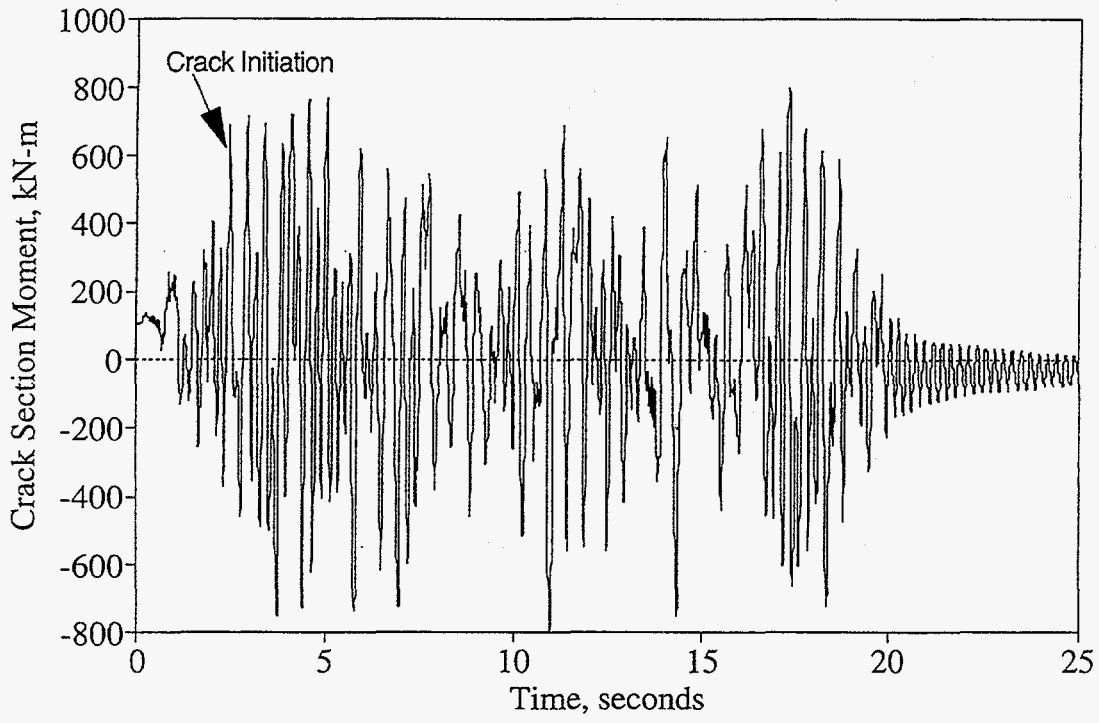

(a) "Test" forcing function

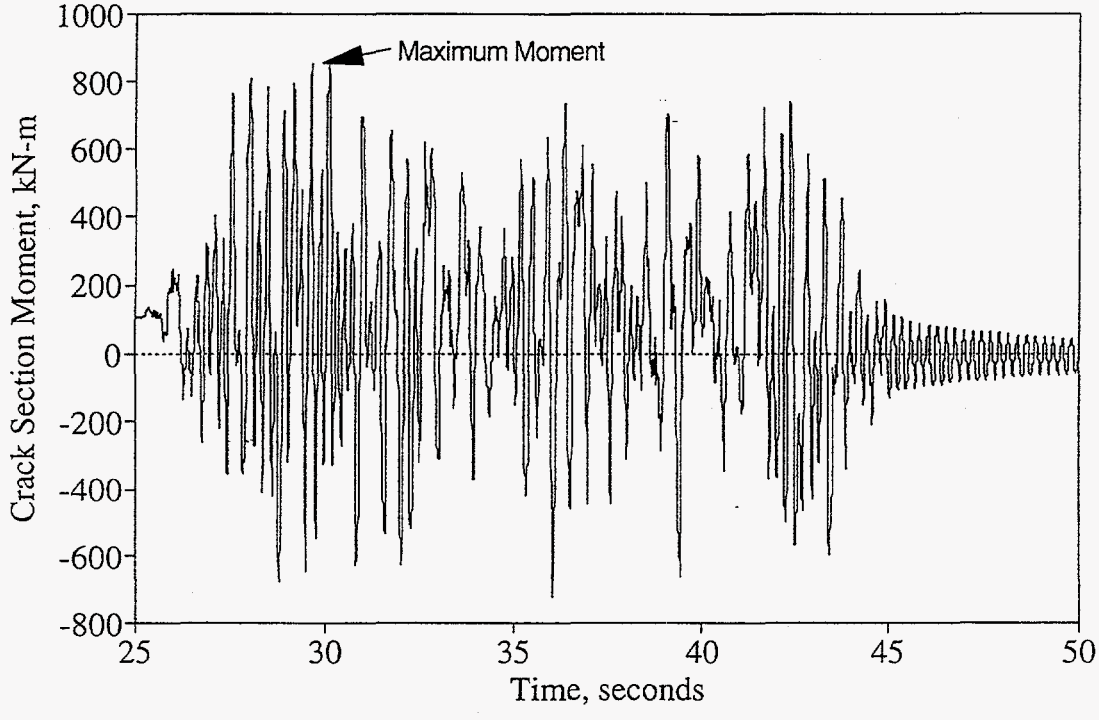

(b) "Decision Tree" forcing function

Figure 4.79 Experiment 1-7 crack-section moment versus time history

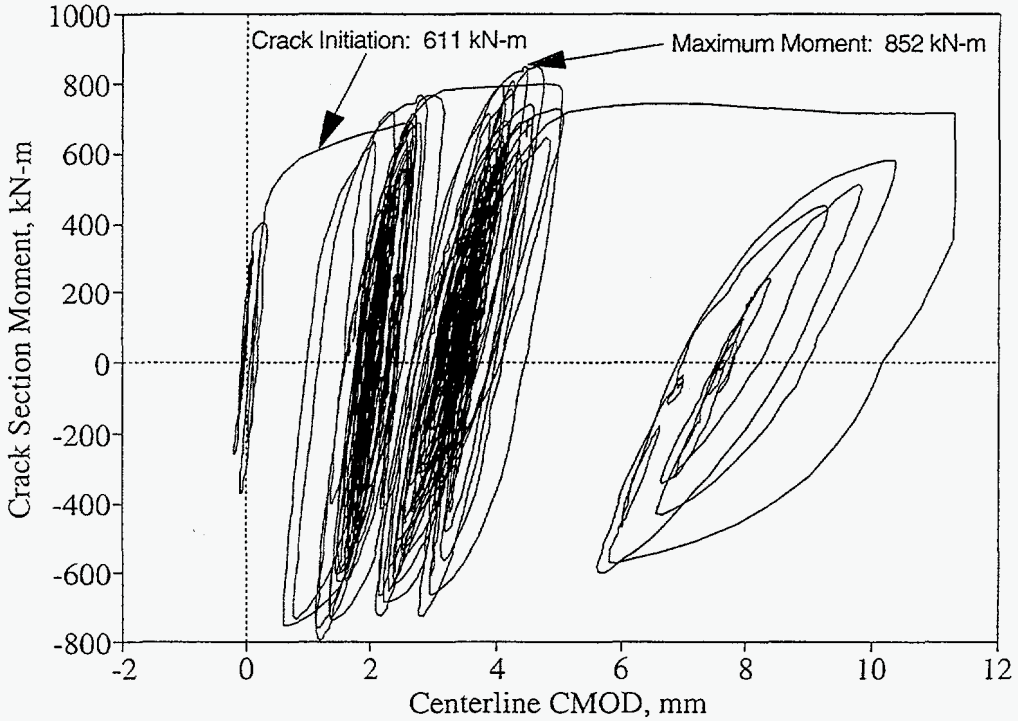

Figure 4.80 Crack-section moment versus crack-mouth-opening displacement (CMOD) for the entire time history of Experiment 1-7

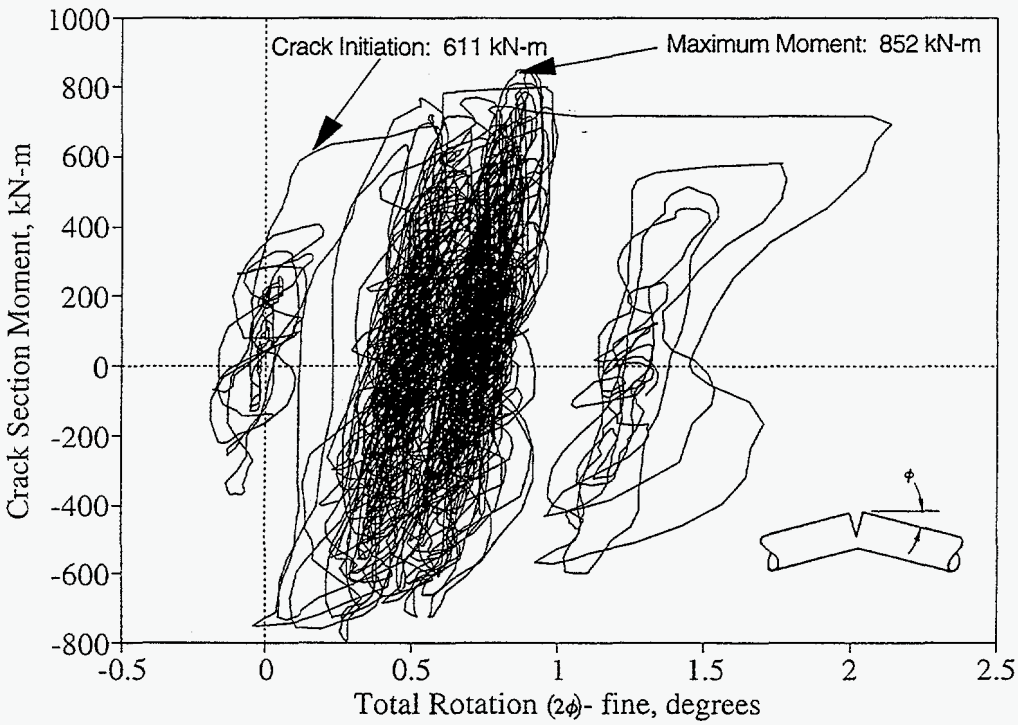

Figure 4.81 Crack-section moment versus total rotation for the entire time history of Experiment 1-7

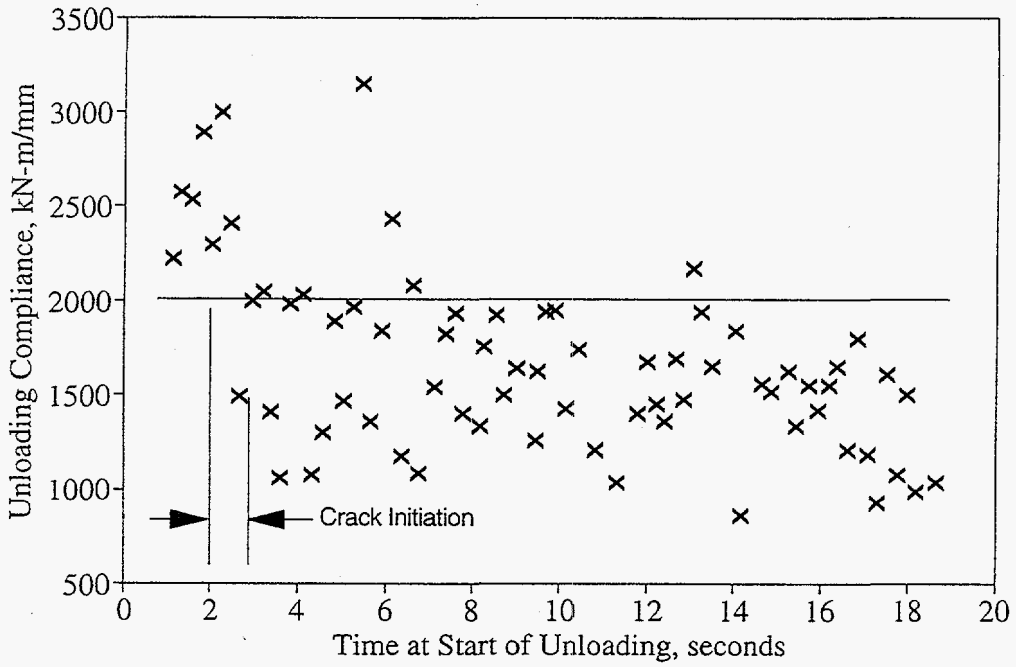

Figure 4.82 Unloading compliance data for the "Test" forcing function for Experiment 1-7

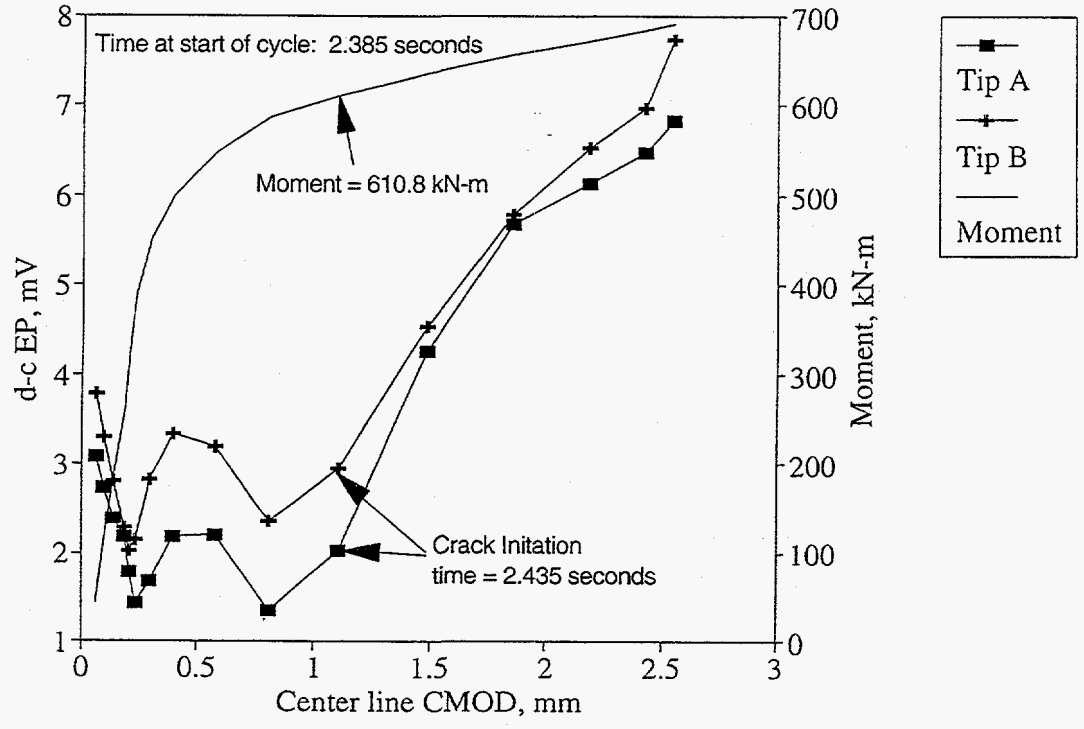

Figure 4.83 Experiment 1-7 d-c EP and crack-section moment as a function of the crack centerline crack-mouth-opening displacement for the loading portion of the cycle starting 2.385 seconds into the "Test" forcing function

the large amplitude cycle at approximately 2.4 seconds into the "Test" forcing function. The increase in slope of the d-c EP versus CMOD plot at approximately 1.15 mm (0.045 inch) of CMOD is indicative of crack initiation. This occurred 2.435 seconds into the "Test" forcing function. (Note, the prior cycles exhibited linear-elastic behavior in the moment-CMOD behavior, see Figure 4.80, so that one would not expect the crack to have initiated during one of these earlier cycles. Furthermore, when the d-c EP data were plotted against the CMOD data for the earlier cycles, no evidence of slope change in the response was observed.) The crack section moment value at crack initiation was found to be approximately 611 kN-m (5,410 in-kips), which is approximately 72 percent of the maximum moment for the experiment.

Figure 4.84 shows a post-test photograph of the crack growth pattern for the test specimen with the external sealing patch removed. The crack grew asymmetrically at an angle of 30 degrees from the original crack plane. Such asymmetric crack growth is common for carbon steel pipes (Ref. 4.8). The crack penetrated the patch 17.4 seconds after the start of the "Decision Tree" forcing function. The crack grew less than 3.3 mm (0.13 inch) beyond the patch weld.

4.4.2.2 Experiment 1-8 Results

Experiment 1-8 was the companion quasi-static monotonic experiment to the short through-wall crack simulated seismic experiment just discussed, Experiment 1-7. Figure 4.85 presents the total applied load (including the "dead-weight" load) as a function of the pipe displacement at the load point. The pipe displacement at the load point is the displacement at the load points due solely to the pipe and crack with all machine compliance removed. The load versus pipe displacement curve shown in Figure 4.85 shows a relatively smooth behavior up to a pipe displacement of approximately 250 mm (10 inches). At this point

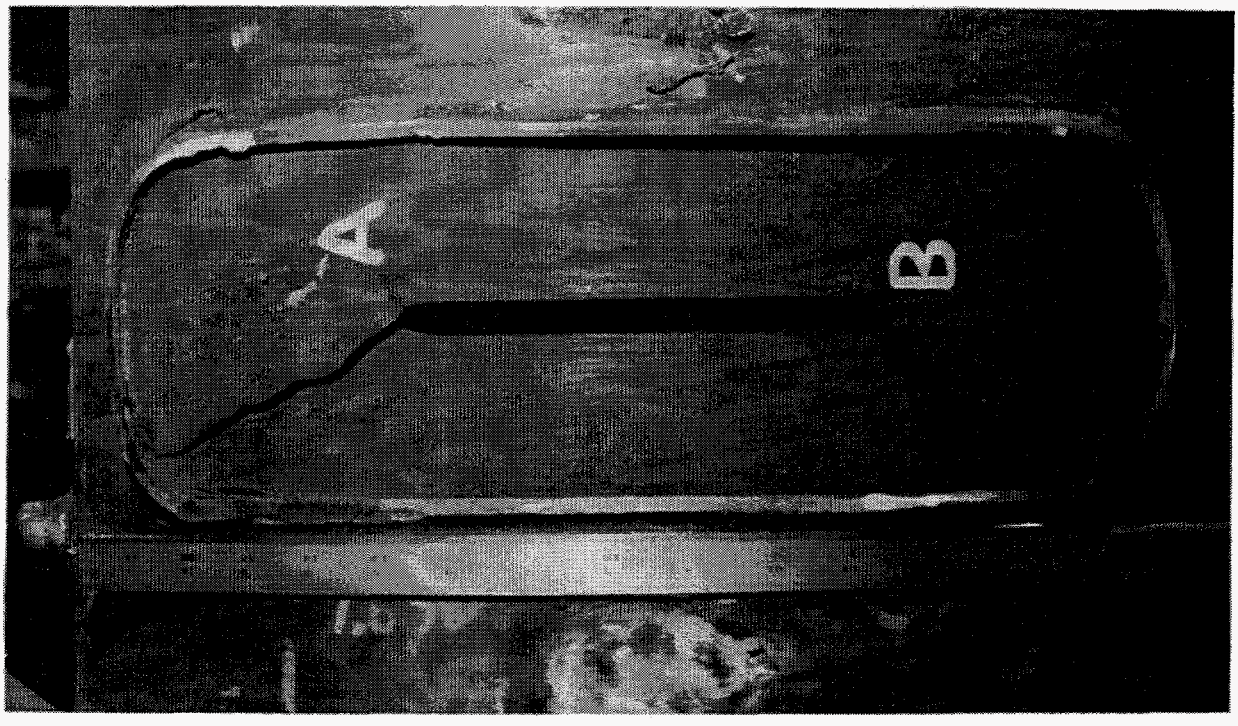

Figure 4.84 Photograph of crack growth after Experiment 1-7

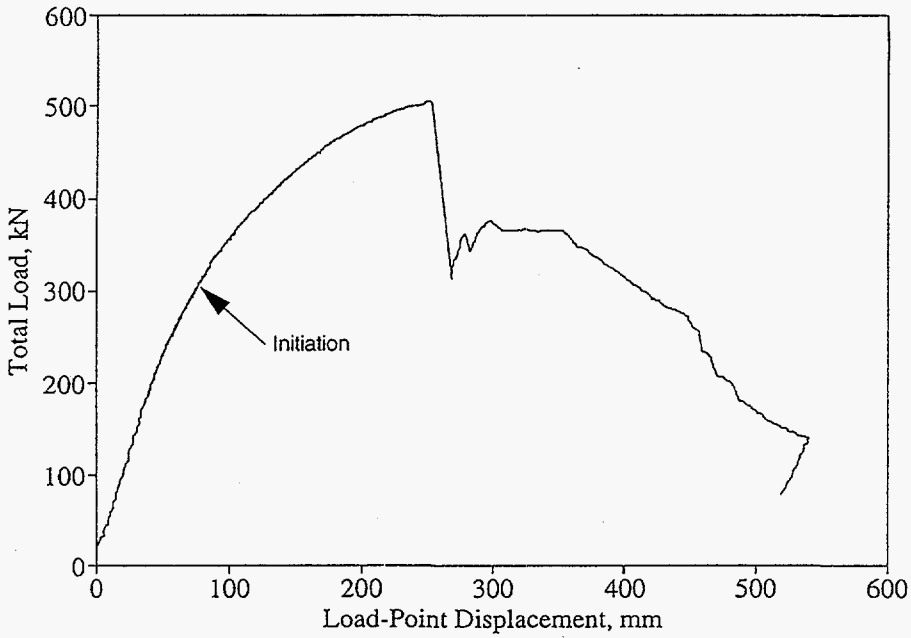

Figure 4.85 Load as a function of pipe displacement at the load point for Experiment 1-8

the load dropped from 504.4 kN (113.4 kips), the maximum load for the experiment, to 313.3 kN (70.4 kips). A post-test examination of the specimen suggests that a crack jump occurred when the through-wall crack grew through the edge of the patch.

Figures 4.86 and 4.87 are plots of the crack section moment data as a function of the crack centerline crack-mouth-opening displacement (CMOD) and crack section rotation data, respectively, for Experiment 1-8. The CMOD data were obtained from a high pressure/high temperature LVDT mounted across the crack on the inside pipe surface. The rotation data were obtained from inclinometers mounted on the pipe 254 mm (10 inches) on either side of the crack plane. The moments were calculated from the total applied load data (including the "dead weight" load) and the fixed moment arm length. The maximum moment for the experiment was 1037.7 kN-m (9,185 in-kips).

Crack initiation was determined from the d-c EP data. Figure 4.88 is a plot of the d-c EP data at Crack Tip B as a function of the crack centerline CMOD data. The instant of crack initiation is taken as the point when the slope of the d-c EP versus CMOD curve increases, i.e., the d-c EP signal deviates from the initial blunting line. From Figure 4.88, it can be seen that the d-c EP data begins to deviate from the blunting line at a crack centerline CMOD value of approximately 1.85 mm (0.073 inches). (From a similar plot for the Crack Tip A d-c EP data, it was shown that the crack at Tip A initiated slightly after the crack initiated at Tip B.) From Figure 4.86, it can be seen that the applied moment value at a crack centerline CMOD value of 1.85 mm (0.073 inches) was 621.3 kN-m (5,499 in-kips), which is approximately 60 percent of the maximum moment for the experiment.

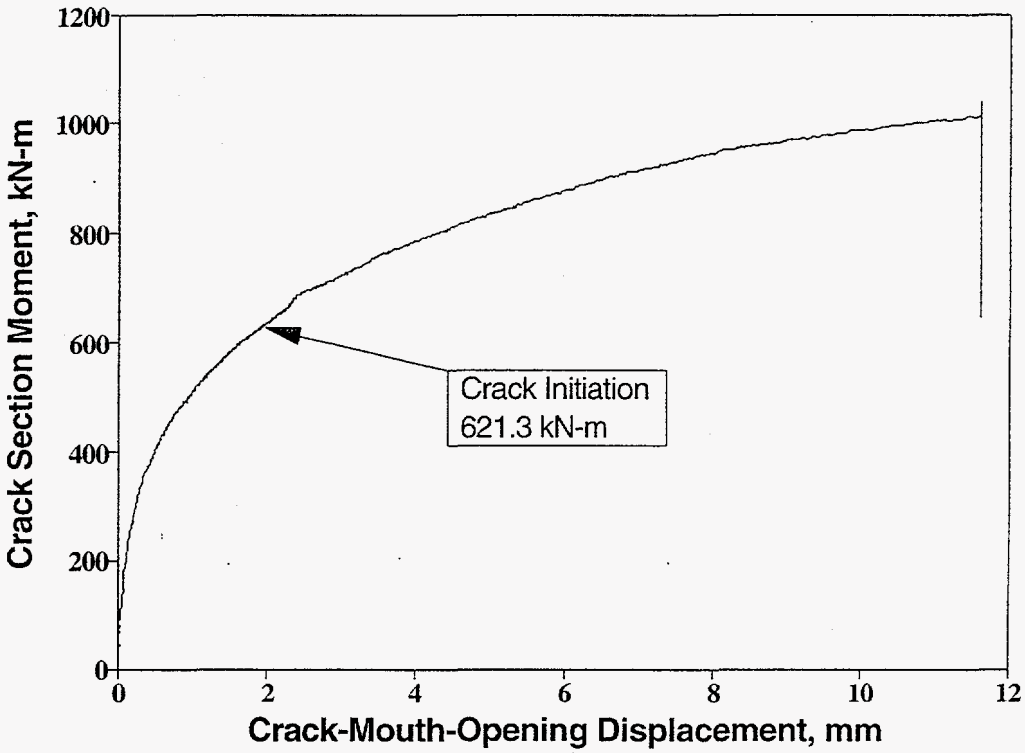

Figure 4.86 Crack-section moment as a function of crack centerline CMOD data for Experiment 1-8

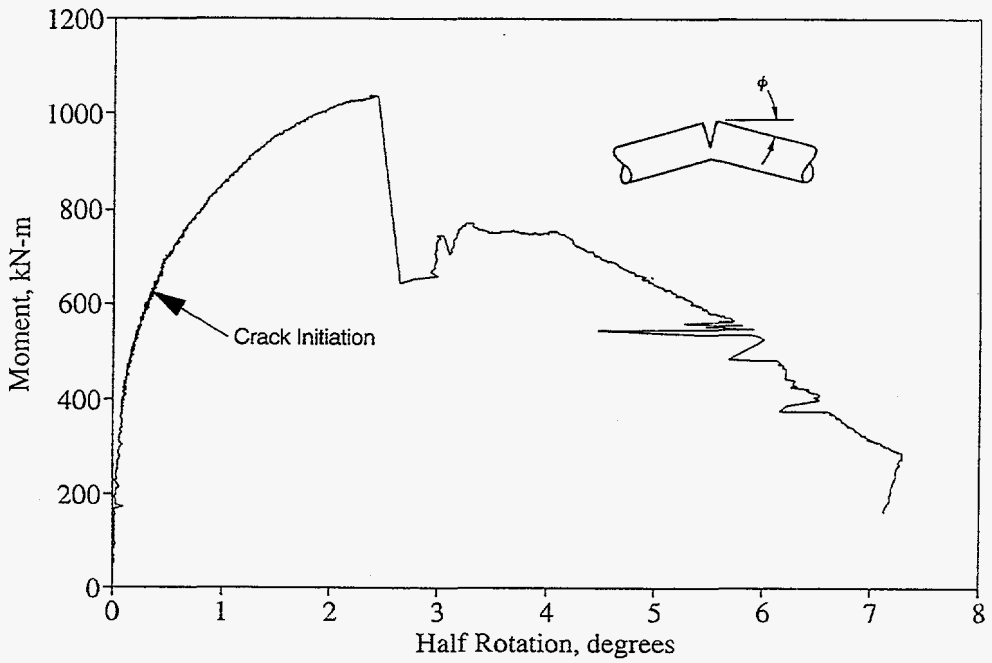

Figure 4.87 Moment as a function of inclinometer half-angle rotation for Experiment 1-8

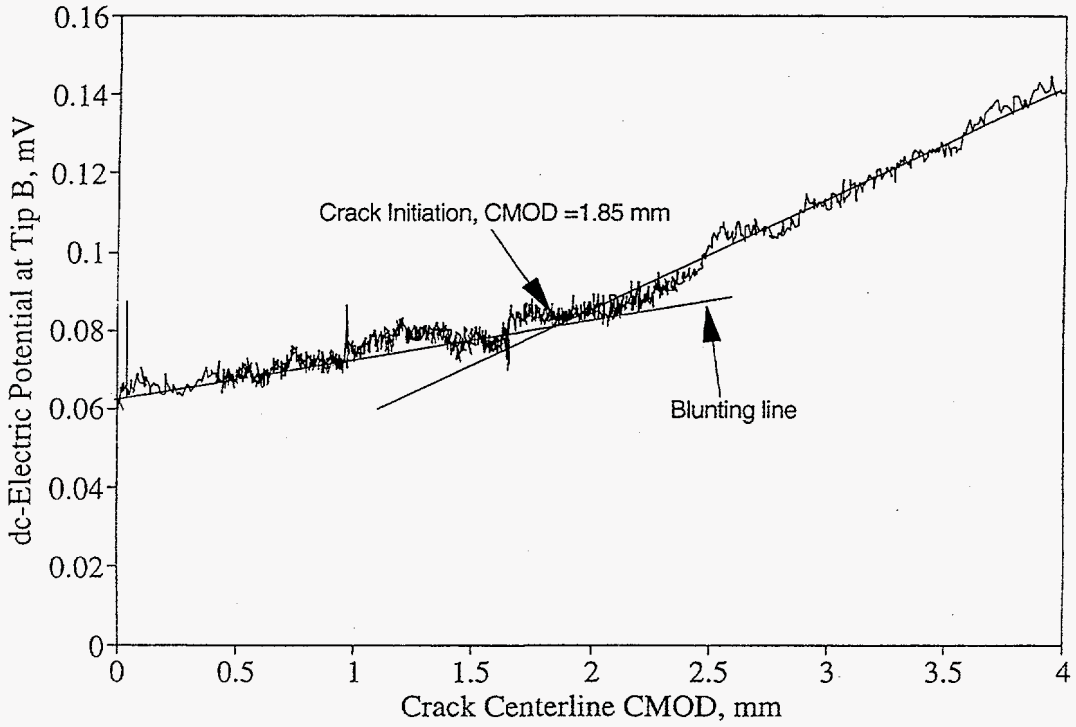

Figure 4.88 Direct-current electric potential at Crack Tip B as a function of the crack centerline crack-mouth-opening displacement showing crack initiation for Experiment 1-8 (lines are from linear regression analysis)

A polynomial fit of the through-wall crack d-c EP calibration data developed by Wilkowski and Maxey (Ref. 4.5) was used to determine the crack growth from the d-c EP data. Two different polynomial expressions were used. The first gave the normalized circumferential crack length in terms of a polynomial fit of the normalized d-c EP data:

$$2c/\pi D_m = 0.275\,E_N - 0.0261\,E_N^2 + 0.00104\,E_N^3 \qquad (4\text{-}4)$$

$$E_N = (EP_c - E_0)/(E_{0.25} - E_0) \qquad (4\text{-}3)$$

where,

D_m = mean pipe diameter
$2c$ = total circumferential through-wall crack length
EP_c = the d-c EP reading at the center of the crack
E_0 = the base metal reference d-c EP normalized by the ratio of the reference probe spacing to the spacing of the probes at the crack centerline
$E_{0.25}$ = the d-c EP reading for a crack 25 percent of the pipe circumference in length
E_N = normalized d-c EP

The second fit gave the normalized electric potential in terms of the normalized circumferential crack length:

$$E_N = 3.777(2c/\pi D_m) + 0.259(2c/\pi D_m)^2 + 2.523(2c/\pi D_m)^3 \quad (4\text{-}5)$$

Figure 4.89 shows the average calculated crack growth from one crack tip based on the d-c EP data for Experiment 1-8. The crack growth determined from Equations 4-3 to 4-5, and shown in Figure 4.89, is the average projected crack growth. The circumferential through-wall crack in this experiment did not remain in the initial crack plane. The angle of the crack growth with respect to the initial crack plane varied from 45 to 65 degrees. Figure 4.90 shows a sketch of the extent of the actual crack at the end of the experiment. The d-c EP data indicates that there was a crack jump at maximum load for this experiment. This crack jump is readily evident in the crack growth data shown in Figure 4.89.

Figures 4.91 and 4.92 are post-test photographs of the two crack tips. For these photographs the external patch is still in place. The patch flattened considerably during the course of the experiment. (For reference, Figure 4.93 is a pretest photograph of the undeformed patch.) The amount that the patch influenced the crack growth behavior is unknown. The crack extension and CMOD values at the time of the crack jump were well beyond the design values for the patch and the patch was almost flat at the end of the experiment. The primary loading of the patch transitioned from bending (which was the design basis for the patch) to tensile during the course of the experiment. The physical shape of the patch changed from an arch in its original configuration to a flat plate at the end of the experiment. The loads needed to deform the arch in bending (i.e., the design basis) are considerably lower than the loads required to deform the resultant plate in tension. Consequently, the loads carried by the patch during the large-crack-growth portion of the experiment were probably higher than expected based on the original design.

4.4.2.3 Experiment 1-9 Results

Since the original intent of this experiment was merely a proof of concept, the amount of data acquired during the experiment was minimal. The results of this experiment illustrate the effect of combined pressure and dynamic bending loads on the fracture behavior of through-wall-cracked pipe. The test specimen contained a through-wall crack that was approximately 25 percent of the pipe circumference in length. The pipe specimen was loaded in four-point bending at dynamic loading rates, 108 mm/second (4.24 inches/second). The time to crack initiation for this dynamic loading was 0.605 seconds. In addition, prior to the dynamic four-point bending phase of the experiment, the test specimen was subjected to a series of relatively small-amplitude cyclic bending loads in order to evaluate the effectiveness of the bellows sealing method under cyclic fatigue type loadings. The amplitude of the displacements for the cyclic loading phase of the experiment was 1.01 to 1.52 mm (0.04 to 0.06 inch). This cyclic loading phase was applied for 60 seconds at a 2 Hz frequency. This phase of the experiment was followed by a second load history consisting of 3 low frequency cycles with the displacement ranging from zero to 25 mm (1 inch). The maximum load obtained during this loading was 18.9 kN (4,250 lbs) with moments peaking at 24.5 kN-m (217 in-kips). There was no sign of crack initiation based on the d-c EP data from either of these cyclic load histories. As a result, the data from these loadings will not be reported.

The third loading consisted of a single computer-controlled ramp up to a displacement of 152 mm (6.0 inches) at a displacement rate of 108 mm/second (4.24 inches/second). The crack initiated during this

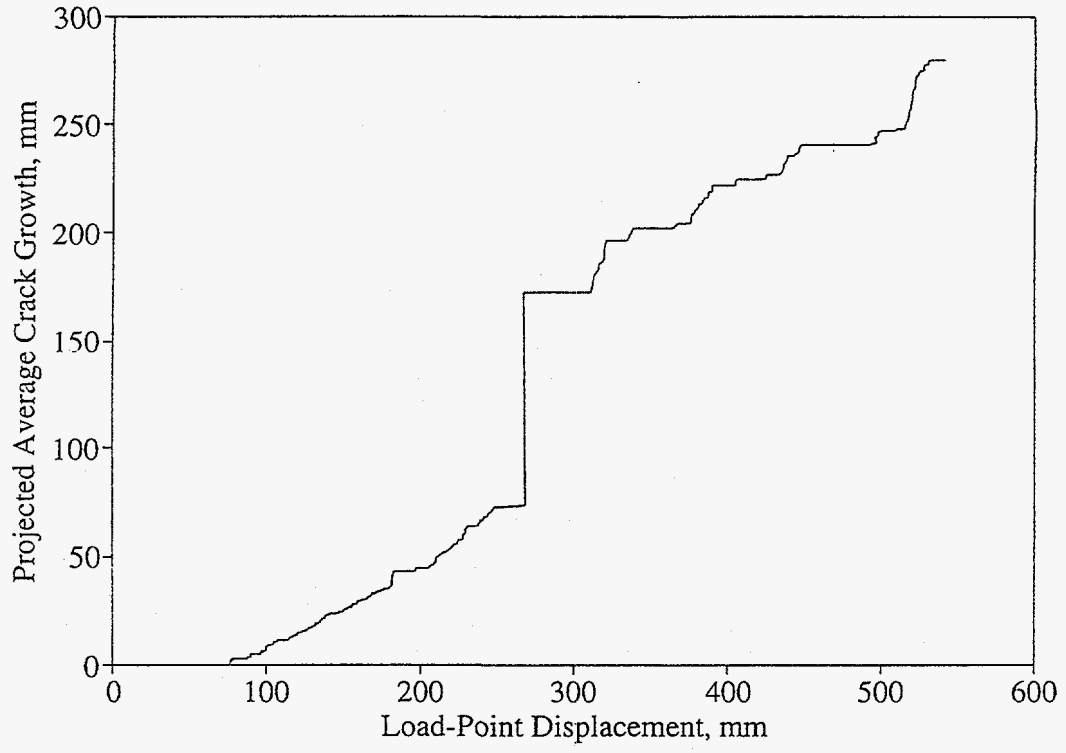

Figure 4.89 Average projected crack growth from both crack tips for Experiment 1-8

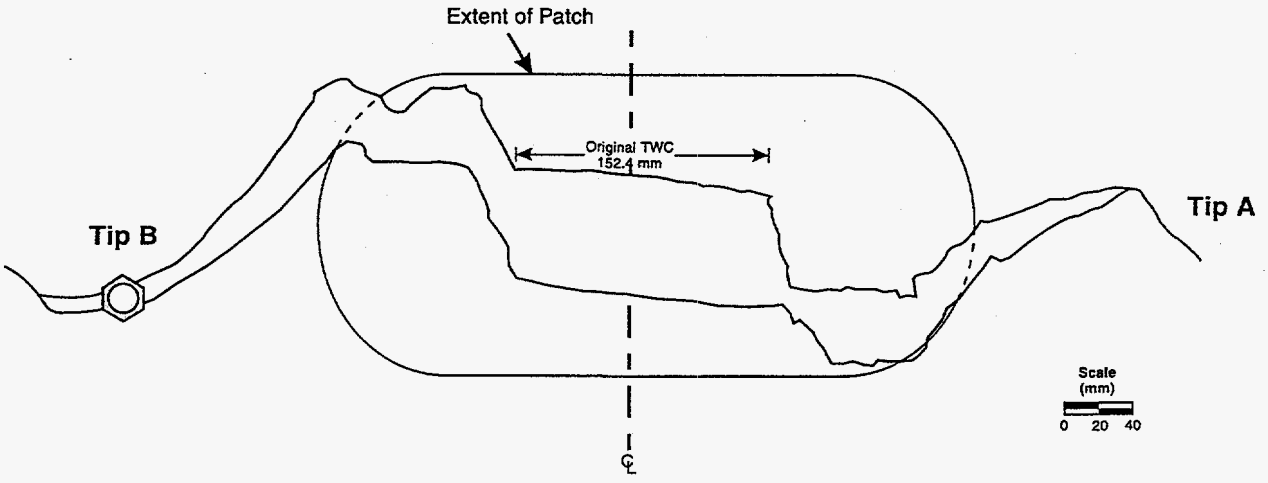

Figure 4.90 Tracing of the through-wall crack at the completion of Experiment 1-8

Figure 4.91 Post-test photograph of Crack Tip A with patch still in place at the completion of Experiment 1-8

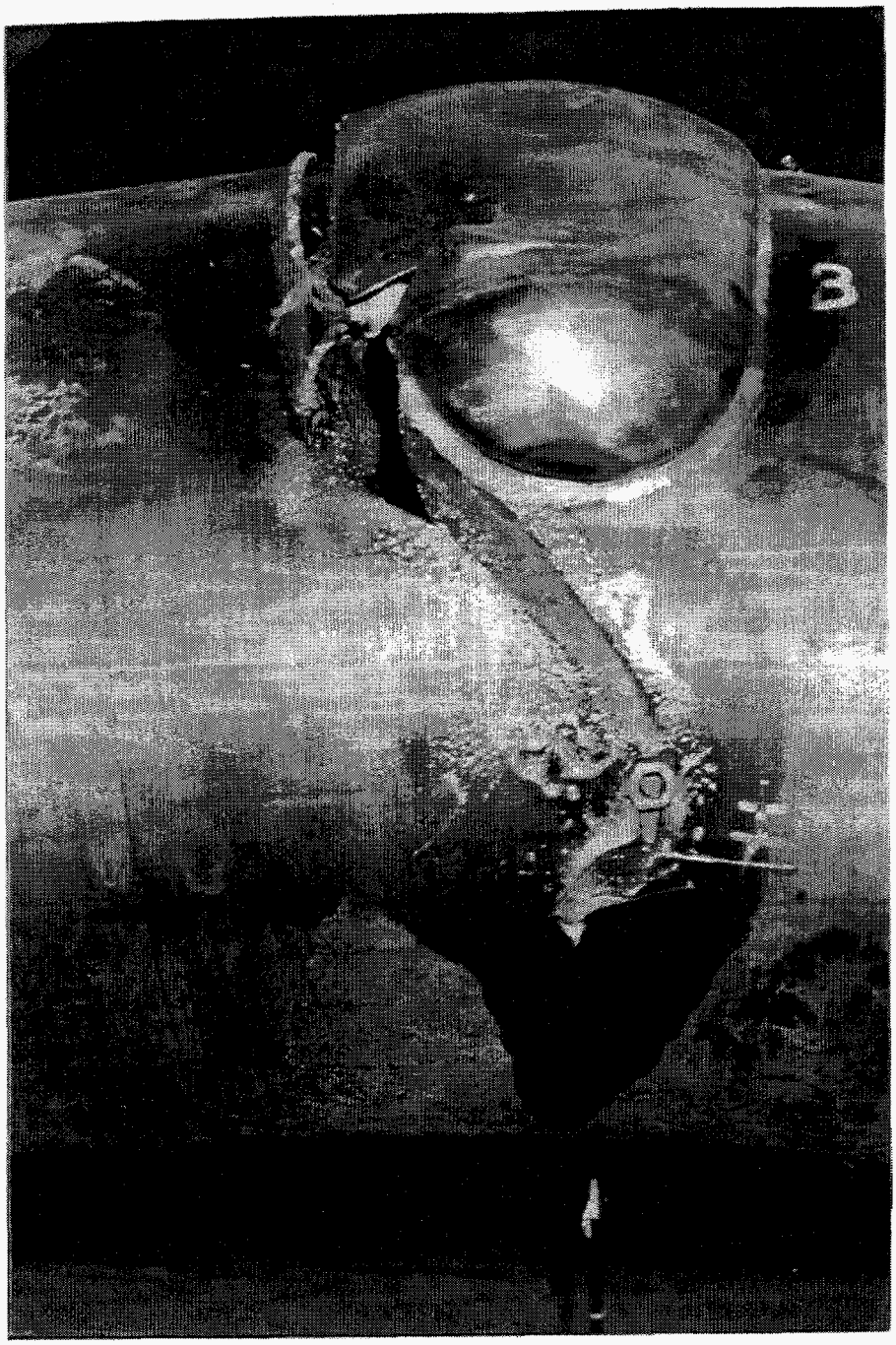

Figure 4.92 Post-test photograph of Crack Tip B with patch still in place at the completion of Experiment 1-8

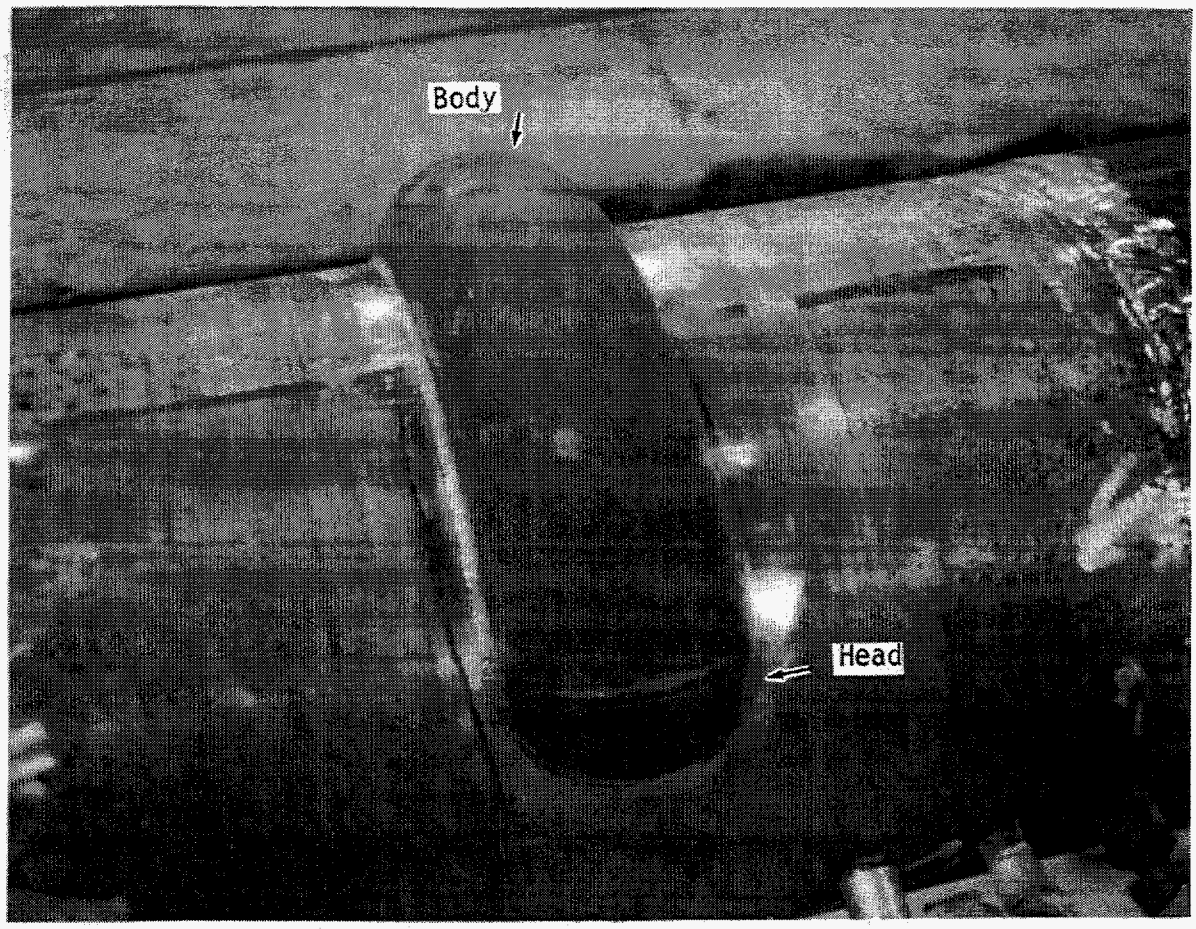

Figure 4.93 Pretest photograph of patch used to seal the through-wall crack in Experiment 1-8

third loading cycle. The fourth loading consisted of a manually-controlled ramp up to a displacement of 237 mm (9.33 inches). At the end of this fourth loading, the pipe severed, i.e., a DEGB occurred.

Figure 4.94 presents the total applied load versus the load-line displacement for both the computer-controlled and manually-controlled dynamic ramps. The total applied load is the sum of the load cell measurements at the two actuators plus the "dead weight" load due to the weight of the pipe, water in the specimen, and fixturing. The load-line displacement data shown in this figure includes the displacements due to the test machine compliance. The actual test machine compliance was not measured for the test configuration used in this experiment. The maximum load and moment for this experiment were 43.2 kN (9,710 lbs) and 54.3 kN-m (481 in-kips), respectively.

Figure 4.95 shows the d-c EP at Crack Tip B data as a function of the load-line displacement data for Experiment 1-9. The increase in slope indicates crack initiation. From this figure, it can be seen that the crack initiated at a load-line displacement value of 38.3 mm (1.51 inches). A similar plot was generated for Crack Tip A and it was shown that Crack Tip A initiated shortly after Tip B at a load-line displacement value of 38.7 mm (1.52 inches). From Figure 4.94, it can be seen that the total applied load at crack initiation was 37.7 kN (8,475 lbs), which is approximately 87 percent of the maximum load for the experiment.

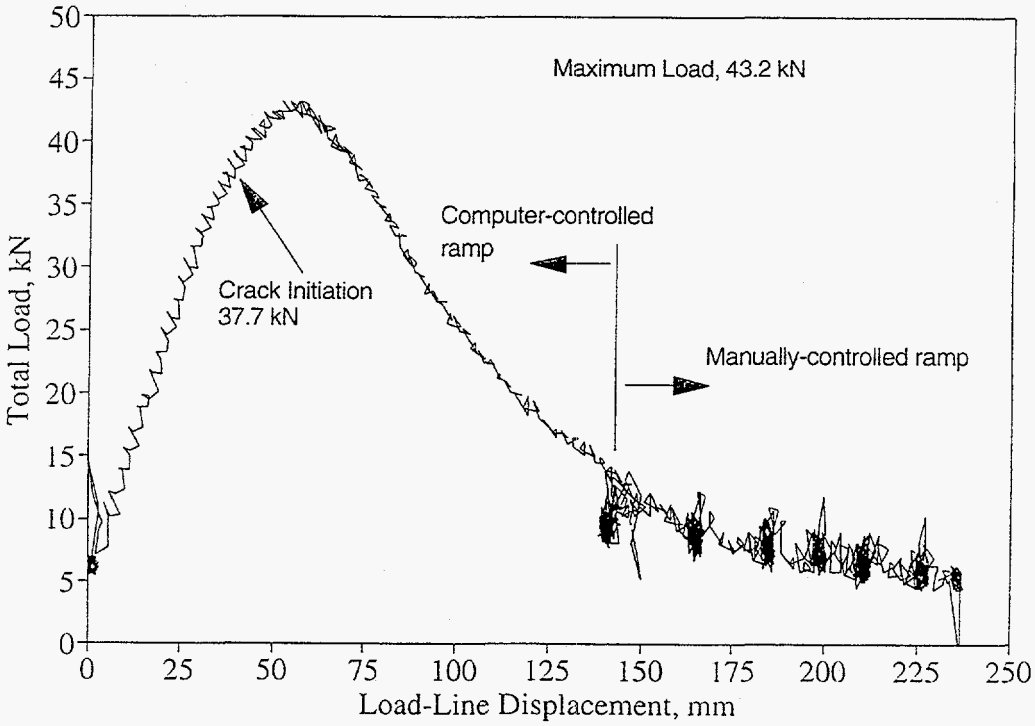

Figure 4.94 Total load as a function of load-line displacement data for Experiment 1-9

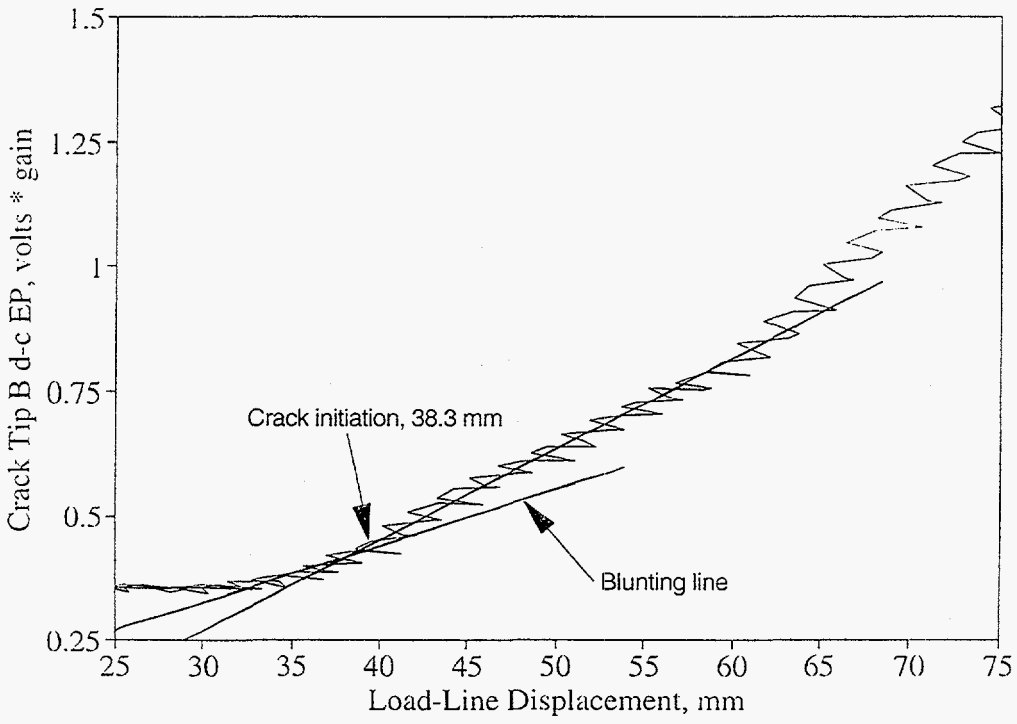

Figure 4.95 Crack Tip B d-c EP data as a function of load-line displacement data showing crack initiation for Experiment 1-9

Figure 4.96 is a plot of the crack section moment as a function of the total rotation data for Experiment 1-9. The moment at crack initiation is 47.5 kN-m (420.4 in-kips) and the maximum moment is 54.3 kN-m (480.6 in-kips).

The through-wall crack growth was calculated from the d-c EP data using the same basic procedures as previously discussed for Experiment 1-8. The only difference is that when the calculated final crack length was compared with the actual final crack length measured after the experiment, it was found that the calculated length was 8.7 percent longer than the actual length. As a result, the calculated crack lengths for the entire loading sequence were then normalized by the ratio of the actual-to-calculated crack lengths at the end of the third loading phase of the experiment. Figure 4.97 shows the average crack growth at one crack tip as a function of the load-line displacement data.

Figure 4.98 is a post-test photograph of the fracture surface for Experiment 1-9. The extent of the crack growth at the end of the third loading can be seen by the tinting (i.e., difference in color) of the fracture surface. The crack growth occurred at an angle of 30 degrees with respect to the initial crack plane. The growth of the crack out of the initial crack plane resulted in the loose piece of pipe that can be seen in Figure 4.98. The two crack tips grew parallel to one another and finally joined up with the original crack plane. This resulted in a DEGB and the loose piece of pipe shown in Figure 4.98.

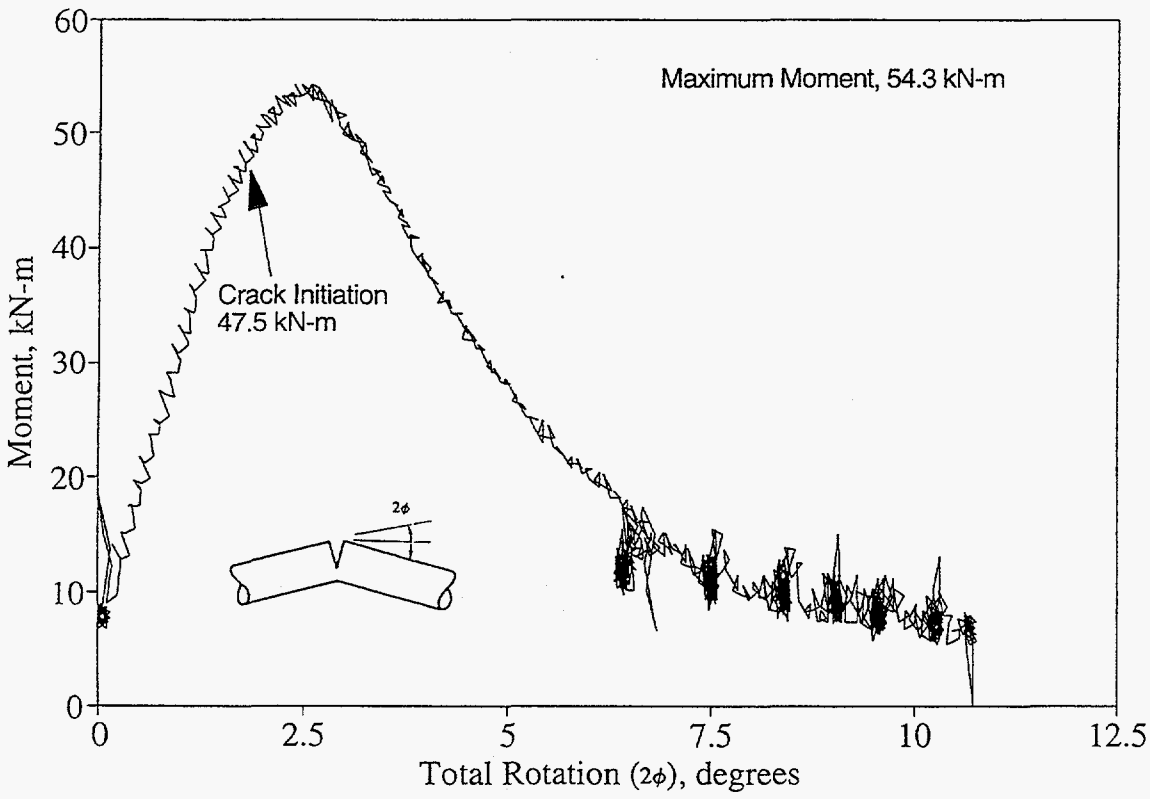

Figure 4.96 Applied moment as a function of rotation data for Experiment 1-9

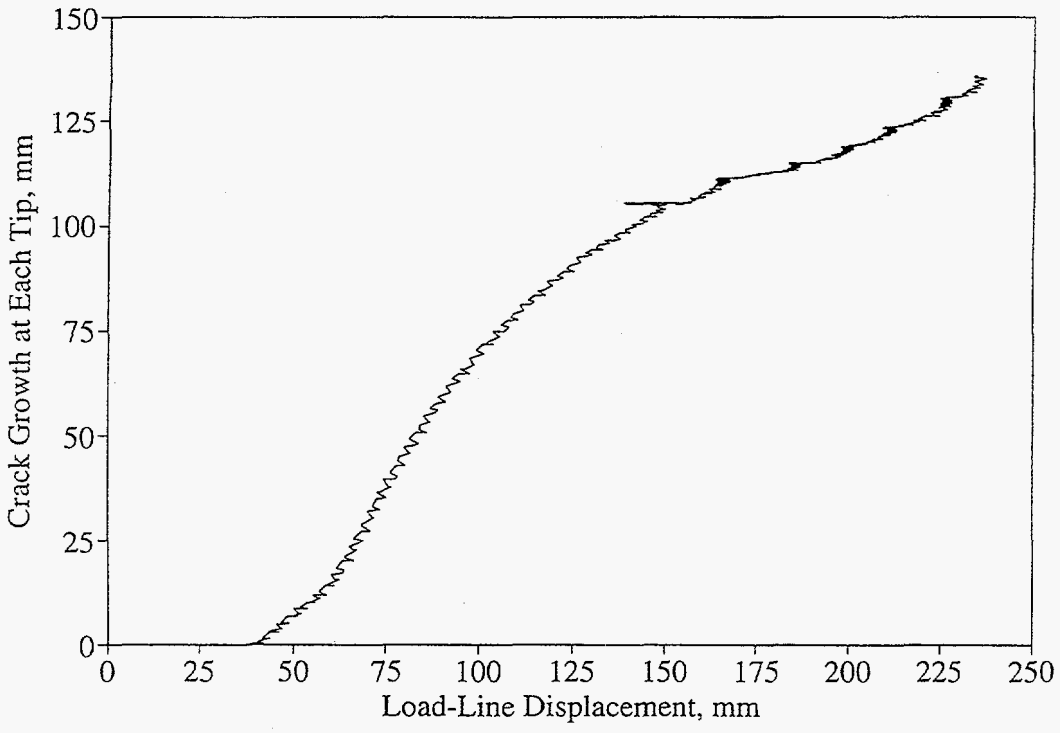

Figure 4.97 Average crack growth at one tip as a function of load-line displacement for Experiment 1-9

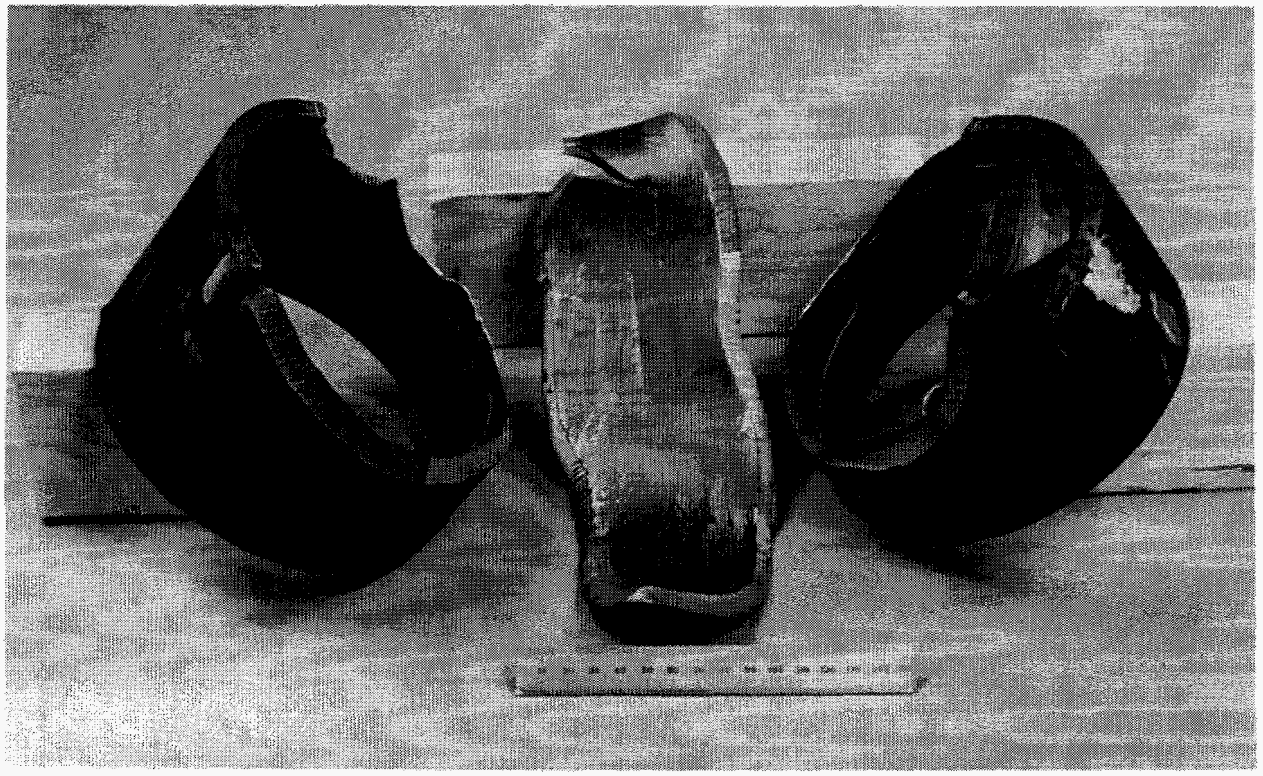

Figure 4.98 Photograph of fracture surface for Experiment 1-9

4.5 References

4.1 Wilkowski, G. M., and others, "Degraded Piping Program - Phase II: Summary of Technical Results and Their Significance to Leak-Before-Break and In-Service Flaw Acceptance Criteria - March 1984 - January 1989," NUREG/CR-4082, Vol. 8, March 1989.

4.2 Scott, P. M., and others, "The IPIRG-1 Pipe System Fracture Tests: Experimental Results," PVP Vol. 280, pp 135-151, June 1994.

4.3 Kanninen, M. F., and others, "Instability Predictions for Circumferentially Cracked Type 304 Stainless Steel Pipes Under Dynamic Loadings," Final Report on EPRI Project T118-2, by Battelle Columbus Laboratories, EPRI Report Number NP-2347, April 1982.

4.4 Olson, R., and others, "Design of the IPIRG-2 Simulated Seismic Forcing Function," NUREG/CR-6439, February 1996.

4.5 Wilkowski, G. M. and Maxey, W. A., "Review and Application of the Electric Potential Method for Measuring Crack Growth in Specimens, Flawed Pipe and Pressure Vessels," ASTM STP 791, 1983.

4.6 Krishnaswamy, P., and others, "Fracture Behavior of Short Circumferentially Surface-Cracked Pipe," NUREG/CR-6298, November 1995.

4.7 Scott, P., and others, "Stability of Cracked Pipe Under Inertial Stresses," Subtask 1.1 Final Report from IPIRG-1 Program, NUREG/CR-6233, Vol. 1, August 1994.

4.8 Mohan, R., and others, "Effects of Toughness Anisotropy and Combined Tension, Torsion, and Bending Loads of Fracture Behavior of Ferritic Nuclear Pipe," NUREG/CR-6299, April 1995.

5.0 ANALYSIS OF EXPERIMENTS

In this section, the results from the analyses of the IPIRG-2 Task 1 and companion pipe experiments from related programs will be presented. Three different types of analysis efforts were undertaken:

- Pipe system finite element analyses (FEA),
- Maximum load predictions, and
- Comparison of J_i values from pipe tests with specimens tests.

First, the results from the linear elastic finite element analyses of these experiments are presented in Section 5.1. Because an uncracked pipe elastic stress analysis is generally part of a Leak-Before-Break (LBB), ASME Section XI, or R6 flaw evaluation analysis, it is useful to know how well such linear elastic stress analysis methods can predict the actual stresses in a dynamic pipe system experiment. If the piping system stresses are high relative to the yield strength of the pipe material, as would be the case when the crack size is small or the crack is in a higher toughness material, then the amount of plastic deformation should be significant, and one would expect that the elastic stress analyses would overpredict the actual stresses. However, if the piping system stresses are low relative to the yield strength of the material, as would be the case when the crack size is large or the crack is in a lower toughness material, then the amount of plastic deformation should be small, and one would expect that the elastic stress analysis should be fairly accurate. This was essentially what was found during IPIRG-1 for the relatively large crack sizes evaluated during that program. It was expected that for the shorter cracks considered in some of the IPIRG-2 Task 1 experiments, that the reverse would be true and more of the piping system would experience plastic deformation and the elastic analysis would significantly overpredict the experimental stresses. Unfortunately, it was not possible to test this hypothesis. It was found that the dynamic stress analyses did not predict some of the IPIRG-2 experiments even during the initial elastic cycles. This problem appears to have its roots in the modeling of the primary restraint system which was used in these pipe system experiments. As such, the elastic finite element results for these experiments are not presented. However, a description of the method and the problem which arose are presented. The experimental data themselves are believed to be correct, only the FEM analyses had problems in reproducing the experimental results.

The second set of analyses associated with this effort involved comparisons of the maximum experimental loads from these experiments with predictions from the various fracture prediction analyses and failure avoidance criteria which have been developed. The purpose of this set of analyses was not to assess the accuracy of the various methods. That has been done in the past as part of prior programs. The purpose of this set of analyses was to normalize the results from the Task 1 and companion experiments so that each could be compared on an equal basis, without the undue bias due to differences in the physical dimensions of the crack and/or pipe. In this manner, the results from the Task 1 experiments could be compared with the companion experiments from this and related programs so that such questions as the effect of seismic loading histories, the effect of cracks at geometric discontinuities such as at an elbow girth welds, the effect of smaller crack sizes, and the effect of through-wall cracks on the fracture behavior could be addressed. These analyses are discussed in detail in Section 5.2.

The final set of analyses associated with this effort involved the calculation of the fracture toughness value at crack initiation, J_i, for each of the applicable pipe experiments. The results from these analyses were then compared with the results from a series of C(T) and SEN(T) specimen tests on the same pipe materials. These analyses are discussed in detail in Section 5.3.

5.1 Comparisons with Linear Elastic Finite Element Analyses

Because an uncracked pipe elastic stress analysis is generally part of a Leak-Before-Break (LBB), ASME Section XI, or R6 flaw evaluation analysis, it is useful to understand where there may be conservatism in the evaluation procedures. The elastic stress ratio is a measure of how well a linear elastic stress analysis predicts the actual stresses of an experiment. In this report, it is defined as the ratio of the elastically calculated stress or moment from a finite element analysis to the experimental stress or moment. The calculated stress or moment value is the maximum value from a linear elastic analysis using the actual experimental displacement-time history applied to the pipe system for the duration of the experimental excitation. Elastic stress ratios greater than 1.0 suggest that an elastic analysis will overestimate the applied loads, and hence overpredict the crack-driving force for fracture analyses.

One of the findings from the IPIRG-1 program was that the elastic stress ratios were close to 1.0 for the cracked IPIRG-1 pipe-system experiments (Ref. 5.1), hence the pipe system with these flaws behaved in an elastic manner with little effect of cracked section plasticity on the elastic stress ratio. This was in contrast to what was found for the uncracked pipe-system experiments conducted as part of the EPRI/NRC Piping Reliability program (Ref. 5.2). Lower elastic stress ratios for the cracked IPIRG-1 pipe-system experiments were attributed to the fact that the crack sizes evaluated in that program were relatively large such that the plasticity was confined to the cracked section. Furthermore, the nonlinear deformation at the surface-cracked section was relatively small compared with the overall displacements. As such, it was expected that if smaller crack sizes were evaluated, with associated higher moment and stress values, then the extent of plasticity remote from the crack section would increase, and the elastic stress ratios would increase proportionately. Hence, the elastic stress ratios for the short surface-cracked and short through-wall-cracked pipe-system experiments should be between the value of approximately 1.0 observed in the IPIRG-1 pipe-system experiments and the value of approximately 30 from the uncracked pipe-system experiments from Reference 5.2. However, this was not the case. If anything, the calculated elastic stress ratio for the short surface-cracked pipe-system experiment (Experiment 1-5) was slightly less than the elastic stress ratio for the companion long surface-cracked pipe-system experiment from IPIRG-1 (Experiment 1.3-5). This was not expected.

In trying to resolve this apparent discrepancy, two major points were discovered. First, it appears that the presence of the double-ended-guillotine-break (DEGB) restraint device used in the IPIRG-2 straight pipe-system experiments, and discussed in Section 3.2, amplifies the experimentally measured moments (and associated displacements) when compared with the experimental moments measured when the restraint device was not present in the pipe system. Secondly, finite element analyses of the pipe system with measured material and pipe section properties fail to predict this difference. Finite element analyses, with and without the restraint device in the model, do not show significant differences in piping system response.

To illustrate these two points, Figure 5.1 shows the measured moment-time response for two experiments in which the DEGB restraint device was not used, one experiment is the IPIRG-1 SSW experiment (Experiment 1.3-5) and one experiment is the IPIRG-2 carbon steel elbow girth weld experiment (Experiment 1-3). As can be seen in Figure 5.1, there is no substantive difference between the two moment-time histories. The conditions for the experimental data plotted in Figure 5.1 are:

(1) The same displacement-time forcing function,

(2) The same nominal crack size,

(3) The same location for reporting the moment values (i.e., the north moment cell), and

(4) Different crack locations and test specimen materials. (The crack in the IPIRG-1 stainless steel weld pipe-system experiment (1.3-5) was 1.37 m (54 inches) north of the elbow/straight pipe girth weld which contained the crack in the IPIRG-2 carbon steel elbow girth weld pipe-system experiment [1-3].)

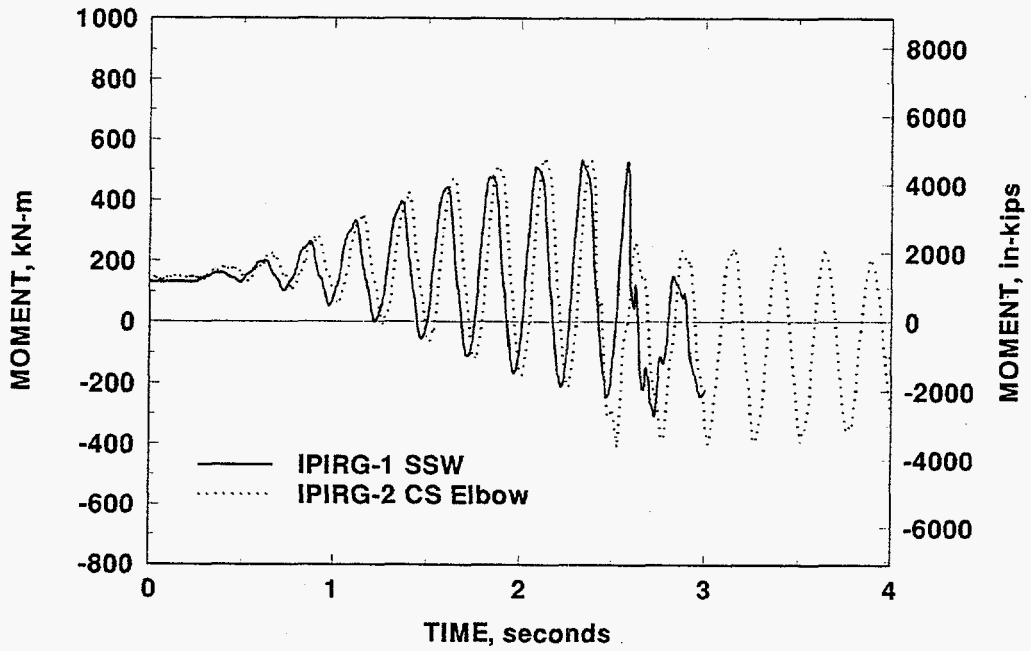

Figure 5.1 Measured moment-time response for two experiments for which the DEGB restraint device was not used showing that there is no substantive difference between the IPIRG-1 and IPIRG-2 pipe loop system response

These data suggest that even after the pipe system was rebuilt for IPIRG-2, and in spite of a different crack location and test specimen material, the response of the pipe system to the same input forcing function was basically the same.

Contrasting the data shown in Figure 5.1, Figure 5.2 compares the north moment cell experimentally measured moments for two experiments, one with (IPIRG-2 short surface crack in stainless steel weld with the restraint system, Experiment 1-5) and one without the DEGB restraint device in the pipe system (Experiment 1.3-5). In this case the crack sizes were different, but the test specimen material, crack location, and forcing function were all the same. The expectation was that the responses for these two experiments would be similar for at least the first few seconds where the behavior is elastic, but such was not the case. The measured moments for the IPIRG-2 experiment, with the restraint device in place, were significantly higher than those for the IPIRG-1 experiment, which did not have the restraint device in place.

In an attempt to explain this discrepancy, ANSYS finite element analyses of the IPIRG-2 pipe system, both with and without the DEGB restraint device included, were conducted. Two different models of the restraint device were tried. The first model used lumped masses to model the restraint system, while the

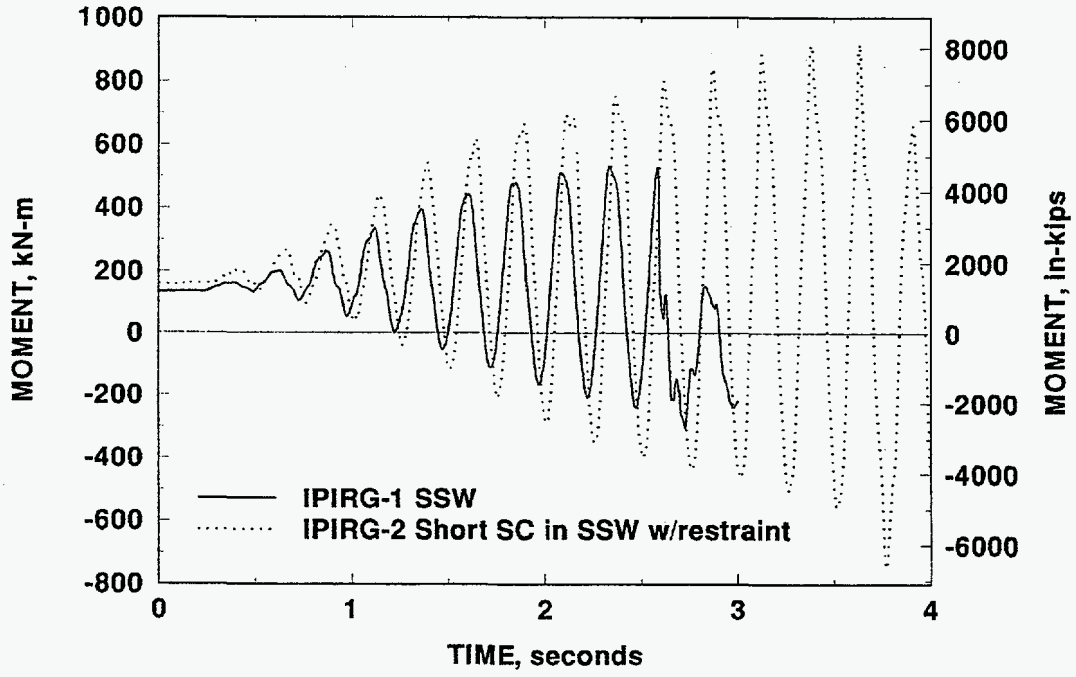

Figure 5.2 Comparison of the measured moment-time response for two experiments, one of which included the DEGB restraint device and one which did not

second model included all of the details of the restraint device, i.e., the springs, plates, and rod, directly in the pipe-system finite element model. The results for the two analyses, for both restraint system models, are virtually identical, see Figure 5.3. These results, contrary to the experimental data, indicate that the restraint device does not change the piping system moment response.

After this discrepancy was discovered, a substantial effort was put into trying to explain why the experimentally measured moments for the single-frequency experiment with the restraint device in place were so different from all of the other single-frequency experiments, and why the finite element analyses failed to replicate these differences. Seven pipe-system experiments were conducted in IPIRG-1 and IPIRG-2 which used the same single-frequency excitation. The seven experiments included a range of materials and crack locations. Some of the experiments were done in the original pipe system, while others were done after the pipe system was rebuilt. In spite of these differences, all of the experiments, except Experiment 1-5, have moments that look very similar for the first two seconds. The positive moments from Experiment 1-5 are significantly higher than the moments from the other experiments. Furthermore, the Experiment 1-5 negative moments are also much greater than those from the other experiments.

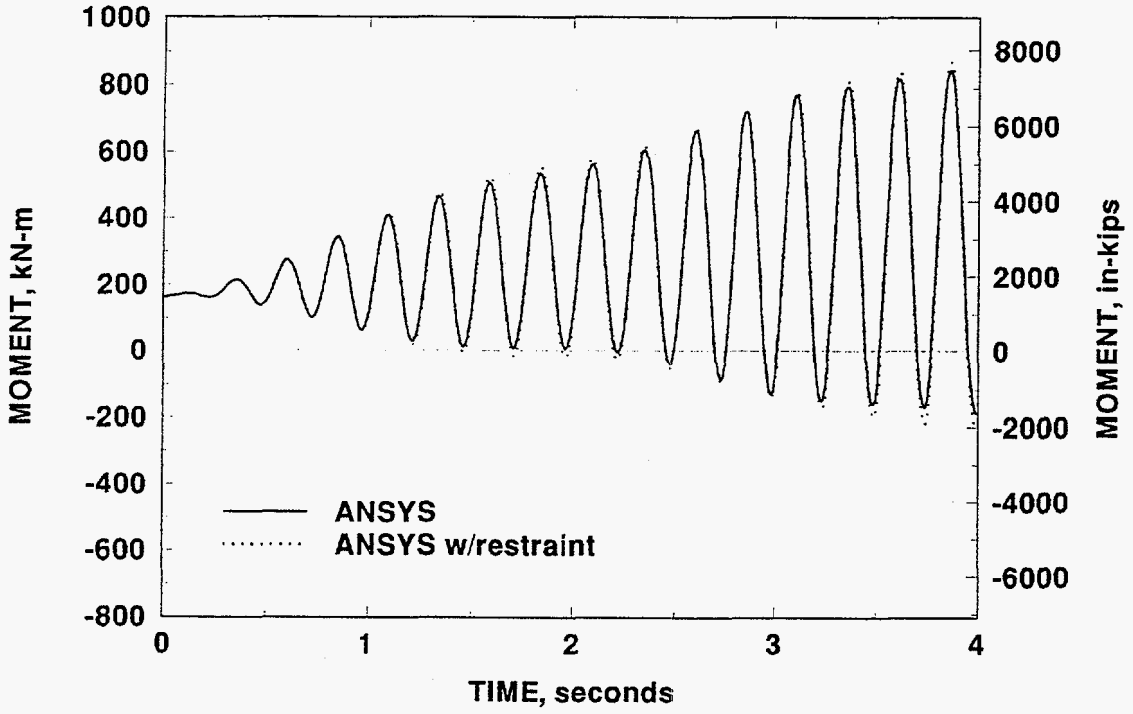

Figure 5.3 Comparison of the ANSYS predicted moment-time response for two analyses, one of which included the DEGB restraint device and one which did not

The obvious features that distinguish Experiment 1-5 from the others are the crack size and the presence of the restraint device. From a technical perspective, the crack size should not affect the system response at the early times, so the differences are assumed to be due to the restraint device. One possible explanation for this discrepancy that was considered was that there was a problem with the experimental data for Experiment 1.5, either with the applied displacements or the measured moment values. However, when the applied displacements from Experiment 1-5 were compared with the applied displacements from the other single-frequency pipe-system experiments, the displacements agreed very closely with each other, see Figure 5.4. Furthermore, the measured pipe-system displacements 1.37 m (54 inches) north of Elbow 4 are larger for Experiment 1-5 than they are for the other single-frequency pipe-system experiments, see Figure 5.5. This suggests that the larger moments for Experiment 1-5 are consistent with the measured motion of the pipe loop.

A second possible explanation for this discrepancy was that there was some feature associated with Experiment 1-5 that was not being fully captured by the analyses. To evaluate this possibility, a series of finite element analyses were performed to try to rationalize the Experiment 1-5 results. A total of 11 different finite element analyses were performed in an attempt to find an explanation for the moment response observed in Experiment 1-5. None of the modified boundary conditions/input parameters tried could duplicate the observed moments. Except where noted, the analyses used the measured pipe diameters and wall thicknesses, the measured elastic modulus, and the forcing function equation (as opposed to the actual measured displacement-time history). The rod and spring model for the restraint system is as shown in Figure 5.6. In this model, the restraint device rod is a beam connected to the pipe with soft springs in series with stiff springs at each end. Except as noted, the spring stiffnesses used were from the measured load-deflection data of two disc springs in parallel. Consistent with the restraint device design, the FEA boundary conditions for the beam was that it was free to rotate where it passes through the baffle plates.

Some of the variations in the FEA tried in an attempt to resolve this apparent discrepancy between the analyses and the experimental results included:

(1) Reducing the stiffness of the soft series of springs by an order of magnitude. It was felt that if the springs were actually softer than modeled, then the moments may have been amplified. It was shown that there was practically no difference between the two solutions.

(2) Restricting the rotation of the restraint device. The design of the restraint device was supposed to permit relatively free rotation of the cracked-pipe section. If such rotations were restrained, it was hypothesized that the bending moments may build up in front of the stiff rotation-restricted section, i.e., at the moment cells. To test this hypothesis, an analysis was conducted in which the restraint device rod was assumed to be rigidly attached to the baffle plates. The moments were virtually unchanged by restricting these rotations, thus invalidating this hypothesis.

(3) Changing the damping value used in the analyses. The measured damping of the IPIRG pipe loop was approximately 0.5 percent. Changing the damping value to 0.25 and 2.0 percent had little or no effect on the piping system moment response.

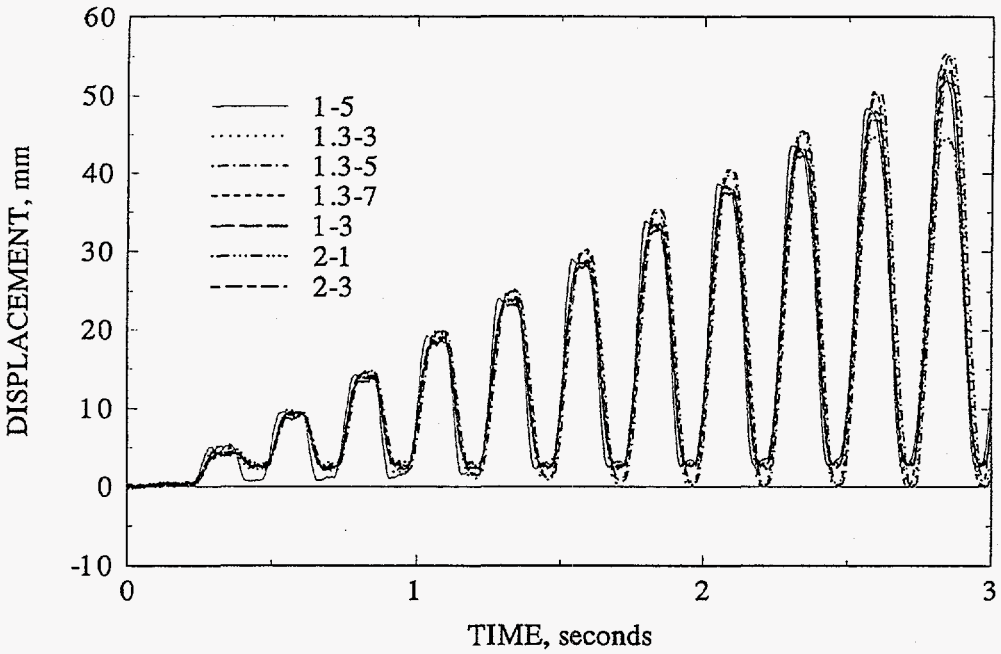

Figure 5.4 Measured input excitation for all IPIRG pipe-system experiments that used the same single-frequency excitation

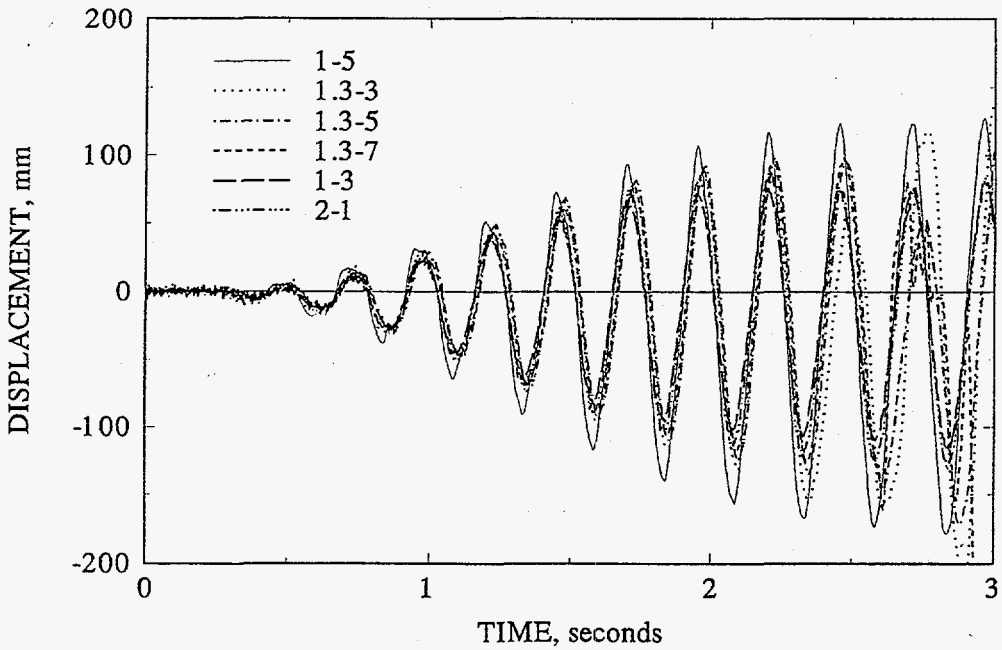

Figure 5.5 Measured Y-directed displacement 1.37 meters north of Elbow 4 for all IPIRG pipe-system experiments that used the same single-frequency excitation

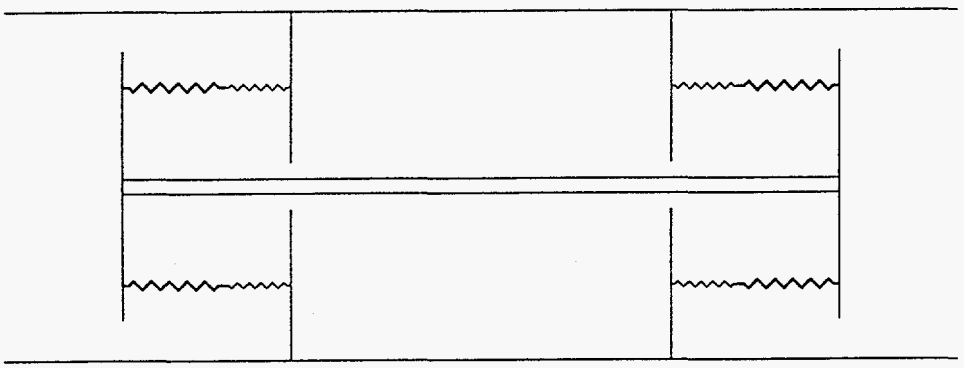

Figure 5.6 Restraint system model

(4) Adding an element of flexibility at the east-end hanger. This idea was tried since part of the spherical bearing at that location moved axially along the length of the pipe during the precracking of some of the experiments. Credibility for this scenario is added by the fact that the bearing in question appears to have been temporarily repaired after Experiment 1-5 and permanently repaired after the following experiment. To model a "loose" bearing situation, a lateral spring was placed between the pipe and the hanger. This change did not have a significant effect on the piping system response.

In all of the cases discussed above, the guiding principle was to only investigate things which could explain the differences observed between Experiment 1-5 and the other experiments that can be directly related to physical change in the pipe loop. For instance, doubling the mass of the restraint system was not considered because the mass can be readily calculated and it was verified by measurement. Using this approach, no reasonable physical explanation for the behavior of Experiment 1-5 is apparent.

In contrast to the physically-based philosophy followed above, the TAG representatives from CEA in France investigated the problem from a theoretical perspective. Basically, they reasoned that the pipe system should behave much like a one degree-of-freedom system does to changes in forcing function excitation frequency or system natural frequency. Specifically, the natural frequency of a one degree-of-freedom system is given by

$$\omega_0 = \sqrt{\left(\frac{k}{m}\right)} \tag{5-1}$$

where

k stiffness of the system
m mass of the system.

Under forced excitation at frequency ω with a damping ratio of ζ (fraction of critical damping), the dynamic response, X, is amplified over the static response

$$\frac{X}{X_0} = \frac{1}{\sqrt{\left(1-\frac{\omega^2}{\omega_0^2}\right)^2 + 4\zeta^2\frac{\omega^2}{\omega_0^2}}} \qquad (5\text{-}2)$$

where X_0 is the static system response. Figure 5.7 shows a plot of Equation 5-2. Looking at Figure 5.7, it is clear that small changes in excitation frequency (or conversely changes in system natural frequency at a fixed excitation frequency) can result in large changes in the dynamic amplification factor. For a fixed-frequency excitation, a decrease of the natural frequency by only 3 percent dramatically changes the system response for a system with only 0.5 percent damping, Figure 5.8. Because the IPIRG pipe system has low damping and the excitation is very near the first natural frequency for the single-frequency experiments, the small change in mass caused by adding the restraint system may cause the observed large change in system response.

To test this theoretical explanation for the observed behavior of Experiment 1-5, CEA performed a series of finite element calculations. Consistent with the Battelle calculations, CEA got very poor agreement between the Experiment 1-5 measured moments and their predictions when they used all of the measured pipe section properties and Young's modulus using a lumped mass model for the restraint system. However, keeping everything else constant, when they reduced Young's modulus by 12 percent throughout the whole pipe loop, they got very good agreement with the moments for the SSE loading phase loading of Experiment 1-1 and dramatically improved agreement with moments for Experiment 1-5. When they remove the restraint lumped masses from their model, the natural frequency increased 3 percent and the moment amplitudes reduced by about 40 percent. This behavior is completely consistent with Figure 5.7.

From a theoretical perspective, the CEA results explain the behavior observed in Experiment 1-5. Low damping and the proximity of the excitation frequency to the first natural frequency of the system change the response magnitude dramatically when just the mass of the restraint system is added or removed. Unfortunately, for the CEA analyses to replicate the observed behavior, Young's modulus had to be reduced by 12 percent. This results in a 6 percent reduction in the first natural frequency. From a practical perspective, this is difficult to justify in light of the consistent modulus measurements made on multiple specimens in both IPIRG-1 and IPIRG-2, see Section 2 in this report. Other mass or stiffness effects might contribute to a frequency shift, but again, these are hard to physically justify.

At this time the CEA analyses offer a theoretically plausible explanation for the Experiment 1-5 observations. However, there is no way to technically justify reducing the elastic modulus of the whole

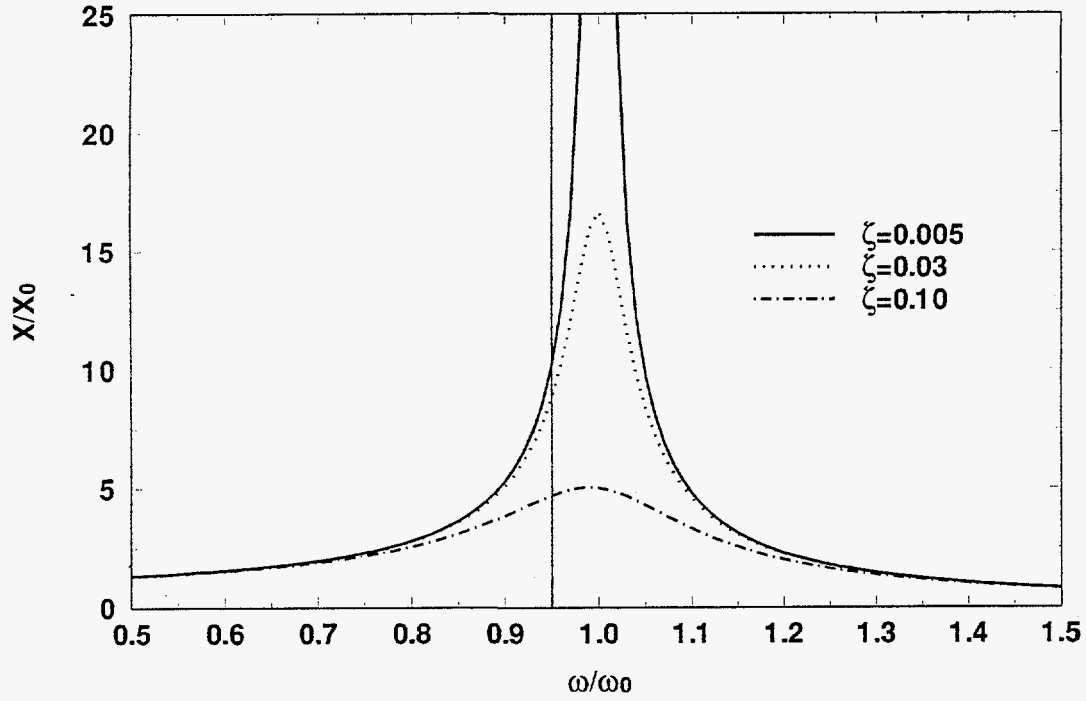

Figure 5.7 Single degree-of-freedom dynamic amplification curves

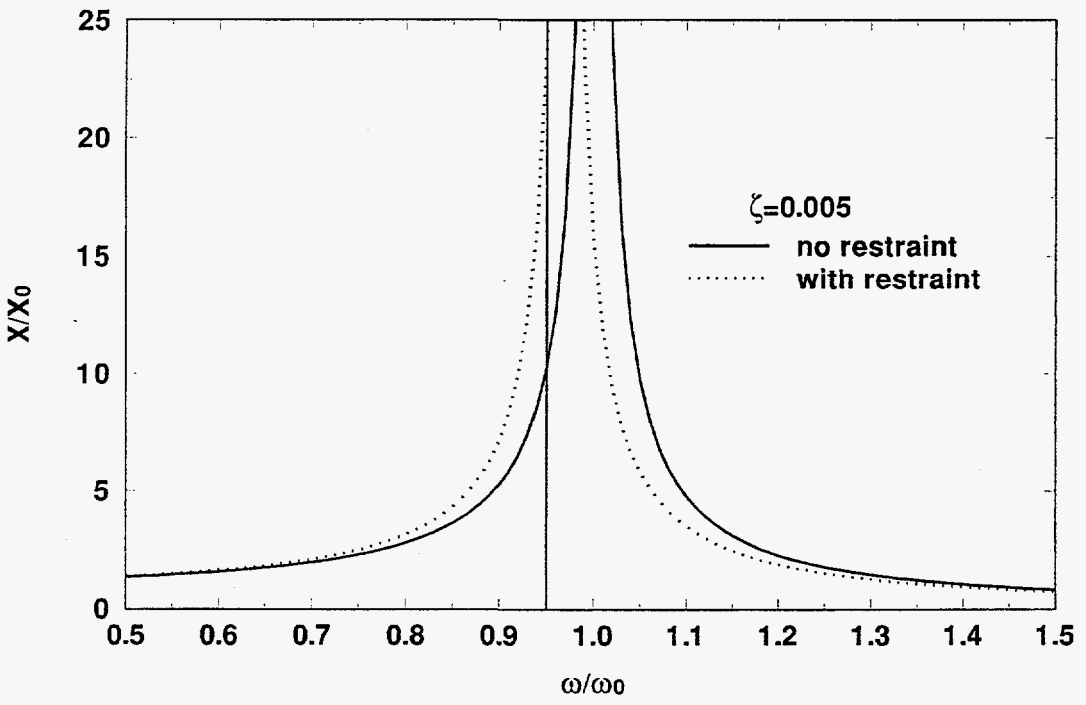

Figure 5.8 Dynamic amplification curves showing the effect of a 3 percent shift of natural frequency

pipe loop. Because such a change is not supported by the measured Young's modulus data, there is a concern that elastic stress ratios calculated using a reduced modulus may not provide an accurate view of the cracked pipe-system behavior. As demonstrated by the Battelle calculations, elastic stress ratios using the measured modulus values are not credible either.

Because there are questions about the validity of the elastic stress ratio for the single-frequency excitation IPIRG-2 experiment where the restraint device was used, there is also, by implication, a question about the validity of the elastic stress ratios for the other experiments that used the restraint device, i.e., the simulated-seismic experiments. As a result, the elastic stress ratio calculations, that were conducted as part of the IPIRG-1 program, may be of questionable value for the IPIRG-2 experiments with the restraint system, and therefore were not calculated or reported for any of the IPIRG-2 pipe-system experiments. Nevertheless, all the supporting data suggest that the experimental results from those experiments are correct, only the FEM boundary conditions, section properties, or material properties are not known well enough. Further attention should be given to this problem.

5.2 Comparisons of Maximum Experimental Stresses with Fracture Analyses Predictions

In this section of the report, the maximum experimental stresses (bending plus axial membrane due to internal pipe pressure) from the nine IPIRG-2 Task 1 pipe experiments, as well as the eight companion pipe experiments from the Degraded Piping (Ref. 5.3), IPIRG-1 (Ref. 5.4), and Battelle/EPRI (Ref. 5.5) programs, will be compared with analytical predictions from various fracture prediction analyses. The fracture analyses methods considered include:

- Simple limit-load analyses such as the Net-Section-Collapse (NSC) analysis (Ref. 5.6),
- Dimensionless-Plastic-Zone-Parameter (DPZP) analysis (Ref. 5.7),
- Various J-estimation scheme analyses such as SC.TNP1 (Ref. 5.8), SC.TNP2 (Ref. 5.9), SC.ENG1 (Ref. 5.9), and SC.ENG2 (Ref. 5.9) for surface-cracked pipe and GE/EPRI (Ref. 5.10), LBB.NRC (Ref. 5.11), and LBB.ENG2 (Ref. 5.12) for through-wall-cracked pipe,
- The ASME Section XI Appendix C approach for austenitic piping (Refs. 5.13 and 5.14), the ASME Section XI Appendix H approach for ferritic piping (Refs. 5.15 and 5.16), the ASME Code Case N-494-3* approach for both austenitic and ferritic piping (Refs. 5.17 and 5.18), and
- The R6 Revision 3 Option 1 method (Refs. 5.19 and 5.20) as programmed in NRCPIPES (Version 3.0).

Details of each of these methods can be found in the appropriate references. The NRCPIPES Computer Code, Version 3.0, was used for all these analyses.

---

* Code Case N-494-3 was approved during the preparation of this report, but was not published at the time this report was completed.

Prior to comparing the experimental stresses with the predictions some of the key input parameters, i.e., flaw size definition and material property data, needed for these analyses need to be discussed.

5.2.1 Crack Size Definitions in Fracture Analyses

In analyzing the Task 1 pipe experiments from IPIRG-2, it was found that the results of the analysis predictions depend greatly on the crack size definition used in the analysis. In this report the term most consistent crack size will be frequently used. In this context "most consistent" crack size is that crack size definition which results in the "most consistent" predictions for the experiments considered in this effort when compared with predictions for a larger set of more controlled experiments (i.e., constant depth, base metal cracks) analyzed during the Short Cracks in Piping and Piping Welds program (Ref. 5.9).

Most of the surface cracks in the Task 1 pipe experiments were fatigue precracked in order to sharpen the machined notch. This was done to eliminate the influence of notch acuity on the results. As a result of this precracking, a number of the resultant cracks were not uniform in depth. Specifically, there were cases where the deepest location along the crack front was not at the crack centerline where the bending stress was the highest. For example, Figure 5.9 is a sketch of the resultant fracture surface for Experiment 1-2, i.e., the carbon steel base metal simulated-seismic pipe system experiment. As can be seen in Figure 5.9, the crack was deeper at a location approximately 33 degrees around the pipe circumference from the crack centerline than it was at the crack centerline location. In addition to this "off-centered crack" phenomenon, there are other realistic crack geometry conditions which must be considered in the fracture analyses.

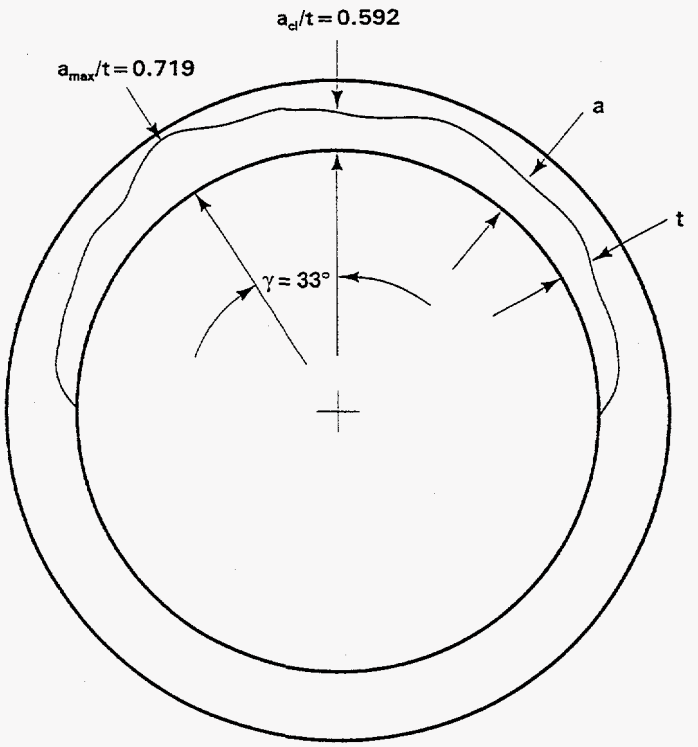

Figure 5.9 Sketch of the resultant fracture surface for Experiment 1-2 showing that the deepest location along the crack was not at the crack centerline

These other geometric conditions typically involve cracks in welds, i.e., how does one account for such effects as weld counterbores and weld crowns. In the sections that follow, the effects of these realistic variables, i.e., off-centered cracks and weld crack geometries, will be considered in a systematic approach by analyzing selected sets of experiments for which these effects are most pronounced. At the end of this discussion, an assessment will be made as to which flaw size definition is most consistent with the findings from the Short Cracks program (Ref. 5.9). Both this "most consistent" definition, along with the ASME Code definition of flaw size, will then be used in all subsequent fracture analyses. By comparing the results of the analyses for the "most consistent" flaw size definition to the results for the ASME Code definition of flaw size, one will be able to assess the inherent margins associated with the ASME Code analyses as a result of its choice of flaw size definition. This comparison will be made later in the Discussion of Results section of this report (Section 6.0).

5.2.1.1 ASME Code Definition of Flaw Size

In Section XI of the ASME Code, Figure IWA-3310-1 provides illustrations of flaw configurations for determining the flaw dimensions "a" (depth) and "l" (length) of surface planar flaws oriented in plane normal to the pressure retaining surface, see Figure 5.10. As shown in Figure 5.10, and further stated in IWA-3300 of Section XI, the flaws shall be sized by the bounding rectangle for the purpose of description and dimensioning. The dimensions of a flaw shall be determined by the size of a rectangle that fully contains the area of the flaw. Consequently, for the assessment of the experiments conducted as part of this effort, the ASME Code definition conservatively assumes that the flaw has a uniform depth and that depth is the depth of the flaw at its deepest location and that the flaw length is the total flaw length. As

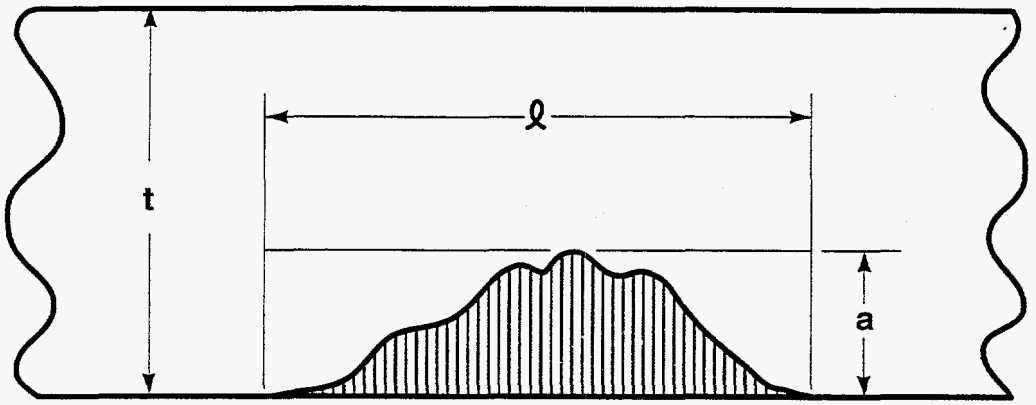

Figure 5.10 Illustration of ASME Section XI method of defining the flaw dimensions for an in-service flaw evaluation

illustrated in Figure 5.11, which compares the ASME flaw size definition with the actual flaw dimensions for Experiment 1-2, the ASME Code approximation of the flaw size can significantly overestimate the severity of the actual flaw shape. As can be seen in Figure 5.11, not only is the flaw for Experiment 1-2 not uniform in depth, but the deepest segment of the flaw is at a location where the bending stress is considerably less than the bending stress at the flaw centerline where the bending stress is highest.

5.2.1.2 Effect of Off-Centered Cracks

In order to evaluate the effect of off-centered cracks, three experiments with cracks in an A106 Grade B (CSBM) pipe (DP2-F29) were analyzed in detail. The three experiments were Experiment 4112-8 from the Degraded Piping program (Ref. 5.3), Experiment 1.3-2 from the IPIRG-1 program (Ref. 5.4), and Experiment 1-2 from this program. Experiments 4112-8 and 1.3-2 had fairly uniform, symmetric, surface-crack geometries while Experiment 1-2 had a surface-crack geometry which was deeper at a location approximately 100 mm (4 inches) around the pipe circumference from the crack centerline than it was at the crack centerline, see Figure 5.9.

In order to examine the effect of off-centered cracks, the fracture ratios for Experiments 4112-8, 1.3-2, and 1-2 were calculated and compared. The fracture ratios, which is the ratio of the maximum experimental stress (bending stress plus pressure-induced membrane stress) to the maximum predicted stress (bending stress plus pressure-induced membrane stress), were calculated using three analysis methods, i.e., DPZP, SC.TNP1, and SC.TNP2. The DPZP and SC.TNP1 analysis methods were chosen because they were found to be the most accurate of the various analysis methods considered when compared with

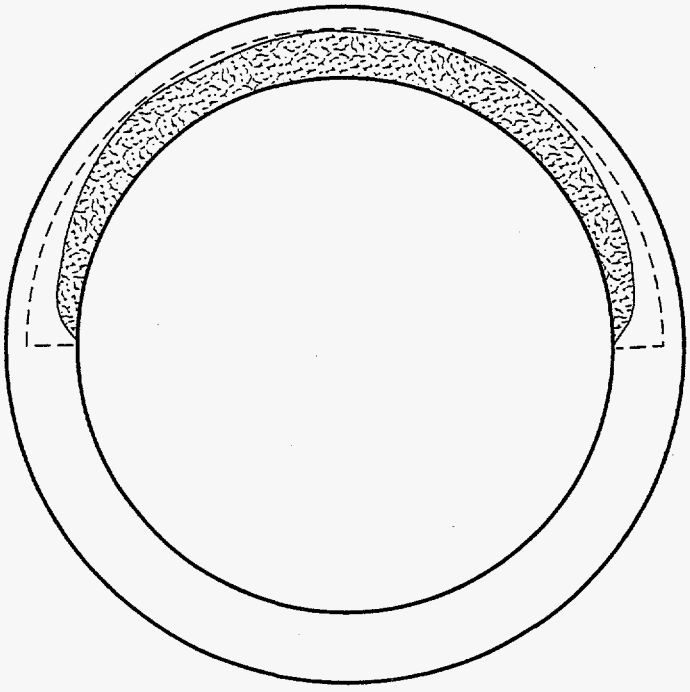

Figure 5.11 Comparison of the ASME flaw size definition with the actual flaw dimensions for Experiment 1-2

experimental data during the Short Cracks in Piping and Piping Welds program (Ref. 5.9). The SC.TNP2 analysis method was chosen because it was found to be the best predictor of J during the Short Cracks in Piping and Piping Welds program (Ref. 5.9). Table 5.1 lists the input parameters used in these analyses.

Table 5.1 Input parameters used in analysis of the effect of off-centered cracks on the fracture analysis predictions

Experiment No.	Outside Diameter, mm	Wall Thickness, mm	θ/π[1]	Pipe Pressure, MPa	Off-Center Crack Angle (ψ)[2], degrees
4112-8	402.6	26.4	0.532	0	0
1.3-2	403.9	25.7	0.525	15.5	0
1-2	405.1	24.8	0.525	15.5	33

(1) θ measured on inside surface.
(2) Angle between location where crack is deepest and crack centerline.

For each of the analysis conducted as part of this assessment, the crack length was defined as the total crack length on the inside pipe surface. Three different sets of assumptions of crack depth and bending stress were considered in these analyses. For each of these sets of assumptions, the surface crack depth was assumed to be constant for the entire length of the surface crack. The first set assumed that the surface-crack depth was the depth of the surface crack at the crack centerline location ($a = a_{cl}$), i.e., at the location of the highest bending stress. The second set assumed that the surface-crack depth was the depth of the surface crack at the location where the crack was the deepest ($a = a_{max}$). The third set of assumptions also assumed that the surface-crack depth was equal to a_{max}, but the experimental applied bending stress term in the numerator of the fracture ratio was reduced by a $\cos(\psi)$ term, where the angle ψ is the angle between the centerline of the crack and the location where the crack is the deepest. This $\cos(\psi)$ term was applied to account for the fact that the applied bending stress at the location where the crack was the deepest was reduced as a result of the distance between this point and the neutral bending axis being reduced by the factor $\cos(\psi)$. For the first two sets of assumptions, the total applied bending stress was used in the fracture ratio calculations.

In addition, three sets of material property data were to be used in these analyses. The first series of analyses used the quasi-static stress-strain curves and quasi-static J-R curves in the analyses of all three experiments. The second set of analyses used the dynamic stress-strain and dynamic J-R curves in the analyses of the two dynamically loaded pipe experiments. The final set of analyses used the quasi-static stress-strain curves and dynamic J-R curves in the analyses of the dynamically loaded pipe experiments. This final set of analyses was considered in that results from the Japanese pipe tests conducted as part of the IPIRG-2 program (Ref. 5.21) indicated that there was minimal difference in the experimental load-displacement records between the quasi-static, monotonic and dynamic, monotonic Japanese pipe experiments, see Figure 5.12, even though there was a substantial decrease in the dynamic stress-strain curve for this pipe material when compared with the quasi-static stress-strain curve, see Figure 5.12b. One possible explanation for this behavior is that the calculated strain rate in the uncracked pipe for the dynamically loaded pipe experiments (approximately 10^{-3}/s) is approximately three orders of magnitude slower than the strain rate for the high speed tensile tests conducted on this material (approximately 1/s), and one order of magnitude faster than the strain rate for the quasi-static tensile tests conducted on this material (approximately 10^{-4}/s). Similarity, the calculated strain rate in the uncracked pipe for the carbon

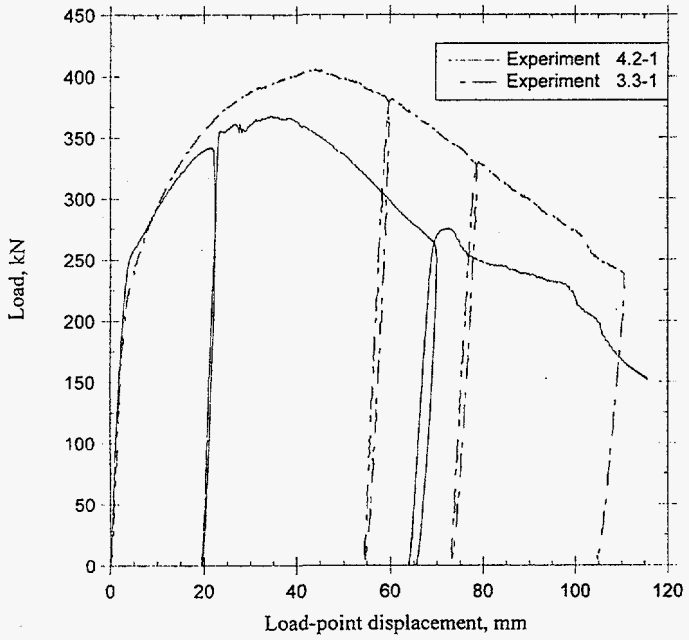

(a) Load-displacement data from pipe experiments

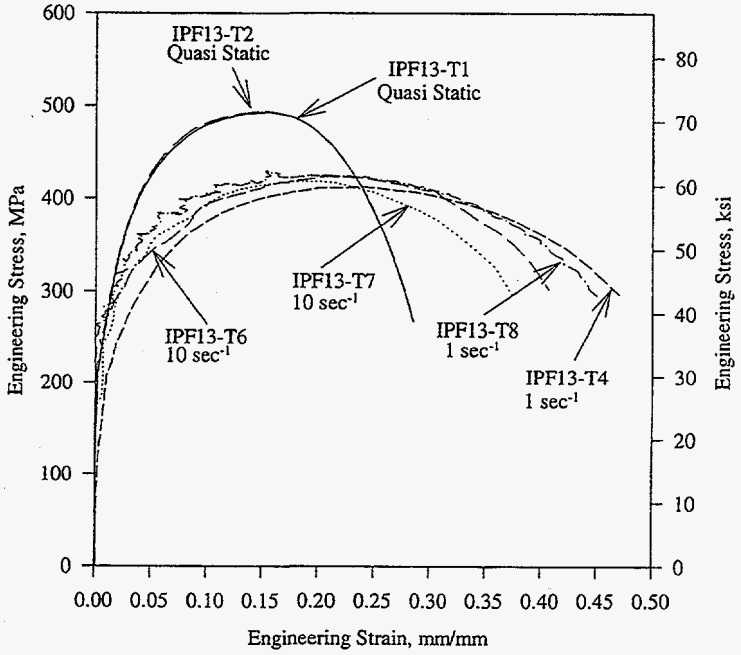

(b) Stress-strain data

Figure 5.12 Comparisons of load-displacement curves for the quasi-static, monotonic, Japanese STS410 carbon steel pipe experiment (3.3-1) and the dynamic, monotonic, STS410 pipe experiment (4.2-1) and comparisons of quasi-static and dynamic stress-strain data for this STS410 carbon steel material

steel simulated-seismic pipe system experiment (Experiment 1-2) was approximately 10^{-2}/s which is approximately two orders of magnitude slower than the strain rate for the slower high speed tensile test conducted on this material (approximately 1/s), and approximately two orders of magnitude faster than the strain rate for the quasi-static tensile tests conducted on this material (approximately 10^{-4}/s). In order to fill this gap in the material database, two additional "intermediate speed" tensile tests with a strain rate of 10^{-2}/s and a test temperature of 288 C (550 F) were conducted on this carbon steel pipe material. Regardless of the choice of material data, the flow stress used in the analyses was defined as the average of the yield and ultimate strengths. The effect of using other definitions for flow stress, e.g., $2.4S_m$ or $3S_m$ will be discussed later.

Table 5.2 shows the results from those intermediate strain-rate tensile tests. Also shown in Table 5.2 are the summary results from the quasi-static and dynamic tensile tests previously conducted. As can be seen in Table 5.2, there is little change in yield strength with strain rate, but there is a large effect on the ultimate strength. The ultimate strength for the intermediate strain rate tensile tests is about 10 percent less than the ultimate strength for the quasi-static loading rate tests and about 10 percent greater than the ultimate strength for the slower dynamic loading rate tensile tests, i.e., 1/s. As a result of this finding, a fourth set of material data were used in the analyses of these dynamic carbon steel base metal (DP2-F29) experiments, i.e., Experiments 1.3-2 and 1-2. This fourth series of analyses used the intermediate strain-rate stress-strain curves and the dynamic J-R curves.

Table 5.2 Comparison of intermediate strain-rate (10^{-2}/s) tensile test results test results with quasi-static and dynamic strain-rate tensile test results

Material	Strain Rate, 1/s	Yield Strength, MPa	Yield Strength, ksi	Ultimate Strength, MPa	Ultimate Strength, ksi
DP2-F29	$2x10^{-4}$	241	34.9	618	89.7
DP2-F29	$2.6x10^{-2}$	236	34.2	554	80.4
DP2-F29	1	235	34.1	503	72.9
DP2-F29	10	234	34.0	443	64.2

The results of all of these analyses are shown in Table 5.3 and Figures 5.13 through 5.15. Figure 5.13 shows the results for the Dimensionless-Plastic-Zone-Parameter analysis, Figure 5.14 shows the results for the SC.TNP1 analysis, and Figure 5.15 shows the results from the SC.TNP2 analysis. The results for each analysis method are very similar. As a result, discussion will be limited to the DPZP analysis method, see Figure 5.13. In Figure 5.13, the solid horizontal line represents the mean value of the fracture ratio for 16 combined pressure and bend, surface-cracked-pipe, fracture experiments analyzed as part of the Short Cracks program (Ref. 5.9). The mean value of the fracture ratios for these 16 experiments was 1.05. The dashed horizontal lines represent the mean value plus or minus one standard deviation from the mean value. The standard deviation for the DPZP analysis method was found to be 0.13 for these 16 combined pressure and bend experiments. The dotted horizontal lines in Figure 5.13 represent the mean value plus or minus two standard deviations from the mean value. Plus or minus two standard deviations is approximately the same as a 95-percent confidence band on the data. As can be seen in reviewing Figure 5.13, when the quasi-static four-point bend experiment (4112-8) was analyzed using quasi-static material data, the fracture ratio was within the mean plus or minus one standard deviation interval.

When the pipe system experiment from IPIRG-1 (1.3-2) was analyzed, it was found that the fracture ratio for this experiment was highly dependent on the material property data chosen for the analysis.

If quasi-static data were chosen for analysis, then the calculated fracture ratio was more than two standard deviations below the mean value for this analysis method. (The same finding was true for the SC.TNP1 analysis method, see Figure 5.14). This is not surprising since the carbon steel pipe material used in this set of experiments was a material highly sensitive to dynamic strain aging effects (Ref. 5.27). As such, both the strength and toughness of this material decreased dramatically with increasing strain rate. If the dynamic J-R curve was used in the analysis, then the calculated fracture ratios were easily within the mean value plus or minus two standard deviation band for this analysis method regardless of the stress-strain curve chosen for analysis.

Table 5.3 Results of analysis of the effect of off-centered cracks on the fracture analysis predictions

Case No.	Experiment No.	Crack Depth	σ-ϵ[1] Curve	J-R[1] Curve	Analysis Method	Fracture[2] Ratio	Adjusted[3] Fracture Ratio
1	4112-8	$a_{cl} = a_{max}$	QS	QS	DPZP	0.935	NA[4]
2	1.3-2	$a_{cl} = a_{max}$	QS	QS	DPZP	0.742	NA
3	1.3-2	$a_{cl} = a_{max}$	10/s	Dyn	DPZP	1.003	NA
4	1.3-2	$a_{cl} = a_{max}$	QS	Dyn	DPZP	0.876	NA
5	1.3-2	$a_{cl} = a_{max}$	$2.6x10^{-2}$/s	Dyn	DPZP	0.913	NA
6	1-2	a_{cl}	10/s	Dyn	DPZP	0.989	NA
7	1-2	a_{cl}	QS	Dyn	DPZP	0.872	NA
8	1-2	a_{cl}	$2.6x10^{-2}$/s	Dyn	DPZP	0.906	NA
9	1-2	a_{max}	10/s	Dyn	DPZP	1.289	1.136
10	1-2	a_{max}	QS	Dyn	DPZP	1.124	0.991
11	1-2	a_{max}	$2.6x10^{-2}$/s	Dyn	DPZP	1.172	1.033
12	4112-8	$a_{cl} = a_{max}$	QS	QS	SC.TNP1	1.021	NA
13	1.3-2	$a_{cl} = a_{max}$	QS	QS	SC.TNP1	0.783	NA
14	1.3-2	$a_{cl} = a_{max}$	10/s	Dyn	SC.TNP1	1.155	NA
15	1.3-2	$a_{cl} = a_{max}$	QS	Dyn	SC.TNP1	0.903	NA
16	1.3-2	$a_{cl} = a_{max}$	$2.6x10^{-2}$/s	Dyn	SC.TNP1	1.146	NA
17	1-2	a_{cl}	10/s	Dyn	SC.TNP1	1.188	NA
18	1-2	a_{cl}	QS	Dyn	SC.TNP1	0.943	NA
19	1-2	a_{cl}	$2.6x10^{-2}$/s	Dyn	SC.TNP1	1.187	NA
20	1-2	a_{max}	10/s	Dyn	SC.TNP1	1.480	1.303
21	1-2	a_{max}	QS	Dyn	SC.TNP1	1.155	1.018
22	1-2	a_{max}	$2.6x10^{-2}$/s	Dyn	SC.TNP1	1.467	1.292
23	4112-8	$a_{cl} = a_{max}$	QS	QS	SC.TNP2	1.310	NA
24	1.3-2	$a_{cl} = a_{max}$	QS	QS	SC.TNP2	1.022	NA
25	1.3-2	$a_{cl} = a_{max}$	10/s	Dyn	SC.TNP2	1.534	NA
26	1.3-2	$a_{cl} = a_{max}$	QS	Dyn	SC.TNP2	1.182	NA
27	1.3-2	$a_{cl} = a_{max}$	$2.6x10^{-2}$/s	Dyn	SC.TNP2	1.471	NA
28	1-2	a_{cl}	10/s	Dyn	SC.TNP2	1.524	NA
29	1-2	a_{cl}	QS	Dyn	SC.TNP2	1.197	NA
30	1-2	a_{cl}	$2.6x10^{-2}$/s	Dyn	SC.TNP2	1.473	NA
31	1-2	a_{max}	10/s	Dyn	SC.TNP2	1.970	1.735
32	1-2	a_{max}	QS	Dyn	SC.TNP2	1.513	1.333
33	1-2	a_{max}	$2.6x10^{-2}$/s	Dyn	SC.TNP2	1.883	1.659

(1) QS = quasi-static, Dyn = dynamic.
(2) Fracture ratio = $(\sigma_{B_{expt}} + \sigma_m) / (\sigma_{B_{analysis}} + \sigma_m)$.
(3) Adjusted fracture ratio = $(\sigma_{B_{expt}} \cos\psi + \sigma_m) / (\sigma_{B_{analysis}} + \sigma_m)$.
(4) NA = not applicable.

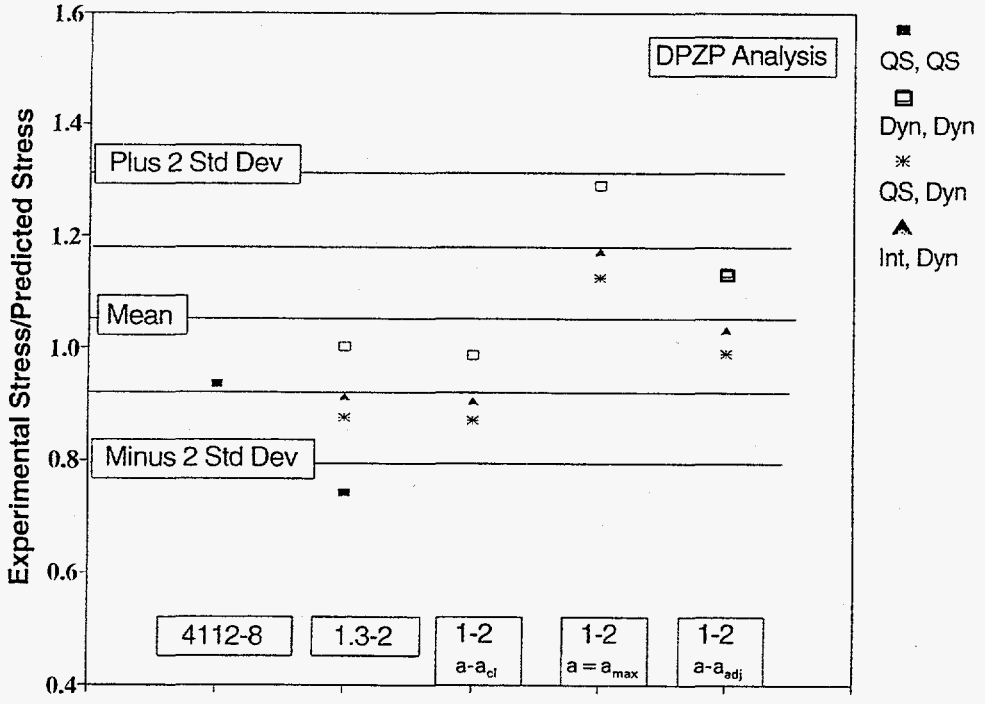

Figure 5.13 Results of "off-centered" crack analysis using Dimensionless-Plastic-Zone-Parameter analysis

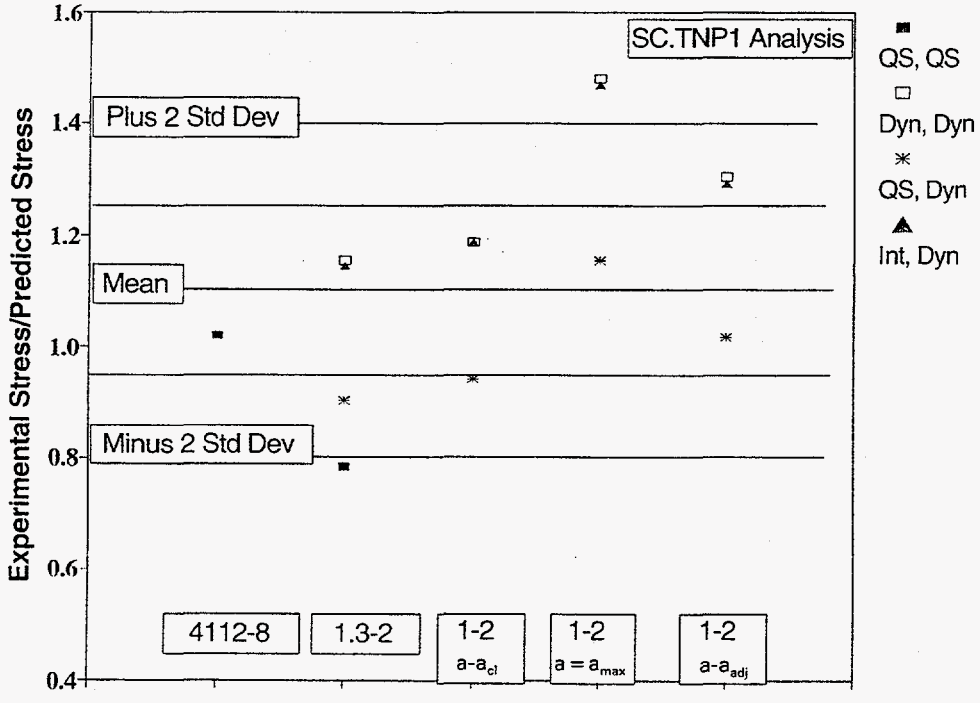

Figure 5.14 Results of "off-centered" crack analysis using SC.TNP1 analysis

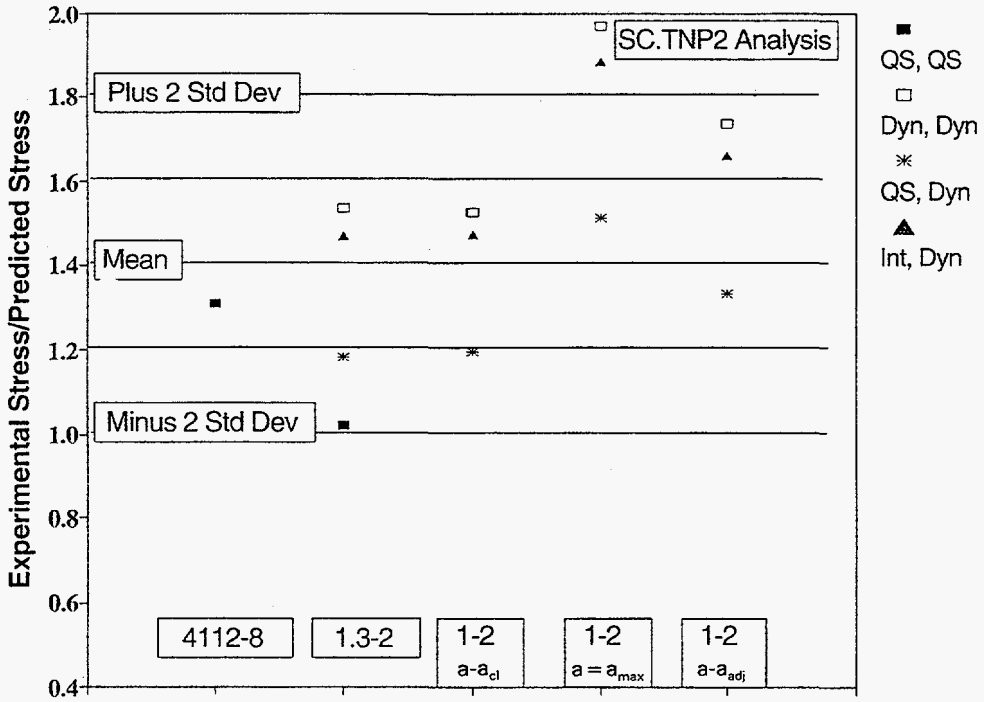

Figure 5.15 Results of "off-centered" crack analysis using SC.TNP2 analysis

When simulated-seismic pipe system Experiment 1-2 from IPIRG-2 was analyzed, a number of crack depth and applied stress combinations were considered. Experiment 1-2 was the one experiment from this set of three which had a significant off-center crack. The other two experiments (4112-8 and 1.3-2) were fairly uniform in depth. Consequently, by considering the different combinations of crack depth and applied stress, in light of the results from the other two experiments, it may be possible to make an assessment of which crack size definition is most consistent for analyzing off-center cracks. Based on the results from Experiment 1.3-2, it was concluded that there was no need to consider the case where the quasi-static J-R curve was used in the analyses of this dynamic experiment. As a result, the analyses of Experiment 1-2 are limited to the cases where the dynamic J-R curve was used. If examining Figure 5.13, it can be seen that the overall best agreement with the data developed previously is for the case where the intermediate-strain-rate stress-strain curve is used along with the dynamic J-R curve and the crack depth is defined as the crack depth at its deepest location (i.e., $a = a_{max}$) and the applied stress is reduced by the term $\cos(\psi)$ to account for the fact that the crack is an off-center crack.

Note, however, that the results for the case when the quasi-static stress-strain curve is used, in conjunction with the same J-R curve (i.e., dynamic), crack depth definition, and applied stress term, are not that different than the results for the case when the intermediate strain-rate stress-strain curve is used. Consequently, since no intermediate strain rate tensile data exist for the other materials, it was decided for the sake of consistency that for the subsequent analysis of dynamically-loaded experiments that the quasi-static strain rate stress-stain data and dynamic J-R curve data would be used. Furthermore, for experiments which involved a crack that was significantly "off-centered", the maximum crack depth would be used for the analysis, but the applied experimental stress would be reduced by the $\cos(\psi)$ term to account for the off-center crack.

5.2.1.3 Effect of Weld Geometry

In order to evaluate the effect of weld geometry on the calculated fracture ratios, a set of four experiments with cracks in a stainless steel submerged-arc weld (SAW) were analyzed in detail. The four experiments were Experiment 4141-4 from the Degraded Piping program (Ref. 5.3), Experiment 1.3-5 from IPIRG-1 (Ref. 5.4), and Experiments 1-5 and 1-6 from this program. In each case, the depth of the crack at the crack centerline was nearly as deep as the depth of the crack at the deepest location of the crack. Consequently, there was no need to consider the effect of off-centered cracks as discussed above. This greatly simplified this analysis.

The SC.TNP1 analysis procedure was used exclusively to calculate the fracture ratios for this comparative analysis. For each of the individual analyses conducted as part of this assessment, the crack length was defined as the total crack length on the inside pipe surface. Table 5.4 lists the input data used in each of these analyses. Figure 5.16 is a schematic of the weld geometry used for these stainless steel submerged-arc weld experiments. Four different sets of assumptions of crack depth and wall thickness were considered. Each set of assumptions assumed that the surface-crack depth was constant for the entire length of the surface crack.

Table 5.4 Input parameters used in analysis of the effect of the weld geometry on the fracture analysis predictions

Experiment No.	Outside Diameter, mm	Pipe Pressure, MPa	θ/π (1)	a_2/t_2 (2)	a_1/t_1 (2)	a_1/t_3 (2)	a_2/t_4 (2)
4141-4	413.5	11.0	0.50	0.633	0.668	0.613	0.575
1.3-5	416.1	15.5	0.532	0.574	0.627	0.601	0.548
1-5	415.3	15.5	0.267	0.427	0.495	0.442	0.376
1-6	412.8	15.5	0.27	0.649	0.687	0.620	0.578

(1) θ = maximum value on inside surface.
(2) See Figure 5.16.

- The first set assumed that the wall thickness was the nominal wall thickness of the pipe less the depth of the counterbore (t_2 in Figure 5.16), and that the surface crack depth was the depth of the crack with respect to the inside surface of the counterbore (a_2 in Figure 5.16). This set seems to be the set most closely aligned with the spirit of the ASME Code in that Paragraph NB-3641.1 of Section III specifies that "the wall thickness 't' is the specified or actual wall thickness of the pipe minus material removed by counterboring, among other things."

- The second set of assumptions assumed that the wall thickness was the nominal wall thickness of the pipe (t_1), and the crack depth was the depth of the crack with respect to the inside surface of the nominal pipe (a_1).

- The third set assumed that the wall thickness was the nominal wall thickness of the pipe plus the weld crown height (t_3), and the crack depth was the depth of the crack with respect to the inside surface of the pipe (a_1).

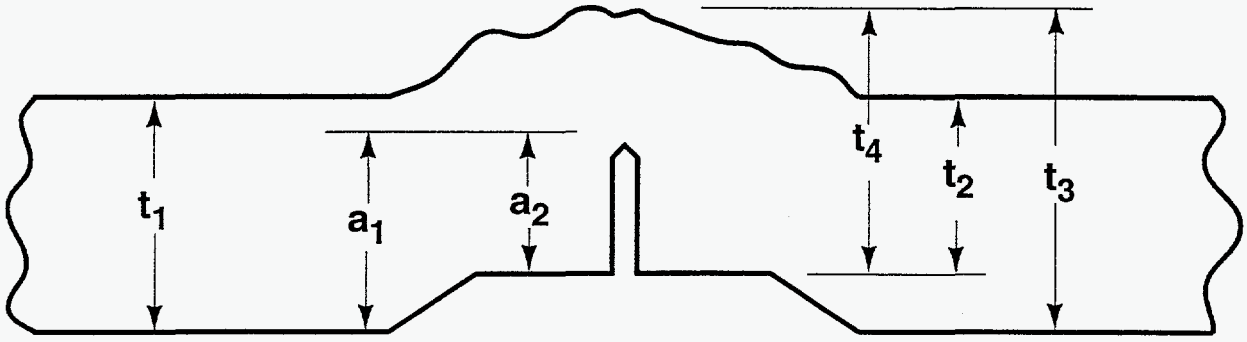

Figure 5.16 Schematic of the weld geometry used for the stainless steel submerged-arc weld (SAW) experiments

- The fourth set assumed that the wall thickness was the nominal wall thickness of the pipe plus the weld crown height but less the depth of the counterbore (t_4), and the crack depth was the depth of the crack with respect to the inside surface of the counterbore region (a_2).

By comparing the results for the first set of assumptions to the second and the third set to the fourth, one can make an assessment of the effect of the counterbore on the fracture analyses. By comparing the results for the first set of assumptions to the fourth, and the second set to the third, one can make an assessment of the effect of the weld crown height on the fracture analyses.

For this comparative analysis, the quasi-static stress-strain curve of the base metal and the quasi-static J-R curve for the weld metal were used in the analyses of the two quasi-static bend experiments (4141-4 and 1-6), and the quasi-static stress-strain curve for the base metal and the dynamic J-R curve for the weld metal were used in the analyses of the two dynamic pipe system experiments (1.3-5 and 1-5). This combination of material property data seemed to be most consistent from the off-center crack analysis discussed previously in Section 5.2.1.2. The results of the fracture ratio analyses for the four experiments under consideration for the four sets of assumed wall thickness and crack depth definitions for this set of material property data are presented in Table 5.5 and Figure 5.17.

As was the case for Figures 5.13 through 5.15, the solid horizontal line represents the mean value of the fracture ratios for the 16 combined pressure and bend pipe fracture experiments analyzed as part of the Short Cracks program (Ref. 5.9). The mean value of the fracture ratios for the SC.TNP1 analysis for these

Table 5.5 Results of analysis of the effect of weld geometry on the fracture analysis predictions

Case No.	Experiment No.	Crack[1] Depth	Wall[1] Thickness	σ-ϵ Curve	J-R Curve	Fracture[2] Ratio
1	4141-4	a_2	t_2	QS	QS	1.318
2	4141-4	a_1	t_1	QS	QS	1.268
3	4141-4	a_1	t_3	QS	QS	1.082
4	4141-4	a_2	t_4	QS	QS	1.113
5	1-6	a_2	t_2	QS	QS	1.372
6	1-6	a_1	t_1	QS	QS	1.288
7	1-6	a_1	t_3	QS	QS	1.117
8	1-6	a_2	t_4	QS	QS	1.184
9	1.3-5	a_2	t_2	QS	Dyn	1.255
10	1.3-5	a_1	t_1	QS	Dyn	1.210
11	1.3-5	a_1	t_3	QS	Dyn	1.111
12	1.3-5	a_2	t_4	QS	Dyn	1.145
13	1-5	a_2	t_2	QS	Dyn	1.192
14	1-5	a_1	t_1	QS	Dyn	1.081
15	1-5	a_1	t_3	QS	Dyn	0.981
16	1-5	a_2	t_4	QS	Dyn	1.034

(1) See Figure 5.16.
(2) Maximum moment predictions based on SC.TNP1 method.

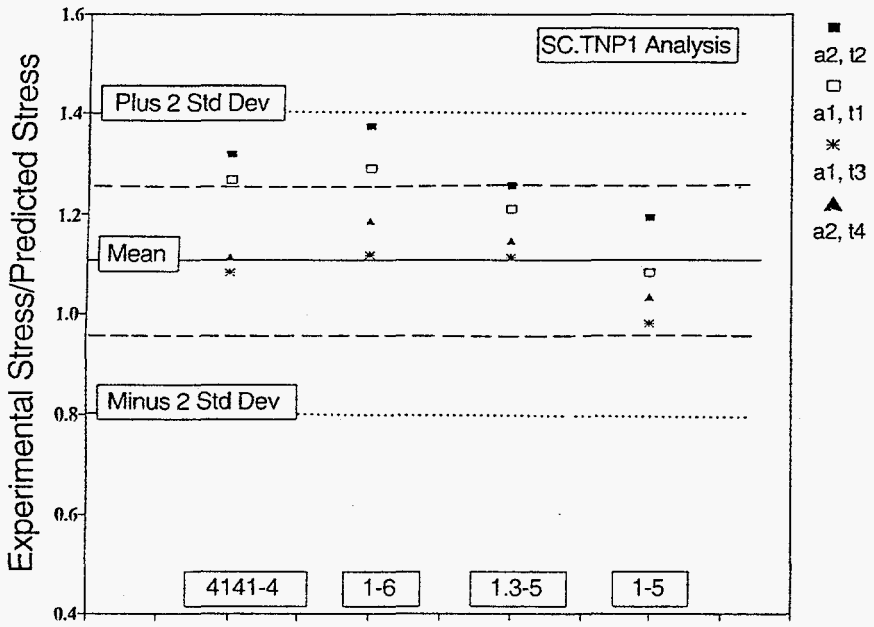

Figure 5.17 Results of weld geometry analysis using SC.TNP1 analysis using quasi-static stress-strain and quasi-static J-R curve data to analyze the quasi-static experiments (4141-4 and 1-6) and quasi-static stress-strain and dynamic J-R curve data to analyze the dynamic experiments

16 experiments is 1.10. The dashed horizontal lines represent the mean value plus or minus one standard deviation from the mean value. The standard deviation for the SC.TNP1 analysis method was found to be 0.15 for these 16 combined pressure and bend experiments. The dotted horizontal line in Figure 5.14 represents the mean value plus two standard deviations from the mean value.

As can be seen in Figure 5.17, if one assumes that the wall thickness is the wall thickness of the pipe less the depth of the counterbore (t_2 in Figure 5.16) and that the surface-crack depth is the depth of the crack with respect to the inside surface of the counterbore (a_2 in Figure 5.16), then the calculated fracture ratios are significantly higher than the mean value established previously for the SC.TNP1 analyses for combined pressure and bending experiments (Ref. 5.9). As alluded to earlier, this combination of wall thicknesses and crack depths seems to be most closely aligned with the spirit of the ASME Code. This finding illustrates the relative conservatism of the ASME approach.

The most consistent of the four sets of wall thickness/flaw size definitions considered in Figure 5.17 (at least when compared with the mean value established previously for the SC.TNP1 approach) appears to be when the wall thickness is defined as the wall thickness of the pipe plus the weld crown height (t_3 in Figure 5.16) and the crack depth is defined as the depth of the crack with respect to the inside surface of the pipe (a_1 in Figure 5.16). Applying this set of wall thicknesses and flaw depths to the four experiments considered as part of this exercise resulted in calculated fracture ratios which were consistently within one standard deviation of the previously established mean value for all four of the experiments considered.

5.2.1.4 Effect of Crack Length Definition

In order to evaluate the effect of the crack length definition, i.e., total crack length versus equivalent crack length, a set of eight pipe fracture experiments were analyzed using the SC.TNP1 analysis method. Seven of the eight experiments were conducted as part of the IPIRG-1 and IPIRG-2 programs. The eighth experiment was Experiment EPRI 13S from the previously conducted Battelle/EPRI program (Ref. 5.5). For each experiment both the total and equivalent crack length were reported in the documentation for the experiments. The equivalent crack length is defined as the total crack area divided by the maximum crack depth. The maximum moments and fracture ratios, i.e., the ratio of the maximum experimental stress (bending plus membrane stress due to the internal pipe pressure) to the maximum predicted stress (bending plus membrane stress due to the internal pipe pressure), for each of these experiments are shown in Table 5.6 for both the case when the crack length used in the SC.TNP1 analysis is based on the total crack length and when it is based on the equivalent crack length. Note, for the analysis of the weld experiments in Table 5.6 the wall thickness was assumed to be wall thickness of the pipe plus the weld crown height (t_3 in Figure 5.16) and the crack depth was taken to be the depth of the crack with respect to the inside surface of the pipe (a_1 in Figure 5.16). As can be seen in Table 5.6, on average the SC.TNP1 predictions based on the total crack length definition are closer to the experimental results than the SC.TNP1 predictions based on the equivalent crack length. In fact, using the SC.TNP1 analysis method and the equivalent crack length overpredicts the experimental values by an average of approximately 7 percent.

5.2.1.5 "Most Consistent" Flaw Size Definition

Based on the above discussion, the "most consistent" definition of flaw size to be used in the subsequent fracture ratio analyses is the total crack length and the maximum crack depth, but the experimentally applied bending stress will be reduced by the cosine of the angle between the maximum crack depth location and the crack centerline location if the crack is not symmetric, i.e., the maximum crack depth is

Table 5.6 Results of analysis of the effect of crack length definition on the fracture analysis predictions

Expt. No.	Crack Location[1]	Loading Conditions	Outside Diameter, mm	Wall Thickness, mm	Total Crack Length			Equivalent Crack Length		
					θ/π	M_{max}[3] kN-m	Fracture Ratio	θ/π	M_{max}[3] kN-m	Fracture Ratio
1.3-2	CSBM	Single frequency	403.9	25.70	0.525	395.8	0.903	0.439	453.4	0.819
1.3-4	CSW	Single frequency	402.6	25.48	0.535	702.2	0.902	0.481	717.9	0.886
EPRI 13S	SSBM	QS 4-Pt Bend[2]	413.5	28.32	0.580	1251	1.008	0.475	1272	0.991
1.3-3	SSBM	Single frequency	415.8	26.19	0.552	500.6	0.890	0.468	529.9	0.854
1-1	SSBM	Simulated seismic	417.1	25.53	0.527	598.6	0.999	0.383	713.5	0.871
1.3-5	SSW	Single frequency	416.1	25.68	0.532	425.4	1.111	0.442	460.7	1.050
1-5	SSW	Single frequency	415.3	25.76	0.267	794.8	0.981	0.228	847.8	0.930
1-6	SSW	QS 4-Pt bend	412.7	25.65	0.270	605.8	1.117	0.230	662.5	1.041
						Avg.	0.989			0.930
						Std. Dev.	0.084			0.082

(1) CSBM = Carbon steel base metal; CSW = Carbon steel weld; SSBM = Stainless steel base metal; SSW = Stainless steel weld.
(2) Ambient temperature, unpressurized experiment; all other experiments 288 C (550 F) temperature and 15.5 MPa (2,250 psi) pressure.
(3) Maximum predicted moment from SC.TNP1 analysis using quasi-static stress-strain and quasi-static J-R curve data for the quasi-static experiments and quasi-static stress-strain and dynamic J-R curve data for the dynamic experiments.

off-centered. If the experiment under consideration is an experiment for which the crack is in a weld, then the wall thickness will be taken to be the wall thickness of the pipe plus the weld crown height (t_3 in Figure 5.16) and the crack depth will be the depth of the crack with respect to the inside surface of the pipe wall (a_1 in Figure 5.16). By using this "most consistent" definition of flaw size in the subsequent fracture analyses, one will be able to make a fairer comparison of fracture ratios between experiments in order to better answer such questions as "What effect does seismic loading have on the fracture behavior?" and "What is the effect of long versus short crack lengths?"

In addition, by comparing the results for the "most consistent" and "ASME" flaw size definitions for the same experiments, one can begin to appreciate the degree of conservatism associated with invoking the idealized ASME constant depth flaw size definition on realistic flaw shapes such as occurred in some of the experiments considered as part of this effort. Such a comparison will be made in Section 6.0.

5.2.2 Material Property Data to be Used in Fracture Analyses

As discussed in Section 5.2.1.2, quasi-static tensile and quasi-static J-R curves will be used in the analyses of the quasi-statically loaded pipe experiments. For the dynamic experiments, quasi-static tensile data, and dynamic J-R curve data will be used.

5.2.2.1 Tensile Data

For the limit-load (i.e., Net-Section-Collapse) or modified limit-load (i.e., Dimensionless-Plastic-Zone-Parameter) analyses, the tensile property required is the flow stress of the material. The flow stress for these analyses has been defined as the average of the yield and ultimate strengths at the test temperature under consideration. For the ASME Section XI Code approaches, i.e., IWB-3640 and Appendix C for austenitic steels and IWB-3650 and Appendix H for ferritic steels, the flow stress has been defined as $3S_m$ and $2.4S_m$, respectively, per Section XI procedures. The ASME Code Design Stress Intensity (S_m) has been defined to be the S_m values from Table 2A of Part D of Section II of the 1995 Edition of the ASME

Code, i.e., S_m(Code), or in the spirit of the Code using the criteria specified in Article 2110 of Appendix III of Section III Division 1 of the 1989 Edition of the ASME Code, i.e., S_m(Actual). The S_m(Code) definition provides a direct comparison of the experiments to the ASME Code procedures. The S_m(Actual) definition was used to evaluate the technical basis of the Code procedures and is an attempt to analyze the pipe experiments as if the pipes used had the minimum properties defined in Section II from the ASME Code. In this manner, it was possible to account for the fact that each of the pipes tested in this program had different strength values relative to the Code specified values. The term S_m(Actual) was calculated using the actual quasi-static tensile properties of the pipes tested adhering to the spirit of Article 2110 of Appendix III Division 1 of Section III of the 1989 Edition of the Code as the lowest of:

(1) One-third of the actual room temperature ultimate tensile strength (for both ferritic and austenitic pipes),

(2) One-third of the actual ultimate tensile strength at the pipe test temperature (for both ferritic and austenitic pipes),

(3) Two-thirds of the actual yield strength at room temperature (for both ferritic and austenitic pipes), and

(4) Two-thirds of the actual yield strength at the pipe test temperature (for ferritic pipes), or 90 percent of the actual yield strength at the pipe test temperature (for austenitic pipes).

For the J-estimation schemes considered, i.e., SC.TNP1, SC.TNP2, SC.ENG1, and SC.ENG2, for the surface-cracked pipe experiments and GE/EPRI, LBB.NRC, and LBB.ENG2, for the through-wall-cracked pipe experiments, and for the R6 analysis method, the material stress-strain behavior was needed for the analyses. This stress-stain behavior was modeled using a Ramberg-Osgood relationship, see Equation 5-3.

$$\epsilon/\epsilon_o = \sigma/\sigma_o + \alpha \left(\sigma/\sigma_o\right)^n \qquad (5\text{-}3)$$

where

σ = Stress
σ_o = Reference stress
ϵ = Strain
ϵ_o = Reference strain
α = Ramberg-0sgood parameter
n = Strain-hardening exponent.

The Ramberg-Osgood equation was fit to the engineering stress-strain curve data in the range of 0.1 percent strain to the strain corresponding to 80 percent of the ultimate strength. The fit of the stress-strain data to the Ramberg-Osgood equation was made using a Battelle-written computer program, ROFIT. Table 5.7 shows the quasi-static tensile properties of the pipe materials used in the Task 1 experiments*.

* During the course of the IPIRG-2 program, it was discovered that the stainless steel pipe material which had always been referred to as DP2-A8 was actually from two different heats of stainless steel pipe. The tensile properties for these two heats (referred to as DP2-A8I and DP2-A8II) were nearly identical. Therefore the tensile properties from Specimen A8-40 were used in the analysis of all the elevated temperature stainless steel base metal and stainless steel weld experiments. The J-R curves for the two heats were different, and as such, heat specific J-R curves were used in the analysis of Experiments 1.3-3 and 1-1, i.e., the two elevated temperature stainless steel base metal experiments.

Included in Table 5.7 are the yield strengths, ultimate strengths, Ramberg-Osgood coefficients (i.e., reference stress, reference strain, α, and n), and S_m(Code) and S_m(Actual) values for the five base metal materials used in the Task 1 experiments. In addition, Table 5.7 includes the specimen number on which the Ramberg-Osgood coefficients are based. The actual stress-strain data from which the data in Table 5.7 were derived are shown in Figures 2.2, 2.4, 2.6, 2.9, and 2.19 in Section 2.0. The Ramberg-Osgood representations of these stress-strain curves are shown in Figures 5.18 and 5.19. Figure 5.18 shows the Ramberg-Osgood representations for the carbon steel materials (F22, F23, F29, and FE17) and Figure 5.19 shows the Ramberg-Osgood representations for the stainless steel material (A8) at the two temperatures evaluated in a pipe experiment. Note, for the weld metal tests the base metal tensile properties were used in the analyses. As such, no tensile data for the weld materials are shown in Table 5.7. The weld metal tensile data are included in Section 2.0 of this report. Also, note that for the elbow girth weld experiments that both the elbow and straight pipe tensile data were used in the analyses of these experiments.

Table 5.7 Tensile properties of pipe materials used in IPIRG-2 Task 1 and companion pipe experiments

Material Ident.	Material Grade	Applicable Pipe Experiments	Nominal Pipe/Elbow Diameter, inch	Quasi-static Data					Tensile Spec. No.	S_m (Code), MPa	S_m (Actual), MPa
				$\sigma_y = \sigma_o$, MPa	σ_u, MPa	ϵ_o	α	n			
DP2-A8[1]	TP304	1-1, 1.3-3, 1-5, 1-6, 4141-4, 1.3-5	16	171	456	0.000936	5.34	4.17	A8-40	117	152
DP2-A8[2]	TP304	EPRI 13S	16	295	743	0.00162	3.93	5.07	A8-35	138	197
DP2-F29	A106B	1-2, 4112-8, 1.3-2, 4141-8, 1.3-4	16	241	618	0.00127	2.19	3.39	F29-5	125	160
IP2-FE17	A106B	1-3, 1-4	16	215	446	0.001114	3.92	3.70	FE17T2	125	143
DP2-F23	A106B	1-3, 1-4, 1-7, 1-8	16	223	514	0.001154	2.37	4.03	F23-3t	125	148
DP2-F22	A106B	1-9	6	259	588	0.00136	2.76	3.56	F22-t1	125	173

(1) The tensile properties for the two heats of DP2-A8 were nearly identical, therefore the tensile properties from Specimen A8-40 were used in the analysis of all the elevated temperature stainless steel base metal and stainless steel weld experiments.
(2) Room temperature data; all other data shown for 288 C (550 F) tensile tests.

5.2.2.2 J-R Curve Data

As indicated previously, quasi-static J-R curves were found to be most consistent for the analysis of the quasi-static experiments and dynamic J-R curves were found to be most consistent for the analysis of the dynamic experiments. The J-R curves typically used were for monotonically loaded specimens. However, where available, cyclic J-R curves were also used in selected analyses. The results of these analyses are reported on in Section 5.2.4. Table 5.8 presents the extrapolated J-R curve constants for the test materials, i.e., base metals and welds, used in the Task 1 experiments. Included in Table 5.8, are the applicable constants, i.e., C_2, and m_1, from Equation 5-4 for each material and loading condition. Where available, Table 5.8 also includes the applicable constants for the C(T) specimen cyclic J-R curves. In addition, Table 5.8 includes the specimen number on which the extrapolated J-R curve constants are based.

$$J = J_i + C_2(\Delta a)^{m_1} \qquad (5\text{-}4)$$

The actual J-R curve data from which the data in Table 5.8 were derived are shown in Figures 2.25, 2.27, 2.29, 2.30, 2.32, 2.34, and 2.35 in Section 2.0. The extrapolated J-R curve representations of these J-R curves are shown in Figures 5.20 through 5.22. Figure 5.20 shows the extrapolated J-R curve representations for the quasi-static data, Figure 5.21 shows the extrapolated J-R curve representations for the dynamic data, and Figure 5.22 shows the extrapolated J-R curve representations for the C(T) specimen cyclic data.

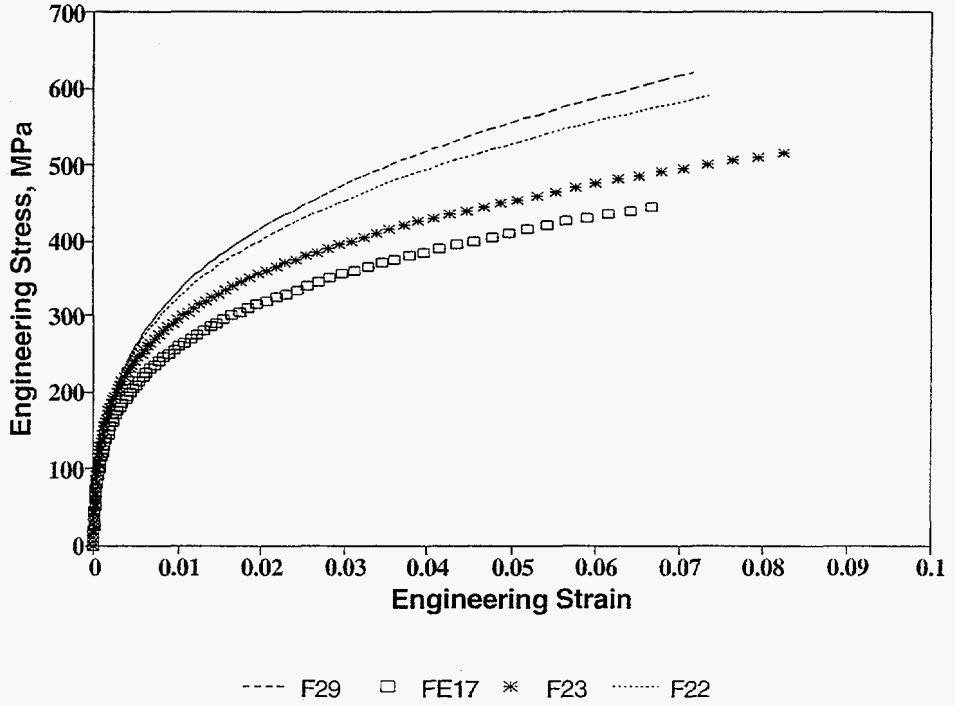

Figure 5.18 Ramberg-Osgood representations of the Task 1 carbon steel materials

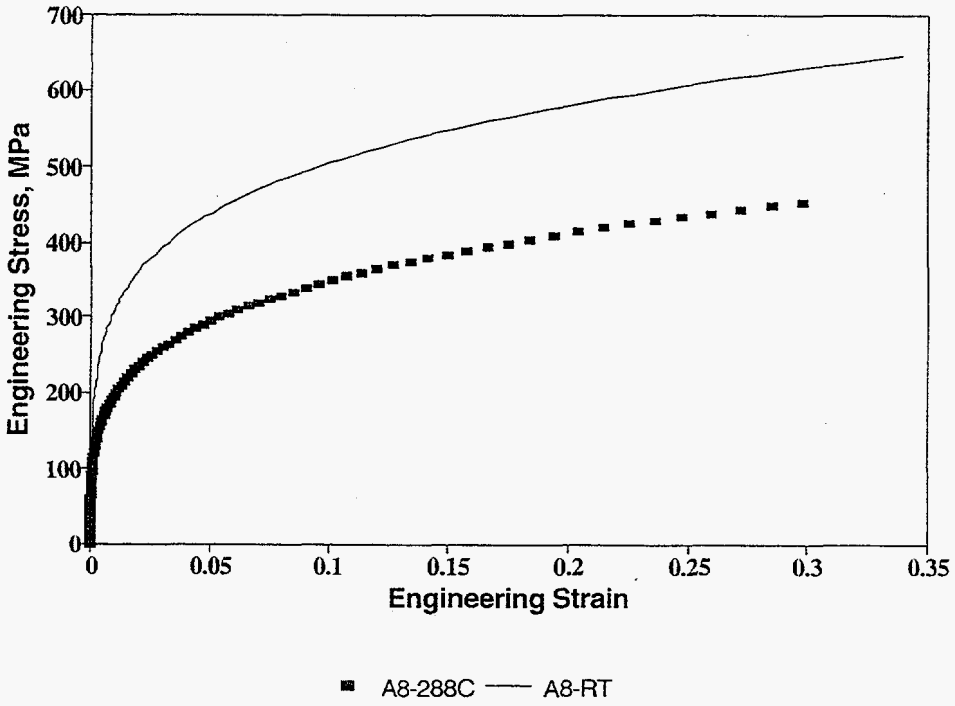

Figure 5.19 Ramberg-Osgood representations of the Task 1 stainless steel at the two temperatures evaluated in a pipe experiment, i.e., room temperature and 288 C (550 F)

Table 5.8 Extrapolated J-R curve constants[1] for the pipe materials used in the IPIRG-2 Task 1 and companion pipe experiments

Material Ident.	Material Grade	Applicable Pipe Experiments	Nominal Pipe/Elbow Diameter, inch	Stress Ratio (R)	Quasi-static Data				Dynamic Data			
					J_i, kJ/m^2	C_2	m_1	Spec No.	J_i, kJ/m^2	C_2	m_1	Spec. No.
Monotonic Data												
DP2-A8I	TP304	1-1	16	1.0	854	452	0.769	A8-12a	1,302	510	0.739	A8-9a
DP2-A8II	TP304	1.3-3	16	1.0	546	300	0.615	A8II-17	815	336	0.612	A8II-20
DP2-A8 [2]	TP304	EPRI 13S	16	1.0	2,277	1,292	0.502	(2)	ND[3]	ND	ND	NA[4]
DP2-F29	A106B	1-2, 4112-8, 1.3-2	16	1.0	149	92.6	0.470	F29-18	68.3	67.1	0.622	F29-9
DP2-F29W	SAW	4141-8, 1.3-4	16	1.0	82.0	78.9	0.630	F29W-12	118	123	0.618	F29W-9
DP2-F55W	SAW	1-3, 1-4	Plate	1.0	65.4	53.3	0.554	F55W-2	91.2	132	0.484	F55W-3
DP2-A8W	SAW	1-5, 1-6, 4141-4, 1.3-5	16	1.0	55.0	153	0.576	A8W-110	140	209	0.704	A8W-107
DP2-F23	A106B	1-7, 1-8	16	1.0	74.3	120	0.698	F23-1	94.9	124	0.604	F23-3
DP2-F22	A106B	1-9	6	1.0	77.1	120	0.566	F22-3	43.6	67.5	0.359	F22-2
Cyclic Data												
DP2-A8I	TP304	1-1	16	-0.3	952	571	0.462	A8-13	1,297	395	0.776	A8I-22
DP2-A8I	TP304	1-1	16	-1.0	356	283	0.432	A8-14	ND	ND	ND	ND
DP2-A8II	TP304	1.3-3	16	-0.3	652	261	0.643	A8II-21	395	154	0.721	A8II-15
DP2-A8II	TP304	1.3-3	16	-1.0	313	140	0.708	A8II-18	ND	ND	ND	ND
DP2-A8W	SAW	1-5, 1-6	16	-0.6	46.4	72.3	0.750	A8W-103c	60.2	88.8	0.641	A8W-108c
DP2-A8W	SAW	4141-4, 1.3.5	16	-1.0	39.3	38.0	0.614	A8W-101c	33.6	78.5	0.675	A8W-107c
DP2-F40W	SAW	4141-8, 1.3-4,	Plate	-0.6	47.3	32.6	0.694	F40W-7	33.4	71.2	0.501	F40W-13c
DP2-F40W	SAW	1-3, 1-4	Plate	-1.0	30.1	44.4	0.384	F40W-5	38.6	59.6	0.402	F40W-10c

(1) $J = J_i + C_2(\Delta a)^{m_1}$.
(2) Average fit for Specimens A8a-1, A8a-2, and A8a-3.
(3) ND = not determined.
(4) NA = not applicable.

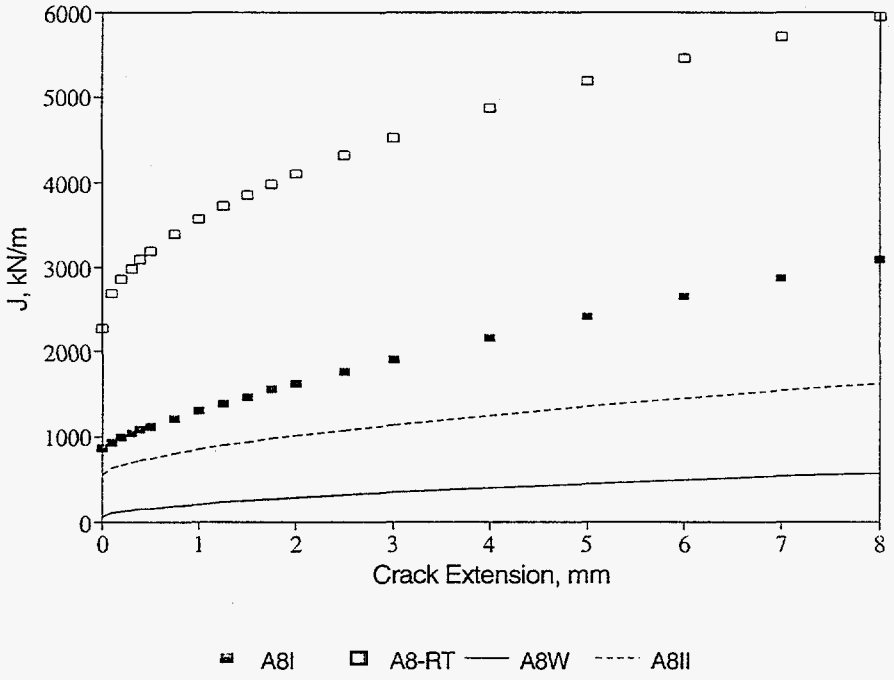

(a) Austenitic materials

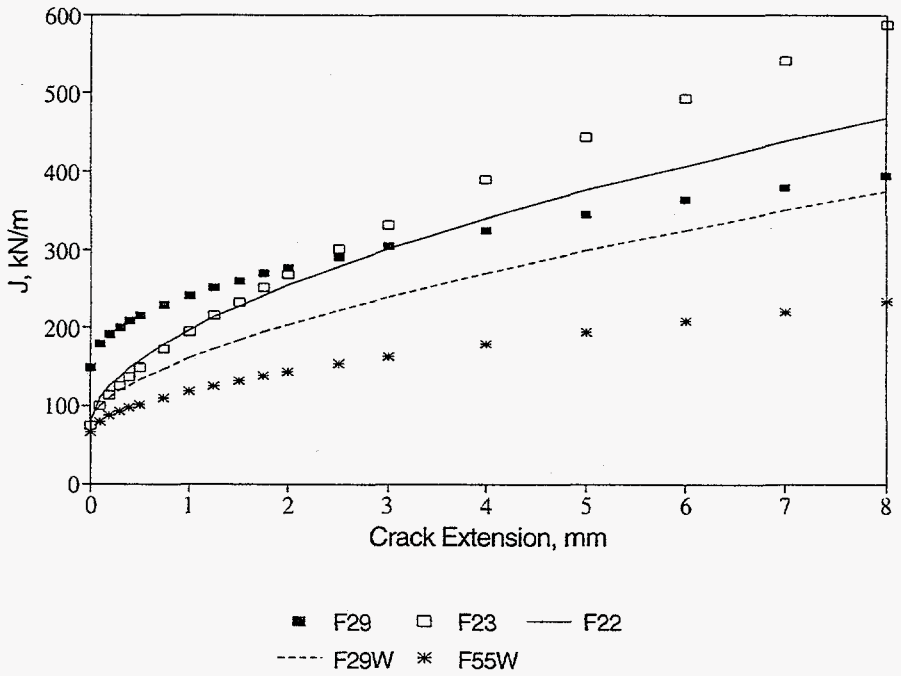

(b) Ferritic materials

Figure 5.20 Extrapolated J-R curve representations for the quasi-static, monotonic Task 1 fracture toughness data

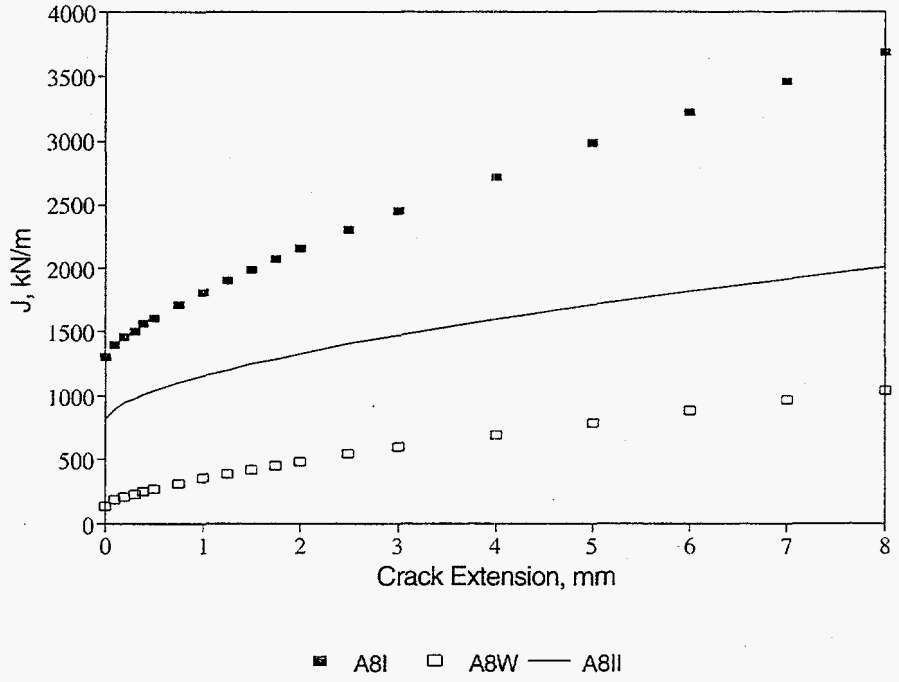

(a) Austenitic materials

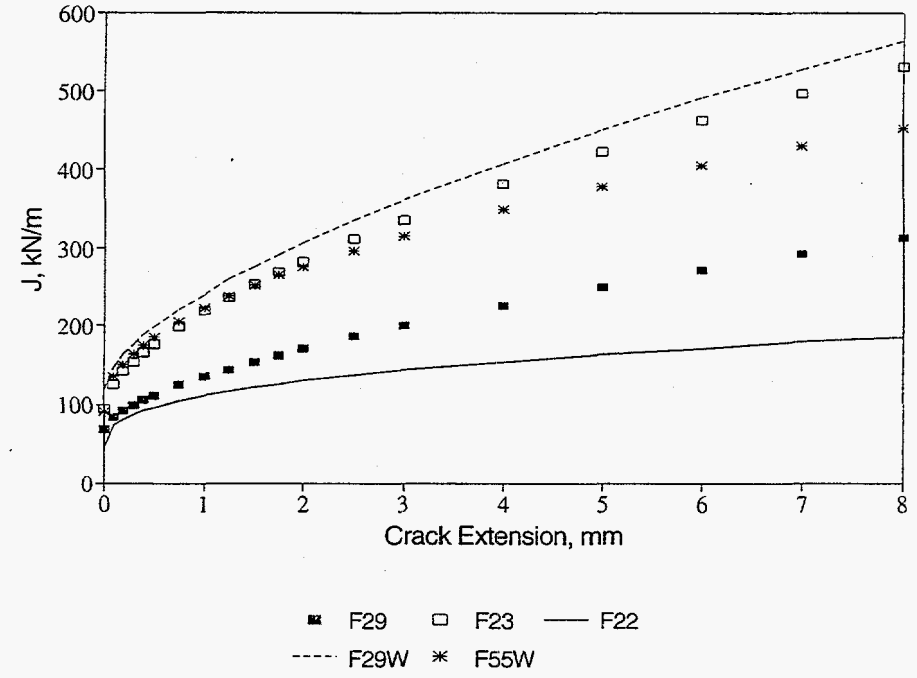

(b) Ferritic materials

Figure 5.21 Extrapolated J-R curve representations for the dynamic, monotonic Task 1 fracture toughness data

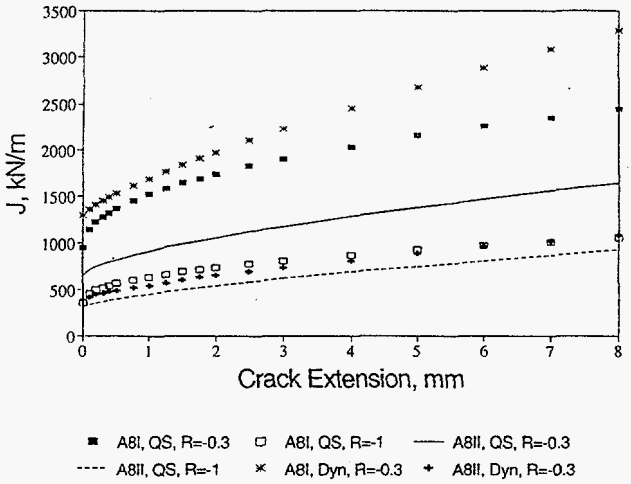

(a) Austenitic base metal, quasi-static and dynamic loading rates

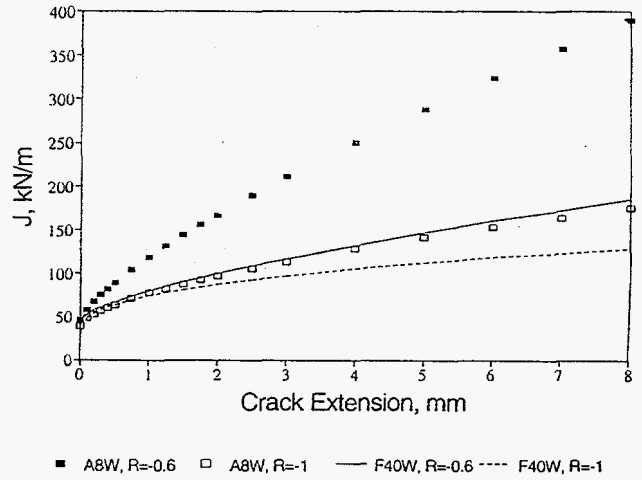

(b) Austenitic and ferritic welds, quasi-static loading rate

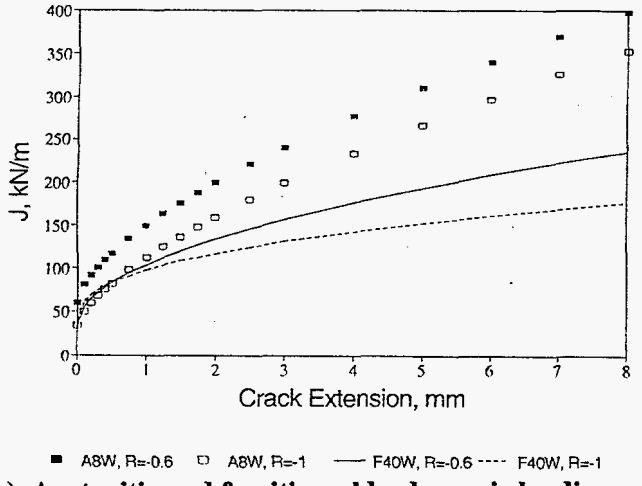

(c) Austenitic and ferritic welds, dynamic loading rate

Figure 5.22 Extrapolated J-R curve representations for the Task 1 C(T) specimen cyclic fracture toughness data

5.2.3 Comparison of Maximum Stress Predictions from Fracture Prediction Analysis Methods with Experimental Data

In this section, comparisons of maximum stress predictions from the various fracture prediction analysis methods are made with the experimental data developed as part of Task 1 and with experimental data developed for the previously conducted companion experiments. The experimental data are compared only with the predictive analysis methods, i.e., Net-Section-Collapse, Dimensionless-Plastic-Zone-Parameter, and J-estimation schemes. Comparisons with the failure avoidance criteria, or code approaches, with their inherent conservatisms, i.e., the ASME and R6 approaches, are deferred to Section 5.2.4. In addition, the predictions in this section are all based on monotonically-loaded J-R curve tests. Comparisons between experimental data and predictions based on cyclic J-R curve data are deferred to Section 5.2.5. To facilitate the calculations needed for these comparisons, the NRCPIPE (Version 2.0) and NRCPIPES (Version 2.0a) computer codes for through-wall-crack and surface-cracked pipe, respectively, were used.

Prior to making the actual comparisons between the experiments and analysis predictions, the various fracture prediction analysis methods are discussed.

5.2.3.1 Analysis Methods Used in Fracture Predictions

The predictive fracture analyses to which the experimental data were compared include:

- The Net-Section-Collapse analysis (Ref. 5.6),
- The Dimensionless-Plastic-Zone-Parameter (DPZP) analysis (Ref. 5.7),
- Various J-estimation schemes for surface-cracked pipes such as,
  - SC.TNP1 (Ref. 5.8),
  - SC.TNP2 (Ref. 5.9),
  - SC.ENG1 (Ref. 5.9), and
  - SC.ENG2 (Ref. 5.9).
- Various J-estimation schemes for circumferential flaws for through-wall-cracked pipes such as,
  - GE/EPRI (Ref. 5.10),
  - LBB.NRC (Ref. 5.11), and
  - LBB.ENG2 (Ref. 5.12).

Net-Section-Collapse Analysis for Circumferential Flaws

The original Net-Section-Collapse (NSC) analysis method was included in this comparative analysis because it is the analysis method which forms the basis for the flaw evaluation procedures in Section XI of the ASME Code, i.e., IWB-3640 and Appendix C for austenitic piping and IWB-3650 and Appendix H for ferritic piping. [Note, Kurihara (Ref. 5.23) modified the basic approach to account for very deep cracks. Comparisons between the Kurihara modified version of the Net-Section-Collapse analysis with the

experimental data and not included herein.] The original NSC analysis is a simple limit-load analysis and as such assumes maximum moment/stress occurs when the pipe section containing the crack becomes fully plastic, and that there is insignificant crack growth from crack initiation to maximum load. Another major assumption embodied in the Net-Section-Collapse analysis is that the toughness of the material is sufficiently high such that failure is governed by the strength of the material (i.e., the flow stress or collapse stress) and is not sensitive to the toughness of the material. The flow stress is a value between the yield and ultimate strength of the material and represents an average critical net-section stress reach throughout the flawed ligament of the structure, see Figure 5.23. This assumption that the net-section stress reaches a fully-plastic condition is easily satisfied for smaller diameter pipes and pipes made from high toughness materials, i.e., stainless steel. However, for lower toughness ferritic pipes, especially larger diameter ferritic pipes, this assumption of fully-plastic conditions is not necessarily satisfied. For these larger diameter, lower toughness pipes, contained plasticity conditions often exist, and the resultant failure stresses are typically below those predicted by the Net-Section-Collapse analysis.

Dimensionless-Plastic-Zone-Parameter Analysis for Circumferential Flaws

As part of the Degraded Piping program (Ref. 5.3), a semi-empirical analysis method was developed which allows one to make an assessment of whether or not the assumptions embodied in the Net-Section-Collapse analysis, i.e., fully-plastic conditions, are satisfied. This analysis was then extended as part of Reference 5.7 such that the failure stresses for these contained plasticity experiments could be predicted. As part of this analysis method, the ratio of the predicted failure stress-to-the Net-Section-Collapse predicted failure stress was found to be a function of a dimensionless-plastic-zone-size parameter. This dimensionless-plastic-zone-size parameter is the ratio of the plastic-zone size to the remaining tensile ligament of the cracked pipe, i.e., the distance from the crack centerline for surface-cracked pipe or the

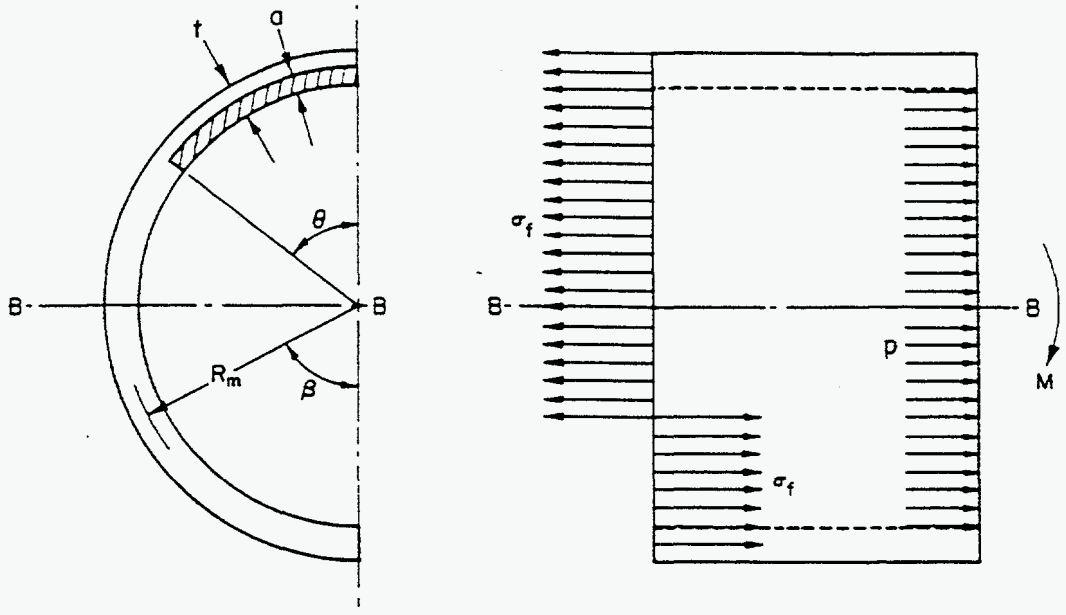

Figure 5.23 Representation of critical net-section-stress (flow stress) reached throughout the flawed ligament of a structure under fully plastic conditions

crack tip for through-wall-cracked pipe to the neutral bending axis, see Figure 5.24. The simplified dimensionless-plastic-zone-size parameter (DPZP) is proportional to the toughness of the material and inversely proportional to the pipe diameter and flow stress of the material, see Equation 5-5. (The simplified DPZP does not account for the effect of the crack size on the fully plastic neutral axis. This was a second order effect and hence neglected in Reference 5.7.)

$$DPZP = 2EJ_i/\left(\pi^2 D_m \sigma_f^2\right) \tag{5-5}$$

where

DPZP = Dimensionless-plastic-zone-parameter
E = Elastic modulus
J_i = Value of J at crack initiation from a C(T) specimen test
D_m = Mean pipe diameter
σ_f = Flow stress, average of the yield and ultimate strengths.

As part of References 5.7 and 5.9, "best-fit" curves were fit to the experimental data relating the ratio of the experimental failure stress-to-the Net-Section-Collapse stress and the simplified Dimensionless-Plastic-Zone-Parameter (DPZP), see Figure 5.25*. Separate curve fits were made for surface-cracked and through-wall-cracked pipe experiments, see Equation 5-6.

$$P/P_{NSC} = \frac{2}{\pi} \text{Arccos}\left(e^{-C_1[DPZP]}\right) \tag{5-6}$$

where

P = DPZP predicted failure stress
P_{NSC} = Net-Section-Collapse predicted failure stress
C_1 = Empirically derived constant.

For surface-cracked pipe, the "best-fit" empirically derived constant was found to be 34. For through-wall-cracked pipe, the "best-fit" empirically derived constant, was found to be 18.3, see Figure 5.25.

Knowing the value of J at crack initiation (J_i) from a C(T) specimen test and the flow stress of the material, one can calculate the simplified dimensionless-plastic-zone-parameter (DPZP). With the flow stress, one can calculate the Net-Section-Collapse stress. Knowing these quantities, one can calculate the DPZP predicted stress at maximum load using Equation 5-6. This method was found to be very accurate for predicting the maximum experimental stresses, especially for surface-cracked pipe (Ref. 5.9).

---

* The "best-fit" curve for the through-wall-cracked pipe data were recently updated based on the data in the CIRCUMCK pipe fracture database (Ref. 5.24).

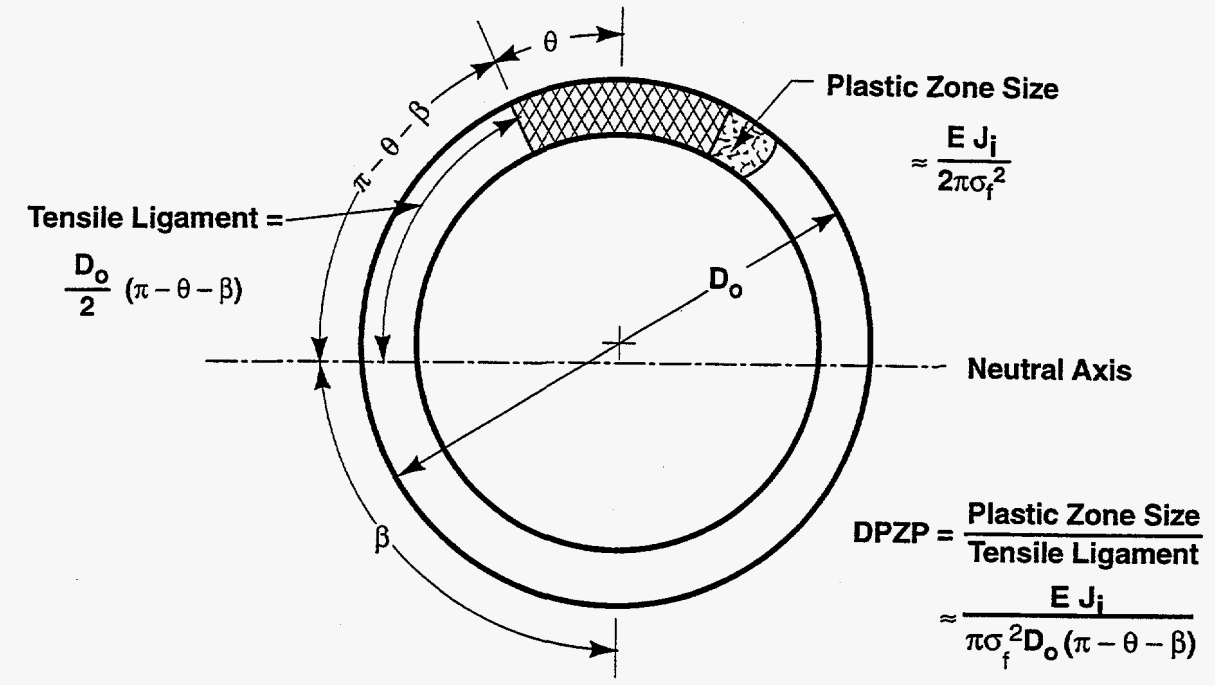

(a) Through-Wall Crack

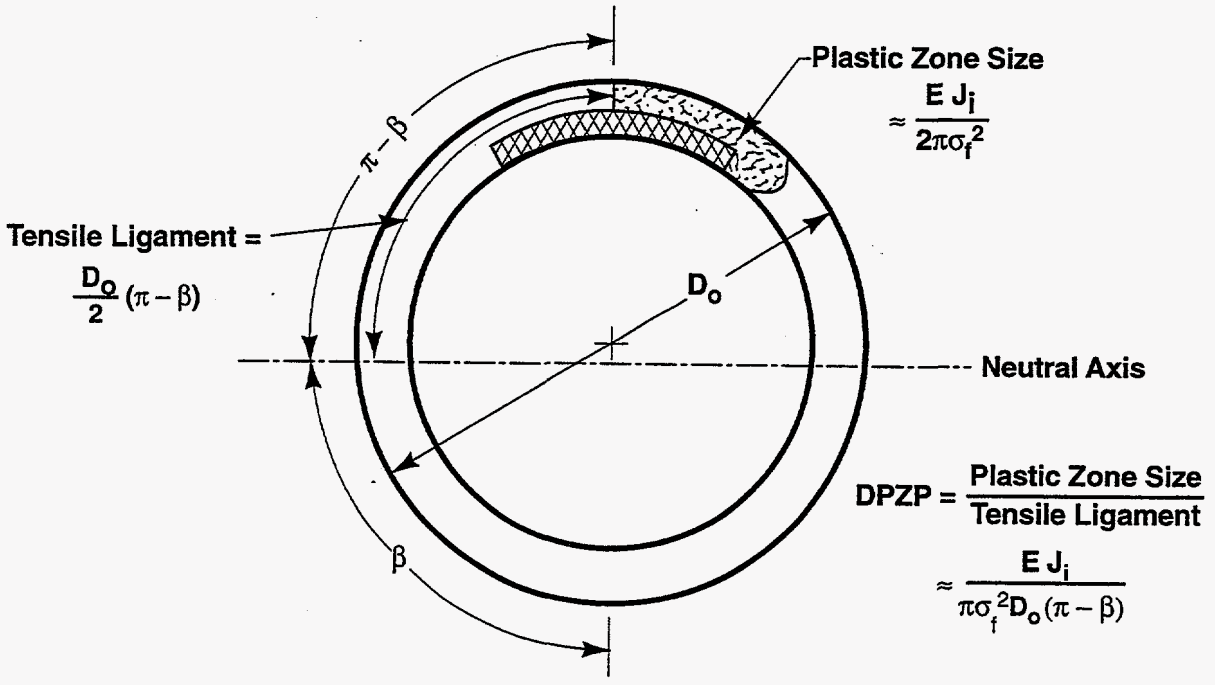

(b) Surface Crack

Figure 5.24 Representation of the Dimensionless-Plastic-Zone-Size parameter

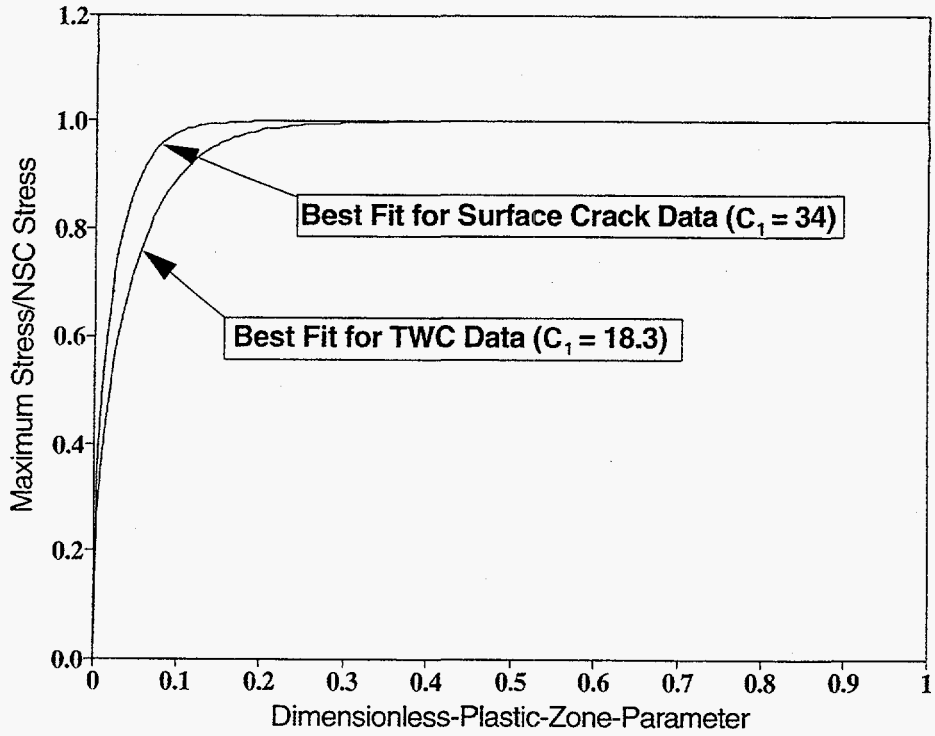

Figure 5.25 Plot of the ratio of the failure stress-to-Net-Section-Collapse stress as a function of the Dimensionless-Plastic-Zone-Parameter

SC.TNP1 and SC.TNP2 J-Estimation Scheme Analyses for Circumferential Surface-Cracked Pipe

The SC.TNP analysis method for finite-length surface cracks was first developed as part of the Degraded Piping program (Ref. 5.8). This method is a modification of the GE/EPRI solution for 360-degree surface-crack pipe in tension that accounts for finite-length surface-cracked pipe in bending. Whereas the Net-Section-Collapse and DPZP analyses required only the flow stress as input for the material's tensile properties, the SC.TNP analysis requires a full stress-strain curve representation through the use of the Ramberg-Osgood relationship. Furthermore, whereas the Net-Section-Collapse analysis was independent of the fracture toughness of the material and the DPZP required only the fracture toughness value at crack initiation (J_i) as input, the SC.TNP analysis method requires the full J-R curve for analysis. As such, the complexity of the SC.TNP analysis method is much more significant than it is for the Net-Section-Collapse or Dimensionless-Plastic-Zone-Parameter analyses. This is evident by the fact that the SC.TNP analysis requires the use of a personal computer program, NRCPIPES, to complete an analysis of a cracked pipe and the Net-Section-Collapse and DPZP analyses are single one line equations that can be solved without the aid of a computer.

The SC.TNP methodology uses a length parameter, L, which is the distance from the crack plane to the plane for which the stresses in the pipe wall can be assumed to be equal to that in the uncracked pipe. Since a clear definition of this length parameter is elusive, the parameter was initially chosen to be approximately equal to the thickness of the pipe wall (Ref. 5.8). This original definition of L (i.e., L = t) was that used in the original version of SC.TNP, i.e., SC.TNP1. As part of the Short Cracks in Piping and Piping Welds program (Ref. 5.7), the effect of changing this length parameter, L, was examined. It was

shown that predictions of J using SC.TNP agreed well with finite element results when L was chosen to be between 2t and 3t for a strain-hardening exponent (n) value of 3, whereas L needs to be closer to 9t for the case of n = 10. This finding demonstrated the influence of the strain-hardening level of the material on the choice of L. Based on the dependence of the SC.TNP predictions on the length parameter, L, it appeared that the SC.TNP method could be modified by incorporating the dependence of L on the hardening exponent. For the modified version of SC.TNP, i.e., SC.TNP2, L is defined as (n-1)t, where t is the wall thickness of the pipe and n is the strain-hardening exponent of the material.

In Reference 5.9, it was shown that the modified version of SC.TNP, i.e., SC.TNP2, results in more accurate predictions of J when compared with finite element results. However, as part of this same reference, it was shown that the original version of SC.TNP, i.e., SC.TNP1, results in more accurate predictions of the maximum experimental stress when compared with experimental data. This apparent discrepancy has been attributed to the fact that original version of SC.TNP, i.e., SC.TNP1, tends to underpredict the crack-driving force (J) for a given applied bending moment, but that this underprediction is offset by the fact that the crack growth resistance (J_R) for a surface crack growing radially through the pipe wall is being underpredicted by a J-R curve established from L-C oriented C(T) specimens due to a combination of anisotropy and constraint.

SC.ENG1 and SC.ENG2 J-Estimation Scheme Analyses for Circumferential Surface-Cracked-Pipe

As part of the U.S. NRC's Short Cracks in Piping and Piping Welds program (Ref. 5.9), a new surface-cracked pipe J-estimation scheme was developed. This method predicted the energy release rates for surface-cracked pipes subjected to remote bending loads. This method of analysis involves determining the moment-rotation behavior based on: (1) classical deformation theory of plasticity, (2) a constitutive law characterized by the Ramberg-Osgood model, and (3) an equivalence criterion incorporating a reduced thickness analogy for simulating the system compliance due to the presence of a crack in a pipe. This reduced thickness analogy, see Figure 5.26, was first developed for through-wall-cracked pipe for the LBB.ENG (Ref. 5.12) analysis method. The SC.ENG method may be applied in the complete range between elastic to fully plastic conditions. Since it is based on J-tearing theory, it is subject to the usual limitations imposed upon this theory, e.g., proportional loading, etc. It also has the implication that the crack growth must be small, although in practice, J-tearing methodology is used far beyond the limits of its theoretical validity with acceptable results (Ref. 5.25). Furthermore, the extent of surface crack growth in piping is often relatively small.

As indicated in the derivation of the SC.ENG method in Reference 5.9, the evaluation of the plastic component of J (J_p) requires determination of the terms H(a/t) and dH(a/t)/d(a/t). According to the definition of H(a/t) in this derivation, this also requires estimating the equivalent thickness, t_e, for the uncracked pipe, see Figure 5.26. In the equivalence method proposed in Reference 5.9, t_e can be determined by forcing the Net-Section-Collapse moment of the equivalent uncracked pipe to be equal to the Net-Section-Collapse moment of the actual cracked pipe. For an uncracked pipe with reduced thickness, t_e, the Net-Section-Collapse moment, M_L^d, is

$$M_L^d = 4\sigma_f R_m^2 t_e \qquad (5\text{-}7)$$

where σ_f is the flow or collapse stress of the material and R_m is the mean radius of the pipe. In determining

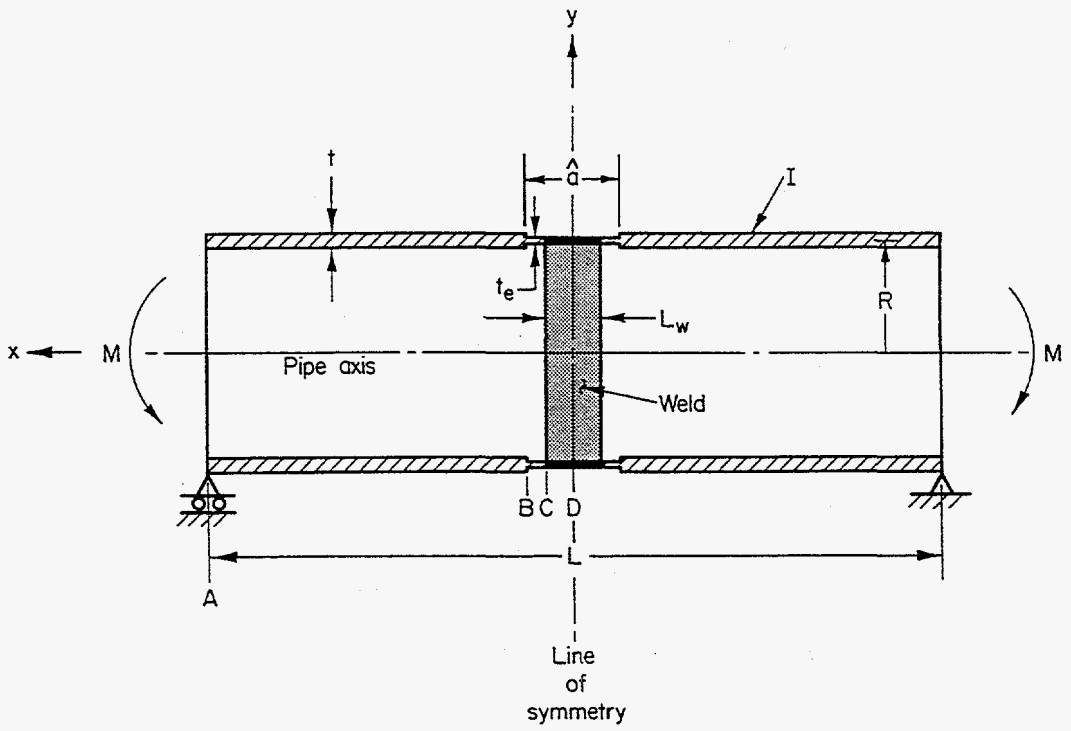

Figure 5.26 The reduced thickness analogy used in the SC.ENG and LBB.ENG analyses

the Net-Section-Collapse moment, M_L^c, for circumferentially surface-cracked pipe, several solutions are available in the literature. In Reference 5.9, two such equations, based on the original Net-Section-Collapse criterion (Ref. 5.6) and the Kurihara modification (Ref. 5.23) to the Net-Section-Collapse criterion, are used to determine H(a/t) and its derivative for the evaluation of J_p. Accordingly, the expressions of J_p based on H(a/t) and dH(a/t)/d(a/t) obtained from the original Net-Section-Collapse equations and the Kurihara modification to the Net-Section-Collapse equations are referred to as SC.ENG1 and SC.ENG2, respectively.

GE/EPRI J-Estimation Scheme Method for Circumferential Through-Wall-Cracked Pipe

The original GE/EPRI method is based on a curve fit through finite-element solutions for through-wall-cracked (TWC) pipes using deformation theory of plasticity. These solutions are catalogued in References 5.10, 5.26, and 5.27 for various geometric and material parameters. For through-wall-cracked pipes subjected to pure bending, the J-integral is calculated by breaking it down into its elastic and plastic components. The elastic and plastic components of J are given in References 5.10, 5.26, and 5.27 as

$$J_e = f_1\left(\theta/\pi, R_m/t\right)M^2/E \tag{5-8}$$

$$J_p = \alpha\sigma_o\epsilon_o R_m\theta\left(1-\theta/\pi\right)h_1\left(\theta/\pi, R_m/t, n\right)\left(M/M_o\right)^{n+1} \tag{5-9}$$

where the elastic f_I and plastic h_I functions are influence functions calculated from finite element results and tabulated in References 5.10, 5.26, and 5.27. M_o is the limit-moment of a through-wall-cracked pipe under pure bending.

As part of the Short Cracks program (Ref. 5.28), a number of improvements were made to the GE/EPRI method. Specifically, finite element solutions were compiled to improve the F-, V-, and h-functions for Ramberg-Osgood strain-hardening exponents (n) of 1, 2, 3, 4, 5, and 10 for both the case of short cracks, such as evaluated in Experiments 1-7 and 1-8, and longer cracks, such as evaluated in Experiment 1-9. In addition, for the short through-wall-cracked pipe case, the effect of combined tension and bending was considered. This method was included in this comparative analysis because it tends to be the most widely used of all of the through-wall-cracked pipe J-estimation schemes. Furthermore, this method tends to underpredict experimental loads the most, so it is a bounding solution relative to the other J-estimation schemes.

LBB.NRC J-Estimation Scheme for Circumferential Through-Wall-Cracked Pipe

The LBB.NRC method (Ref. 5.11) for through-wall-cracked pipe subjected to bending was developed primarily for use by the U.S. NRC staff as a means to evaluate Leak-Before-Break submittals by the nuclear industry. It is based on earlier work by Paris and Tada in NUREG/CR-3464 (Ref. 5.29) with modifications developed by the NRC staff to account for the strain-hardening characteristics of typical nuclear power plant piping materials.

LBB.ENG2 J-Estimation Scheme for Circumferential Through-Wall-Cracked Pipe

The LBB.ENG2 method was originally developed by Brust and Gilles during the Degraded Piping program (Refs. 5.12, 5.30, and 5.31) to compute the energy release rates for through-wall-cracked pipes subjected to bending loads. It involves an equivalence criterion incorporating a reduced thickness analogy, similar to that included in the SC.ENG analysis methods for surface-cracked pipe, for simulating the system compliance due to the presence of a through-wall crack in a pipe.

The elastic and plastic components of J (J_e and J_p) are given in Equations 5-10 and 5-11 below:

$$J_e = K_I^2/E \tag{5-10}$$

$$J_p = \left\{\alpha/\left(E\sigma_o^{n-1}\right)\right\}\left\{\pi R_m/(2[n+1])\right\} H_B(n,\theta)L_B(n,\theta)I_B(\theta)\left\{M/\pi R_m^2 t\right\}^{n+1} \tag{5-11}$$

where $H_B(n,\theta)$, $L_B(n,\theta)$, and $I_B(\theta)$ are conveniently defined elementary functions with explicit forms available in References 5.12, 5.30, and 5.31.

As part of the Short Cracks in Piping and Piping Welds program (Ref. 5.28), this method was extended to consider the case of a through-wall-cracked pipe subjected to combined tensile and bending loading conditions, as well as account for a crack in a weld, where the weld metal stress-strain curve is

incorporated. The method is similar to the case of pure bending and is also based on deformation plasticity, Ramberg-Osgood constitutive model, and an equivalence criterion incorporating a reduced thickness analogy for simulating the cracked-pipe compliance. Further details of this method regarding energy release rates due to combined bending and tension can be obtained from Reference 5.32.

Further details of each of these fracture prediction methods can be found in the appropriate references.

5.2.3.2 Comparisons of Maximum Load Predictions with Experimental Data from the Simulated-seismic Surface-Cracked Pipe Experiments

Two simulated-seismic surface-cracked pipe system experiments were conducted as part of the IPIRG-2 Task 1 efforts, i.e., Experiments 1-1 and 1-2. The cracks for Experiments 1-1 and 1-2 were internal circumferential surface cracks located in sections of 16-inch nominal diameter, Schedule 100, TP304 stainless steel pipe (DP2-A8I) and A106 Grade B carbon steel pipe (DP2-F29), respectively. The crack in the stainless steel test specimen was not fatigue precracked prior to testing, while the crack in the carbon steel test specimen was. Prior research had shown that the effect of notch acuity was insignificant for higher toughness materials such as this stainless steel (Ref. 5.33). The crack in the carbon steel specimen was fatigue precracked using pressure cycling techniques. As a result of this pressure cycling, the resultant surface-crack geometry was not uniform. The crack was deeper (a/t = 0.719) at a location approximately 100 mm (4 inches) from the crack centerline than it was at the crack centerline location (a/t = 0.592), see Figure 5.27.

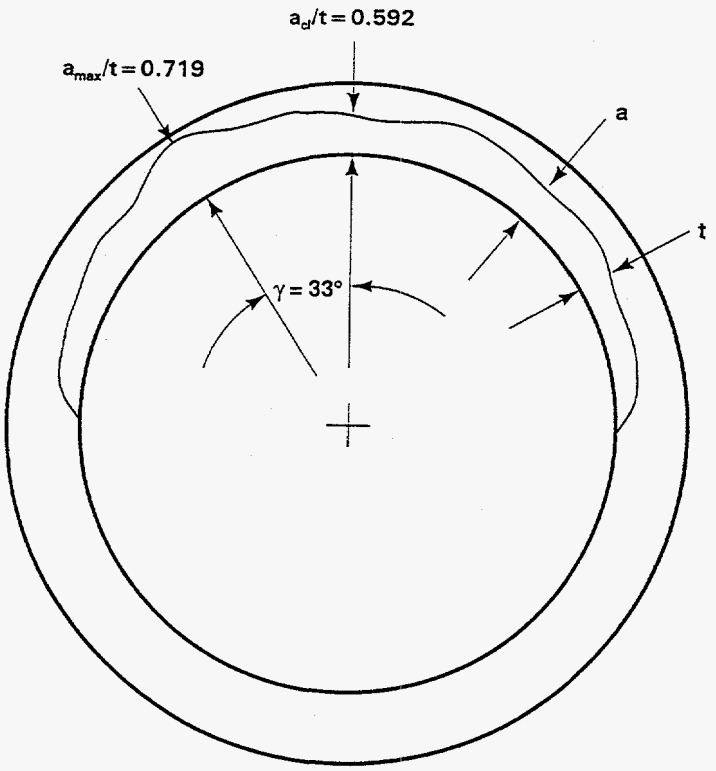

Figure 5.27 Surface crack geometry for Experiment 1-2 showing off-center crack

As a result of this off-centered crack for Experiment 1-2, the fracture ratios for this simulated-seismic experiment and the companion quasi-static four-point bend and single-frequency pipe system experiments were calculated using the "most consistent" definition of flaw size as discussed previously in Section 5.2.1.5 of this report. For these base metal cracks, this amounted to using the equivalent crack length and the maximum crack depth, but reducing the experimentally applied bending stress by the cosine of the angle between the maximum crack depth location and the crack centerline for Experiment 1-2. This accounted for the fact that the applied bending stress at the maximum crack depth location was reduced due to the fact that the distance to the neutral bending axis was reduced.

In calculating the fracture ratios for these experiments, as well as for the other Task 1 experiments discussed later, the fracture ratios (i.e., the ratio of experimental stress [bending plus membrane stress due to internal pipe pressure] to the predicted stress [bending plus membrane stress]) were calculated by converting the bending moments (experimental and predicted) to bending stresses through a simple strength of materials formulation (i.e., Mc/I) where c is the outside pipe radius and I equals $0.0491(D_o^4-D_i^4)$, where D_o is the outside pipe diameter and D_i is the inside pipe diameter. The membrane stress term was calculated using the simple thin-wall equation, $pD_o/4t$, following the guidance provided in ASME Section III, Equation 9.

Table 5.9 presents the results of the fracture ratio calculations for the two simulated-seismic pipe-system experiments and the four companion four-point bend and single-frequency pipe-system experiments using the "most consistent" definition of flaw size. During the analyses of these experiments, quasi-static stress-strain curves have been used throughout. Furthermore, quasi-static, monotonic J-R curves have been used to analyze the quasi-static four-point-bend experiments and dynamic, monotonic, J-R curves have been used to analyze the dynamic pipe-system experiments. As has been stated previously, the stainless steel pipe material DP2-A8 was actually from two different heats of stainless steel pipe. The J-R curves for these two heats were substantially different. Consequently, heat specific J-R curves were used in the analysis of the two stainless steel base metal pipe-system experiments, 1-1 and 1.3-3.

As can be seen in Table 5.9, the fracture ratios for the single-frequency pipe-system experiments are slightly less than the fracture ratios for the simulated-seismic pipe-system experiments. Initially, it was thought that this may be due to cyclic degradation. However, when the applied stress ratios were calculated for the four pipe-system experiments, it was found that the stress ratios (R) for the simulated-seismic experiments were more negative than the stress ratios for the companion single-frequency experiments for both materials, see Table 5.9. Yet, when the crack-section moments were plotted against the crack-mouth-opening displacements for the various experiments, it was found that the cycles prior to maximum load for the simulated-seismic experiments were primarily elastic, see Figure 5.28, whereas the cycles prior to maximum load for the single-frequency experiments exhibited significant amount of plasticity. This was especially true for the stainless steel single-frequency experiment, see Figure 5.29. The fact that the cycles prior to maximum moment were essentially elastic for the simulated-seismic experiments implies that these experiments could probably be analyzed much in the same manner as one would analyze a dynamic monotonic pipe experiment. This observation is probably an artifact of the forcing function used. If some other simulated-seismic forcing function had been used, with a more gradual buildup of large amplitude cycles, then more cyclic degradation may have occurred during these simulated-seismic experiments.

In reviewing Table 5.9, it can also be seen that for the case of the Net-Section-Collapse analysis, that the fracture ratios for the two carbon steel dynamic pipe system experiments (i.e., Experiments 1.3.2 and 1-2),

are significantly less (25 to 30 percent less) than the fracture ratio for the quasi-static four-point bending carbon steel experiment (i.e., Experiment 4112-8). For the other analysis methods, the agreement between the fracture ratios for the quasi-static experiment and the two dynamic pipe system experiments was much better. This is probably attributed to the fact that the Net-Section-Collapse analysis is a limit-load analysis

Table 5.9 Results of fracture ratio calculations for the two simulated-seismic surface-cracked pipe system experiments plus two companion quasi-static four-point-bend and two companion single-frequency pipe-system experiments (using quasi-static stress-strain curve and quasi-static, monotonic, J-R curve data to analyze the quasi-static bend experiments and quasi-static stress-strain curve and dynamic, monotonic, J-R curve data to analyze the dynamic pipe-system experiments)

Experiment Number	Material	Load History	Effective Stress Ratio (R)[1]	Fracture Ratios[2]					
				NSC	DPZP	SC.TNP1	SC.TNP2	SC.ENG1	SC.ENG2
EPRI 13S	TP304	QS Bend	1.0	1.144	1.144	1.008	1.316	1.324	1.522
1.3-3	TP304	Single Freq.	-0.2	0.975	0.975	0.890	1.165	1.155	1.342
1-1	TP304	Sim. Seismic	-0.5	1.156	1.156	0.999	1.291	1.222	1.403
4112-8	A106B	QS Bend	1.0	0.894	0.935	1.021	1.310	1.362	1.567
1.3-2	A106B	Single Freq.	0.3	0.709	0.876	0.903	1.182	1.325	1.617
1-2[3]	A106B	Sim. Seismic	-0.1	0.801	0.991	1.018	1.333	1.485	1.801

(1) $R_{effective} = (\sigma_{B_{min}} + \sigma_m) / (\sigma_{B_{max}} + \sigma_m)$.

(2) Fracture ratio = $(\sigma_{B_{expt}} + \sigma_m) / (\sigma_{B_{analysis}} + \sigma_m)$.

(3) Fracture ratio for Experiment 1-2 had been adjusted to account for the deepest part of the crack not being at the crack centerline where the stress was the highest, i.e., fracture ratio = $(\sigma_{B_{expt}} \cos(\psi) + \sigma_m) / (\sigma_{B_{analysis}} + \sigma_m)$ where $\psi = 33$ degrees.

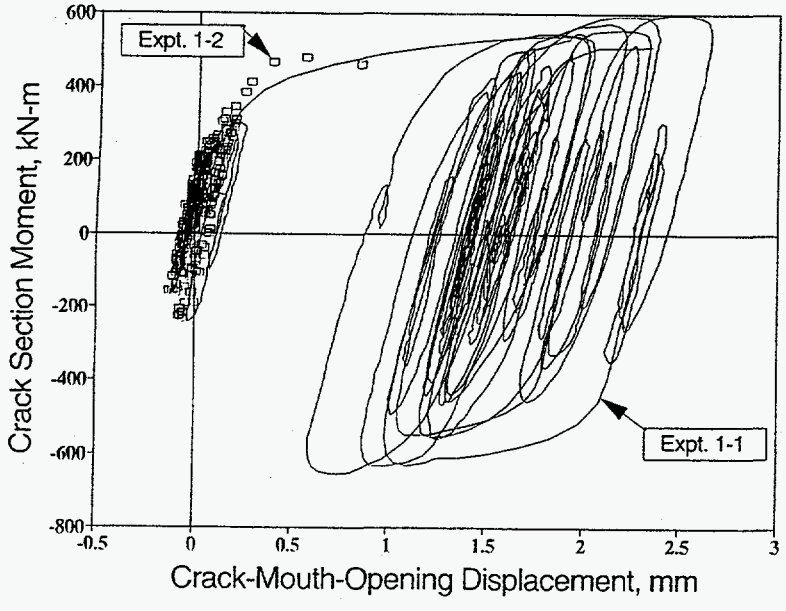

Figure 5.28 Moment-CMOD response for the two simulated-seismic pipe-system experiments, i.e., Experiments 1-1 and 1-2

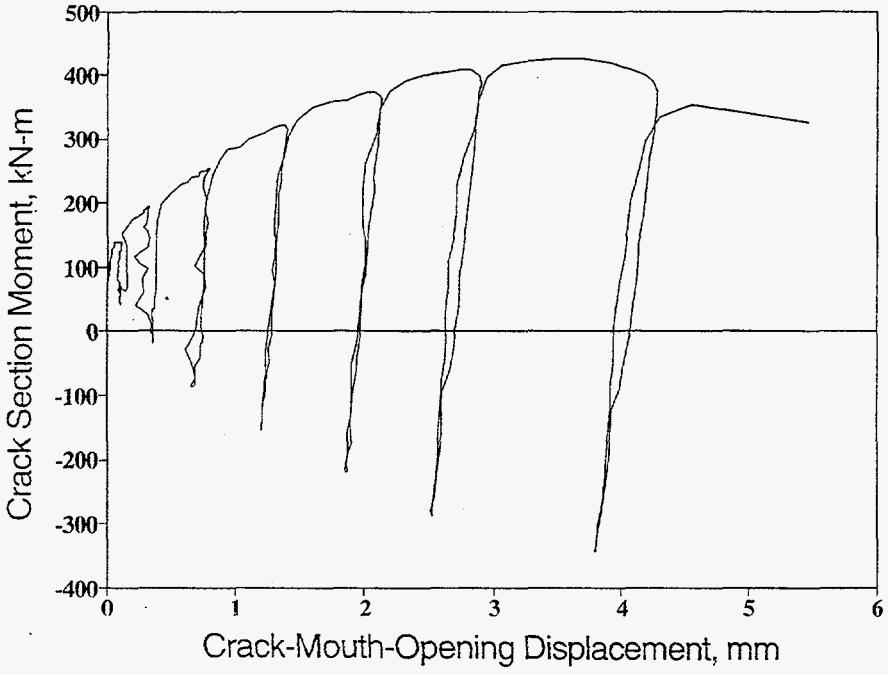

Figure 5.29 Moment-CMOD response for the stainless steel base metal single-frequency pipe-system experiment from IPIRG-1, i.e., Experiment 1.3-3

and, as such, does not consider the toughness of the material in the analysis. Quasi-static tensile properties were used to obtain the analysis results presented in Table 5.9. Since the Net-Section-Collapse analysis only considers the material's strength properties, and not the toughness, there has been no accounting for the dynamic loading rate effects on the material properties for this analysis. On the other hand, the other analysis methods considered are elastic-plastic methods for which the effect of the dynamic loading rate on the material's toughness has been taken into account by using dynamic J-R curve data in the analysis of the two dynamic pipe-system experiments.

5.2.3.3 Comparisons of Maximum Stress Predictions with Experimental Data from the Elbow Girth Weld Pipe Experiments

Two experiments with internal circumferential surface cracks in a girth weld joining a section of 16-inch diameter straight pipe to a 16-inch diameter, Schedule 100, long-radius 90-degree elbow were conducted as part of Task 1 of the IPIRG-2 program, i.e., Experiments 1-3 and 1-4. For these two experiments, both the elbows and straight pipe sections were fabricated from A106 Grade B material. The pipes and elbows were from different manufacturers, and hence did not have identical material properties. The weld procedure used for these experiments was a C-Mn-Mo-Ni submerged-arc weld (SAW) procedure developed by Babcock and Wilcox and fabricated by the United McGill Corporation in Columbus, Ohio. This was the same weld procedure used in the companion single-frequency pipe-system and quasi-static four-point-bend straight pipe-to-pipe weld experiments conducted as part of the IPIRG-1 (Ref. 5.4) and Degraded Piping programs (Ref. 5.3), respectively. The flaws in both of these elbow girth weld experiments were fatigue precracked prior to testing. The same was true for the two companion straight pipe-to-pipe weld experiments conducted earlier. For the two companion experiments, the fatigue crack

extension from the tip of the electric-discharged-machined notch was fairly uniform. For the single-frequency, pipe-system, elbow, girth weld experiment (Experiment 1-3), the fatigue crack was much deeper at one of the 45-degree locations (a/t = 0.710) than it was at the crack centerline (a/t = 0.601). The same was true for the quasi-static, bend, elbow, girth weld experiment (Experiment 1-4), but to a lesser degree. The normalized crack depth (a/t) at one of the 45-degree locations was 63.9 percent of the pipe wall but only 60.5 percent of the pipe wall at the crack centerline location.

In addition to having to account for the off-center cracks for Experiments 1-3 and 1-4, the weld cross-section geometry also had to be accounted for in the analyses of these experiments. Figure 5.30 shows a comparison of the weld cross-section geometry for the straight pipe-to-pipe girth welds tested in the companion experiments and the pipe-to-elbow girth welds tested in these IPIRG-2 experiments. As discussed in Section 5.2.1.3, when considering cracks in welds, the best agreement with other surface-cracked pipe fracture data occurs when the crack depth is referenced to the inside pipe surface (a_1), and not the counterbore surface, and the pipe wall thickness is the wall thickness of the pipe plus the weld crown height (t_3), see Figure 5.16. In analyzing these elbow girth weld experiments, there is the further complication that the inside pipe surfaces of the pipes and elbows do not match up. The inside pipe surfaces of the original Schedule 140 straight pipe sections were machined such that the resultant wall thicknesses of the straight pipes were the same as the average wall thicknesses of the test elbows. However, since the outside diameters of the elbows were slightly larger than the outside diameters of the straight pipe sections, the inside diameters did not match, see Figure 5.30. As a result, fracture prediction analyses were conducted using both the straight pipe and elbow dimensions in the analyses. For both cases, the crack depths were referenced to the inside surface of the pipe or elbow, and the wall thicknesses included the relative height of the weld crown. In addition, for the case where the straight pipe dimensions

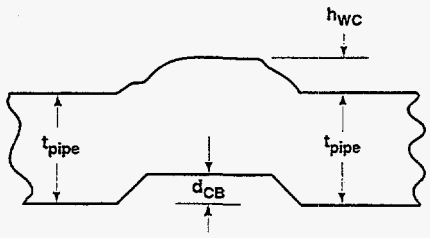

Straight pipe-to-straight pipe weld

h_{WC} = Weld Crown Height
d_{CB} = Counterbore Depth

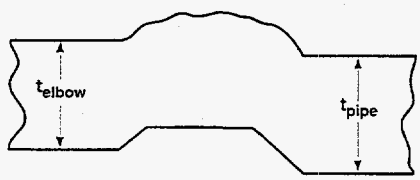

Elbow-pipe girth weld

Figure 5.30 Comparison of the weld cross-section geometry for the straight pipe-to-pipe welds evaluated in the companion experiments and the pipe-to-elbow welds evaluated in the elbow-girth weld experiments

were used in the analyses, the stress-strain curve for the straight pipe material was used, and for the case where the elbow dimensions were used, the elbow stress-strain curve was used. The results of those analyses are shown in Table 5.10.

As can be seen in Table 5.10, the fracture ratios for the straight pipe experiments agree closely with those for the elbow girth weld experiments, especially for the case when the straight pipe dimensions and straight pipe stress-strain curve were used in the analyses. For instance, when the SC.TNP1 analysis method was used, the fracture ratios for the two elbow girth weld and two straight pipe weld experiments all agreed within 5 percent of each other. This finding suggests that straight pipe analyses can be used to predict the behavior of cracks located in elbow-to-straight pipe girth welds. This is significant since it implies that special analysis procedures for the case of surface cracks in elbow-to-straight pipe girth welds need not be developed. One can simply use the straight pipe analyses previously developed.

5.2.3.4 Comparisons of Maximum Stress Predictions with Experimental Data from Short Surface-Cracked Pipe Experiments

Two pipe experiments with relatively short (25 percent of the pipe circumference) internal circumferential surface cracks in stainless steel pipe-to-pipe girth welds were conducted as part of Task 1 of the IPIRG-2 program, i.e., Experiments 1-5 and 1-6. The weld procedure used in fabricating the test welds for these two experiments was the same submerged-arc weld procedure used previously in two long crack (50 percent of the pipe circumference) pipe experiments conducted as part of the Degraded Piping (Ref. 5.1) and IPIRG-1 (Ref. 5.2) programs, i.e., Experiments 4141-4 and 1.3-5, respectively. The weld procedure was originally supplied to Battelle by General Electric (GE) as part of the Degraded Piping program (Ref. 5.3).

The results of the fracture ratio calculations for the two short and two long surface-cracked pipe experiments for the six analysis methods considered are shown in Table 5.11. As can be seen in Table 5.11, the results for the quasi-static, bend, short-surface-crack experiment (Experiment 1-6) agree very closely with the results from both of the long-surface-crack experiments (Experiments 4141-4 and 1.3-5). As can be seen in Table 5.11, the agreement in fracture ratios between these three experiments is typically within 5 to 7 percent of each other, well within the experimental scatter band typically observed for this type of experiment. However, the calculated fracture ratios for the various analysis methods for the short surface-cracked pipe system experiment (Experiment 1-5 from IPIRG-2) are up to 30 percent less than the fracture ratios for the other three stainless steel weld experiments. This finding has been attributed to the fact that the cyclic damage for short surface-cracked pipe system experiment was probably greater than the cyclic damage for the long surface-cracked pipe system experiment or the two quasi-static monotonic experiments. Figure 5.31 shows plots of the moment-rotation behavior for both the short and long surface-cracked pipe system experiments. As can be seen in Figure 5.31, the magnitude of the compressive moments for the short surface-cracked pipe system experiment is approximately twice that for the long surface-cracked pipe system experiment even though the same actuator forcing function was used for both experiments. (The restraint system is believed to cause the greater compressive loads, see Section 5.1.)

In Section 5.2.4, comparisons of the maximum stress predictions using cyclic J-R curve data will be made with the experimental data for these two stainless steel weld pipe system experiments. At that time, it will be possible to determine if the more compressive cyclic load history for Experiment 1-5 was the reason for lower fracture ratios for this experiment.

Table 5.10 Results of fracture ratio calculations for the two elbow girth weld pipe experiments plus the companion, quasi-static, four-point-bend, straight-pipe experiment and the companion, single-frequency, pipe-system, straight-pipe experiment (using quasi-static stress-strain curve and quasi-static J-R curve data to analyze the quasi-static bend experiments and quasi-static stress-strain curve and dynamic J-R curve data to analyze the dynamic pipe-system experiments)

Experiment No.	Material	Weld Configuration	Load History	Effective Stress Ratio[1]	Pressure, MPa	Fracture Ratios[2]					
						NSC	DPZP	SC.TNP1	SC.TNP2	SC.ENG1	SC.ENG2
Elbow Girth Weld Experiments Using Straight Pipe Dimensions and Stress-Strain Curve											
1-3	A106B SAW	Elbow Girth Weld	Single Freq.	-0.55	15.5	0.802	0.863	0.887	1.154	1.210	1.480
1-4	A106B SAW	Elbow Girth Weld	QS Bend	1.0	15.5	0.679	0.783	0.882	1.131	1.156	1.326
Elbow Girth Weld Experiments Using Elbow Dimensions and Stress-Strain Curve											
1-3	A106B SAW	Elbow Girth Weld	Single Freq.	-0.55	15.5	0.857	0.896	0.956	1.225	1.262	1.494
1-4	A106B SAW	Elbow Girth Weld	QS Bend	1.0	15.5	0.818	0.903	1.058	1.341	1.357	1.546
Straight Pipe Experiments											
4141-8	A106B SAW	Straight Pipe Weld	QS Bend	1.0	15.5	0.696	0.817	0.923	1.164	1.157	1.295
1.3-4	A106B SAW	Straight Pipe Weld	Single Freq.	-0.15	15.5	0.754	0.816	0.902	1.143	1.149	1.282

(1) $R_{effective} = (\sigma_{B_{min}} + \sigma_m)/(\sigma_{B_{max}} + \sigma_m)$.

(2) The fracture ratios for Experiments 1-3 and 1-4 have been adjusted to account for the crack being off-center, i.e., fracture ratio = $(\sigma_{B_{expt}}\cos(\psi)+\sigma_m)/(\sigma_{B_{analysis}}+\sigma_m)$ where $\psi = 43$ degrees for Experiments 1-3 and 1-4.

Table 5.11 Fracture ratios for stainless steel weld pipe experiments (using quasi-static stress-strain curve and quasi-static J-R curve data to analyze the quasi-static bend experiments and quasi-static stress-strain curve and dynamic J-R curve data to analyze the dynamic pipe-system experiments

Experiment No.	Material	Load History	Pressure, MPa	Effective Stress Ratio[1]	a/t[2]	θ/π[3]	Fracture Ratios[4]					
							NSC	DPZP	SC.TNP1	SC.TNP2	SC.ENG1	SC.ENG2
1-5	TP304 SAW	Single Freq.	15.5	-0.5	0.442	0.267	0.815	0.822	0.981	1.217	1.029	1.166
1-6	TP304 SAW	QS Bend	15.5	1.0	0.620	0.270	0.844	0.955	1.117	1.431	1.319	1.677
4141-4	TP304 SAW	QS Bend	11.0	1.0	0.613	0.50	0.801	0.906	1.082	1.396	1.340	1.555
1.3-5	TP304 SAW	Single Freq.	15.5	-0.2	0.601	0.532	0.917	0.924	1.111	1.441	1.389	1.585

(1) $R_{effective} = (\sigma_{B_{min}} + \sigma_m)/(\sigma_{B_{max}} + \sigma_m)$.

(2) Using the crack depth/wall thickness definitions that agree best with other surface-cracked pipe fracture data (a_i/t_3; see Figure 5.16).

(3) Using maximum θ value on inside surface.

(4) Fracture ratio = $(\sigma_{B_{expt}} + \sigma_m)/(\sigma_{B_{analysis}} + \sigma_m)$.

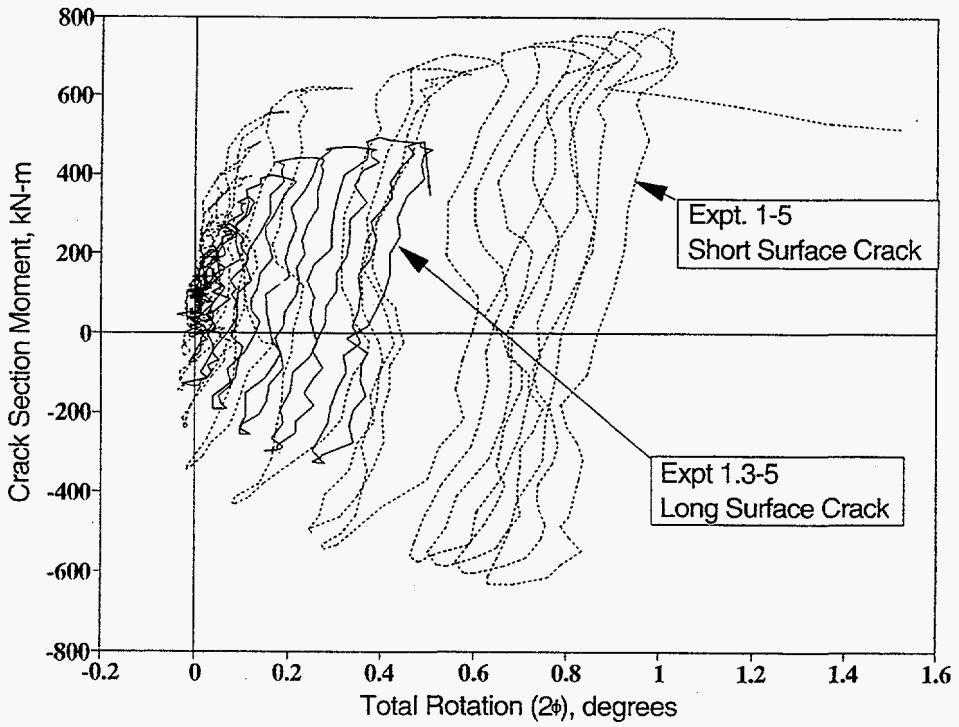

Figure 5.31 Plots of the moment-rotation behavior for both the short and long surface-cracked stainless steel weld pipe-system experiments

Regardless, the overall results of the analyses represented by Table 5.11 tend to indicate that the analyses methods previously developed and validated for the case of long surface cracks work well for the case of a relatively short surface crack, if the effects of cyclic loading can be properly accounted for. This result is supported by the findings in Reference 5.9.

5.2.3.5 Comparisons of Predictions with Experimental Data from Short Through-Wall-Cracked Pipe Experiments

Three relatively short-through-wall-cracked pipe experiments were conducted as part of Task 1 of the IPIRG-2 program. For Experiments 1-7 and 1-8, the through-wall-cracks were located in the base metal of a 16-inch nominal diameter A106 Grade B carbon steel pipe with a wall thickness equal to Schedule 100 specifications. The through-wall crack lengths for these two experiments were 12 percent of the pipe circumference. Experiment 1-7 was a simulated-seismic, pipe-system experiment using a slightly increased amplitude version of the seismic forcing function used in Experiments 1-1 and 1-2. Experiment 1-8 was a quasi-static, monotonic four-point bending experiment. In both cases the test specimens were pressurized with subcooled water to a test pressure of 15.5 MPa (2,250 psi). The internal pipe pressure for these two experiments was sealed with an external patch, see Figure 5.32. The third experiment (Experiment 1-9) was a 6-inch nominal diameter through-wall-cracked pipe experiment. The through-wall crack for this experiment was approximately 25 percent of the pipe circumference in length. The load history for this experiment was dynamic, monotonic four-point bend plus internal pipe pressure. The test specimen for this experiment was also pressurized to 15.5 MPa (2,250 psi) prior to applying the dynamic monotonic loading. The internal pipe pressure for this experiment was sealed with an internal bellows.

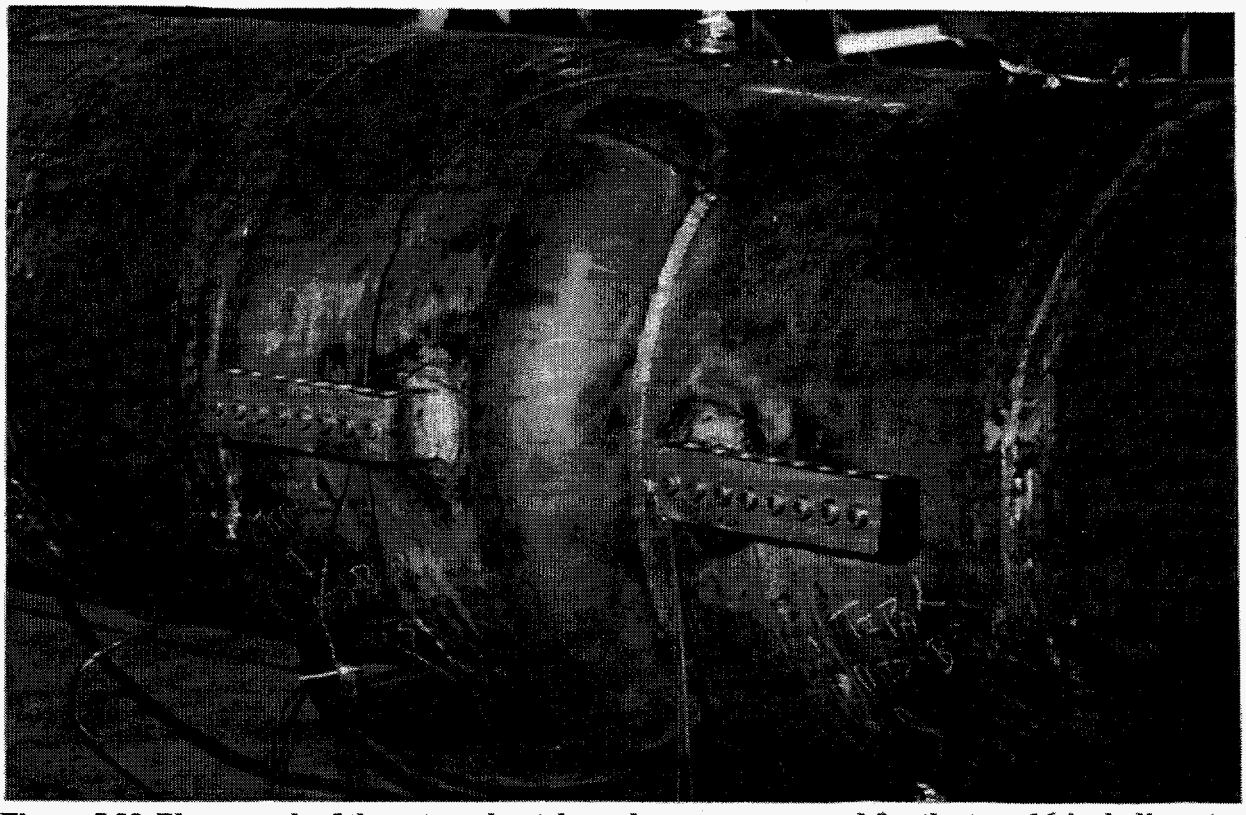

Figure 5.32 Photograph of the external patch used as a pressure seal for the two, 16-inch diameter, through-wall-cracked, pipe experiments conducted as part of Task 1 in IPIRG-2

The results of the fracture ratio calculations for these three through-wall-cracked pipe experiments are shown in Table 5.12. As can be seen in Table 5.12, the calculated fracture ratios for the 16-inch diameter simulated-seismic experiment (Experiment 1-7) are approximately 15 percent less than the corresponding calculated fracture ratios for the companion 16-inch diameter, quasi-static, monotonic, four-point-bend experiment (Experiment 1-8). This decrease in load-carrying capacity for the simulated-seismic experiment when compared with that of the quasi-static, monotonic experiment may be attributed to cyclic loading effects. As can be seen in Figure 5.33, which is the moment versus crack-mouth-opening-displacement (CMOD) response for this experiment, there was a number of large amplitude plastic cycles, in addition to a large number of elastic cycles, which occurred prior to the attainment of maximum moment for this experiment. In addition, the magnitude of the compressive moment values is approximately the same as the magnitude of the tensile component of the moment values. The combined result of these large amplitude plastic cycles and the large compressive moments creates a situation in which significant cyclic damage could occur.

Another possible explanation for the observed reduction in load-carrying capacity for the pipe system experiment is dynamic loading rate effects. However, dynamic loading rates did not appear to have a large impact on either the stress-strain or J-R curves for this material (DP2-F23). At dynamic rates the yield strength increased slightly when compared with the quasi-static values and the ultimate strength decreased approximately the same amount, see Table 2.3. Consequently, the flow stress, when defined as the average of the yield and ultimate strengths, would be virtually unchanged as a result of this increase in strain rate. Similarly there was not a dramatic change in the J-R curves between the quasi-static and dynamic loading rate C(T) specimen tests for this material, see Figure 2.27. As can be seen in Figure 2.27, the J-R curve for

Table 5.12 Results of fracture ratio calculations for the three through-wall-cracked pressure plus bending pipe experiments conducted as part of IPIRG-2 Task 1 (using quasi-static stress-strain curve and quasi-static, monotonic, J-R curve data to analyze the quasi-static bend experiment and quasi-static stress-strain curve and dynamic, monotonic, J-R curve data to analyze the dynamic pipe experiments)

Experiment No.	Material	Load History	Pressure, MPa	θ/π	Fracture Ratios[1]				
					NSC	DPZP	GE/EPRI	LBB.NRC	LBB.ENG2
1-7	A106B	Sim. Seismic	15.5	0.12	0.869	1.066	1.247	1.153	1.106
1-8	A106B	QS Bend	15.5	0.12	1.039	1.375	1.436	1.333	1.268
1-9	A106B	Dyn. Bend	15.5	0.249	0.949	1.236	1.720	1.602	1.731

(1) Fracture ratio = $(\sigma_{B_{exp}} + \sigma_m)/(\sigma_{B_{analysis}} + \sigma_m)$. Quasi-static stress-strain and J-R curve data were used in these analyses. The dynamic J-R curve was similar to the quasi-static J-R curve.

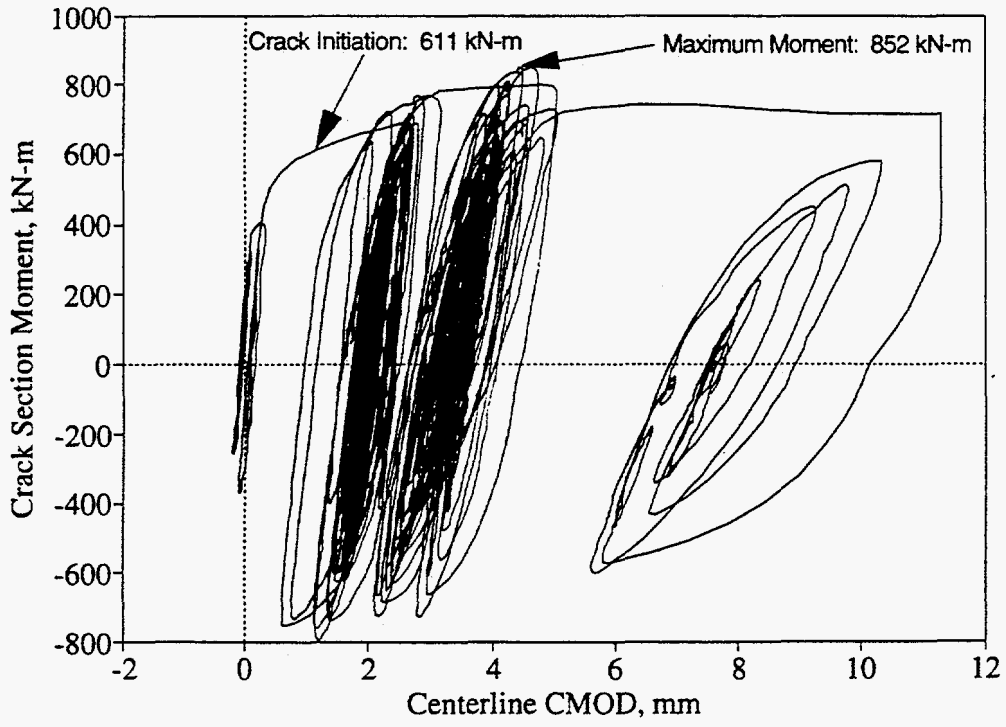

Figure 5.33 Moment-CMOD response for the simulated-seismic, through-wall-cracked, pipe-system experiment (Experiment 1-7)

one of the quasi-static C(T) specimen tests agreed almost exactly with the J-R curves for the two dynamic C(T) specimen tests. The other quasi-static J-R curve was somewhat higher than the J-R curves for the other three C(T) specimen tests.

Another possible explanation for this reduction in load-carrying capacity for the pipe system experiment when compared with the quasi-static experiment is that the through-wall crack in the quasi-static experiment grew at a much greater angle with respect to the circumferential crack plane than did the through-wall crack for the pipe system experiment. The through-wall crack in the quasi-static experiment grew at an angle approximately 60 degrees from the circumferential crack plane at one crack tip and at an angle approximately 75 degrees from the circumferential crack plane at the other crack tip. The through-wall crack in the pipe system experiment grew at angles of approximately 35 and 50 degrees from the circumferential plane at the two crack tips. As noted in Reference 5.34 the maximum loads for through-wall-cracked experiments which exhibited angled crack growth are greater than those which exhibited straight crack growth. Consequently, it stands to reason that as the crack growth angle increases, the maximum loads should also increase.

A fourth possible explanation for this observed reduction in load-carrying capacity for the pipe system experiment when compared with the quasi-static experiment is that the experimental data are suspect. The design of the external patch used to seal the internal pipe pressure for these through-wall-cracked pipe experiments was a definite challenge. On the one hand, the patch had to be robust and stiff enough such that it would contain the internal pipe pressure, while on the other hand, it had to be flexible enough so as not to carry appreciable bending load, and thus affect the experimental results. The toroidal-shaped external patch design seemed to offer the best hope of mutually satisfying these seemingly competing design constraints. As long as the patch remained cylindrical in shape, it was thought that the patch would act primarily as a hinge and not carry appreciable bending loads. In post-test examination of the patch for Experiment 1-7, i.e., the simulated-seismic pipe system experiment, see Figure 5.34a, it was found that the patch had indeed remained cylindrical in shape. However, the patch for Experiment 1-8, i.e., the quasi-static, four-point bend experiment, flattened appreciably during the course of the experiment, see Figure 5.34b. As such the patch for Experiment 1-8 was probably carrying a portion of the bending loads across the crack such that the experimentally measured bending loads, and thus moments, for this experiment were probably slightly higher than what they would have been if the patch had not been in place.

Consequently, the higher fracture ratios for the quasi-static bend experiment when compared with those for the pipe system experiment are probably attributed to either; (1) cyclic effects, (2) angled through-wall crack growth, (3) a problem with the experimental data, i.e., the patch was carrying a portion of the load for the quasi-static experiment, or (4) a combination of the above. As a result of the fact that the experimental data for Experiment 1-8 are even the least bit suspicious, the data for this experiment should be used with caution.

5.2.4 Comparison of Maximum Stress Predictions from Failure Avoidance Criteria with Experimental Data

In this section, comparisons of maximum stress predictions with two failure avoidance criteria, i.e., the ASME Section XI and R6 approaches, are made. Two different approaches to define a "fracture ratio" have been considered. In the first approach (Approach 1), the experimental stresses are compared with the

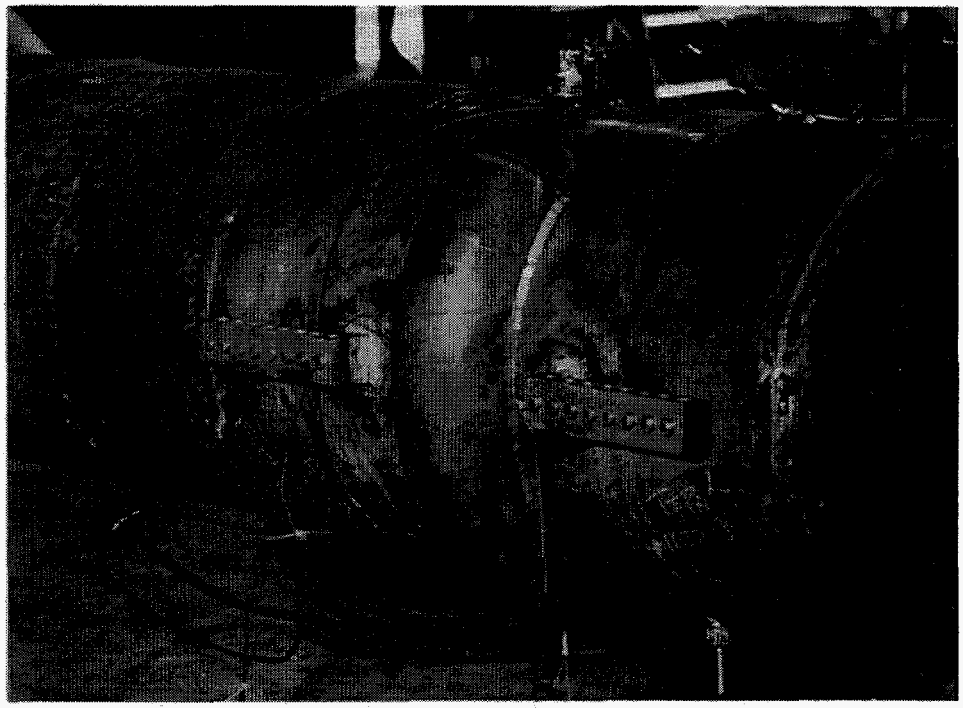

(a) Experiment 1-7

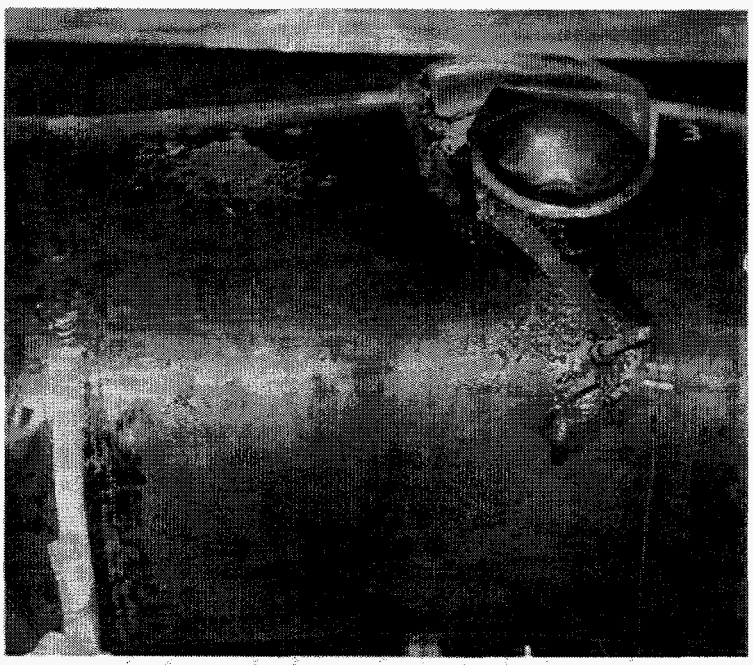

(b) Experiment 1-8

Figure 5.34 Post-test photographs of patches used in the two IPIRG-2, 16-inch diameter, through-wall-cracked, pipe experiments

ASME and R6 predicted stresses without applied safety factors. Basically, this approach evaluates the source equations, but it ignores the prediction of the crack driving force, i.e., the piping stress analysis and its associated safety factors. The second approach (Approach 2) considers not only the "allowable stresses" but also the calculated "applied stresses" from an uncracked pipe elastic stress analysis relative to the actual moments experimentally generated. Thus, Approach 2 provides an assessment of the complete flaw evaluation procedures, including all implicit or explicit safety factors on the different stress components.

To perform an Approach 1 assessment, the stresses on the flaw at the maximum applied load condition, the post-test measured flaw geometry, and code-specified material properties are required. For the Approach 2 analysis, all of the Approach 1 information plus the results of an elastic stress analysis are required. Given a prescription of the analysis equations, the "fracture ratio" is calculated as the experimental stress divided by the predicted stress.

5.2.4.1 Failure Avoidance Criteria

The methods described previously in Section 5.2.2.1 were all fracture prediction methodologies typically used to give reasonably accurate predictions of the actual failure stresses. In the following sections, three flaw evaluation methodologies embodied in Section XI of the ASME Code and one of the analysis approaches in the R6 document are considered. The failure avoidance criteria to which the experimental data are compared include:

- ASME Section XI,
- Appendix C for austenitic piping (Refs. 5.13 and 5.14),
- Appendix H for ferritic piping (Refs. 5.15 and 5.16),
- Code Case N-494-3* (Refs. 5.17 and 5.18), and
- R6 Revision 3 Option 1 (Refs. 5.19 and 5.20).

These methods are intended to be failure avoidance criteria rather than accurate predictive tools, and hence, should consistently underpredict the experimental results.

For each of these methods the experiments considered were analyzed using the ASME Code definition of the flaw size as described in Section 5.2.1.1, i.e., a constant depth flaw with a flaw depth equal to the maximum flaw depth and a flaw length equal to the total flaw length.

ASME Section XI IWB-3640 and Appendix C Flaw Evaluation Criteria for Austenitic Piping

The technical basis for the ASME Section XI IWB-3640 and Appendix C flaw evaluation criteria for austenitic piping is the Net-Section-Collapse (NSC) criterion (Ref. 5.6). However, there are two distinct differences between the Appendix C and NSC criteria.

---

* Code case N-494-3 was approved during the preparation of this report, but was not published at the time this report was completed.

(1) The flow stress definition in the Appendix C criteria is defined as 3 times the design stress intensity factor (S_m) as defined in Section II Part D of the ASME Code rather than the average of the measured yield and ultimate strengths as used in the NSC analyses discussed above. As discussed previously, the flow stress defined as $3S_m$ was based on an S_m based on actual material property data following the procedures specified in Article 2110 of Appendix III Section III Division 1 of the 1989 edition of the ASME code, i.e., S_m(Actual), as well as the code values in Section II, Part D, i.e., S_m(Code).

(2) A Z-factor is introduced in the analyses to account for the lower toughness flux welds in predicting the maximum allowable stresses of these welds.

ASME Section XI IWB-3650 and Appendix H Flaw Evaluation Criteria for Ferritic Piping

The ASME Section XI Appendix H flaw evaluation criteria for ferritic piping (Ref. 5.15) is fundamentally different than the Appendix C criteria for austenitic piping in that the Appendix H criteria incorporates a screening criterion to establish the failure mechanism of the flawed pipe (i.e., linear-elastic, elastic-plastic, or limit-load) depending on the pipe and flaw sizes, as well as the strength and fracture toughness of the cracked pipe material. For these lower toughness ferritic pipes and their associated weldments, Appendix H incorporates a stress multiplier (i.e., Z-factor) on the limit-load solution for the elastic-plastic analysis to account for the crack being in a lower-toughness material. This Z-factor approach is similar to that used for the austenitic criteria in Appendix C for the case of cracks in lower toughness austenitic flux welds, i.e., submerged-arc and shielded-metal-arc welds. As part of previous programs (Refs. 5.1 and 5.9), it has been shown that the elastic-plastic Z-factor solutions for the Appendix H ferritic criteria are much more conservative than the Z-factor solutions embodied in the Appendix C austenitic criteria. In the past, it has been shown that the calculated fracture ratios (i.e., the ratio of the experimental stress [bending plus membrane due to internal pipe pressure]-to-the maximum predicted stress [bending plus membrane due to internal pipe pressure]) for the Appendix C criterion for austenitic piping are on average slightly greater than one while the calculated fracture ratios for the elastic-plastic criterion embodied in Appendix H for ferritic piping are on average approximately two.

ASME Code Case N-494-3 Approach

The Code Case N-494-2 approach (Ref. 5.17) is similar to the R6 method (discussed next) in that it involves a failure assessment diagram (FAD). Code Case N-494-3 is based on deformation plasticity and uses some of the GE/EPRI functions to specify the bounding failure assessment curve for surface-cracked pipe. This method is essentially the same as the EPFM approach used in the GE/EPRI J-estimation scheme. While safety factors may be specified externally in this method, it suffers from the same limitations as those for the R6 approach, namely that rotations and/or displacements are not predicted. The shape of the FAD curve is stress-strain curve and geometry dependent. This method is currently being incorporated into the ASME Section XI Flaw Evaluation Procedures by using a lower bound FAD curve shape (Ref. 5.17). At the time this report was written, this Code Case was extended to consider both austenitic and ferritic materials.

R6 Revision 3 Option 1 Method

This approach for evaluating the integrity of flawed structures was originally developed by the Central Electric Generating Board (CEGB) in the United Kingdom (Refs. 5.19 and 5.20). The basic method

involves a diagram of the toughness ratio (K_r) versus the load ratio (L_r) as shown in Figure 5.35. The value of K_r for a flawed structure is the ratio of the linear-elastic stress intensity factors (K_I) to the material toughness (K_{Ic}). The value of L_r is the ratio of the nominal stress in the component to the yield stress of the material. If the point (L_r, K_r) falls within the failure assessment curve, shown in Figure 5.35, then the structure is deemed to be safe. If the assessment point (L_r, K_r) falls outside the failure assessment diagram, the structure is not necessarily unsafe, but should be evaluated using some other evaluation method, e.g., R6 Option 2 or 3. The R6 document recommends the use of best estimate material data. Such data were used in the analyses reported herein.

This method has some inherent safety factors incorporated into the Failure Assessment Curve (FAC), $K_r = f(L_r)$, and hence, the predicted failure loads should never be lower than the experimental values. The ratio of the distance from the origin to the FAC through the assessment point (L_r, K_r) to the distance from the origin to the assessment point (L_r, K_r) in Figure 5.35 is the margin of safety for the structure. Note, the moment-rotation behavior of the cracked pipe cannot be predicted using this method as is possible using some of the J-estimation scheme analysis methods.

Further details of each of these failure avoidance methods can be found in the appropriate references.

5.2.4.2 Approach 1 Fracture Ratios

As indicated previously, Approach 1 is an evaluation of the source equations for cracked-pipe load-carrying capacity. That is, the maximum experimentally applied bending plus pressure stress is compared with the maximum predicted flaw bending plus pressure stress capacity using no factors of safety.

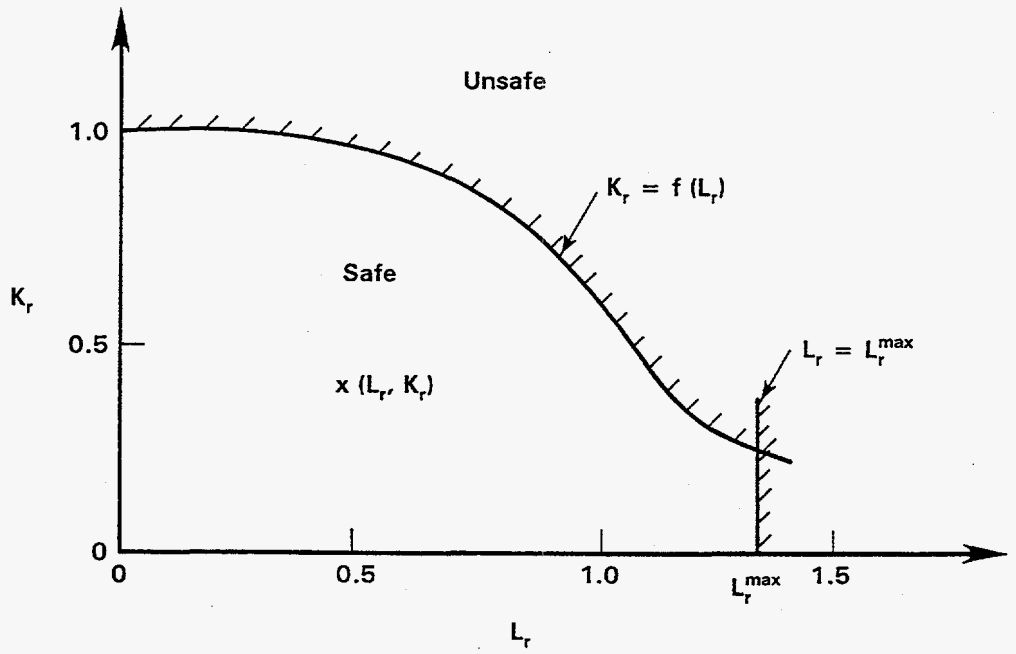

Figure 5.35 R6 failure assessment diagram

Table 5.13 shows the Approach 1 fracture ratios for the IPIRG-2 Task 1 and companion pipe experiments for the ASME Section XI and R6 Revision 3 Option 1 failure avoidance criteria*.

The crack shape/size assumed in all of these analyses are a rectangular crack shape with the crack depth equal to the crack depth at the deepest location along the crack front ($a = a_{max}$) and the crack length equal to the total crack length. For the weld crack experiments, the crack depth (a) and wall thickness (t) are referenced with respect to the counterbore surface, i.e., $a = a_2$ and $t = t_2$, per the specifications of Paragraph NB-3641.1 of Section III of the ASME Code. This was consistent for both the ASME and R6 calculations. For the ASME Appendices C and H approaches, the flow stress has been based on both S_m(Code) and S_m(Actual). As can be seen in Table 5.13, the Appendix H criteria predictions for ferritic pipe result in higher fracture ratios (more conservative) than the Appendix C criteria for austenitic pipes. This finding has been reported previously on several occasions (Refs. 5.1 and 5.7). In fact, the fracture ratios for the two elevated temperature, dynamic cyclic pipe system stainless steel base metal experiments (Experiments 1.3-3 and 1-1) are close to 1.0 when the flow stress is based on S_m(Code) values and considerably less than 1.0 when the flow stress is based on S_m(Actual) properties. Remember the S_m(Actual) analyses were performed in order to see the what values of fracture ratios which may have been obtained if the pipe materials evaluated had strength properties near the Code values from 2A of Part D of Section II of the ASME Code. Consequently, it appears that if the strength properties of the stainless steel base metal evaluated in these experiments had been near those specified in Section II, then the experimental moments may have been less than predicted using the Appendix C criteria in conjunction with the S_m(Code) values from Section II.

It is also of note from Table 5.13 that the fracture ratios for the four stainless steel weld experiments were greater than 1.0 regardless of whether the flow stress was based on S_m(Code) or S_m(Actual). (Note, for these calculations, the Z-factors are based on 16-inch nominal diameter pipe and not the assumed 24-inch diameter pipe used in the stainless steel flux weld Z-factor calculations embodied in the 1995 edition of Section XI of the ASME Code. This change to the methodology for calculating Z-factors was approved at the March 1996 meeting of the Section XI Working Group on Pipe Flaw Evaluation. As noted earlier, the predicted moments/stresses for these stainless steel weld experiments were calculated assuming that the wall thickness "t" was the wall thickness of the pipe less the counterbore depth (and excluding the weld crown height), i.e., t_2 in Figure 5.16, and the crack depth "a" was the depth of the crack with respect to the inside surface of the counterbore, i.e., a_2 in Figure 5.16. This set of assumptions seems to be most closely aligned with the spirit of the ASME Code in that Paragraph NB-3641.1 of Section III specifies that "the wall thickness 't' is the specified or actual wall thickness of the pipe minus material removed by counterboring, among other things". If one were to define the wall thickness as the actual wall thickness (less the weld crown height), i.e., t_1 in Figure 5.16, and the depth of the crack being referenced with respect to the inside surface of the pipe, i.e., a_1 in Figure 5.16, then the calculated fracture ratios for these stainless steel weld experiments are somewhat less than those shown in Table 5.13, see Table 5.14. Even so, as can be seen in Table 5.14, the calculated fracture ratios for the Appendix C criteria, for both the case when the flow stress is based on S_m(Code) and S_m(Actual), are still greater than 1.0 for all for stainless steel

* For the R6 calculations, the limit-load solution used in the calculation of the L_r term was the original Net-Section-Collapse (NSC), Refs. 5.5 and 5.6, equations, but using the yield strength instead of the flow stress in both the moment and β-term calculations. The cutoff value along the X-axis on the FAD curve (L_r^{max}) was calculated as the ratio of the NSC stress using the flow stress to the NSC stress using the yield strength. The K-solution used to calculate the K_r term along the Y-axis was based on the K-solution given in ASME Section XI Appendix H. This K-solution does not have an R/t dependence, and hence is only valid for pipes with R/t values between 5 and 10.

Table 5.13 Comparison of maximum experimental stresses for IPIRG-2 Task 1 pipe experiments and companion experiments with maximum stress predictions from ASME Section XI and R6 Revision 3 Option 1 methods

					Fracture Ratios[1]							
					Appendix C		Appendix H		Code[5] Case	Code [6] Case		
Expt. No.	Material	Load History	a/t[2,3]	θ/π[4]	S_m(Code)	S_m(Actual)	S_m(Code)	S_m(Actual)	N-494-3	N-494-3	R6[5]	R6[6]
EPRI 13S[7]	TP304	QS Bend	0.660	0.580	1.533	1.074	NA	NA	1.319	1.319	1.377	1.377
1.3-3	TP304	Single Freq.	0.660	0.552	0.977	0.728	NA	NA	1.182	1.182	1.570	1.490
1-1	TP304	Sim. Seismic	0.628	0.527	1.154	0.865	NA	NA	1.326	1.326	1.722	1.634
4112-8	A106B	QS Bend	0.662	0.532	NA	NA	2.007	1.565	1.554	1.554	1.504	1.504
1.3-2	A106B	Single Freq.	0.727	0.525	NA	NA	1.785	1.329	1.107	1.250	1.268	1.347
1-2	A106B	Sim. Seismic	0.719	0.525	NA	NA	2.293	1.704	1.418	1.613	1.632	1.729
1-3[8]	A106B SAW	Single Freq.	0.766	0.50	NA	NA	3.746	3.053	2.671	2.000	2.780	2.675
1-4[8]	A106B SAW	QS Bend	0.677	0.50	NA	NA	3.042	2.520	2.328	2.328	2.313	2.313
4141-8	A106B SAW	QS Bend	0.670	0.50	NA	NA	2.478	1.871	1.642	1.642	1.704	1.704
1.3-4	A106B SAW	Single Freq.	0.692	0.535	NA	NA	2.863	2.141	1.834	1.630	1.935	1.875
1-5	TP304 SAW	Single Freq.	0.427	0.267	1.397	1.078	NA	NA	1.663	1.511	1.672	1.594
1-6	TP304 SAW	QS Bend	0.649	0.27	1.486	1.139	NA	NA	1.819	1.819	1.889	1.889
4141-4	TP304 SAW	QS Bend	0.633	0.50	1.405	1.066	NA	NA	1.501	1.501	1.780	1.780
1.3-5	TP304 SAW	Single Freq.	0.574	0.532	1.489	1.116	NA	NA	1.646	1.485	2.003	1.929

(1) Fracture ratio $= (\sigma_{B_{expt}} + \sigma_m)/(\sigma_{B_{analysis}} + \sigma_m)$.
(2) $a = a_{max}$.
(3) For weld tests the wall thickness "t" is the wall thickness of the pipe less the counterbore depth and excluding the weld crown height, i.e., t_2 in Figure 5.16, and the crack depth "a" is the crack depth with respect to the inside surface of the counterbore, i.e., a_2 in Figure 5.16.
(4) θ = maximum value on inside surface.
(5) Using actual quasi-static yield and ultimate strength values, and quasi-static, monotonic, J-R curves in analyzing all experiments.
(6) Using actual quasi-static yield and ultimate strength values, and quasi-static, monotonic, J-R curves in analyzing the quasi-static experiments and dynamic, monotonic, J-R curves in analyzing the dynamic, pipe-system experiments.
(7) Room temperature test; all other tests conducted at 288 C (550 F).
(8) Elbow girth weld experiment; using straight pipe dimensions in analysis.

Table 5.14 Comparison of maximum experimental stresses with the ASME Appendix C predicted stresses for the four stainless steel weld experiments (wall thickness is assumed to be the actual full wall thickness of the pipe and the depth of the crack is referenced to the inside surface of the pipe)

Experiment Number	Wall Thickness, mm	a/t	θ/π	Fracture Ratios	
				S_m(Code)	S_m(Actual)
1-5	25.76	0.495	0.267	1.286	0.992
1-6	25.65	0.687	0.270	1.386	1.063
4141-4	26.19	0.668	0.500	1.368	1.104
1.3-5	25.68	0.635	0.532	1.481	1.109

weld experiments, with one minor exception, when the wall thickness and crack depth are referenced to the inside surface of the pipe and not the counterbore surface. The only exception was for Experiment 1-5 when the flow stress was based on S_m(Actual). For that case, the fracture ratio was 0.992 which is quite acceptable.

It is also of note from Table 5.13 that the fracture ratios for the ASME Code Case N-494-3 approach for the austenitic and ferritic steels and the R6 Option 1 Revision 3 approach are very comparable. Both of these methods (N-494-3 and R6) are based on predictions using a failure assessment diagram (FAD) approach. For both methods the calculated fracture ratios range from approximately 1.2 to 1.9 for the straight pipe experiments and 2.2 to 2.7 for the elbow girth weld experiments. The reason why the fracture ratios for the elbow girth weld experiments are so much greater than the fracture ratios for the straight pipe experiments probably has to do with the assumed wall thicknesses and crack depths for the two elbow girth weld experiments. The actual wall thicknesses of the straight pipe sections and elbows for these two experiments were approximately 33.5 mm (1.32 inches) while the assumed wall thickness for these code-type analyses were in the range of 26.0 to 27.1 mm (1.02 to 1.07 inches) due to the significant counterbores associated with these girth welds.

It is also of note from Table 5.13 that calculations for the Code Case N-494-3 and R6 approaches were made using both quasi-static, monotonic and dynamic, monotonic J-R curves for the pipe-system experiments. (Quasi-static stress-strain curves were always used for the analysis of these experiments, and quasi-static J-R curves were always used for the analysis of the quasi-static experiments.) In comparing the fracture ratios for the pipe-system experiments for the cases when quasi-static and dynamic, monotonic J-R curves were used, it can be seen that choice of J-R curve made little difference in the fracture ratios from these two analysis methods. Typically, the difference was on the order of 5 to 10 percent. In fact, for the two stainless steel base metal experiments, the calculated fracture ratios using quasi-static and dynamic J-R curve data were identical. This is the result of the fact that these were essentially limit-load failures, and as such, the results should be independent of fracture toughness.

5.2.4.3 Approach 2 Fracture Ratios

Approach 2 fracture ratios consider not only the source equations for the flaw capacity, but also the underlying piping stress analysis and the factors of safety applied to various stress components.

To calculate the Approach 2 fracture ratios, a linear elastic stress analysis is required. Five components of stress are of concern: dead weight, thermal, inertial, seismic anchor motion-induced (SAM), and pressure-induced membrane stresses. For the IPIRG pipe loop facility, the dead weight stresses are negligible. Typically, the other stress components are calculated as follows:

- The thermal and pressure stresses come from the stress state at time = 0,
- The SAM stress comes from a static anchor motion, displacement-loaded analysis, and
- For the IPIRG experiments, the inertial stress was calculated as the total stress less the sum of the SAM plus thermal plus pressure stress terms.

The predicted stresses are combined according to specified rules to find the Code-prescribed total applied stress. Where specified, factors of safety are applied to various stress components or stress components are ignored altogether to reflect the perceived propensity of the stress to cause crack growth. (For instance, in ASME Section XI, Appendix C, thermal expansion stresses are ignored for stainless steel base metal flaws thus suggesting that the Code authors did not think that thermal expansion stresses contribute to the crack propagation process for tough materials.) In a similar manner, the flawed pipe source equations, with specified safety factors, can be manipulated to find an expression for the total allowable stress. The ratio of the total applied stress to the total allowable stress is the fracture ratio.

In concept, the calculations enumerated above are simple to perform. In the present case, however, for some of the IPIRG-2 pipe system experiments, the validity of the linear elastic results is questionable. Because using the questionable linear elastic analysis results would compromise the usefulness of the fracture ratios, it was decided to not report any Approach 2 fracture ratio results in this report.

The difficulties encountered with the linear elastic analysis are documented in Section 5.1. Basically, for experiments that included the DEGB restraint system, the predicted moment-time response of the pipe system, even using the most sophisticated nonlinear spring cracked pipe analysis, does not agree with the experimental results, even for the first few seconds of the experiment when the crack and entire pipe system behaved elastically. Because the analysis could not be made to match the "linear" portion of the response, the whole analysis was deemed suspect. Although the linear analysis for the experiments without the DEGB restraint appear to be "correct", it was felt that to be consistent, an "all or none" philosophy should be followed on reporting Approach 2 fracture ratios.

To try to circumvent the problem with the linear analyses, an attempt was made to try to use the experimental data to predict what the linear response would be. These efforts included trying to directly use the experimental maximum moment and extrapolating the linear portions of the experimental displacement-moment plots. These efforts were either completely futile or the resulting fracture ratios were nonsensical (some were actually negative).

For consistency with what was done in IPIRG-1 (Ref. 5.1), it would have been nice to be able to present Approach 2 fracture ratios. However, it was deemed essential to use a consistent approach to doing the calculations. The position that was adopted was to abandon reporting Approach 2 fracture ratios, since it was deemed technically prudent to avoid reporting fracture ratios that may give a false sense of security, or alarm, about the failure avoidance criteria.

5.2.5 Comparison of Maximum Stress Predictions Using Cyclic J-R Curve Data with Experimental Data

In this section of the report, comparisons are made of the experimental data with the maximum stress predictions using cyclic J-R curve data. Comparisons are made between the cyclic pipe data developed as part of IPIRG-2 Task 1 as well as with the cyclic pipe data developed for the previously conducted single-frequency pipe-system experiments from IPIRG-1 with predictions using monotonically loaded C(T) specimens and cyclically loaded C(T) specimens (Ref. 5.35). Comparisons are made using the DPZP and SC.TNP1 analysis methods because past research has shown these two methods to be the best predictors of the maximum experimental stresses (Ref. 5.9). Comparisons are made only for those experiments/materials for which cyclically loaded C(T) specimen data were developed as part of this program, i.e., the stainless steel base metals (DP2-A8I and DP2-A8II), the stainless steel weld (DP2-A8W) and the carbon steel weld (DP2-F40W). For the stainless and carbon steel weld experiments, the cyclic J-R curves used in the analyses were the dynamic, R = -0.6 C(T) specimen J-R curves. The dynamic J-R curves were chosen since previously it was shown that the dynamic J-R curves worked better than the quasi-static curves when it comes to predicting the dynamic pipe-system experiments. The R = -0.6 J-R curves were chosen instead of the R = -1 J-R curves because the stress ratios for the pipe-system experiments were closer to -0.6 than -1. For the analyses of the two stainless steel base metal experiments, the dynamic, R = -0.3 C(T) specimen data were used in these analyses.

The results of the analyses using the cyclically loaded J-R curve data are shown in Table 5.15. As can be seen in Table 5.15, the use of the dynamic, R = -0.3 C(T) specimen J-R curve data had little impact on the fracture ratios for Experiment 1-1. This is because there was not much difference between the dynamic, monotonic and dynamic, cyclic (R = -0.3) C(T) specimen J-R curve data for this material (DP2-A8I). For Experiment 1.3-3, the use of the cyclic J-R curve resulted in a 16 percent increase in the fracture ratio when compared with the case where the dynamic, monotonic, J-R curve was used in the analysis. This increase in the fracture ratio is the direct result of a significant lowering the J-R curve of this material (DP2-A8II) when cyclically loaded, see Figure 5.36.

For the carbon steel weld experiments, the use of the cyclic J-R curves raised the fracture ratios (i.e., lowered the predictions) by approximately 30-45 percent when using the DPZP analysis and 15-20 percent when using the SC.TNP1 analysis. For the stainless steel weld experiments, the use of the cyclic J-R curves raised the fracture ratios by approximately 10 percent when using the DPZP analysis method and 20 percent when using the SC.TNP1 analysis method.

In comparing the results from Table 5.15 with the results from Table 5.11 for the stainless steel weld experiments, it can be seen that if the dynamic, cyclic (R = -0.6) J-R curve for this weld is used in the analyses of Experiment 1-5, which experienced the much larger compressive moments ($R_{effective}$ = -0.5 versus -0.2 for Experiment 1.3-5), then the calculated fracture ratios for Experiment 1-5 agree very closely with the calculated fracture ratios for the other three stainless steel weld experiments when monotonic J-R curve data were used in the analyses of these three experiments. For the DPZP and SC.TNP1 analysis methods, the calculated fracture ratios following such an approach ranged from 0.905 to 0.955 and 1.082 to 1.16, respectively. It was shown previously in Table 5.11 that if monotonic J-R curve data were used to analyze Experiment 1-5, then the DPZP and SC.TNP1 calculated fracture ratios for Experiment 1-5 were

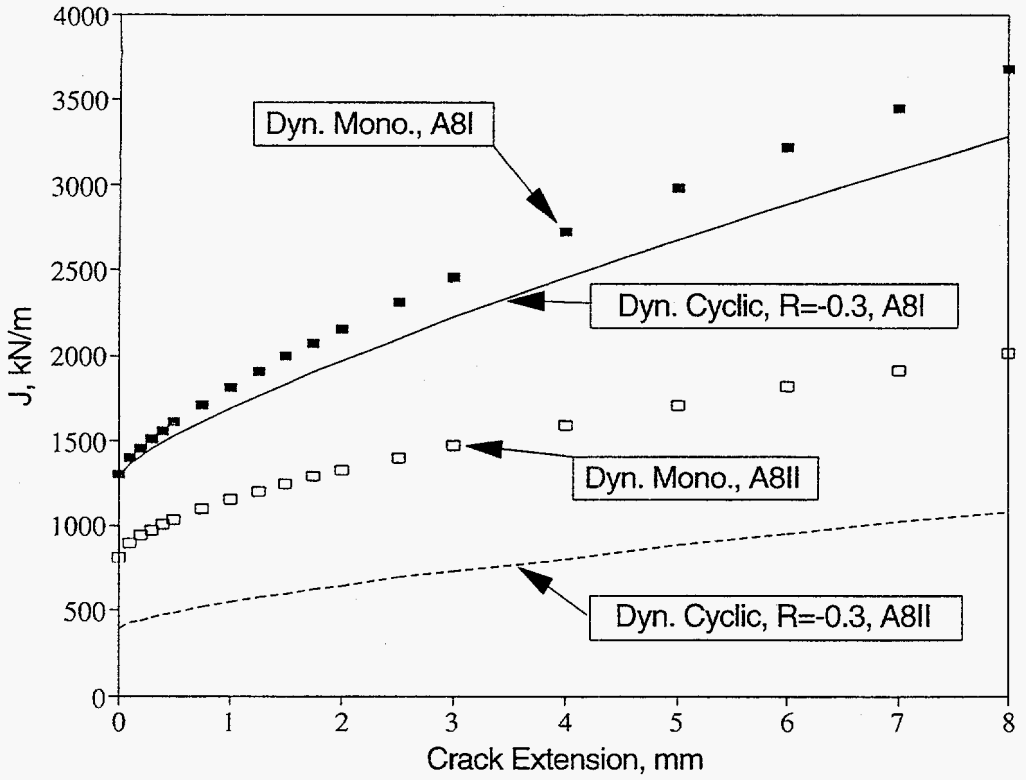

Figure 5.36 Comparison of dynamic, monotonic and dynamic, cyclic (R = -0.3) C(T) specimen J-R curve data for pipe materials DP2-A8I and DP2-A8II

Table 5.15 Comparison of fracture ratios for six pipe system experiments when using monotonic and cyclic J-R curves in the analyses

Expt. No.	Test Specimen Material[2]	Forcing Function	Fracture Ratios Using Dynamic Monotonic C(T) Specimen J-R Curves		Fracture Ratios Using Dynamic Cyclic (R = -0.3 or R = -0.6) C(T) Specimen J-R Curves[1]	
			DPZP	SC.TNP1	DPZP	SC.TNP1
1.3-3	SSBM	Single Freq. Sim.	0.975	0.890	0.975	1.036
1-1	SSBM	Seismic	1.156	0.999	1.156	1.011
1.3-4	CSW	Single Freq.	0.816	0.902	1.197	1.080
1-3[2]	CSW	Single Freq.	0.863[3,4]	0.887[3,4]	1.137[3,4]	1.029[3,4]
1.3-5	SSW	Single Freq.	0.924	1.111	1.019	1.321
1-5	SSW	Single Freq.	0.822	0.981	0.905	1.160

(1) For the two stainless steel base metal experiments, the dynamic, cyclic (R = -0.3) C(T) specimen J-R curves were used, and for the carbon and stainless steel SAW experiments, the dynamic, cyclic (R = -0.6) C(T) specimen J-R curves were used.
(2) SSBM = stainless steel base metal; CSW = carbon steel weld; SSW = stainless steel weld.
(3) Using the straight pipe dimensions and straight pipe material data in the analyses.
(4) Adjusted fracture ratio to account for off-center crack.

0.822 and 0.981, respectively. These ratios are significantly below the values for the other three stainless steel weld experiments. Thus, it appears cyclic J-R curve data improve the accuracy in predicting such an experiment. Furthermore, it appears in comparing Tables 5.11 and Table 5.15, that Experiment 1.3-5, which had an effective stress ratio of -0.2, is probably best analyzed using monotonic J-R curve data instead of cyclic J-R curve data.

5.3 η-Factor Analyses of Pipe Experiments

In this section, the results of a series of η-factor calculations for a subset of the surface-cracked Task 1 and companion pipe experiments from related programs (Refs. 5.3 and 5.4) will be discussed. The η-factor analysis (Refs. 5.36 and 5.37) is a simple method for estimating the fracture resistance of a pipe material from a pipe test experimental record, used in lieu of three-dimensional finite element analyses. In calculating J using the η-factor analysis, J is separated into its elastic and plastic components.

$$J = J_e + J_p \tag{5-12}$$

where the elastic component of J is

$$J_e = K_I^2/E' \tag{5-13}$$

where

$$K_I = K_{Im} + K_{Ib} \tag{5-14}$$

and

$$E' = E/(1 - \upsilon^2) \tag{5-15}$$

and K_{Im} and K_{Ib} can be calculated using the equations embodied in Paragraph H-4220 of Appendix H to ASME Section XI.

The plastic component of J, J_p, is the energy absorbed during the test, i.e., the area under the plastic portion of the moment-rotation curve, multiplied by a geometric term, i.e., the η-factor.

As part of this effort, the η-factor analyses were conducted only for those surface-cracked pipe experiments for which valid cracked-section rotation data existed. In addition, only J values at crack initiation (J_i) were calculated since the crack growth was not uniform all along the crack front which greatly complicates the analysis.

The J_i values for the various pipe experiments from these η-factor calculations are presented in Table 5.16, along with the J_i values from the C(T) specimen tests. Both quasi-static and dynamic C(T) specimen J_i values are shown in Table 5.16. In addition, where available, J_i values from the quasi-static and dynamic, cyclic C(T) specimen J-R curve tests are presented.

Table 5.16 Comparison of J_i values from η-factor analyses of surface-cracked pipe experiments and J_i values from C(T) specimen tests

	J_i Values, kJ/m^2				
Experiment Number	Pipe Experiment	Quasi-Static Monotonic C(T) Specimen	Dynamic Monotonic C(T) Specimen	Quasi-Static Cyclic C(T) Specimen	Dynamic Cyclic C(T) Specimen
Stainless Steel Base Metal (DP2-A8)					
1-1 (Seismic)	583	854	1,302	952 (R = -0.3) 356 (R = -1)	1,297 (R = -0.3) ND[1] (R = -1)
1.3-3 (Single-Frequency)	233	546	815	652 (R = -0.3) 313 (R = -1)	395 (R = -0.3) ND (R = -1)
Carbon Steel Weld					
4141-8 (QS-Mono)	130	82.0	NA[2]	NA	NA
Stainless Steel Weld					
1-5 (Seismic)	673	55.0	140	46.4(R = -0.6) 39.3 (R = -1)	60.2(R = -0.6) 33.6 (R = -1)
1-6 (QS-Mono)	419	55.0	NA	NA	NA
4141-4 (QS-Mono)	585	55.0	NA	NA	NA
1.3-5 (Single-Frequency)	252	55.0	140	46.4(R = -0.6) 39.3 (R = -1)	60.2(R = -0.6) 33.6 (R = -1)

(1) ND = Not determined.
(2) NA = Not applicable.

In making these calculations, the experimental moment-rotation curves were input into the analyses along with the appropriate pipe and crack dimensions and material property data. The elastic displacements were subtracted from the total displacements, leaving the plastic displacements, which were assumed to be due only to the crack. For each analyses, actual pipe and crack dimensions were used. For the weld crack experiments, the wall thicknesses include the weld crown height (t_3 in Figure 5.16) and the crack depths were referenced to the inside pipe surface (a_1 in Figure 5.16). The crack depths and lengths used in these analyses were the maximum crack depths and the total crack lengths.

In examining Table 5.16, it can be seen that there does not appear to be a direct correlation between the η-factor J_i values from the pipe experiments and the C(T) specimen J_i values for a number of the pipe experiments. Especially poor were the correlations between the η-factor and the C(T) specimen J_i values for some of the stainless steel weld pipe experiments (1-5, 1-6, and 4141-4). If one plots the η-factor J_i value from the pipe experiments against the crack-mouth-opening displacement (CMOD) value at crack initiation from the pipe experiments, which is proportional to J, one sees that there is a nice linear relationship between J_i and CMOD for all of the experiments, except for the stainless steel weld short surface-cracked pipe system experiment (1-5), see Figure 5.37.

A couple possible explanations can be offered as to why the results from Experiment 1-5 do not agree with the rest of the data. One possible explanation for the behavior observed for Experiment 1-5 is that since

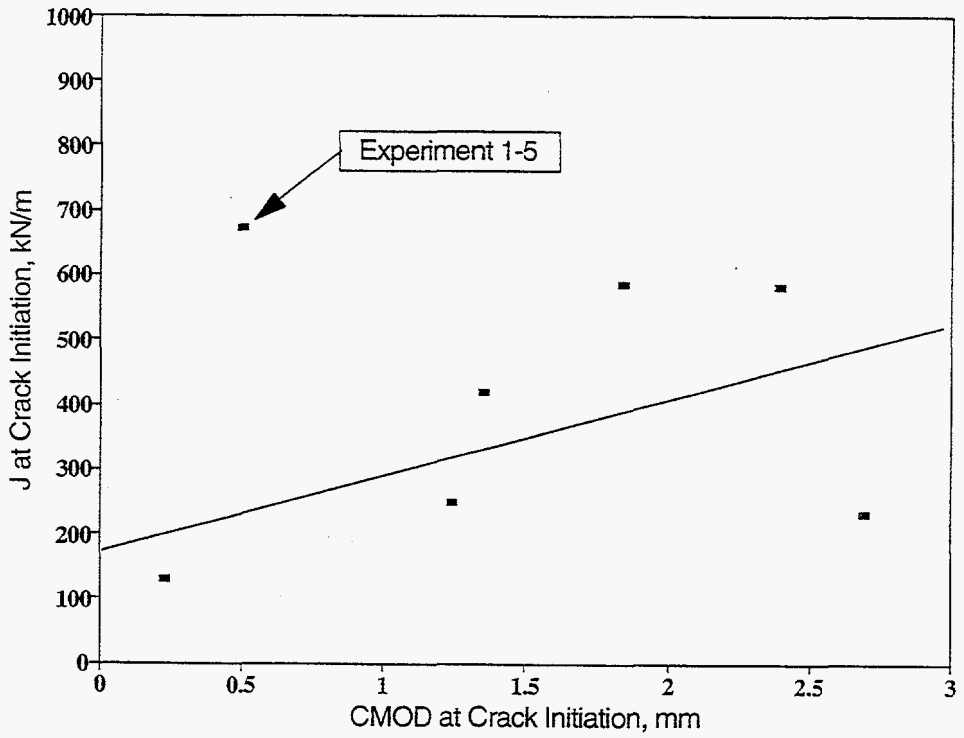

Figure 5.37 J at crack initiation from η-factor analyses as a function of crack-mouth-opening displacement, which is proportional to J, for a subset of the IPIRG-2 Task 1 and companion pipe experiments from related programs (Refs. 5.3 and 5.4)

the crack size was smaller for this experiment, the applied loads to initiate the crack were higher. As a result, for this experiment, the nominal pipe stress in the uncracked pipe, was 36 percent higher than the elevated temperature yield strength of the material. If the applied loads, and thus stresses, are high enough to cause yielding of the uncracked pipe, then the exiting η-factor solution is not appropriate. A new η-factor solution which accounts for this yielding may need to be developed since the existing solution does not account for uncracked pipe plastic rotations. To support this contention, the reader is referred to Figure 5.38 which shows two η-factor J-R curves for a short through-wall-cracked pipe experiment from the Short Cracks program (Ref. 5.28), Experiment 1.1.1.21, along with a J-R curve from a finite element analysis of this pipe experiment and C(T) specimen J-R curves for the test specimen material. The two η-factor J-R curves are for the cases where no correction was made for uncracked pipe plasticity and where a correction was made for uncracked pipe plasticity. As can be seen in Figure 5.38, the two η-factor solutions bound the finite element results. Furthermore, accounting for plasticity lowers the J-R curve, which is what would be needed to bring the results from Experiment 1-5 more in line with the results for the other experiments. In fact, from Figure 5.38, it can be seen that the J_i value for the plasticity correction solution is a factor of 3 less than the J_i value for the uncorrected solution. Applying this factor of three reduction to the η-factor J_i values for Experiment 1-5, brings the results for this experiment into much better agreement with the results for the other experiments considered, see Figure 5.39. The problem with this explanation is that there were two other pipe experiments (1-1 and 1-6) which had stresses in the uncracked pipe at crack initiation which were a higher percentage of the yield strength of the test specimen material. If plasticity was the sole explanation for the observed discrepancy for Experiment 1-5, then why did the results from these other two experiments show so much better agreement?

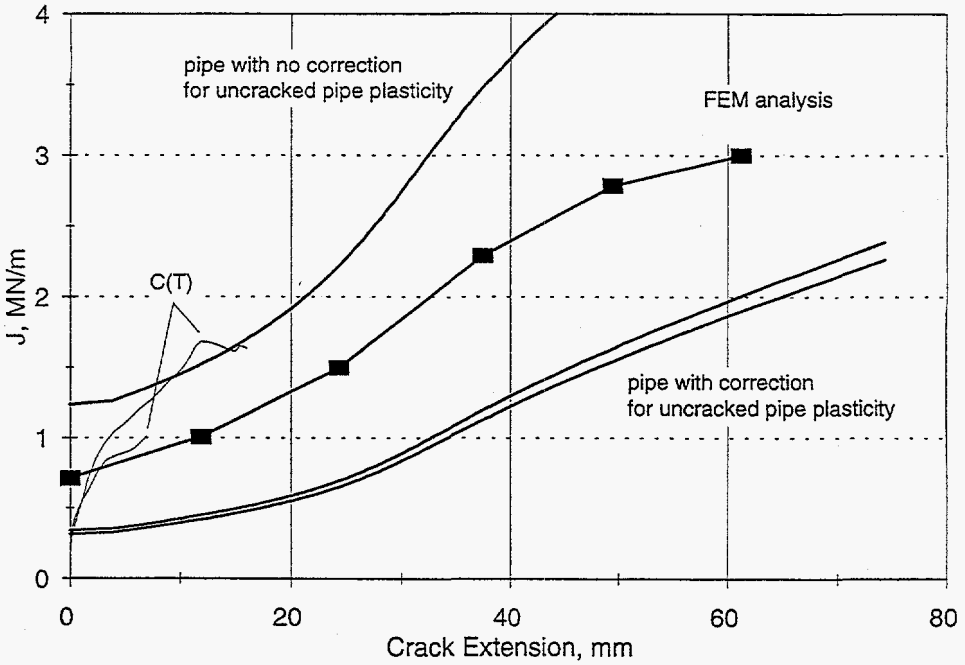

Figure 5.38 Comparison of two η-factor calculated J-R curves, one with and one without a correction for plasticity of the uncracked pipe, for Experiment 1.1.1.21 from the Short Cracks program (Ref. 5.28) with a finite element calculated J-R curve for this pipe experiment and C(T) specimen J-R curves for this pipe material

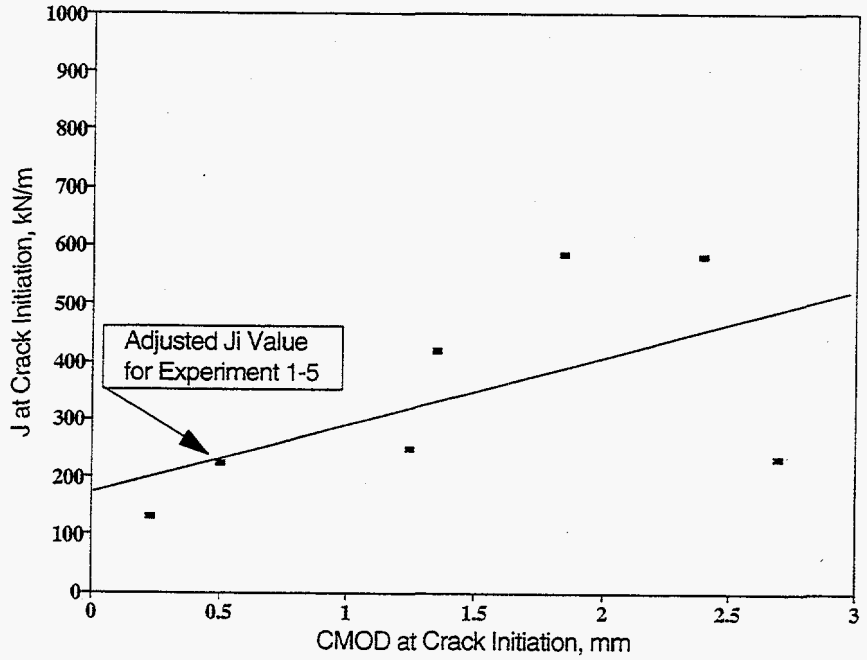

Figure 5.39 J at crack initiation from an η-factor analysis as a function of crack-mouth-opening displacement for a subset of the IPIRG-2 Task 1 and companion pipe experiments from related programs (Refs. 5.3 and 5.4) for which the J_i values for the stainless steel weld, short-surface-cracked, pipe-system experiment (1-5) has been adjusted to account for plasticity of the uncracked pipe

Another explanation for the apparent discrepancy in behavior for Experiment 1-5 is that the existing η-factor solution breaks down for shallower crack depths. Of all the experiments considered, Experiment 1-5 had the shallowest crack. Its normalized crack depth (a/t), accounting for the weld crown height, was 44 percent of the pipe wall thickness. The next shallowest crack considered was 59 percent of the pipe wall thickness in depth.

5.3.1 Validity of η-Factor Analyses for Surface-Cracked Pipe

A more basic question than why does the calculated η-factor for Experiment 1-5 disagree with the C(T) specimen data, is how good is the η-factor approach for surface cracks in general? The basic philosophy of an η-factor analysis is that the plastic part of J is related to the integration of a load versus plastic displacement or moment versus plastic rotation relationship. The η-factor function is a multiplier on this integral that accounts for specimen and crack geometry aspects. In the typical η-factor analysis, the elastic displacements are subtracted from the total displacements, leaving plastic displacements that may be due to the crack and possibly from the uncracked structure. If there are plastic displacements due to the uncracked specimen (typically from the fracture loads being above yield), then these need to be eliminated, otherwise the J values will be too high.

During the NRC's Short Cracks in Piping and Piping Welds program, an effort was undertaken to assess the various proposed η-factor solutions for circumferentially surface-cracked pipe. In the short surface-cracked pipe experiments conducted in that program, the loads at crack initiation were above yield, so that the uncracked-pipe plastic displacements needed to be accounted for. Such a correction was attempted by finite element simulation of the cracked-pipe experiment and then also conducting an uncracked-pipe analyses. The results of these analyses showed that there was insignificant difference in the moment versus rotation curve from the cracked and uncracked pipe FEM analyses. This is shown in Figure 5.40, where the rotations in this case were measured 1.375 diameters either side of the crack. Hence, it appears that an η-factor solution based on far-field displacement (or rotation) measurements may be too insensitive to capture the plasticity due to the crack.

A similar experience was found in analyzing circumferential surface cracks in elbows, Ref. 5.38. In that work, the rotations of the cracked elbow were found to be the same as the uncracked elbow, so that the GE/EPRI type h_4 function could not be defined, see Figure 5.41 from Reference 5.38. Consequently, an η-factor solution using the rotations located at either end of the elbow could also not be defined.

In order to make an η-factor analysis of a circumferentially surface-cracked pipe or elbow, it is believed that if the crack-mouth-opening displacements were used with either the load or moment, then an η-factor function could be developed that is more sensitive to the plastic displacements due to the crack, and would not be sensitive to plasticity in the uncracked pipe or elbow regions. Such an η-factor function could be developed with knowledge of the GE/EPRI h_1 (J versus moment) and h_2 (CMOD versus moment) functions. However, since most surface-cracked pipe h-functions have been developed using line-spring elements and the line-spring method does not compute the CMOD, the h_2 functions do not exist for surface-cracked pipes or elbows. Three-dimensional FEM analyses are needed to develop such functions.

As a results of these finite element analyses which were to validate surface-cracked pipe and elbow η-factor solutions, the confidence in the pipe J_i values in Table 5.16 is not very high.

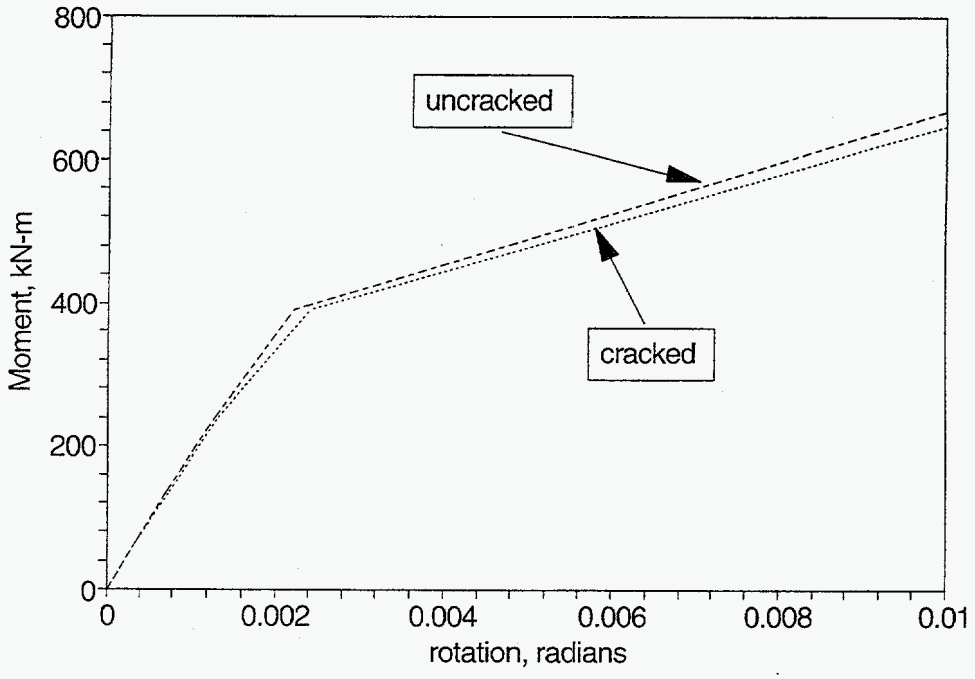

Figure 5.40 FEM predicted moment-rotation response for a cracked and uncracked pipe showing the insignificant difference between the two predictions

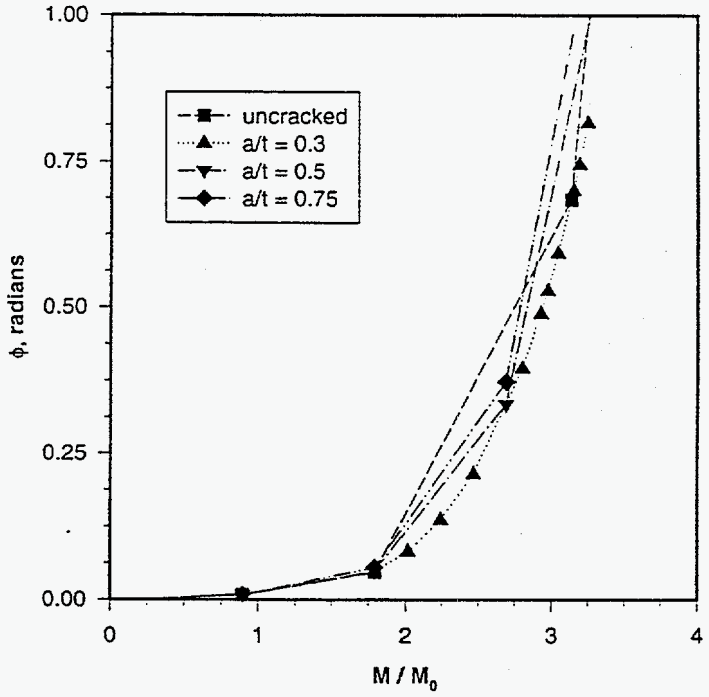

Figure 5.41 Comparisons of FEM rotations at the junction of a straight pipe and elbow for uncracked and circumferentially cracked elbows with several a/t ratios and $R_m/t = 10$ for a strain-hardening exponent n = 5 (from Ref. 5.38)

5.4 References

5.1 Scott, P., and others, "The IPIRG-1 Pipe System Fracture Tests: Analytical Results," PVP Vol. 280, pp 153-163, June 1994.

5.2 "Piping and Fitting Dynamic Reliability Program - Project Summary," Vol. 1, EPRI TR-102792, Vols. 1-5, 1995.

5.3 Wilkowski, G. M., and others, "Degraded Piping Program - Phase II, Summary of Technical Results and Their Significance to Leak-Before-Break and In-Service Flaw Acceptance Criteria," March 1984 - January 1989, NUREG/CR-4082, Vol. 8, March 1989.

5.4 Scott, P., and others, "The IPIRG-1 Pipe System Fracture Tests: Experimental Results," PVP Vol. 280, pp 135-151, June 1994.

5.5 Kanninen, M. F., and others, "Instability Predictions for Circumferentially Cracked Type 304 Stainless Steel Pipes Under Dynamic Loadings," EPRI Report NP-2347, April 1982.

5.6 Kanninen, M. F., and others, "Mechanical Fracture Predictions for Sensitized Stainless Steel Piping with Circumferential Cracks," Final Report, EPRI NP-192, September 1976.

5.7 Wilkowski, G. M., and Scott, P. M., "A Statistical Based Circumferentially Cracked Pipe Fracture Mechanics Analysis for Design or Code Implementation," *Nuclear Engineering and Design*, Vol. 111, pp 173-187, 1989.

5.8 Scott, P., and Ahmad, J., "Experimental and Analytical Assessment of Circumferentially Surface-Cracked Pipes Under Bending," NUREG/CR-4872, April 1987.

5.9 Krishnaswamy, P., and others, "Fracture Behavior of Short Circumferentially Surface-Cracked Pipe," NUREG/CR-6298, November 1995.

5.10 Kumar, V., German, M., and Shih, C., "An Engineering Approach for Elastic-Plastic Fracture Analysis," EPRI Report NP-1931, July 1981.

5.11 Klecker, R., Brust, F., and Wilkowski, G., "NRC Leak-Before-Break (LBB.NRC) Analysis Method for Circumferentially Through-Wall-Cracked Pipe Under Axial Plus Bending Loads," NUREG/CR-4572, May 1986.

5.12 Brust, F. W., "Approximate Methods for Fracture Analyses of Through-Wall Cracked Pipes," NUREG/CR-4853, February 1987.

5.13 ASME Boiler and Pressure Vessel Code, Section XI, Appendix C, 1992 Edition, July 1995.

5.14 "Evaluation of Flaws in Austenitic Steel Piping," (Technical basis document for ASME IWB-3640 analysis procedures), prepared by Section XI Task Group for Piping Flaw Evaluation, EPRI Report NP-4690-SR, April 1986.

5.15 ASME Boiler and Pressure Vessel Code, Section XI, Appendix H, 1995 Edition, July 1995.

5.16 "Evaluation of Flaws in Ferritic Piping," EPRI Report NP-6045, prepared by Novetech Corporation, October 1988.

5.17 ASME Boiler and Pressure Vessel Code, Code Case N-494-2, 1995 Edition, July 1995.

5.18 Bloom, J. M., and Malik, S. N., "A Procedure for the Assessment of Integrity of Structures Containing Defects," EPRI Report NP-2431, June 1982.

5.19 Milne, I., Ainsworth, R. A., Dowling, A. R., and Stewart, A. T., "Assessment of the Integrity of Structures Containing Defects," CEGB Report R/H/R6 - Revision 3, 1986.

5.20 Milne, I., Ainsworth, R. A., Dowling, A. R., and Stewart, A. T., "Background to and Validation of CEGB Report R/H/R6 - Revision 3," January 1987.

5.21 Rudland, D., and others, "The Effect of Cyclic and Dynamic Loads on Carbon Steel Pipe," NUREG/CR-6438, February 1996.

5.22 Marschall, C. W., and others, "Effect of Dynamic Strain Aging on the Strength and Toughness of Nuclear Ferritic Piping At LWR Temperatures," NUREG/CR-6226, October 1994.

5.23 Kurihara, R., Ueda, S., and Sturm, D., "Estimation of the Ductile Unstable Fracture of Pipe with a Circumferential Surface Crack Subjected to Bending," *Nuclear Engineering and Design*, Vol. 106, pp 265-273, 1988.

5.24 Scott, P. M., and Wilkowski, G. M., "Development and Application of a Database of Pipe Fracture Experiments," PVP - Vol. 323, Fatigue and Fracture, Vol. 1, July 1996.

5.25 Kanninen, M., and Popelar, C., *Advanced Fracture Mechanics*, Oxford University Press, New York, 1985.

5.26 Kumar, V., and others, "Advances in Elastic-Plastic Analysis," EPRI Final Report NP-3607, August 1984.

5.27 Brust, F., Rahman, S., and Ghadiali, N., "Elastic-Plastic Analysis of Small Cracks in Tubes," *Journal of Offshore Mechanics and Arctic Engineering*, Vol. 117, pp 57-62, February 1995.

5.28 Brust, F. W., and others, "Assessment of Short Through-Wall Circumferential Cracks in Pipes," NUREG/CR-6235, April 1995.

5.29 Paris, P. C., and Tada, H., "The Application of Fracture Proof Design Methods Using Tearing Instability Theory to Nuclear Piping Postulating Circumferential Through-Wall Cracks," NUREG/CR-3464, September 1983.

5.30 Gilles, P., and Brust, F., "Approximate Fracture Methods for Pipes - Part I: Theory," *Nuclear Engineering and Design*, Vol. 127, pp 1-27, 1991.

5.31 Gilles, P., Chao, K. S., and Brust, F., "Approximate Fracture Methods for Pipes - Part II: Applications," *Nuclear Engineering and Design*, Vol. 127, pp 13-31, 1991.

5.32 Brust, F. W., and Gilles, P., "Approximate Methods for Fracture Analysis of Tubular Members Subjected to Combined Tensile and Bending Loads," ASME, *Journal of Offshore Mechanics and Arctic Engineering*, Vol. 116, pp 221-227, November 1994.

5.33 Wilkowski, G. M., and others, "Degraded Piping Program - Phase II," Second Semiannual Report, October 1984 - March 1985, NUREG/CR-4082, Vol. 2, July 1985.

5.34 Mohan, R., and others, "Effects of Toughness Anisotropy and Combined Tension, Torsion, and Bending Loads on Fracture Behavior of Ferritic Nuclear Pipe," NUREG/CR-6299, April 1, 1995.

5.35 Rudland, D., and others, "The Effects of Cyclic and Dynamic Loading on the Fracture Resistance of Nuclear Piping Steels," NUREG/CR-6440, August 1996.

5.36 Zahoor, A., and Kanninen, M. F., "A Plastic Fracture Mechanics Prediction for Fracture Instability in a Circumferentially Cracked Pipe in Bending - Part I. J-Integral Analysis," *Journal of Pressure Vessel Technology*, Vol. 103, pp 352-358, 1981.

5.37 Pan, J., and others, "Application of a Tearing Instability Analysis for Strain Hardening Materials to a Circumferentially Cracked Pipe in Bending," ASTM STP 833, pp 721-748, 1984.

5.38 Mohan, R., and others, "Development of a J-Estimation Scheme for Internal Circumferential and Axial Surface Cracks in Elbows," NUREG/CR-6445, June 1996.

6.0 DISCUSSION OF RESULTS

In this section, the results of the pipe experiments and subsequent analyses of those pipe experiments will be discussed.

6.1 Discussion of Results from Elastic Stress Analyses

As discussed in Section 5.1, there were a number of questions regarding the validity of the dynamic finite element elastic stress calculations for the IPIRG-2, single-frequency, pipe-system experiments where the restraint device was used. Consequently, by implication, that created a situation where questions also arose as to the validity of the elastic stress calculations for all the other pipe system experiments that used the restraint device. As a result, the elastic stress ratio calculations that were conducted in the IPIRG-1 program were not performed. Such evaluations are useful because they provide insight and understanding as to where there may be conservatism in Leak-Before-Break or in-service flaw analyses.

The lack of credible elastic dynamic stress analyses for the pipe system experiments precluded the analysis of the pipe system experiments to ascertain the effect of secondary stresses (seismic anchor motion plus thermal expansion stresses) on the fracture behavior. As part of the analysis of the IPIRG-1, single-frequency, pipe-system experiments (Ref. 6.1), it was shown that if the piping system stresses were below yield, then the global secondary stresses, such as the thermal expansion and seismic anchor motion stresses, contributed equally to the fracture process as did the primary bending and membrane stresses, see Figure 6.1. Figure 6.1 is a bar chart comparing the normalized failure stresses of the IPIRG-1 pipe system experiments (normalized by the Net-Section-Collapse predicted stress) with the normalized failure stresses from the companion, quasi-static, monotonic experiments. The normalized failure stresses for the pipe system experiments are broken down by stress component so that the effect of the different stress components on the fracture behavior can be assessed. As can be seen in Figure 6.1, the total normalized failure stresses (including both the primary and secondary stress components) for the pipe system experiments agree closely with the normalized failure stresses for the quasi-static, monotonic experiments. If the secondary stresses are ignored, then the normalized failure stresses for the IPIRG-1 pipe system experiments would have only been a fraction of the normalized failure stresses for the quasi-static, monotonic experiments. The lack of a credible elastic analysis for the experiments which used the primary restraint device dictated that it would not be possible to conduct similar analyses of the effect of secondary stresses for the case of simulated seismic load histories and shorter crack lengths for which stresses in excess of the yield strength may occur.

Finally, the lack of a viable or credible elastic analysis implied that it would not be possible to compare the IPIRG-2 pipe system experiments with a strict ASME or R6 in-service flaw evaluation for which elastically calculated stresses are used in the crack driving force portion of the analysis. Similarly, it would not be possible to make an assessment as to how the applied elastic-calculated stresses compared with the various service level limits from Section III.

The net impact of these limitations probably warrants revisiting these elastic stress calculations at a later date in order to take full advantage of the experimental data which have been developed.

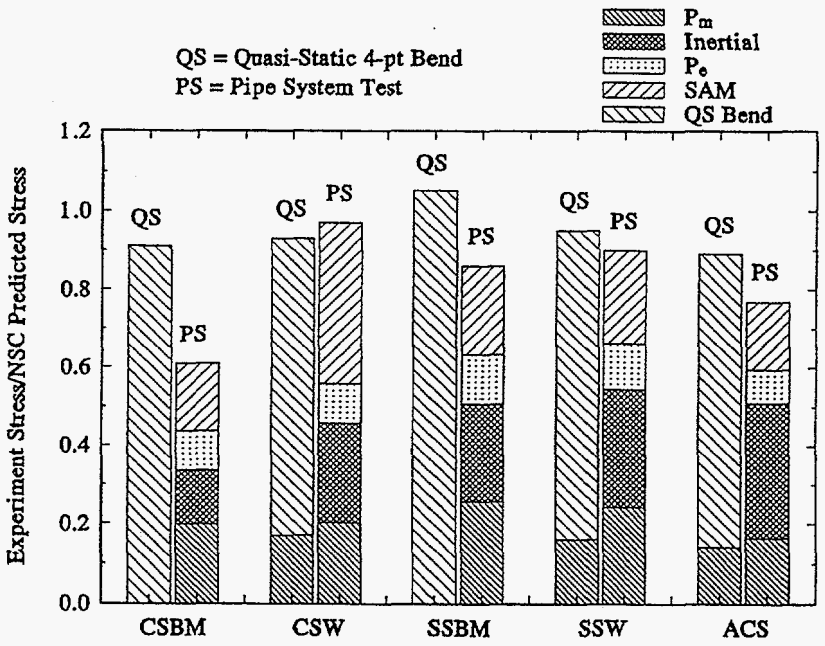

Figure 6.1 Bar chart showing the effect of the different stress components (i.e., primary membrane, primary bending, secondary thermal expansion, and secondary seismic anchor motion) on the fracture behavior of the IPIRG-1 pipe-system experiments

6.2 Discussion of Results from Comparisons with Fracture Prediction Analyses

In Section 5.2, comparisons were made between the maximum experimental stresses and the maximum predicted stresses for a number of fracture prediction analysis methods.

Comparisons of fracture ratios (i.e., the ratio of the maximum experimental stress to the maximum predicted stress) for different load histories (simulated seismic versus single frequency versus quasi-static four-point bending), different crack locations (straight pipe versus elbow girth welds), and different crack lengths (short versus long) were made to examine the effect of each of these parameters on the fracture behavior of cracked piping systems. At the beginning of the IPIRG-2 program, these issues (load history, crack location, and crack length) were areas where experimental data were lacking. As such, the rationale for and objective of Task 1 of the IPIRG-2 program were to help fill these gaps. In the sections that follow, the results of the IPIRG-2 Task 1 experiments and the companion experiments from previous programs (Ref. 6.1, 6.2, and 6.3) will be discussed in light of how the results helped address these gaps in the experimental database. The questions will be addressed as to what effect does a seismic load history or an elbow girth weld crack or a shorter crack length have on the fracture behavior of a cracked piping system. However, before specifically addressing these issues, a couple of other more fundamental issues which arose during the course of this effort need to be discussed. Namely, what is the effect on the fracture analyses of the choice of crack size definition or choice of material property data?

6.2.1 Comparison of "Most Consistent" with ASME Code Definition of Crack Size

A number of the experiments considered in Section 5.2 involved cracks in welds. The assessment of cracks in welds introduces the added complications to the analyses of weld crowns and counterbores. As a result, an assessment was made in Section 5.2.1 as to what was the "most consistent" definition of crack size to use in the fracture prediction analyses in order to account for these complications so that the results of these experiments could be compared on an equal basis. In this context "most consistent" crack size definition means that crack size definition which results in the most consistent predictions for the experiments considered in this effort when compared with predictions for a larger set of more controlled experiments (i.e., constant depth, base metal cracks) analyzed during the Short Cracks in Piping and Piping Welds program (Ref. 6.4). This "most consistent" definition of crack size involved assuming the crack was constant depth with a length equal to the total crack length and the depth equal to the maximum crack depth, much in the spirit of a crack size definition used in a Code-type flaw evaluation. For the experiments which involved cracks in welds, the wall thickness was assumed to be the actual wall thickness of the pipe plus the weld crown height and the crack depth was referenced to the inside surface of the pipe. This is somewhat different than what would be assumed for an ASME Code type analysis in that Paragraph NB-3641.1 of Section III suggests that the wall thickness should be the wall thickness of the pipe less the material removed for counterboring. Consistent with this definition of wall thickness, it seems likely that an ASME Code-type analysis would reference the crack depth to the inside surface of the counterbore and not the inside pipe surface. In addition, the height of the weld crown would in all likelihood be ignored in such an analysis.

Table 6.1 shows a comparison of maximum moment predictions between using the "most consistent" and ASME Code definitions of crack size for seven of the eight Task 1 and companion experiments which involved cracks in welds. The predictions were made using the SC.TNP1 analyses since that analysis method, along with the DPZP analysis method, was found to be most accurate when compared with experimental data (Ref. 6.4). As can be seen in Table 6.1, the predictions using the ASME Code definition of crack size are on average 20 percent lower than the predictions using the "most consistent" definition of crack size for the case where the cracks were in straight pipe-to-straight pipe girth welds and 40 percent lower for the case where the cracks were in straight pipe-to-elbow girth welds. The larger underprediction in using the ASME definition of flaw size for the elbow girth weld experiments is the result of a more significant counterbore for the elbow girth weld experiments.

Note, for all of the experiments considered in Table 6.1, the crack was centered in the weld metal. In the ASME Code, any crack within a region one-half the wall thickness on either side of the weld centerline is considered a weld crack, and should be analyzed as such. For weld cracks which are offset from the weld centerline, the effect of the weld crown and counterbore will be less.

In addition to the complications associated with analyzing cracks in welds, there is also the effect of "off-center" cracks that needs to be considered. An off-center crack is a crack which has a nonuniform crack front and not the idealized constant depth crack shape typically assumed in a Section XI or R6 type analyses. The deepest part of the crack is also at some location other than the crack centerline where the bending stresses are the highest. Note, the effect of "off-centered" cracks is not an issue of concern in an actual plant in-service flaw evaluation in that the plant operators may have little or no idea of the seismic

Table 6.1 Comparison of predictions for seven weld crack experiments when using the ASME Code definition of crack size with predictions when using the "most consistent" definition of crack size as established in Section 5.0 showing the effect of the weld crown and counterbore on the fracture predictions

Experiment No.	Outside Pipe Diamter, mm	"Most Consistent" Flaw Size Definition			ASME Flaw Size Definition			SC.TNP1 Predicted[a] Moments, kN-m		Predicted Moment Ratio (ASME/ "Most Consistent")
		t, mm	a/t	θ/π	t, mm	a/t	θ/π	"Most Consistent"	ASME Definition	
Carbon Steel Weld Experiments										
1-3[b]	406.7	38.38	0.709	0.50	27.10	0.765	0.50	691.3	411.0	0.595
1-4[b]	406.9	39.19	0.639	0.50	26.01	0.676	0.50	682.0	411.0	0.603
1.3-4	402.6	29.18	0.590	0.535	25.76	0.669	0.535	702.2	535.0	0.762
Stainless Steel Weld Experiments										
1-5	415.3	28.14	0.442	0.267	22.15	0.427	0.267	794.8	622.6	0.783
1-6	412.7	28.45	0.620	0.27	22.86	0.649	0.27	605.8	461.0	0.761
4141-4	413.5	28.55	0.613	0.50	23.65	0.633	0.50	454.0	349.9	0.771
1.3-5	416.1	26.80	0.601	0.532	22.56	0.574	0.532	425.4	355.7	0.836

(a) Using quasi-static stress-strain curve and quasi-static J-R curve data to analyze the quasi-static bend experiments and quasi-static stress-stain curve and dynamic J-R curve data to analyze the dynamic pipe-system experiments.

(b) Using straight pipe dimensions and straight pipe stress-strain curve in analyses.

bending plane. Consequently, they would most likely assume the location where the crack is deepest as being centered on the bending plane. However, in an attempt to compare the results from the "off-centered" crack experiments on an equal basis with the more uniform depth crack experiments, an attempt was made in the analyses presented in this report to account for the fact that the maximum crack depth location may not coincide with the location of maximum bending stress. In order to assess the effect of "off-center" cracks, consider the crack shown in Figure 6.2 which is a representation of the crack shape geometry for Experiment 1-2. This was a carbon steel base metal experiment which was precracked using pressure cycling techniques. As a result of the pressure cycling, the fatigue crack was deeper at a location approximately 100 mm (4 inches) removed from the crack centerline. Since this was a base metal experiment, there was not a weld crown or counterbore to complicate the analyses. The shaded area in Figure 6.2 shows the actual surface of the initial fatigue crack plus EDM notch for Experiment 1-2. The dashed line shows the boundaries of the idealized constant depth crack shape for this experiment. In Section 5.2 it was shown that one promising way of analyzing such a crack was to consider the crack as a constant depth crack with a depth equal to the maximum crack depth and a length equal to the total crack length, and reducing the applied stress by the factor $\cos(\psi)$, where the angle ψ is the angle between the crack centerline and the location where the crack is the deepest.

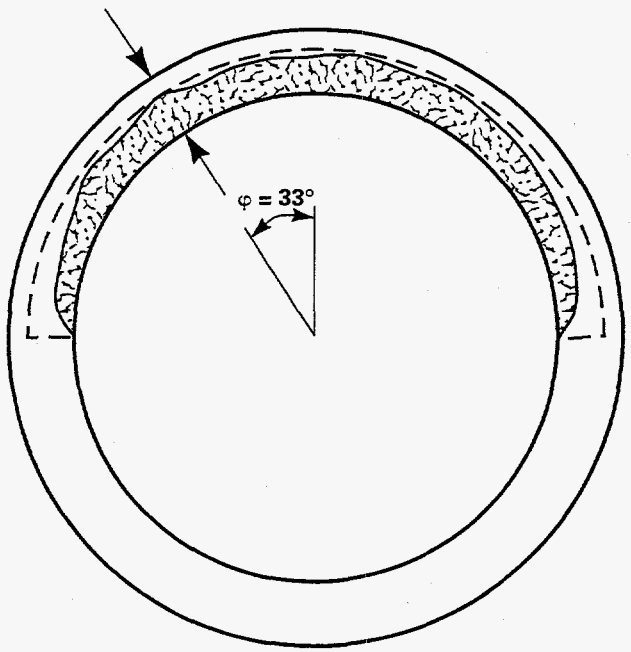

Figure 6.2 Actual crack shape geometry for Experiment 1-2 with an idealized representation of the crack shown by the dashed line

In order to see what effect an "off-center" crack has on the fracture predictions, a series of calculations were made for the crack shape shown in Figure 6.2. The assumed pipe dimensions for these calculations were those for Experiment 1-2. The results of those calculations are shown in Table 6.2.

Case 1 in Table 6.2 shows the results for the case where the crack was analyzed using the SC.TNP1 method using the idealized constant depth crack shape per the Section XI procedures, i.e., the maximum crack depth and the total crack length.

Case 2 shows the results for basically the same conditions as Case 1, except the predicted bending stress has been increased by a $1/\cos(\psi)$ term to account for fact that the crack was deeper at a location remote from the crack centerline where the bending stresses would be highest.

Case 3 shows the results for the case where the crack was analyzed using the Net-Section-Collapse (NSC) analysis method using the same idealized constant depth crack shape as used for Case 1.

Case 4 shows the results for the case where the crack was again analyzed using the NSC analysis except the location of the neutral bending axis was calculated with a separate program by inputting the actual crack shape and piecewise integrating around the pipe circumference to satisfy the force and equilibrium requirements at the crack section. This angle between the neutral axis and the point on the pipe circumference opposite the crack centerline, i.e., the stress inversion angle β in the classical NSC analysis, was then input into the NSC analysis to calculate the NSC limit-moment which was used to calculate the bending stress for Case 4. For this type analysis, the assumed stress distribution at the crack section is the same stress distribution as assumed in the

Table 6.2 Comparison of predicted bending stresses for Experiment 1-2 for two analysis methods and two different methods for accounting for the fact that the crack was deeper at a location remote from the location of highest bending stress

Case No.	Analysis Method	Crack Depth	Crack Length	Assumed Crack Shape	Experimental Bending Stress/Predicting Bending Stress[1, 2]
1[3]	SC. TNP1[4]	a_{max}	Total	Constant Depth	1.232
2[5]	SC.TNP1[4]	a_{max}	Total	Constant Depth	1.033
3[3]	NSC	a_{max}	Total	Constant Depth	0.887
4[6]	NSC	a_{max}	Total	Actual	0.691

(1) Bending stress = $M(D_o)/2I$ where $I = 0.0491(D_o^4 - D_i^4)$.
(2) Experimental bending stress = 180.4 MPa (26.2 ksi).
(3) Assuming an idealized constant depth crack shape with a depth = a_{max} and a length equal to the total crack length.
(4) Using quasi-static stress-strain curve and dynamic J-R curve data.
(5) Assuming the same idealized constant depth crack shape as for Case 1, but the calculated bending stress is increased by a $1/\cos(\psi)$ term to account for the fact that the deepest location of the crack is offset from the location of highest bending stress ($\psi = 33°$).
(6) Assuming the actual crack shape and the location of the neutral bending axis is calculated with a separate computer program (ANSC.FOR) by inputting the actual crack shape and piece wise integrating around the pipe circumference to satisfy the force and moment equilibrium requirements at the crack section.

original NSC analysis for which the stresses both above and below the neutral axis reach a constant value equal to the flow stress of the material, see Figure 6.3. In addition, for this type analysis one must assume that the crack shape is symmetric.

As can be seen in Table 6.2, the predicted bending stresses using the idealized constant depth crack shape (Cases 1 and 3 in Table 6.2) are 20 to 30 percent less than the predicted bending stresses when using an adjusted bending stress term or alternative crack shape to account for the off-center crack (Cases 2 and 4 in Table 6.2) for both the SC.TNP1 and Net-Section-Collapse analysis methods. It is also of note from Table 6.2 data the most accurate prediction of the experimental stress was for the SC.TNP1 analysis method when adjusting the predicted bending stress by the 1/cos (ψ) term to account in the crack being off-center. These comparisons show the degree of conservatism associated with using the idealized crack shape geometry in the analysis of real cracks found in service.

Based on comparisons with the experimental data, the "most consistent" definition of flaw size to use in a fracture prediction analysis is the total crack length with a constant depth equal to the maximum crack depth, with the applied bending stress being reduced by the cosine of the angle between the maximum crack depth location and the crack centerline location, where the bending stress is the highest, to account for the effect of an "off-center" crack. If considering a crack in a weld, then the wall thickness should be assumed to be the full wall thickness of the pipe plus the weld crown height and the crack depth should be referenced to the inside pipe surface.

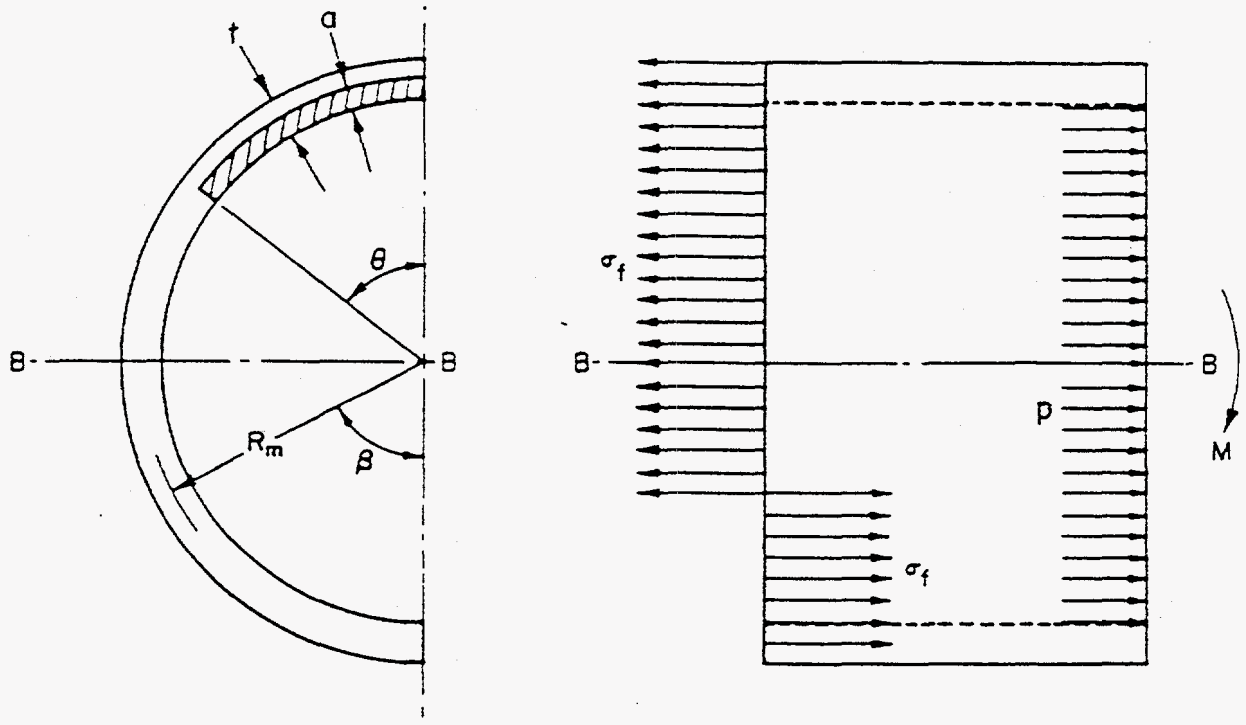

Figure 6.3 Assumed stress distribution at the crack section for the Net-Section-Collapse analysis

6.2.2 Effect of the Choice of Material Property Data on the Fracture Ratio Calculations

The material property data required for a fracture analysis are the tensile and fracture toughness properties. For limit-load analyses (e.g., Net-Section-Collapse or ASME Section XI Appendix C for stainless steel base metal cracks) or modified limit-load analyses (e.g., Dimensionless-Plastic-Zone-Parameter), the tensile property required is the flow stress of the material. If actual material data are available, the flow stress is typically defined as the average of the yield and ultimate strengths. For the ASME Section XI Code approaches, i.e., IWB-3640 and Appendix C for austenitic steels and IWB-3650 and Appendix H for ferritic steels, the flow stress is defined as $3S_m$ and $2.4S_m$, respectively, where S_m is the ASME Code Design Stress Intensity from Table 2A of Part D of Section II. For elastic-plastic analyses (i.e., J-estimation schemes or R6), a representation of the full stress-strain curve is required for such analyses. In this effort, for these types of analyses, the stress-strain behavior was modeled using a Ramberg-Osgood relationship. In all likelihood, for a plant-specific in-service flaw evaluation, the plant engineer doing the evaluation using either R6 or one of the J-estimation schemes will not have a full stress-strain curve at temperature for the material under consideration. If such is the case, he or she may resort to estimating the stress-strain behavior by using tensile data from a material property database such as PIFRAC (Ref. 6.5) for the material/temperature combination of interest to his or her application.

For the ferritic materials evaluated in this program, the stress-strain behavior at LWR temperatures was oftentimes significantly affected by the strain rate. Typically, the ultimate tensile strength decreased as the strain rate was increased. For pipe material DP2-F29, which was used in the carbon steel base metal simulated seismic experiment and a number of the companion experiments, the ultimate tensile strength decreased approximately 30 percent as the strain rate was increased from quasi-static strain rates to strain rates approaching 10/s. For this material, the yield strength did not change significantly as the strain rate increased. However, for other ferritic materials, it was found that as the strain rate increased, the yield strength increased slightly, see Table 2.4, although the ultimate strengths still decreased with increasing strain rate. (For the austenitic material evaluated in this program, i.e., DP2-A8, the stress-strain behavior was not affected significantly by an increase in strain rate, see Table 2.5.)

This dependence of the strength properties on the strain rate for ferritic materials has been attributed to dynamic strain aging (DSA), Ref. 6.6. Dynamic strain aging is a phenomenon observed in many carbon steels at light-water reactor operating temperatures. It involves interactions between highly mobile nitrogen and carbon atoms dissolved in the steel and moving dislocations associated with plastic strain.

As a result of the DSA phenomenon, there was a need to make an assessment of which tensile properties were most appropriate for use in the fracture prediction analyses. In Section 5.2.2, it was concluded that using quasi-static tensile properties of the base material to analyze both the quasi-static and dynamic experiments tended to result in the most accurate predictions of the experiments when compared with past results from Reference 6.4. (Note, for pipe material DP2-F29, the use of stress-strain data obtained for an intermediate strain rate, i.e., 2.6×10^{-2}, resulted in slightly more accurate predictions than using quasi-static data, but since intermediate-strain-rate data only existed for this single material, it was decided for the sake of consistency to use quasi-static tensile data for all of the analyses.) It is not known if this conclusion is valid for the case of small flaws or uncracked pipe behavior where a larger portion of the pipe would experience plasticity at the higher strain rates.

DSA can affect not only the tensile properties of a ferritic steel but also the fracture toughness of the steel. In fact, at certain combinations of strain rate and temperature, the interactions between the nitrogen and carbon atoms dissolved in the steel and the moving dislocations associated with plastic strain can lower the crack-growth resistance and can cause a stably growing crack to become temporarily unstable, i.e., to jump. Although there were no instances of crack jumps in any of the Task 1 pipe experiments*, the fracture resistance, i.e., J-R curves, of a number of the ferritic steels were affected by strain rate. In Section 5.2.2, it was concluded that quasi-static pipe-fracture behavior (normal operating conditions) can be predicted using quasi-static J-R curves in conjunction with quasi-static stress-strain data, and dynamic pipe fracture behavior (Service Level C or D conditions) can be predicted using dynamic J-R curves in conjunction with quasi-static stress-strain data.

A final issue to be addressed is that of the use of cyclic J-R curve data. That discussion will be deferred to Section 6.2.8 of this report.

6.2.3 Discussion of Results from Simulated Seismic Pipe-System Experiments

One of the questions left unresolved at the conclusion of the IPIRG-1 program was what effect would a seismic load history have on the fracture behavior of a cracked piping system. All of the pipe-system experiments conducted as part of the IPIRG-1 program were experiments for which the forcing function was a well prescribed single-frequency, increasing-amplitude, forcing function. At the end of IPIRG-1, the state-of-the-art of pipe fracture analyses was such that it was possible to predict the fracture behavior of one of these single-frequency, cracked-pipe-system experiments using a nonlinear spring representation of the crack with a high degree of confidence, given that appropriate material property data were available and the dimensions of the pipe and crack were adequately defined. Clearly, the biggest limitation in this type of analyses was not the fracture prediction models, but the definition of the crack size, specifically the crack depth from nondestructive evaluation (NDE) techniques. The calibration/definition of the nonlinear spring constants used in this type of analyses typically involves an SC.TNP1 type analysis to predict the monotonic moment-rotation response of the cracked section. Experience from the IPIRG-1 program indicated that it was possible to predict the response of these single-frequency experiments with such fidelity that the cycle number on which the crack would penetrate the pipe wall could be predicted.

As the IPIRG-2 program was being formulated, the question being asked was how well would this analysis methodology work for the case of a seismic load history with its multiple-frequency content and greater number of cycles. In order to address this question, two simulated-seismic, surface-cracked, pipe-system experiments were conducted as part of Task 1. One involved a crack in the base metal of a carbon steel pipe (DP2-F29) and the other a crack in the base metal of a stainless steel pipe (DP2-A8I). For both materials there were companion, single-frequency, pipe-system experiments conducted as part of the IPIRG-1 program (Ref. 6.1)** and companion, quasi-static, four-point-bend, pipe experiments conducted in earlier work, Refs. 6.2 and 6.3.

---

* The only crack jump which occurred in any of the Task 1 experiments was the jump which occurred when the crack in the quasi-static, monotonic, through-wall-cracked pipe experiment (i.e., Experiment 1-8) grew through the patch. However, it is not clear if dynamic strain aging contributed to this instability.

** For the stainless steel case, the companion single-frequency, pipe-system experiment (1.3-3) was conducted on a test specimen prepared from a different heat of DP2-A8 (i.e., DP2-A8II).

In Section 5.2, the fracture ratios for these simulated-seismic, pipe-system experiments and the applicable companion experiments were calculated. It was found that the fracture ratios for the simulated-seismic experiments were actually slightly higher than the fracture ratios for the companion, single-frequency experiments. Initially this finding was somewhat perplexing in that the number of cycles associated with the simulated-seismic experiments was significantly higher than the number of cycles associated with the single-frequency experiments. Furthermore, the effective stress ratio ($R_{effective}$), accounting for the stress contribution due to internal pipe pressure, was more negative for the simulated-seismic experiments than it was for the single-frequency experiments. As such, it was expected that the extent of cyclic degradation, and consequential reduction in load-carrying capacity, for the simulated-seismic experiments should be greater than for the single-frequency experiments. However, as evident from the fracture ratio calculations, this was not the case. To shed light on this apparent discrepancy, the crack-section moment data for the single-frequency and simulated-seismic, pipe-system experiments were plotted against the crack-mouth-opening displacements for the respective experiments. It was found that the cycles prior to maximum load for the simulated-seismic experiments were primarily elastic, see Figure 6.4, whereas the cycles prior to maximum load for the single-frequency experiments exhibited a significant amount of plasticity. This was especially true for the case of the stainless steel base metal, single-frequency, pipe-system experiment (Experiment 1.3-3), see Figure 6.5. The fact that the cycles prior to maximum moment were essentially elastic for the simulated-seismic experiments implies that these experiments could probably be analyzed much in the same manner as one would analyze a dynamic, monotonic, pipe experiment. This observation is probably an artifact of the forcing function used for these simulated seismic experiments. If some other simulated-seismic history were used, with a more gradual buildup of the large amplitude cycles, then the extent of cyclic degradation that occurred during these simulated-seismic experiments may have increased.

It is of note that as part of the IPIRG-2 round-robin analyses (Ref. 6.7), four different but "equal" displacement time histories were created from the same peak-broadened acceleration response spectrum. The maximum moments induced in a linear finite element model of the IPIRG piping system were similar (to within 20-percent), but the timing, number, and build-up of moment peaks were substantially different.

It is not clear that merely being consistent with a given input spectrum is any guarantee that one will have an upper-bound, lower-bound, or average crack-driving force potential due to differences in loading rate and load history effects. Other prescriptions on spectrum matching are probably required to give bounding crack-driving force behavior. This work showed that although the IPIRG-2 program seismic displacement-time-history forcing function met all of the current ASME, NRC, etc. design requirements, it is not known if it is lower-bound, upper-bound, or average in terms of crack driving force considerations.

6.2.4 Discussion of Results from Elbow Girth Weld Experiments

Another question left unresolved at the end of the IPIRG-1 program was what is the effect of a change in pipe system geometry, such as at the junction of an elbow and a straight pipe section, on the fracture behavior of a cracked-pipe system. The cracks in each of the pipe-system experiments conducted during IPIRG-1 were located in a straight run of pipe, see Figure 6.6. The specific question of interest to a number of the participants in the IPIRG program was could one use fracture analyses previously developed and verified for cracks in straight pipe runs to analyze cracks at geometric discontinuities such as at an elbow girth weld, or was there a need to develop new analysis methods to handle such cases? In order to address this question, two surface-cracked, elbow girth-weld, experiments were conducted as part of

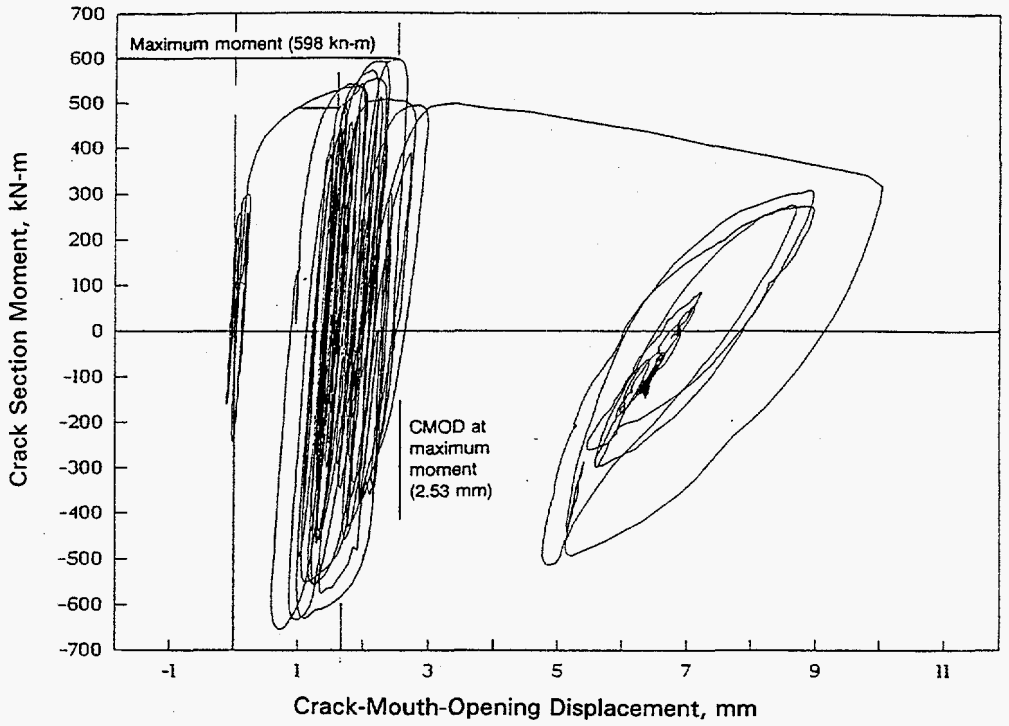

Figure 6.4 Crack-section moment versus crack-mouth-opening-displacement data for the IPIRG-2, stainless steel base metal, simulated-seismic, pipe-system experiment (Experiment 1-1)

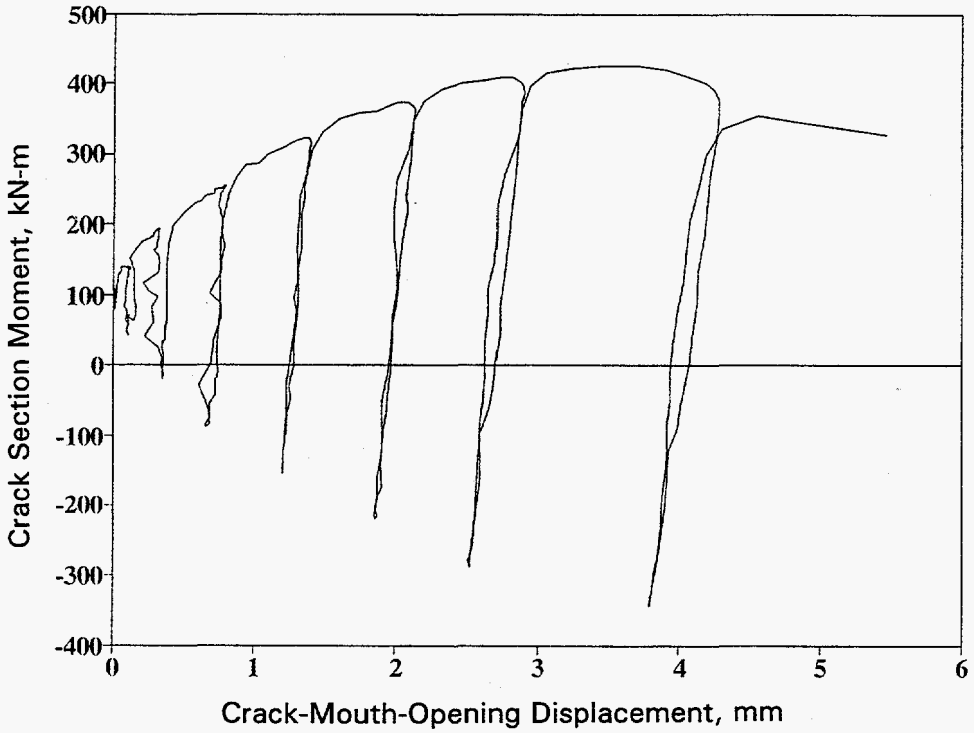

Figure 6.5 Crack-section moment versus crack-mouth-opening displacement data for the IPIRG-1, stainless steel base metal, single-frequency, pipe-system experiment (Experiment 1.3-3)

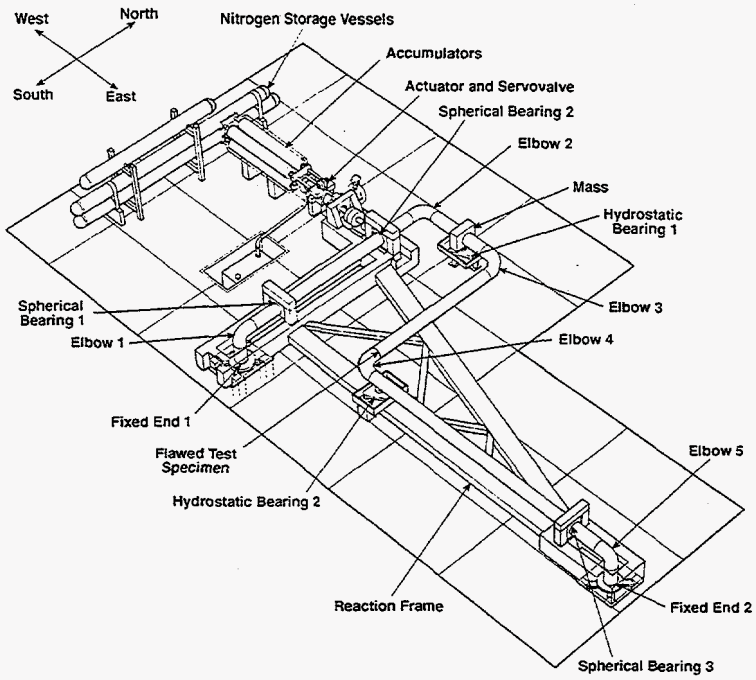

Figure 6.6 Artist conception of the IPIRG-2 pipe loop facility showing the location of the elbow-straight-pipe, girth weld which contained the crack for the elbow-girth-weld, pipe-system experiment conducted as part of the IPIRG-2 program (Experiment 1-3)

Task 1 of the IPIRG-2 program. (Note, the question of cracks in the base metal of the elbows themselves was addressed in Task 2 of the IPIRG-2 program.) One of the elbow, girth-weld experiments conducted as part of Task 1 was a single-frequency pipe system experiment with the internal surface crack in the elbow-straight pipe girth weld joining Elbow 4 to the adjoining north-south pipe run, see Figure 6.6. The other was a companion combined pressure and quasi-static, monotonic bend experiment. The weld procedure used for both of these elbow girth welds was the same carbon steel, C-Mn-Mo-Ni, submerged-arc-weld procedure used in the IPIRG-1 program (Ref. 6.1) and the Degraded Piping program (Ref. 6.2).

Fracture ratios were calculated for the two, circumferential-surface-cracked, elbow girth-weld experiments as well as the companion, straight pipe-to-pipe, girth-weld, quasi-static, monotonic, four-point-bend experiment from the Degraded Piping program (Ref. 6.2) and the companion, straight pipe-to-pipe girth-weld, single-frequency, pipe-system experiment from the IPIRG-1 program (Ref. 6.1). It was shown in Section 5.2 that the fracture ratios for the straight-pipe experiments agreed very closely with those for the elbow girth weld experiments, especially for the case when the straight-pipe dimensions and straight-pipe stress-strain curves were used in the analyses of the elbow-straight-pipe girth-weld experiments conducted as part of Task 1. In fact, for the SC.TNP1 analyses, the calculated fracture ratios for the two, elbow-girth-weld experiments and the two straight-pipe, girth-weld experiments agreed within 5 percent of each other. This finding suggests that straight pipe analyses can be used to predict the load-carrying capacity of surface cracks located in elbow-to-straight pipe girth welds. No new analysis methods for predicting the load-carrying capacity of surface cracked elbow/straight pipe girth welds need to be developed. However, from other work from the NRC's Short Cracks in Piping and Piping Welds program (Ref. 6.8), IPIRG-2 round-robin efforts (Ref. 6.7), and described in the IPIRG-2 report on uncertainty analysis (Ref. 6.9), it

was found that for through-wall cracks, there could be several technical issues that require additional considerations if the crack is close to an elbow or nozzle.

These issues are:

(1) For a crack at a nozzle girth weld, there is a thickness difference on each side of the crack that reduces the crack-opening displacement if the pipe thickness is used.

(2) There is a restraint of pressure induced bending that increases the maximum load, but decreases the crack-opening displacement. This effect is negligible for short through-wall cracks and surface cracks, but is significant for long through-wall cracks, i.e., in LBB applications for smaller diameter pipe, see Reference 6.9.

It is also noted from Table 5.10 that if the pipe dimensions and stress-strain curve were used in the analyses of the carbon steel weld experiments, that the predicted fracture ratios were consistently less than 1.0 for the SC.TNP1 analysis method. For these analyses, the weld crown height was included in the analyses. If the weld crown height had not been included, then these fracture ratios would have been greater than 1.0. Consequently, for flaw evaluation purposes, the weld crown should not be included with the pipe thickness when making moment predictions to insure a conservative underprediction. (In reality, it is unlikely if it is known if the flaw is in the center of the weld or near the weld toe, where the weld crown is less.

For the analyses discussed above, monotonic C(T) specimen J-R curve data were used exclusively. If the dynamic, cyclic (R = -0.6), C(T) specimen, J-R curve data were used, then the agreement between the quasi-static, monotonic, four-point-bend, experimental results and the dynamic, cyclic, pipe-system, experimental results gets worse. The use of the cyclic J-R curve data raises the fracture ratios for the pipe system experiments such that they are 17 percent higher than the fracture ratios for the quasi-static companion experiments when using the SC.TNP1 analysis method. Consequently, it appears that for this material, it is better to use monotonic C(T) specimen J-R curve data than cyclic C(T) specimen J-R curve data in the fracture analyses. As noted in Section 5.2.5, this is not always the case. Based on the results from the IPIRG-2 and companion experiments, it appears that it is sometimes better to use cyclic J-R curve data if such data are available. The discussion of when to use cyclic J-R curve data will be deferred to Section 6.2.8.

6.2.5 Discussion of Results from Short Surface-Cracked and Short Through-Wall-Cracked Experiments

During the Degraded Piping (Ref. 6.2) and IPIRG-1 (Ref. 6.1) programs, the nominal crack sizes used in the pipe experiments were relatively large, i.e., 37 percent of the pipe circumference in length for the through-wall cracked pipe experiments and 50 percent of the pipe circumference long and 66 percent of the pipe wall thickness deep for the surface-cracked pipe experiments. These larger crack sizes were chosen so the maximum loads were low enough such that most of the plasticity was concentrated at the crack section.

However, while these larger crack sizes facilitated the analyses, they were not representative of the crack sizes typically considered in leak-before-break (LBB) or in-service flaw evaluation analyses. For the U.S.

NRC LBB analysis procedure, the postulated through-wall crack should be such that the calculated leakage rate of fluids discharged from the flaw under normal operating loads should be detectable with a prescribed margin. In the U.S. NRC Standard Review Plan (SRP) 3.6.3 (Ref. 6.10), a margin of 10 on leakage detection is required unless a detailed justification can be provided which accounts for the effects of potential uncertainties, e.g., particulate plugging, measurement techniques, personnel qualifications, and frequency of monitoring. For large diameter pipes, these criteria typically result in a postulated through-wall crack size of 6 to 8 percent of the pipe circumference.

For surface-cracked pipe, the nominal crack size used in the IPIRG-1 and Degraded Piping programs was at the limit or outside the limit on flaw sizes considered for evaluation in Table H-5310-1 for ferritic pipe and Table IWB-3641-1 for austenitic pipe, respectively. As a result, it was decided to include a series of shorter crack experiments (both through-wall and surface-cracked pipe) in Task 1 to demonstrate that the analyses previously developed and validated for the long crack case were adequate for the case of shorter cracks. As part of the U.S. NRC Short Cracks in Piping and Piping Welds program (Ref. 6.11) a number of shorter crack pipe experiments were conducted, but the loading conditions were always quasi-static, monotonic, four-point bending. No dynamic or cyclic loadings, such as will be introduced during a pipe system experiment, were included.

A major finding from the stainless steel pipe-to-pipe girth weld experiments is that cyclic J-R curve data may be needed to predict the behavior of flaws that have significant compressive loading. Using monotonic J-R curve data, the short-surface-crack, pipe-system, submerged-arc weld (SAW) test (Experiment 1-5) fracture ratio was 30 percent less than the companion quasi-static, short-surface-cracked SAW test (Experiment 1-6), and the long-surface-crack, quasi-static and pipe-system tests (Experiments 4141-4 and 1.3-5). The only feature associated with Experiment 1-5 that can explain this apparent anomaly is that the stress ratio is considerably more negative than for the other three SAW experiments, see Figure 6.7. Analyzing Experiment 1-5 using cyclic J-R data brings it much closer to the other experiments' fracture ratios.

For the case of the short-through-wall-cracked, pipe experiments, no data from companion experiments from other programs existed for comparison. Thus, the only comparisons to be made were between the quasi-static, monotonic four-point bend experiment conducted as part of Task 1 (i.e., Experiment 1-8) and the simulated seismic pipe system experiment conducted as part of Task 1 (i.e., Experiment 1-7). Unfortunately, as discussed in Section 5.2.2.5, it appears that the maximum moment values for the quasi-static experiment may be suspect due to the possibility that the patch may have reinforced the cracked section. (Another possible explanation as to why the fracture ratios for the quasi-static experiment (1-8) were so much higher than the fracture ratios for the pipe-system experiment (1-7) was that the through-wall crack in the quasi-static experiment grew at a much greater angle with respect to the circumferential plane than did the through-wall crack for the pipe-system experiment. Previous results from Reference 6.12 tend to indicate that as the crack growth angle increases, the maximum load should also increase.) Regardless, due to the fact that data for the quasi-static experiment have even been drawn into question due to the flattening of the patch, the discussion of results for these through-wall-cracked pipe experiments will focus on results for the simulated seismic, through-wall-cracked, pipe-system experiment.

In reviewing the fracture ratios for the three J-estimation schemes considered in this effort, i.e., GE/EPRI, LBB.NRC, and LBB.ENG2, it was found that the fracture ratios for Experiment 1-7 agreed very closely with the average fracture ratios reported for these three methods for six quasi-static pressure and bend experiments previously analyzed during the Short Cracks program (Ref. 6.13). From Table 4.31 of

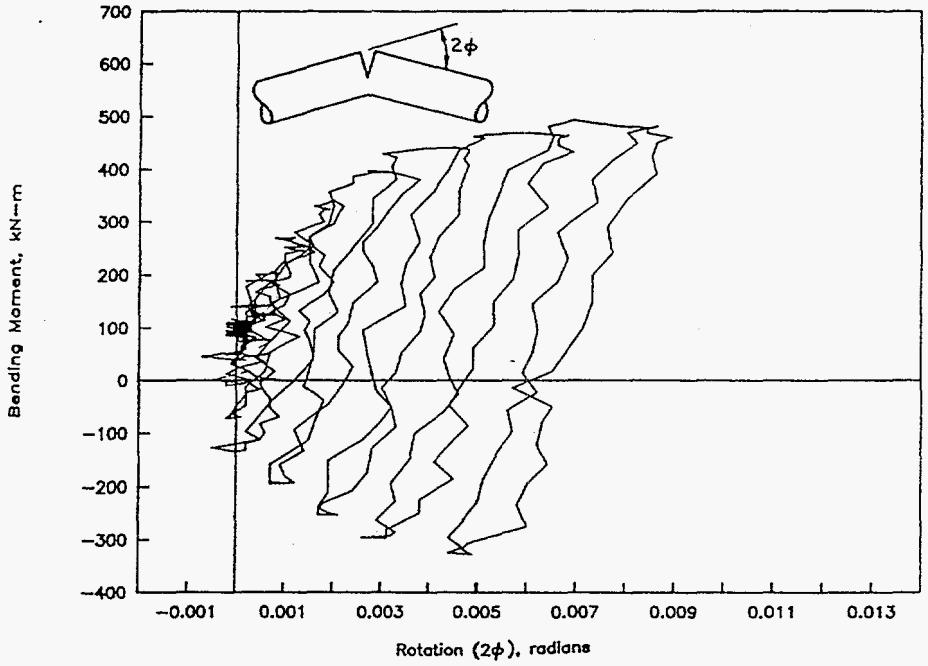

(a) Long-surface-cracked pipe-system experiment (1.3-5)

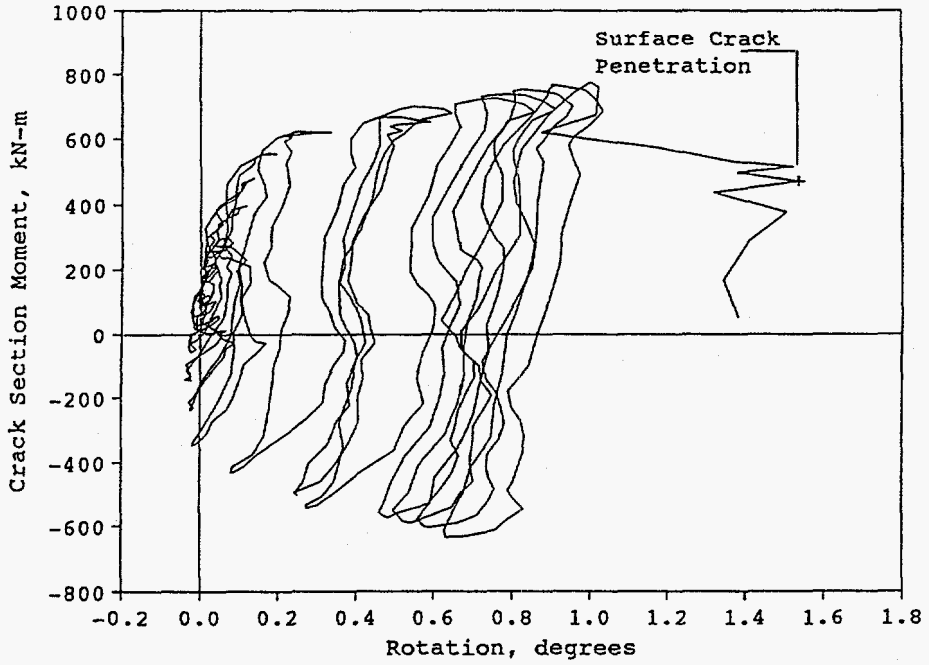

(b) Short-surface-cracked pipe-system experiment (1-5)

Figure 6.7 Plots of the moment-rotation response for both the long- (1.3-5) and short -(1-5) surface-cracked stainless steel weld pipe-system experiments

Reference 6.13, the average fracture ratios for the six previously conducted pressure and bend through-wall cracked experiments were 1.31 for the GE/EPRI method, 1.17 for the LBB.NRC method, and 1.18 for the LBB.ENG2 method. These values compare well, within 2 to 7 percent, see Table 5.12. Consequently, based on this comparison, it appears that the previously developed through-wall-cracked analyses, which had been previously only verified using quasi-static, monotonic pipe fracture data, work equally well for the case of a through-wall-cracked dynamic, cyclic pipe system experiment.

6.2.6 Discussion of Inaccuracies Inherent in ASME Section XI Procedures

It has been reported that the fracture ratios for the ASME Section XI Appendix H criteria for ferritic piping were significantly higher than the fracture ratios for the ASME Section XI Appendix C criteria for austenitic piping (Ref. 6.1). Since both criteria are based on the Net-Section-Collapse analysis, modified, as necessary, with a stress multiplier (i.e., Z-factor) to account for the cases where the crack is located in a low toughness material, a question arose as to why the fracture ratios for the ferritic experiments were so much higher than the fracture ratios for the austenitic experiments. In order to address this question both the differences in flow stress definition and differences in the Z-factor formulation between the two criteria were addressed. As a result of this assessment it was concluded that the higher fracture ratios for the ferritic experiments had more to do with the differences in the flow stress definition than with the differences in the Z-factor formulation.

6.2.6.1 Flow Stress Considerations

The various failure avoidance criteria considered as part of this effort (ASME Appendices C and H, ASME Code Case N-494-3, and R6) all have different technical bases for the flow stress definition they use.

The technical basis document for the ASME Section XI Appendix C criterion for austenitic piping defines the flow stress as $3S_m$. This definition is based on a value close to the mean value of some actual Type 304 stainless steel data at elevated temperature for which the flow stress had been defined as 1.15 times the average of the actual yield and ultimate strengths. Since the Appendix C flow stress definition is based on mean strength data, and not lower bound strength data, the criterion does not allow one to use actual strength properties to define S_m since actual properties tend to be higher than Code values. It was felt by the authors of this appendix that using actual properties would be taking double credit for the increase in strength of actual properties.

The technical basis document for the ASME Section XI Appendix H criterion for ferritic piping defines the flow stress as $2.4S_m$. This definition is based on a lower bound flow stress from an axially-cracked pipe test documented in Reference 6.14. Since this definition is based on lower bound data instead of mean data, the Code allows the user to use actual material data (average of yield and ultimate strengths) to define the flow stress as an alternative to the $2.4S_m$ definition.

ASME Code Case N-494-3 allows for the use of actual material properties, but Code values (S_y and S_u) can also be used.

The R6 document specifies that conservative material properties are generally to be used, but actual properties can be used, if available.

As alluded to, the ASME Section XI Appendices C and H approaches specify that the flow stress may be defined in terms of the Code Design Stress Intensity (S_m) value from Table 2A of Part D of Section II of the ASME Code. For the analyses conducted in Section 5.2.3, the S_m value was established both using values from Table 2A of Part D of Section II of the ASME Code, i.e., S_m(Code), and in the spirit of the Code using the criteria specified in Article 2110 of Appendix III of Section III Division 1 of the 1989 Edition of the ASME Code, i.e., S_m(Actual). Figure 6.8 is a bar chart showing a comparison of the flow stresses using actual tensile data, i.e., the average of yield and ultimate strengths, the S_m(Code) values, and the S_m(Actual) values for the materials used in some of the IPIRG experiments. From Figure 6.8, it can be seen that the flow stress based on S_m(Actual) was within 12 percent of the flow stress based on the average of the measured yield and ultimate strength values for the five ferritic materials considered. For four of the five ferritic materials, the flow stress based on S_m(Actual) was within 5 percent of the flow stress based on measured values. On the other hand, the flow stresses based on S_m(Code) were 10 to 35 percent less than the flow stresses based on measured tensile properties. These findings support the contention that using the S_m(Actual) definition for flow stress provides a reasonable means for evaluating the technical basis of the Code procedures by analyzing the pipe experiments as if the pipes used had the minimum properties defined in Section II of the ASME Code, at least for the case of the ferritic experiments.

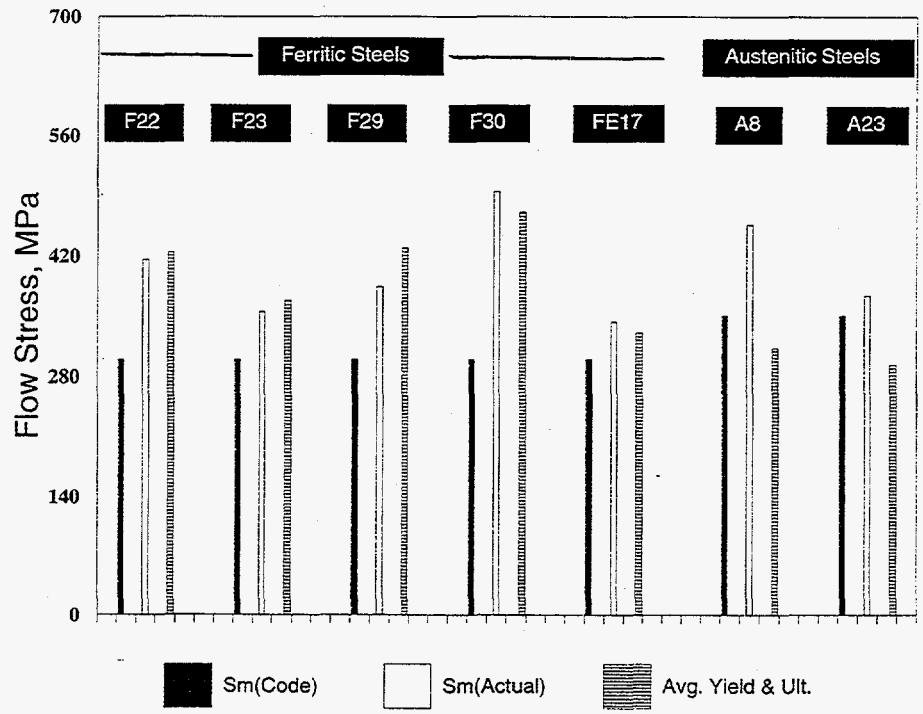

Figure 6.8 Comparison of flow stress definitions for the pipe materials evaluated in the IPIRG-2 program

For the austenitic material considered in Task 1 (i.e., DP2-A8), the flow stress based on the average of the yield and ultimate strengths was approximately 10 percent less than the flow stress based on the S_m(Code) value and was approximately 30 percent less than the flow stress based on the S_m(Actual) value. This finding is significant in that the strength properties of this stainless steel material at 288 C (550 F) were not as high as one might expect based on Table 2A of Part D of Section II of the Code. This finding is even more significant when one considers the fact that the other stainless steel pipe material used in the IPIRG-1 program (i.e., DP2-A23), had even lower strength properties (Ref. 6.15), see Figure 6.8. The flow stress based on the average of yield and ultimate was approximately 16 percent less than the $3S_m$(Code) flow stress value for DP2-A23. This suggests that the ASME Code definition of flow stress, i.e., $3S_m$, for Type 304 stainless steel may overestimate the strength of this material specification. This may be part of the reason why the calculated fracture ratios for the Appendix C approach for the two elevated temperature stainless steel base metal pipe-system experiments (i.e., Experiments 1.3-3 and 1-1) were so low, see Table 5.13. (Note, for the single room temperature stainless steel base metal experiment [i.e., EPRI 13S], the calculated fracture ratio for the Appendix C criteria [1.533, see Table 5.13] was very high with respect to the corresponding fracture ratios for the elevated temperature pipe-system experiments [i.e., 0.977 and 1.154] when the flow stress was based on S_m(Code) values. Based on the room temperature data, the flow stress based on the average of the measured yield and ultimate strengths was 25 percent higher than the flow stress based on $3S_m$(Code) whereas for the 288 C (550 F) data, the average of yield and ultimate flow stress was 11 percent less than the $3S_m$(Code) value.)

As can be seen in Table 5.13, the calculated fracture ratios using the Appendix C procedures for the two elevated temperature stainless steel base metal experiments (i.e., Experiments 1.3-3 and 1-1) were only 0.977 and 1.154 when the S_m(Code) definition of flow stress was used. These values are significantly below the fracture ratios calculated for the stainless steel weld experiments, which were analyzed using a Z-factor approach to account for the low toughness submerged-arc weld (SAW), or the fracture ratios for the carbon steel experiments, which were also analyzed using a Z-factor approach to account for the crack being in a lower toughness carbon steel material. Based on the analyses of the stainless steel weld experiments, it appears that some of the conservatism associated with the Z-factor approach offsets the fact that the actual flow stress of this particular stainless steel at 288 C (550 F) is slightly less than might be expected based on strength properties specified in Section II of the Code.

6.2.6.2 Z-Factor Considerations

To illustrate the basic inaccuracies/conservatisms associated with the use of ASME Appendices C and H elastic-plastic Z-factor approaches, consider Figures 6.9 and 6.10. As alluded to earlier, the simplified Dimensionless-Plastic-Zone-Parameter analysis was found to be one of the most accurate of the analysis methods considered as part of Reference 6.4. As part of Reference 6.4, Z-factors based on the DPZP analyses were calculated as a function of pipe diameter and compared with the ASME Code Z-factors from Appendices C and H, see Figures 6.9 and 6.10. The DPZP calculated Z-factors were calculated for lower bound default J_i values specified in the technical basis documents for Appendices C and H for the different material categories considered by these approaches. For the DPZP analysis, Z-factors were calculated using both a "best-fit" of the pipe fracture data which formed the basis for the DPZP analysis and for a 95-percent confidence level for that data. As can be seen in Figure 6.9 for the austenitic case, the "best-fit" Z-factor curves from the DPZP analysis are well below the Z-factor curves from IWB-3640 and Appendix C. (There is much better agreement between the Appendix C Z-factors and the DPZP 95-percent confidence level curve Z-factors, especially for the shielded-metal-arc weld (SMAW) case, see

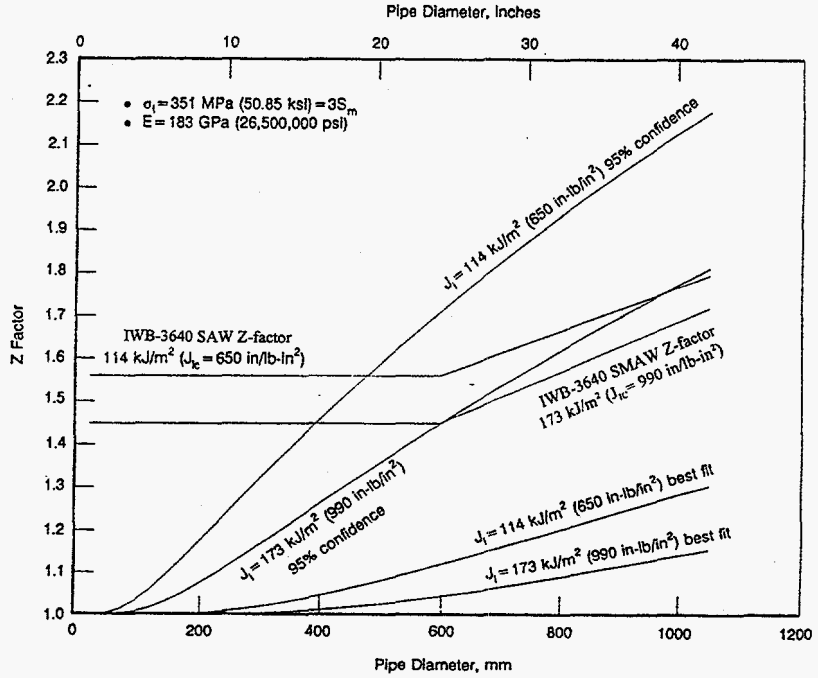

Figure 6.9 Comparison of Z-factors from DPZP analysis with Z-factors from ASME IWB-3640 analysis for austenitic steels using a flow stress definition of $3S_m$(Code)

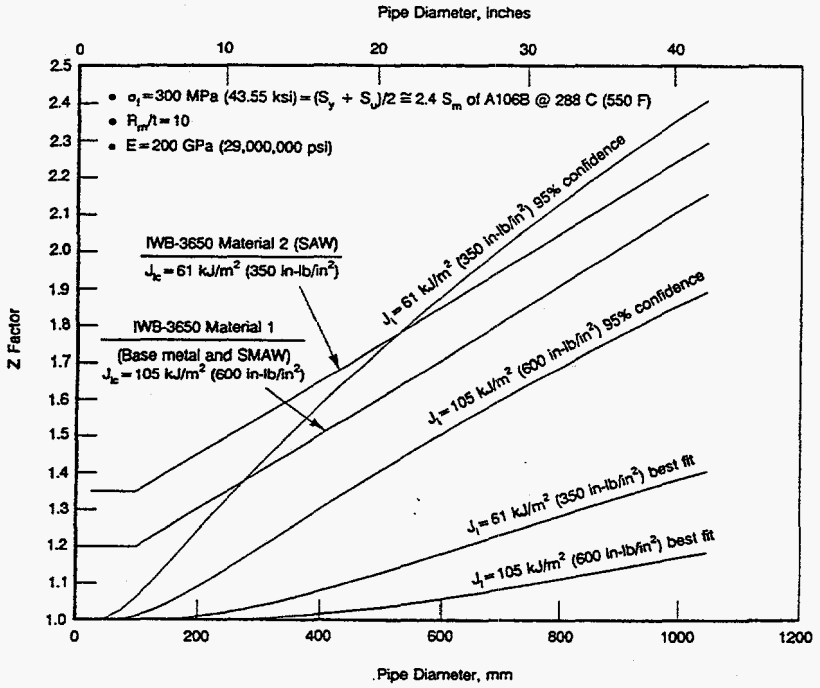

Figure 6.10 Comparison of Z-factors from DPZP analysis with Z-factors from ASME IWB-3650 analysis for ferritic steels using a flow stress definition of $2.4S_m$(Code)

Figure 6.9.) Considering the case of a 16-inch nominal diameter pipe such as evaluated in the Task 1 experiments, Figure 6.9 shows that the ratio of the IWB-3640 Z-factor for submerged-arc welds to the DPZP "best fit" Z-factor for submerged-arc welds is approximately 1.5. It can be seen from Table 5.13 that the calculated fracture ratios for the four elevated temperature stainless steel submerged-arc weld experiments for the Appendix C method for the case when the flow stress was defined as $3S_m$(Code) ranged from approximately 1.4 to 1.5. Comparing these fracture ratios with the calculated fracture ratios for the two elevated temperature stainless steel base metal pipe system experiments, with a Z-factor of 1.0, for the same flow stress definition, shows that the fracture ratios for the weld experiments relative to that of the base metal experiments were also approximately 1.4. This agreement demonstrates the degree of inherent conservatism associated with the Z-factor correction embodied in Appendix C for austenitic flux welds.

A similar story can be told for the case of the ferritic Z-factor approach embodied in IWB-3650 and Appendix H. From Figure 6.10, it can be seen that the ASME Code Z-factor for a crack in the base metal of a 16-inch diameter carbon steel pipe would be approximately 1.5. On the other hand the DPZP "best-fit" Z-factor for the same crack in the same pipe would only be about 1.03. Consequently, the ASME Z-factor for a base metal crack in a 16-inch diameter pipe is approximately 45 percent greater than the DPZP "best-fit" Z-factor using the "best fit" curve in Figure 6.10. Combining this inaccuracy with the fact that the flow stress for Pipe DP2-F29, based on the average of the measured yield and ultimate strengths, is 43 percent higher than the flow stress based on a S_m(Code) definition results in an overall inaccuracy of approximately 2.1 (i.e., 1.45 times 1.43). As can be seen in Table 5.13, the calculated fracture ratios for two of the three carbon steel base metal experiments for the Appendix H criteria for the case when the flow stress is based on S_m(Code) agree very closely with this level of inaccuracy, i.e., fracture ratios of 1.94 and 2.18. The third carbon steel base metal experiment (i.e., 1.3-2) had a fracture ratio of 1.69.

Similarly, for the case of the ferritic straight pipe-to-pipe girth weld experiments, the ratio of the Code Z-factor to the DPZP "best fit" Z-factor is approximately 1.53 for cracks in a 16-inch diameter pipe. Combining this with the fact that the flow stress based on actual properties is approximately 43 percent higher than the flow stress based on S_m(Code) values suggests that the fracture ratios for these two experiments (i.e., Experiments 4141-8 and 1.3-4) should approach 2.2. In reality, the fracture ratios for these two experiments for the Appendix H approach when using the S_m(Code) value for flow stress were 2.48 and 2.86, respectively, which agree fairly well with the value of 2.2, especially for the case of Experiment 4141-8 (i.e., the quasi-static four-point bend experiment). The slightly higher value for the fracture ratio for Experiment 1.3-4 (i.e., the dynamic pipe system experiment) may be an artifact of the fact that the toughness of this carbon steel weld (DP2-F29W) increases significantly with strain rate.

As a result of this discussion it appears that contrary to what has been published in the past, the degree of inaccuracy, or conservatism, associated with the Appendix H approach may not be that more excessive than that for the Appendix C approach. The higher fracture ratios for the Appendix H approach when compared with the Appendix C approach may be more the result of the fact that the strength of the carbon steel pipe material evaluated (DP2-F29) is significantly higher than what one might expect based on Code properties, while the strength of the stainless steel pipe material evaluated (DP2-A8), is slightly less than what one might expect based on Code properties.

In conclusion, both the Appendix C and Appendix H elastic-plastic Z-factor approaches have a degree of inaccuracy or conservatism of approximately 1.4 to 1.5 for 16-inch diameter pipe for a material with

strength properties near the lower bound strength properties provided in Section II. As can be seen in Figures 6.9 and 6.10 this degree of inaccuracy or conservatism would increase as the pipe diameter increases.

Note, in Reference 6.4 a similar finding was found to hold true based on the SC.TNP1 analysis method. Figure 6.11 shows a comparison of the SC.TNP1 calculated Z-factors to the ASME Section XI Appendix H Z-factors for ferritic submerged-arc welds. As was the case for the DPZP-based analyses, the Appendix H Z-factors are much higher than the SC.TNP1 calculated Z-factors, and the level of disagreement between the SC.TNP1 Z-factors and the Appendix H Z-factors increases as the pipe diameter increases.

6.2.7 Discussion of Inaccuracies Inherent in the R6 Revision 3 Option 1 and ASME Code Case N-494-3 Methods

As is the case for the ASME criteria, the R6 method is more of a failure avoidance criteria than a fracture prediction criteria. Consequently, there is a degree of conservatism built into this method. As can be seen in Table 5.13, the calculated fracture ratios for the R6 method (as programmed in NRCPIPES Version 3.0) are on average comparable to those for the ASME criteria. For the 12 straight pipe experiments considered in Table 5.13, the average fracture ratio for the R6 method is approximately 1.6. On average, the R6 fracture ratios for stainless steel experiments are slightly higher than the Section XI Appendix C fracture ratios for these same stainless steel experiments. Conversely, the R6 fracture ratios for the carbon steel experiments are less than the Section XI Appendix H fracture ratios for these same carbon steel experiments. The explanation for this observation is that the R6 method uses actual material property data

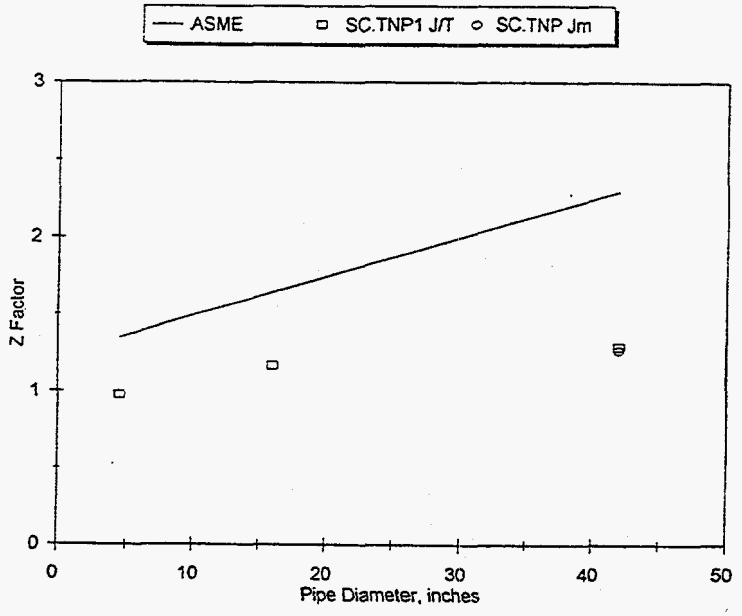

Figure 6.11 Comparison of the SC.TNP1 Z-factors with the ASME Appendix H Z-factors

instead of Code-specified strength values, and actual material properties were used in the analyses which formed the basis for Table 5.13. (Note, the R6 method also allows for the use of code strength properties, i.e., S_y and S_u values, but the analyses which formed the bases for Table 5.13 did not do so.) As was shown in the previous section, the actual strength of the stainless steel pipe used in these experiments was less than what would be expected based on the Code strength values. As a result, if one uses the Code-specified strength properties, the predicted stress (i.e., the denominator in the fracture ratio term) will be higher than what would be expected based on actual properties resulting in a lower fracture ratio. The opposite will be true for the case of the carbon steel experiments. Based on this discussion, it appears that the degree of inaccuracy, or conservatism, associated with the R6 Revision 1 Option 1 method is comparable to that for the ASME Appendices C and H approaches, if one accounts for the differences in material property data.

It is also of note from Table 5.13 that the degree of inaccuracy or conservatism associated with the ASME Code Case N-494-3 approach for austenitic and ferritic pipes is comparable to that for the R6 method. Like the R6 method, the ASME Code Case N-494-3 approach for ferritic pipes allows use of actual yield and ultimate strength data instead of Code-specified strength parameters, i.e., S_m values.

6.2.8 Effect of Using Cyclic J-R Curves

The use of the dynamic, cyclic (R = -0.6) C(T) specimen J-R curve brought the results for the short surface-cracked, pipe-system experiment from IPIRG-2 (Experiment 1-5) more in line with the results for the other three stainless steel weld experiments. When monotonic C(T) specimen data were used in the analyses of these experiments, the calculated fracture ratios for Experiment 1.5 were up to 30 percent less than the corresponding fracture ratios for the other three stainless steel weld experiments. (For these other three experiments, there was excellent agreement in the calculated fracture ratios for each of the analysis methods considered.) When the dynamic, cyclic C(T) specimen J-R curve data were used to analyze the two stainless steel weld pipe system experiments, the calculated fracture ratios for Experiment 1-5 agreed closely with the fracture ratios for the other experiments, however, the calculated fracture ratios for the long surface crack, pipe-system experiment (Experiment 1.3-5) was now 17 to 22 percent higher than the fracture ratios for the other three stainless steel weld experiments. This tends to indicate that it was probably better to analyze the short surface-cracked, pipe-system experiment using cyclic C(T) specimen data and to analyze the long surface-cracked, pipe-system experiment using monotonic C(T) specimen data. This can probably be explained by the differences in the effective stress ratio between the two experiments. The effective stress ratio was -0.5 for Experiment 1-5 and -0.2 for Experiment 1.3-5. Consequently, there appears to be a threshold effective stress ratio value above which the effect of cyclic loading can be ignored. A similar finding was reported previously for some 6-inch nominal diameter pipe tests conducted as part of IPIRG-1 (Ref. 6.16).

This threshold value of $R_{effective}$ appears to be material dependent in that the most consistent predictions for the four carbon steel weld experiments were realized when using monotonic C(T) specimen J-R curve data for all of the experiments. The effective stress ratio for the IPIRG-2 pipe system elbow girth weld experiment was -0.55 (less than that for the short surface-cracked, stainless steel weld, pipe-system experiment discussed above), and yet, the fracture ratios for this experiment agreed best with the fracture ratios for the other three carbon steel weld experiments when monotonic C(T) specimen data were used in the analyses.

This dependence on the need for cyclic J-R curve data has been attributed to the toughness of the material (Ref. 6.17). Figure 6.12 is a schematic representation of the toughness degradation due to cyclic loading (J_{cyc}/J_{mono}) as a function of stress ratio and material toughness. As illustrated in Figure 6.12, lower toughness materials will begin to see a more pronounced effect of cyclic loading at higher (i.e., more positive) stress ratios. This dependence of the cyclic degradation on the toughness has been attributed to the relative crack tip and void sharpening characteristics of the materials (Ref. 6.17). The higher toughness materials required greater compressive loads to resharpen the crack tip and voids ahead of the crack after a tensile loading than do the lower toughness materials. However, in applying this logic to the two experiments of concern to this discussion, one would expect that both experiments would be affected by cyclic loading to essentially the same degree since the toughness of the two welds are comparable. Consequently, it is still unclear why the predictions for Experiment 1-5 are more consistent using cyclic data and the predictions for Experiment 1-3 are more consistent using monotonic data.

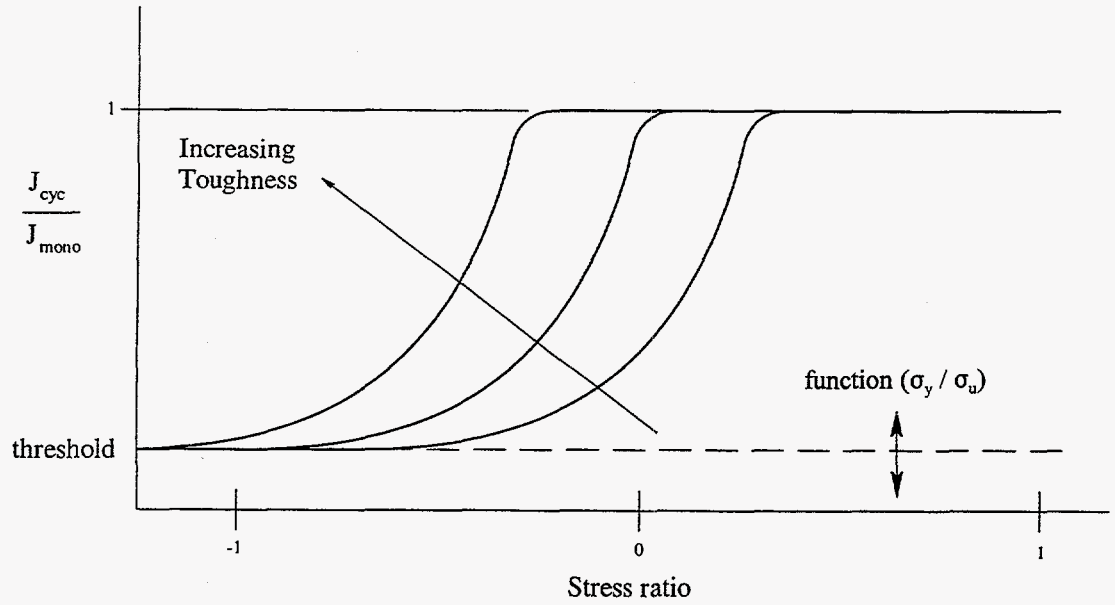

Figure 6.12 Schematic representation of the toughness degradation due to cyclic loading as a function of stress ratio and material toughness

6.3 References

6.1 Scott, P., and others, "The IPIRG-1 Pipe System Fracture Tests: Experimental Results," PVP Vol. 280, pp 135-151, June 1984.

6.2 Wilkowski, G. M., and others, "Degraded Piping Program - Phase II, Summary of Technical Results and Their Significance to Leak-Before-Break and In-Service Flaw Acceptance Criteria," March 1984 - January 1989, NUREG/CR-4082, Vol. 8, March 1989.

6.3 Kanninen, M. F., and others, "Instability Predictions for Circumferentially Cracked Type 304 Stainless Steel Pipes Under Dynamic Loading," EPRI Report NP-2347, April 1982.

6.4 Krishnaswamy, P., and others, "Fracture Behavior of Short Circumferentially Surface-Cracked Pipe," NUREG/CR-6298, November 1995.

6.5 Wilkowski, G. M., and others, "Short Cracks in Piping and Piping Welds," Semiannual Report, March 1993 - December 1994," NUREG/CR-4599, Vol. 4, No. 1, April 1995.

6.6 Marschall, C. W., and others, "Effect of Dynamic Strain Aging on the Strength and Toughness of Nuclear Ferritic Piping at LWR Temperatures," NUREG/CR-6226, October 1994.

6.7 Rahman, S., and others, "Summary of Results from the IPIRG-2 Round-Robin Analyses," NUREG/CR-6337, February 1996.

6.8 Rahman, S., and others, "Probabilistic Pipe Fracture Evaluations for Leak-Rate-Detection Applications," NUREG/CR-6004, April 1995.

6.9 Ghadiali, N., and others, "Deterministic and Probabilistic Evaluations for Uncertainty in Pipe Fracture Parameters in Leak-Before-Break and In-Service Flaw Evaluations," NUREG/CR-6443, September 1996.

6.10 Solicitation for Public Comment on Standard Review Plan 3.6.3 "Leak-Before-Break Evaluation Procedures," *Federal Register*, Vol. 52, No. 167, pp 32626-32633, Friday, August 28, 1987.

6.11 Wilkowski, G. M., and others, "Short Cracks in Piping and Piping Welds," Semiannual Report, March-September 1990, NUREG/CR-4599, Vol. 1, No. 1, May 1991.

6.12 Mohan, R., and others, "Effects of Toughness Anisotropy and Combined Tension, Torsion, and Bending Loads on Fracture Behavior of Ferritic Nuclear Pipe," NUREG/CR-6299, January 1995.

6.13 Brust, F. W., and others, "Assessment of Short Through-Wall Circumferential Cracks in Pipes," NUREG/CR-6235, April 1995.

6.14 Eiber, R. J., and others, "Investigation of the Initiation and Extent of Ductile Pipe Rupture," Battelle Memorial Institute Report to the Atomic Energy Commission, BMI-1908, 1971.

6.15 Marschall, C. W., and others, "Loading Rate Effects on Strength and Fracture Toughness of Pipe Steels Used in Task 1 of the IPIRG Program," NUREG/CR-6098, October 1993.

6.16 Scott, P., and others, "The Effect of Dynamic and Cyclic Loading During Ductile Tearing on Circumferentially Cracked Pipe: Experimental Results," PVP Vol. 280, pp 207-220, June 1994.

6.17 Rudland, D., and others, "The Effects of Cyclic and Dynamic Loading on the Fracture Resistance of Nuclear Piping Steels," NUREG/CR-6440, November 1996.

7.0 CONCLUSIONS

As a result of the efforts associated with Task 1 of the IPIRG-2 program, the following conclusions were drawn:

(1) The load-carrying capacity of a cracked pipe subjected to a simulated-seismic load history is no worse than the load-carrying capacity of a cracked pipe subjected to a single-frequency, cyclic load history. This conclusion should be qualified by saying that it may be an artifact of the specific simulated-seismic forcing function applied during these Task 1 experiments in that the cycles prior to maximum load were primarily elastic for this simulated-seismic history while the cycles prior to maximum load for the companion single-frequency, pipe-system experiments exhibited a significant amount of cyclic plasticity. This was especially true for the stainless steel base metal, single-frequency, pipe-system experiment from IPIRG-1, i.e., Experiment 1.3-3. The fact that the cycles prior to maximum load were essentially elastic for the simulated-seismic experiments implies that these experiments could probably be analyzed much in the same manner as one would analyze a dynamic monotonic experiment. If some other simulated-seismic history were used, with a more gradual buildup of the large amplitude cycles, then the extent of cyclic degradation that occurs may be greater than that which occurs for the seismic forcing function used in this program. It is of note that as part of one of the IPIRG-2 round-robin problems, that four different but "equal" displacement-time histories were created from the same peak-broadened acceleration response spectrum. For these displacement-time histories, the maximum moments induced in a linear finite element model of the IPIRG pipe system were similar (to within 20 percent), but the timing, number, and build-up of the moment peaks were substantially different. Based on experience from this program and the IPIRG-1 program, we believe that the most damaging seismic function can be bounded by a gradually increasing single-frequency load history. In this case, once the maximum load (or surface-crack penetration) is reached, then the amplitude would be held constant for approximately 10 cycles to assess the extent of crack propagation.

(2) The load-carrying capacity of surface cracks at geometric discontinuities, such as at the junction of an elbow to a straight pipe section, can be analyzed using analysis methods previously developed for surface cracks in straight pipe sections. Note, however, that for through-wall cracks, there could be other technical issues, such as thickness gradients and restraint of pressure induced bending, that may require additional consideration if the crack is close to an elbow or nozzle.

(3) The analysis methods previously developed and verified for large surface cracks, for which the plasticity is confined to the cracked section, are appropriate for the analysis of smaller crack sizes for which plasticity may not be confined to the crack section. This conclusion is supported by findings from the Short Cracks in Piping and Piping Welds program (Ref. 7.1). However, the results from this program extended the finding from Reference 7.1 to the case of dynamic loadings. For a pipe system with a "short" crack, it is expected that plasticity remote from the crack could become significant and add an inherent margin by effectively acting to increase damping. The magnitude of this inherent margin will vary with the pipe system geometry, i.e., how much of the pipe system experiences plasticity.

(4) The previously developed through-wall-cracked pipe analyses, which had only been verified using quasi-static, monotonic pipe fracture data, work equally well for the case of a through-wall-cracked, dynamic, cyclic, pipe-system experiment.

(5) The use of an idealized constant depth crack shape geometry assumed by such documents as ASME Section XI and R6, can result in a significant underprediction of the failure stresses for a situation where the crack is in a weld or the crack is irregular in shape. If real cracks are found in service, then additional inspection efforts may be warranted to further define the crack shape in order to avoid excess conservatism.

(6) For flaw evaluation purposes, the weld crown should not be included with the pipe thickness when making moment predictions to insure a conservative underprediction. (In reality, it is unlikely if it will be known if the flaw is centered in the weld or near the toe where the weld crown is less.) Furthermore, if the weld crown was ground off, then the results from this effort suggest that the analyses of the stainless steel weld experiments are still sufficiently conservative, however, this may not be the case for the carbon steel weld experiments. In hindsight, it might have been better to conduct the IPIRG experiments with the weld crown removed, especially in light of the fact that typically for UT flaw sizing, the weld crown is ground off in service.

(7) The use of quasi-static stress-strain data and quasi-static J-R curve data results in the best predictions of the quasi-static pipe experiments for the crack sizes investigated in this program. The use of quasi-static stress-strain data and dynamic J-R curve data results in the best predictions of the dynamic experiments. Consequently, the development of dynamic stress-strain data is probably not necessary. However, it is not known if this is also true for very small flaws or uncracked pipe behavior where a large amount of pipe would experience plasticity at high strain rates. It is of further note that for the ASME Code Case N-494-3 and R6 approaches, the differences in the predictions for the dynamic pipe-system experiments when using quasi-static and dynamic J-R curve data were relatively insignificant. Consequently, for these code approaches, one should be able to use quasi-static stress strain and quasi-static J-R curve data.

(8) For the ferritic materials evaluated in this program, a flow stress based on actual material property data (i.e., the average of yield and ultimate) agrees closely with the ASME Code definition of flow stress of $2.4S_m$, where S_m is based on actual material data adhering to the spirit of the criteria specified in Article 2110 of Appendix III of Section III Division 1 of the 1989 Edition of the ASME Code, i.e, S_m(Actual). On the other hand, the flow stresses based on actual material data for the ferritic materials were up to 40 percent higher than the 2.4 S_m(Code) values. However, for the austenitic materials evaluated, a flow stress based on actual material data (e.g., the average of the measured yield and ultimate strengths) is significantly less than the flow stress based on a $3S_m$(Actual) definition while the average of yield and ultimate strength definition of flow stress was approximately 10 percent less than the $3S_m$(Code) definition. The S_m(Actual) term was introduced as a means for evaluating the technical basis of the ASME Code procedures by analyzing the pipe experiments as if the pipes used had the minimum properties defined in Section II of the ASME Code.

These differences are a result of the stainless steel $3S_m$ value being correlated to the mean value of flow stress using $1.15\ (\sigma_y + \sigma_u)/2$, whereas $2.4S_m$ for ferritic steels was based on lower bound pipe

data. The ASME Section XI Working Group on Pipe Flaw Evaluation is currently reassessing these flow stress definitions.

(9) There appears to be a threshold for the effective stress ratio ($R_{effective}$) above which the effect of cyclic loading can be ignored. The most consistent predictions for the stainless steel weld experiments were realized when cyclic J-R curve data were used in the analyses of the IPIRG-2, short-surface-cracked, pipe-system experiment and monotonic J-R curve data were used for the analyses of the IPIRG-1, stainless steel weld, pipe-system experiment. The effective stress ratios for the IPIRG-1 and IPIRG-2 stainless steel weld, pipe-system experiments were -0.2 and -0.5, respectively. The more negative effective stress ratio for the IPIRG-2 pipe-system experiment may explain why it was best analyzed using cyclic J-R curve data while the IPIRG-1 pipe-system experiment was best analyzed using monotonic J-R curve data. This finding suggests the existence of a threshold value of $R_{effective}$. For the carbon steel weld experiments, the most consistent predictions were realized when using monotonic C(T) specimen J-R curve data for the analyses of all of the experiments. The effective stress ratio for the IPIRG-2, carbon steel, elbow-girth weld, pipe-system experiment was -0.55 (less than that for the IPIRG-2, stainless steel weld, pipe-system experiment), and yet, the fracture ratios for this carbon steel weld, pipe-system experiment agreed best with the fracture ratios for the other three carbon steel weld experiments when monotonic C(T) specimen data were used in the analyses. This observation suggests that the threshold value of $R_{effective}$ may be material dependent. This material dependence of the threshold value of $R_{effective}$ is supported by the findings from Task 3 of this program (Ref. 7.2). The dependence on the need for cyclic J-R curve data has been attributed to the relative toughness of the material. The higher toughness materials require greater compressive loads (more negative stress ratios) to resharpen the crack tip and voids ahead of the crack after a tensile loading than do the lower toughness materials.

(10) For 16-inch nominal diameter pipe, and accounting for differences between the actual strength of the material and the code specified strength parameter (i.e., S_m), the ASME Section XI Z-factors for austenitic weld and ferritic base metal and weld cracks each have an inherent margin (i.e., underprediction or conservatism) of approximately 1.4 to 1.5 when compared with the Dimensionless-Plastic-Zone-Parameter (DPZP) "best fit" Z-factors from Reference 7.1. This finding is contrary to what has been reported in the past where it was indicated that the degree of inaccuracy, or conservatism, associated with the ferritic criteria was much greater than that for the austenitic criteria (Ref. 7.3). The differences in fracture ratios between the two criteria are more the result of differences in the relative strength factors between actual and code properties than they are the result of differences in the basic criteria of Z-factor formulations. The inherent margin between the current Section XI Z-factors and the DPZP "best-fit" Z-factors increases with pipe diameter. The ASME Section XI Z-factors agree fairly closely with the DPZP Z-factors based on the 95-percent confidence level fits of the experimental data.

(11) The degree of inaccuracy, or conservatism, associated with the R6 Revision 3 Option 1 method (as programmed in NRCPIPES Version 3.0) is comparable with that for the ASME criteria when the safety factors of 1.39 for Service Levels C and D and 2.78 for Service Levels A and B are not included in the ASME analyses.

(12) The degree of inaccuracy, or conservatism, associated with the ASME Code Case N494-3 approach for cracks in both austenitic and ferritic pipes is comparable to that for the R6 and ASME Appendices C and H approaches. Like the R6 approach, the ASME Code Case N-494-3 is a

FAD-based approach that allows for the use of actual yield and ultimate strength data instead of Code specific strength parameters, i.e., S_m values.

7.1 References

7.1 Krishnaswamy, P., and others, "Fracture Behavior of Short Circumferentially Surface-Cracked Pipe," NUREG/CR-6298, November 1995.

7.2 Rudland, D., and others, "The Effects of Cyclic and Dynamic Loading on the Fracture Resistance of Nuclear Piping Steels," NUREG/CR-6440, November 1996.

7.3 Scott, P., and others, "The IPIRG-1 Pipe System Fracture Tests: Analytical Results," PVP Vol. 280, pp 153-163, June 1994.

APPENDIX A

DETAILED GEOMETRY OF IPIRG PIPE LOOP FACILITY

APPENDIX A DETAILED GEOMETRY OF IPIRG PIPE LOOP FACILITY

Appendix A - Detailed Geometry of the IPIRG Pipe Loop Facility

This appendix provides the geometric details of the pipe loop facility used in the IPIRG-2 Task 1 pipe system experiments. Detailed material property data of the pipe loop materials are provided in Section 2.

The IPIRG pipe loop experimental facility is constructed in the shape of an expansion loop with five long-radius elbows and approximately 30 meters (100 feet) of 406-mm (16-inch) nominal diameter pipe. Figure A.1 is an artist's conception of the overall facility while Figure A.2 shows the overall dimensions. For the most part, the straight pipe used in the construction of the pipe loop is Schedule 100 pipe. Elbows 1, 2, 3, and 5 are also Schedule 100. The straight pipe in the loop is fabricated from ASTM A710, Grade A, Class 3 pipe steel and Elbows 1, 2, 3, and 5 are WPHY-65 material. These materials (A710, Grade A, Class 3 and WPHY-65) were chosen for their strength and weldability. As discussed below, the material and schedule for Elbow 4 was different for the two kinds of experiments that were run.

Figures A.3 and A.4 show the locations for the strain gages and string potentiometers on the pipe loop. The strain gages were used to measure moments, while the string potentiometers were used to determine pipe loop global displacements.

A.1 Detailed Dimensions of the Pipe Loop Facility Used in the Four Straight Pipe, Pipe System Experiments

The geometric details of the pipe loop facility used in the four straight pipe, pipe system experiments (Experiments 1-1, 1-2, 1-5, and 1-7) are shown in Figures A.5 through A.11. In these experiments, Elbow 4 was a nominal Schedule 160 WPHY-65 elbow.

A restraint device was used in all of the straight pipe experiments to control the motion of the pipe in case there was a double-ended guillotine break (DEGB) at the test section. Figures A.12 through A.14 summarize all of the design details for the restraint device.

A.2 Detailed Dimensions of the Pipe Loop Facility Used in the Elbow Girth Weld Pipe System Experiment

The pipe loop was modified in order to conduct Experiment 1-3, the elbow girth weld experiment. The modifications included replacing Elbow 4 with a Schedule 100 A106-90 elbow, removal of the DEGB restraint device, putting in end caps to limit the amount of energy available to drive pipe whip in the event of a DEGB, and adding strain gages on Leg 4 to measure moment. Figures A.15 through A.22 provide all of the details for the modified geometry.

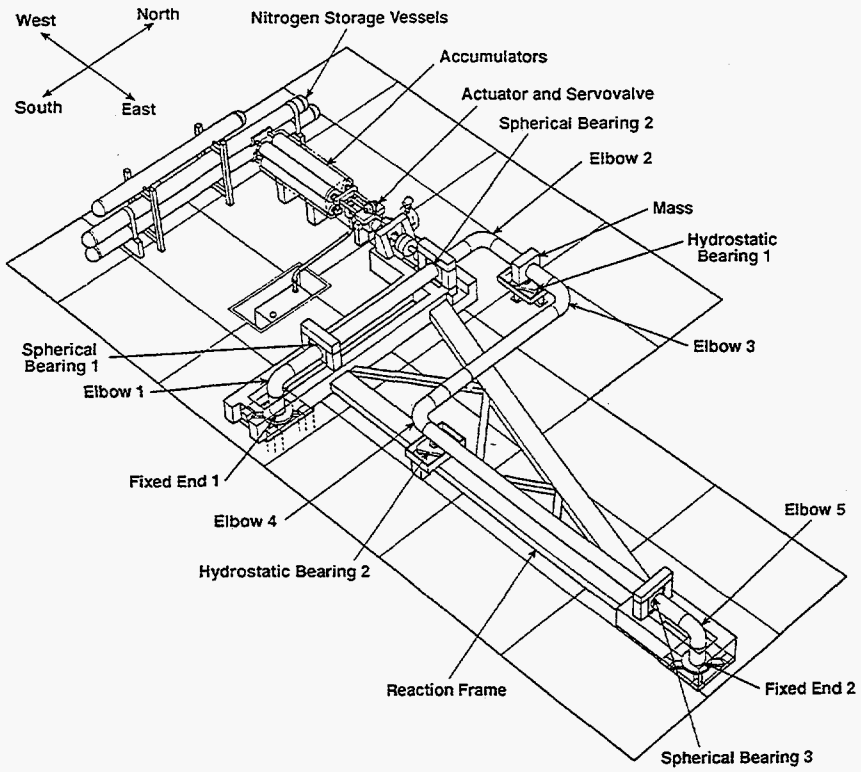

Figure A.1 Artist's conception of the IPIRG pipe loop test facility

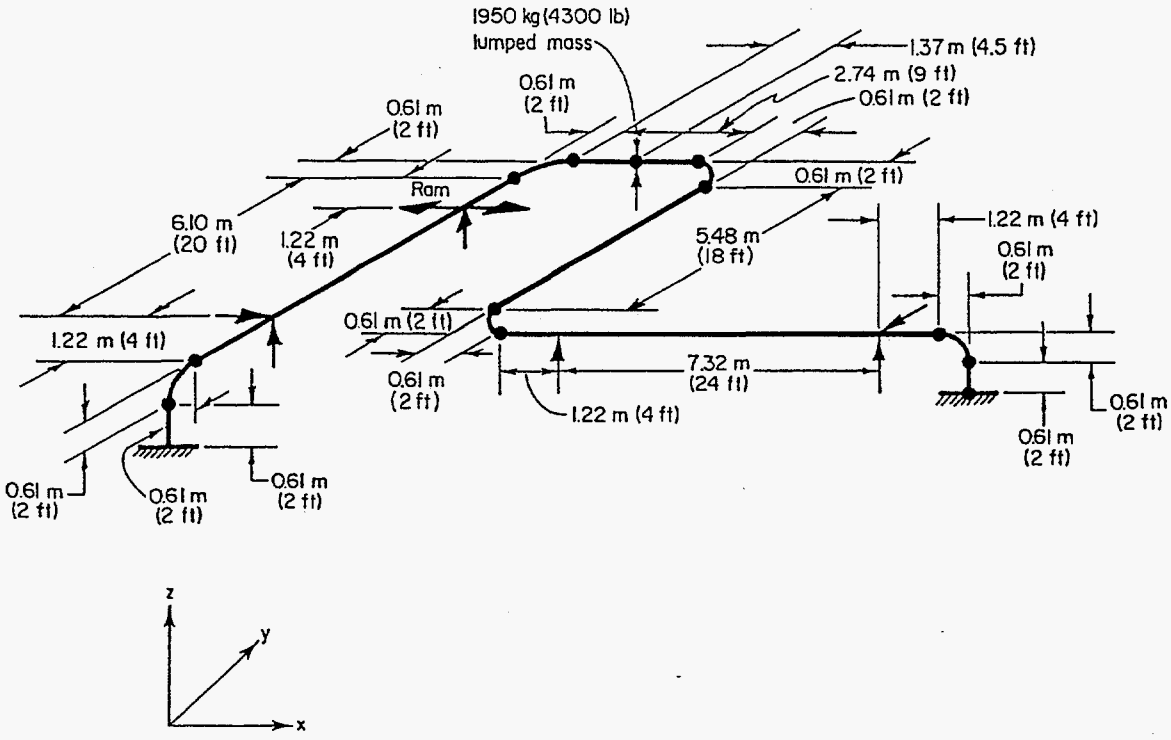

Figure A.2 Overall dimensions of the IPIRG pipe loop test facility

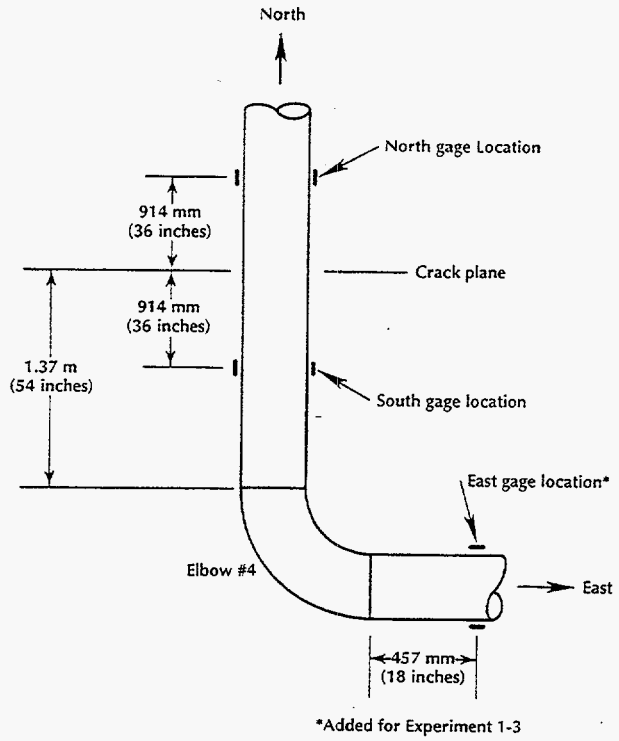

Figure A.3 Layout of strain gages for the IPIRG-2 pipe system experiments

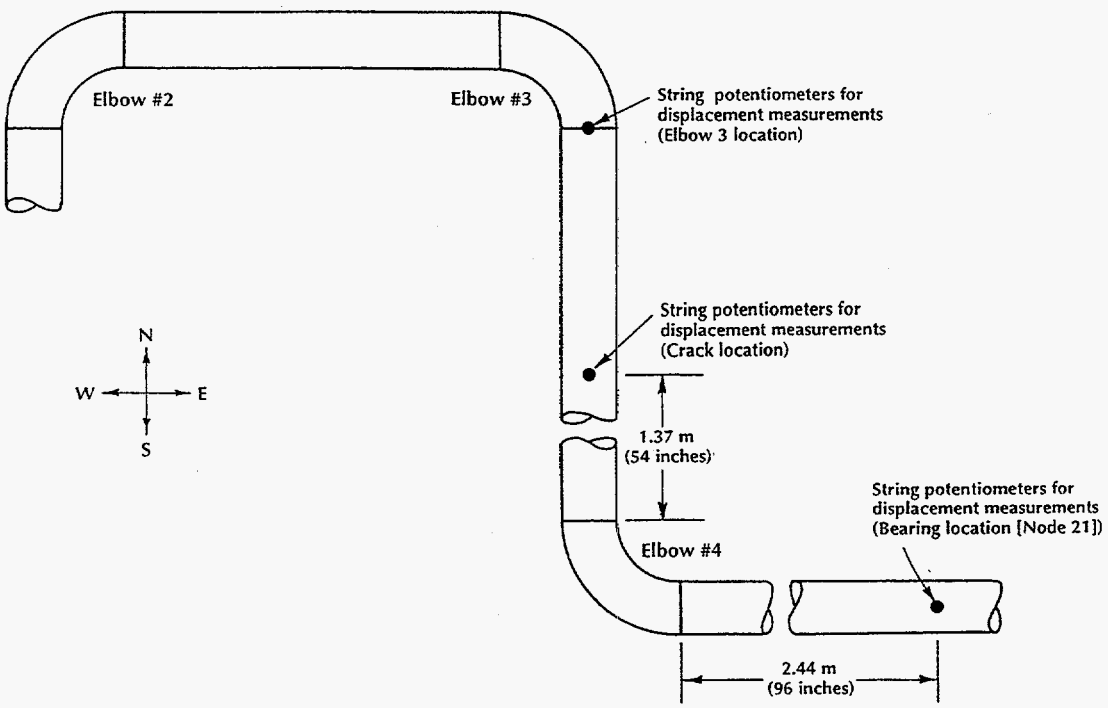

Figure A.4 String potentiometer locations for the IPIRG-2 pipe system experiments

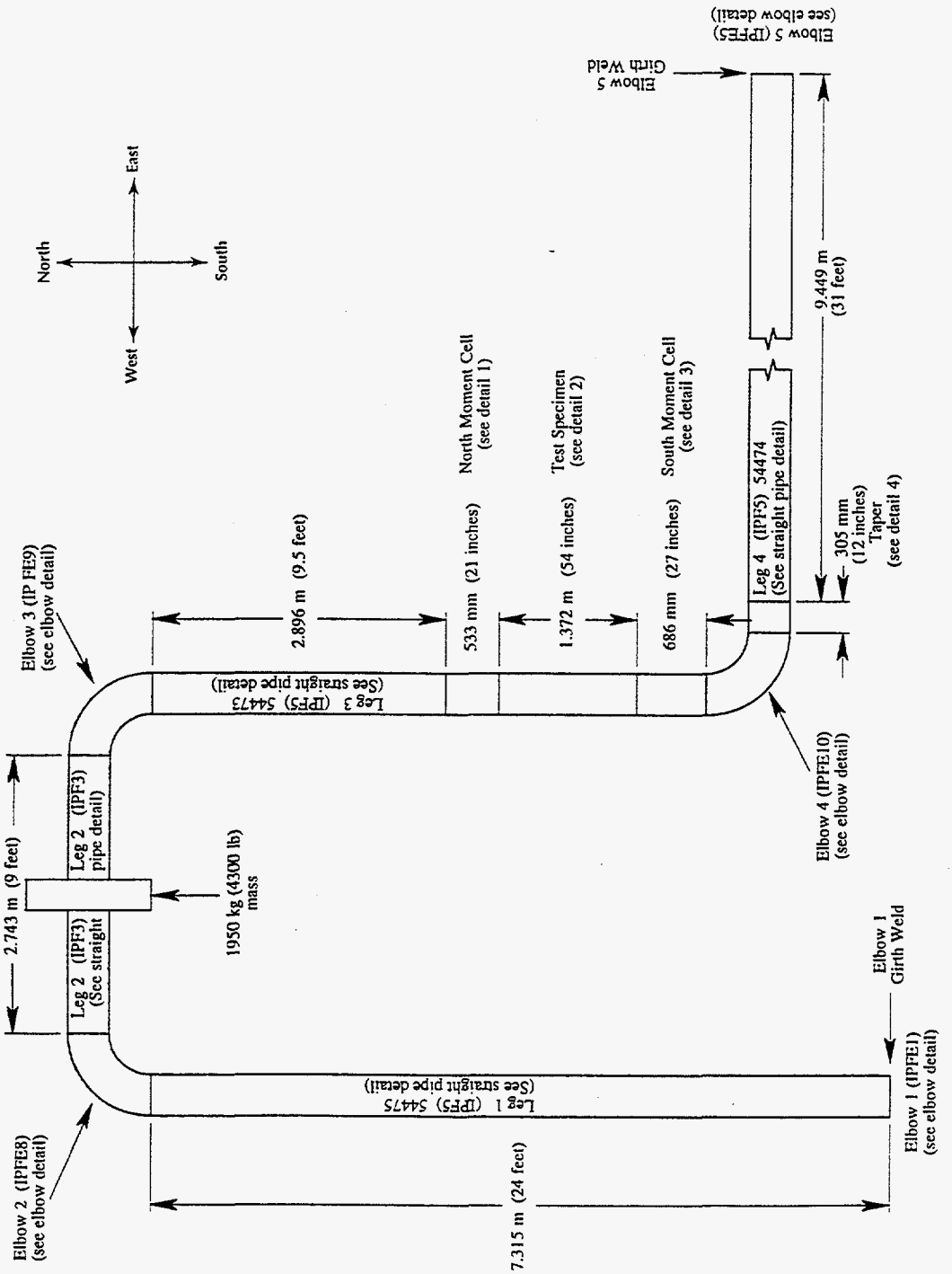

Figure A.5 Straight pipe experiments pipe loop geometry

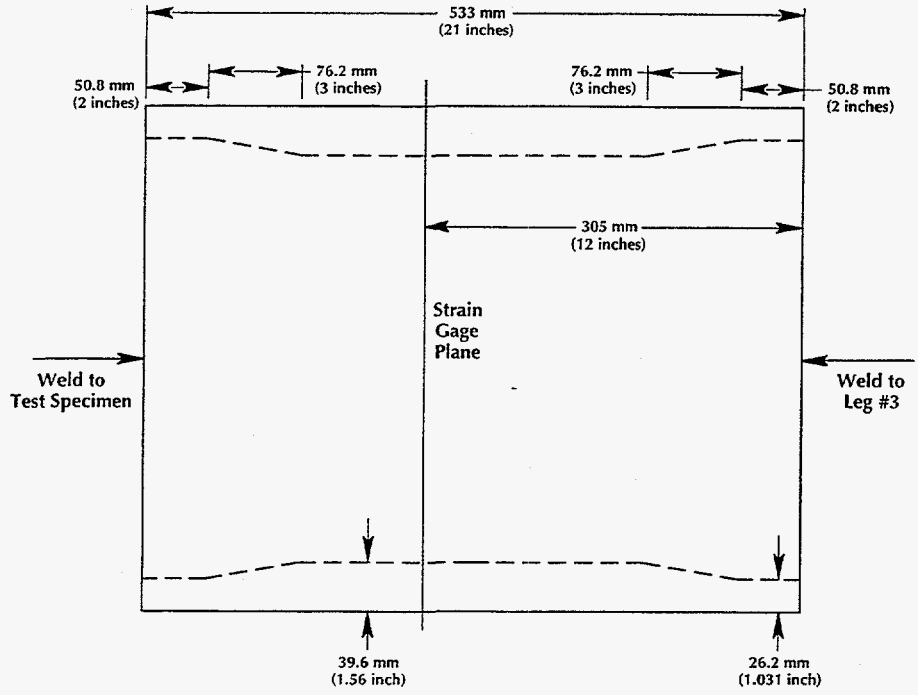

Figure A.6 North moment cell geometry

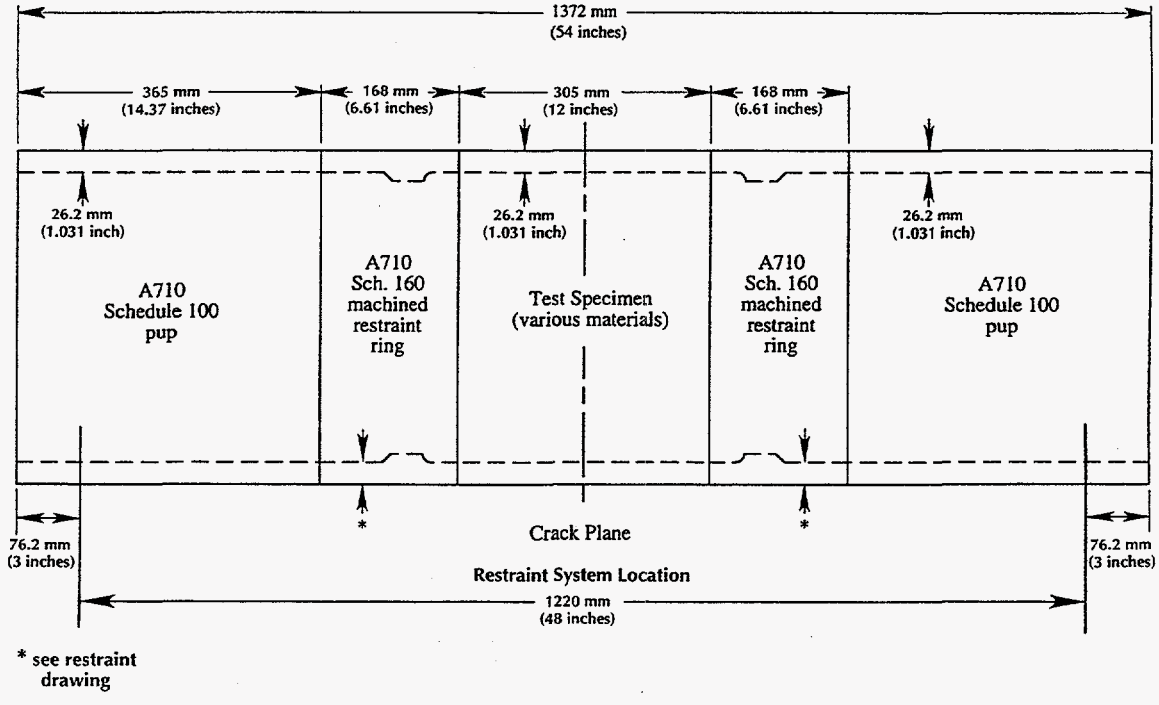

Figure A.7 Test specimen geometry

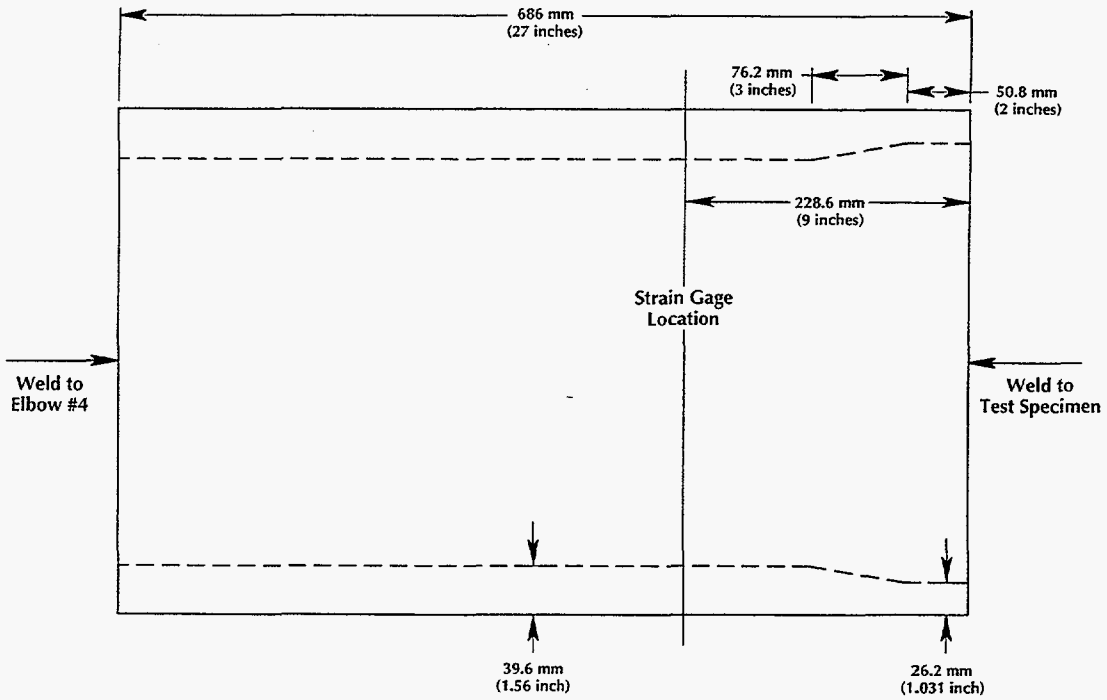

Figure A.8 South moment cell geometry

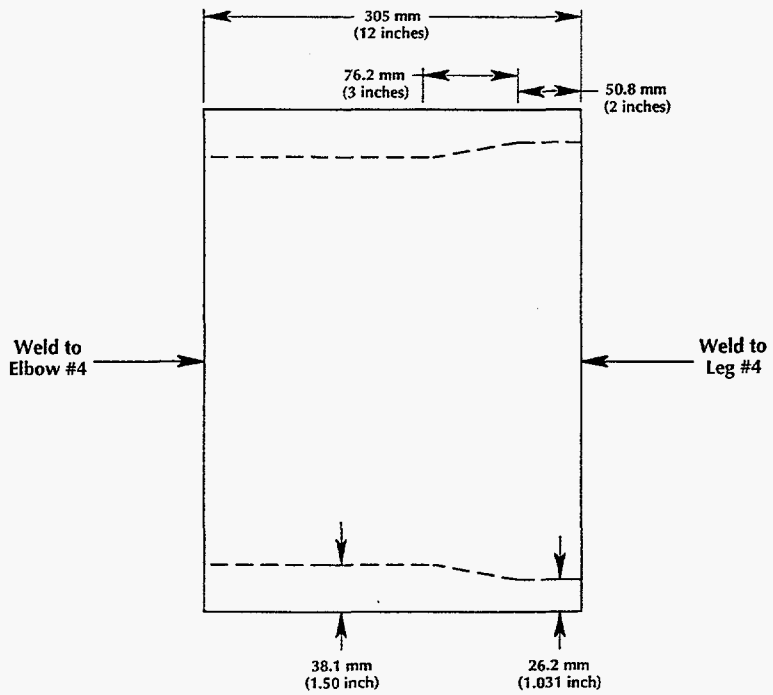

Figure A.9 Tapered section geometry

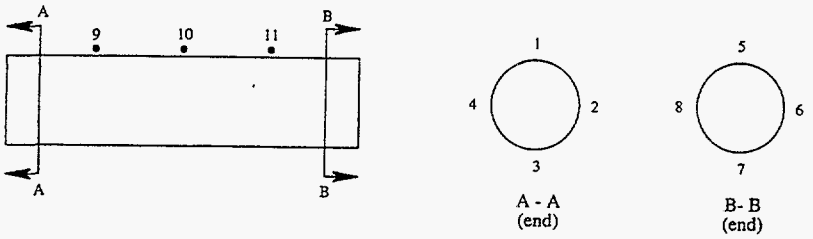

			Wall Thickness, mm Location											
Leg #	Pipe ID # (a)	Pipe Serial #	1	2	3	4	5	6	7	8	9	10	11	Avg
1	IPF5	54475	26.8	25.5	25.6	27.2	27.2	25.5	26.6	25.8	27.5	27.4	27.3	26.6
2	IPF3	(b)	27.1	27.9	28.5	(c)	26.9	(c)	28.6	(c)	(c)	(c)	(c)	27.8
3	IPF5	54473	26.2	25.8	27.0	28.6	26.3	26.6	26.9	26.8	25.9	25.8	26.8	26.6
4	IPF5	54474	28.2	25.9	25.6	27.9	27.2	26.3	25.7	26.6	27.8	27.5	27.9	26.9

(a) IPF3 was procured as part of IPIRG-1; IPF5 was procured as part of IPIRG-2
(b) Unknown, but either 47453, 47454, 47455, or 47456
(c) Not measured

Figure A.10 Straight pipe wall thickness measurements

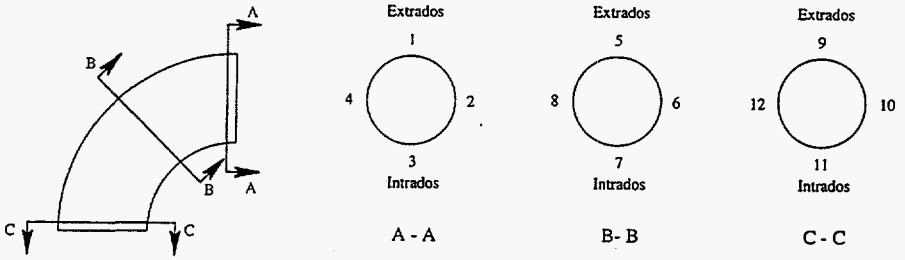

							Wall Thickness, mm Location							
Elbow # (a)	1	2	3	4	5	6	7	8	9	10	11	12	Avg
1	(b)	(b)	(b)	(b)	31.1	32.1	32.3	33.2	(b)	(b)	(b)	(b)	32.2
2	37.2	38.4	41.7	38.6	33.5	37.4	38.2	37.1	35.5	37.8	43.1	36.7	37.9
3	37.2	35.8	41.0	36.8	33.2	37.0	37.0	37.1	36.1	37.3	41.6	36.8	37.2
4	51.9	50.1	54.2	51.9	48.2	50.5	49.1	50.1	53.0	50.8	56.5	50.2	51.4
5	(b)	(b)	(b)	(b)	31.7	32.6	32.4	32.8	(b)	(b)	(b)	(b)	32.4

(a) Elbows 1 and 5 were procured as part of IPIRG-1; Elbows 2, 3, and 4 were procured as part of IPIRG-2
(b) Not measured

Figure A.11 Elbow wall thickness measurements

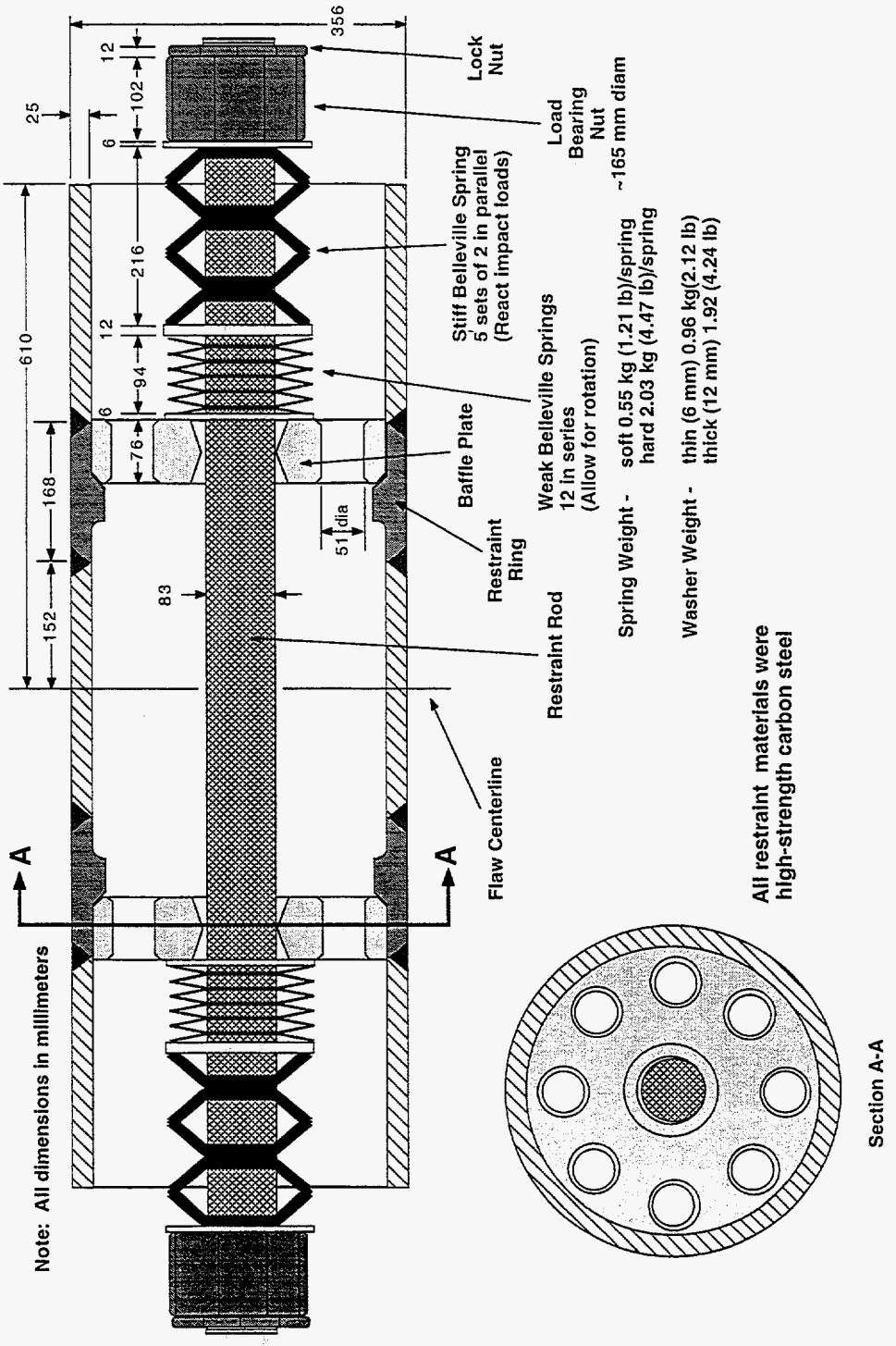

Figure A.12 DEGB restraint device

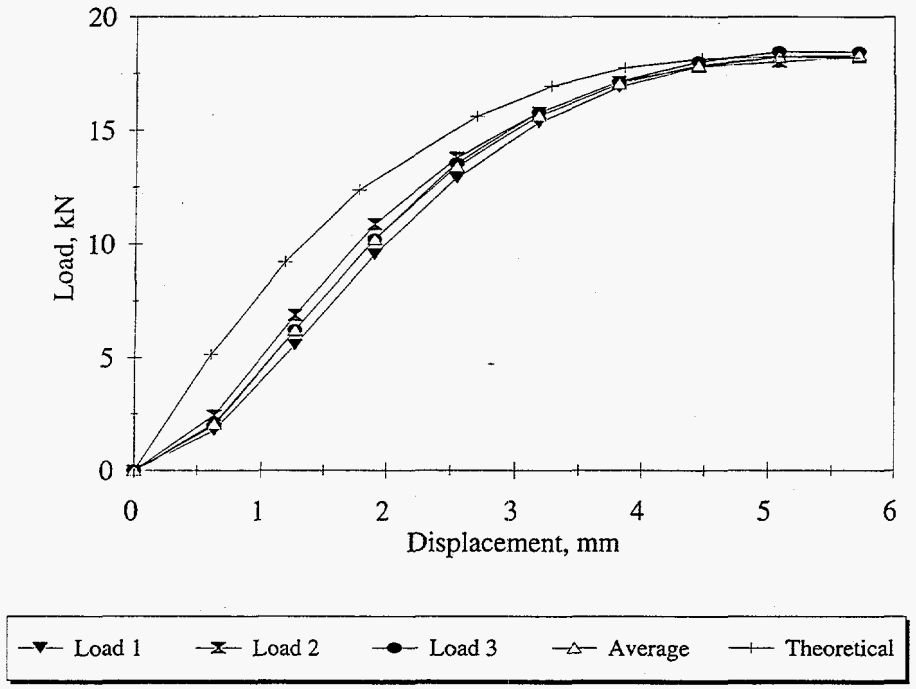

Figure A.13 DEGB restraint device weak Belleville spring stiffness

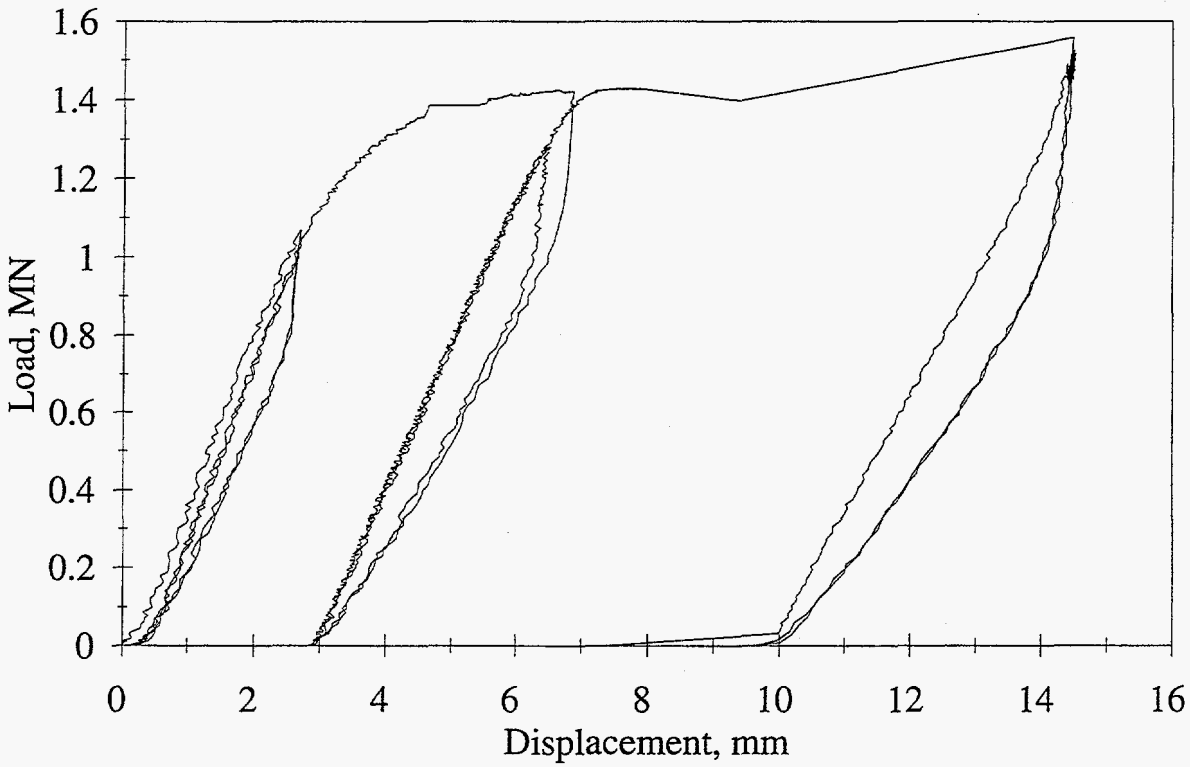

Figure A.14 DEGB restraint device stiff Belleville spring stiffness

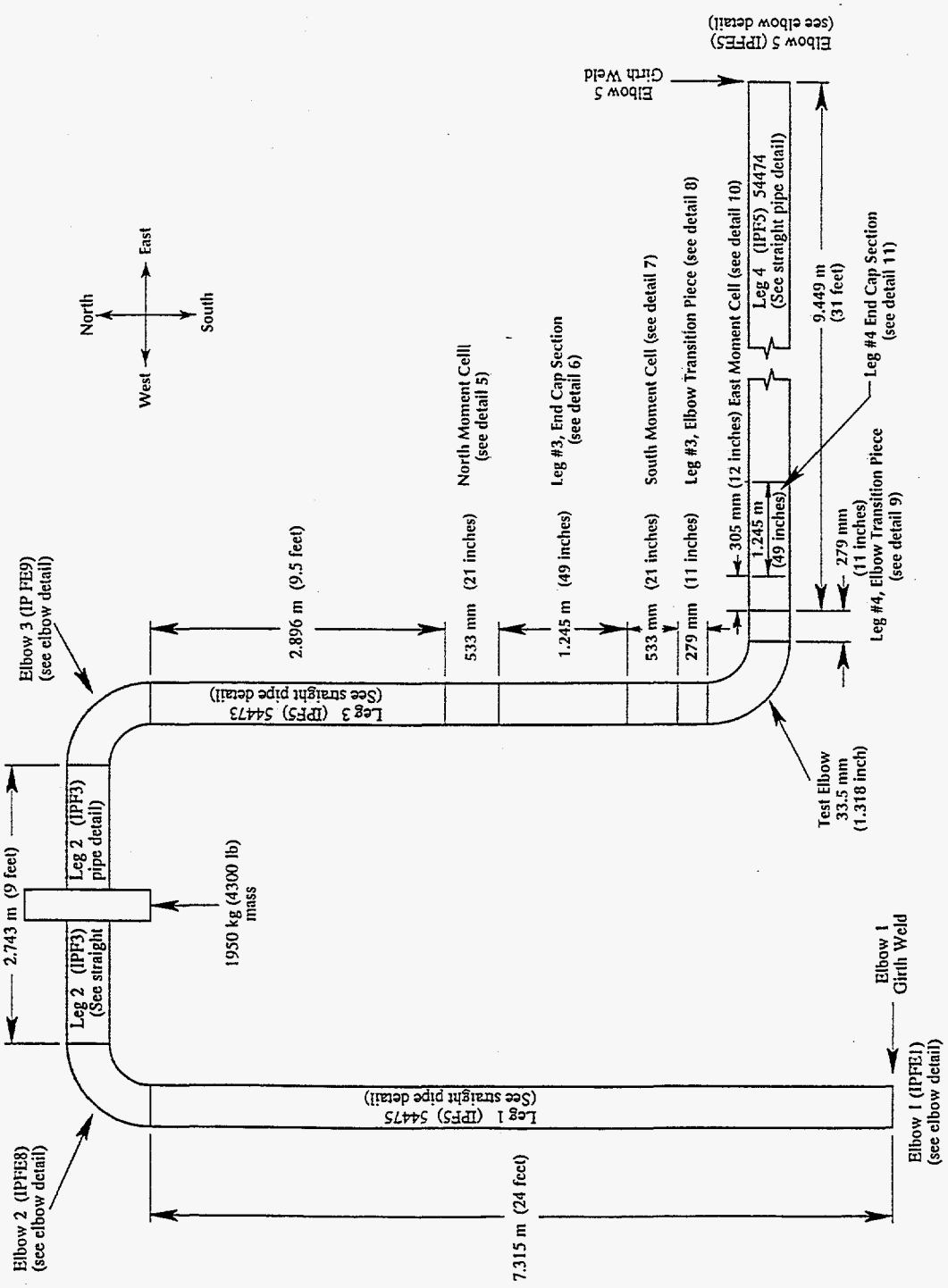

Figure A.15 Elbow girth weld experiment pipe loop geometry

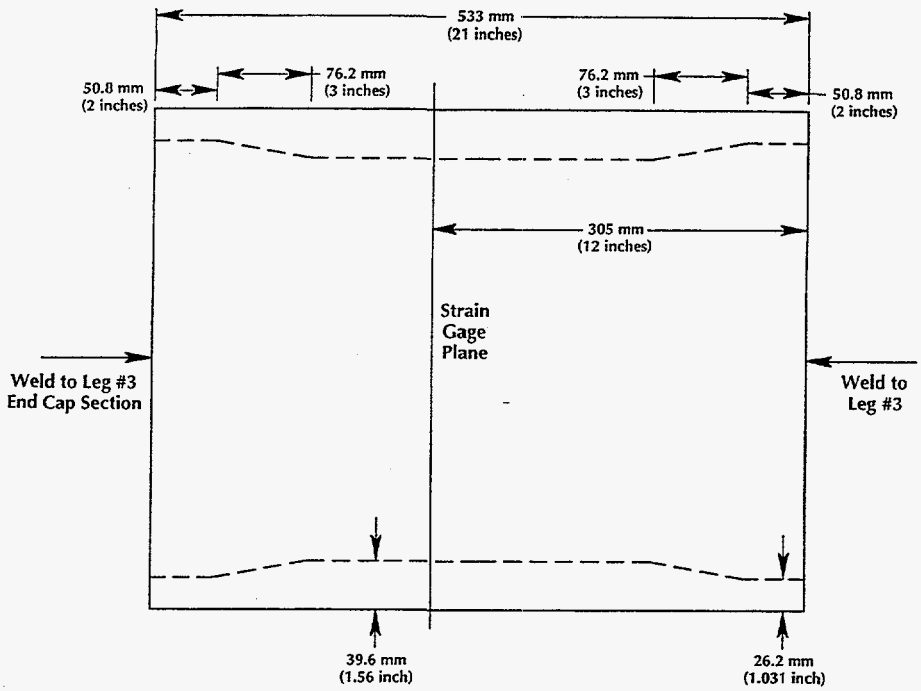

Detail 5

Figure A.16 North moment cell geometry

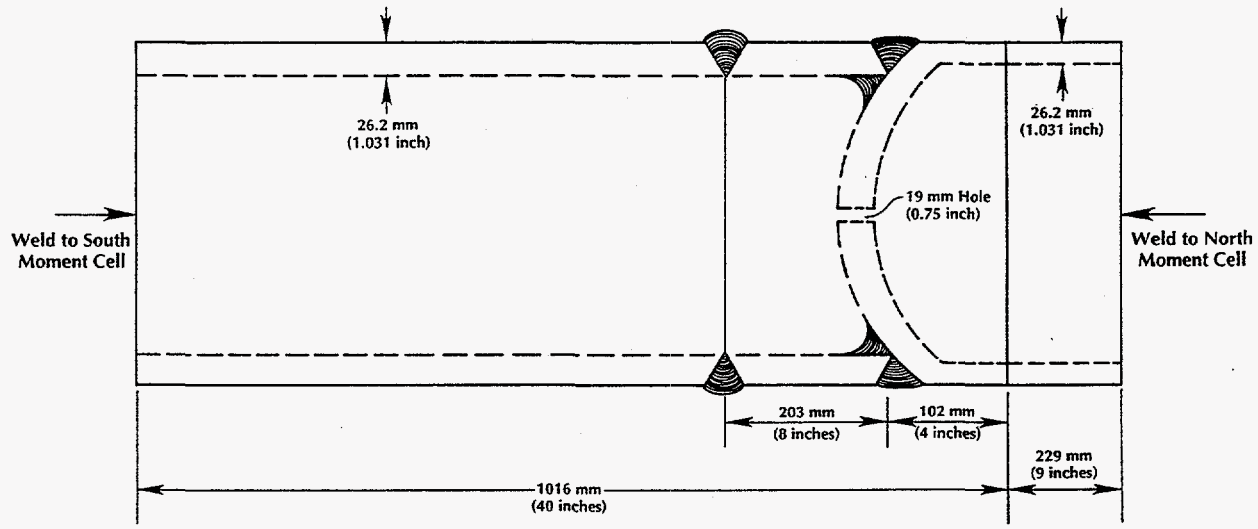

Detail 6

Figure A.17 Leg 3 end cap section

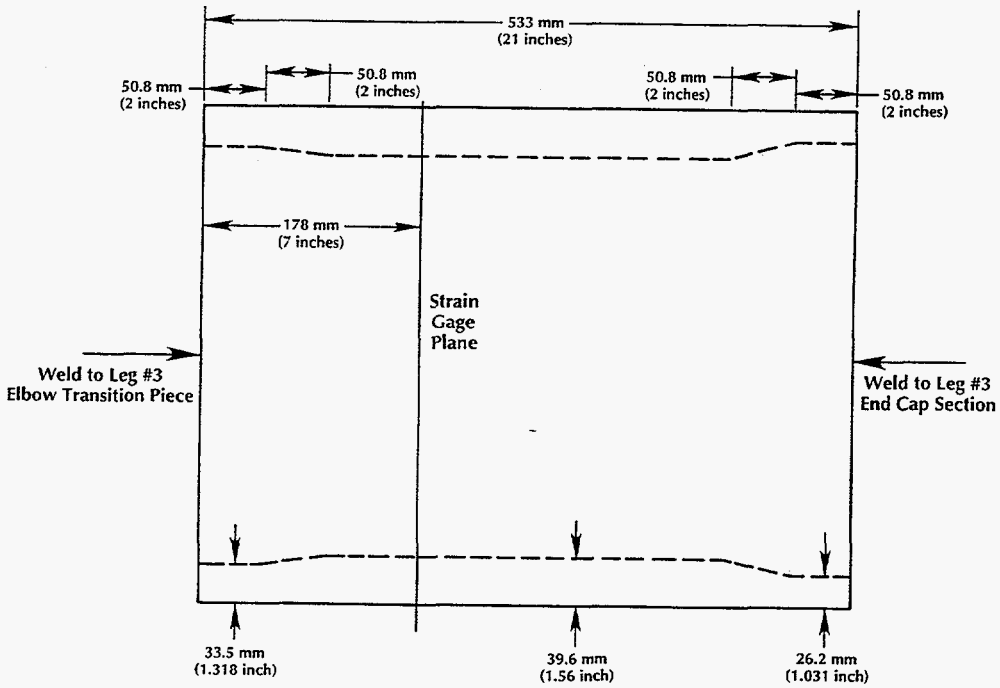

Detail 7

Figure A.18 South moment cell

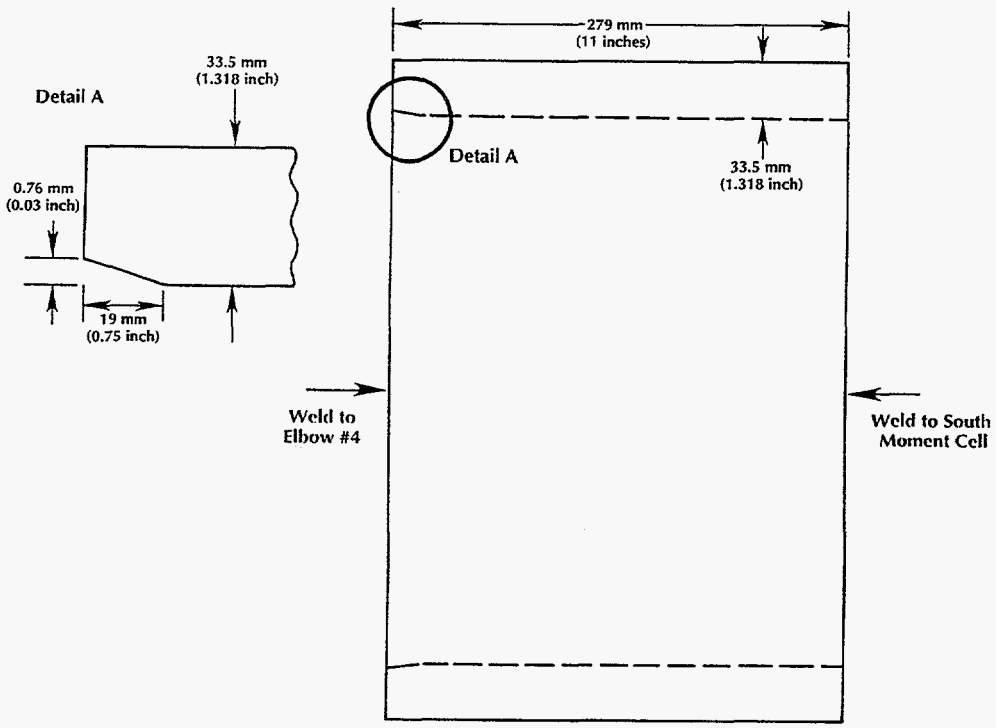

Detail 8

Figure A.19 Leg 3 elbow transition piece

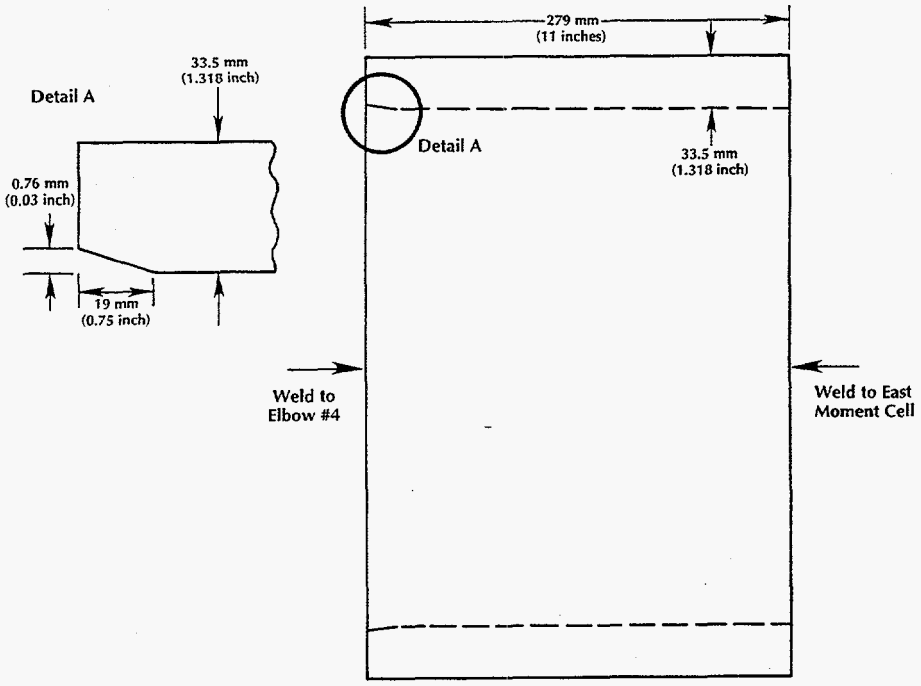

Detail 9

Figure A.20 Leg 4 elbow transition piece

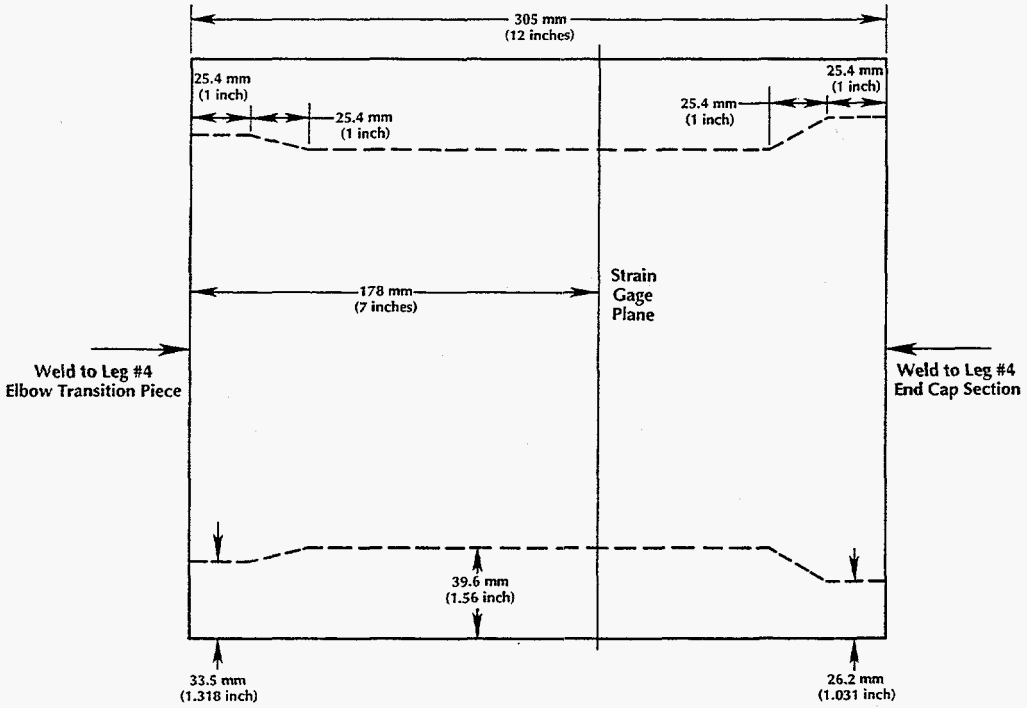

Detail 10

A.21 East moment cell

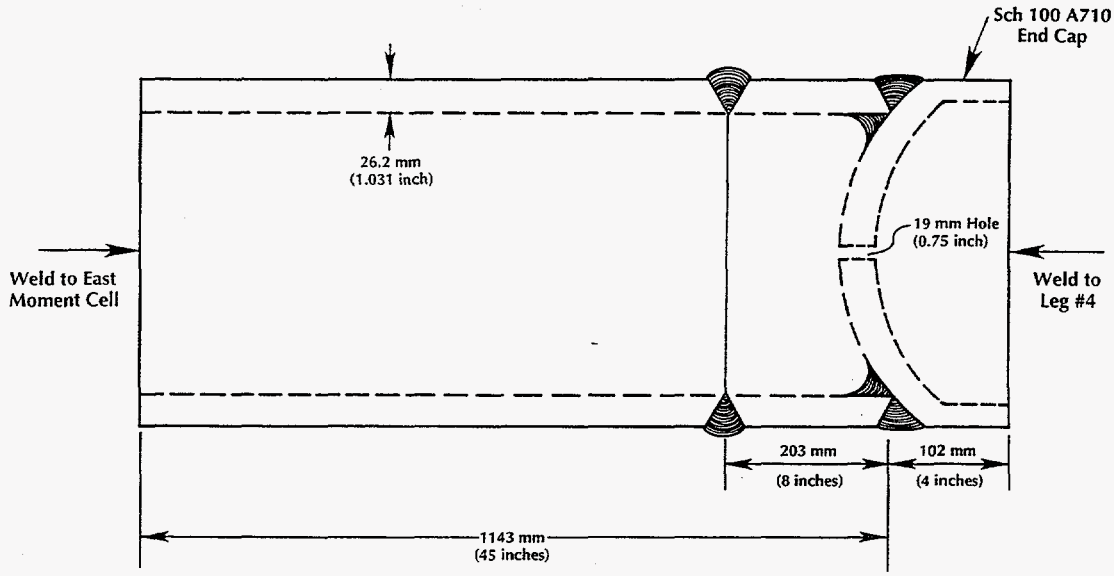

Detail 11

Figure A.22 Leg 4 end cap section

APPENDIX B

INPUT DATA FOR FINITE ELEMENT ANALYSES OF THE PIPE SYSTEM EXPERIMENTS

APPENDIX B INPUT DATA FOR FINITE ELEMENT ANALYSES OF THE PIPE SYSTEM EXPERIMENTS

Input Data for Finite Element Analyses of the Pipe System Experiments

Detailed listings of the input files used for ANSYS finite element analyses of the IPIRG-2 Task 1 pipe system experiments are provided for the two different test geometries. Table B.1 is a listing for the straight pipe experiments and Table B.2 is a listing for the elbow girth weld experiment. The major differences between the two models are: (1) Differences in pipe wall thicknesses in the vicinity of Elbow 4 due to the modifications made to the pipe loop for the elbow girth weld experiment (the addition of a new moment cell and end caps), and (2) The rod and spring restraint device is in straight pipe model.

Appendix A provides the detailed geometry information used to develop the finite element models. Comments are provided in the listings to synchronize the input data with the drawings in Appendix A and to permit correct interpretation of the ANSYS-specific input formats. All data in the models are given in U.S. customary units.

Table B.1 IPIRG straight pipe ANSYS finite element model (U.S. customary units)

```
/PREP7
/TITLE, FINAL IPIRG-2 MODEL OPTION 33D, STRAIGHT PIPE VERSION W/RESTRAINT
C***KAN,0        *STATIC ANALYSIS
C***KAN,2        *EIGENVALUE ANALYSIS
C***KAY,2,5
KAN,4    *DYNAMIC ANALYSIS
KAY,5,2

C*** DEFINE DAMPING 0.5% @ 1ST 0.5% @ 4TH
C*** 4.73 14.55 15.43 19.16
ALPHAD,2.384e-1
BETAD,6.662e-5

C*** ELEMENT TYPE DEFINITION (ET,set#,type,parameters)

ET,1,16,,,,,,2              * straight pipe (for output control)
ET,2,16,,,,,,2              * straight pipe
ET,3,18,,,1,,,2             * curved pipe
ET,4,21,,,2                 * lumped X-Y-Z mass
ET,5,40,,,6                 * spring-slider for SC
ET,6,8                      * truss for TWC

C***$$$$$$$$$$$$$$$$$$$$$$$$$$$$$$$$$$$$$$$$$$$$$$$$$$$$$$$$$$$$$$$$
ET,7,1                      * spar for the springs
ET,8,4                      * beam for the rod & nuts
C***$$$$$$$$$$$$$$$$$$$$$$$$$$$$$$$$$$$$$$$$$$$$$$$$$$$$$$$$$$$$$$$$

C*** NODE DEFINITIONS (N,node#,x,y,z)

N,1,0,0,48          * fixed end
N,2,0,0,60
N,3,0,0,72          * elbow
N,4,0,7.03,88.97    * elbow 1
N,5,0,24,96             * elbow
N,42,0,60,96
N,6,0,72,96             * hanger
N,43,0,84,96
N,7,0,120,96
N,37,0,168,96
N,8,0,216,96
N,44,0,252,96
N,38,0,264,96           * actuator
N,45,0,276,96
```

```
N,9,0,312,96                * elbow
N,10,7.03,328.97,96         * elbow 2
N,11,24,336,96      * elbow
N,12,78,336,96      * mass/support
N,13,132,336,96     * elbow
N,14,148.97,328.97,96       * elbow 3/string pot
N,15,156,312,96     * elbow
N,52,156,282,96
N,39,156,252,96
N,53,156,194.5,96   * taper
N,16,156,186,96     * sg location
N,60,156,180.5,96   * taper
N,61,156,162.6,96   * baffle
N,46,156,159.6,96   * baffle
N,40,156,150,96     * crack plane
N,100,155,150.005,96
N,101,156,150,96
N,102,155,149.995,96
N,41,156,150,96     * crack plane
N,47,156,140.4,96   * baffle
N,62,156,137.4,96   * baffle
N,63,156,119.5,96   * taper
N,48,156,114,96     * sg location
N,17,156,96,96      * elbow
N,18,163.03,79.03,96        * elbow 4
N,19,180,72,96      * elbow
N,49,188.5,72,96    * taper
N,20,228,72,96      * support
N,21,276,72,96      * string pot
N,22,324,72,96
N,23,372,72,96
N,24,420,72,96
N,25,468,72,96
N,50,504,72,96
N,26,516,72,96      * hanger
N,51,528,72,96
N,27,564,72,96      * elbow
N,28,580.97,72,88.97        * elbow 5
N,29,588,72,72      * elbow
N,30,588,72,60
N,31,588,72,48      * fixed end
N,32,0,24,72                * el 1 center
N,33,24,312,96      * el 2 center
N,34,132,312,96     * el 3 center
N,35,180,96,96      * el 4 center
N,36,564,72,72      * el 5 center
```

```
C***$$$$$$$$$$$$$$$$$$$$$$$$$$$$$$$$$$$$$$$$$$$$$$$$$$$$$$
N,300,156,180.24,96         * end of nut
N,301,156,175.75,96         * nut/hard spring interface
N,302,156,166.77,96         * hard/soft spring interface
C*** ties to Node 61 on the north baffle plate
N,303,156,162.6,96 * baffle location
N,304,156,150,96   * middle of rod
N,305,156,137.4,96 * baffle location
C*** ties to Node 62 on the south baffle plate
N,306,156,133.23,96         * soft/hard spring interface
N,307,156,124.25,96         * hard spring/nut interface
N,308,156,119.76,96         * end of nut
C***$$$$$$$$$$$$$$$$$$$$$$$$$$$$$$$$$$$$$$$$$$$$$$$$$$$$$$

C*** DEFINE REAL CONSTANTS

RWT=6.9099E-5

C***(R,set#,OD,wall thickness,,,,fluid density)
R,1,16,1.047,,,,RWT               * leg 1
R,2,16,1.094,,,,RWT               * leg 2
R,3,16,1.047,,,,RWT               * leg 3
R,4,16,1.059,,,,RWT               * leg 4
R,5,16,7.625,,,,RWT               * end cap
R,6,16,1.560,,,,RWT               * moment cell pipe
R,7,16,1.031,,,,RWT               * test pipe pups
R,9,16,1.500,,,,RWT               * taper section
R,10,16,1.031,,,,RWT        * nominal Sch 100
R,11,16,1.593,,,,RWT        * nominal Sch 160
R,12,16,6.000,,,,RWT        * baffle plate

C***(R,set#,mass)
R,15,11.128                       * simulated valve lumped mass
R,16,0.175                        * spring & washer mass

C***(R,set#,OD,wall thickness,radius,sifI,sifJ,,fluid density)
R,21,16,1.268,24,1,1,,RWT         * elbow 1
R,22,16,1.492,24,1,1,,RWT         * elbow 2
R,23,16,1.465,24,1,1,,RWT         * elbow 3
R,24,16,2.024,24,1,1,,RWT         * elbow 4
R,25,16,1.276,24,1,1,,RWT         * elbow 5

C***(R,set#,OD,wall thickness,,,,fluid density)
R,40,16,1.031,,,,RWT        * straight test section pipe
R,41,16,1.318,,,,RWT        * elbow transition pipe
R,42,16,1.318,24,1,1,,RWT         * girth weld test elbow
```

```
C***$$$$$$$$$$$$$$$$$$$$$$$$$$$$$$$$$$$$$$$$$$$$$$$$$$$
C***(R,set#,area)
R,100,4.31713e-3                * soft springs
R,101,7.11920e-1                * hard springs
C***(R,set#,area,i_zz,i_yy,thickness_z,thickness_y)
R,102,8.386,5.597,5.5597,3.268,3.268    * rod
R,103,33.183,87.624,87.624,6.5,6.5           * nuts
C***$$$$$$$$$$$$$$$$$$$$$$$$$$$$$$$$$$$$$$$$$$$$$$$$$$$

C*** DEFINE MATERIAL PROPERTY TABLES (MP,property,set#,value)

/COM
/COM    ASTM A710 Gr A Cl 3
/COM
MP,EX,1,28.34E6
MP,NUXY,1,0.285
MP,DENS,1,7.324E-4
MP,ALPX,1,6.5E-6

/COM
/COM    WPHY-65
/COM
MP,EX,2,28.34E6
MP,NUXY,2,0.285
MP,DENS,2,7.324E-4
MP,ALPX,2,6.5E-6

/COM
/COM    UNCRACKED PIPE TEST SECTION MATERIAL - ASTM A710 GR A CL 3
/COM

MP,EX,10,28.34E6
MP,NUXY,10,0.285
MP,DENS,10,7.324E-4
MP,ALPX,10,6.5E-6

/COM
/COM    ELBOW TEST SECTION PUP MATERIAL
/COM

MP,EX,11,28.34E6
MP,NUXY,11,0.285
MP,DENS,11,7.324E-4
MP,ALPX,11,6.5E-6

/COM
```

```
/COM   ELBOW TEST SECTION MATERIAL
/COM

MP,EX,12,28.34E6
MP,NUXY,12,0.285
MP,DENS,12,7.324E-4
MP,ALPX,12,6.5E-6

C*** ######################################################
/COM
/COM   NRCPIPE EXP 1-5 (A8W short SC w/Jm-R TWC), PRESSURE CORRECTED
/COM
C***
C***   surface crack
C***
C***(R,set#,stiffness_1,,,gap,F_slide,stiffness_2)
R,31,6.06354e9,0,0,0,3.32411e6
R,32,3.75317e8,0,0,0,1.58049e6
R,33,6.66172e6,0,0,0,7.53977e4
C***
C***   crack closure spring
C***
R,34,0,0,0,1E-6,0,2E11
C***
C***   break away element
C***
R,35,5.9e9.,0.,0.,0.,-9959988.
C***
C***   through-wall crack
C***
MP,EX,13,1473944.6
C***(NL,set#,kinematic hardening flag,strains)
NL,13,13,17,3.0114,5.8431,8.6282,31.7010,80.7213
C***(NL,set#,table_location,temperature,stresses)
NL,13,19,72.,4438636.7,4766130.8,4722769.3,2239808.6,347764.0
C***(R,set#,area)
R,36,1.
C***
C***   balance of pipe in the test section
C***
C***MP,EX,10,26.37E6
C***MP,NUXY,10,.285
C***MP,DENS,10,7.324E-4
C***MP,ALPX,10,6.5E-6
C*** ######################################################

C***$$$$$$$$$$$$$$$$$$$$$$$$$$$$$$$$$$$$$$$$$$$$$$$$$$$$
```

```
C***
C***    Restraint System
C***
MP,EX,100,29.e6
MP,NUXY,100,.285
MP,DENS,100,7.324e-4
MP,ALPX,100,6.5e-6
C***$$$$$$$$$$$$$$$$$$$$$$$$$$$$$$$$$$$$$$$$$$$$$$$$$$$$$$$$

C*** ELEMENT DEFINITIONS (EN,el#,i,j,k)

MAT,1
TYPE,2  $REAL,10  $EN,1,1,2  $EN,2,2,3
MAT,2
TYPE,3  $REAL,21  $EN,3,3,4,32  $EN,4,4,5,32          * elbow 1
MAT,1
TYPE,2  $REAL,1  $EN,5,5,42
EN,6,42,6   $EN,7,6,43
EN,8,43,7   $EN,9,7,37
EN,10,37,8  $EN,11,8,44
EN,12,44,38 $EN,13,38,45
EN,14,45,9
MAT,2
TYPE,3  $REAL,22  $EN,15,9,10,33  $EN,16,10,11,33     * elbow 2
MAT,1
TYPE,2  $REAL,2  $EN,17,11,12
TYPE,4  $REAL,15 $EN,18,12                    * valve mass
TYPE,2  $REAL,2  $EN,19,12,13
MAT,2
TYPE,3  $REAL,23  $EN,20,13,14,34  $EN,21,14,15,34    * elbow 3
MAT,1
TYPE,2  $REAL,3  $EN,22,15,52  $EN,23,52,39
TYPE,2  $REAL,3  $EN,24,39,53
TYPE,2  $REAL,6  $EN,25,53,16  $EN,26,16,60          * moment cell
TYPE,2  $REAL,7  $EN,27,60,61

C***$$$$$$$$$$$$$$$$$$$$$$$$$$$$$$$$$$$$$$$$$$$$$$$$$$$$$$$$
MAT,100
C***TYPE,8  $REAL,103 $EN,28,300,301,38               * nut
C***TYPE,8  $REAL,102 $EN,29,301,303,38               * rod
C***CP,7,UX,61,303                  * rigid connection in Ux
C***CP,8,UZ,61,303                        * rigid connection in Uz
C***TYPE,7  $REAL,101 $EN,30,301,302          * hard spring
C***TYPE,4  $REAL,16  $EN,31,302              * spring mass
C***TYPE,7  $REAL,100 $EN,32,302,61                  * soft spring
C***TYPE,8  $REAL,102 $EN,33,303,304,38              * rod
```

```
MAT,1
C***$$$$$$$$$$$$$$$$$$$$$$$$$$$$$$$$$$$$$$$$$$$$

C***TYPE,2  $REAL,12  $EN,34,61,46                    *baffle plate
MAT,10
TYPE,2  $REAL,40  $EN,34,61,46                        * baffle plate removed

MAT,10
TYPE,1  $REAL,40  $EN,35,46,40                        * test section pipe
C***TYPE,5  $REAL,35  $EN,36,40,101                   * break-away
C***TYPE,5  $REAL,31  $EN,37,101,41                   * SC1
C***TYPE,5  $REAL,32  $EN,38,101,41                   * SC2
C***TYPE,5  $REAL,33  $EN,39,101,41                   * SC3
C***TYPE,5  $REAL,34  $EN,40,40,41                    * crack closure
MAT,13
C***TYPE,6  $REAL,36  $EN,41,100,102                  * TWC
C***CE,1,0., 100,UY,1., 40,UY,-1., 40,ROTZ,1.         * TWC constraint
C***CE,2,0., 102,UY,1., 41,UY,-1., 41,ROTZ,1.         * TWC constraint
CP,1,UX,40,41                  * X rigid
CP,2,UY,40,41                  * Y rigid
CP,3,UZ,40,41                  * Z rigid
CP,4,ROTX,40,41                * X_rot rigid
CP,5,ROTY,40,41                * Y_rot rigid
CP,6,ROTZ,40,41   * constrait for uncracked analysis on ROTZ
MAT,10
TYPE,1  $REAL,40  $EN,42,41,47                        * test section pipe

MAT,10
TYPE,2  $REAL,40  $EN,43,47,62                        * baffle plate (removed)
MAT,1
C***TYPE,2  $REAL,12  $EN,43,47,62                    * baffle plate

C***$$$$$$$$$$$$$$$$$$$$$$$$$$$$$$$$$$$$$$$$$$$$
MAT,100
C***TYPE,8  $REAL,102 $EN,44,304,305,38               * rod
C***TYPE,7  $REAL,100 $EN,45,62,306                   * soft spring
C***TYPE,4  $REAL,16  $EN,46,306                * spring mass
C***TYPE,7  $REAL,101 $EN,47,306,307            * hard spring
C***CP,9,UX,62,305             * rigid connection in Ux
C***CP,10,UZ,62,305            * rigid connection in Uz
C***TYPE,8  $REAL,102 $EN,48,305,307,38               * rod
C***TYPE,8  $REAL,103 $EN,49,307,308,38               * nut
MAT,1
C***$$$$$$$$$$$$$$$$$$$$$$$$$$$$$$$$$$$$$$$$$$$$

TYPE,2  $REAL,7  $EN,50,62,63
TYPE,2  $REAL,6  $EN,51,63,48  $EN,52,48,17           * moment cell
```

```
MAT,2
TYPE,3  $REAL,24  $EN,53,17,18,35  $EN,54,18,19,35     * elbow 4
MAT,1
TYPE,2  $REAL,9   $EN,55,19,49
TYPE,2  $REAL,4   $EN,56,49,20
TYPE,2  $REAL,4   $EN,57,20,21
TYPE,2  $REAL,4   $EN,58,21,22
TYPE,2  $REAL,4   $EN,59,22,23
TYPE,2  $REAL,4   $EN,60,23,24
TYPE,2  $REAL,4   $EN,61,24,25
TYPE,2  $REAL,4   $EN,62,25,50
TYPE,2  $REAL,4   $EN,63,50,26
TYPE,2  $REAL,4   $EN,64,26,51
TYPE,2  $REAL,4   $EN,65,51,27
MAT,2
TYPE,3  $REAL,25  $EN,66,27,28,36  $EN,67,28,29,36     * elbow 5
MAT,1
TYPE,2  $REAL,10  $EN,68,29,30  $EN,69,30,31

C*** MASTER DEGREES OF FREEDOM FOR EIGENVALUE ANALYSIS
TOTAL,40

C***
C*** DEFINE LOADS
C***

/COM
/COM gravity
/COM
ACEL,,,386.4

/COM
/COM pressure
/COM
EP,ALL,PINT,2250
C***EP,ALL,PINT,0

C***$$$$$$$$$$$$$$$$$$$$$$$$$$$$$$$$$$$$$$$$$$$$$$$$$$$$
C***
C*** REMOVE PRESSURE FROM SOME ELEMENTS
C***
EPDELE,18,,,ALL        * lumped mass
EPDELE,28,,,ALL        * restraint nut beam
EPDELE,29,,,ALL        * restraint rod beam
EPDELE,30,,,ALL        * hard spring
EPDELE,31,,,ALL        * spring mass
```

```
EPDELE,32,,,ALL          * soft spring
EPDELE,33,,,ALL          * restraint rod beam
EPDELE,36,,,ALL          * break away
EPDELE,37,,,ALL          * SC1
EPDELE,38,,,ALL          * SC2
EPDELE,39,,,ALL          * SC3
EPDELE,40,,,ALL          * crack closure
EPDELE,41,,,ALL          * TWC
EPDELE,44,,,ALL          * restraint rod beam
EPDELE,45,,,ALL          * soft spring
EPDELE,46,,,ALL          * spring mass
EPDELE,47,,,ALL          * hard spring
EPDELE,48,,,ALL          * restraint rod beam
EPDELE,49,,,ALL          * restraint nut beam
C***$$$$$$$$$$$$$$$$$$$$$$$$$$$$$$$$$$$$$$$$$$$$$$$$

/COM
/COM temperature
/COM
KTEMP,0  *DEFINES WHERE TEMPERATURE LOADS ARE TO BE FOUND(TUNIF)
TREF,72
TUNIF,550 *ASSIGNS A UNIFORM TEMPERATURE TO ALL NODES
C***TUNIF,72

C***
C*** DEFINE NODE CONSTRAINTS
C***
D,1,ALL              * west fixed end
D,6,UX,0.,,,,UZ      * node 6 hanger
D,38,UZ              * actuator
D,12,UZ              * lumped mass
D,20,UZ              * hydrostatic bearing
D,26,UZ,0.,,,,UY     * end hanger
D,31,ALL             * end fixed end

KBC,1
ITER,1,1,1
PODISP,1             * write displacements every iteration
POSTR,1,1,3                  * write pipe moment every iteration
POSTR,1,5,3                  * write spring-sliders every iteration
POSTR,1,6,3                  * write truss every iteration

C***
C*** DEFINE LOAD STEPS
C***
C*** AMP,FREQ,RAMP,SLOPE      9.500     3.950   225.000     0.375
TIME, 0.0   $D,38,UX, 0.000   $LWRITE
```

```
AFWRITE
FINISH
/INPUT,27
FINISH
```

Table B.2 IPIRG girth weld experiment ANSYS finite element model (U.S. customary units)

```
/PREP7
/TITLE, FINAL IPIRG-2 MODEL OPTION 33D, ELBOW GIRTH WELD TEST VERSION
C***KAN,0          *STATIC ANALYSIS
C***KAN,2          *EIGENVALUE ANALYSIS
C***KAY,2,5
KAN,4      *DYNAMIC ANALYSIS
KAY,5,2

C*** DEFINE DAMPING 0.5% @ 1ST 0.5% @ 4TH
C*** 4.74 14.53 15.39 18.45
ALPHAD,2.369e-1
BETAD,6.863e-5

C*** ELEMENT TYPE DEFINITION (ET,set#,type,parameters)

ET,1,16,,,,,,2              * straight pipe (for output control)
ET,2,16,,,,,,2              * straight pipe
ET,3,18,,,1,,,2             * curved pipe
ET,4,21,,,2                 * lumped X-Y-Z mass
ET,5,40,,,6                 * spring-slider for SC
ET,6,8                      * truss for TWC

C*** NODE DEFINITIONS (N,node#,x,y,z)

N,1,0,0,48          * fixed end
N,2,0,0,60
N,3,0,0,72          * elbow
N,4,0,7.03,88.97    * elbow 1
N,5,0,24,96                 * elbow
N,42,0,60,96
N,6,0,72,96                 * hanger
N,43,0,84,96
N,7,0,120,96
N,37,0,168,96
N,8,0,216,96
N,44,0,252,96
N,38,0,264,96               * actuator
N,45,0,276,96
N,9,0,312,96                * elbow
N,10,7.03,328.97,96         * elbow 2
N,11,24,336,96      * elbow
N,12,78,336,96      * mass/support
N,13,132,336,96     * elbow
N,14,148.97,328.97,96       * elbow 3/string pot
```

```
N,15,156,312,96     * elbow
N,52,156,282,96
N,39,156,252,96
N,53,156,194.5,96   * taper
N,16,156,186,96     * sg location
N,60,156,180.5,96   * taper
N,61,156,162,96     * end cap
N,46,156,161,96     * end cap
N,47,156,144,96
N,62,156,125,96     * taper
N,48,156,114,96     * sg location
N,63,156,110,96     * taper
N,17,156,107,96
N,40,156,96,96      * crack plane/elbow
N,100,155,96.005,96
N,101,156,96,96
N,102,155,95.995,96
N,41,156,96,96      * crack plane/elbow
N,18,163.03,79.03,96        * elbow 4
N,19,180,72,96      * elbow
N,70,191,72,96
N,71,192.5,72,96    * taper
N,72,198,72,96      * sg location
N,73,201.5,72,96    * taper
N,20,228,72,96      * support
N,74,245,72,96      * end cap
N,75,246,72,96      * end cap
N,21,276,72,96      * string pot
N,22,324,72,96
N,23,372,72,96
N,24,420,72,96
N,25,468,72,96
N,50,504,72,96
N,26,516,72,96      * hanger
N,51,528,72,96
N,27,564,72,96      * elbow
N,28,580.97,72,88.97        * elbow 5
N,29,588,72,72      * elbow
N,30,588,72,60
N,31,588,72,48      * fixed end
N,32,0,24,72                * el 1 center
N,33,24,312,96      * el 2 center
N,34,132,312,96     * el 3 center
N,35,180,96,96      * el 4 center
N,36,564,72,72      * el 5 center
```

```
C*** DEFINE REAL CONSTANTS

RWT=6.9099E-5

C***(R,set#,OD,wall thickness,,,,fluid density)
R,1,16,1.047,,,,RWT          * leg 1
R,2,16,1.094,,,,RWT          * leg 2
R,3,16,1.047,,,,RWT          * leg 3
R,4,16,1.059,,,,RWT          * leg 4
R,5,16,7.625,,,,RWT          * end cap
R,6,16,1.560,,,,RWT          * moment cell pipe
R,7,16,1.031,,,,RWT          * test pipe pups
R,9,16,1.500,,,,RWT          * taper section
R,10,16,1.031,,,,RWT     * nominal Sch 100
R,11,16,1.593,,,,RWT     * nominal Sch 160
R,12,16,6.000,,,,RWT     * baffle plate

C***(R,set#,mass)
R,15,11.128                  * simulated valve lumped mass

C***(R,set#,OD,wall thickness,radius,sifI,sifJ,,fluid density)
R,21,16,1.268,24,1,1,,RWT    * elbow 1
R,22,16,1.492,24,1,1,,RWT    * elbow 2
R,23,16,1.465,24,1,1,,RWT    * elbow 3
R,24,16,2.024,24,1,1,,RWT    * elbow 4
R,25,16,1.276,24,1,1,,RWT    * elbow 5

C***(R,set#,OD,wall thickness,,,,fluid density)
R,40,16,1.031,,,,RWT     * straight test section pipe
R,41,16,1.318,,,,RWT     * elbow transition pipe
R,42,16,1.318,24,1,1,,RWT    * girth weld test elbow

C*** DEFINE MATERIAL PROPERTY TABLES (MP,property,set#,value)

/COM
/COM   ASTM A710 Gr A Cl 3
/COM
MP,EX,1,28.34E6
MP,NUXY,1,0.285
MP,DENS,1,7.324E-4
MP,ALPX,1,6.5E-6

/COM
/COM   WPHY-65
/COM
MP,EX,2,28.34E6
MP,NUXY,2,0.285
```

```
MP,DENS,2,7.324E-4
MP,ALPX,2,6.5E-6

/COM
/COM   UNCRACKED PIPE TEST SECTION MATERIAL - ASTM A710 GR A CL 3
/COM

MP,EX,10,28.34E6
MP,NUXY,10,0.285
MP,DENS,10,7.324E-4
MP,ALPX,10,6.5E-6

/COM
/COM   ELBOW TEST SECTION PUP MATERIAL
/COM

MP,EX,11,28.34E6
MP,NUXY,11,0.285
MP,DENS,11,7.324E-4
MP,ALPX,11,6.5E-6

/COM
/COM   ELBOW TEST SECTION MATERIAL
/COM

MP,EX,12,28.34E6
MP,NUXY,12,0.285
MP,DENS,12,7.324E-4
MP,ALPX,12,6.5E-6

C*** ##########################################################
/COM
/COM   NRCPIPE F29 50% LONG, 66% DEEP SURFACE CRACK, PRESSURE CORRECTED
/COM
C***
C***   surface crack
C***
C***(R,set#,stiffness_1,,,gap,F_slide,stiffness_2)
R,31,1.10756e10,0,0,0,1.96759e6
R,32,1.10264e9,0,0,0,1.42276e6
R,33,4.28777e8,0,0,0,1.25108e6
C***
C***   crack closure spring
C***
R,34,0,0,0,1E-6,0,2E11
C***
```

```
C***  break away element
C***
R,35,9.0e9.,0.,0.,0.,-9282872.
C***
C***  through-wall crack .
C***
MP,EX,13,1266801.
C***(NL,set#,kinematic hardening flag,strains)
NL,13,13,17,0.3810,0.9585,1.3925,2.3833,3.2419
C***(NL,set#,table_location,temperature,stresses)
NL,13,19,72.,482651.2,763202.8,745032.5,432909.2,143918.3
C***(R,set#,area)
R,36,1.

C*** ##########################################################

C*** ELEMENT DEFINITIONS (EN,el#,i,j,k)

MAT,1
TYPE,2  $REAL,10  $EN,1,1,2  $EN,2,2,3
MAT,2
TYPE,3  $REAL,21  $EN,3,3,4,32  $EN,4,4,5,32          * elbow 1
MAT,1
TYPE,2  $REAL,1  $EN,5,5,42
EN,6,42,6  $EN,7,6,43
EN,8,43,7  $EN,9,7,37
EN,10,37,8  $EN,11,8,44
EN,12,44,38  $EN,13,38,45
EN,14,45,9
MAT,2
TYPE,3  $REAL,22  $EN,15,9,10,33  $EN,16,10,11,33     * elbow 2
MAT,1
TYPE,2  $REAL,2  $EN,17,11,12
TYPE,4  $REAL,15  $EN,18,12                  * valve mass
TYPE,2  $REAL,2  $EN,19,12,13
MAT,2
TYPE,3  $REAL,23  $EN,20,13,14,34  $EN,21,14,15,34    * elbow 3
MAT,1
TYPE,2  $REAL,3  $EN,22,15,52  $EN,23,52,39
TYPE,2  $REAL,3  $EN,24,39,53
TYPE,2  $REAL,6  $EN,25,53,16  $EN,26,16,60           * moment cell
TYPE,2  $REAL,10  $EN,27,60,61
TYPE,2  $REAL,5  $EN,28,61,46                         * end cap
TYPE,2  $REAL,10  $EN,29,46,47  $EN,30,47,62
TYPE,2  $REAL,6  $EN,31,62,48  $EN,32,48,63           * moment cell
MAT,11
TYPE,2  $REAL,41  $EN,33,63,17                        * elbow pup
```

```
TYPE,2  $REAL,41   $EN,35,17,40

C***$$$$$$$$$$$$$$$$$$$$$$$$$$$$$$$$$$$$$$$$$$$$$$$$$$$$$$$$

C***TYPE,5  $REAL,35   $EN,36,40,101              * break-away
C***TYPE,5  $REAL,31   $EN,37,101,41              * SC1
C***TYPE,5  $REAL,32   $EN,38,101,41              * SC2
C***TYPE,5  $REAL,33   $EN,39,101,41              * SC3
C***TYPE,5  $REAL,34   $EN,40,40,41               * crack closure
MAT,13
C***TYPE,6  $REAL,36   $EN,41,100,102             * TWC
C***CE,1,0., 100,UY,1., 40,UY,-1., 40,ROTZ,1.     * TWC constraint
C***CE,2,0., 102,UY,1., 41,UY,-1., 41,ROTZ,1.     * TWC constraint
CP,1,UX,40,41                     * X rigid
CP,2,UY,40,41                     * Y rigid
CP,3,UZ,40,41                     * Z rigid
CP,4,ROTX,40,41                   * X_rot rigid
CP,5,ROTY,40,41                   * Y_rot rigid
CP,6,ROTZ,40,41   * constraint for uncracked analysis on ROTZ
MAT,12
TYPE,3   $REAL,42  $EN,41,41,18,35  $EN,42,18,19,35     * elbow 4

C***$$$$$$$$$$$$$$$$$$$$$$$$$$$$$$$$$$$$$$$$$$$$$$$$$$$$$$$$

MAT,11
TYPE,2   $REAL,41  $EN,44,19,70                         * elbow pup
MAT,1
TYPE,2   $REAL,41  $EN,45,70,71
TYPE,2   $REAL,6   $EN,46,71,72   $EN,47,72,73          * moment cell
TYPE,2   $REAL,10  $EN,48,73,20   $EN,49,20,74
TYPE,2   $REAL,5   $EN,50,74,75                         * end cap
TYPE,2   $REAL,4   $EN,57,75,21
TYPE,2   4REAL,4   $EN,58,21,22
TYPE,2   $REAL,4   $EN,59,22,23
TYPE,2   $REAL,4   $EN,60,23,24
TYPE,2   $REAL,4   $EN,61,24,25
TYPE,2   $REAL,4   $EN,62,25,50
TYPE,2   $REAL,4   $EN,63,50,26
TYPE,2   $REAL,4   $EN,64,26,51
TYPE,2   $REAL,4   $EN,65,51,27
MAT,2
TYPE,3   $REAL,25  $EN,66,27,28,36  $EN,67,28,29,36     * elbow 5
MAT,1
TYPE,2   $REAL,10   $EN,68,29,30  $EN,69,30,31

C*** MASTER DEGREES OF FREEDOM FOR EIGENVALUE ANALYSIS
```

```
TOTAL,40

C***
C*** DEFINE LOADS
C***

/COM
/COM gravity
/COM
ACEL,,,386.4

/COM
/COM pressure
/COM
EP,ALL,PINT,2250
C***EP,ALL,PINT,0

C***$$$$$$$$$$$$$$$$$$$$$$$$$$$$$$$$$$$$$$$$$$$$$$$$$$$$$$$$$$$$
C***
C*** REMOVE PRESSURE FROM SOME ELEMENTS
C***
EPDELE,18,,,ALL        * lumped mass
EPDELE,36,,,ALL        * break away
EPDELE,37,,,ALL        * SC1
EPDELE,38,,,ALL        * SC2
EPDELE,39,,,ALL        * SC3
EPDELE,40,,,ALL        * crack closure
EPDELE,41,,,ALL        * TWC
C***$$$$$$$$$$$$$$$$$$$$$$$$$$$$$$$$$$$$$$$$$$$$$$$$$$$$$$$$$$$$

/COM
/COM temperature
/COM
KTEMP,0   *DEFINES WHERE TEMPERATURE LOADS ARE TO BE FOUND(TUNIF)
TREF,72
TUNIF,550 *ASSIGNS A UNIFORM TEMPERATURE TO ALL NODES
C***TUNIF,72

C***
C*** DEFINE NODE CONSTRAINTS
C***
D,1,ALL            * west fixed end
D,6,UX,0.,,,,UZ    * node 6 hanger
D,38,UZ            * actuator
D,12,UZ            * lumped mass
D,20,UZ            * hydrostatic bearing
D,26,UZ,0.,,,,UY   * end hanger
```

```
D,31,ALL          * end fixed end

KBC,1
ITER,1,1,1
PODISP,1 * write displacements every iteration
POSTR,1,1,3       * write pipe moment every iteration
POSTR,1,5,3       * write spring-sliders every iteration
POSTR,1,6,3       * write truss every iteration

C***
C*** DEFINE LOAD STEPS
C***
C*** AMP,FREQ,RAMP,SLOPE     9.500    3.950  225.000    0.375
TIME, 0.0  $D,38,UX, 0.000  $LWRITE

AFWRITE
FINISH
/INPUT,27
FINISH
```

NRC FORM 335 (2-89) NRCM 1102, 3201, 3202

U.S. NUCLEAR REGULATORY COMMISSION

BIBLIOGRAPHIC DATA SHEET

(See instructions on the reverse)

1. REPORT NUMBER (Assigned by NRC, Add Vol., Supp., Rev., and Addendum Numbers, if any.)

NUREG/CR-6389
BMI-2187

2. TITLE AND SUBTITLE

IPIRG-2 Task 1 - Pipe System Experiments With Circumferential Cracks in Straight-Pipe Locations

Final Report
September 1991- November 1995

3. DATE REPORT PUBLISHED

MONTH	YEAR
February	1997

4. FIN OR GRANT NUMBER

D2060

5. AUTHOR(S)

P. Scott, R. Olson, C. Marschall, D. Rudland, R. Francini, R. Wolterman, A. Hopper, and G. Wilkowski

6. TYPE OF REPORT

Technical

7. PERIOD COVERED *(Inclusive Dates)*

9/91 - 11/95

8. PERFORMING ORGANIZATION – NAME AND ADDRESS *(If NRC, provide Division, Office or Region, U.S. Nuclear Regulatory Commission, and mailing address; if contractor, provide name and mailing address.)*

Battelle
505 King Avenue
Columbus, OH 43201-2693

9. SPONSORING ORGANIZATION – NAME AND ADDRESS *(If NRC, type "Same as above"; if contractor, provide NRC Division, Office or Region, U.S. Nuclear Regulatory Commission, and mailing address.)*

Division of Engineering Technology
Office of Nuclear Research
U.S. Nuclear Regulatory Commission
Washington, D.C. 20555

10. SUPPLEMENTARY NOTES

M. Mayfield, NRC Project Manager

11. ABSTRACT *(200 words or less)*

This report presents the results from Task 1 of the Second International Piping Integrity Research Group (IPIRG-2) program. The rationale for and objective of Task 1 was to build on the results of the First IPIRG program by evaluating: (1) the fracture behavior of circumferentially cracked pipe subjected to more complex load histories, such as simulated seismic load histories, (2) cracks at geometric discontinuities, such as elbow girth welds, (3) smaller circumferential surface cracks, more typical of those considered in in-service flaw evaluations, subjected to dynamic, cyclic load histories, and (4) circumferential through-wall-cracked pipe subjected to dynamic, cyclic load histories. As a result of these Task 1 efforts, it was shown that: (1) the load-carrying capacity of a cracked pipe subjected to a simulated seismic load history is no worse than that of a cracked pipe subjected to the single-frequency excitation evaluated in IPIRG-1, (2) cracks at elbow girth welds can be adequately analyzed using methods previously developed for cracks in straight pipe, and (3) analysis methods previously developed and verified for large circumferential surface cracks and circumferential through-wall cracks work equally well for smaller cracks, even when subjected to more complex load histories.

12. KEY WORDS/DESCRIPTORS *(List words or phrases that will assist researchers in locating the report.)*

pipe system, surface crack, through-wall crack, fracture toughness, elastic modulus, yield strength, ultimate strength, seismic, elbow, leak-before-break, flaw evaluation, cyclic loading, R6, ASME, carbon steel, stainless steel, submerged-arc weld, circumferential crack, J-integral, nuclear pipe

13. AVAILABILITY STATEMENT

Unlimited

14. SECURITY CLASSIFICATION

(This Page) Unclassified

(This Report) Unclassified

15. NUMBER OF PAGES

16. PRICE